JUSTUS-LIEBIG-
UNIVERSITÄT
GIESSEN

Mesoporöse Materialien für elektrochemische Anwendungen: Porendesign und Konnektivität

---

Kumulative Dissertation
zur Erlangung des akademischen Grades
„Doctor rerum naturalium“
- Dr. rer. nat. -

Eingereicht am Fachbereich
Biologie und Chemie
der
Justus-Liebig-Universität Gießen
von
Lysander Quentin Wagner

Gießen, Dezember 2025

Erstgutachter: Prof. Dr. Bernd M. Smarsly
Zweitgutachterin: Prof. Dr. Anja Henß

So eine Arbeit wird eigentlich nie fertig, man muss sie für fertig erklären,
wenn man nach Zeit und Umständen das Möglichste getan hat.

Johann Wolfgang von Goethe

Selbstständigkeitserklärung

Ich erkläre: Ich habe die vorgelegte Dissertation selbstständig und ohne unerlaubte fremde Hilfe und nur mit den Hilfen angefertigt, die ich in der Dissertation angegeben habe. Alle Textstellen, die wörtlich oder sinngemäß aus veröffentlichten Schriften entnommen sind, und alle Angaben, die auf mündlichen Auskünften beruhen, sind als solche kenntlich gemacht. Ich stimme einer evtl. Überprüfung meiner Dissertation durch eine Antiplagiat-Software zu. Bei den von mir durchgeführten und in der Dissertation erwähnten Untersuchungen habe ich die Grundsätze guter wissenschaftlicher Praxis, wie sie in der „Satzung der Justus-Liebig-Universität Gießen zur Sicherung guter wissenschaftlicher Praxis“ niedergelegt sind, eingehalten.

Angaben zu auf künstlicher Intelligenz (KI) basierender Hilfen wie ChatGPT oder SchulKI von OpenAI oder Gemini von Google zur Erstellung meiner Dissertation (Zutreffendes angekreuzt):

☐ Ich habe bei der Erstellung dieses Textes kein KI-Tool verwendet.

☒ Ich habe ein KI-Tool in den folgenden Bereichen eingesetzt (Mehrfachnennungen möglich):

- ☒ Ideen finden, meine Kreativität anregen
- ☐ Verstehen von Konzepten, Recherche von Fakten und Definitionen
- ☒ Optimierung eines von mir verfassten Textes
- ☐ Erstellen ganzer Textpassagen nach meinen Vorgaben

Folgende KI-Tools habe ich verwendet, damit aufgeführte Teile meines Textes von dem Tool wie folgt profitiert haben:
Ich habe die KI-Tools ChatGPT (OpenAI) und DeepL genutzt, um vereinzelt vorformulierte Textabschnitte sprachlich zu optimieren.

Ort, Datum

Lysander Quentin Wagner

Die vorliegende Arbeit und die zugrundeliegenden Experimente wurden in der Zeit von Oktober 2021 – Dezember 2025 am Physikalisch-Chemischen Institut der Justus-Liebig-Universität Gießen in der Arbeitsgruppe von Prof. Dr. Bernd M. Smarsly angefertigt.

Danksagung

Ein besonderes Dankeschön richte ich an meinen Doktorvater *Prof. Dr. Bernd Smarsly*, in dessen Arbeitsgruppe ich bereits seit meiner Bachelorarbeit im Jahr 2019 forschen darf. Über all die Jahre habe ich deine zutiefst menschliche und fürsorgliche Art der Betreuung sehr genossen. Du hast mich mit diversen Empfehlungsschreiben bei allerlei Bewerbungen mit großer Hingabe unterstützt, mir knapp zwanzig Dienstreisen an die unterschiedlichsten Orte ermöglicht und großen Freiraum gelassen, meinem ehrenamtlichen Engagement nachzugehen. Auch wissenschaftlich hast du mir alle Freiheiten und Mittel gegeben, meine Projektideen umzusetzen, meinen Eifer, wenn nötig, gebremst, aber mir stets mit großer Fachkenntnis und kritischen Nachfragen geholfen. Vielen Dank für die prägende Zeit in deiner Gruppe.

Ich bedanke mich bei *Dr. Eric Prates da Costa* für die tatkräftige Unterstützung bei der Auswertung meiner Tomographiedaten. Dein beeindruckendes Wissen über Python und Blender hat mir bei der Umsetzung diverser Ideen ungemein geholfen.

Weiterhin danke ich meinem langjährigen Büronachbar und besten Freund *Dr. Paul Debes* für die schöne gemeinsame Zeit. Egal ob Freude oder Leid, dienstlich oder privat, du hast stets ein offenes Ohr für allerlei Fragen und eine fundierte zweite Meinung, etwa zum Design meiner Abbildungen oder der Nachvollziehbarkeit meiner Texte, so auch beim Gegenlesen dieser Thesis.

Gleichermaßen gilt mein Dank *Raoul Brand*, der mich während meiner gesamten Zeit in der Arbeitsgruppe begleitet hat. Mit deiner überaus großzügigen Art hast du mich sowohl innerhalb als auch außerhalb der Uni sehr unterstützt. Immer wenn ich eine dringende Physisorptionsmessung hatte, konnte ich mich auf dich als meine erste Anlaufstelle verlassen. Generell möchte ich hiermit dem gesamten „Physteam“ (neben *Raoul* und *Eric*, besonders *Dr. Rafael Meinusch* und *Dr. Sebastian Werner*) für die unzähligen Messungen danken, die ihr über Tage und falls nötig mehrmals durchgeführt habt, um das Optimum aus jeder Probe zu holen.

Mit besonders großer Freude danke ich den Studierenden, die ich während meiner Promotion betreuen durfte und liebevoll meine „Schäfchen“ genannt habe: *Franziska Schmitz*, *Chantal Glatthaar*, *Frederik Breckwoldt*, *Joshua Schober*, *Viktoriia Kuzminska*, *Raphael Neisius*, *Yasothaa Thavayogarajah*, *Andrea Guerrer*, *Marius Lang*, *Smail Mekhilef*, *Boris Pavlovic* und *Tim Jonas Erben*. Es hat mir sehr viel Spaß bereitet, mit euch zusammenzuarbeiten, eure individuellen Talente zu entdecken und eure wissenschaftliche Entwicklung begleiten zu können. Ihr habt mir nicht nur mit eurer Arbeit im Labor beachtlich geholfen, sondern ich konnte mit euch auch viel über die Arbeit mit Menschen lernen. Vor allem bei euch, *Talli* und *Freddi*, freut es mich, euch mittlerweile nicht mehr als Betreuer, sondern als Arbeitskollege und Freund begegnen zu können.

Darüber hinaus bedanke ich mich bei der gesamten Arbeitsgruppe Smarsly, bei *Aline Trommer*, *Usman Ali*, *Luca Cartabia*, *Christian Bauer*, *Melanie Pagel*, *Norman Zweig*, *Fabian Schmitz*, *Felix Boll*, *Pierre Böhme* und allen übrigen, nicht namentlich genannten Mitgliedern der AG von damals und heute. Das familiäre und unterstützende Umfeld habe ich stets sehr genossen. Ich möchte mich auch bei *Antonella D'Ambrosio*, *Kerstin Rose*, *Bjoern Luerßen* und *Gabi Scheller* für die Unterstützung bei administrativen Angelegenheiten bedanken.

Ich danke dem Zentrum für Materialforschung und seinen Mitarbeitenden für den barrierefreien Zugang zu diversen Messgeräten und die bereitwillige Unterstützung. Vor allem *Pascal Dippell*, *David Schäfer* und *Max Elm* danke ich für die kollegiale Kooperation, die zu wertvollen Forschungsergebnissen führte. Außerdem danke ich den Teams der feinmechanischen Werkstatt, der Glasbläserei und der zentralen Analytik für ihre jeweiligen Beiträge zu meiner Forschung.

Des Weiteren danke ich auch allen Kooperationspartnern außerhalb der JLU, insbesondere *Christian Kübel*, *Helmut Schlaad*, *Matthias Thommes*, *Manfred Kriechbaum* und *Katja Schladitz*. Ebenso danke ich meinen Mentoren an der Universität Padua, *Marco Zecca* und *Paolo Centomo*, und an der Kansai-Universität, *Hiromitsu Kozuka*, in deren Laboren ich forschen und viel lernen durfte. Ich danke auch meinem ehemaligen Betreuer *Pascal Cop* für die vielen Erfahrungen, die er mir mitgegeben hat.

Ein großer Dank gilt auch allen aus dem *JCF* und dem *ChemTalk JLU*, vor allem *Mareike Maass* und *Johannes Voigt*. Im Rahmen meines Ehrenamts im Regionalforum, dem Frühjahrssymposium, dem Bundesvorstand und dem EYCN habe ich unglaublich viele tolle Menschen kennengelernt und ebenso viele Erfahrungen gesammelt.

Abschließend möchte ich mich ganz herzlich bei *meiner Familie* und *meinen Eltern* bedanken, die mir diesen Bildungsweg ermöglicht haben und auf die ich mich immer verlassen kann. Auch danke ich *meinen Freunden* (sowohl in Gießen als auch in der Heimat) für die gemeinsame Zeit und die nötige Ablenkung von der Arbeit.

Zusammenfassung

Geordnet mesoporöse Materialien werden aufgrund ihrer hohen Oberfläche in zahlreichen Anwendungsgebieten, beispielsweise in der Katalyse, in Membranen, oder in Batterien, als Modellmaterialien untersucht. Vor allem in der sauren Wasserelektrolyse zur Herstellung des sogenannten grünen Wasserstoffs erscheint ein mesoporöser Elektrokatalysator vielversprechend, um das kritische Iridium auf der Anodenseite möglichst effizient zu nutzen. Allerdings ist unklar, welche Porenstruktur (Porengröße und Wanddicke) eine maximale Stabilität und Aktivität in der Katalyse liefert. Die systematische Beantwortung dieser Frage erfordert maßgeschneiderte Modellmaterialien, weshalb sich diese Arbeit der Etablierung einer Bibliothek solcher mesoporösen Materialien mit variabler Porenstruktur widmet.

In **Publikation 1** wurde dafür zunächst eine einfache Synthese eines Block-Copolymers aus Polyethylenoxid (PEO) und Polyhexylacrylat (PHA) vorgestellt, mit dem mesoporöse Metalloxide mit großen Mesoporen (etwa 40 nm) hergestellt werden können. Da solch große Poren aufgrund des Kompromisses zwischen einer noch hohen Oberfläche und der Vermeidung von Diffusionslimitierungen aussichtsreich erscheinen, aber mit gängigen Methoden wie Physisorption nicht trivial untersucht werden können, wurde eine Routine entwickelt, wie solche Strukturen zuverlässig charakterisiert werden können. Mit dieser Methodik wurde in **Publikation 2** eine Vielzahl an PEO-*b*-PHA-Proben hergestellt und als Templat untersucht und so abgeleitet, wie die Porengröße, Wanddicke und Porenkonnektivität in Silika über die Polymermenge und die PHA-Blocklänge eingestellt werden kann. In **Publikation 3** konnte gezeigt werden, dass das Porensystem im Silika nach *Soft Templating* mit PEO-*b*-PHA analog zu dem in mesoporösem Kohlenstoff aufgebaut ist, sodass die Gültigkeit der zuvor erwähnten Leitfäden zum Porendesign auch für das elektrochemisch relevante Material Kohlenstoff zu erwarten ist. In **Publikation 4** wurden mesoporöse Kohlenstofffilme hergestellt und hinsichtlich ihrer Eignung in der Elektrokatalyse untersucht. Die beobachtete hohe elektrische Leitfähigkeit, elektrochemische Stabilität und variable Zugänglichkeit des Porensystems bestätigen, dass die mesoporösen Dünnfilme ein vielversprechendes Modellsystem für elektrochemische Studien darstellen, beispielsweise als Trägermaterial für die Elektrokatalyse.

Die hier gewonnenen Erkenntnisse bilden die Grundlage für eine Vielzahl systematischer Studien zur Korrelation makroskopischer Eigenschaften mit der Porenstruktur mesoporöser Materialien, zum Beispiel wie die Morphologie von mesoporösem Iridiumoxid mit dessen Aktivität und Stabilität in der sauren Wasserelektrolyse zusammenhängt.

Abstract

Ordered mesoporous materials are investigated in several applications, such as heterogeneous catalysis, membranes, and batteries, as model materials due to their large surface area. In particular in the acidic water electrolysis, a mesoporous electrocatalyst appears promising in order to utilize the critical iridium at the electrolyzer's anode as efficient as possible. However, it remains unclear which pore structure (pore size and wall thickness) possesses maximum activity and stability in catalysis. Answering such questions on a systematic level requires well-defined model materials. Therefore, this project aims at establishing a library of mesoporous materials with tailored pore structure.

P**ublication 1** presents a facile synthesis of a block copolymer comprising a poly(ethylene oxide) (PEO) and a poly(hexyl acrylate) (PHA) block, with which mesoporous metal oxides featuring large mesopores (of about 40 nm) can be prepared. While such large pores might benefit from a tradeoff between a still high surface area and the absence of diffusion limitations, their characterization by conventional methods like physisorption can be challenging. Thus, a routine was developed to accurately characterize those kind of structures. Following this protocol, a set of various PEO-*b*-PHA samples was prepared and applied in soft templating in **publication 2**. Doing so, guidelines were derived on how to modify pore size, wall thickness, and pore connectivity of mesoporous silica by adjusting polymer amount and PHA block length. **Publication 3** shows that the pore system of mesoporous silica after soft templating with PEO-*b*-PHA is analogue to that in mesoporous carbon. Hence, it can be expected that the aforementioned guidelines on the pore design hold true for this electrochemically relevant material as well. In **publication 4**, mesoporous carbon thin films were prepared and investigated with respect to their suitability for electrocatalysis. The observed high electric conductivity, electrochemical stability, and tunable pore accessibility confirm that these mesoporous thin films act as promising model system for electrochemical studies, *e.g.,* as support for electrocatalysts.

The results obtained herein build the basis for a variety of systematic studies for correlating macroscopic properties with the pore structure of mesoporous materials. For instance, the relationship between the morphology of mesoporous iridium oxide and its activity and stability in acidic water splitting can be revealed to boost catalyst performance.

Publikationsliste

Folgende Publikationen sind während meines Promotionsprojekts von 2021 bis 2025 entstanden:

1. **L. Q. Wagner**, E. Prates da Costa, C. Glatthaar, F. Breckwoldt, M. Zecca, P. Centomo, X. Huang, C. Kübel, H. Schlaad, M. Kriechbaum, H. Amenitsch, M. Thommes, B. M. Smarsly, Poly(ethylene oxide)-*block*-poly(hexyl acrylate) Copolymers as Templates for Large Mesopore Sizes ─ A Detailed Porosity Analysis, *Chem. Mater.* **2023**, *35*, 9879 – 9899. DOI: 10.1021/acs.chemmater.3c01255.

2. **L. Q. Wagner**, F. Breckwoldt, X. Huang, C. Kübel, X. Cheng, K. Schladitz, B. M. Smarsly, Porosity Tuning in Soft-templated Mesoporous Silica: The Influence of Block Copolymer Composition and Concentration, *Langmuir* **2025**, *41*, 30948 – 30967. DOI: 10.1021/acs.langmuir.5c02750.

3. **L. Q. Wagner**, L. Brauch, C. Kübel, X. Cheng, K. Schladitz, B. M. Smarsly, On the Interpretation of Physisorption Isotherms: Connectivity *versus* Accessibility of Mesopore Networks, *to be submitted*.

4. **L. Q. Wagner**, J. Schober, P. Dippell, C. Glatthaar, S. Mekhilef, D. Schäfer, H. Hergert, M. Rohnke, M. T. Elm, B. M. Smarsly, Mesoporous Carbon Thin Films with Large Mesopores as Model Material for Electrochemical Applications, *Adv. Funct. Mater.* **2025**, e21031. DOI: 10.1002/adfm.202521031.

5. M. Einert, A. Waheed, S. Lauterbach, M. Mellin, M. Rohnke, **L. Q. Wagner**, J. Gallenberger, C. Tian, B. M. Smarsly, W. Jaegermann, F. Hess, H. Schlaad, J. P. Hofmann, *Small* **2023**, *19*, 2205412. DOI: 10.1002/smll.202205412.

6. C. Glatthaar, M. Wang, **L. Q. Wagner**, F. Breckwoldt, Z. Guo, K. Zheng, M. Kriechbaum, H. Amenitsch, M.-M. Titirici, B. M. Smarsly, *Chem. Mater.* **2023**, *35*, 10416 – 10433. DOI: 10.1021/acs.chemmater.3c01520.

7. M. Einert, H. Sezen, Q. Wu, **L. Q. Wagner**, M. Neumann, A. Waheed, B. Gonzalez-Navarrete, S. Lauterbach, H. Schlaad, J. P. Hofmann, *ACS Appl. Nano Mater.* **2025**, *8*, 14218 – 14229. DOI: 10.1021/acsanm.5c02246.

8. U. Ali, F. Dressler, **L. Q. Wagner**, P. P. Debes, J. Gallego, P. R. Schreiner, B. M. Smarsly, *New J. Chem.* **2025**, *49*, 17271. DOI: 10.1039/D5NJ02915E.

9. Q. Wu, S. Lauterbach, C. Dietz, A. Alkemper, **L. Q. Wagner**, H. Schlaad, J. P. Hofmann, M. Einert, *Small Sci.* **2025**, e202500422. DOI: 10.1002/smsc.202500422.

Konferenzbeiträge

Die gewonnenen Erkenntnisse wurden auf den folgenden externen Veranstaltungen vorgestellt:

Posterpräsentation

L. Q. Wagner, B. M. Smarsly, Influence of the PEO-*b*-PHA Block Lengths on the Mesopore Size, Frühjahrssymposium, Hannover, Deutschland, 2022.

Vortragspräsentation

L. Q. Wagner, B. M. Smarsly, Synthesis of PEO-*b*-PHA Block Copolymers for Mesoporosity Tuning, International Sol-Gel Conference, Lyon, Frankreich, 2022.

Posterpräsentation

L. Q. Wagner, F. Breckwoldt, B. M. Smarsly, Influence of the PEO-*b*-PHA Block Lengths on the Mesopore Size, Bunsen-Tagung, Gießen, Deutschland, 2022.
– *ausgezeichnet mit dem PCCP Poster Award*

Vortragspräsentation

L. Q. Wagner, J. Schober, B. M. Smarsly, Mesoporous Carbon Thin Films as Electrocatalyst Support for the Oxygen Evolution Reaction, Deutsche Zeolith-Tagung, Wien, Österreich, 2023.

Posterpräsentation

L. Q. Wagner, F. Breckwoldt, B. M. Smarsly, PEO-*b*-PHA Block Copolymers as Templates for Mesoporous Metal Oxides with Tailored Pore Size, Deutsche Zeolith-Tagung, Wien, Österreich. 2023.

Vortragspräsentation

L. Q. Wagner, J. Schober, B. M. Smarsly, Mesoporous Carbon Thin Films as Electrocatalyst Support for the Oxygen Evolution Reaction, E-MRS Spring Meeting, Straßburg, Frankreich, 2023.

Vortragspräsentation

L. Q. Wagner, B. M. Smarsly, Mesoporous IrO_2-based Thin Films as Model Catalysts for the Electrocatalytic Water Splitting, NERM, Boston, Vereinigte Staaten von Amerika, 2023.

Posterpräsentation

L. Q. Wagner, F. Breckwoldt, B. M. Smarsly, Tailor-made Mesoporous Metal Oxides: The Role of PEO-*b*-PHA Composition and Concentration, Deutsche Zeolith-Tagung, Jena, Deutschland, 2024.

Posterpräsentation

L. Q. Wagner, F. Breckwoldt, B. M. Smarsly, Tailor-made Mesoporous Metal Oxides: The Role of Template Composition and Concentration, Frühjahrssymposium, Ulm, Deutschland, 2024.

Vortragspräsentation

L. Q. Wagner, B. M. Smarsly, Mesoporous Materials with Tailor-made Porosity from PEO-*b*-PHA Copolymers, International Sol-Gel Conference, Berlin, Deutschland, 2024.

Posterpräsentation

L. Q. Wagner, B. M. Smarsly, Mesoporous Carbon Thin Films on Titanium Substrates as Electrocatalyst Support, Deutsche Zeolith-Tagung, Erlangen, Deutschland, 2025.

Inhaltsverzeichnis

Selbstständigkeitserklärung I

Danksagung II

Zusammenfassung IV

Abstract V

Publikationsliste VI

Konferenzbeiträge VIII

1 Einleitung 1

2 Aktueller Stand der Forschung 4

2.1 Synthese mesoporöser Materialien 4

2.1.1 Sol-Gel-Synthesen 4

2.1.2 Nanostrukturierung mittels Templatierung 7

2.1.3 Porendesign und Blockcopolymere 11

2.2 Charakterisierung mesoporöser Materialien 16

2.2.1 Physisorption 17

2.2.2 Elektronentomographie 24

3 Publikationen 27

3.1 Publikation 1 27

3.2 Publikation 2 75

3.3 Publikation 3 121

3.4 Publikation 4 155

4 Fazit und Ausblick 207

5 Literaturverzeichnis 209

1 Einleitung

Grüner Wasserstoff gilt als Schlüsselelement in der Energiewende, da mit ihm Strom aus erneuerbaren Quellen temporär gespeichert und er als Basischemikalie in der Stahl- und Chemieindustrie eingesetzt werden kann.[1] Seine technische Herstellung über die saure Wasserelektrolyse erfolgt überwiegend mit Iridium als Elektrokatalysator,[2] das zwar weniger aktiv, aber deutlich stabiler als Ruthenium ist.[3] Die jährliche Förderung von Iridium liegt aufgrund seiner Seltenheit allerdings lediglich bei etwa sieben Tonnen, was den großflächigen Ausbau von Elektrolyseuren limitiert (geschätzter Bedarf: 2 t a^{-1}).[4] Vor diesem Hintergrund wird sowohl an Alternativen zu Iridium[5] als auch an dessen effizienteren Nutzung[6] geforscht.

Eine Möglichkeit der effizienteren Nutzung bietet die Verwendung von hochporösen Elektrokatalysatoren. Der Einbau von insbesondere kleinen, sogenannten Mesoporen (2 – 50 nm) in den Katalysator verringert die eingesetzte Masse an Iridium gegenüber einer unporösen Vergleichsprobe, und liefert gleichzeitig eine um etwa zwei Größenordnungen[7] höhere Oberfläche, an der die Katalyse erfolgen kann. Dies führt zu einer höheren katalytischen Aktivität pro Masse an Iridium, was bereits von Kraehnert und Mitarbeitenden für mesoporöses Iridiumoxid (IrO_2) gezeigt wurde.[7,8] Allerdings bleibt die Frage offen, welche Porenstruktur eine optimale Nutzung des Edelmetalls bietet. Zwar maximieren kleine Poren die Oberfläche, können aber den Stofftransport im Porensystem limitieren. Eine solche Diffusionslimitierung mit abnehmender Porengröße wurde in mehreren Arbeiten theoretisch beschrieben[9–12] und in einer aktuellen Studie von Trommer *et al.* auch experimentell bestätigt, in der die Diffusionskoeffizienten organischer Moleküle (vor allem des großen Tocopherolmoleküls) in einem Porensystem mit 6 nm großen Poren gegenüber denen in größeren Poren (10 und 30 nm) signifikant reduziert sind.[13] Insofern erscheinen größere Mesoporen, vor allem im Bereich von 20 – 70 nm, die noch eine hohe Oberfläche gewährleisten, aber Transportlimitierungen möglichst minimieren, besonders vielversprechend.

Darüber hinaus werden die makroskopischen Eigenschaften des mesoporösen Materials, wie die Leitfähigkeit, die elektrische Kapazität und der thermische Transport, nicht nur von der Porengröße[14–20] beeinflusst, sondern auch von anderen morphologischen Parametern, wie der Porenwanddicke[21] und der Konnektivität[22–26] der Poren. Allen voran der elektrische Transport und die mechanische Stabilität sind wichtige Größen für einen Elektrokatalysator, werden aber vom Porenvolumen[27] und der Porenwanddicke[28] bestimmt. Bisherige Studien zur Korrelation der Porenstruktur mit der katalytischen Aktivität in der Elektrokatalyse, wie die von Priamushko *et al.* für die Sauerstoffentwicklung mit mesoporösen Oxiden,[29] mangeln jedoch an einer systematischen Variation einzelner morphologischer Parameter: Die dortige Modifikation der Porengröße über die Kalzinierungstemperatur verunmöglicht eine Trennung des morphologischen (Porengröße) und chemischen (Kristallitgröße) Effekts auf die Leistungsfähigkeit des Katalysators. Deshalb besteht ein Bedarf an mesoporösen Proben, in denen lediglich die morphologischen Parameter, also die Porengröße, die Wanddicke und die Konnektivität, individuell und systematisch variiert werden können, ohne die Chemie des Wandmaterials zu verändern. Stefik und Mitarbeitende präsentierten mit dem Copolymer Polyethylenoxid-*block*-Polyhexylacrylat (PEO-*b*-PHA) ein Templat, das für die Herstellung solcher Proben mit großen Mesoporen geeignet sein könnte, allerdings beschränken sich die Studien bislang auf Dünnfilme und entbehren einer systematischen Variation der Porengröße und -konnektivität.[30]

Ziel dieser Arbeit besteht daher in der Etablierung einer Bibliothek an mesoporösen Materialien für elektrochemische Anwendungen mit großen Kugelporen, deren Größe vor allem im Porengrößenbereich von 20 – 70 nm systematisch variiert werden kann (**Abbildung 1**). Dazu wurde in **Publikation 1** zunächst ein exemplarisches Blockcopolymer der PEO-*b*-PHA-Familie zur Templatierung von SiO_2-Pulvern genutzt und das erfolgreich eingebrachte Porensystem im Detail entschlüsselt. Im Rahmen der morphologischen Charakterisierung wurde außerdem eine Routine etabliert, Systeme mit solch großen Mesoporen (40 nm) verlässlich zu analysieren. Die Polymersynthese wurde in **Publikation 2** auf eine umfassende Matrix aus PEO-*b*-PHA-Copolymeren mit variierter PEO- und PHA-Blocklänge ausgeweitet und die nach Templatierung erhaltenen Oxidpulver gemäß der erprobten Routine analysiert. Auf diese Weise wurde ein Porengrößenbereich von 10 – 80 nm für diese Polymerfamilie identifiziert, der Einfluss der individuellen Blöcke auf die Porengröße quantifiziert und der Zusammenhang zwischen Templatmenge und Porengröße, -verknüpfung und Wanddicke charakterisiert.

Mit diesem synthetischen Leitfaden können Proben für systematische Studien der Porenstruktur und deren Effekt auf beispielsweise die Aktivität und Stabilität von mesoporösem IrO_2 in der sauren Wasserelektrolyse hergestellt werden, um die optimale Porosität ausfindig zu machen. Um darauf aufbauend den Bedarf an notwendigem Iridium weiter zu senken, wäre die Beschränkung des seltenen Aktivmaterials lediglich auf die Oberfläche, die mit dem Elektrolyten in Kontakt und somit für die Katalyse zur Verfügung steht. Dafür wäre ein unkritisches Trägermaterial notwendig, wie zum Beispiel mesoporöser Kohlenstoff, auf dem beispielsweise über Atomlagenabscheidung eine nanoskalige IrO_2-Schicht abgeschieden wird. Kraehnert und Pinna verfolgten einen ähnlichen Ansatz, nutzen allerdings ein mesoporöses Titan/Iridium-Mischoxid als Trägermaterial,[31] das somit den Bedarf an Iridium erhöht. In anderen Studien wurde Kohlenstoff zwar als Trägermaterial für die Elektrokatalyse verwendet, allerdings wurde dort nicht die gesamte Oberfläche beschichtet und teilweise ohne eine nanostrukturierte Oberfläche gearbeitet.[32,33] Im Gegensatz dazu verspricht ein homogen beschichteter, mesoporöser Kohlenstofffilm eine möglichst effiziente Nutzung der gesamten, maximierten Oberfläche, sofern diese für die Edukte leicht zugänglich ist.

In **Publikation 3** wurde die Brücke vom Modellmaterial SiO_2 zum elektrochemisch relevanten Kohlenstoff geschlagen, der ebenso mit einem PEO-*b*-PHA-Templat strukturiert wurde. In einem tiefgründigen Vergleich von Physisorption und Tomographie zur Charakterisierung der Porenkonnektivität wurde das zuvor abgeleitete Porenmodell auch im Kohlenstoff mittels Skelettierung nachgewiesen. **Publikation 4** ebnet abschließend den Weg in Richtung elektrochemischer Anwendung, in der der bereits erwähnte mesoporöse Kohlenstoff in Form eines Dünnfilms auf einem leitfähigen Metallsubstrat synthetisiert, umfassend charakterisiert und im Hinblick auf eine elektrokatalytische Nutzung untersucht wurde. Hierbei zeigte der Dünnfilm eine vielversprechende Leitfähigkeit, Zugänglichkeit und Stabilität, um als Trägermaterial für die elektrokatalytische Wasserspaltung in Frage zu kommen.

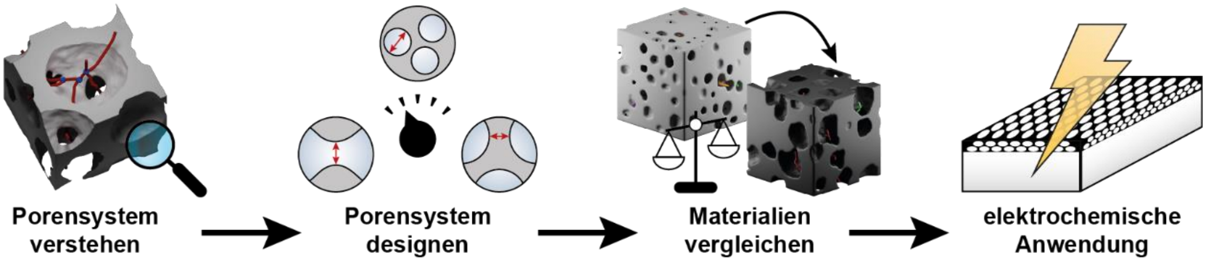

Abbildung 1: Teilschritte des Promotionsprojekts bestehend aus der Charakterisierung der mesoporösen Porenstruktur, dessen Variation hinsichtlich Porengröße, -konnektivität und Wanddicke, dem Transfer auf das elektrochemisch relevante Material Kohlenstoff und schließlich dessen Untersuchung als Dünnfilm im Hinblick auf mögliche elektrochemische Anwendungen.

Die Erkenntnisse dieser Arbeit bieten die Grundlage für eine Vielzahl systematischer Studien von Porosität-Eigenschaftsbeziehungen an Oxiden und Kohlenstoffen, allen voran im elektrochemischen Kontext, in dem gezielte Porenstrukturen hergestellt werden können. Ferner dienen die erarbeiteten Charakterisierungsprotokolle als Blaupause zur Untersuchung mesoporöser Materialien mit großen Kugelporen, besonders hinsichtlich Porenkonnektivität.

2 Aktueller Stand der Forschung

2.1 Synthese mesoporöser Materialien

Mesoporöse Materialien werden in aller Regel, und so auch in dieser Arbeit, auf Basis von molekularen Ausgangsstoffen hergestellt. Hierbei bildet das in einer Sol-Gel-Reaktion erzeugte Material die Struktur eines Templats ab, das nach dessen Entfernung die Porenstruktur im Material zurücklässt. Die einzelnen Teilschritte der Synthese, alternative Herstellungsverfahren und systematische Modifikationen bilden die Bestandteile dieses Kapitels.

2.1.1 Sol-Gel-Synthesen

Das Sol-Gel-Verfahren ist ein nasschemisches Synthesekonzept für anorganische Feststoffe, wie beispielsweise Metalloxide, ausgehend von molekularen Präkursoren. Im Gegensatz zu konventionellen Festkörpersynthesen, die auf der thermischen Behandlung von Pulvergemischen beruhen, liefert dieser sogenannte Bottom-Up-Prozess homogenere Reaktionsprodukte bei gleichzeitig geringeren Reaktionstemperaturen und kürzeren Synthesedauern,[34,35] weswegen er dem Konzept der *Chimie Douce* („sanfte Chemie")[36,37] zugeordnet wird. Der Name „Sol-Gel" wurde Mitte des 19. Jahrhunderts von Graham im Zuge seiner Arbeiten an Salzlösungen (*solution*) und deren Gelierung (*gelation*) geprägt[38,39] und beschreibt die beiden Kernschritte des Verfahrens. Konkreter lässt sich eine Sol-Gel-Synthese in fünf Prozesse unterteilen: (1) die Bildung des Sols, (2) deren Gelierung, (3) Alterung, (4) Trocknung und (5) sofern gewünscht deren Kalzinierung.[34]

Der Präkursor, meist ein Metallalkoxid, -halogenid oder -nitrat,[40,41] wird in einem geeigneten Lösemittel (meist einem Alkohol) gelöst und bildet unter partieller oder vollständiger Hydrolyse durch enthaltenes oder zugegebenes Wasser einen Hydroxidokomplex.[34,42] Dieser kondensiert wie in **Abbildung 2** gezeigt mit anderen Hydroxiden (unter Wasserabspaltung) oder Alkoxiden (unter Alkoholabspaltung), wodurch eine kolloidale Dispersion an Primärpartikeln entsteht – das Sol. Die fortschreitende Polykondensation mündet schließlich in einem weitreichenden Metall-Oxo- beziehungsweise Metall-Hydroxido-Netzwerk, in dessen Poren das abgespaltene Wasser (oder der Alkohol) eingeschlossen wird – das Gel.[34,42] Unter einem Gel wird allgemein laut der Standardisierungsorganisation IUPAC (*International Union of Pure and Applied Chemistry*) ein dreidimensionales, nicht-fließendes Netzwerk verstanden, das durch eine Flüssigkeit aufgequollen ist. Im Falle der Sol-Gel-Chemie ergeben sich hierfür verschiedene Unterarten, die von Flory[43] (1974) zunächst in vier und von Kakihana[35] (1996) später in fünf Typen kategorisiert wurden: kolloidale Gele, Metall-Oxo-Polymere, Metallkomplexe, polymerisierende Komplexe und vernetzte koordinierende Polymere.[34] Eine fortlaufende Kondensation innerhalb des Gels (auch Alterung genannt) führt zum partiellen Ausstoß des eingeschlossenen Lösemittels (Synärese), das im Zuge der anschließenden Trocknung vollständig entfernt wird. Eine abschließende Kalzinierung bei hohen Temperaturen führt unter Entfernung von Wasser aus dem Metall-Oxo-Netzwerk (und je nach Temperatur unter anschließender Kristallisierung) zum finalen Feststoff.[34] Die Entfernung des Lösemittels kann entweder kontrolliert unter Erhalt der ursprünglichen Porosität (zum Beispiel über superkritische Trocknung) erfolgen, was ein hochporöses Aerogel liefert oder unkontrolliert unter Kollaps des porösen Systems zu einem kompakten Xerogel.[41,44–46]

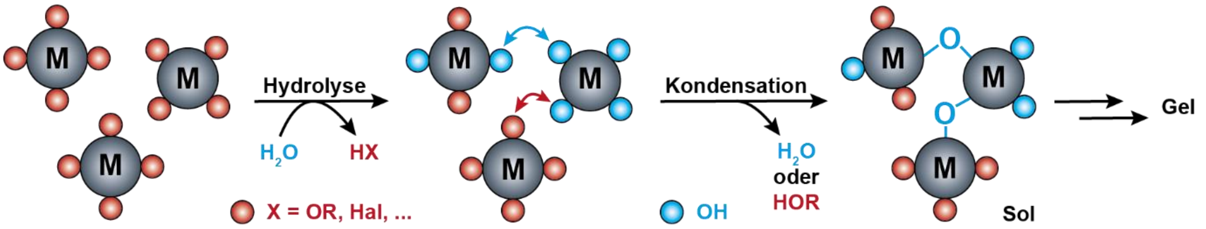

Abbildung 2. Schematischer Ablauf einer Sol-Gel-Synthese mit dem allgemeinen Metalloxidpräkursor MX_4, der (partiell) hydrolysiert und unter Wasser- oder Alkoholabspaltung zunächst zum Sol und später zu einem weitreichenden Netzwerk (Gel) kondensiert.

Die Morphologie des Gels und somit auch des gebildeten Feststoffs kann durch diverse Parameter beeinflusst werden. Erste systematische Studien lieferte die Stöber-Synthese über die Variation des pH-Werts.[47] Sowohl die Hydrolyse als auch die Kondensation des Präkursors können sowohl säure- als auch basekatalysiert werden. Während eine saure Umgebung die Kondensation gegenüber der weiteren Hydrolyse beschleunigt und somit ein kettenförmiges Wachstum des Netzwerks fördert, wird im Basischen die Hydrolyse kinetisch bevorzugt, was in einem quervernetzten Partikelwachstum resultiert.[40,48] Neben dem pH-Wert des Lösemittels ist auch das Lösemittel selbst von großer Bedeutung, da die Viskosität und die Dielektrizitätskonstante der Lösung das Gelierverhalten beeinflussen.[49–51] Darüber hinaus spielt das Metallion und dessen Elektronegativität eine entscheidende Rolle,[52] da beispielsweise Siliziumalkoxide verhältnismäßig langsam hydrolysieren und den Einsatz von Katalysatoren erfordern, wohingegen Zirkoniumverbindungen wesentlich reaktiver sind und deren Hydrolyse mittels Chelatliganden und Minimierung der verwendeten Wassermenge gebremst werden muss.[34,40] Allen voran Zitronensäure und Ethylendiamintetraessigsäure (EDTA) werden häufig als Liganden eingesetzt, um die Kondensation der Metallkomplexe (auch Olation genannt) kinetisch zu kontrollieren.[35]

Eine Sol-Gel-Synthese kann auch durch Polymere wie beispielsweise Polyvinylalkohol oder Polyacrylsäure unterstützt werden, die das Metallion komplexieren und somit dispergieren. Auf diese Weise kann ein Ausfällen reaktiver Präkursoren vermieden und eine gleichmäßige Verteilung der Metallspezies in multinären Systemen gewährleistet werden.[35,53] Dieses synthetische Konzept wird auch in der verbreiteten Pechini-Synthese ausgenutzt, in der Zitronensäure die Präkursoren komplexiert und anschließend mit Ethylenglycol *in-situ* über Veresterung ein polymeres Netzwerk bildet.[54] Somit lassen sich nach thermischer Entfernung des Polymers vor allem für reaktive oder schwer dispergierbare Präkursoren homogene Oxide erhalten, sowie komplexe Verbindungen wie Pigmente und Perowskite herstellen.[55,56] Solch komplexe, multinäre Oxide erfordern allerdings nicht *per se* eine Pechini-Synthese, denn wie Einert *et al*. kürzlich zeigten, können hochentropische Spinelle mit fünf bis sechs verschiedenen Metallen auch über klassische Sol-Gel-Synthesen synthetisiert werden.[57,58]

Mittels Sol-Gel-Synthesen lassen sich nicht nur Keramiken, sondern auch Kohlenstoffmaterialien herstellen. Als Kohlenstoffpräkursor dienen Phenol, Resorcinol oder Phloroglucinol, aber auch natürliche Vorstufen wie Lignin,[59] die mit Formaldehyd oder Glyoxal unter Säure- oder Basenkatalyse quervernetzt werden.[60–62] Hierbei bilden Präkursor und Aldehyd bei Temperaturen von maximal 60 °C zunächst ein Additionsprodukt, welches bei höheren Temperaturen (85 – 100 °C) zu einem weitreichenden Netzwerk thermopolymerisiert – dem Novolak- (säurekatalysiert) beziehungsweise Resolharz (basekatalysiert).[59,61,63–65] Die Polymerisationsgeschwindigkeit und der Grad der Quervernetzungen steigt mit der Anzahl der Hydroxylgruppen im Präkursor (von Phenol zu Phloroglucinol), wobei außerdem der reaktivere Formaldehyd schneller thermopolymerisiert als Glyoxal.[62,66] Präkursor und Vernetzer müssen daher in der Synthese (vor allem für nanostrukturierte Kohlenstoffe) in der Art aufeinander abgestimmt werden, dass zwar ein stabiles Netzwerk ausgebildet wird, allerdings nicht zu schnell, um zu vermeiden, dass ein inhomogenes (Poren-)Netzwerk entsteht.[67]

Das Harz wird anschließend unter inerten Bedingungen bei hohen Temperaturen (>800 °C) zum finalen Kohlenstoff karbonisiert. In diesem Schritt werden Heteroatome wie Sauerstoff aus dem polymeren Netzwerk entfernt und kleine Graphenstapel innerhalb des amorphen Kohlenstoffs gebildet. Auch wenn die Größe dieser Stapel mit steigender Karbonisierungstemperatur zunimmt, lassen sich die sol-gel-basierten Harze selbst bei 3000 °C nicht in Graphit überführen, da die Quervernetzung eine zwischenzeitliche Bildung einer Flüssigphase verhindert, wohingegen andere Kohlenstoffe wie Kohlenteerpeche graphitisierbar sind.[68–70]

Dem gegenüber resultiert die quervernetzte Struktur der nicht-graphitischen Kohlenstoffe in einer hohen chemischen und mechanischen Stabilität,[71] die durch die Graphenstapel von einer hinreichenden elektrischen Leitfähigkeit begleitet wird, wie in **Publikation 4** anhand von mesoporösen Kohlenstofffilmen gezeigt. Auch wenn sich Kohlenstoff über andere Bottom-Up-Synthesen wie die hydrothermale Karbonisierung von Kohlenhydraten herstellen lässt,[72,73] bietet die oben beschriebene Sol-Gel-Synthese von nicht-graphitischem Kohlenstoff neben dessen Stabilität den Vorteil, auch nanostrukturierte Materialien mittels Templatierung herzustellen, worauf im nächsten Kapitel näher eingegangen wird.

2.1.2 Nanostrukturierung mittels Templatierung

Nanostrukturierte Materialien werden aufgrund ihrer hohen Oberfläche in vielen Forschungsfeldern (z. B. Katalyse[74,75] und Sensorik[76,77]) als Modellmaterialien untersucht und für viele Anwendungen (z. B. Wasserfilter und Batterien)[78] bereits industriell genutzt. Unter einer Nanostruktur wird per Definition ein Strukturmerkmal (Partikel, Pore o. Ä.) verstanden, dessen Größe zwischen 1 und 100 nm liegt.[79] Handelt es sich bei diesen Strukturmerkmalen um Poren, wird weiterhin zwischen Mikroporen (< 2 nm), Mesoporen (2 – 50 nm) und Makroporen (> 50 nm) unterschieden.[80] Solche nanoporösen Materialien lassen sich durch die Kombination der zuvor beschriebenen Sol-Gel-Synthesen und geeigneten Templatierungsverfahren herstellen; dazu zählen vor allem das *Hard Templating* und das *Soft Templating*. Grundsätzlich sind mesoporöse Materialien auch durch andere Methoden wie die Selbsttemplatierung oder hydrothermales Ätzen zugänglich, leiden aber häufig unter einer ungeordneten Porenstruktur und sind somit für systematische Studien nicht gut geeignet.[81]

Im Falle von *Hard Templating* wird eine feste Struktur (Templat) mit einem Präkursorsol infiltriert, dieses wie oben beschrieben über Alterung, Trocknung und Kalzinierung in ein Oxid überführt und das feste Templat selektiv herausgelöst. Auf diese Weise verbleibt ein idealer Abguss (Negativ) der Templatstruktur auf der Nanoebene (*nanocasting*).[82] Als Templat werden bereits poröse Materialien aus beispielsweise Silika (z. B. SBA-15, KIT-6), Kohlenstoff (z. B. CMK-1, CMK-3) oder anodischem Aluminiumoxid verwendet, aber auch sphärische Kolloide aus Silika (Stöber-Partikel) oder Polymeren (z. B. Polystyrol (PS) oder Polymethylsäuremethacrylat (PMMA)), die sich in einer flüssigkristallinen Phase gemäß einer dichten Kugelpackung anordnen, auch Opal genannt. Je nach Material, erfolgt die Entfernung des Templats über nasschemisches Ätzen mit Natronlauge oder Flusssäure (bei keramischen Templaten) oder über Pyrolyse (bei Templaten aus Kohlenstoff oder Polymer).[82,83]

Da wie im vorigen Kapitel beschrieben auch Kohlenstoffe über Sol-Gel-Synthesen zugänglich sind, ist die Nanostrukturierung nicht auf Metalloxide beschränkt. So synthetisierten Ryoo *et al*. erstmals den geordnet porösen Kohlenstoff CMK-1 mittels Imprägnierung des mesoporösen Silikas MCM-48 mit einer schwefelsauren Zuckerlösung, anschließender Karbonisierung und abschließender Templatentfernung mit Natronlauge.[84] Auch die Herstellung von invers-opalen Metalloxiden, die erstmalig mit PS-Opalen berichtet wurde,[85,86] lässt sich unter Verwendung von Silika-Opalen auf Kohlenstoff übertragen.[87] Weiterhin ist ein *Hard Templating* von Kohlenstoff mit Nanopartikeln aus anderen Oxiden wie ZnO und MgO, aber auch Salzkristallen (NaCl oder KCl) möglich, die mithilfe von Salzsäure oder Wasser entfernt werden können;[88] auch hierarchisch-meso-/makroporöse Template wie Silikamonolithe aus der Nakanishi-Synthese[89] finden Anwendung in der Nanostrukturierung. Im Falle von letzteren erfolgt die Templatierung über das Volumen der Mesoporen (Negativ des Templats) sowie die Oberfläche der Makroporen (Positiv des Templats).[82] Eine solche Templatierung über die Templatoberfläche wird auch gezielt zur Erzeugung hohler Nanostrukturen genutzt, sodass bei teilweiser Füllung von SBA-15-Silika hohle Kohlenstoffzylinder (CMK-5) erhalten werden können,[90] sowie hohle[91] und poröse[92] Nanopartikel ausgehend von mit Präkursor benetzten Opalen. Der Vorteil des *Hard Templatings* besteht in der Robustheit des Templats, die eine leichte Synthese von einer Vielzahl von Metalloxiden[82] und selbst komplexen Feststoffen wie Perowskiten[93] ermöglicht, sofern eine vollständige Benetzung und Füllung des Templats (unter anderem durch Kapillarkräfte) gewährleistet werden kann.[81,83,94] Nachteilhaft sind allerdings die generell harschen Bedingungen zur Templatentfernung, die das poröse Produkt selbst beschädigen können,[95] sowie eine unter Umständen unvollständige Entfernung des Templats.[88] Außerdem ist die Auswahl an Templaten (sowohl bezüglich Material als auch Strukturgröße) limitiert,[81] auch wenn Modifikationen in der Stöber-Synthese[47,96] und in der Emulsionspolymerisation[97–99] eine gewisse Variation in der Templat- und somit Makroporengröße invers-opaler Materialien ermöglichen.

Auf der anderen Seite beruht das *Soft Templating* auf der Strukturierung mit eher flexiblen organischen Templaten wie Tensiden, Blockcopolymeren und ionischen Flüssigkeiten, die einen amphiphilen Charakter aufweisen. Aufgrund der unterschiedlichen Polarität der hydrophilen und hydrophoben Teile des Templats kommt es zu einer Entmischung des in der Sol-Gel-Mischung gelösten Amphiphils auf der Nanoebene (in Form von bspw. Mizellen), die die Struktur des späteren Feststoffs vorgibt.[100,101] Analog zum *Hard Templating* wird das Hybridmaterial gealtert und getrocknet, bevor die Templatentfernung (über Pyrolyse, nasschemische Extraktion oder UV-Bestrahlung) das finale poröse Produkt liefert.[40] Die verglichen mit *Hard Templates* eher lose Struktur des Templats ermöglicht eine einfache und vollständige Templatenfernung,[81] die selbst ein *Soft Templating* von Kohlenstoffen ermöglicht, sofern die thermische Entfernung unter Sauerstoffausschluss erfolgt, bei der sich das Templat zwar zersetzt, aber das Skelett lediglich karbonisiert,[64] wie erstmals 2004 von Dai und Mitarbeitenden vorgestellt.[102]

Die gezielte Nanostrukturierung mittels *Soft Templating* startete allerdings bereits mit der Synthese der MCM-Silika in den frühen 1990er-Jahren unter Verwendung von kationischen Tensiden, die zylindrische oder sphärische Mizellen bilden und Mesoporen selbiger Form hinterlassen.[103,104] Mechanistisch erfolgt die Templatierung in diesem Fall über das Ausfällen mikrometergroßer, nanostrukturierter Silikapartikel aus der niederkonzentrierten Tensidlösung; gleiches gilt für die Synthese der sogenannten MSU-Silika mit nichtionischen Tensiden, die merklich größere Poren und dickere Porenwände aufweisen.[105,106] Im Gegensatz dazu kann das *Soft Templating* auch aus einer konzentrierten Lösung aus nichtionischem Tensid oder Blockcopolymer erfolgen, in der ein perfekter Abguss der sich bildenden, sogenannten lyotropen Flüssigkristallphase gefertigt wird (*true liquid crystal templating*).[107] Unter einer lyotropen Flüssigkristallphase wird die mesoskalige Selbstanordnung einer Substanz in Lösung verstanden, die eine kristallähnliche Ordnung aufweist und innerhalb gewisser Bedingungen (v. a. Konzentration und Temperatur) auftritt, wobei je nach Bedingungen unterschiedliche Phasen (z. B. kubisch oder lamellar) auftreten können.[108,109] Auf diese Weise lässt sich eine Vielzahl an mesoporösen Metallen und Metalloxiden herstellen,[100,110] deren Morphologie (kubisch, zylindrisch, lamellar, Gyroid) vom Phasendiagramm[111–113] des Blockcopolymers und somit von den jeweiligen Größen und Volumenanteilen der Polymerblöcke sowie deren Wechselwirkung untereinander bestimmt wird.[101] Vor allem die Gyroidstruktur wird aufgrund ihrer durchgängigen und gut zugänglichen Morphologie häufig für katalytische Anwendungen untersucht, auch wenn ihre Synthese herausfordernd ist.[40,114,115] Im Falle von Kohlenstoff ist diese auch direkt aus der Schmelze des Blockcopolymers möglich, sofern ein Block als Präkursor fungierend (z. B. Polyacrylnitril) karbonisieren und das Replika des sich zersetzenden Blocks (z. B. ein Polyacrylat als Templat fungierend) abbilden kann.[116]

Eine dritte und weitverbreitete Möglichkeit des *Soft Templating* bietet die von Brinker und Mitarbeitenden geprägte verdampfungsinduzierte Selbstanordnung (*evaporation-induced self-assembly*, EISA).[117–119] Im Zuge dieser bildet das amphiphile Templat entweder während des

Lösens oder nach ausreichender Verdampfung des Lösemittels und Überschreitung der kritischen Mizellbildungskonzentration (*critical micelle concentration*, CMC) Mizellen, die sich durch weiteres Verdampfen in einer geordneten, dicht gepackten lyotropen Phase anordnen. In den Zwischenbereichen bildet sich im Rahmen einer Sol-Gel-Reaktion das Metalloxid (oder Resolharz), das nach thermischer Entfernung des Templats als mesoporöses Replika der lyotropen Phase verbleibt (**Abbildung 3**). Alternativ kann die Anordnung der Mizellen durch eine Aggregation von Präkursor und Mizellen in Lösung erfolgen (*evaporation-induced aggregating assembly*, EIAA),[120] wodurch allerdings lediglich mesoporöse Pulver zugänglich sind. Im Gegensatz dazu kann die Templatierung über den EISA-Mechanismus auch auf monolithische, mesoporöse Dünnfilme übertragen werden, sofern die Präkursorlösung für die Tauch- oder Rotationsbeschichtung von Substraten eingesetzt wird.[121–124] Ferner bietet die Synthese mittels EISA zwei weitere Vorteile: (1) Zum einen können auch vorgefertigte Nanopartikel als Bausteine für das Porenskelett verwendet werden, was vor allem bei sonst zu reaktiven Präkursoren, aber auch für die Erlangung hoher Kristallinität nützlich sein kann.[125–127] (2) Zum anderen kann die Porenwanddicke anders als im EIAA-Mechanismus leicht über die Anpassung des Templat-zu-Präkursor-Verhältnis modifiziert werden, wie v. a. von Stefik und Mitarbeitenden für mesoporöse Metalloxide und Kohlenstoffe gezeigt.[128–134]

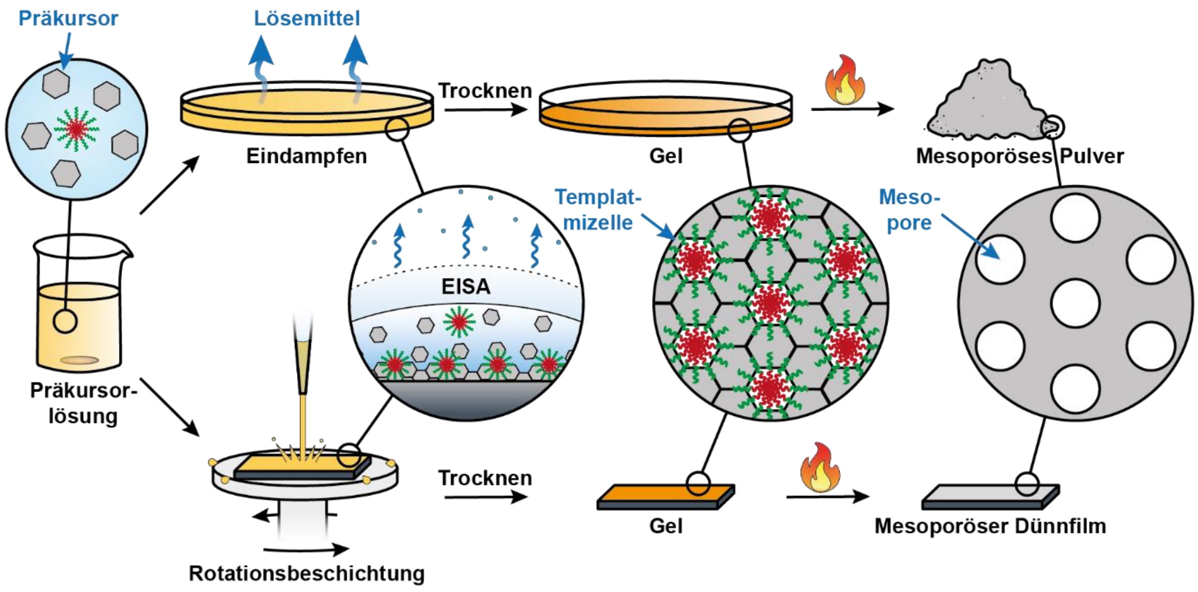

Abbildung 3: Schematische Übersicht über die Synthese von mesoporösen Metalloxiden über den EISA-Mechanismus.

Da die Porenwanddicke und ihre gezielte Variation für die Eigenschaften des mesoporösen Materials eine große Rolle spielen, beispielsweise für den elektrochemischen Transport in der Porenwand von porösen Kondensatoren,[21] aber lediglich im Rahmen des EISA-Mechanismus möglich ist, ist es entscheidend den zugrundeliegenden Templatierungsmechanismus zu kennen. In **Publikation 1** wurde daher eine systematische Studie bezüglich der Mizellisierung des Templats und der Gelierung der Präkursorlösung mittels dynamischer Lichtstreuung und Rheometrie durchgeführt, in welcher der EISA-Mechanismus für die Templatierung von Silika mit PEO-*b*-PHA nachgewiesen werden konnte. Dies wurde im Zuge einer systematischen Variation der Templatmenge und der daraus resultierenden Wanddickenabnahme in **Publikation 2** für mit PEO-*b*-PHA templatiertes Silika bestätigt. Abseits der Wanddicke beeinflussen auch die Größe und Verknüpfung der Mesoporen die Eigenschaften des Materials, deren Modifikation im folgenden Kapitel näher beleuchtet werden soll.

2.1.3 Porendesign und Blockcopolymere

Für das gezielte Design verschiedener morphologischer Parameter, wie Porengröße, Wanddicke und Porenverknüpfung, existieren viele Stellschrauben in der Synthese mesoporöser Materialien (**Abbildung 4**). Die Porenform und -größe hängt prinzipiell von dem verwendeten Templat[113,135] und seiner Größe (Blocklänge)[136,137] ab, kann aber auch durch die Templatmenge (in Form[138,139] und Größe[16]) verändert werden, sowie durch das Lösemittel,[140–142] die Temperatur,[143–146] die Art[147] und Konzentration[144,148] des Säurekatalysators in der Sol-Gel-Reaktion und besonders im Falle von Dünnfilmen durch die Verdampfungsgeschwindigkeit[149] des Lösemittels während der Synthese. Des Weiteren wird die Größe der Mizellen und somit der späteren Mesoporen häufig durch anorganische Additive[150] (NH_4F oder KCl) und sonstige Quellmittel[145,151–157] (kleine organische Moleküle oder Homopolymere) variiert, die je nach Polarität die Poren sowohl verkleinern als auch vergrößern können, aber teilweise zu inhomogenen Porengrößenverteilungen führen.[155]

Bezüglich der Variation der Porenwanddicke ist, wie zuvor beschrieben, maßgeblich das Verhältnis von Templat- zu Präkursormenge verantwortlich,[131] wohingegen die Situation für die Modifikation der Porenkonnektivität weniger offensichtlich ist. Dies liegt unter anderem daran, dass der Begriff selbst nicht klar definiert ist (beispielsweise seitens der IUPAC) und in der Literatur entweder auf die Größe der Porenhälse (Zugänglichkeit)[26,158] oder die Anzahl an verknüpftenden Nachbarporen (Koordinationszahl)[159,160] im Sinne der Perkolationstheorie bezogen wird. Darüber hinaus gibt es nur weniger Berichte, die sich mit der (systematischen) Variation der Porenkonnektivität befassen. So konnten Yoon *et al*. zum Beispiel zeigen, dass die Koordinationszahl der Poren in mesoporösem Kohlenstoff mit zunehmender Reaktionszeit und dadurch zunehmendem Kollaps der Mizell- und daher Porenstruktur abnimmt.[23] Außerdem berichteten Pérez-Mendoza *et al*. von einer Abnahme der Koordinationszahl in

SBA-2-Silika mit zunehmender Kalzinierungstemperatur infolge fortschreitender Kontraktion der Porensystems.[161] Weiterhin können die Synthesetemperatur[162] und der pH-Wert[163,164] die Porenkonnektivität beeinflussen, sowie zusätzliche, verknüpfende Poren (durch parallele Templatierung mit z. B. ionischen Flüssigkeiten)[165,166] eine qualitative Verbesserung der Porenzugänglichkeit herbeiführen.

Da solche externen Parameter (wie Temperatur und pH-Wert) auch das Skelettmaterial verändern können, das heißt z. B. die Kristallitgröße,[167] ist für eine systematische Studie, in der lediglich der Einfluss morphologischer Parameter (Porengröße *etc.*) auf makroskopische Eigenschaften untersucht werden soll, eine Variation des Templats und seiner Menge besser geeignet. Zur Erzielung verschiedener Porengrößen wurden zahlreiche Template untersucht (siehe **Abbildung 4**): Kleine Mesoporen (2 – 4 nm) lassen sich analog zu den oben genannten MCM-[103,104] und MSU-Silika[105,107,168] aus ionischen beziehungsweise nichtionischen Tensiden erhalten, wohingegen die weit verbreiteten und kommerziell erhältlichen Pluronics® Blockcopolymere aus Polyethylenoxid und Polypropylenoxid (PEO-*b*-PPO-*b*-PEO) größere Poren von 5 – 12 nm im Durchmesser erzielen, wie von den Silika der SBA-[169] und KIT-Familie[114] bekannt. Einen Schritt zu merklich größeren Mesoporen (11 – 20 nm) gelang durch die Kombination des PEO-Blocks mit einem hydrophoben Block aus Poly(ethylen-*co*-butylen) ((PE/B)-*b*-PEO), den sogenannten KLE-Polymeren.[170,171] Mit Blockcopolymeren aus PEO und Polyisobutylen (PIB-*b*-PEO)[18,172,173] und Polyisopren (PI-*b*-PEO)[174–176] synthetisierten Brezesinski beziehungsweise Wiesner und Mitarbeitende sogar diverse mesoporöse Metalloxide mit Kugelporen von bis zu 40 nm Durchmesser, wobei auch Template auf Basis von PMMA (PEO-*b*-PMMA)[120] für diesen Bereich (18 – 33 nm) bereits genutzt wurden.

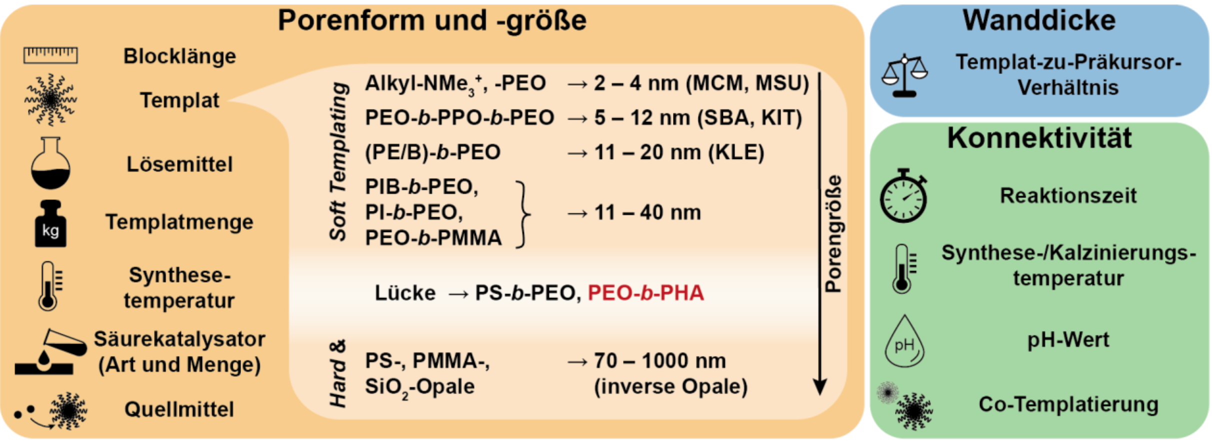

Abbildung 4: Übersicht über Parameter, die ein Design des Porensystems ermöglichen, sowie eine Auswahl an Templaten für *Soft* und *Hard Templating* mit den dazugehörigen Porengrößenbereichen.

Für den Zwischenbereich von 40 – 70 nm (Lücke in **Abbildung 4**), oberhalb dessen Kugelporen variabler Größe bereits über *Hard Templating* mit Opalen aus PS,[85] PMMA[98,99] oder Silika[177,178] leicht zugänglich sind, ist die Auswahl an Templaten aus Blockcopolymeren begrenzt. Abgesehen von PI-*b*-PS-*b*-PEO[179] und PMMA-*b*-PEO[180], die solche Porengrößen lediglich in Form der Gyroidstruktur induzieren, sind vor allem Blockcopolymere aus Polystyrol (PS-*b*-PEO,[181–183] PDMA-*b*-PS,[137] PS-*b*-PAA-*b*-PEO,[184] PI-*b*-PS-*b*-PVP,[185] PEO-*b*-PMMA-*b*-PS[128]) oder Polyhexylacrylat (PEO-*b*-PHA)[130] in der Literatur für sehr große Kugelporen (10 – 56 nm) bekannt, was unter anderem an der geringen Löslichkeit der meisten Polymere liegt, deren molare Masse für solch große Poren sehr groß sein muss.[186–189]

Generell muss ein geeignetes Templat für diesen Porengrößenbereich mehrere Voraussetzungen erfüllen: (1) Zum einen muss das Blockcopolymer über eine ausreichend hohe thermische Stabilität verfügen, damit sich das Templat erst zersetzt, nachdem eine stabile Porenwand ausgebildet wurde.[190] (2) Des Weiteren muss der Kontrast der Polarität zwischen den hydrophilen und hydrophoben Blöcken groß sein, damit sich in einem geeigneten Lösemittel bei geringer Polymerkonzentration Mizellen ausbilden (niedrige CMC).[176,191,192] Zur Abschätzung der Selektivität (das heißt Eignung) eines Lösemittels werden Polymerblöcke und Lösemittel anhand von Löslichkeitsparametern verglichen, beispielsweise mit dem Parameter δ nach Hildebrand, der mit zunehmender Polarität steigt.[193–195] Je nach Polarität (δ) des Lösemittels im Vergleich zu den Löslichkeiten der Polymerblöcke, erfolgt keine Lösung, eine Lösung als Mizelle (normal oder invers) oder eine als molekulare Kette (**Abbildung 5**).[130,132,196] In jedem Fall sollte die Löslichkeit des Templats (als Mizelle) hoch sein, um eine hohe Porosität erzielen zu können. (3) Schließlich muss das Templat über eine möglichst leichte Synthese im Grammmaßstab zugänglich sein, die eine wohl definierte Variation des Polymerisationsgrads selbst bei hohen Molmassen ermöglicht.[30,112,190] Im Zuge der Blocklängenvariation ist allerdings zu beachten, dass damit auch die Löslichkeit verändert wird,[197–199] sowie möglicherweise auch die Polymer- und somit Porenmorphologie gemäß des Konzepts der geometrischen Packung der Mizellen nach Israelachvili[101,113,200] und gemäß des Phasendiagramms des Copolymers (als Funktion von Polymer-Polymer- und Polymer-Lösemittel-Wechselwirkung, Volumenanteil der Blöcke und Blocklänge).[101,111]

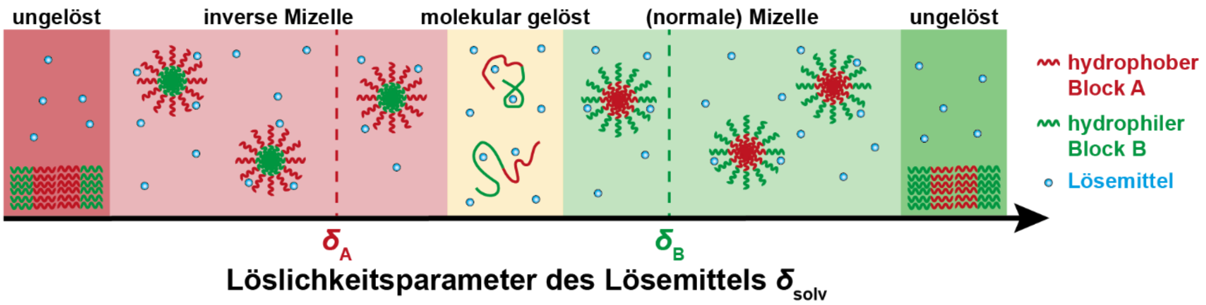

Abbildung 5: Morphologie eines Blockcopolymers in Lösung in Abhängigkeit der Polarität des Lösemittels.

Die Synthese von Blockcopolymeren erfolgte ursprünglich häufig über eine lebende anionische Polymerisation,[112] die allerdings sehr sensibel auf Verunreinigungen reagieren und somit ein besonders hohe Reinheit der Chemikalien und Syntheseschritte erfordern.[115,201] Radikalische Polymerisationen hingegen sind zwar robuster gegenüber Verunreinigungen, allerdings aufgrund der hohen Reaktivität der aktiven Ketten zu unkontrolliert für eine Templatsynthese.[202] Dies änderte sich 1967 mit der Entdeckung[203] kontrollierter radikalischer Polymerisationen und deren Weiterentwicklung in den 90er-Jahren,[204,205] die ein definiertes, lineares Kettenwachstum und schmale Molmassenverteilungen ermöglichen. Zu diesen laut IUPAC-Empfehlung[206] genannten reversibel deaktivierten radikalischen Polymerisationen (RDRP) zählen die NMP (*nitroxide-mediated polymerization*),[207,208] OMRP (*organometallic mediated polymerization*)[209,210] und RAFT (*reversible addition-fragmentation chain transfer polymerization*).[211,212] Neben der RAFT wird für die Templatsynthese besonders häufig eine vierte kontrollierte Polymerisationsmethode eingesetzt: die 1995 unabhängig voneinander von Matyjaszewski (mit Kupferkomplexen als Katalysator)[213] und Sawamoto (mit Rutheniumkomplexen)[214] entdeckte ATRP (*atom transfer radical polymerization*). Die Kontrolle über die sonst unkontrollierte radikalische Polymerisation beruht bei der ATRP auf dem Ausbalancieren der Geschwindigkeiten der Initiierung und der Kettenreaktion: eine schnelle Initiierung der Polymerisation gewährleistet ein gleichzeitiges Wachstum aller Ketten und die Verlangsamung der Kettenreaktion durch eine temporäre, reversible Inaktivierung der aktiven Ketten mithilfe eines Metallkomplexes[215] im ATRP-Gleichgewicht (**Schema 1**) vermindert die Wahrscheinlichkeit für Abbruchreaktionen und hält die Anzahl wachsender Ketten konstant.[201]

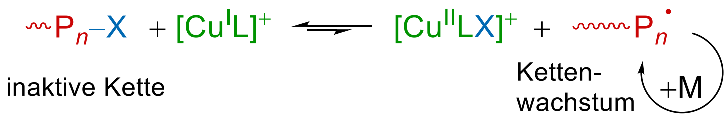

Schema 1: ATRP-Gleichgewicht zwischen der halogenterminierten inaktiven Kette P_n–X und der aktiven Kette $P_n^{\bullet}$, die mit dem Monomer (M) radikalisch polymerisieren kann, am Beispiel eines allgemeinen Kupferkomplexes $[CuL]^{+}$.

Die Geschwindigkeit der ATRP wird von vielen Faktoren beeinflusst, wie zum Beispiel vom Lösemittel,[216,217] dem pH-Wert,[218] der Temperatur,[219,220] dem Liganden des Katalysators,[221,222] der Stabilität des gebildeten Radikals[221] und dem Halogen[223] des Initiators. Neben vor allem der Ligandentwicklung sind weitere Optimierungen der ATRP durch konzeptionelle Anpassungen der Initiierung möglich, die eine bessere Kontrolle über die Polymerisation erlauben, die teilweise Inaktivierung des Katalysators durch Regeneration ausgleichen und so die Toleranz gegenüber Sauerstoffspuren erhöhen.[201] Dazu zählen zum Beispiel die elektrochemisch (*e*ATRP),[224] photochemisch (*photo*ATRP),[225,226] organokatalytisch (*o*ATRP)[227] und mittels Ultraschalls (*sono*ATRP)[228] betriebenen Polymerisationen. Allen voran die ATRP mit einem Metall (wie Cu^0) als zusätzlichen Aktivator und Reduktionsmittel (*supplemental activator and reducing agent*, SARA)[229] erlaubt eine leichte Katalysatorregeneration über eine Komproportionierung[230,231] und somit hohe Kontrolle über den Polymerisationsgrad (das heißt die Blocklänge) des Templats, der durch das Konzentrationsverhältnis von Monomer zu Initiator bestimmt wird.

In **Publikation 1** wurde ein PEO-*b*-PHA-Copolymer mittels SARA ATRP von Hexylacrylat mit einem PEO-Makroinitiator und Tris(2-pyridylmethyl)aminkupfer(I) als Katalysator synthetisiert und dessen Eignung als Templat für große Mesoporen untersucht. Diese leicht realisierbare Polymersynthese wurde in **Publikation 2** verwendet, um eine Bibliothek an PEO-*b*-PHA-Templaten mit variabler PHA-Blocklänge (50 bis 500 Wiederholungseinheiten) im Grammmaßstab herzustellen. Durch deren Einsatz im *Soft Templating* von Silika konnte geschlussfolgert werden, dass diese Polymerfamilie in der Lage ist, Kugelporen einzuführen, die einen Größenbereich von 10 – 80 nm abdecken, und somit ebenjene Lücke zwischen gängigen *Soft* und *Hard Templates* schließt. Da im Falle der Templatierung von Silika bekannt ist, dass letzteres ein perfektes Replika der lyotropen Phase bildet[105,106,171,232,233] (gemäß Avnirs Konzept des *molecular imprinting*[234] sogar bis auf molekularer Ebene), konnte darüber hinaus das Verhalten der Mizellen im Templatierungsprozess polymerphysikalisch näher untersucht werden, allen voran der Kollaps der PEO-Ketten auf dem Kern der Mizellen. Wie in **Publikation 4** beschrieben, eignet sich PEO-*b*-PHA von Silika abgesehen auch zur Templatierung von elektrochemischen relevanten Materialien wie Kohlenstoff und IrO_2.

Eine gezielte Synthese mesoporöser Materialien und systematische Studien der Templatierung erfordern präzise Methoden zur morphologischen Charakterisierung (Porengröße, Porenvolumen und Konnektivität), welche im nächsten Kapitel vorgestellt werden.

2.2 Charakterisierung mesoporöser Materialien

Zur Untersuchung poröser Strukturen gibt es ein großes Repertoire an Methoden, die verschiedene Porengrößenbereiche abdecken und unterschiedliche Informationen liefern. So bieten bildgebende Verfahren wie die Rastertunnel-[235] und Transmissionselektronenmikroskopie (TEM) für Mikroporen, die Rasterelektronenmikroskopie (REM) für Mesoporen sowie die REM und Lichtmikroskopie für Makroporen zweidimensionale Einblicke in die Porenstruktur. Größe und Volumen von Meso- und Makroporen können außerdem mittels Quecksilberporosimetrie[236,237] bestimmt werden. Mesoporöse Materialien lassen sich darüber hinaus über Physisorption,[236] Kleinwinkel-Röntgen- und Neutronenstreuung (SAXS und SANS),[238,239] Positronen-Annihilations-Spektroskopie,[240] Thermoporosimetrie,[241] Kernspinresonanz (NMR)-Kryoporosimetrie[242] und NMR-Relaxometrie[243] untersuchen. Ferner ermöglicht die ellipsometrische Porosimetrie[244] die Porengrößenbestimmung in mesoporösen Dünnfilmen, sowie die inverse Größenausschlusschromatographie[245–247] diese in flüssiger Phase (z. B. von porösen Gelen). Routinemäßig wird die Porengröße mesoporöser Pulver, wie in **Abbildung 6** anhand der jeweils farblich entsprechenden Porengrößenverteilung zusammengefasst, durch stichprobenartiges Ausmessen der Poren in REM-Bildern, aus der Hysterese der Physisorptionsisotherme und durch Modellierung von SAXS-Daten (bspw. im Falle zufällig verteilter Kugelporen unter Annahme eines Formfaktors für Kugeln und eines Percus-Yevick-Gitterfaktors[248–250]) bestimmt, was mit anderen Methoden (wie der Elektronentomographie in dieser Arbeit) verglichen werden kann.

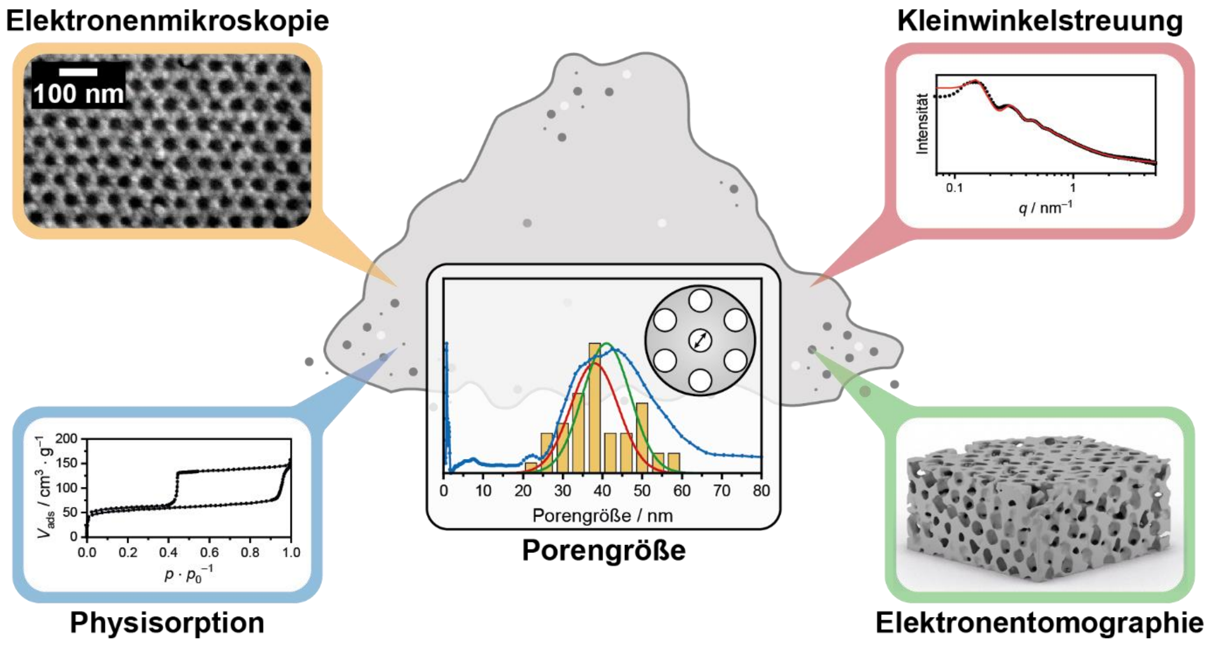

Abbildung 6: Charakterisierungsmethoden zur Bestimmung der Porengröße in mesoporösen Pulvern.

Die Bestimmung der Porenwanddicke kann prinzipiell aus REM-Bildern oder tomographischen Rekonstruktionen[251] lokal bestimmt werden, wird allerdings typischerweise aus SAXS-Experimenten erhalten: entweder aus der Differenz von Porenabstand und -durchmesser unter Annahme eines Packungsmodells der Poren[130] oder (v. a. für ungeordnet poröse Materialien) durch Modellierung und Bestimmung einer sogenannten Sehnenlängenverteilung.[252]

Die Verknüpfung von Mesoporen lässt sich über Physisorption,[236] vor allem durch Kopplung mit SAXS-[253] oder SANS-Experimenten[166], aber auch dreidimensional aufgelöst über Elektronen-[254] oder Röntgentomographie[255] studieren. Darüber hinaus ermöglichen NMR-basierte Methoden die Quantifizierung der Diffusion von Testmolekülen im Porensystem,[13,256] sowie deren Fähigkeit, Poren zu erreichen.[243] Abseits davon kann die Zugänglichkeit eines Porensystems auch indirekt bestimmt werden. So infiltrierten zum Beispiel Hartmann *et al.* einen mesoporösen Oxidfilm mit einem Referenzelektrolyten und untersuchten dessen Verteilung im Film *ex-situ* mittels Sekundarionen-Massenspektrometrie (SIMS).[257] Dieser praxisorientierte Ansatz wurde in **Publikation 1** und **4** ausgenutzt, um die Zugänglichkeit des PEO-*b*-PHA-induzierten Porensystems dreidimensional zu bestätigen, was vor allem im Falle des Kohlenstofffilms ein guter Indikator für die Zugänglichkeit des Films ist, da hier erst nach einer elektrochemischen Nachbehandlung ein zugängliches Porensystem nachweisbar war.

In dieser Arbeit wurden sowohl Physisorptionsexperimente als auch die Elektronentomographie besonders intensiv zur Charakterisierung mesoporöser Pulver herangezogen und dabei diverse morphologische Parameter wie Porengröße und -konnektivität analysiert. Vor diesem Hintergrund wird auf diese Methoden im Folgenden näher eingegangen.

2.2.1 Physisorption

Physisorptionsexperimente zählen zu den gängigsten Charakterisierungsmethoden mikro- und mesoporöser Materialien hinsichtlich Oberfläche, Porenvolumen, -größe und -konnektivität. Die Messung basiert auf der Anlagerung (Adsorption) von Atomen oder Molekülen des zur Analyse herangezogenen Gases (Adsorptiv bzw. nach Adsorption Adsorpt genannt) an der Oberfläche des porösen Feststoffs (Adsorbens).[258] Abhängig von der Stärke der Adsorpt-Adsorbens-Wechselwirkung spricht man im Falle großer Adsorptionsenthalpien (> 100 kJ mol^{-1}) von Chemisorption, bei der die Wechselwirkung eher einer kovalenten Bindung entspricht. Dieser Fall tritt beispielsweise zwischen Kohlenstoffmonooxid (CO) und diversen Edelmetallen wie Platin auf und wird im Rahmen der CO-Strippung zur Bestimmung der elektrochemisch aktiven Oberfläche von Elektrokatalysatoren genutzt.[259,260] Entspricht die Wechselwirkung eher einer Van-der-Waals-Wechselwirkung mit einer Adsorptionsenthalpie < 100 kJ mol^{-1}, spricht man von Physisorption und der Adsorptionsprozess kann als Kondensation auf der Oberfläche verstanden werden. Dieser Fall erfolgt zum Beispiel zwischen Stickstoff oder Argon und oxidischen Feststoffen und findet in Physisorptionsmessungen Anwendung. Experimentell wird dabei bei konstanter Temperatur die Menge an adsorbiertem Adsorptiv in Abhängigkeit des Partialdrucks des Gases gemessen und als sogenannte Physisorptionsisotherme aufgetragen. Konkret wird zunächst der Partialdruck bis zum Sättigungsdampfdruck p_0 erhöht (Adsorptionszweig) und im Anschluss wieder Richtung Vakuum erniedrigt, um den gegenteiligen Prozess zu untersuchen (Desorptionszweig). Die Messtemperatur wird sehr gering gewählt – in der Regel die Siedetemperatur des gasförmigen Adsorptivs – damit die Desorption von der Oberfläche die Adsorption nicht überwiegt und eine vollständige Benetzung der Oberfläche erreicht werden kann.[236]

Die Form der Isothermen liefert wichtige Hinweise auf die Morphologie des Adsorbens (Porenform und –größe) und die Wechselwirkung zwischen Adsorptiv und Probe (Be- oder Entnetzung). Gemäß IUPAC werden sechs Typen von Isothermen unterschieden, die in **Abbildung 7** gezeigt sind.[258] Mikroporöse Materialien (Porengröße < 2 nm) zum Beispiel zeigen lediglich einen starken Anstieg im adsorbierten Volumen bei kleinen Relativdrücken ($p/p_0 < 0{,}15$), da die kleinen Poren aufgrund des starken Adsorptionspotentials bei kleinen Drücken bereits vollständig gefüllt werden (siehe Typ I). Im Falle von Mesoporen (2 – 50 nm) sind höhere Relativdrücke notwendig, um die Poren zu füllen, wobei der dafür notwendige Relativdruck mit der Porengröße zunimmt. Üblicherweise wird für Mesoporen allerdings festgestellt, dass Adsorptions- und Desorptionszweig nicht übereinanderliegen. Denn übersteigt die Porengröße einen Wert von etwa 4 nm, sind die gegenüberliegenden Porenwände zu weit voneinander entfernt, als dass sich ihre Adsorptionspotentialkurven beeinflussen könnten. Somit erfolgt die Adsorption des Gases nicht im thermodynamischen Gleichgewicht (binodal), sondern als aktivierter, kinetischer Nukleationsprozess (spinodal), was mit einer Nukleationsbarriere verknüpft ist. Die Entleerung der Pore während des Verdampfens hingegen verläuft über einen rückläufigen Flüssigkeitsmeniskus im Gleichgewicht beim Überschreiten der Binodalen im Phasendiagramm.[158,258,261,262] Durch die Verschiebung des Adsorptionszweigs in Richtung höherer Relativdrücke spaltet sich die Isotherme somit zu einer Hystereseschleife auf (Typ IV), dessen Form von Temperatur, Adsorptiv, Porenform und Porenzugänglichkeit abhängt. Dieser Isothermentyp (**Abbildung 7** rechts) wird für die allermeisten Materialien in den **Publikationen 1 – 4** beobachtet und ist charakteristisch für mesoporöse Proben.

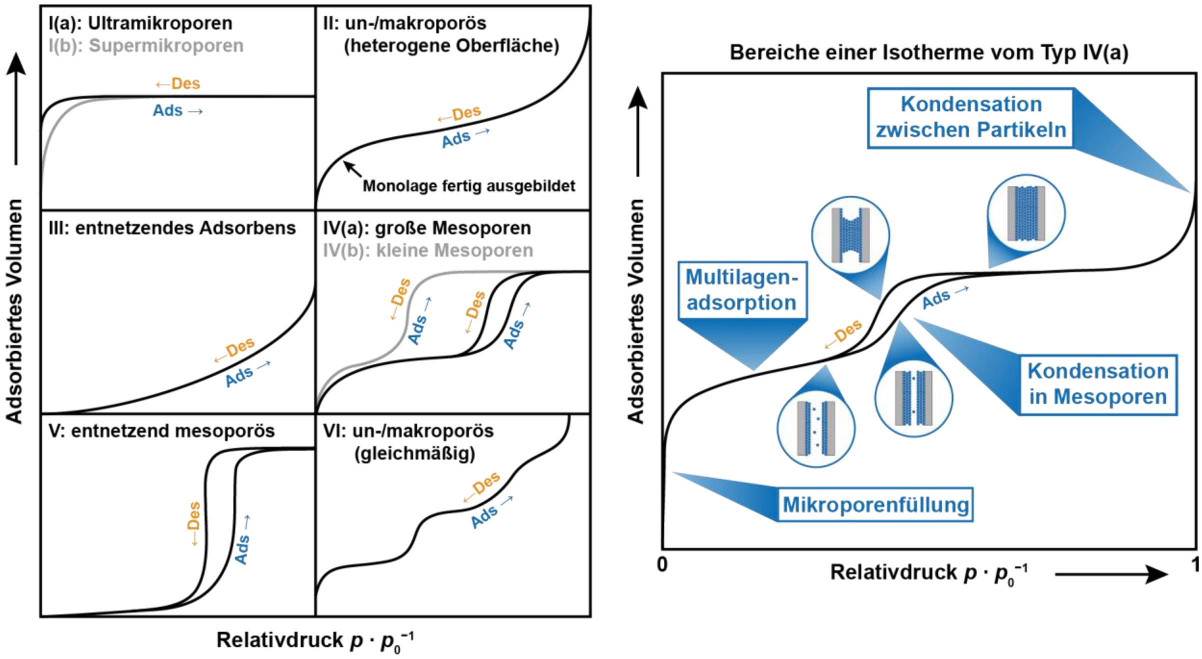

Abbildung 7: IUPAC-Klassifizierung von Physisorptionsisothermen (links) und Beschreibung der einer Isothermen zugrundeliegenden Prozesse mit schematischer Darstellung der Mesoporenfüllung und -entleerung (rechts).

Zwischen Mikro- und Mesoporenfüllung (etwa $p/p_0 = 0{,}05 – 0{,}30$) erfolgt die Adsorption reversibel unter Ausbildung eines flüssigkeitsähnlichen Films (den Multilagen) auf der Oberfläche. Die Gleichmäßigkeit der Oberfläche bestimmt hierbei, wie ungehindert die Multilage wachsen kann, das heißt, ob Mono- und anschließende Multilagen schichtweise (Typ VI) oder gleichzeitig wachsen (Typ II). Dieser Teil der Isothermen bietet die Grundlage für die Bestimmung der spezifischen Oberfläche einer Probe wie im Folgenden erklärt.[258]

Es gibt verschiedene Ansätze zur Beschreibung einer Adsorptionsisothermen, beispielsweise von Langmuir,[263,264] Freundlich[265] oder Temkin,[266] wobei das Modell nach Brunauer, Emmet und Teller (BET)[267] unter diesen am weitesten verbreitet ist und auch die Ausbildung von Multilagen inkludiert. In jedem Fall ist zu beachten, dass all diese Modelle nur die Adsorption auf einer flachen Oberfläche beschreiben und somit keine Porenfüllung betrachten, wodurch dieser Ansatz nur für den Bereich der Isothermen gültig ist, in dem weder Mikro- noch Mesoporenfüllung stattfinden. Unter der Annahme, dass sich eine Monolage ausbildet, auf der eine zufällige Multilage mit konstanter Adsorptionsenthalpie kondensiert, ergibt sich die BET-Gleichung. Mit ihrer Hilfe ergibt sich aus einer linearisierten Auftragung die Stoffmenge an Adsorpt in der Monolage. Diese lässt sich mit dem spezifischen Flächenbedarf eines einzelnen

Adsorptmoleküls und der Masse an verwendeter Probe in eine spezifische Oberfläche S_{BET} umrechnen. Der so erhaltene Wert beschreibt allerdings nicht die tatsächliche Oberfläche der Probe, sondern lediglich die für das Adsorptiv zugängliche Oberfläche, da die endliche Größe des Adsorptivatoms/-moleküls verhindert, dass jede Pore erreicht und jede Rauigkeit der Oberfläche ideal abgebildet werden kann. Ferner ist die Wahl des Adsorptivs relevant: Die IUPAC empfiehlt einatomige Adsorptive wie Argon oder Krypton, die als kugelförmige Adsorptive im Gegensatz zum zweiatomigen und somit stabförmigen Stickstoff einen konstanten Platzbedarf auf der Probenoberfläche einnehmen.[258]

Eine quantitative Auswertung der Physisorptionsisothermen im Hinblick auf die Porengrößenverteilung (*pore size distribution*, PSD) ermöglichen die von dem BET-Modell nicht erfassten Bereiche der Kapillarkondensation, das heißt die Mikro- und Mesoporenfüllung. Denn wie zuvor angemerkt, hängt der Relativdruck, bei dem die Kondensation in einer Pore auftritt, von der Größe der Pore ab und nimmt mit zunehmender Porengröße zu. Einen Ansatz, den Porenradius r_{P} mit dem Relativdruck der Porenfüllung zu korrelieren, liefert unter Annahme einer sphärischen Porengeometrie die in Gleichung **(1)** gezeigte Kelvin-Cohan-Gleichung (mit der Oberflächenspannung γ und dem molaren Volumen V_{m} des flüssigen Adsorptivs, dem Kontaktwinkel θ, der idealen Gaskonstante R, der Temperatur T und der Dicke t_{c} der Adsopt-Multilage vor dem Eintritt der Kapillarkondensation):

$$r_{\mathrm{P}} = -\frac{2\,\gamma\,V_{\mathrm{m}}\cos\theta}{\mathrm{R}\,T\ln\left(\frac{p}{p_0}\right)} + t_{\mathrm{c}} \qquad \mathbf{(1)}$$

Viele traditionelle (makroskopische) Methoden wie die Barrett-Joyner-Halenda-Methode,[268] die auf den Kelvin-Cohan-Gleichungen[269,270] beruht, oder die Derjaguin-Broekhoff-de-Boer-Theorie[271,272] liefern für große Mesoporen (> 15 – 30 nm) gute Ergebnisse. Im Falle kleiner Poren mit Durchmessern unterhalb von 20 nm unterschätzen diese jedoch aufgrund der zunehmenden Ungenauigkeit in der Bestimmung von t_{c} die Porengröße signifikant, z. B. um 30% für Mesoporen von 10 nm Größe. Moderne (mikroskopische) Methoden auf Basis von großkanonischen Monte-Carlo-Simulationen[273,274] oder der Dichtefunktionaltheorie[275] (meist *non-local* bzw. für Kohlenstoff optimiert *quenched solid density functional theory*, NLDFT[276,277] bzw. QSDFT[278,279]) überwinden diese Schwäche und bieten durch die akkurate Modellierung des Phasendiagramms des nanoskalig eingeschlossenen Fluids über den gesamten Mikro- und Mesoporenbereich zuverlässige Ergebnisse. Der DFT-Ansatz beruht auf der Anpassung einer experimentellen Isothermen mit einem Satz (*Kernel*) von simulierten

Isothermen für ein vorgegebenes Adsorptiv, Adsorbens, Temperatur, Porengeometrie und Porengröße. Da die ersten vier Parameter bekannt bzw. angenommen werden, können die (somit nur noch) porengrößenabhängigen Isothermen additiv überlagert werden, um die Messdaten möglichst gut anzupassen, wodurch sich die PSD als Gewichtungsfunktion ergibt.

Auf die oben beschriebene Weise kann für einheitliche und gut zugängliche Poren, der Porendurchmesser aus dem Desorptionszweig bestimmt werden, aber auch aus dem Adsorptionszweig der Hysterese unter Verwendung eines geeigneten DFT-Kernels, der die Nukleationsbarriere der Adsorption korrekt inkludiert.[280] Allerdings wird wie oben angedeutet die Form der Hystereschleife von der Porenform und –zugänglichkeit beeinflusst, wodurch sich die nach der IUPAC in fünf Typen klassifizierten Hystereseschleifen ergeben,[258] was unter Umständen bei der Interpretation der PSD beachtet werden muss (siehe **Abbildung 8** links).

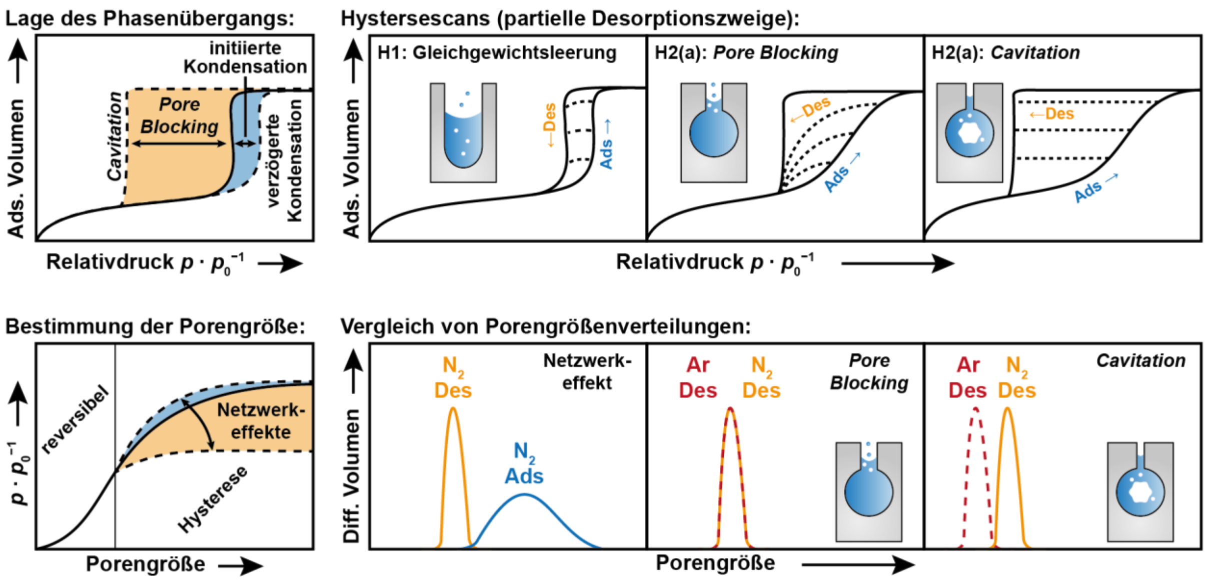

Abbildung 8: Lage des Phasenübergangs und Korrelation dieser mit der Porengröße für die Verdampfung im Gleichgewicht (durchgezogene Linie) sowie für durch Netzwerkeffekte beeinflusste Porensysteme (links). Zusätzlich sind Wege zur Bestimmung des vorliegenden Netzwerkseffekts mit möglichen Porenschemata gezeigt (rechts).

Treten zum Beispiel Netzwerkeffekte auf, das heißt ist eine Mesopore nur durch eine kleine Porenöffnung zugänglich, ist die Verdampfung des Fluids aus der Pore verzögert und der Desorptionszweig verglichen mit der Hysterese für offene und einheitliche Poren (Typ H1) in Richtung niedrigerer Relativdrücke verschoben (Typ H2(a)).[236,258,277] Die Entleerung der größeren Mesopore erfolgt erst bei dem niedrigeren Relativdruck, bei dem der engere, limitierende Porenhals entleert wird (orange gekennzeichneter Bereich in **Abbildung 8** links). Aus diesem Grund entspricht die PSD, die aus dem Desorptionszweig abgeleitet wird in diesem auch als *Pore Blocking* bezeichneten Desorptionsmechanismus nicht der eigentlichen PSD, sondern der Größenverteilung der Porenhälse. Unterschreitet die Porenöffnung aber eine kritische Größe (von etwa 4 – 5 nm für Stickstoff bei 77 K), verringert sich der zur Entleerung notwendige Relativdruck so weit, dass die Stabilitätsgrenze der Flüssigkeit erreicht wird und die gesamte Pore samt Hals über eine spontane Bildung von Gasblasen entleert wird. Dieser Grenzfall wird als *Cavitation* bezeichnet und erfolgt beim Kavitationsdruck, der durch das Adsorptiv, die Temperatur und die Größe der großen (limitierten) Pore bestimmt wird.[281] Hierbei liefert die aus dem Desorptionszweig bestimmte PSD keine morphologischen Informationen, sondern stellt ein thermodynamisches Artefakt dar; über die Größe der Porenöffnung kann lediglich geschlussfolgert werden, dass diese unterhalb des kritischen Werts liegt. Für solche Porensysteme muss die PSD aus dem Adsorptionszweig abgeleitet werden. In **Publikation 1** wurde hierfür am Beispiel von mesoporösem Silika demonstriert, dass die Analyse der Porengröße anhand der Adsorption sogar für große Kugelporen von etwa 40 nm zuverlässig möglich ist, für die bisherige NLDFT-Methoden noch nicht programmiert wurden.

Da die Bedeutsamkeit der desorptionsbasierten PSD davon abhängt, ob die Porenentleerung über *Pore Blocking* oder *Cavitation* erfolgt, ist eine experimentelle Unterscheidung beider Prozesse von großer Relevanz. Diese ist über zwei Wege möglich: über einem Adsorptivvergleich[280] und über Hysteresescans,[253,282] wie in **Abbildung 8** rechts gezeigt. (1) Im ersten Fall wird zunächst die adsorptionsbasierte PSD der desorptionsbasierten gegenübergestellt. Ist letztere im direkten Vergleich nicht deckungsgleich, sondern zu kleineren Porengrößen verschoben, ist die Verdampfung verzögert und ein Netzwerkeffekt liegt vor. Im zweiten Vergleich werden die desorptionsbasierten PSDs aus zwei Physisorptionsmessungen mit unterschiedlichen Adsorptiven (meist Stickstoff und Argon) übereinandergelegt. Da im Falle von *Pore Blocking* die PSD einen morphologischen Ursprung hat, müssen beide Verteilungen kongruent sein; im Falle von *Cavitation* hängt die PSD-Verschiebung von der Thermodynamik des Adsorptivs ab und die Verteilungen sollten sich demnach unterscheiden. (2) Alternativ können einer Physisorptionsmessung mehrere partielle Zyklen angeschlossen werden, bei der die Mesoporen sukzessive weniger gefüllt werden, bevor die Desorption gestartet wird. Die Form der partiellen Desorptionszweige hängt hierbei davon ab, ob die Desorption über *Pore Blocking* oder *Cavitation* erfolgt. Im Falle von letzterem behalten die partiellen Scans die Form der ursprünglichen Isothermen bei, da Desorption ausschließlich beim Kavitationsdruck erfolgt (alle Teilkurven sind parallel zueinander). Im Falle von *Pore Blocking* bilden die schrittweise ungefüllt bleibenden Mesoporen neue Fluid-Dampf-Grenzphasen, die die Verdampfung aus benachbarten Poren erleichtern. In der Folge gestalten sich die partiellen Isothermen merklich von der ursprünglichen Form verändert und münden alle in einem gemeinsamen Schnittpunkt. Da vor allem in ungeordnet porösen Netzwerken die PSD der Porenhälse sehr breit sein kann, liegt nicht immer nur ein Grenzfall von offenen Poren, *Pore Blocking* oder *Cavitation* vor, sondern es können auch Zwischenfälle von teilweise blockierten und offenen Poren vorliegen. Für solche ungeordnet porösen Materialien konnten Kube *et al*. am Beispiel von Silika-Monolithen durch eine Kopplung von Hysteresescans mit *in-situ*-SAXS-Experimenten zeigen, dass ein Porengrößengradient im Metalloxid vorliegt.[253]

Netzwerkeffekte können nicht nur den Desorptionzweig beeinflussen, sondern auch den Adsorptionsprozess. In den meisten mesoporösen Systemen (sofern die Mesoporen größer als etwa 4 nm sind) ist die Adsorption durch die Nukleationsbarriere verglichen mit dem binodalen Gleichgewichtsprozess verschoben. Diese Verschiebung kann in gewissen, stark vernetzten Porennetzwerken allerdings reduziert oder gar aufgehoben werden (blau gekennzeichneter Bereich in **Abbildung 8** links), wenn das flüssige Adsorptiv aus bereits gefüllten Mesoporen in größere, benachbarte Mesoporen, die mit metastabilem Dampf gefüllt sind, eindringt. Auf diese Weise kann die Nukleationsbarriere gesenkt oder gar umgangen werden. Dieser Fall einer initiierten Kondensation[158,283–285] verhindert eine valide Porengrößenbestimmung auf Basis des Adsorptionszweigs.

Abgesehen von der überwiegend qualitativen Analyse der Porenverknüpfung bieten moderne Evaluationsmethoden Ansätze zur quantitativen Untersuchung der Konnektivität. Mithilfe von Netzwerkmodellen, die auf der Perkolationstheorie und Monte-Carlo-Simulationen beruhen, lassen sich experimentelle Hysteresescans anpassen und so die Anzahl, Größe und Ordnung der verknüpfenden Poren quantifizieren.[159,160,286,287]

Da die Netzwerkanalyse mittels Physisorptionsexperimenten auf Porenhälse limitiert ist, die die Desorption beschränken, sind andere Messmethoden wie zum Beispiel Elektronentomographie notwendig, um auch größere Porenverknüpfungen sowie deren räumliche Verteilung zu studieren. In **Publikation 3** wird die Physisorption der Tomographie zur Untersuchung der Porenkonnektivität gegenübergestellt. Es zeigt sich, dass beide Methoden auf dem ersten Blick widersprüchlich, tatsächlich aber komplementär zueinander sind und in Kombination ein volles Bild des Porensystems liefern, da Physisorption die Zugänglichkeit des Porennetzwerks beschreibt, während die Tomographie Einblicke in die lokale Verknüpfung liefert. Die Grundlagen dieser bildgebenden Methode werden im nächsten Kapitel beschrieben.

2.2.2 Elektronentomographie

Konventionelle elektronenmikroskopische Aufnahmen liefern lediglich zweidimensionale Bilder eines dreidimensionalen Objekts, wohingegen tomographische Methoden ein dreidimensionales Modell rekonstruieren. Dafür wird eine Serie an winkelabhängigen TEM-Bildern aufgenommen und aus diesen Projektionen der porösen Probe über ein Rekonstruktionsalgorithmus, wie beispielsweise DART (*discrete algebraic reconstruction technique*), ein 3D-Modell der Porenstruktur berechnet.[288,289] Die Qualität der Rekonstruktion hängt von der Anzahl an aufgenommenen TEM-Bildern und der Größe des Winkelbereichs ab,[290] der aufgrund der Probenhalterung nicht bei ±90°, sondern maximal bei etwa ±70° liegt.[289] Vor allem mittels DART werden akkurate Rekonstruktionen auf der Nanoebene erhalten, die im Gegensatz zu anderen Charakterisierungsmethoden poröser Materialien keine Annahmen bezüglich der Porengeometrie benötigen und auch isolierte Poren abbilden.[291,292]

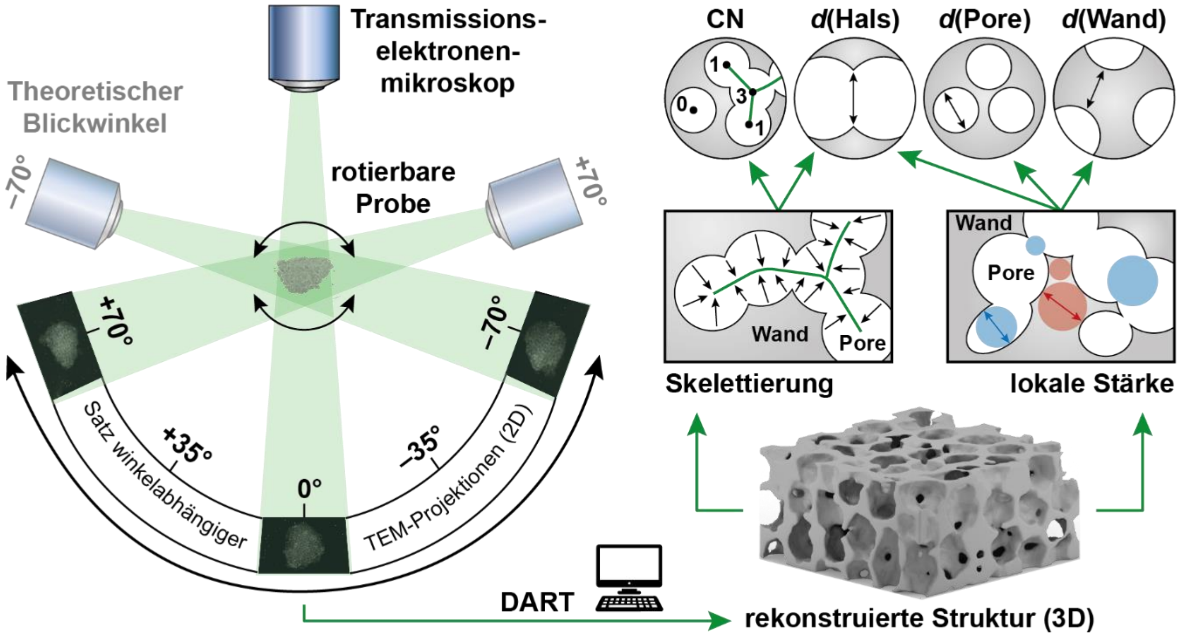

Abbildung 9: Prinzip der Elektronentomographie zur Untersuchung morphologischer Parameter, wie der Koordinationszahl (CN) der Poren, der Größe der Poren und deren Hälse, sowie der Wanddicke.

Auf Basis der rekonstruierten Porenstruktur können viele morphologische Parameter untersucht werden. Über eine iterative Verkleinerung des Porenraums (Skelettierung)[293] kann das Porenskelett als zentraler Pfad durch das Porensystem erhalten werden (**Abbildung 9**), dessen Verzweigung (Koordinationszahl, CN) Aufschluss über die lokale Verknüpfung liefert.[294] Tallarek und Mitarbeitende simulierten auf Basis des Porenskeletts, dessen Tortuosität („Gewundenheit“) und der Porengröße die Transportprozesse und -limitierungen von katalytischen Reaktionen in mesoporösen Materialien.[295] In **Publikation 3** wurden die

Skelettierung genutzt, um das Vorhandensein von separierten Subnetzwerken selbst in stark vernetzten Porensystemen zu bestätigen, die in Physisorptionsmessungen zu ausgeprägten Netzwerkeffekten führen.

Darüber hinaus können sowohl die Porengröße als auch die Wanddicke statistisch erfasst werden. Hierfür werden entweder die Sehnenlängenverteilungen für den Poren- und Wandraum (im Gegensatz zu SAXS) unabhängig voneinander generiert[296–298] oder die lokale Stärke der jeweiligen Phase ortsaufgelöst bestimmt.[251,254] Letztere ist definiert durch den Durchmesser der größten Kugel, die sich an gegebenem Voxel gerade noch in die eine Phase einfügt, ohne die andere zu penetrieren.[299] Die Bestimmung der lokalen Stärke des Porenraums inkludiert auch den Porenhals, sodass mittels Elektronentomographie wie in den **Publikationen 1 – 3** gezeigt nicht nur Anzahl, sondern auch Größe der verknüpfenden Poren quantifiziert werden kann. Auch wenn die Tomographie wie alle mikroskopischen Verfahren eine lokale Methode ist, konnten Prates da Costa *et al*. aus der tomographischen Rekonstruktion eine SAXS-Kurve simulieren und durch den Vergleich mit experimentellen Streudaten zeigen, dass die rekonstruierten Partikel repräsentativ für die gesamte Probe sind.[251,300]

3 Publikationen

3.1 Publikation 1

Poly(ethylene oxide)-*block*-poly(hexyl acrylate) Copolymers as Templates for Large Mesopore Sizes ─ A Detailed Porosity Analysis

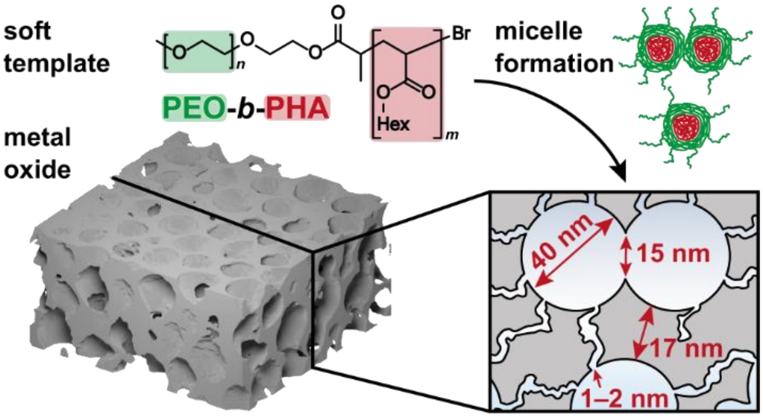

Reprinted with permission from

L. Q. Wagner, E. Prates da Costa, C. Glatthaar, F. Breckwoldt, M. Zecca, P. Centomo, X. Huang, C. Kübel, H. Schlaad, M. Kriechbaum, H. Amenitsch, M. Thommes, B. M. Smarsly, Poly(ethylene oxide)-*block*-poly(hexyl acrylate) Copolymers as Templates for Large Mesopore Sizes ─ A Detailed Porosity Analysis, *Chem. Mater.* **2023**, *35*, 9879 – 9899.

DOI: 10.1021/acs.chemmater.3c01255

CHEMISTRY OF MATERIALS

pubs.acs.org/cm Article

Poly(ethylene oxide)-*block*-poly(hexyl acrylate) Copolymers as Templates for Large Mesopore Sizes—A Detailed Porosity Analysis

Published as part of Chemistry of Materials virtual special issue "In Honor of Prof. Clement Sanchez".

Lysander Q. Wagner, Eric Prates da Costa, Chantal Glatthaar, Frederik Breckwoldt, Marco Zecca, Paolo Centomo, Xiaohui Huang, Christian Kübel, Helmut Schlaad, Manfred Kriechbaum, Heinz Amenitsch, Matthias Thommes, and Bernd M. Smarsly*

Cite This: *Chem. Mater.* 2023, 35, 9879−9899 **Read Online**

ACCESS | Metrics & More | Article Recommendations | Supporting Information

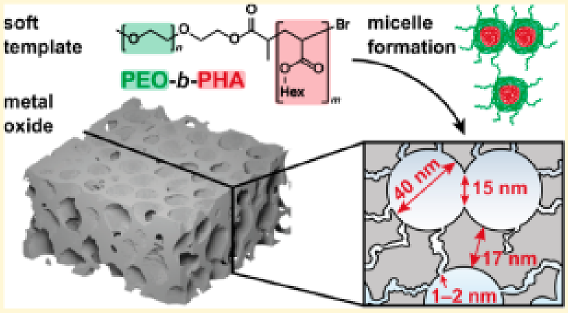

ABSTRACT: Mesoporous materials with defined pore geometry act as important models for porous substances being applied in various fields of materials research due to their large surface area—from catalysis to coatings and from solar cells to batteries and capacitors. Thus, understanding structure-property relationships requires the capability of deliberately and precisely tuning the mesoporosity, i.e., pore diameter, connectivity, and wall thickness. However, especially for the interesting pore size range between 35 and 70 nm, only a few convenient block copolymer templates are available using micellar self-assembly. In this study, we synthesized poly(ethylene oxide)-*block*-poly(hexyl acrylate) copolymers (PEO-*b*-PHA) by a supplemental activator reducing agent atom transfer radical polymerization (SARA ATRP) and employed them as soft templates for the preparation of ordered mesoporous metal oxide powders with spherical mesopores of ca. 40 nm in diameter, as shown by scanning electron microscopy (SEM), scanning transmission electron microscopy (STEM), and small-angle X-ray scattering (SAXS). With the aid of argon physisorption, STEM-based tomography, and time-of-flight secondary ion mass spectrometry (ToF-SIMS), we performed in-depth elucidation of pore shape and their mutual connection. In the case of mesoporous silica, 40 nm spherical mesopores are connected to 3−4 adjacent pores by 15 nm pore windows as well as 1−2 nm-sized micropores. These micropores seem to originate from single PEO chains penetrating the 17 nm thick pore wall. Compared to such mesoporous silica, mesoporous, crystalline zirconia possesses significantly higher pore accessibility. Furthermore, we prepared a set of PEO-*b*-PHA block copolymers with different block lengths, showing that mainly the PHA block length governs the mesopore size and thus enables mesopore size tuning. These results highlight that PEO-*b*-PHA is a promising template for the preparation of mesoporous metal oxides (in particular, crystalline ones) with tailored mesopore sizes, which enables systematic studies on property-porosity relationships.

■ INTRODUCTION

Ordered mesoporous metal oxides play a central role as promising model materials in various applications such as heterogeneous catalysis,[1−3] photocatalysis,[4−6] coatings,[7,8] adsorption and biocatalysis,[9,10] and electronic devices.[11−13] While mesoporosity is generally advantageous due to the large and readily accessible interface area it introduces,[4,14] mesoporous materials possessing defined pore shape and connectivity allow elucidating fundamental aspects of transport and interaction. Pore size, wall thickness, and pore connectivity are crucial parameters governing electrical, optical, and mechanical properties as well as determining heat and mass transport in porous catalysts.[5,15−17] An accurate in-depth characterization and fine-tuning of the mesoporosity are of fundamental importance to tailor those properties. Adjusting the transport of fluids and gases through the pore system can maximize the catalytic activity[4,5,17] but is also crucial for coating protocols such as the atomic layer deposition.[18,19] Thus, suitable procedures are required to synthesize and accurately study model materials, enabling a systematic variation of the aforementioned parameters on the mesoscale. In this field, major contributions to sol−gel chemistry and the preparation of hierarchically ordered materials were achieved by the group of Clément

Received: May 23, 2023
Revised: October 30, 2023
Accepted: October 31, 2023
Published: November 20, 2023

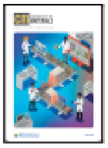

ACS Publications

https://doi.org/10.1021/acs.chemmater.3c01255
Chem. Mater. 2023, 35, 9879−9899

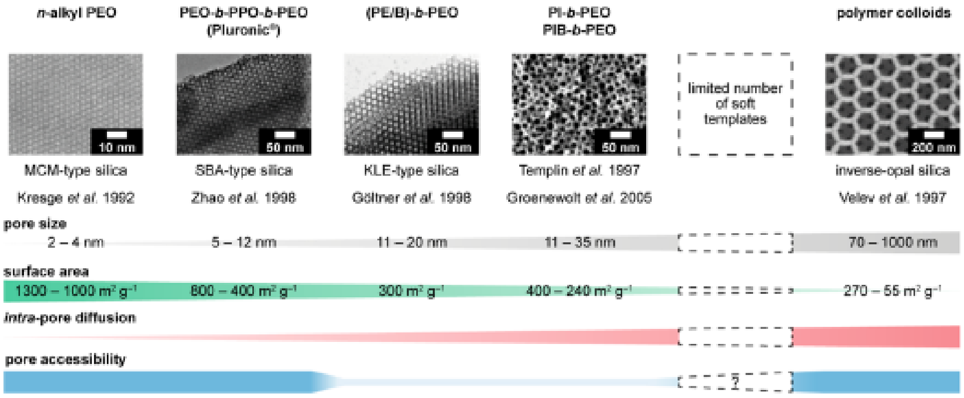

Figure 1. Overview of selected soft templates and the resulting silica pore structures dependent on the pore size. In addition, the influence of the pore size on surface area as well as the diffusion within and into the pore is given together with the original citations of the templates. SEM and TEM images, respectively, are reprinted with permission from left to right from ref 30, copyright 1992 American Chemical Society (MCM-type silica), from ref 42, copyright 2006 American Chemical Society (SBA-type silica), from ref 45, copyright 2003 American Chemical Society (KLE-type silica), and from ref 56, copyright 2007 Elsevier (inverse-opal silica). The fourth SEM image of PIB-b-PEO-derived silica was recorded in this work as described in the Experimental Section.

Sanchez.[20−23] One frequently used method to prepare ordered mesoporous metal oxides was significantly pushed forward also by Brinker and co-workers and is based on the evaporation-induced self-assembly (EISA) mechanism[24−26] applying amphiphilic soft templates. The latter form micelles in appropriate solvents (either directly or upon solvent evaporation), which arrange themselves in an ordered array upon proceeding evaporation.[25] Embedded in a gel from a hydrolyzed and condensed metal oxide precursor or using preformed dispersible nanoparticles,[27] an ordered array of mesopores within a metal oxide matrix is obtained after calcination. The pore dimension thus directly depends on the template used.

On the length scale of pore sizes (Figure 1), several structure-directing agents have been developed starting from soft templates for micro- and mesopores and hard templating approaches for macropores.[23,28,29] In detail, ionic surfactants like *n*-alkyl ammonium compounds (yielding MCM-type silica)[30,31] and nonionic surfactants like *n*-alkyl poly(ethylene oxide) (yielding MSU-type silica)[32−34] are applied to induce small pores in a range between 2 and 4 nm. Going one step toward larger pore sizes, block copolymers consisting of blocks of poly(ethylene oxide) and poly(propylene oxide)—PEO-*b*-PPO-*b*-PEO—are frequently used in form of the two representatives Pluronic P123 and F127. Employing this kind of polymers, pore sizes between 5 and 10 nm are accessible as known from the well-studied silica materials of the SBA and KIT family.[35−43] Larger mesopores can be obtained with different block copolymers such as poly(ethylene-*co*-butylene)-*block*-poly(ethylene oxide)[44,45]—commonly referred to as KLE—and poly(isobutylene)-*block*-poly(ethylene oxide) (PIB-*b*-PEO). While KLE polymers typically lead to defined spherical mesopores with diameters in the range of 13−22 nm, the combination of a KLE polymer with an ionic liquid yielded a network of spherical 14 nm pores connected via 2.6 nm pores and by that to an improvement of the mutual connection of these spherical mesopores.[46,47] PIB-*b*-PEO-derived materials are able to cover a range of pore sizes from 11 to 40 nm.[15,48,49] Also, poly(isoprene)-*block*-poly(ethylene oxide) (PI-*b*-PEO),[50−52] poly(ethylene oxide)-*block*-poly(methyl methacrylate) (PEO-*b*-PMMA),[53] and poly(*N*,*N*-dimethylacrylamide)-*block*-poly(styrene) (PDMA-*b*-PS)[54] copolymers are capable of generating pore sizes above 20 nm by soft templating. If hard templates are used, then a variety of different-sized macropores can be introduced. While colloidal poly(styrene) (PS) or poly(methyl methacrylate) (PMMA) spheres lead to highly porous inverse opals with a narrow pore size distribution and tailored pore size between 70 and 300 nm,[55−58] SiO_2 beads, e.g., Stöber particles, give access to macropores from 100 nm until several microns in diameter.[59] Figure 1 provides an overview of accessible pore size regimes by selected templates, while a detailed collection of templates, which have been investigated during the past 30 years, and their resulting pore sizes can be found in Table S1. Note that this table focuses on the mesoporous materials obtained by the templating action of the template in the respective, typical synthesis without further modifications of the synthesis, such as the addition of swelling agents in order to compare the individual templates.

The gap between soft and hard templates, i.e., the pore size regime from 35 to 70 nm, is difficult to fill by soft templating, especially aiming at defined pore geometries. Block copolymers with a sufficiently high molar mass often suffer from low solubility and therefore impede the EISA or nanocasting procedure. However, it is particularly this pore size region that is very relevant for ordered mesoporous oxides due to the following consideration: as shown in Figure 1, the surface area of a porous system increases with decreasing pore size. Based solely on this trend, a small pore size would be ideal for a catalytic application. Yet, the intra-pore diffusion is highly restricted in confined systems (small pores) and generally is expected to increase with increasing pore size. Indeed, photocatalytic studies using ordered mesoporous $CsTaWO_6$ of varying pore sizes between 5 and 15 nm confirm an enhanced catalytic activity due to two effects: an improved mass transport in case of larger pores and, concomitantly, a larger dimension of $CsTaWO_6$ nanocrystals, which can be accommodated.[5] Based on these two aspects (surface area and intra-pore diffusion), a medium pore size of about 40−50 nm should represent a trade-off between a still high surface area and a mostly unrestricted diffusion within a pore, especially, for larger reactant and product species in case of catalysis. Still, one further parameter must be taken into account—namely, the pore accessibility, i.e., the connectivity within the mesopore space. Neither a high surface area nor an unrestricted diffusion of reactants within a single pore can provide a high catalytic performance if diffusion into the pore is hindered. Herewith, transport into the pore may show no obvious dependency on the pore size (Figure 1, bottom) but depends on the inter-pore connectivity. Unfortunately, several of the block copolymers which were designed to produce larger mesopore sizes and, in addition, to withstand the crystallization conditions of the metal oxide (e.g., a high synthesis temperature) were shown to exhibit a tendency to form spherical micelles owing to the large poly(ethylene oxide) block (see the concept of the packing parameter[60,61]). As a result, the minor micelle overlap leads to a poor pore connectivity and overall mass transport in case of KLE-type and PIB-*b*-PEO-derived metal oxides (both spherical mesopores),[62] while MCM- and SBA-type materials with cylindrical pores normally possess a nearly unrestricted mesopore accessibility as well as mass transport within one cylindrical mesopore for small molecular species. For instance, this was shown for MCM-48 silica by the absence of network effects in physisorption experiments[63] as well as for the unrestricted immobilization in SBA-15 silica.[64] In contrast to KLE-type and PIB-*b*-PEO-derived materials, inverse-opal silica is readily accessible despite being derived from spherical templates. However, their pore window sizes are sufficiently large to ensure a good accessibility.[65]

Despite the shortage of suitable templates for the medium pore size regime, a few possible candidates exist to fill this gap. For example, poly(ethylene oxide)-*block*-poly(styrene) (PEO-*b*-PS) gives access to spherical pores of 20[66] to 50 nm[67] in diameter depending on the block lengths and the solvent used for templating. Also, swelling agents influence the pore size and give access to mesopores being significantly larger than normally achievable with the pure template.[35,68−71] However, this approach requires an accurate synthesis protocol to guarantee a uniform swelling of all micelles and avoid a significant increase in polydispersity of the resulting pore size. Structure-directing agents for achieving metal oxide gyroid structures with 30 and 40 nm pores, respectively, are poly(styrene)-*block*-poly(L-lactide)[72,73] and poly(isoprene)-*block*-poly(styrene)-*block*-poly(ethylene oxide),[6,74,75] respectively. A further diblock copolymer for spherical pores was proposed by Lokupitiya et al.[76] consisting of a hydrophilic poly(ethylene oxide) block and a hydrophobic poly(hexyl acrylate) block (PHA). With a polymer of this class, that is, PEO$_{453}$-*b*-PHA$_{431}$, the authors prepared metal oxide thin films with a pore size of around 50 nm. On the one hand, however, this polymer system seems to be underestimated for soft templating. On the other hand, all morphological investigations were performed on thin films. Yet, mesoporous powders are frequently used as model catalysts, too, and they are more suitable for a meticulous in-depth analysis of the pore system, especially the pore connectivity and accessibility. Thus, in this work, we focus on the synthesis of metal oxide powders using PEO-*b*-PHA as well as deep analysis of the resulting pore network by physisorption, electron microscopy, small-angle X-ray scattering, electron tomography, and secondary-ion mass spectrometry. Although spherical mesopores typically suffer from low pore connectivity, we target this pore morphology because (1) they might enable property improvements,[15] and (2) we strive to understand if the pore connectivity of these large mesopores is actually as poor as expected, and if it can be possibly controlled. Starting with silica as a model metal oxide, which can be robustly elucidated as well as yields a perfect replica in soft templating, we investigate the templating behavior of PEO-*b*-PHA and apply various state-of-the-art structural characterization to provide in-depth inside into the mesopore space. Following this study, our focus turns to ZrO$_2$ as a crystalline material to compare the pore accessibility with amorphous silica. By this comparison, we show how the pore morphology depends on the metal oxide used, and by varying the template's block lengths, we investigate how the porosity can be tuned by adjusting the PEO-*b*-PHA composition. In particular, the latter is a prerequisite for systematic studies of porosity-property relationships of any metal oxide.

■ EXPERIMENTAL SECTION

Synthesis of the Macroinitiator PEO−Br. Three samples of α-methyl-ω-hydroxy poly(ethylene oxide) (PEO−OH) with nominal average molecular weights of 5, 10, and 20 kDa (as provided by the supplier) were purchased from Sigma-Aldrich. According to ^{1}H NMR end group analysis, the number-average molecular weights (M_n) of the PEO−OH samples were 5.8 kDa (131 EO units), 9.4 kDa (214 EO units), and 15.7 kDa (355 EO units), respectively.

The macroinitiators PEO−Br were synthesized by a Steglich esterification as described by Lokupitiya et al.[76] In an exemplary procedure, a 50 mL Schlenk round-bottom flask was dried by applying two heating-evacuating steps of 10 min each. Then, 4.000 g (0.20 mmol, 1.0 equiv) of poly(ethylene oxide) methyl ether (PEO−OH, 20 kDa, Sigma-Aldrich) was dissolved in 10 mL of anhydrous dichloromethane (DCM, 99.8%, Acros Organics) under argon yielding a slightly viscous colorless solution after 15 min of stirring at room temperature. Then, 22 μL (0.24 mmol, 1.2 equiv) of 2-bromopropionic acid (99%, Acros Organics) was added with a syringe under argon flow. The colorless solution was cooled with an ice bath and 10 mg (0.08 mmol, 0.4 equiv) 4-dimethylaminopyridine (DMAP, ≥99%, Sigma-Aldrich) and 95 mg (0.46 mmol, 2.3 equiv) *N,N′*-dicyclohexylcarbodiimide (DCC, 99%, Sigma-Aldrich) were added. The solution became opaque, and after removal of the ice bath, the mixture was stirred under an argon atmosphere at room temperature for 22 h. To ensure a complete conversion of excess DCC, 5 μL of a 1 M hydrochloric acid (Grüssing GmbH) was added. After 15 min of stirring, the turbid reaction mixture was diluted with 40 mL of DCM and filtered over a paper filter. The clear colorless filtrate was concentrated under reduced pressure, yielding a colorless solid. The residue was dissolved in 17 mL of tetrahydrofuran (THF, technical grade, Thermo Scientific, purified over a 5 cm long column of basic aluminum oxide to remove peroxides) and precipitated in 200 mL of cold diethyl ether (being cooled with an ice bath). The colorless precipitation was recovered by filtration over a Büchner funnel and dissolved again in 20 mL of THF by gentle warming with a water bath. Following a second precipitation and filtration cycle, the colorless residue was dried in a vacuum oven at 40 °C for 25 h, leading to 3.735 g (0.19 mmol, 93%) of colorless powder.

The same protocol was used for the esterification of PEO−OH (10 kDa, Sigma-Aldrich, 87% yield) and PEO−OH (5 kDa, Sigma-Aldrich, 65% yield).

Synthesis of the PEO-*b*-PHA Copolymer. The PEO-*b*-PHA block copolymers were synthesized by a supplemental activator reducing agent atom transfer radical polymerization (SARA ATRP) combining the protocols of Lokupitiya et al.[76] and Kopeč et al.[77] In an exemplary synthesis, metallic Cu used as the reducing agent was activated as follows:[77,78] a copper wire (10 cm long and 1 mm in diameter) was wrapped around a stirring bar and stirred for 30 min at room temperature in a mixture of 12 mL methanol (HPLC grade, ChemSolute) and 12 mL hydrochloric acid (36−38%, ORG Laborchemie GmbH). The yellow solution was disposed of, and the wire was washed twice with pure methanol (about 25 mL each) under flowing argon. Then, the wire was rinsed in approximately 20 mL methanol for 30 min before drying the lusterless metal for about 5 h under flowing argon. As for the reaction, a 50 mL Schlenk round-bottom flask was dried by applying two heating-evacuating steps of 10 min each. Next, 500 mg (0.05 mmol, 1.0 equiv) PEO−Br and 43 mg (0.15 mmol, 3.0 equiv) tris(2-pyridylmethyl)amine (TPMA, >98.0%,

https://doi.org/10.1021/acs.chemmater.3c01255
Chem. Mater. 2023, 35, 9879−9899

TCI CO.) were dissolved in 0.65 mL anhydrous *N*,*N*-dimethylformamide (DMF, 99.8%, Acros Organics) by stirring at 40 °C yielding a beige suspension. Then, 11 mg (0.05 mmol, 1.0 equiv) $CuBr_2$ (>99%, water free, Acros Organics) was added under flowing argon leading to a bright green suspension. One freeze—pump—thaw cycle was carried out before 2.35 mL (13.36 mmol, 270 equiv) hexyl acrylate (98%, Sigma-Aldrich, removed from inhibitors by passing over a column of 9 cm basic aluminum oxide and 2 cm dried potassium carbonate on top) were added to the solution. After stirring for 10 min, two further freeze—pump—thaw cycles were applied and the mixture was heated to 50 °C after each thawing step to obtain a green clear solution. The stirring bar was exchanged by the copper-coated one under flowing argon. The reaction flask was heated to 70 °C, sealed, and it was stirred for 17 h. Upon heating, the initially green solution turned orange. The polymerization was stopped by cooling to room temperature and exposing the reaction mixture to air. The orange gel was diluted with 50 mL THF (purified by column chromatography with alumina) and heated to 40 °C yielding a dark yellow solution, which was passed over a column of 8 cm basic aluminum oxide; a blue/green band of roughly 1 cm on top could be observed. The column was washed with around 30 mL purified THF, and the slightly yellow filtrate was concentrated under reduced pressure forming a yellow gel. The residue was dissolved in 17 mL THF and precipitated in 200 mL cold methanol (cooled with an ethyl acetate/liquid nitrogen freezing mixture). The fine colorless precipitation was recovered by filtration over a Büchner funnel and dissolved again in 17 mL purified THF. After a second precipitation and filtration cycle, the colorless residue was transferred to a Petri dish and dried in a vacuum oven at 40 °C for 15 h leading to 1.757 g of a slightly yellow gel (for characterization by NMR and GPC, see below).

Additional PEO-*b*-PHA samples with different molecular weights and compositions were prepared by the same protocol; see Table S2 in the Supporting Information for the respective batch sizes.

Synthesis of Mesoporous SiO_2 Powders. Mesoporous SiO_2 powders were prepared based on a sol—gel procedure described by Weller et al.[6] and Cop et al.[3] 130 μL tetraethyl orthosilicate (TEOS, 98%, Sigma-Aldrich) was dissolved in 0.5 mL absolute ethanol (99.8%, Fisher Chemical) by stirring at room temperature for 20 min. In a second vial, 20 mg PEO-*b*-PHA was dissolved in 1 mL absolute ethanol upon sonication at 40 °C and 37 kHz for 20 min [in the case of PIB-*b*-PEO-derived mesoporous silica shown in Figure 1, 20 mg PIB_{50}-*b*-PEO_{45} (BASF) was used instead analogously to our comparable templating procedures[3,15,27,79,80]]. Both solutions were combined, and 40 μL of water was added. After further 5 min of stirring, 10 μL of concentrated hydrochloric acid was added, and the solution was stirred at room temperature for 1 h. The reaction mixture was transferred to a 5 mL PTFE cup and heated at 40 °C under a glass dome for 2 days followed by a drying step in a vacuum oven at 50 °C for 1 day. The colorless gel was calcined at 350 °C for 1 h and at 500 °C for 4 h (heating ramp each: 2 K min^{-1}) yielding about 35 mg of a colorless solid. In the case of the template concentration variation, 33 mg (volume fraction of $\Phi = 0.69$), 58 mg ($\Phi = 0.80$), and 82 mg ($\Phi = 0.85$), respectively, PEO-*b*-PHA, were used instead.

Preparation of Mesoporous SiO_2 Thin Films. Mesoporous SiO_2 thin films were fabricated with the aid of an EISA approach based on a protocol reported by Lokupitiya et al.[76] 50 mg PEO-*b*-PHA was dissolved in 770 μL absolute ethanol by stirring at 60 °C for 1 h. In a second vial, 126 mg of TEOS was mixed with 61 mg of 0.1 M HCl and 424 μL of absolute ethanol analogously. After cooling to room temperature, both solutions were combined and stirred at room temperature for a further 3 h. The solution was passed through a 0.25 μm PTFE syringe filter and sonicated at 80 kHz for 5 min. A 2 cm × 2 cm aluminum oxide wafer was cleaned with water, acetone, and isopropanol, respectively, by sonication for 15 min at 37 kHz each, and after drying, further cleaning was executed with an UV ozone cleaner for 15 min prior use. 100 μL of the precursor solution was deposited on the wafer rotating at 1200 rpm for 60 s applying a spin-coater setup SCK-200P provided by Instras Scientific. The film was kept for three further minutes in the chamber at a constant relative humidity of 20% guaranteed by a custom-made humidity control. The film was treated at 90 °C for 3 h and 100 °C for 4 h in a preheated oven to evaporate the solvent and calcined at 350 °C for 8 h and 600 °C for 2 h for template removal and crystallization (heating ramp each: 5 K min^{-1}).

Preparation of Mesoporous ZrO_2 Thin Films. The preparation of mesoporous ZrO_2 thin films was carried out in accordance to a procedure given by Cop et al.[79] As for the precursor solution, 92 mg of $ZrOCl_2 \cdot 8H_2O$ (98%, Alfa Aesar) was dissolved in 0.5 mL of absolute ethanol and 0.5 mL of 2-methoxy ethanol (≥99.9%, Sigma-Aldrich) by sonication at 80 kHz and 45 °C for 30 min. In a second vial, 48 mg of PEO-*b*-PHA was dissolved in 0.5 mL of absolute ethanol in the same way. Both solutions were combined and stirred at room temperature for 5 min. After the addition of 50 μL water, the solution was stirred at room temperature for further 3 h. The slightly yellow solution was passed through a 0.25 μm PTFE syringe filter and sonicated at 80 kHz for 5 min. The spin coating process was similar to that for the fabrication of SiO_2 thin films. Briefly described, a 2 cm × 2 cm silicon wafer was cleaned in an ozone cleaner for 15 min. Next, 100 μL of the precursor solution was poured on the wafer rotating at 2600 rpm for 60 s at a relative humidity of 20%. The film was kept at this humidity for further 3 min before exposing to 130 °C in an oven for 4 h. As for the drying and calcination step, the thin film was treated at 300 °C for 12 h and 600 °C for 2 h (heating rate each: 5 K min^{-1}).

Synthesis of Mesoporous ZrO_2 Powders. The ZrO_2 counterpart was prepared in the style of a protocol proposed by Cop et al.[3] 161 mg $ZrOCl_2 \cdot 8H_2O$ was dissolved in a mixture of 330 μL absolute ethanol and 330 μL 2-methoxy ethanol by sonication at 40 °C and 80 kHz for 30 min. In a second vial, 21 mg of PEO-*b*-PHA was dissolved in 660 μL of absolute ethanol and 170 μL of acetic acid (100%, Carl Roth GmbH) in the same manner. Both solutions were combined, stirred for 10 min at room temperature, and 10 μL water was added. After further 10 min of stirring, the solution was treated at 40 °C under a glass dome for 3 days. The gel was further dried in a vacuum oven at 50 °C for 24 h prior to calcination at 350 °C for 1 h and at 500 °C for 4 h (heating ramp: each 2 K min^{-1}). Since the powder appeared gray, a second calcination step was performed at 300 °C for 12 h and 550 °C for 20 min (heating ramps: 0.75 and 4.5 K min^{-1}, respectively), yielding 50 mg of gray powder.

Characterization Techniques. Proton-nuclear magnetic resonance (^1H NMR) spectra were recorded with a Bruker Avance II 400 MHz and Bruker Avance III 400 MHz HD at 25 °C and evaluated with MestReNova 14.1.2. $CDCl_3$ was used as the solvent, and signals were referenced to the solvent signal at $\delta = 7.26$ ppm. Gel permeation chromatography (GPC) with simultaneous UV (TSP UV 1000) and differential refractive index (Shodex RI-101) detection was executed at room temperature using tetrahydrofuran as an eluent at a flow rate of 0.5 mL min^{-1}. The stationary phase consisted of a 300 mm × 8 mm PSS SDV linear M column packed with 3 μm particles (molar mass range of 10^2 to 10^6 Da). Prior to the injection of 100 μL of sample solution containing around the 0.15 wt % polymeric sample, they were filtered through 0.45 μm filters. Poly(styrene) standards (PSS, Mainz, Germany) were used for calibration. Dynamic light scattering (DLS) experiments were performed on a Zetasizer Nano series from Malvern. For each measurement, the sample solution was diluted with the respective solvent by the factor of 1:1000 and characterized in three runs of 13 cycles. The data were exported using the corresponding application, Zetasizer Software. Nitrogen physisorption experiments were carried out at 77 K on a Quadrasorb evo (Quantachrome Instruments, Boynton Beach, FL), while argon physisorption experiments were performed at 87 K on an Autosorb iQ (Quantachrome Instruments, Boynton Beach, FL). The data obtained were analyzed with the aid of the software ASiQwin by applying nonlocal density functional theory (NLDFT) methods dedicated to nitrogen and argon at 77 and 87 K, respectively, on siliceous/oxidic materials assuming a cylindrical pore geometry. In both cases, the pore size distribution was obtained from the adsorption branch by applying a dedicated metastable adsorption branch kernel, which correctly takes into account the delay in pore condensation due to metastable pore fluid.[46] All metal oxide samples were degassed at 200 °C for 6 h in order to remove the attached water and gases prior measurement. The scanning electron microscopy (SEM) images were obtained on a Merlin scanning secondary electron microscope by Zeiss. All samples were sputter-coated for 60 s with platinum (1 kV, 40 mA) in order to increase the conductivity of the specimens. Additionally, thin films were connected to conducting silver varnish for cross-section imaging. A working distance of 2.2 to 3.2 mm combined with a voltage of 2 kV and a current of 78 pA were applied. For focused-ion-beam (FIB)-cutting SEM imaging, a drop of polymer solution was deposited with a metal rod onto a copper block cooled with liquid nitrogen and covered with an argon atmosphere. After sputtering with a 2 nm thick carbon layer, the sample was transferred with a Leica EM VCT500 transfer module (Leica Microsystems GmbH) to a XEIA3 FIB-SEM setup (TESCAN GmbH). Under permanent cooling with liquid nitrogen, a crater of 20 μm in width and depth, respectively, was cut with Xe^+ ions, and SEM micrographs of the cross-section were recorded under an angle of 55° with a voltage of 3 kV. The evaluation of all SEM images was performed with the software ImageJ. Small-angle X-ray scattering (SAXS) measurements were carried with the laboratory SAXS instrument SAXSpoint 2.0 by Anton Paar using point-focused (spot size of 500 μm) and slit-collimated Cu Kα radiation (λ = 0.1541 nm) from a microsource operating at 50 W and a Dectris EIGER2 R 1M hybrid pixel area X-ray detector. Powder samples were placed into an Anton Paar solid sample holder comprising a 1 mm thick metal plate with 20 squared holes mounted on a motorized X/Y-stage. The sample plate was sealed at both sides with a vacuum-tight sealing tape. SAXS images of the samples and the background (sealing tapes) were recorded in vacuum (around 1 mbar and 25 °C) at a sample-to-detector distance of 575.65 mm. Per each sample and background, respectively, 25 single images with 2 min exposure time each were recorded, averaged, and radially integrated in order to obtain the 1D-SAXS curves. The scattering curves were fitted using the software SASfit 0.94.11 with a model consisting of a form factor for spheres with a Gaussian size distribution and a lattice factor by applying the implemented decoupling approximation. In the case of measurements in solution, sealed quartz glass capillaries (1.5 mm outer diameter, 0.01 mm wall thickness, Hilgenberg GmbH) were used instead, and the background measurement was performed with the respective solvent without polymer. As for the partly condensed gels, the synthesis of mesoporous silica (57 vol % template) was stopped before (denoted as weakly condensed) and after 48 h of drying (denoted as highly condensed). The aliquots were sealed in the sample tube and measured 2 weeks later. Rheological experiments were carried out at 40 °C in oscillation mode on a MCR 92 rheometer by Anton Paar equipped with a D-CP/PP 7 probe head and a single-use D-PP25/AL/S07 measuring plate (gap of 1 mm between the stage and measuring plate). Scanning transmission electron microscopy (STEM)-based tomography was executed with a Thermo Fisher Scientific Themis 300 transmission electron microscope equipped with probe aberration correction and operated at an acceleration voltage of 300 kV. The silica powder (around 10 mg) was ground, suspended in ethanol, and dropped on a 100 × 400 mesh carbon-coated copper grid purchased from Quantifoil Micro Tools GmbH. Gold nanoparticles ($d_{\text{Au-np}}$ = 12 nm) were deposited onto the sample as fiducial markers for image alignment. The grid was cleaned twice for 30 s using a Fischione 1070 Plasmacleaner in an argon–oxygen atmosphere with a power of 50%. A high-angular annular dark-field (HAADF)-STEM tilt series with a tilt range of −72–70° (step size: 2°) and with a pixel size of 0.81 nm was gathered using the Xplore3D software (Thermo Fisher Scientific) with auto focus and tracking before acquisition. A small convergence angle of roughly 8.5 mrad was used to increase the depth of focus. With the aid of the gold nanoparticles, an image alignment was done in IMOD Version 4.11.7 (University of Colorado) with a residual alignment error of 0.606 nm (0.374 px). The 3D reconstruction [with a voxel size of $(1.62\ \text{nm})^3$] was obtained from the aligned tilt series with a simultaneous iterative reconstruction technique (SIRT) and 100 iterations in Inspect 3D 4.4 (Thermo Fisher Scientific). Denoising with a median filter in ImageJ and binarization by global thresholding in Avizo 2021.1 (Thermo Fisher Scientific) of the tomograms yielded initial segmentation. The segmented volume was purified by removal of unconnected islands being smaller than 15 voxels, which originate from reconstruction artifacts. Skeletonization of a cropped region of the image stack was executed as reported by Cheng et al.[81] in order to elucidate the local pore connectivity. Pore and wall size distributions were obtained with a local thickness evaluation using the corresponding plugin in ImageJ after subtracting the background with a Python code applying a rolling ball radius of 30 pixels (48.6 nm) as recently described by us.[82] In addition, the chord length distribution (CLD) of the wall phase was created by an analysis described by Bruns et al.[83] For this, points in the solid space were randomly chosen (referred to as seed points), and a set of 26 angularly evenly spaced vectors was built up pointing in all directions until the first phase border is hit. The length of two opposing vectors sums up to the chord length. In total, 10^7 chords were gathered neglecting chords touching the image boundary. The CLD was binned and fitted by a k-gamma function to obtain the mean chord length. For the shown time-of-flight secondary ion mass spectrometry (ToF-SIMS) study, we carried out the measurements on a ToF-SIMS 5 instrument by IonTOF GmbH, which is equipped with a 25 keV Bi cluster primary ion gun for analysis and a dual source column including an O_2^+ low energy gun for depth profiling. Prior to analysis, each thin film was immersed by a tracing solution. For this reason, 143 mg of $Co(NO_3)_2 \cdot 6H_2O$ (Acros) was dissolved in 5 mL of isopropanol upon stirring at room temperature for 10 min. The films were cut into 1 cm × 1 cm pieces and one drop of the violet tracing solution was dropped on every sample with the aid of a Pasteur pipet. The films were dried under ambient conditions for 20 min and remaining droplets carefully removed with a tissue. For further drying, the samples were heated in an oven at 80 °C for 8 h and 130 °C for 1 h. Depth profiles were recorded in spectrometry mode (bunched mode), providing a high signal intensity and mass resolution (full width at half-maximum $m/\Delta m$ of roughly 5000 at m/z = 17.00 for OH^-). A Bi^+ primary ion gun with an acceleration voltage of 25 kV and a current of 1.3 pA was applied to generate a 100 μm × 100 μm crater, and an O_2^+ sputter ion beam (1 kV and 240 nA) was used over an area of 300 μm × 300 μm in addition. Between two sputter frames, an analysis was performed after waiting for 2 s in random raster mode and by measuring one frame with 128 px × 128 px and one shot per pixel. All measurements were done in positive ion mode with a cycle time of 100 μs and evaluated with aid of the corresponding software SurfaceLab 7.2. The depth of the sputtered crater was determined from a depth profile measured with a cantilever. Here, the Alpha-Step D-600 profilometer by KLA Tencor was operated with the corresponding software AlphaStep D Profiler. Crystallinity of the thin films was studied by grazing incidence X-ray diffraction (GIXRD) using an X'Pert MRD diffractometer by PANalytical and an incidence angle of 0.5°. A 2θ range of 10 until 90° was covered with a step size of 0.1° and a scanning rate of 0.01° s^{-1}. Powder X-ray diffraction (XRD) data were acquired from an Empyrean Series 2 diffractometer by PANalytical in Bragg-Bretano geometry using monochromatized Cu Kα radiation (λ = 0.1541 nm, a Ni filter was used to suppress Cu Kβ radiation) in ambient atmosphere and a 2θ range of 10 until 90°. All diffraction data were exported by using the software HighScore Plus. The thickness and refractive index of the thin films were measured with an SE400Adv laser ellipsometer by Sentech equipped with a 633 nm HeNe laser. An angle of 70° was used for the measurement, and a model consisting of an overlaying air layer (n = 1.0000), a 100 nm SiO_2 (n = 1.4570), and ZrO_2 (n = 1.8608) deposition layer, respectively, as well as a silicon substrate (n = 3.8714) was assumed.

RESULTS AND DISCUSSION

Block Copolymer Synthesis. Block copolymers composed of poly(ethylene oxide) and poly(hexyl acrylate) were synthesized by atom transfer radical polymerization (ATRP) as summarized in Scheme S1. In the first step, the ATRP-active C−Br bond was introduced to PEO−OH (20 kDa, 355 repeating units according to ^{1}H NMR spectroscopy) by Steglich esterification as described by Lokupitiya et al.[76] The ^{1}H NMR end group analysis of the obtained PEO−Br macroinitiator confirmed the successful attachment of the halide moiety to the PEO−OH homopolymer with a degree of esterification of 97% (Figure S1). In the second step, the PEO−Br macroinitiator was

https://doi.org/10.1021/acs.chemmater.3c01255
Chem. Mater. 2023, 35, 9879−9899

used to initiate the polymerization of hexyl acrylate by ATRP. While Lokupitiya et al.[76] used a copper(I)-based ATRP with 1,1,4,7,10,10-hexamethyltriethylentetramine (HMTETA) as the ligand, here, we decided to use tris(2-pyridylmethyl)amine (TPMA) as the ligand, which increases the ATRP activity by 3 orders of magnitude[84] and thus speeds up the polymerization of hexyl acrylate being otherwise rather slow (less stable radical intermediate compared to, e.g., the polymerization of styrene).[84] In addition, performing the polymerization as a supplemental activator reducing agent (SARA) ATRP offers the advantage of keeping the catalyst concentration very stable since Cu(II) species originating from oxidation events can be regenerated.[84,85] Furthermore, the reducing agent (Cu wire) acts as an initiator activator and generates the active catalyst, as shown in Figure 2. Consequently, the synthesis gains robustness and reproducibility. Following this protocol, we obtained copolymer PEO$_{355}$-*b*-PHA$_{171}$ with a number-average molar mass of 42.6 kDa determined by ^{1}H NMR spectroscopy (Figure S2). According to GPC analysis (Figure S3), the copolymer exhibited a rather broad molar mass distribution with a dispersity of 1.55 and contained some residual PEO homopolymer (estimated to about 20 wt %, see Figure S3B). Hence, the true average length of the PHA block of the copolymer should be larger than the 171 repeating units determined by ^{1}H NMR spectroscopy. The large amount of unreacted PEO homopolymer is possibly a matter of reactor design. Here, we used a Schlenk flask (as depicted in Figure 2) suffering from a low mixing in the upper part of the reaction mixture, especially with consecutively increasing viscosity. The syntheses of other PEO-*b*-PHA samples (see below, Table 1) were thus performed in round-bottom flasks instead, by which the amount of PEO homopolymer could be reduced substantially to less than 10 wt % (see Figure S11). However, PEO homopolymers cannot form micelles during the soft templating process and thus are not expected to interfere in the following step.

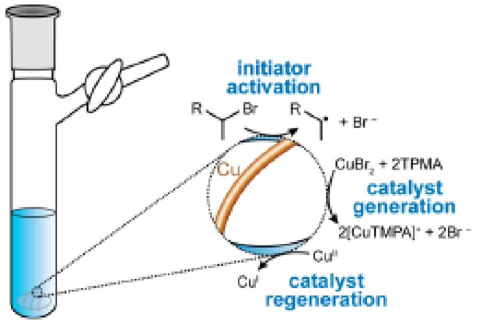

Figure 2. Schematic representation of the role of the copper wire in a SARA ATRP.

To investigate the influence of the two block lengths on the templating behavior, four further samples were synthesized: two with a PEO block length of 131 repeating units and two with a PEO block length of 214 repeating units (see Figures S4 and S5 for the NMR spectra of the corresponding macroinitiators). Besides the PEO block, the PHA block length was varied from 57 to 396 repeating units (see the ^{1}H NMR spectra in Figures S6−S9 and GPC traces in Figure S10). Table 1 provides an overview of the synthesized block copolymers and their molecular parameters.

While the PEO$_{355}$-*b*-PHA$_{171}$ copolymer was used for deeply investigating the pore structure after soft templating in the first part of this work, the remaining four samples were used to elucidate the individual influence of the two blocks on the pore size in the last section of this article.

Soft Templating. The application of the PEO$_{355}$-*b*-PHA$_{171}$ copolymer as soft template follows an evaporation-induced self-assembly (EISA) mechanism.[24−26] As shown in Figure 3, both the silica precursor and template are brought into ethanolic solution before water and hydrochloric acid are added to promote the sol−gel reaction. Above the critical micelle concentration (CMC), block copolymer micelles are formed, which act as template. Upon solvent evaporation, the latter form an ordered array of micelles within an inorganic phase. The final annealing step leads to pyrolysis of the organic phase, leaving an ordered mesoporous metal oxide behind.

According to DLS, PEO$_{355}$-*b*-PHA$_{171}$ does not seem to form micelles in ethanol (Figure S12) in contrast to other block copolymer soft templates such as PIB-*b*-PEO possessing a very low critical micelle concentration due to the high hydrophilic−hydrophobic contrast.[15,27,86] A hydrodynamic diameter of 13 nm hints at a polymer coil instead of a micelle. This interpretation is supported by the findings of Sarkar et al.,[87] who observed absence of micellization of PEO-*b*-PHA in pure ethanol as well. However, DLS measurements of the polymer in pure TEOS lead to a hydrodynamic diameter of 85 nm, which is plausible for micelles of such large polymers.[87,88] Since these large colloids are not observed in pure TEOS (reference experiment without polymer), the formation of SiO$_2$ particles in the precursor can be ruled out as the origin of the 85 nm colloids. Hence, these findings suggest that micellization occurs in a TEOS-enriched solution upon solvent evaporation, as depicted in Figure 3. To verify this assumption, a more detailed DLS study was performed by recording the particle size distribution in various ethanol-TEOS mixtures (Figure 4B). Over a range from 0 vol % TEOS (pure ethanol) to 70 vol % TEOS, the same hydrodynamic diameter of around 13 nm in diameter is

Table 1. Overview on the Block Copolymers Prepared and Used as Templates in This Study Comprising the Average Degree of Polymerization of the PEO (n) and PHA (m) Blocks, the Degree of Esterification (f) of the Parent Macroinitiator, the Number-Average Molecular Weight (M_n), and the Mole Fraction of PEO (x) in the Block Copolymer Based on NMR, as Well as the Apparent Number-Average Molecular Weight (M_n^{app}) and the Dispersity Index ($Đ$) Based on GPC

sample	n(PEO)	m(PHA)	f	M_n/kDa	x(PEO)	M_n^{app}/kDa	$Đ$
PEO$_{355}$-*b*-PHA$_{171}$	355	171	0.97	42.6	0.67	60.2	1.55
PEO$_{214}$-*b*-PHA$_{322}$	214	322	0.92	59.9	0.40	62.9	1.42
PEO$_{214}$-*b*-PHA$_{83}$	214	83	0.92	22.5	0.72	18.5	1.77
PEO$_{131}$-*b*-PHA$_{396}$	131	396	0.92	67.8	0.25	47.4	1.29
PEO$_{131}$-*b*-PHA$_{57}$	131	57	0.92	14.9	0.70	15.4	1.41

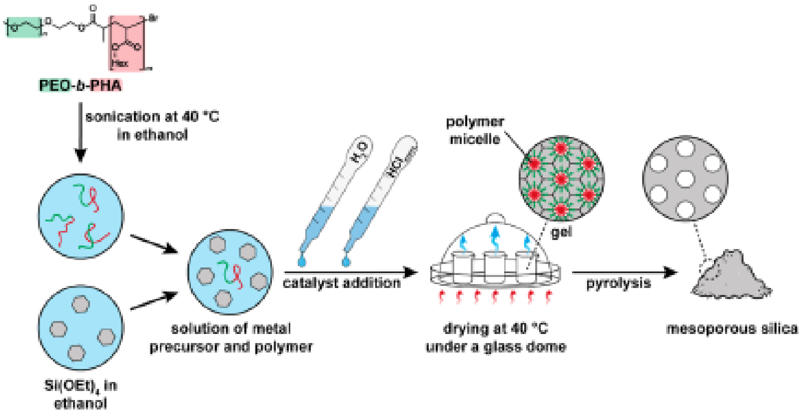

Figure 3. Schematic overview of the sol–gel synthesis for preparing mesoporous silica powders by soft templating.

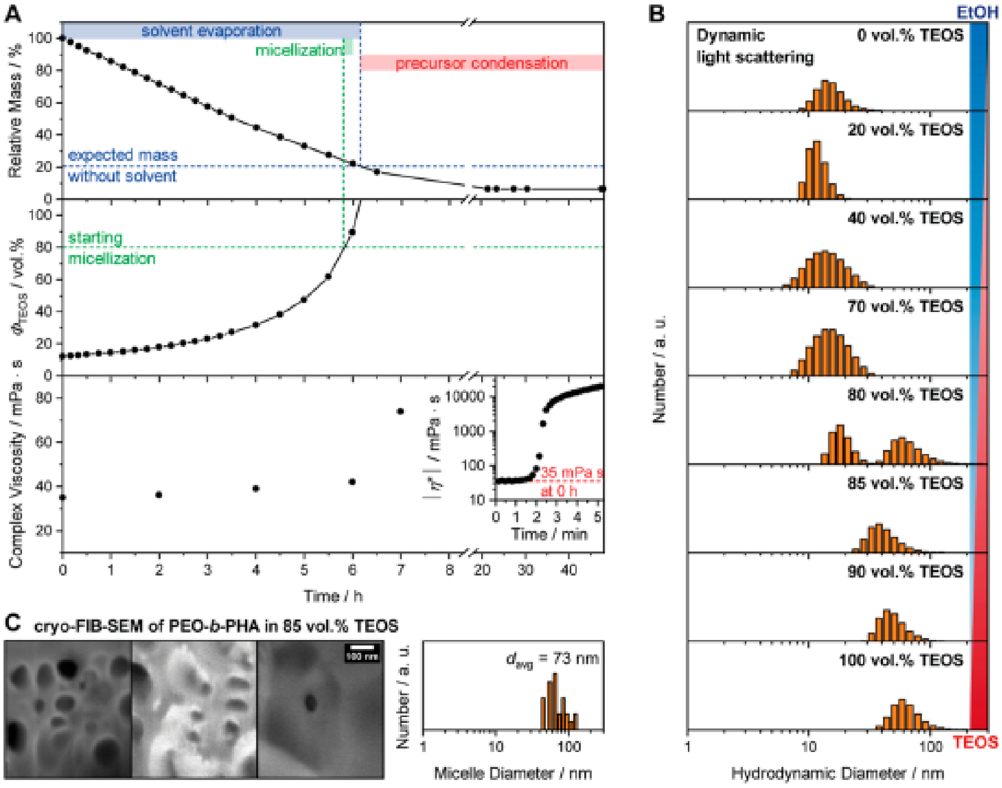

Figure 4. Evaluation of the underlying soft templating mechanism comprising (A) a gravimetric study of the relative mass loss of the reaction mixture during the solvent evaporation (top), the estimated TEOS volume fraction calculated from the mass loss (middle), and the evolution of the initial complex viscosity measured at 40 °C with single ex situ rheological measurements, as shown in the inset for the measurement after 0 h (bottom). The underlying processes are labeled on a timeline on the top. (B) DLS study of PEO_{355}-*b*-PHA_{171} dissolved in different mixtures of ethanol and TEOS is given as well as (C) cryo-SEM images of three different spots and the resulting particle size distribution of the polymer dissolved in an ethanol-TEOS mixture (85 vol % TEOS) recorded at the cross-section after cutting the frozen droplet with a focused ion beam (FIB).

observed similar to the coil conformation occurring in pure ethanol as discussed before (Figure S12). However, at a concentration of 80 vol % TEOS, a superposition of the aforementioned small particles and larger entities hints for starting micellization. This interpretation is supported by the size distributions recorded in 85, 90, and 100 vol % TEOS showing only larger entities (mode hydrodynamic diameter of 70–80 nm). As independent method to back up the presence of micellization, cryo-FIB-SEM images were recorded. Here, a drop of the polymer solution in 85 vol % TEOS was frozen onto a copper block cooled by liquid nitrogen. Then, the frozen droplet was cut with a focused ion beam (FIB), and the cross-section is regarded by SEM. The SEM images (Figure 4C) confirm the presence of spherical objects with an average diameter of 73 nm, being in good agreement with the DLS results. Both size and shape of these dark spots observed in SEM support the hypothesis that micellization occurs upon TEOS enrichment in a region of 80−85 vol % TEOS. Small-angle X-ray scattering provides additional confirmation, e.g., performed on polymer dissolved in 85 vol % TEOS and pure TEOS (Figure S13A,B). In a log−log plot at large q (above 0.2 nm^{-1}), both SAXS curves follow a linear trend with a slope significantly lower than circa −2 as expected from a form factor of a perfect Gaussian coil (F_{chain}) with a diameter of 13 nm.[89,90] Instead, a slope of about −4 is found (Porod law) being typical for a two-phase material with sharp interfaces between the two phases (such as a dense micelle versus solvent). The absence of sharp form factor minima and a slope of zero at low q values found in other studies[91,92] is due to the polydispersity of the micelles and render an accurate size determination difficult. Yet, the presence of micelles instead of Gaussian coils still becomes apparent from the slope at large q values. This evaporation-induced micellization is in particular important as it evokes a direct dependency of the soft templating process on the precursor used.

Next to the EISA mechanism explained above, an evaporation-induced aggregating assembly (EIAA) of the micelles could be assumed as an alternative self-assembly process. While following an EISA mechanism, the micelle assembly occurs at the solid (substrate/bottom of beaker)-liquid (solution) interface during solvent evaporation and precursor condensation takes place only after solvent evaporation, an assembly of micelles as building blocks occurs at the liquid−liquid interface in solution (condensation during evaporation) in case of an EIAA mechanism.[53] To distinguish between the both mechanisms, the mass (solvent evaporation) and complex viscosity (extent of TEOS condensation) of the reaction mixture were monitored ex situ at several points in time. More precisely, the synthesis was executed as described in Experimental Section with 20 mg template per batch (PTFE cup in Figure 3) with eight batches: three for tracking the mass of the reaction mixture and five for measuring the viscosity at five points in time with the aid of a rheometer. The starting point (0 h in Figure 4A) corresponds to the step at which the reaction mixture was exposed to 40 °C.

Looking at the relative mass of the reaction mixture (Figure 4A, top), a consecutive mass loss due to solvent evaporation appears. As the relative mass of the reaction mixture without ethanol (pure TEOS, template, water, and HCl) is known to be 20.7% (192 mg) compared to the starting value at 0 h (927 mg corresponding to 100%), the evaporation of ethanol is expected to be finished after 6.2 h. Yet, a further mass loss can be observed even after 6 h, which is due to the fact that also TEOS itself can release ethanol (up to four equiv per equivalent TEOS) upon hydrolysis and/or condensation. In case all ethoxy moieties are converted to ethanol, an additional mass loss of 9% is expected for complete conversion of TEOS and is in fair agreement with the final value found at 48 h. Assuming that only ethanol evaporation is responsible for the observed mass loss, the mass difference between a respective measurement and the initial mass can be transformed roughly into a volume fraction of TEOS (Figure 4A, middle). With the knowledge of the DLS results, the micellization of the block copolymer is expected to start at 80 vol % TEOS and thus after roughly 5.8 h. This implies that micelle formation starts before solvent evaporation is finished. The fact that TEOS also releases ethanol leads to a TEOS volume fraction exceeding 100% after 6 h and, however, enables only a rough estimation of the TEOS concentration. Yet, the micellization has to occur before complete solvent evaporation because otherwise no soft templating would be possible. The extent of TEOS condensation can be evaluated through the complex viscosity of the reaction mixture (Figure 4A, bottom). Upon gelation (TEOS condensation), a steep increase in complex viscosity $|\eta^*|$ is expected,[93] and this behavior is also found here, as shown in the inset of Figure 4A on the bottom. However, due to the small gap between the measurement plates, i.e., small amount of sample, the absence of the glass dome, and the higher heat transport of the sample stage (heated to 40 °C) compared to the reaction setup (PTFE cup under a glass dome), an in situ measurement is not representative of the reaction conditions. Instead, the initial complex viscosity was measured ex situ (see the red dotted line in the inset of Figure 4A) after 0, 2, 4, 6, and 7 h of exposure to 40 °C under the glass dome. As expected from proceeding solvent evaporation, the viscosity of the reaction mixture increases with exposure time, but even after 7 h, a value is observed being too low to originate from a significantly gelated sample (beyond 1000 mPa s) when compared to the upper part of the curve in the inset of Figure 4A. No values were recorded beyond 7 h because the reaction mixture forms a transparent brittle gel afterward, which cannot be studied in a rheometer due to its nonmonolithic nature. Thus, pronounced gelation does not take place before 7 h and consequently occurs after solvent evaporation. As a result, this combined gravimetric and rheological study confirms the synthesis to follow most likely an EISA mechanism.

Porosity Analysis. Ordered mesoporous metal oxide powders, compared to the corresponding thin films, provide the opportunity to study the porosity and general physisorption phenomena more deeply, especially in terms of pore connectivity. Among several aspects, the deformation of the micelles and mesopores perpendicular to the surface is a frequently observed feature especially for large micelles, which was observed already in the early works in this field, especially, by the team of Clément Sanchez and in our cooperation with him.[26,38,43,49,62,86,94] Moreover, if used for heterogeneous catalysis studies, mesoporous oxides need to be used in the form of powders. Therefore, understanding the pore morphology in the powder state is crucial. In the case of PEO_{355}-*b*-PHA_{171}-derived silica, argon physisorption (see Figure 5A,B) reveals a steep uptake at high relative pressures in the adsorption branch speaking for quite large mesopores with uniform size and thus supporting SEM analysis. Evidently, the most striking feature is a very pronounced hysteresis of type H2 indicative of delayed desorption/capillary evaporation. Furthermore, we observe an intrinsic nonclosure of the adsorption and desorption branches at lower pressure, which would suggest irreversible changes (e.g., deformation) of the porous materials matrix.

Applying a dedicated NLDFT adsorption branch kernel on the adsorption branch (see Experimental Section) of the argon 87 K data (Figure 5A) reveals a bimodal pore size distribution (Figure 5B) exhibiting well-defined micropores centered at around 1 nm and a defined mesoporous system centered at 31 nm (assuming a cylindrical pore geometry). It should be noted that assuming here a cylindrical pore geometry instead of a spherical oneleads to an underestimation of the mode pore diameter of approximately 35% as outlined in ref 95 in detail.[95] Thus, the true mode pore diameter of the spherical mesopores should be around 42 nm. Indeed, the latter mode pore diameter is observed in the SEM analysis (Figure 5C). The widths of the mesopore size distributions derived from physisorption and

https://doi.org/10.1021/acs.chemmater.3c01255
Chem. Mater. 2023, 35, 9879−9899

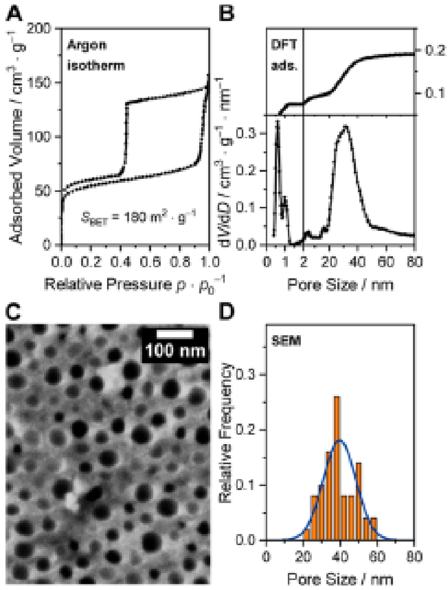

Figure 5. (A) Argon isotherm at 87 K of mesoporous silica derived from PEO$_{355}$-*b*-PHA$_{171}$ and (B) corresponding pore size distribution obtained from the adsorption branch with an NLDFT kernel for cylindrical pores. In addition, a (C) SEM image of the mesoporous system is given with the (D) resulting pore size distribution from electron microscopy.

SEM (Figure 5D) are in good agreement. The SEM-based pore diameter of (42 ± 9) nm was determined by building an average diameter of 50 pores observed in Figure 5C. Beside the limitations of SEM, such as being only a local method, this approach is expected to yield a slightly smaller pore size as a cut through the mesoporous system most likely will not occur along the center of the spherical pores (see Figure S14). However, as discussed in the Supporting Information in more detail, this underestimation (of 9 nm at maximum) is comparable to the width of the pore size distribution, and the pore size evaluation by SEM is supported by further experiments as well (see below).

Comparing the pore size distribution derived from the adsorption branch (which considers the delay in condensation due to the metastable pore fluid) with that of the desorption branch (using argon, Figure S15B), quite distinct different distributions are obtained. From this mismatch, a delayed mesopore emptying can be concluded and attributed to either pore blocking or cavitation.[46,95,96] Cavitation-induced evaporation is expected to occur when the neck sizes are smaller than circa 5 to 6 nm, independent of the actual value of the neck size, while pore blocking/percolation occurs for larger neck sizes. In order to distinguish whether pore blocking or cavitation is the underlying phenomenon affecting pore evaporation, we apply a method suggested in ref 46, i.e., which involves the use of two adsorptives: here, nitrogen (at 77 K) and argon (at 87 K); the respective adsorption isotherms are displayed in Figure S15A. While cavitation depends solely on the state of the fluid in the pore cavity (thermodynamics), the pore blocking evaporation–desorption mechanism is controlled by the size of the pore necks/restrictions (morphology). Thus, in the case of pore blocking, the pore size distribution (PSD) should be independent of the adsorptive. However, the desorption-derived PSD from the argon isotherm does not match that of the nitrogen-based one (see Figure S15C). As a result, pore blocking can be excluded, and the pore size distribution from the desorption branch does not provide the actual (small) pore neck size. Thus, cavitation is the dominant emptying mechanism.

Further means to elucidate the pore connectivity and to differentiate between cavitation and pore blocking are possible by recording a hysteresis scan. Here, multiple desorption branches are measured after partial pore filling. These partial desorption branches converge in the lower closing point of the adsorption and desorption branch in the case of pore blocking. In the case of cavitation, all partial desorption branches show a horizontal behavior down to the relative cavitation pressure, at which an abrupt and entire pore emptying occurs in all cases. The hysteresis scan shown in Figure 6 corresponds to the second case, i.e., confirms the presence of cavitation. The underlying process is sketched in the inset of Figure 6: with decreasing relative pressure, no evaporation can initially take place due to the small pore neck. At the relative cavitation pressure—in this case 0.45 for argon—a sudden and complete evaporation occurs because the liquid state becomes thermodynamically unstable, and bubbles are formed within the filled mesopore spontaneously. This thermodynamically driven cavitation pressure depends on both the adsorptive (and temperature) and weakly on the size of the underlying restricted mesopore, as shown in Figure S16.[41] In the case of nitrogen as adsorptive (Figure S15A), cavitation-based pore emptying occurs at a relative pressure of 0.50, which represents the bulk cavitation pressure of nitrogen and continues the saturation curve of cavitation pressure versus mesopore size reported by Rasmussen et al.[41] and summarized in Figure S16.

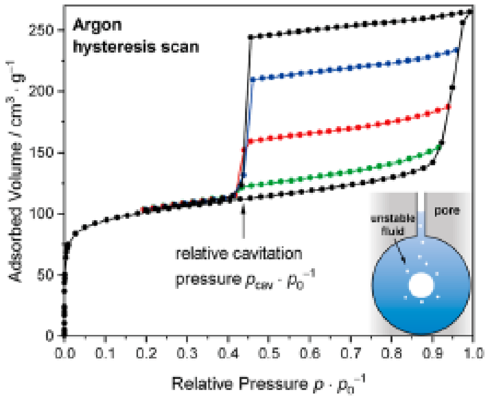

Figure 6. Argon hysteresis scan at 87 K of mesoporous silica derived from PEO$_{355}$-*b*-PHA$_{171}$ consisting of the boundary loop (black), the first (blue), second (red), and third (green) desorption scans. Furthermore, the relative cavitation pressure is labeled and a scheme showing the pore emptying upon cavitation is depicted.

While the pore size distribution in Figure 5B claims the presence of micropores of 1 nm in size, the cavitation study reveals that the spherical mesopores are mainly interconnected by very small pores, likely the aforementioned micropores. Based on these findings, two boundary cases are feasible to describe the pore morphology: (1) the spherical block copolymer micelles barely overlap during the templating process, causing a small pore window as illustrated in model 1 in Figure 7. As an alternative, (2) the spherical micelles might be isolated with the PEO block partly collapsing onto the PHA core

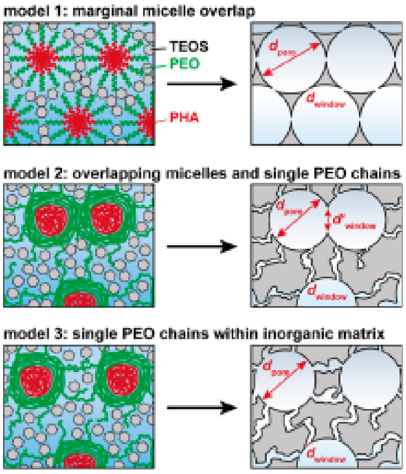

Figure 7. Possible pore models comprise (1) spherical mesopores with a low micelle overlap and thus small pore windows, (2) spherical mesopores being connected by large mesopore windows or small micropore channels, and (3) spherical mesopores being solely connected with each other by micropores. The pore formation via the micelles consisting of a PEO (green) and PHA block (red) is shown on the left-hand side.

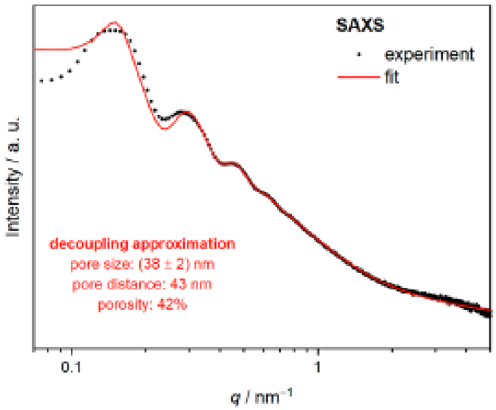

Figure 8. SAXS curve of mesoporous silica derived from 57 vol % PEO_{355}-*b*-PHA_{171} (black) and fitted scattering curve (red) according to a Percus−Yevick model (decoupling approximation) for spherical pores.

and partly penetrating the inorganic gel phase as single chains. Calcination would then lead to almost isolated spherical mesopores being connected only by PEO-single-chain-derived microchannels (model 3 in Figure 7). This model is supported by other templates showing hairy core−shell micelles and a microchannel diameter of 0.5−1 nm found for single PEO chain templating.[34] Generally, a high fraction of PEO is well-known to be embedded in the siliceous phase.[97−99] In between, a third model is plausible, allowing for a less restricted pore connectivity: in the case of readily overlapping hairy micelles, a model can be deduced with mesopores being connected with adjacent pores by smaller mesopore windows and/or microchannels, as shown in model 2 in Figure 7. In this case, cavitation can be explained by the end of a percolation path made up of well-connected large mesopores being connected to the exterior or other percolation paths by microchannels exhibiting characteristic pore diameters below approximately 6 nm (in the case of larger pore windows, cavitation cannot occur).

In order to further elucidate and quantitatively describe the mesopore space, small-angle X-ray scattering (SAXS) was performed. This method helps to understand which of the aforementioned models (Figure 7) of the spatial distribution of the spherical mesopores represent a suitable description of the metal oxide. The SAXS curve of mesoporous silica derived from PEO_{355}-*b*-PHA_{171} exhibits a series of form factor oscillations speaking for a defined pore shape and narrow pore size distribution. By modeling the SAXS curve (Figure 8) with a theoretical function based on the Percus−Yevick structure factor,[38,100−102] pore size, pore-to-pore distance, and the porosity can be estimated using a polydisperse form factor for spheres. In spite of this simple approach, the modeling (Figure 8) is surprisingly good, especially, in regards to the form factor oscillations allowing for at least semiquantitative determination of structural parameters. The average pore diameter obtained from SAXS amounts to 38 nm and is in good agreement with the SEM analysis (42 nm), as shown in Figure 5C,D. Compared with the results of fitting the SAXS curve of the gel prior to calcination (Figure S13C), a shrinkage of the assembled spherical porogen by 17% occurs upon drying and mesopore formation (see Experimental Section and Supporting Information for more details). Regarding the mesoporosity, a volume fraction of 42% determined from SAXS seems reasonable, as a polymer volume fraction of 57% was chosen in the synthesis. This value is given as the volume fraction of template (i.e., corresponding to the pore volume after calcination) with respect to the overall volume (template and metal oxide assuming full conversion of the precursor). A detailed description can be found in the Supporting Information with eqs S5 and S6. A deviation is possible in the case that the polymer blocks are more densely packed in the block copolymer micelles than in the respective homopolymers used for estimating the density of the block copolymer. However, a porosity of only 30% can be derived from the argon physisorption analysis (total pore volume in Figure 5B) according to eq S7 being significantly lower. Since SAXS is capable of probing even isolated pores, one explanation could be that not the entire pore system is accessible to the adsorptive. On the other hand, the porosity determination by SAXS using the aforementioned approach shows a relatively large uncertainty: Only one prominent SAXS maximum of the lattice factor ("Bragg" signals) is observed, the interpretation of which in terms of a defined packing of spheres is impossible. Hence, an exact lattice constant cannot be determined from SAXS. The Percus−Yevick lattice factor used herein provides reasonable semiquantitative values for the pore-to-pore distance and the volume fraction of pores, which suffer from an uncertainty of certainly up to 20%. Still, the pore-to-pore distance obtained from this analysis reveals interesting insights: An average pore distance of 43 nm combined with a pore size of 38 nm would suggest a pore wall thickness of 5 nm according to SAXS. Taking the SEM image (Figure 5C) into account, however, this value appears too small. This underestimation could be a result of some overlapping mesopores (with a pore distance being smaller than the pore size), hinting for model 2 in Figure 7 as a plausible description. The pore distance obtained with this model seems reasonable, as the position of the "Bragg" signal at $q = 0.15$ nm^{-1} hints at a comparable lattice distance of 42 nm (inverse of scattering vector s).

Another general approach to judge the plausibility of model 1 in Figure 7 comprises variation of the polymer concentration

https://doi.org/10.1021/acs.chemmater.3c01255
Chem. Mater. 2023, 35, 9879−9899

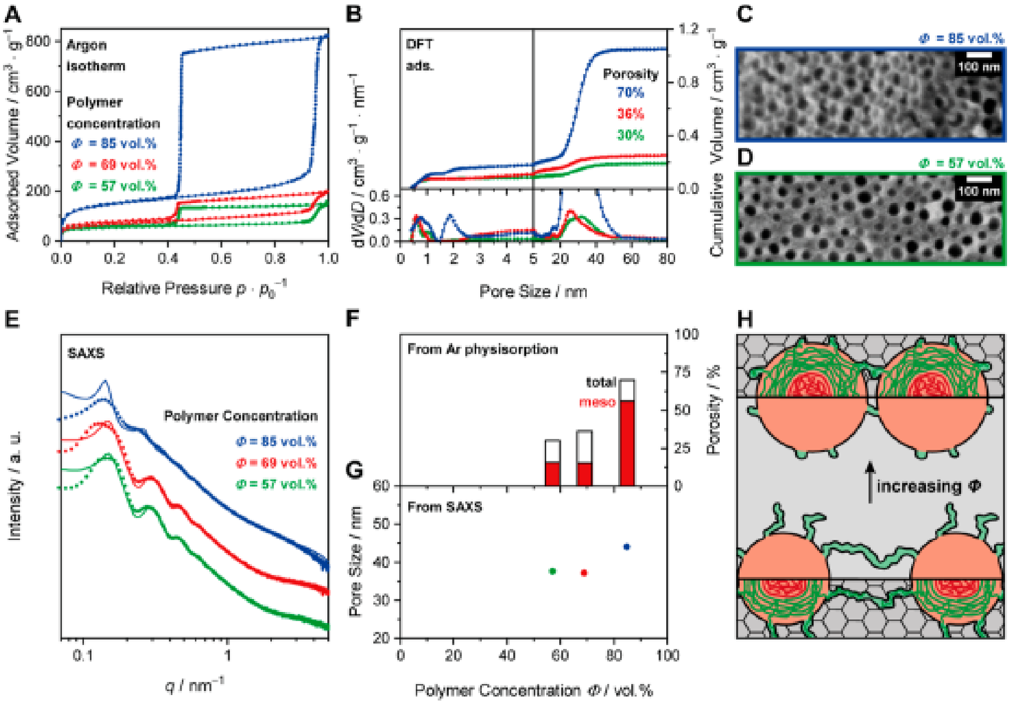

Figure 9. (A) Argon (87 K) isotherms of mesoporous silica prepared with a PEO_{355}-*b*-PHA_{171} volume fraction of 57 (green), 69 (red), and 85 vol % (blue) as well as the (B) respective pore size distributions derived from the adsorption branches with an NLDFT kernel for cylindrical pores. In addition, SEM images of mesoporous silica obtained with the (C) highest and (D) lowest template amount are shown as well as (E) SAXS curves of mesoporous silica prepared with 57 (green), 69 (blue), and 85 vol % PEO_{355}-*b*-PHA_{171} together with the corresponding fits (solid lines). (F) Overall porosity and the contribution of the mesopores (red) are contrasted to the (G) pore size from SAXS as a function of the template amount. (H) Contribution of the PEO block (green) to the micropores is sketched for two different template amounts.

during the templating process. The rationale behind are micelles being forced into closer contact upon increasing template content while keeping the precursor amount constant.[76,88] If model 1 holds true, the mutual mesopore connectivity is then expected to be enhanced and the extent of cavitation in physisorption experiments might be altered compared to the sample, as shown in Figure 5. Looking at the argon physisorption isotherms of silica prepared with different polymer concentrations during the templating step (Figure 9A), a clear increase in specific pore volume and thus porosity with increasing template amount can be seen, as shown in Figures 5, 6, and 8. In addition, the SEM images of the highest (Figure 9C) and the lowest polymer amount (Figure 9D) confirm a decrease in pore-to-pore distance with increasing template concentration, i.e., the mesopores being in a closer vicinity. However, the pronounced cavitation-based hysteresis remains in all isotherms. Also, the pore size distribution (Figure 9B) is very similar for all template concentrations. Hence, in spite of being of similar size and in closer contact, the pore connectivity is unchanged although the number of accessible mesopores increases. By that, a small connecting pore size as a result of a small pore-to-pore distance (model 1) can be excluded.

It is worth mentioning that the corresponding SAXS curves (Figure 9E) of the mesoporous silica materials reveal a slight increase in pore size of the spherical mesopores with increasing polymer concentration; namely, from 38 nm (57 vol %) to 44 nm (85 vol %) as plotted in Figure 9G. Such a trend was also found for other PEO-containing templates like Pluronic F127[103] and some PEO-*b*-PS[104] copolymers. Furthermore, the contribution of the mesopores to the total pore volume increases with increasing template concentration, considering the cumulative pore size distribution (Figure 9B). Comparing the mesopore volume (red bar in Figure 9F) to the total pore volume (micro- and mesopore volume, white bar in Figure 9F), the mesopore contribution increases from 52% (template concentration of 57 vol %) to 80% (85 vol %)—see eq S8 in the Supporting Information for more details. Since pore connectivity model 1 in Figure 7 can be excluded, the aforementioned two observations can be explained with a consecutive withdrawal of the PEO single chains from the surrounding matrix with increasing template concentration and thus decreasing the micelle-to-micelle distance. As illustrated in Figure 9H, the more the micelles approach each other within the templating step, the more PEO single chains partly collapse onto the PHA core in order to avoid an entropically unfavored chain entanglement. Consequently, a smaller fraction of micropores and a slightly larger mesopore size are observed after calcination. This shows that the template concentration does not affect the pore wall thickness in a trivial fashion as expected from literature,[76] but the behavior of the PEO chains might significantly change upon concentration variation, e.g., because of different solvation and entropy effects as already proposed for other types of PEO-containing block copolymers.[34]

So far, one of the proposed pore connectivity models (Figure 7) can be ruled out, but still, the questions remain whether the mesopores are indeed as poorly connected and thus hardly accessible as the isotherms in Figure 9A suggest. On the other hand, it should be noted that the physisorption analysis

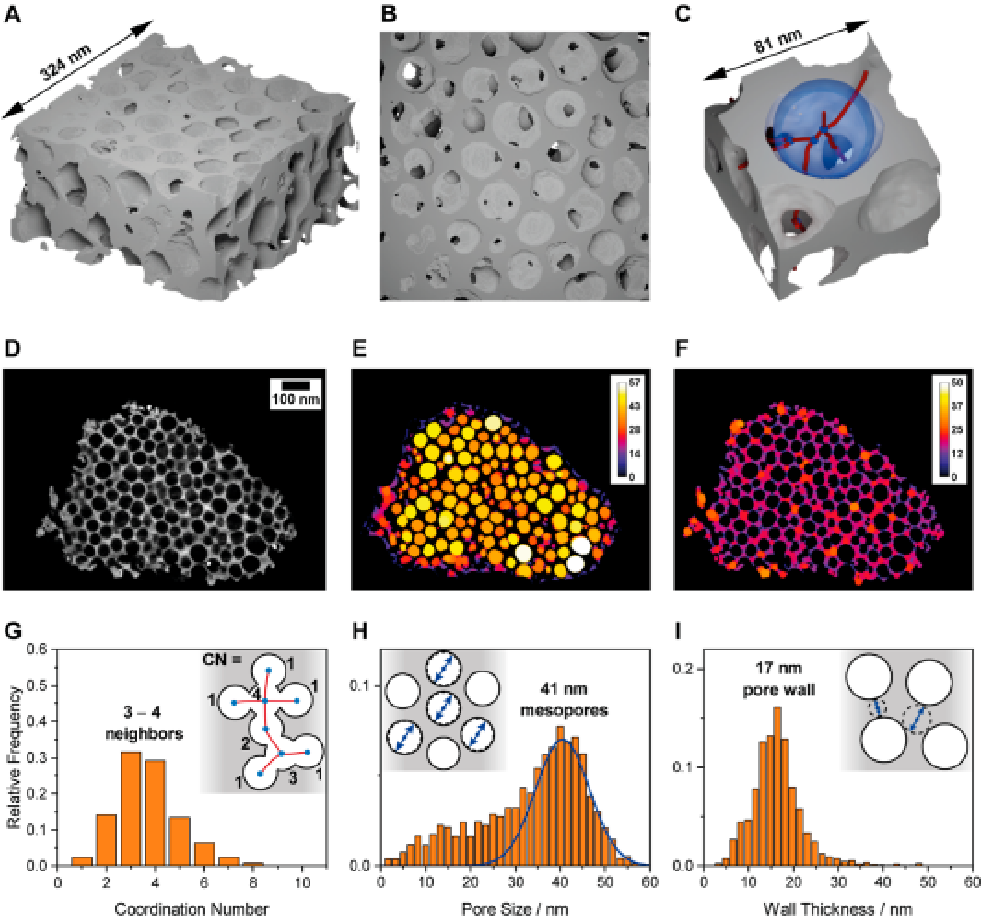

Figure 10. (A) Side- and (B) top-view of the STEM-based three-dimensional reconstruction of the pore system of mesoporous silica prepared with 85 vol % PEO_{355}-*b*-PHA_{171}. (C) Magnified cutout highlights the pore windows by showing the pore skeleton (red) and the sphere (transparent blue) used for determining the coordination number of the pore. Moreover, one slice of the model is exemplified showing the (D) two-dimensional pore morphology, (E) color-coded mesopore sizes from small (dark) to large (bright), and (F) color-coded wall sizes in units of nm each. The respective distributions of the (G) average number of neighbors connected through a mesopore to the regarded pore derived from skeletonization, (H) pore sizes, and (I) wall thickness within the entire reconstructed particle are shown below. The definition of the coordination number (CN) is illustrated by a sketched pore network, including the skeleton (red) and the respective coordination number (black number) for each pore. Similarly, the definition of the pore size and wall thickness by the local thickness approach is shown by a sketched pore system.

performed here provides only limited information on pore connectivity; i.e., this method can only suggest in which way the spherical mesopores are accessible from a surrounding bulk gas phase. However, only limited information on the connectivity between the mesopore cavities in the interior of the particle can be obtained. Hence, to peer into fine details of the mesopore space in PEO_{355}-*b*-PHA_{171}-derived mesoporous silica, a 3D model of the pore system was reconstructed from angle-dependent STEM images of one particle of the material (STEM-based tomography). This method is particularly suitable and accurate here as (1) the alignment and reconstruction errors (e.g., missing wedge) are low due to the large tilt range of 142° and the high electron contrast between the sample and the gold fiducial points and (2) the method provides a resolution down to 1 nm being significantly larger than the pore size.[105,106] The STEM analysis for mesoporous silica prepared with 85 vol % template is shown in Figure 10A,B and nicely reveals an ordered array of spherical mesopores, the shape of them being slightly deformed. Already qualitatively, the reconstruction confirms the presence of spherical mesopores being connected through larger pore windows (in addition to micropore channels as derived from physisorption). Especially, the top-view in Figure 10B shows several pore windows being larger than 10 nm and enabling a view even through the entire cutout. We will discuss this apparent contradiction between tomography and physisorption in regards to the connectivity between the spherical mesopores afterward. A few exemplary pore windows are highlighted in a smaller magnified cutout in Figure 10C.

A statistical description is possible by a skeletonization approach in which the binary pore system is iteratively thinned to the centerline until a one-pixel thick skeleton is obtained (red skeleton in Figure 10C). All spheres (representing the pores) from a local thickness determination are aligned to this skeleton, and the number of branches leaving a sphere is counted (transparent blue sphere in Figure 10C). For instance, the sphere in Figure 10C contains three junctions of the skeleton (small solid blue spheres), which are summarized, leading to one pore with a coordination number of six (the definition of the coordination number is illustrated in Figure 10G). A detailed description of this algorithm can be found elsewhere.[81,82] According to this evaluation, each spherical mesopore is on average connected to three to four adjacent spherical mesopores as shown in the distribution of the coordination number in Figure 10G. Since electron tomography is not able to resolve micropores, each visible pore window has a dimension of mesopores. The size of these connecting mesopore windows can be estimated by determining the minimum diameter (in the local thickness of the pore phase) along the skeleton connecting two different pores.[82] As shown in the pore neck size distribution in Figure S17A, the connecting pores most frequently possess a diameter of 15 nm. Still, the distribution is very broad, and rather a range of 10−30 nm should be concluded. The reason why such a number of pore connections does not arise from the 2D slice of the reconstruction (Figure 10D) is the fact that the large mesopores do not necessarily have to be connected along this slice plane but might be linked in all remaining directions of space. This significantly decreases the probability of finding a pore window in one single plane and causes a pore image appearing rather isolated. The same holds true for the top-view obtained from SEM: Only a few pore windows can be observed in Figure 9C, which is further hampered by the low lateral resolution of this method. Yet, a certain number of well-connected mesopores can also be found by SEM, e.g., in a mesoporous silica prepared with 80 vol % PEO_{355}-*b*-PHA_{171} (Figure S18).

Besides pore connectivity, STEM-based tomography offers the opportunity of a precise pore size and even wall thickness evaluation. Especially the latter is normally not directly accessible in form of a size distribution by other methods such as SAXS. Using the local thickness approach (plugin of ImageJ), the pore size and pore wall thickness can be determined on a local level as shown in the heat maps of the exemplary slice in Figure 10D for the pore size (Figure 10E) and wall thickness (Figure 10F). Here, the diameter of the largest sphere still fitting in one phase without intruding into the second phase is determined at any point, yielding the local thickness at the given point as shown in the schemes of Figure 10H,I. A more general picture arises from evaluating all slices of the particle yielding the overall pore size distribution in Figure 10H and the overall wall thickness distribution in Figure 10I. The pore wall exhibits a homogeneous thickness of about 17 nm, which is relatively small compared with the pore size but rather large in absolute values. Other templates such as PIB-*b*-PEO lead to pore walls of only 10 nm thickness,[3] which might limit the crystallite growth in crystalline metal oxides and by that negatively influences certain properties (e.g., conductivity in case of conductive metal oxides). A second approach to describe the wall thickness the chord length distribution[82,83] (Figure S17B). A chord is a straight line within the pore wall without passing a phase border. The length of this path depends on the direction, because a chord connecting two adjacent pores is shorter than a tangential chord bypassing several pores. In a statistical description, instead of the minimum diameter of a sphere at one point still fitting in the solid phase (local thickness), a set of chords through a given point connecting the border of the void space each is generated (see Experimental Section and scheme in Figure S17B). The average of this distribution describes the mean length of a straight path through the pore wall connecting two opposing phase borders. This mean chord length might be more useful in terms of e.g., solid-state diffusion (diffusion pathways) in the case of conducting solids, while the local-thickness-based wall thickness might be more useful for mechanical studies. In this case, a mean chord length of 42 nm is obtained being naturally larger than the average wall thickness (17 nm) from local thickness.

The mean pore size of 41 nm is in good agreement with those of SEM (Figure 5D) and SAXS (Figure 8). Additionally, a significant number of small pores contribute to the tomography-based pore size distribution. However, these pores result from an artifact of the background subtraction. The latter is necessary to avoid that the local thickness analysis regards the background as one large pore. However, the pores located at the particle surface, i.e., the small pores at the particle border shown in violet in Figure 10E are then assigned to 10−15 nm pores because they are not entirely covered by the silica phase, although they are actually as large as the mesopores in the bulk. For this reason, a distribution as shown in blue in Figure 10H is more representative (leading to a mean pore size of 41 nm) than the entire histogram shown in orange (mean pore size of 35 nm). The deviation of the blue fit from the measured histogram in Figure 10H between 20 and 30 nm can be explained with the contribution of the pore windows (Figure S17A) to the pore size distribution, which exhibit a significant fraction of pores of this size. Still, the blue distribution is more accurate to estimate the size of only the spherical mesopores, subtracting the surface artifacts and the pore windows. Regarding the possible error while deducing the pore size by STEM tomography, a pixel size of 1.62 nm must be considered. In the worst case, the two voxels at each end point of the diameter of the pore (better to say: largest sphere still fitting in the pore in the local thickness approach) are incorrectly assigned to the wrong phase. This leads to an uncertainty of the pore size of roughly 3 nm, as shown in Figure S17C.

Furthermore, tomography gives access to a statistical evaluation of the pore-to-pore distance. Building an average of 114 mesopores and plotting the distance of the respective pore to all remaining pores in the particle (1388 detected pores) yielded the distribution depicted in Figure S17D. From the first maximum, a mean distance between two adjacent pores of 56 nm can be estimated, which is in good alignment with the sum of the average mesopore size (Figure 10H) and wall thickness (Figure 10I). Yet, by modeling the SAXS curve using the aforementioned theoretical scattering function (Percus−Yevick-type analysis,[38] blue data in Figure 9E), a pore-to-pore distance of 48 nm is obtained, which is different from STEM analysis but of a comparable order of magnitude and further supports the STEM-based result. Note that the average pore-to-pore distance obtained from SAXS analysis lacks accuracy as described above, and a deviation of 15% is within the uncertainty of this analysis. The Percus−Yevick approach is based on a statistical spatial distribution according to a hard sphere potential of spheres providing a lattice factor with an average distance and fraction of spheres. However, if the arrays of spheres might possess a more regular packing, the first SAXS maximum has to be converted into a pore-to-pore distance by a different geometrical relationship (e.g., face-centered cubic lattice), which goes beyond this study. For this reason, we present a more extensive and accurate evaluation of the SAXS data in a follow-up study. Counting the respective number of pores, i.e., the integral of the blue curve in Figure S17D, gives an idea of the total coordination number (including also the pores connected by micropores and isolated ones), which amounts roughly to 12. However, the coordination number determination is strongly hampered by the distances to the pores of the second coordination sphere (expected at approximately 85 nm in Figure S17D assuming a face-centered cubic lattice) overlapping with the first one. A coordination number of 12 hints at a face-centered packing of the pores, but further studies will be conducted in the near future. Summing up, the STEM-based tomography shows that the 40 nm mesopores are better connected than the argon physisorption suggests and pore windows of >10 nm are present, which connect the large mesopores with each other. Thus, a pore model as depicted in model 2 in Figure 7 is suitable to describe the PEO_{355}-*b*-PHA_{171}-derived pore system best. The pronounced cavitation observed in physisorption (Figure 9) most likely is thus a consequence of dead-ends, which represent the end of a percolation path made up of well-connected mesopores. These dead-ends are then connected to other percolation paths or the exterior only by micropores and act as a bottleneck for evaporation (see Figure 11). Yet, this does not exclude the presence of some isolated mesopores (model 3) being only connected by micropores to the surrounding mesopore space. These can be found to a certain minor extent in the reconstruction as well.

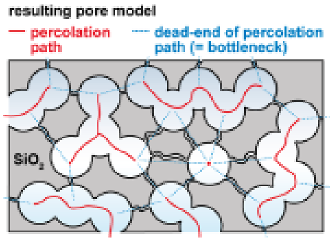

Figure 11. Schematic representation of the pore connectivity model of mesoporous silica based on physisorption, SAXS, and electron tomography comprising percolation paths (red solid line) of well-connected mesopores, which are connected to other percolation paths or the exterior by micropores (blue dotted line).

Mesoporous Zirconium Dioxide. Despite the state-of-the-art analysis, the origin of the connecting micropores remains an important feature with respect to the usability of these PHA-*b*-PEO block copolymers. In principle, there are two possibilities: (1) the micropores originate from single PEO chains leaving microchannels behind after calcination or (2) the micropores belong to random, intrinsic cracks of the silica material. To tackle this question, a mesoporous silica thin film was prepared by spin coating using PEO_{355}-*b*-PHA_{171} as a soft template. In addition to the mesoporous thin film, a reference film without a structure-directing agent was synthesized. The basic idea to study the connectivity between the spherical mesopores is to drop cast a tracing solution (here: cobalt nitrate) and monitor the distribution of Co^{2+} ions within the thin films by ToF-SIMS.[14] By that, the depth profile can provide information on the accessibility of the mesopore structure for an electrolyte solution on the one hand and, on the other hand, whether intrinsic cracks allow for a decent accessibility as well. In the case of a silica thin film, a silicon wafer is not suitable because the substrate and thin film are barely distinguishable. For this reason, an alumina wafer was used, which possesses, however, a very rough structure (as shown in Figure S19G,I). Thus, a mesoporous zirconium dioxide thin film on a silicon wafer was prepared in addition. This system benefits from knocking out the strong roughness of the alumina wafer and, on top, delivers information on the mesopore accessibility for a crystalline metal oxide (which are frequently used as catalytic materials). In contrast to amorphous silica acting as ideal replica of the template,[32,45,107,108] a crystalline material might yield a different pore connectivity since an increase in density takes place upon crystallization. The latter occurs by a change in volume and thus might result in a widening of the pore windows. In addition, the DLS study in Figure 4B evokes a potential dependency of the soft templating on the metal oxide precursor used. Thus, the suitability of PEO-*b*-PHA as a template for other metal oxides might not be straightforward. According to the SEM image of the mesoporous ZrO_2 thin film (Figure 12G), the pore size amounts to (41 ± 7) nm and matches the pore size of the silica counterpart (e.g., Figure S19H). Consequently, PEO-*b*-PHA is apparently able to yield ordered mesoporous ZrO_2 as well. An investigation by ellipsometry yields a film thickness of 122 nm and a refractive index of 1.2945, which corresponds to a porosity of 66%.[27] Besides the morphological investigation, the presence of crystalline ZrO_2 can be confirmed by grazing incidence (GI) XRD. The diffraction pattern in Figure S20A reveals that the thin film consists mostly of monoclinic ZrO_2 but traces of the tetragonal phase are discernible as well. As for the ZrO_2 thin films, the depth profile of different ion species after electrolyte impregnation and drying is shown in Figure 12A for the mesoporous case and in Figure 12B for the untemplated (dense) counterpart. Comparing the evolution of the Co^+ signal with that of the ZrO^+ signal in the depth profile of the mesoporous film (Figure 12A), we find an almost perfect agreement of both shape and intensity. After an initial plateau, both profiles show a decay with proceeding sputtering. In contrast, the SiO^+ signal originating from the substrate offers the exact opposite behavior: at the beginning, i.e., at the film's surface, almost no Si species is detected, but with increasing sputtering time the SiO^+ signal gains intensity simultaneously to the decay of the ZrO^+ and Co^+ signals. While the opposing trends of the ZrO^+ and SiO^+ signals are expected for a layered structure, the high concentration of cobalt ions deep in the ZrO_2 thin film and especially the comparable shape of the Co^+ and the ZrO^+ signal evolution suggest an in-depth infiltration by a cobalt-ion-containing solution and hence an interconnected pore system. Consequently, the 3D overlay in Figure 12C clearly confirms a homogeneous and complete infiltration of the pore system by the tracing solution, as schematically sketched in Figure 12D.

As for the dense reference film, the ZrO^+ and SiO^+ signals in the depth profile (Figure 12B) behave similarly to those of the mesoporous film (Figure 12A) but the Co^+ signal quickly drops at short sputtering time and shows a relatively low intensity afterward. This trend strongly hints at a Co-based wetting layer on the ZrO_2 surface, which is further supported by the overlay in Figure 12E, in which a three-layered structure is discernible, as illustrated in Figure 12F. Hence, the absence of infiltration by the tracing solution can be derived. Albeit the thin film is very smooth, a sharp transition between the thin film and the wafer can be observed neither in the mesoporous sample (Figure 12A) nor in the dense one (Figure 12B). Also, the transition is blurred in the overlays in Figure 12C,E implying an interdiffusion between the ZrO_2 and Si phase. However, this does not necessarily represent the actual spatial distribution, as an ion mixing effect leading to a delay between the intensity increase of the substrate's ion signals and the decay of the coating signals is often observed in SIMS.[14] As a consequence of the rather harsh bombardment of the secondary ions, sharp interfaces cannot be

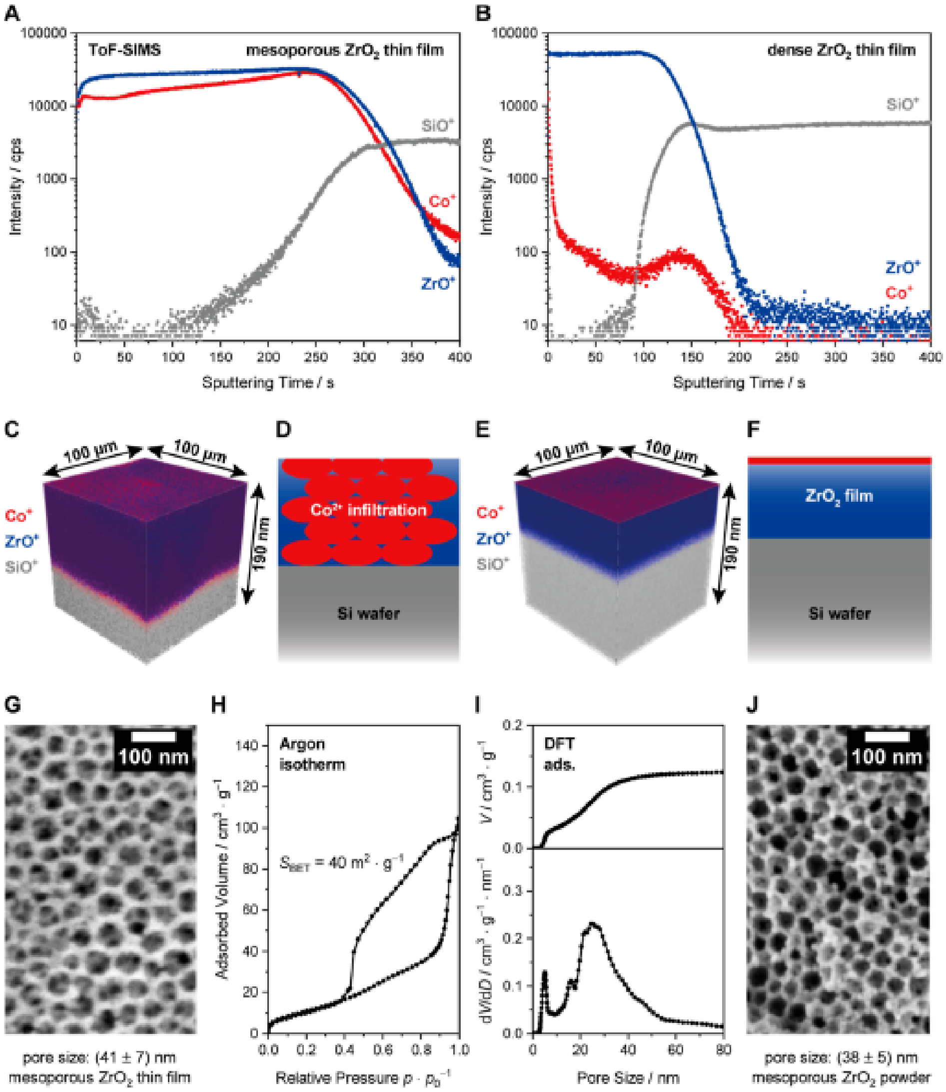

Figure 12. ToF-SIMS depth profile of a (A) mesoporous ZrO_2 thin film infiltrated with a cobalt nitrate solution including the signals of the ions Co^+ (m/z = 59), ZrO^+ (106), and SiO^+ (44) and a (B) dense ZrO_2 reference film without PEO-*b*-PHA template including the signals of Co^+, ZrO^+, and SiO^+. The 3D overlay of the Co^+, ZrO^+, and SiO^+ signals as well as a schematic representation of the underlying situation is shown for the (C,D) mesoporous and (E,F) dense ZrO_2 film. Additionally, SEM images of the (G) mesoporous ZrO_2 thin film and (J) mesoporous ZrO_2 powder are given for comparison, as well as the (H) argon isotherm at 87 K of the mesoporous ZrO_2 powder with the (I) corresponding pore size distribution derived from the adsorption branch with an NLDFT kernel for mesoporous silica with cylindrical pores.

resolved. The crater depth was determined by profilometry and amounts to 190 nm in both cases. Since the sputtering rate, i.e., the crater depth evolution with sputtering time, depends on the material, only the sputtering time is given in Figure 12A,B and consequently only the overall crater depth can be obtained. Compared to the thin film thickness of 122 nm obtained from ellipsometry, however, this value for the crater depth is reasonable.

In the case of templated and untemplated silica films (Figure S19), an analogous result is observed although the rough substrate causes a height difference within the thin film leading to a rather blurred profile for the dense film (Figure S19B,E). Collecting the results of the mesoporous and the dense reference film together, the interconnected pore structure observed in the tomography of mesoporous silica powder is confirmed by the full impregnation of the porous silica film. The cobalt wetting layer in the case of the dense film, however, shows no penetration of the tracing solution, which implies that only the pores generated by the template are responsible for the infiltration observed in Figure 12C. Thus, the micropores that connect the mesopores in the case of the mesoporous system are most likely the result of single PEO chains and not of random cracks.

The influence of crystallinity on pore connectivity is difficult to investigate in the thin film state. Indeed, Figure 12G clearly shows the pore structure even below the surface of the ZrO_2 thin film, which thus seems to be readily accessible from the top. Also, the ellipsometric porosimetry measurements of a mesoporous metal oxide thin film by Lokupitiya et al.[76] gave rise to a type IV isotherm suggesting an easily accessible pore network. However, a quantitative interpretation is hardly possible by, e.g., gas physisorption experiments. For this reason, a mesoporous ZrO_2 powder was prepared by a sol−gel approach similar to that of SiO_2 in order to investigate the porosity in terms of pore blocking by physisorption. The presence of tetragonal ZrO_2 (and traces of the monoclinic phase) according to powder XRD (Figure S20B) confirms the successful synthesis of a crystalline material. As for the morphological characterization, spherical mesopores of (38 ± 5) nm in diameter arise from the SEM image (Figure 12J) similar to those of mesoporous silica (Figure 5C). Opposed to the parent silica system, the argon physisorption isotherm in Figure 12H, however, reveals significant evaporation already before the cavitation pressure. Additionally, mesoporous zirconia shows a low amount of micropores, which is an explanation for the apparent low surface area (40 $m^2\,g^{-1}$). Even taking into account that ZrO_2 is almost 3-fold denser than amorphous SiO_2, the surface area of the ZrO_2 powder was adjusted to about 100 $m^2\,g^{-1}$, which is still lower than that of silica (180 $m^2\,g^{-1}$). Instead of micropores, a significant amount of mesopores of ca. 5 nm in size arise from the pore size distribution in Figure 12I hinting at a pore window widening upon crystallization. In conclusion, a comparable pore size and shape are observed in a crystalline metal oxide, but according to physisorption, the pore system is better accessible than in the case of amorphous silica.

Influence of the Block Lengths. Based on the aforementioned results, PEO-*b*-PHA block copolymers seem to be promising soft templates for targeting a large mesopore size of about 40 nm, especially for crystalline metal oxides. However, pore size tuning would be very important for systematic studies and tailoring of porosity-dependent properties. As a proof of concept, four different PEO-*b*-PHA block copolymers were synthesized: two pairs of a constant PEO block length (131 and 214 repeating units, respectively) each with a short (57 and 83) and a long PHA block (322 and 396 repeating units). This set of block copolymers enables a rough estimation of which polymer block governs the mesopore size and to which extent. The SEM images of the mesoporous silica powders after soft templating are collected in Figure 13 together with the corresponding average pore diameter.

It turns out that the average mesopore size increases from 20 to over 40 nm by increasing the PHA block length from ca. 70 to over 300 repeating units (for both PEO block lengths). However, the PEO block length does not seem to affect the pore size significantly. Especially in the case of the short PHA block, doubling the PEO block length, surprisingly, keeps the mesopore diameter untouched (20 nm in both cases). These observations are qualitatively confirmed by the pore size distributions derived from argon physisorption (Figure S21B) although slight shifts of the pore size distribution between the silica powders from PEO_{131}-*b*-PHA_{57} and PEO_{214}-*b*-PHA_{83} as well as between PEO_{131}-*b*-PHA_{396} and PEO_{214}-*b*-PHA_{322} are apparent. This, however, can be explained by the PHA block length not being exactly of the same size each. However, the PEO_{131}-*b*-PHA_{396}-derived silica renders an exception from this trend. There, the pore structure seems less ordered and homogeneous than in the other three samples. One reason might be that a very short PEO block combined with a very large PHA block might not be sufficient to screen the entire PHA core from the polar solvent, and hence, no stable micelles are formed. Following the concept of the packing parameter, the formation of vesicles might be favored,[60,61] which is supported by the rather heterogeneously shaped mesopores in the SEM image (Figure 13D) partly containing small metal oxide spheres in the pore center. As a result, the polydispersity in pore size as seen in SEM is rather large, and the PSD from argon physisorption is too blurred to be accurately evaluated. Similarly, Dunphy et al. observed a phase separation of Pluronic polymers during soft templating of silica for small PEO amounts yielding large pores due to the packing-related formation of vesicles.[103] Still, comparing the four argon isotherms to each other, the shapes are very similar in all cases, highlighting the reproducibility of the synthesis as well as the homogeneity of the pore structure along the sample series.

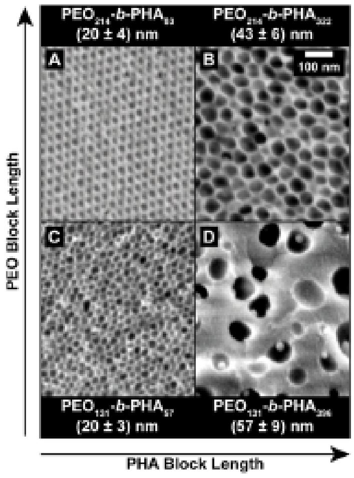

Figure 13. SEM images and average pore sizes of mesoporous silica synthesized with PEO-*b*-PHA block copolymers of varying PEO and PHA block lengths: (A) PEO_{214}-*b*-PHA_{83}, (B) PEO_{214}-*b*-PHA_{322}, (C) PEO_{131}-*b*-PHA_{57}, and (D) PEO_{131}-*b*-PHA_{396}. The last sample is not included in the quantitative comparison due to the pore structure most likely not resulting from soft templating with polymer micelles.

If the pore structures are very similar and the PEO block length does not influence the pore size, then the question arises whether the PEO block affects the templating process after all. Reconsidering the aforementioned model of hairy micelles, i.e., a PHA core on which the PEO block partly collapses, while the rest remains as single stretched out PEO chains, the PEO block length should govern the amount of micropores (see scheme in Figure S21C) after templating and should affect the mesopore volume only moderately. In this regard, the mesopore volume fraction Φ_{meso} defined by the mesopore volume (red fraction in Figure S21D) divided by the total pore volume (sum of red and green part in Figure S21D) is a suitable descriptor to investigate the relative amount of meso- and micropores, respectively. With increasing PEO block length, the contribution of the mesopore volume to the total pore volume decreases from 62% (PEO_{131}-*b*-PHA_{57}) to 54% (PEO_{214}-*b*-PHA_{83}) being in good agreement with the expectation that the mesopores contribute less to the overall pore volume because more micropores are present. Analogously, Φ_{meso} increases with increasing PHA block length from 54% (PEO_{214}-*b*-PHA_{83}) to 64% (PEO_{214}-*b*-PHA_{322}) confirming the increasing amount of mesopores keeping the micropore fraction constant. Within this sample matrix, the PEO_{131}-*b*-PHA_{396}-derived silica should possess the highest value, comprising the shortest PEO and the longest PHA block. However, in this case, Φ_{meso} = 54% is observed but this value cannot be compared with the other materials due to the different pore structure (vesicles versus micelles). As the polymer volume used for templating was kept constant in all samples, it can be concluded that the PEO block length mainly governs the micropore amount, while the PHA block length influences the mesopore dimension. Regarding the template system poly(*N,N*-dimethylacrylamide)-*block*-poly(styrene), Billet et al.[54] observed a mesopore size increase with increasing PS block length, i.e., micelle core size. This monovariant study confirms the crucial role of the micelle core, although the role of the second block length is not sufficiently understood. Nevertheless, a word of caution is necessary since the number of studied polymers is very small here. Especially, the PEO_{131}-*b*-PHA_{396}-derived silica forms a missing puzzle piece because this template does not result in an ordered mesopore system and is not suitable for comparison. Here, further studies with a larger library of block copolymers are necessary to deeply understand the role of both block lengths for soft templating. Still, the small series in Figure 13 confirms that pore size tailoring is possible with the PEO-*b*-PHA block copolymer system.

CONCLUSIONS AND OUTLOOK

In this study, a facile synthesis of PEO-*b*-PHA block copolymers based on a supplemental activator reducing agent atom transfer radical polymerization is presented, establishing a block copolymer system with tunable PEO and PHA block lengths. These polymers have been used up until now for the preparation of mesoporous metal oxide thin films, and building on this we expand the soft templating procedure to metal oxide powders as well and confirmed an underlying EISA mechanism. In addition, we show that SEM, argon and nitrogen physisorption, SAXS, and STEM-based tomography provide an in-depth comprehensive investigation of the pore system, mesopore connectivity, and templating behavior. In the case of PEO_{355}-*b*-PHA_{171}, the deduced pore model comprises spherical mesopores of 40 nm in diameter being connected by mesopore windows (above 10 nm in diameter) to three to four adjacent mesopores. In addition, the pore connection through the pore walls being 17 nm thick on average occurs via micropores of 1−2 nm, representing the bottleneck if they are the only connecting pores of the regarded mesopore. Infiltration of mesoporous metal oxide thin films by an electrolyte solution and subsequent ToF-SIMS measurements confirm that these micropores originate from the block copolymer (e.g., from single PEO chains penetrating the inorganic matrix) and not from random intrinsic cracks of the inorganic phase. Furthermore, this experiment demonstrated that the mesoporous scaffold is accessible for a liquid electrolyte, which is of great interest for, e.g., electrocatalytic applications. Especially a crystalline metal oxide (here: ZrO_2 compared to amorphous SiO_2) turned out to possess an ordered mesopore structure with better accessibility than that for SiO_2, as shown by physisorption. In the future, we will simulate a SAXS curve from the STEM-based reconstruction and compare it with the experimental one in order to evaluate if the particle investigated by STEM is representative for the entire sample, and if the tomography-derived results are generally applicable.

By changing the block lengths of both the PEO and the PHA block, the resulting mesoporous silica materials showed a clear dependency of the mesopore size on the PHA block length, while the PEO block mainly governs the amount of micropores in the metal oxide. These results verify that PEO-*b*-PHA block copolymers represent a very promising soft template to target large mesopores (20−50 nm), especially for catalytically relevant metal oxides (often requiring the crystalline state). In particular, the facile pore size variation by adjusting the block lengths pave the way toward systematic studies concerning porosity-property relationships, such as the influence of pore and wall size on the catalytic activity and stability.

ASSOCIATED CONTENT

Supporting Information

The Supporting Information is available free of charge at https://pubs.acs.org/doi/10.1021/acs.chemmater.3c01255.

Image stack of the STEM-based reconstruction of the silica particle; 3D object of a cutout of the STEM-based reconstruction containing the skeleton (ZIP)

Literature review on templating of metal oxides; additional experimental details; ^1H NMR spectra and GPC RI traces of all macroinitiators and block copolymers; further supplemental DLS and SAXS data of the polymer solutions; comparison of adsorptives used; relative cavitation pressure as a function of the mesopore size; STEM-based distributions of the pore neck size, wall chord length, and pore-to-pore distance; ToF-SIMS analysis of silica thin films with corresponding SEM images; XRD patterns of all zirconia samples; argon (87 K) physisorption isotherms and corresponding pore size distributions of all mesoporous silica powders (PDF)

AUTHOR INFORMATION

Corresponding Author

Bernd M. Smarsly − *Institute of Physical Chemistry, Justus-Liebig University, D-35392 Giessen, Germany; Center of Materials Research, Justus-Liebig University, D-35392 Giessen, Germany;* orcid.org/0000-0001-8452-2663; Email: bernd.smarsly@phys.chemie.uni-giessen.de

Authors

Lysander Q. Wagner − *Institute of Physical Chemistry, Justus-Liebig University, D-35392 Giessen, Germany; Center of Materials Research, Justus-Liebig University, D-35392 Giessen, Germany;* orcid.org/0009-0007-9366-6969

Eric Prates da Costa − *Institute of Physical Chemistry, Justus-Liebig University, D-35392 Giessen, Germany; Center of Materials Research, Justus-Liebig University, D-35392 Giessen, Germany; Umicore AG & Co. KG, D-63457 Hanau, Germany;* orcid.org/0000-0001-8163-7828

Chantal Glatthaar − *Institute of Physical Chemistry, Justus-Liebig University, D-35392 Giessen, Germany;* orcid.org/0009-0000-7413-5926

Frederik Breckwoldt − *Institute of Physical Chemistry, Justus-Liebig University, D-35392 Giessen, Germany;* orcid.org/0009-0004-4284-820X

Marco Zecca − *Department of Chemical Sciences, University of Padova, I-35131 Padova, Italy*

Paolo Centomo − *Department of Chemical Sciences, University of Padova, I-35131 Padova, Italy;* orcid.org/0000-0002-0124-9284

Xiaohui Huang − *Institute of Nanotechnology, Karlsruhe Institute of Technology, D-76344 Eggenstein, Leopoldshafen, Germany; Department of Materials and Earth Science, Technical University Darmstadt, D-64287 Darmstadt, Germany*

Christian Kübel – *Institute of Nanotechnology, Karlsruhe Institute of Technology, D-76344 Eggenstein, Leopoldshafen, Germany; Department of Materials and Earth Science, Technical University Darmstadt, D-64287 Darmstadt, Germany; Karlsruhe Nano Micro Facility, Karlsruhe Institute of Technology, D-76344 Eggenstein, Leopoldshafen, Germany;* orcid.org/0000-0001-5701-4006
Helmut Schlaad – *Institute of Chemistry, University of Potsdam, D-14476 Potsdam, Germany;* orcid.org/0000-0002-5824-7204
Manfred Kriechbaum – *Institute of Inorganic Chemistry, Graz University of Technology, A-8010 Graz, Austria*
Heinz Amenitsch – *Institute of Inorganic Chemistry, Graz University of Technology, A-8010 Graz, Austria*
Matthias Thommes – *Department of Chemical and Bioengineering, Friedrich-Alexander University, D-91058 Erlangen, Germany;* orcid.org/0000-0002-3702-4976

Complete contact information is available at:
https://pubs.acs.org/10.1021/acs.chemmater.3c01255

Author Contributions

The manuscript was written through contributions of all authors. All authors have given approval to the final version of the manuscript.

Funding

The research was financially supported by the Funds of the Chemical Industry.

Notes

The authors declare no competing financial interest.

■ ACKNOWLEDGMENTS

The authors thank Raoul Brand and Rafael Meinusch (both Justus-Liebig University) for gas physisorption experiments as well as Sascha Prentzel (University of Potsdam) for GPC measurements. Also, they would like to thank Abdirisak Isse (University of Padova) for useful discussions on the synthesis of the block copolymer. In addition, Svenja Otto (Justus-Liebig University) is acknowledged for ToF-SIMS measurements, Melvin Pradja (Justus-Liebig University) for profilometry and Boris Mogwitz (Justus-Liebig University) for cyro-FIB-SEM experiments. The authors would also like to thank the support of Karlsruhe Nano Micro Facility (KNMFi) for providing access to the TEM instrument as well as the CERIC–ERIC Consortium for the access to experimental facilities and financial support. L.W. thanks the Funds of the Chemical Industry for financial support. X.H. acknowledges the China Scholarship Council (CSC) for the support of her Ph.D. at Karlsruhe Institute of Technology and the Technical University of Darmstadt.

■ REFERENCES

(1) Yarulina, I.; De Wispelaere, K.; Bailleul, S.; Goetze, J.; Radersma, M.; Abou-Hamad, E.; Vollmer, I.; Goesten, M.; Mezari, B.; Hensen, E. J. M.; Martínez-Espín, J. S.; Morten, M.; Mitchell, S.; Perez-Ramirez, J.; Olsbye, U.; Weckhuysen, B. M.; Van Speybroeck, V.; Kapteijn, F.; Gascon, J. Structure-Performance Descriptors and the Role of Lewis Acidity in the Methanol-to-Propylene Process. *Nat. Chem.* **2018**, *10*, 804–812.

(2) Wang, Y.; Arandiyan, H.; Scott, J.; Bagheri, A.; Dai, H.; Amal, R. Recent Advances in Ordered Meso/Macroporous Metal Oxides for Heterogeneous Catalysis: A Review. *J. Mater. Chem. A* **2017**, *5*, 8825–8846.

(3) Cop, P.; Maile, R.; Sun, Y.; Khalid, O.; Djerdj, I.; Esch, P.; Heiles, S.; Over, H.; Smarsly, B. M. Impact of Aliovalent/Isovalent Ions (Gd, Zr, Pr, and Tb) on the Catalytic Stability of Mesoporous Ceria in the HCl Oxidation Reaction. *ACS Appl. Nano Mater.* **2020**, *3*, 7406–7419.

(4) Luna, A. L.; Matter, F.; Schreck, M.; Wohlwend, J.; Tervoort, E.; Colbeau-Justin, C.; Niederberger, M. Monolithic Metal-Containing TiO_2 Aerogels Assembled from Crystalline Pre-Formed Nanoparticles as Efficient Photocatalysts for H_2 Generation. *Appl. Catal., B* **2020**, *267*, 118660.

(5) Weller, T.; Sann, J.; Marschall, R. Pore Structure Controlling the Activity of Mesoporous Crystalline $CsTaWO_6$ for Photocatalytic Hydrogen Generation. *Adv. Energy Mater.* **2016**, *6*, 1600208.

(6) Weller, T.; Deilmann, L.; Timm, J.; Dörr, T. S.; Beaucage, P. A.; Cherevan, A. S.; Wiesner, U. B.; Eder, D.; Marschall, R. A Crystalline and 3D Periodically Ordered Mesoporous Quaternary Semiconductor for Photocatalytic Hydrogen Generation. *Nanoscale* **2018**, *10*, 3225–3234.

(7) Burgess, I. B.; Koay, N.; Raymond, K. P.; Kolle, M.; Lončar, M.; Aizenberg, J. Wetting in Color: Colorimetric Differentiation of Organic Liquids with High Selectivity. *ACS Nano* **2012**, *6*, 1427–1437.

(8) Reid, B.; Taylor, A.; Chen, Y.; Schmidt-Hansberg, B.; Guldin, S. Robust Operation of Mesoporous Antireflective Coatings under Variable Ambient Conditions. *ACS Appl. Mater. Interfaces* **2018**, *10*, 10315–10321.

(9) Fried, D. I.; Brieler, F. J.; Fröba, M. Designing Inorganic Porous Materials for Enzyme Adsorption and Applications in Biocatalysis. *ChemCatChem* **2013**, *5*, 862–884.

(10) Fried, D. I.; Tropp, K.; Fröba, M. On the Way to Cofactor Regeneration in Nanopores: Tailoring Porous Materials for Glucose-6-Phosphate Dehydrogenase Immobilization. *ChemCatChem* **2013**, *5*, 931–938.

(11) O'Regan, B.; Grätzel, M. A Low-Cost, High-Efficiency Solar Cell Based on Dye-Sensitized Colloidal TiO_2 Films. *Nature* **1991**, *353*, 737–740.

(12) Bach, U.; Lupo, D.; Comte, P.; Moser, J. E.; Weissörtel, F.; Salbeck, J.; Spreitzer, H.; Grätzel, M. Solid-State Dye-Sensitized Mesoporous TiO_2 Solar Cells with High Photon-to-Electron Conversion Efficiencies. *Nature* **1998**, *395*, 583–585.

(13) Kreissl, J. J. A.; Petit, J.; Oppermann, R.; Cop, P.; Gerber, T.; Joos, M.; Abert, M.; Tübke, J.; Miyazaki, K.; Abe, T.; Schröder, D. Electrochemical Lithiation/Delithiation of ZnO in 3D-Structured Electrodes: Elucidating the Mechanism and the Solid Electrolyte Interphase Formation. *ACS Appl. Mater. Interfaces* **2021**, *13*, 35625–35638.

(14) Hartmann, P.; Lee, D. K.; Smarsly, B. M.; Janek, J. Mesoporous TiO_2: Comparison of Classical Sol-Gel and Nanoparticle Based Photoelectrodes for the Water Splitting Reaction. *ACS Nano* **2010**, *4*, 3147–3154.

(15) von Graberg, T.; Hartmann, P.; Rein, A.; Gross, S.; Seelandt, B.; Röger, C.; Zieba, R.; Traut, A.; Wark, M.; Janek, J.; Smarsly, B. M. Mesoporous Tin-Doped Indium Oxide Thin Films: Effect of Mesostructure on Electrical Conductivity. *Sci. Technol. Adv. Mater.* **2011**, *12*, 025005.

(16) van den Bergh, W.; Lokupitiya, H. N.; Vest, N. A.; Reid, B.; Guldin, S.; Stefik, M. Nanostructure Dependence of T-Nb_2O_5 Intercalation Pseudocapacitance Probed Using Tunable Isomorphic Architectures. *Adv. Funct. Mater.* **2021**, *31*, 2007826.

(17) Weller, T.; Timm, J.; Deilmann, L.; Doerr, T. S.; Greve, C.; Cherevan, A. S.; Beaucage, P. A.; Wiesner, U. B.; Herzig, E. M.; Eder, D.; Marschall, R. Effects of Periodic Pore Ordering on Photocatalytic Hydrogen Generation with Mesoporous Semiconductor Oxides. *Small Struct.* **2022**, *4*, 2200184.

(18) Rauda, I. E.; Augustyn, V.; Saldarriaga-Lopez, L. C.; Chen, X.; Schelhas, L. T.; Rubloff, G. W.; Dunn, B.; Tolbert, S. H. Nanostructured Pseudocapacitors Based on Atomic Layer Deposition of V_2O_5 onto Conductive Nanocrystal-Based Mesoporous ITO Scaffolds. *Adv. Funct. Mater.* **2014**, *24*, 6717–6728.

(19) Cop, P.; Göttlicher, M.; Schörmann, J.; Boissiere, C.; Beyer, A.; Becker, C.; Volz, K.; Over, H.; Smarsly, B. M. Atomic Layer Deposition of Titania in Ordered Mesoporous Cerium Zirconium Oxide Thin Films: A Case Study. *J. Phys. Chem. C* **2019**, *123*, 12851–12861.

(20) Livage, J.; Henry, M.; Sanchez, C. Sol-Gel Chemistry of Transition Metal Oxides. *Prog. Solid State Chem.* **1988**, *18*, 259–341.

(21) Crepaldi, E. L.; Soler-Illia, G. J. d. A. A.; Grosso, D.; Cagnol, F.; Ribot, F.; Sanchez, C. Controlled Formation of Highly Organized Mesoporous Titania Thin Films: From Mesostructured Hybrids to Mesoporous Nanoanatase TiO_2. *J. Am. Chem. Soc.* **2003**, *125*, 9770–9786.

(22) Soler-Illia, G. J. D. A. A.; Sanchez, C.; Lebeau, B.; Patarin, J. Chemical Strategies to Design Textured Materials: From Microporous and Mesoporous Oxides to Nanonetworks and Hierarchical Structures. *Chem. Rev.* **2002**, *102*, 4093–4138.

(23) Yang, X. Y.; Chen, L. H.; Li, Y.; Rooke, J. C.; Sanchez, C.; Su, B. L. Hierarchically Porous Materials: Synthesis Strategies and Structure Design. *Chem. Soc. Rev.* **2017**, *46*, 481–558.

(24) Lu, Y.; Fan, H.; Stump, A.; Ward, T. L.; Rieker, T.; Brinker, C. J. Aerosol-Assisted Self-Assembly of Mesostructured Spherical Nanoparticles. *Nature* **1999**, *398*, 223–226.

(25) Brinker, C. J.; Lu, Y.; Sellinger, A.; Fan, H. Evaporation-Induced Self-Assembly: Nanostructures Made Easy. *Adv. Funct. Mater.* **1999**, *11*, 579–585.

(26) Grosso, D.; Cagnol, F.; Soler-Illia, G. J. de A. A.; Crepaldi, E. L.; Amenitsch, H.; Brunet-Bruneau, A.; Bourgeois, A.; Sanchez, C. Fundamentals of Mesostructuring Through Evaporation-Induced Self-Assembly. *Adv. Funct. Mater.* **2004**, *14*, 309–322.

(27) Cop, P.; Hess, K.; Werner, S.; Meinusch, R.; Smarsly, B. M.; Kozuka, H. Comparison of In-Plane Stress Development in Sol-Gel- and Nanoparticle-Derived Mesoporous Metal Oxide Thin Films. *Langmuir* **2019**, *35*, 16427–16437.

(28) Suib, S. L. A Review of Recent Developments of Mesoporous Materials. *Chem. Rec.* **2017**, *17*, 1169–1183.

(29) Szczęśniak, B.; Choma, J.; Jaroniec, M. Major Advances in the Development of Ordered Mesoporous Materials. *Chem. Commun.* **2020**, *56*, 7836–7848.

(30) Beck, J. S.; Vartuli, J. C.; Roth, W. J.; Leonowicz, M. E.; Kresge, C. T.; Schmitt, K. D.; Chu, C. T. W.; Olson, D. H.; Sheppard, E. W.; McCullen, S. B.; Higgins, J. B.; Schlenker, J. L. A New Family of Mesoporous Molecular Sieves Prepared with Liquid Crystal Templates. *J. Am. Chem. Soc.* **1992**, *114*, 10834–10843.

(31) Kresge, C. T.; Leonowicz, M. E.; Roth, W. J.; Vartuli, J. C.; Beck, J. S. Ordered Mesoporous Molecular Sieves Synthesized by a Liquid-Crystal Template Mechanism. *Nature* **1992**, *359*, 710–712.

(32) Bagshaw, S. A.; Prouzet, E.; Pinnavaia, T. J. Templating of Mesoporous Molecular Sieves by Nonionic Polyethylene Oxide Surfactants. *Science* **1995**, *269*, 1242–1244.

(33) Attard, G. S.; Glyde, J. C.; Göltner, C. G. Liquid-Crystalline Phases as Templates for the Synthesis of Mesoporous Silica. *Nature* **1995**, *378*, 366–368.

(34) Smarsly, B.; Polarz, S.; Antonietti, M. Preparation of Porous Silica Materials via Sol-Gel Nanocasting of Nonionic Surfactants: A Mechanistic Study on the Self-Aggregation of Amphiphiles for the Precise Prediction of the Mesopore Size. *J. Phys. Chem. B* **2001**, *105*, 10473–10483.

(35) Zhao, D.; Huo, Q.; Feng, J.; Chmelka, B. F.; Stucky, G. D. Nonionic Triblock and Star Diblock Copolymer and Oligomeric Surfactant Syntheses of Highly Ordered, Hydrothermally Stable, Mesoporous Silica Structures. *J. Am. Chem. Soc.* **1998**, *120*, 6024–6036.

(36) Zhao, D.; Feng, J.; Huo, Q.; Melosh, N.; Fredrickson, G. H.; Chmelka, B. F.; Stucky, G. D. Triblock Copolymer Syntheses of Mesoporous Silica with Periodic 50 to 300 Angstrom Pores. *Science* **1998**, *279*, 548–552.

(37) Kleitz, F.; Hei Choi, S.; Ryoo, R. Cubic Ia3d Large Mesoporous Silica: Synthesis and Replication to Platinum Nanowires, Carbon Nanorods and Carbon Nanotubes. *Chem. Commun.* **2003**, *3*, 2136.

(38) Weidmann, C.; Brezesinski, K.; Suchomski, C.; Tropp, K.; Grosser, N.; Haetge, J.; Smarsly, B. M.; Brezesinski, T. Morphology-Controlled Synthesis of Nanocrystalline η-Al_2O_3 Thin Films, Powders, Microbeads, and Nanofibers with Tunable Pore Sizes from Preformed Oligomeric Oxo-Hydroxo Building Blocks. *Chem. Mater.* **2012**, *24*, 486–494.

(39) Voss, G. J. B.; Chavez Panduro, E. A.; Midttveit, A.; Fløystad, J. B.; Høydalsvik, K.; Gibaud, A.; Breiby, D. W.; Rønning, M. Mesostructured Alumina as Powders and Thin Films. *J. Mater. Chem. A* **2014**, *2*, 9727–9735.

(40) Djinović, P.; Batista, J.; Levec, J.; Pintar, A. Comparison of Water-Gas Shift Reaction Activity and Long-Term Stability of Nanostructured CuO-CeO_2 Catalysts Prepared by Hard Template and Co-Precipitation Methods. *Appl. Catal., A* **2009**, *364*, 156–165.

(41) Rasmussen, C. J.; Vishnyakov, A.; Thommes, M.; Smarsly, B. M.; Kleitz, F.; Neimark, A. V. Cavitation in Metastable Liquid Nitrogen Confined to Nanoscale Pores. *Langmuir* **2010**, *26*, 10147–10157.

(42) Kleitz, F.; Czuryszkiewicz, T.; Solovyov, L. A.; Lindén, M. X-Ray Structural Modeling and Gas Adsorption Analysis of Cagelike SBA-16 Silica Mesophases Prepared in a F127/Butanol/H_2O System. *Chem. Mater.* **2006**, *18*, 5070–5079.

(43) Boissiere, C.; Grosso, D.; Lepoutre, S.; Nicole, L.; Bruneau, A. B.; Sanchez, C. Porosity and Mechanical Properties of Mesoporous Thin Films Assessed by Environmental Ellipsometric Porosimetry. *Langmuir* **2005**, *21*, 12362–12371.

(44) Göltner, C. G.; Berton, B.; Krämer, E.; Antonietti, M. Nanoporous Silica from Amphiphilic Block Copolymer (ABC) Aggregates: Control over Correlation and Architecture of Cylindrical Pores. *Chem. Commun.* **1998**, 2287–2288.

(45) Thomas, A.; Schlaad, H.; Smarsly, B.; Antonietti, M. Replication of Lyotropic Block Copolymer Mesophases into Porous Silica by Nanocasting: Learning about Finer Details of Polymer Self-Assembly. *Langmuir* **2003**, *19*, 4455–4459.

(46) Thommes, M.; Smarsly, B.; Groenewolt, M.; Ravikovitch, P. I.; Neimark, A. V. Adsorption Hysteresis of Nitrogen and Argon in Pore Networks and Characterization of Novel Micro- and Mesoporous Silicas. *Langmuir* **2006**, *22*, 756–764.

(47) Sel, O.; Brandt, A.; Wallacher, D.; Thommes, M.; Smarsly, B. Pore Hierarchy in Mesoporous Silicas Evidenced by In-Situ SANS during Nitrogen Physisorption. *Langmuir* **2007**, *23*, 4724–4727.

(48) Groenewolt, M.; Brezesinski, T.; Schlaad, H.; Antonietti, M.; Groh, P. W.; Iván, B. Polyisobutylene-*block*-Poly(ethylene oxide) for Robust Templating of Highly Ordered Mesoporous Materials. *Adv. Mater.* **2005**, *17*, 1158–1162.

(49) Wang, Y.; Brezesinski, T.; Antonietti, M.; Smarsly, B. Ordered Mesoporous Sb-Nb-and Ta-Doped SnO_2 Thin Films with Adjustable Doping Levels and High Electrical Conductivity. *ACS Nano* **2009**, *3*, 1373–1378.

(50) Templin, M.; Franck, A.; Du Chesne, A.; Leist, H.; Zhang, Y.; Ulrich, R.; Schädler, V.; Wiesner, U. Organically Modified Aluminosilicate Mesostructures from Block Copolymer Phases. *Science* **1997**, *278*, 1795–1798.

(51) Lee, J.; Christopher Orilall, M.; Warren, S. C.; Kamperman, M.; DiSalvo, F. J.; Wiesner, U. Direct Access to Thermally Stable and Highly Crystalline Mesoporous Transition-Metal Oxides with Uniform Pores. *Nat. Mater.* **2008**, *7*, 222–228.

(52) Stefik, M.; Song, J.; Sai, H.; Guldin, S.; Boldrighini, P.; Orilall, M. C.; Steiner, U.; Gruner, S. M.; Wiesner, U. Ordered Mesoporous Titania from Highly Amphiphilic Block Copolymers: Tuned Solution Conditions Enable Highly Ordered Morphologies and Ultra-Large Mesopores. *J. Mater. Chem. A* **2015**, *3*, 11478–11492.

(53) Wei, J.; Wang, H.; Deng, Y.; Sun, Z.; Shi, L.; Tu, B.; Luqman, M.; Zhao, D. Solvent Evaporation Induced Aggregating Assembly Approach to Three-Dimensional Ordered Mesoporous Silica with Ultralarge Accessible Mesopores. *J. Am. Chem. Soc.* **2011**, *133*, 20369–20377.

(54) Billet, J.; Vandewalle, S.; Meire, M.; Blommaerts, N.; Lommens, P.; Verbruggen, S. W.; De Buysser, K.; Du Prez, F.; Van Driessche, I. Mesoporous TiO_2 from Poly(*N*, *N*-Dimethylacrylamide)-*b*-Polystyrene Block Copolymers for Long-Term Acetaldehyde Photodegradation. *J. Mater. Sci.* **2020**, *55*, 1933–1945.

(55) Umeda, G. A.; Chueh, W. C.; Noailles, L.; Haile, S. M.; Dunn, B. S. Inverse Opal Ceria-Zirconia: Architectural Engineering for Heterogeneous Catalysis. *Energy Environ. Sci.* **2008**, *1*, 484–486.

(56) Waterhouse, G. I. N.; Waterland, M. R. Opal and Inverse Opal Photonic Crystals: Fabrication and Characterization. *Polyhedron* **2007**, *26*, 356–368.

(57) Wang, T.; Sel, O.; Djerdj, I.; Smarsly, B. Preparation of a Large Mesoporous CeO_2 with Crystalline Walls Using PMMA Colloidal Crystal Templates. *Colloid Polym. Sci.* **2006**, *285*, 1–9.

(58) Bian, S.-W.; Zhang, Y.-L.; Li, H.-L.; Yu, Y.; Song, Y.-L.; Song, W.-G. γ-Alumina with Hierarchically Ordered Mesopore/Macropore from Dual Templates. *Microporous Mesoporous Mater.* **2010**, *131*, 289–293.

(59) Malgras, V.; Tang, J.; Wang, J.; Kim, J.; Torad, N. L.; Dutta, S.; Ariga, K.; Hossain, M. S. A.; Yamauchi, Y.; Wu, K. C. W. Fabrication of Nanoporous Carbon Materials with Hard- and Soft-Templating Approaches: A Review. *J. Nanosci. Nanotechnol.* **2019**, *19*, 3673–3685.

(60) Israelachvili, J. N.; Mitchell, D. J.; Ninham, B. W. Theory of Self-Assembly of Hydrocarbon Amphiphiles into Micelles and Bilayers. *J. Chem. Soc., Faraday Trans. 2* **1976**, *72*, 1525.

(61) Cummins, C.; Lundy, R.; Walsh, J. J.; Ponsinet, V.; Fleury, G.; Morris, M. A. Enabling Future Nanomanufacturing through Block Copolymer Self-Assembly: A Review. *Nano Today* **2020**, *35*, 100936.

(62) Sallard, S.; Schröder, M.; Boissière, C.; Dunkel, C.; Etienne, M.; Walcarius, A.; Oekermann, T.; Wark, M.; Smarsly, B. M. Bimodal Mesoporous Titanium Dioxide Anatase Films Templated by a Block Polymer and an Ionic Liquid: Influence of the Porosity on the Permeability. *Nanoscale* **2013**, *5*, 12316–12329.

(63) Thommes, M.; Köhn, R.; Fröba, M. Sorption and Pore Condensation Behavior of Nitrogen, Argon, and Krypton in Mesoporous MCM-48 Silica Materials. *J. Phys. Chem. B* **2000**, *104*, 7932–7943.

(64) Serra, E.; Mayoral, Á.; Sakamoto, Y.; Blanco, R. M.; Díaz, I. Immobilization of Lipase in Ordered Mesoporous Materials: Effect of Textural and Structural Parameters. *Microporous Mesoporous Mater.* **2008**, *114*, 201–213.

(65) Stein, A. Achieving Functionality and Multifunctionality through Bulk and Interfacial Structuring of Colloidal-Crystal-Templated Materials. *Langmuir* **2023**, *39*, 2890–2910.

(66) Yin, S.; Song, L.; Xia, S.; Cheng, Y.; Hohn, N.; Chen, W.; Wang, K.; Cao, W.; Hou, S.; Müller-Buschbaum, P. Key Factors for Template-Oriented Porous Titania Synthesis: Solvents and Catalysts. *Small Methods* **2020**, *4*, 1900689.

(67) Liang, S.; Guan, T.; Yin, S.; Krois, E.; Chen, W.; Everett, C. R.; Drewes, J.; Strunskus, T.; Gensch, M.; Rubeck, J.; Haisch, C.; Schwartzkopf, M.; Faupel, F.; Roth, S. V.; Cheng, Y.-J.; Müller-Buschbaum, P. Template-Induced Growth of Sputter-Deposited Gold Nanoparticles on Ordered Porous TiO_2 Thin Films for Surface-Enhanced Raman Scattering Sensors. *ACS Appl. Nano Mater.* **2022**, *5*, 7492–7501.

(68) Schmidt-Winkel, P.; Lukens, W. W.; Zhao, D.; Yang, P.; Chmelka, B. F.; Stucky, G. D. Mesocellular Siliceous Foams with Uniformly Sized Cells and Windows. *J. Am. Chem. Soc.* **1999**, *121*, 254–255.

(69) Huang, L.; Kruk, M. Versatile Surfactant/Swelling-Agent Template for Synthesis of Large-Pore Ordered Mesoporous Silicas and Related Hollow Nanoparticles. *Chem. Mater.* **2015**, *27*, 679–689.

(70) Sarkar, A.; Thyagarajan, A.; Cole, A.; Stefik, M. Widely Tunable Persistent Micelle Templates *Via* Homopolymer Swelling. *Soft Matter* **2019**, *15*, 5193–5203.

(71) Huang, L.; Yan, X.; Kruk, M. Synthesis of Ultralarge-Pore FDU-12 Silica with Face-Centered Cubic Structure. *Langmuir* **2010**, *26*, 14871–14878.

(72) Hsueh, H. Y.; Chen, H. Y.; She, M. S.; Chen, C. K.; Ho, R. M.; Gwo, S.; Hasegawa, H.; Thomas, E. L. Inorganic Gyroid with Exceptionally Low Refractive Index from Block Copolymer Templating. *Nano Lett.* **2010**, *10*, 4994–5000.

(73) Hsueh, H. Y.; Ho, R. M. Bicontinuous Ceramics with High Surface Area from Block Copolymer Templates. *Langmuir* **2012**, *28*, 8518–8529.

(74) Stefik, M.; Wang, S.; Hovden, R.; Sai, H.; Tate, M. W.; Muller, D. A.; Steiner, U.; Gruner, S. M.; Wiesner, U. Networked and Chiral Nanocomposites from ABC Triblock Terpolymer Coassembly with Transition Metal Oxide Nanoparticles. *J. Mater. Chem.* **2012**, *22*, 1078–1087.

(75) Cherevan, A. S.; Robbins, S.; Dieterle, D.; Gebhardt, P.; Wiesner, U.; Eder, D. Ordered Gyroidal Tantalum Oxide Photocatalysts: Eliminating Diffusion Limitations and Tuning Surface Barriers. *Nanoscale* **2016**, *8*, 16694–16701.

(76) Lokupitiya, H. N.; Jones, A.; Reid, B.; Guldin, S.; Stefik, M. Ordered Mesoporous to Macroporous Oxides with Tunable Isomorphic Architectures: Solution Criteria for Persistent Micelle Templates. *Chem. Mater.* **2016**, *28*, 1653–1667.

(77) Kopeč, M.; Yuan, R.; Gottlieb, E.; Abreu, C. M. R.; Song, Y.; Wang, Z.; Coelho, J. F. J.; Matyjaszewski, K.; Kowalewski, T. Polyacrylonitrile-*b*-Poly(butyl acrylate) Block Copolymers as Precursors to Mesoporous Nitrogen-Doped Carbons: Synthesis and Nanostructure. *Macromolecules* **2017**, *50*, 2759–2767.

(78) Fantin, M.; Isse, A. A.; Venzo, A.; Gennaro, A.; Matyjaszewski, K. Atom Transfer Radical Polymerization of Methacrylic Acid: A Won Challenge. *J. Am. Chem. Soc.* **2016**, *138*, 7216–7219.

(79) Cop, P.; Celik, E.; Hess, K.; Moryson, Y.; Klement, P.; Elm, M. T.; Smarsly, B. M. Atomic Layer Deposition of Nanometer-Sized CeO_2 Layers in Ordered Mesoporous ZrO_2 Films and Their Impact on the Ionic/Electronic Conductivity. *ACS Appl. Nano Mater.* **2020**, *3*, 10757–10766.

(80) Cop, P.; Kitano, S.; Niinuma, K.; Smarsly, B. M.; Kozuka, H. In-Plane Stress Development in Mesoporous Thin Films. *Nanoscale* **2018**, *10*, 7002–7015.

(81) Cheng, X.; Föhst, S.; Redenbach, C.; Schladitz, K. Detecting Branching Nodes of Multiply Connected 3D Structures. *Proceedings of the Mathematical Morphology and its Applications to Signal and Image Processing: 14th international symposium, ISMM 2019; Saarbrücken, Germany, July 8–10, 2019*; Burgeth, B., Kleefeld, A., Naegel, B., Passat, N.; Perret, B., Eds.; Springer International Publishing: Cham, 2019; Vol. *11564*, pp 441–455.

(82) Prates da Costa, E.; Huang, X.; Kübel, C.; Cheng, X.; Schladitz, K.; Hofmann, A.; Göbel, U.; Smarsly, B. M. Effects of Hydrothermal Treatment on Mesopore Structure and Connectivity in Doped Ceria-Zirconia Mixed Oxides. *Langmuir* **2023**, *39*, 177–191.

(83) Bruns, S.; Müllner, T.; Kollmann, M.; Schachtner, J.; Höltzel, A.; Tallarek, U. Confocal Laser Scanning Microscopy Method for Quantitative Characterization of Silica Monolith Morphology. *Anal. Chem.* **2010**, *82*, 6569–6575.

(84) Ribelli, T. G.; Lorandi, F.; Fantin, M.; Matyjaszewski, K. Atom Transfer Radical Polymerization: Billion Times More Active Catalysts and New Initiation Systems. *Macromol. Rapid Commun.* **2019**, *40*, 1800616.

(85) Matyjaszewski, K.; Coca, S.; Gaynor, S. G.; Wei, M.; Woodworth, B. E. Zerovalent Metals in Controlled/"living" Radical Polymerization. *Macromolecules* **1997**, *30*, 7348–7350.

(86) Smarsly, B.; Grosso, D.; Brezesinski, T.; Pinna, N.; Boissière, C.; Antonietti, M.; Sanchez, C. Highly Crystalline Cubic Mesoporous TiO_2 with 10-nm Pore Diameter Made with a New Block Copolymer Template. *Chem. Mater.* **2004**, *16*, 2948–2952.

(87) Sarkar, A.; Evans, L.; Stefik, M. Expanded Kinetic Control for Persistent Micelle Templates with Solvent Selection. *Langmuir* **2018**, *34*, 5738–5749.

(88) Sarkar, A.; Stefik, M. How to make persistent micelle templates in 24 hours and know it using X-ray scattering. *J. Mater. Chem. A* **2017**, *5*, 11840–11853.

(89) Pedersen, J. S.; Svaneborg, C.; Almdal, K.; Hamley, I. W.; Young, R. N. A Small-Angle Neutron and X-Ray Contrast Variation Scattering Study of the Structure of Block Copolymer Micelles: Corona Shape and Excluded Volume Interactions. *Macromolecules* **2003**, *36*, 416–433.

(90) Pedersen, J. S.; Gerstenberg, M. C. The Structure of P85 Pluronic Block Copolymer Micelles Determined by Small-Angle Neutron Scattering. *Colloids Surf., A* **2003**, *213*, 175–187.

(91) Derry, M. J.; Fielding, L. A.; Warren, N. J.; Mable, C. J.; Smith, A. J.; Mykhaylyk, O. O.; Armes, S. P. In Situ Small-Angle X-Ray Scattering Studies of Sterically-Stabilized Diblock Copolymer Nanoparticles

Formed during Polymerization-Induced Self-Assembly in Non-Polar Media. *Chem. Sci.* **2016**, *7*, 5078–5090.

(92) Guild, J. D.; Knox, S. T.; Burholt, S. B.; Hilton, E. M.; Terrill, N. J.; Schroeder, S. L. M.; Warren, N. J. Continuous-Flow Laboratory SAXS for In Situ Determination of the Impact of Hydrophilic Block Length on Spherical Nano-Object Formation during Polymerization-Induced Self-Assembly. *Macromolecules* **2023**, *56*, 6426–6435.

(93) Meinusch, R.; Ellinghaus, R.; Hormann, K.; Tallarek, U.; Smarsly, B. M. On the Underestimated Impact of the Gelation Temperature on Macro- and Mesoporosity in Monolithic Silica. *Phys. Chem. Chem. Phys.* **2017**, *19*, 14821–14834.

(94) Brezesinski, T.; Fischer, A.; Iimura, K. I.; Sanchez, C.; Grosso, D.; Antonietti, M.; Smarsly, B. M. Generation of Self-Assembled 3D Mesostructured SnO_2 Thin Films with Highly Crystalline Frameworks. *Adv. Funct. Mater.* **2006**, *16*, 1433–1440.

(95) Thommes, M.; Schlumberger, C. Characterization of Nanoporous Materials. *Annu. Rev. Chem. Biomol. Eng.* **2021**, *12*, 137–162.

(96) Schlumberger, C.; Thommes, M. Characterization of Hierarchically Ordered Porous Materials by Physisorption and Mercury Porosimetry—A Tutorial Review. *Adv. Mater. Interfaces* **2021**, *8*, 2002181.

(97) De Paul, S. M.; Zwanziger, J. W.; Ulrich, R.; Wiesner, U.; Spiess, H. W. Structure, Mobility, and Interface Characterization of Self-Organized Organic-Inorganic Hybrid Materials by Solid-State NMR. *J. Am. Chem. Soc.* **1999**, *121*, 5727–5736.

(98) Melosh, N. A.; Lipic, P.; Bates, F. S.; Wudl, F.; Stucky, G. D.; Fredrickson, G. H.; Chmelka, B. F. Molecular and Mesoscopic Structures of Transparent Block Copolymer-Silica Monoliths. *Macromolecules* **1999**, *32*, 4332–4342.

(99) Kruk, M.; Jaroniec, M.; Ko, C. H.; Ryoo, R. Characterization of the Porous Structure of SBA-15. *Chem. Mater.* **2000**, *12*, 1961–1968.

(100) Percus, J. K.; Yevick, G. J. Analysis of Classical Statistical Mechanics by Means of Collective Coordinates. *Phys. Rev.* **1958**, *110*, 1–13.

(101) Ashcroft, N. W.; Lekner, J. Structure and Resistivity of Liquid Metals. *Phys. Rev.* **1966**, *145*, 83–90.

(102) Wertheim, M. S. Exact Solution of the Percus-Yevick Integral Equation for Hard Spheres. *Phys. Rev. Lett.* **1963**, *10*, 321–323.

(103) Dunphy, D. R.; Sheth, P. H.; Garcia, F. L.; Brinker, C. J. Enlarged Pore Size in Mesoporous Silica Films Templated by Pluronic F127: Use of Poloxamer Mixtures and Increased Template/SiO_2 Ratios in Materials Synthesized by Evaporation-Induced Self-Assembly. *Chem. Mater.* **2015**, *27*, 75–84.

(104) Nisticò, R.; Scalarone, D.; Magnacca, G. Preparation and Physico-Chemical Characterization of Large-Mesopore Silica Thin Films Templated by Block Copolymers for Membrane Technology. *Microporous Mesoporous Mater.* **2014**, *190*, 208–214.

(105) Weyland, M.; Midgley, P. A.; Thomas, J. M. Electron Tomography of Nanoparticle Catalysts on Porous Supports: A New Technique Based on Rutherford Scattering. *J. Phys. Chem. B* **2001**, *105*, 7882–7886.

(106) Ercius, P.; Alaidi, O.; Rames, M. J.; Ren, G. Electron Tomography: A Three-Dimensional Analytic Tool for Hard and Soft Materials Research. *Adv. Mater.* **2015**, *27*, 5638–5663.

(107) Prouzet, E.; Pinnavaia, T. J. Synthese mesoporöser Silicate mit wurmlochartigen Strukturmotiven unter Verwendung von nichtionischen Detergentien: Steuerung der Porengröße durch Variation der Synthesetemperatur. *Angew. Chem.* **1997**, *109*, 533–536.

(108) Tanev, P. T.; Pinnavaia, T. J. A Neutral Templating Route to Mesoporous Molecular Sieves. *Science* **1995**, *267*, 865–867.

Supporting Information

Poly(ethylene oxide)-*block*-poly(hexyl acrylate) Copolymers as Templates for Large Mesopore Sizes – a Detailed Porosity Analysis

Lysander Q. Wagner[a,b], *Eric Prates da Costa*[a,b,c], *Chantal Glatthaar*[a], *Frederik Breckwoldt*[a], *Marco Zecca*[d], *Paolo Centomo*[d], *Xiaohui Huang*[e,f], *Christian Kübel*[e,f,g], *Helmut Schlaad*[h], *Manfred Kriechbaum*[i], *Heinz Amenitsch*[i], *Matthias Thommes*[j], *and Bernd M. Smarsly*[a,b]*

a. Institute of Physical Chemistry, Justus-Liebig University, Heinrich-Buff-Ring 17, D-35392 Giessen, Germany
b. Center of Materials Research, Justus-Liebig University, Heinrich-Buff-Ring 16, D-35392 Giessen, Germany
c. Umicore AG & Co. KG, Rodenbacher Chaussee 4, D-63457 Hanau, Germany
d. Department of Chemical Sciences, University of Padova, via Marzolo 1, I-35131 Padova, Italy
e. Institute of Nanotechnology, Karlsruhe Institute of Technology, Hermann-von-Helmholtz-Platz 1, D-76344 Eggenstein-Leopoldshafen, Germany
f. Department of Materials and Earth Science, Technical University Darmstadt, Alarich-Weiss-Str. 2, D-64287 Darmstadt, Germany
g. Karlsruhe Nano Micro Facility, Karlsruhe Institute of Technology, Hermann-von-Helmholtz-Platz 1, D-76344 Eggenstein-Leopoldshafen, Germany
h. Institute of Chemistry, University of Potsdam, Karl-Liebknecht-Str. 24-25, D-14476 Potsdam, Germany
i. Institute of Inorganic Chemistry, Graz University of Technology, Stremayrgasse 9, A-8010 Graz, Austria
j. Department of Chemical and Bioengineering, Friedrich-Alexander University, Egerlandstr. 3, D-91058 Erlangen, Germany

Table S1. Overview of important templates for the synthesis of mesoporous metal oxides with cylindrical and spherical mesopores of varying pore size. Note that the focus lays on pure-template-derived pore systems to enable a comparison between the templates. However, pore size variations are possible with swelling agents and adjustment of solvent and temperature during or hydrothermal treatments after the synthesis.

Reference	**Template**	**Silica Type**	**Pore Size**	**Pore Morphology**
Beck *et al.* 1992[1]	$C_8H_{17}NMe_3^+$	MCM-41	1.8 nm	hexagonal cylinders
Beck *et al.* 1992[1]	$C_9H_{19}NMe_3^+$	MCM-41	2.1 nm	hexagonal cylinders
Beck *et al.* 1992[1]	$C_{10}H_{21}NMe_3^+$	MCM-41	2.2 nm	hexagonal cylinders
Kresge *et al.* 1992[2]	$C_{12}H_{25}NMe_3^+$	MCM-41	3.0 nm	hexagonal cylinders
Beck *et al.* 1992[1]	$C_{14}H_{29}NMe_3^+$	MCM-41	3.0 nm	hexagonal cylinders
Kresge *et al.* 1992[2]	$C_{16}H_{33}NMe_3^+$	MCM-41	4.0 nm	hexagonal cylinders
Huo *et al.* 1996[3]	$C_{16}H_{33}NMe_3^+$ (post-synthesis treatment)	MCM-41	6.0 nm	hexagonal cylinders
Kresge *et al.* 1992[2]	$C_{16}H_{33}NMe_3^+$ (higher template concentration)	MCM-48	2.9 nm[4]	cubic phase[5]
Bagshaw *et al.* 1995[6]	Tergitol $C_{11-15}H_{23-31}$-PEO_9	MSU-1	2.5 nm	hexagonal-like channels
Bagshaw *et al.* 1995[6]	Tergitol $C_{11-15}H_{23-31}$-PEO_{12}	MSU-1	3.1 nm	hexagonal-like channels
Bagshaw *et al.* 1995[6]	Tergitol $C_{11-15}H_{23-31}$-PEO_{15}	MSU-1	2.6 nm	hexagonal-like channels
Bagshaw *et al.* 1995[6]	Tergitol $C_{11-15}H_{23-31}$-PEO_{20}	MSU-1	4.8 nm	hexagonal-like channels

Reference	Template	Silica Type	Pore Size	Pore Morphology
Bagshaw *et al.* 1995[6]	Tergitol $C_{11-15}H_{23-31}$-PEO_{30}	MSU-1	4.5 nm	hexagonal-like channels
Bagshaw *et al.* 1995[6]	Triton-X C_8H_{17}-PEO_8	MSU-2	2.0 nm	hexagonal-like channels
Bagshaw *et al.* 1995[6]	Triton-X C_8H_{17}-PEO_{10}	MSU-2	3.5 nm	hexagonal-like channels
Bagshaw *et al.* 1995[6]	Igepal $C_{12}H_{25}$-PEO_{18}	MSU-2	2.1 nm	hexagonal-like channels
Bagshaw *et al.* 1995[6]	Pluronic PEO_{13}-PPO_{30}-PEO_{13}	MSU-3	5.8 nm	hexagonal-like channels
Smarsly *et al.* 2001[7]	C_8H_{17}-PEO_4	MSU-like	2.2 nm	hexagonal cylinders
Attard *et al.* 1995[8]	$C_{12}H_{25}$-PEO_8	MSU-like	2.8 nm	hexagonal cylinders
Smarsly *et al.* 2001[7]	$C_{14}H_{29}$-PEO_4	MSU-like	2.7 nm	hexagonal cylinders
Attard *et al.* 1995[8] Smarsly *et al.* 2001[7]	$C_{16}H_{33}$-PEO_8	MSU-like	3.1 nm	cubic phase
Smarsly *et al.* 2001[7]	Brij $C_{12}H_{25}$-PEO_{30}	MSU-like	3.3 nm	hexagonal cylinders
Smarsly *et al.* 2001[7]	Brij $C_{16}H_{33}$-PEO_{10}	MSU-like	3.5 nm	hexagonal cylinders
Smarsly *et al.* 2001[7]	Brij $C_{18}H_{37}$-PEO_{20}	MSU-like	3.7 nm	hexagonal cylinders
Zhao *et al.* 1998[9]	Pluronic P123 PEO_{20}-PPO_{70}-PEO_{20}	SBA-15	4.7 nm	hexagonal cylinders
Zhao *et al.* 1998[9]	Pluronic P85 PEO_{26}-PPO_{39}-PEO_{26}	SBA-15	6.0 nm	hexagonal cylinders
Zhao *et al.* 1998[9]	Pluronic L121 PEO_5-PPO_{70}-PEO_5	SBA-15	10 nm	hexagonal cylinders
Zhao *et al.* 1998[9]	Pluronic F127 PEO_{106}-PPO_{70}-PEO_{106}	SBA-16	5.4 nm	cubic phase

Reference	Template	Silica Type	Pore Size	Pore Morphology
Kleitz *et al.* 2003[10]	Pluronic P123 PEO_{20}-PPO_{70}-PEO_{20} (with *n*-butanol, 35 °C)	KIT-6	4.0 nm	cubic phase
Kleitz *et al.* 2003[10]	Pluronic P123 PEO_{20}-PPO_{70}-PEO_{20} (with *n*-butanol, 130 °C)	KIT-6	12 nm	cubic phase
Zhang *et al.* 2018[11]	PS_{50}-$P4VP_{36}$	–	6.2 nm	hexagonal cylinders
Xiao *et al.* 2013[12]	PS_{60}-PAA_{100}	–	13 nm	cubic phase
Yu *et al.* 2000[13]	PEO_{39}-PBO_{47}-PEO_{39}	FDU-1	12 nm	cubic phase
Thomas *et al.* 2003[14]	KLE-1 $(PE_{0.67}/B_{0.33})_{99}$-$PEO_{72}$	KLE-type	12 nm	cubic phase
Thomas *et al.* 2003[14]	KLE-2 $(PE_{0.67}/B_{0.33})_{104}$-$PEO_{56}$	KLE-type	13 nm	cubic phase
Thomas *et al.* 2003[14]	KLE-3 $(PE_{0.67}/B_{0.33})_{104}$-$PEO_{52}$	KLE-type	16 nm	cubic phase
Lee *et al.* 2008[15]	PI_{380}-PEO_{175}	–	23 nm[a]	hexagonal cylinders
Stefik *et al.* 2015[16]	PI_{928}-PEO_{652}	–	32 nm[a]	cubic phase
Wei *et al.* 2011[17]	PEO_{44}-$PMMA_{103}$	–	18 nm	cubic phase
Wei *et al.* 2011[17]	PEO_{125}-$PMMA_{174}$	–	33 nm	cubic phase
Tanaka *et al.* 2018[18]	PS_{162}-PAA_{113}-PEO_{46}	–	39 nm[a]	cubic phase
von Graberg *et al.* 2010[19]	PIB_{50}-PEO_{45}	–	23 nm[a]	cubic phase
von Graberg *et al.* 2010[19]	PIB_{353}-PEO_{454}	–	40 nm[a]	cubic phase
Billet *et al.* 2020[20]	$PDMA_{58}$-PS_{67}	–	8 nm[a]	cubic phase
Billet *et al.* 2020[20]	$PDMA_{58}$-PS_{288}	–	45 nm[a]	cubic phase
Yu *et al.* 2001[21]	PS_{35}-PEO_{109}	–	5 nm	cubic phase
Yu *et al.* 2001[21]	PS_{215}-PEO_{100}	–	18 nm	cubic phase
Liang *et al.* 2022[22]	PS_{576}-PEO_{818}	–	48 nm[a]	cubic phase

Reference	Template	Silica Type	Pore Size	Pore Morphology
Lokupitiya *et al.* 2016[23]	PEO_{453}-PHA_{279}	–	25 nm[a]	cubic phase
Lokupitiya *et al.* 2016[23]	PEO_{453}-PHA_{431}	–	56 nm[a]	cubic phase
Velev *et al.* 1997[24]	PS bead (d = 200 nm)	inverse opal	150 nm	cubic phase
Waterhouse *et al.* 2007[25]	PMMA bead (d = 224 nm)	inverse opal	180 nm	cubic phase
Waterhouse *et al.* 2007[25]	PMMA bead (d = 317 nm)	inverse opal	260 nm	cubic phase
Velev *et al.* 1997[24]	PS bead (d = 560 nm)	inverse opal	380 nm	cubic phase
Zakhidov *et al.* 1998[26]	SiO_2 bead (d = 200 nm)	inverse opal	160 nm[a]	cubic phase
Chai *et al.* 2004[27]	SiO_2 bead (d = 1000 nm)	inverse opal	806 nm[a]	cubic phase

[a]pore size from a material different than silica

Table S2. Overview of the amounts of macroinitiator (PEO-Br), hexyl acrylate (monomer), ligand (TPMA), and $CuBr_2$ for the SARA ATRP reactions used in this work.

Sample	PEO-Br	Monomer	TPMA	$CuBr_2$
PEO_{355}-*b*-PHA_{171}	1001 mg	4.2 mL	39 mg	16 mg
PEO_{214}-*b*-PHA_{322}	500 mg	2.35 mL	43 mg	11 mg
PEO_{214}-*b*-PHA_{83}	1000 mg	3.83 mL	86 mg	22 mg
PEO_{131}-*b*-PHA_{396}	501 mg	5.1 mL	85 mg	22 mg
PEO_{131}-*b*-PHA_{57}	500 mg	3.45 mL	85 mg	22 mg

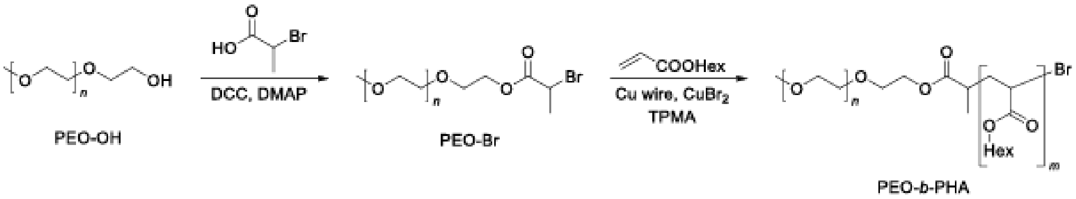

Scheme S1. Two-step synthesis of PEO-*b*-PHA block copolymers comprising (1) a Steglich esterification of the PEO-OH homopolymer to give the PEO-Br macroinitiator with a terminal C–Br bond and (2) the SARA ATRP with hexyl acrylate.

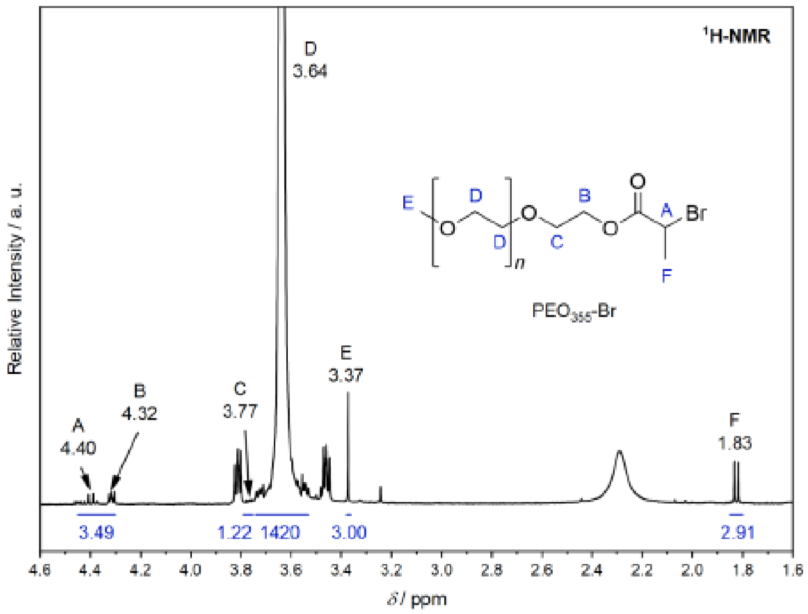

Figure S1. ^{1}H-NMR (400 MHz) spectrum of the PEO-Br macroinitiator (20 kDa) in $CDCl_3$. The peaks are assigned according to the given structure.

The degree of polymerization of the PEO block *n* is determined from the integrals in the ^{1}H-NMR spectrum of the macroinitiator. In this regard, signal D arising from the repeating unit has to be compared with the head-group's signal. Signal E in **Figure S1** is well separated, and thus provides an accurate determination of the PEO block length according to equation (S1)

$$n = \frac{3\,I_\mathrm{D}}{4\,I_\mathrm{E}} \tag{S1}$$

The degree of esterification of the PEO-Br macroinitiator can be directly determined by the comparison of signals E and F, *i.e.*, the ratio of the integral of signal F to the integral of signal E in **Figure S1**.

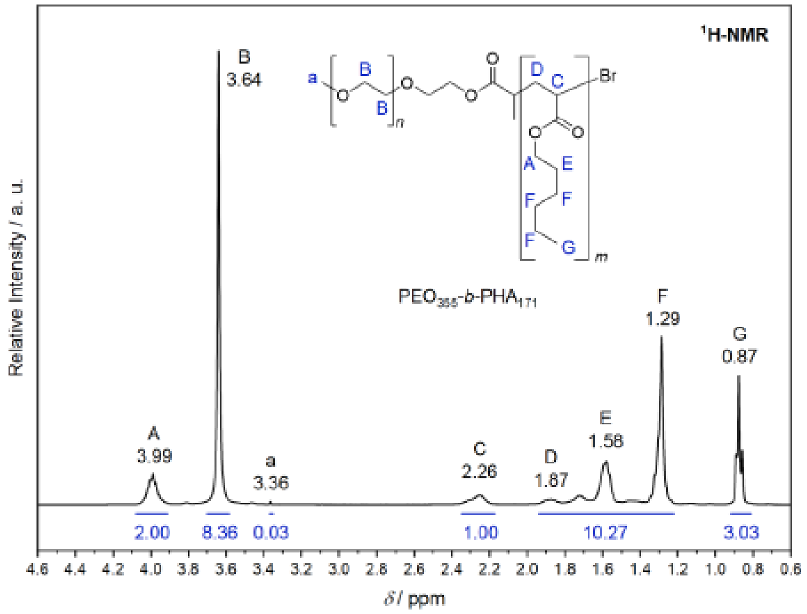

Figure S2. ^{1}H-NMR (400 MHz) spectrum of the PEO$_{355}$-*b*-PHA$_{171}$ block copolymer in CDCl$_3$. The peaks are assigned according to the given structure.

The degree of polymerization of the PHA block *m* is determined from the integrals in the ^{1}H-NMR spectrum of the block copolymer. Since the product of nuclei per repeating unit and degree of polymerization divided by the respective integral is a constant for each block, m can be obtained from the integral I_i of the respective NMR signal if the degree of polymerization of the PEO block n is known (see above). Note that the number four in the denominator on the right-hand side of equation (S2) arises from the number of summands for the PHA block in the nominator:

$$m = \frac{4\,n}{I_B} \cdot \frac{\frac{I_A}{2} + \frac{I_C}{1} + \frac{I_D + I_E + I_F}{10} + \frac{I_G}{3}}{4} \qquad \text{(S2)}$$

Due to the tacticity-derived resonances,[23] signal D in **Figure S2** is less intense than expected while signals E and F possess a higher intensity. Thus, signals D, E, and F are treated as one signal in equation (S2).

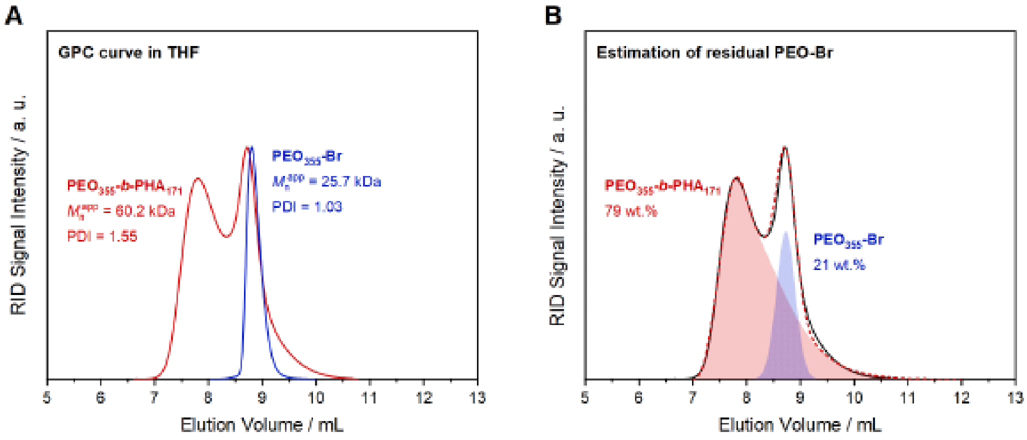

Figure S3. (A) GPC RI traces of the macroinitiator PEO-Br (blue) and the PEO-*b*-PHA block copolymer (red) in THF. (B) The GPC trace of the PEO-*b*-PHA block copolymer (black) was fitted (red, dotted line) by a combination of two functions, one for PEO-*b*-PHA (red area) and one for PEO-Br (blue area) in order to estimate the amount of residual macroinitiator in the final product.

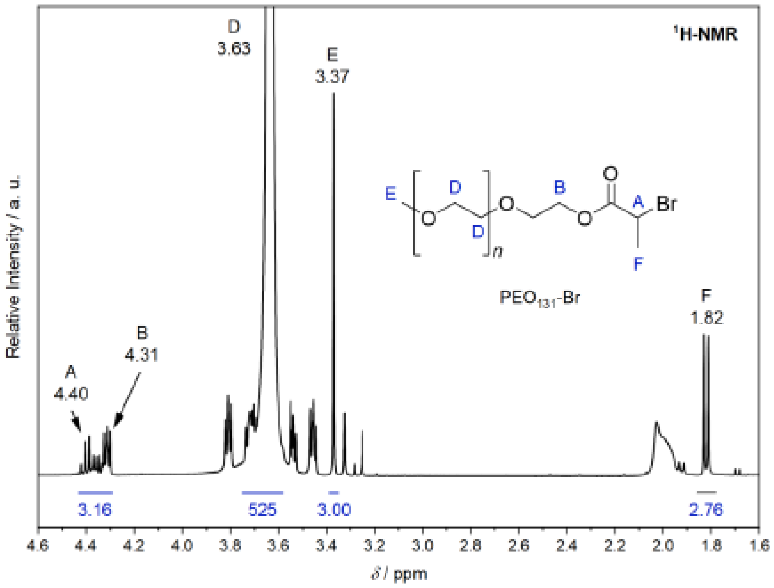

Figure S4. ^{1}H-NMR (400 MHz) spectrum of the PEO-Br macroinitiator (5 kDa) in $CDCl_3$. The peaks are assigned according to the given structure.

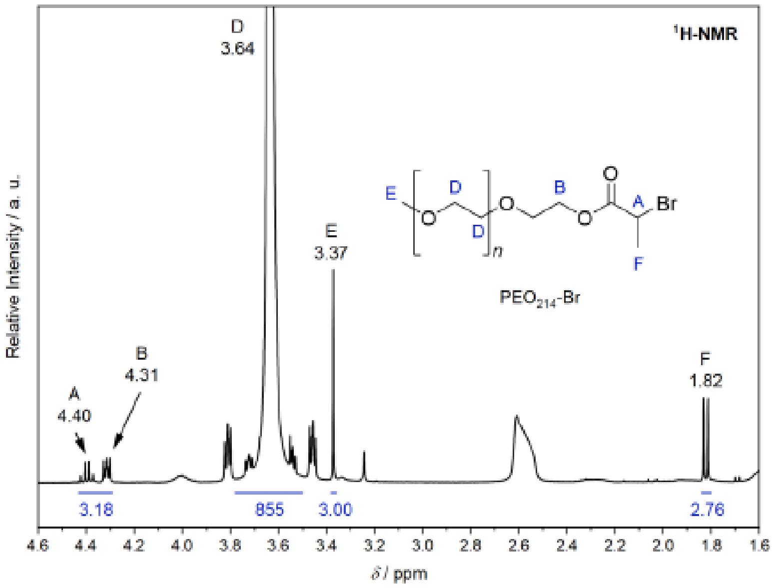

Figure S5. ^{1}H-NMR (400 MHz) spectrum of the PEO-Br macroinitiator (10 kDa) in $CDCl_3$. The peaks are assigned according to the given structure.

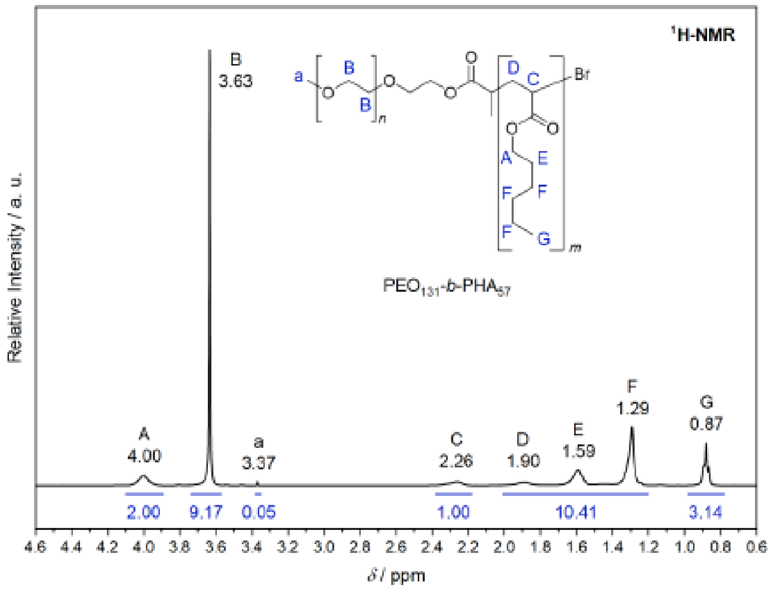

Figure S6. ^{1}H-NMR (400 MHz) spectrum of the PEO$_{131}$-*b*-PHA$_{57}$ block copolymer in CDCl$_3$. The peaks are assigned according to the given structure.

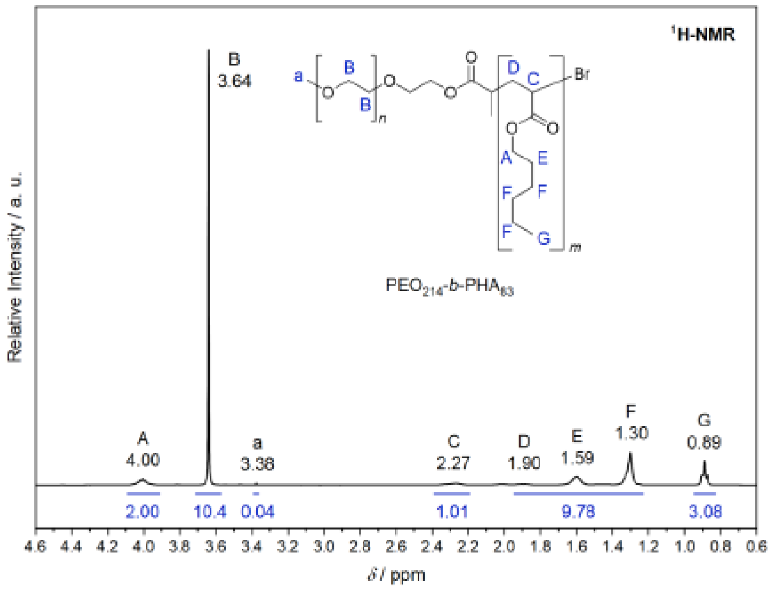

Figure S7. ^{1}H-NMR (400 MHz) spectrum of the PEO$_{214}$-*b*-PHA$_{83}$ block copolymer in CDCl$_3$. The peaks are assigned according to the given structure.

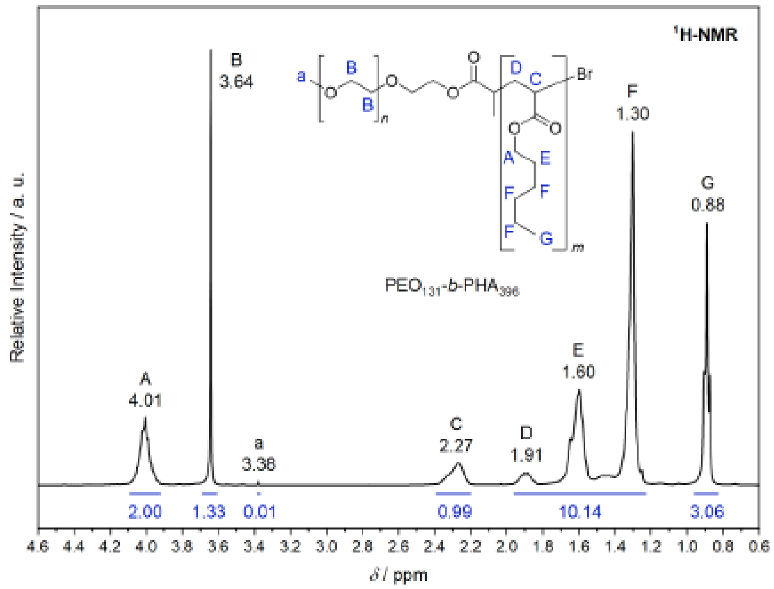

Figure S8. ^{1}H-NMR (400 MHz) spectrum of the PEO$_{131}$-*b*-PHA$_{396}$ block copolymer in CDCl$_3$. The peaks are assigned according to the given structure.

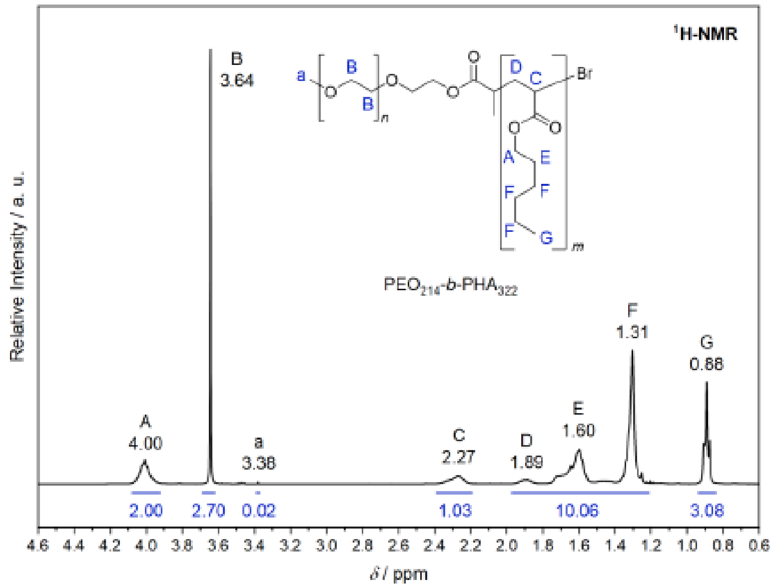

Figure S9. ^{1}H-NMR (400 MHz) spectrum of the PEO$_{214}$-*b*-PHA$_{322}$ block copolymer in CDCl$_3$. The peaks are assigned according to the given structure.

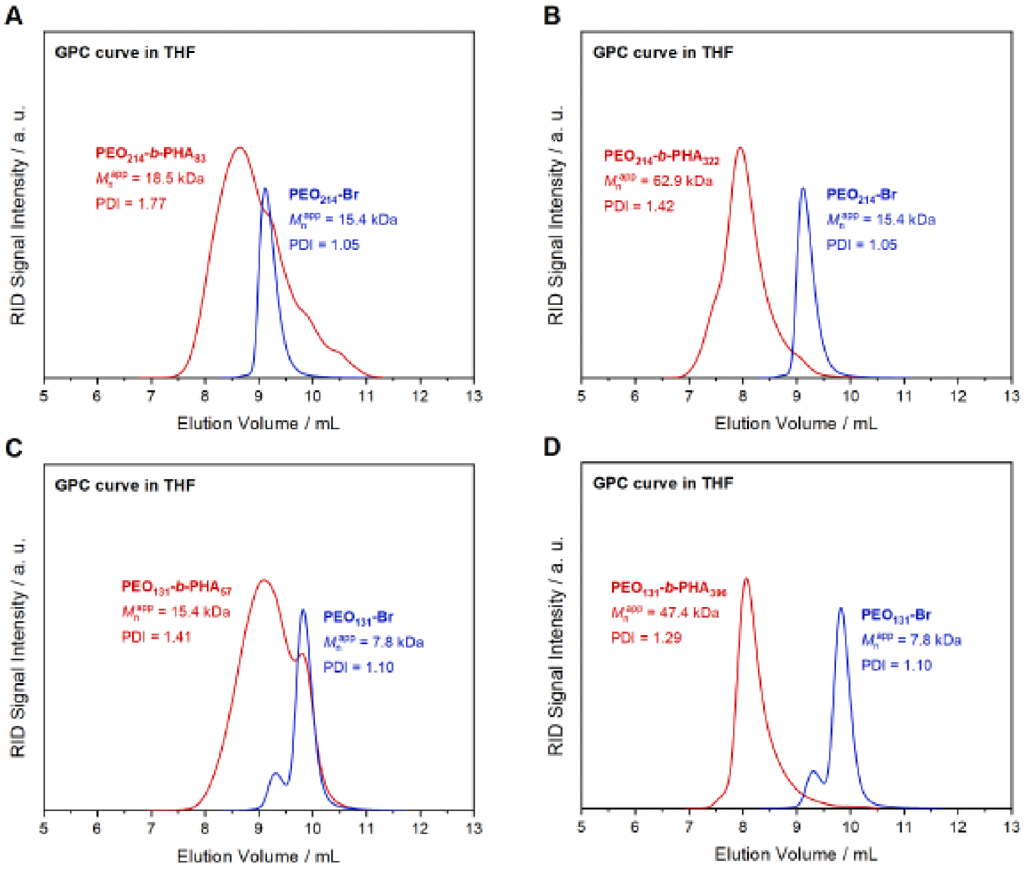

Figure S10. GPC RI traces of (A) PEO$_{214}$-*b*-PHA$_{83}$, (B) PEO$_{214}$-*b*-PHA$_{322}$, (C) PEO$_{131}$-*b*-PHA$_{57}$, and (D) PEO$_{131}$-*b*-PHA$_{396}$ in red, as well as the respective macroinitiators in blue (eluent: THF).

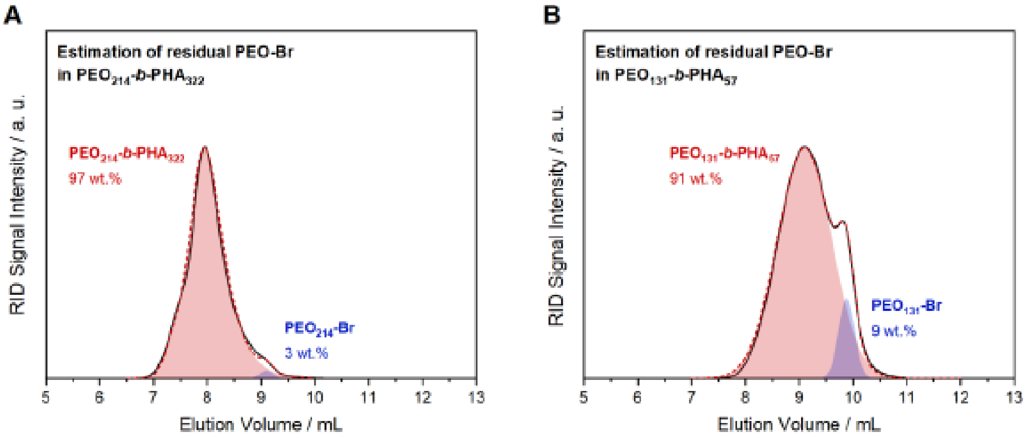

Figure S11. The GPC traces of the block copolymers (A) PEO_{214}-*b*-PHA_{322} and (B) PEO_{131}-*b*-PHA_{57} (black) were fitted (red, dotted line) by a combination of two functions, one for PEO-*b*-PHA (red area) and one for PEO-Br (blue area) in order to estimate the amount of residual macroinitiator in the final product.

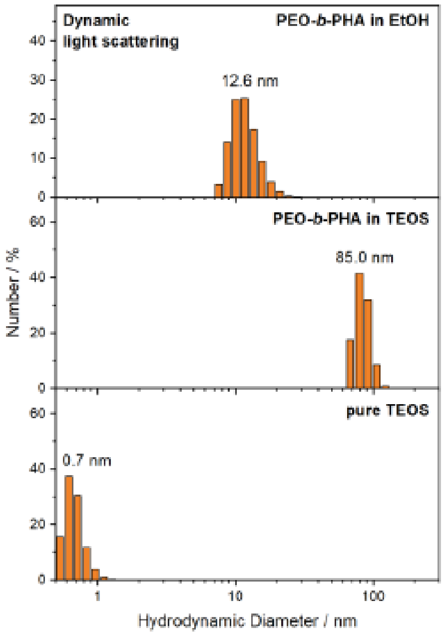

Figure S12. DLS data of PEO_{355}-*b*-PHA_{171} in ethanol (top), PEO_{355}-*b*-PHA_{171} dissolved in the metal oxide precursor (middle), and the pure precursor as blank measurement (bottom).

SAXS curves of a weakly (before 48 h of drying at 40 °C), highly condensed (after drying), and calcined silica-template hybrid gels are collected in **Figure S13C**. Note that the reaction mixture termed weakly condensed was sealed in the measurement tube but measured two weeks later. This allows a partial micelle assembly and condensation even without exposure to 40 °C leading to the observed maxima and minima of the SAXS curve. The sample termed highly condensed was dried at 40 °C in the measurement tube before sealing representing the dried gel state. Following a Percus-Yevick model, the size of the spherical objects, *i.e.*, pore forming micelles in case of the gels and mesopores in case of the calcined metal oxide, can be determined and shows a steady decrease by 4 nm upon drying and calcination, respectively. Deviations of the fits from the data (especially the distance between the first two maxima) might result from the simplicity of the model taking neither imperfect spherical (*i.e.*, ellipsoidal) pores nor ordered lattices into account.

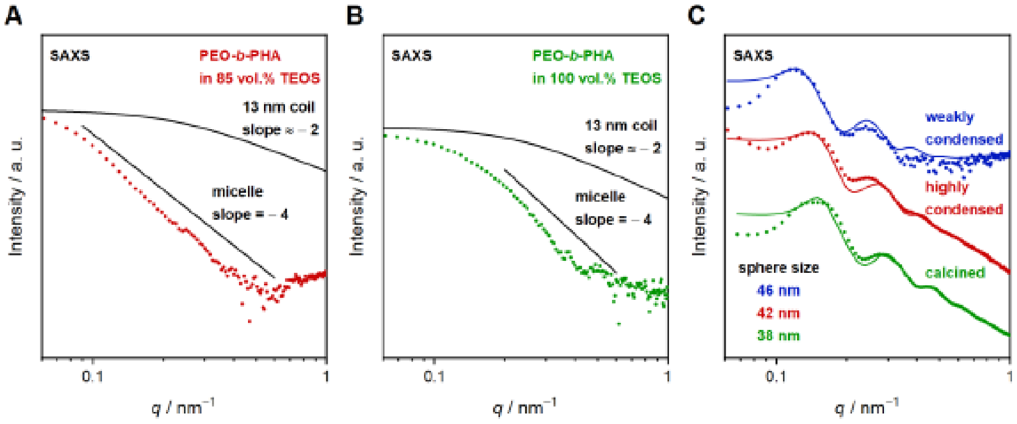

Figure S13. SAXS curves of PEO$_{355}$-*b*-PHA$_{171}$ dissolved in (A) a mixture of TEOS (85 vol.%) and ethanol (15 vol.%) and (B) pure TEOS (dotted lines) compared with simulated SAXS curves for 13 nm Gaussian coils and spherical micelles (solid lines). (C) The SAXS curves of a weakly condensed (blue), dried gel (red), and calcined mesoporous silica synthesized with 57 vol.% PEO$_{355}$-*b*-PHA$_{171}$ are given with the respective fits (solid lines) based on a Percus-Yevick model.

In an SEM image, the mesoporous metal oxide is regarded along a random breaking plane (see **Figure S14A**), along which the particle broke during grinding. As shown in **Figure S14B**, the resulting apparent pore size x from SEM is smaller than the actual pore diameter $2r$. A mathematical description is possible by evaluating the right triangle built up by the pore radius r, the distance d of the breaking plane from the pore center, and the apparent pore radius $0.5x$ yielding the apparent pore size shown in equation (S3) and plotted in **Figure S14C**:

$$x = 2 \cdot \sqrt{r^2 - d^2} \qquad \text{(S3)}$$

A random cut through several pores corresponds statistically to several random cuts through one single pore. Assuming the breaking planes to be located randomly, *i.e.*, all values of d are equally probable, the average apparent pore size x_{avg} thus can be determined from equation (S4). Here, the denominator represents the pore radius r and the numerator one quarter of the ellipse made up from the pore size $2r$ (long radius) and the pore radius r (short radius) leading to the simple form:

$$x_{\text{avg}} = \frac{\int_0^r \left(2 \cdot \sqrt{r^2 - d^2}\right) \mathrm{d}d}{\int_0^r \mathrm{d}d} = \frac{\pi}{4} \cdot 2\,r \qquad \text{(S4)}$$

With a mesopore of 41 nm in diameter (see STEM tomography), an average apparent pore size of 32.2 nm is obtained. Thus, an underestimation of the pore size of 21% by SEM can be expected. Alternatively, **Figure S14C** represents the fraction of pores exceeding a certain threshold pore size (in case of equally distributed breaking planes). This means for instance that 50% ($= 10.25 \cdot 20.5^{-1}$) of the observed pores possess an apparent pore size above 36 nm and 80% ($= 16.4 \cdot 20.5^{-1}$) are still above 25 nm. Yet, all these values correspond to the maximum error as the assumption of the equally distributed might not hold true, *e.g.*, if a breaking plane near the pore center is more likely due to the thinner pore wall, and the actual underestimation might be smaller. In any case, the maximum deviation of the SEM evaluation is in worst case in the range of the width of the pore size distribution, *i.e.*, polydispersity, enlarging the range of the mean pore size by 7 – 10 nm (20 – 25% depending on the evaluation method) in each direction.

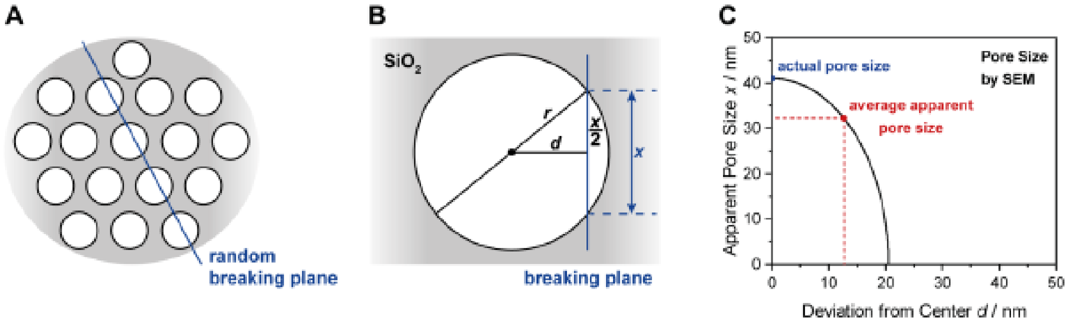

Figure S14. (A) Schematic representation of mesoporous silica with a random breaking plane shown in blue, along which an SEM image would be recorded. (B) The geometric relation between pore diameter and apparent pore size *x* observed in SEM in case of single pore being cut along a breaking plane (blue) with a distance *d* from the pore center yields (C) the dependency of apparent pore size on the cutting distance *d*.

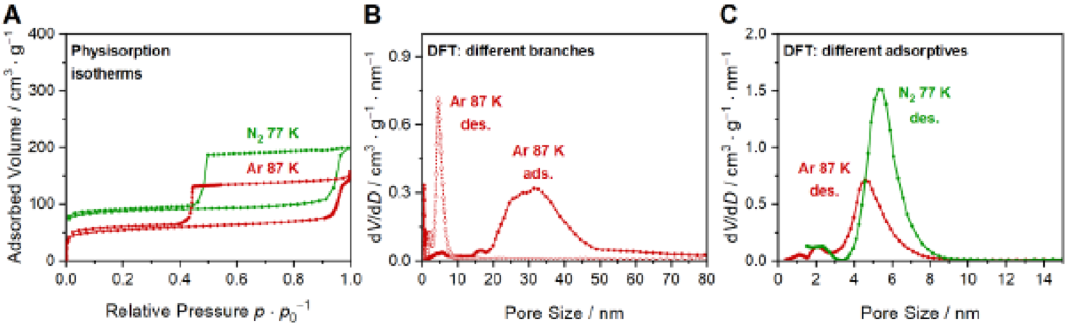

Figure S15. (A) Argon isotherm at 87 K (red) and nitrogen isotherm at 77 K (green) of mesoporous silica derived from PEO$_{355}$-*b*-PHA$_{171}$, as well as (B) a comparison of the pore size distributions derived from the adsorption branch (filled symbols) and desorption branch (open symbols) of the argon isotherm with an NLDFT kernel for cylindrical pores. (C) Comparison of the pore size distributions obtained from the desorption branch of the argon (red) and nitrogen (green) isotherm with an NLDFT kernel for cylindrical pores.

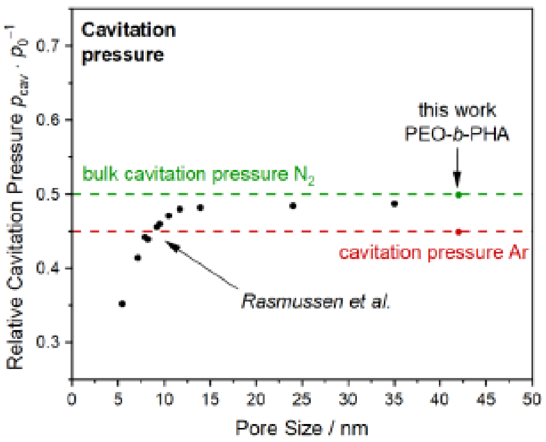

Figure S16. Relative cavitation pressure in dependency on the pore size according to Rasmussen *et al.*[28] (black) for nitrogen, as well as the data points for nitrogen (green) and argon (red) of this work. The dotted lines represent the bulk cavitation pressure of nitrogen (green) and the expected bulk cavitation pressure of argon (red).

The polymer concentration being equal to the theoretical porosity of the final metal oxide is defined by the volume of polymer with respect to the overall volume. Estimating the volume of the polymer requires the knowledge of its density ρ_{BCP}, which can be obtained from the ratio of polymer mass to polymer volume. In detail, this corresponds to the expression shown in equation (S5), where M_{n} defines the number-weighted molar mass from ^{1}H-NMR, n is the degree of polymerization of the PEO block, m is the degree of polymerization of the PHA block, M_{EO} and M_{HA} are the respective molar masses of the repeating units (44 g mol^{-1} and 156 g mol^{-1}, respectively), and ρ_{PEO} and ρ_{PHA} are the respective polymer block's density (1.13 g mL^{-1} and 1.065 g mL^{-1}, respectively)[23]:

$$\rho_{\mathrm{BCP}} = \frac{M_{\mathrm{n}}}{\frac{n\,M_{\mathrm{EO}}}{\rho_{\mathrm{PEO}}} + \frac{m\,M_{\mathrm{HA}}}{\rho_{\mathrm{PHA}}}} \qquad \text{(S5)}$$

This averaged density can be used to convert the polymer mass into a volume V_{BCP} (equaling the pore volume). The metal oxide's volume can be derived as follows: the mass of the precursor (in case of liquids like TEOS, the volume is transformed into the mass using the according density) is converted into a molecular amount using the molar mass. The amount of precursor is then assumed to be equal to the amount of metal oxide, *i.e.*, assuming that all precursor molecules react to the final metal oxide. The amount of metal oxide is then converted to the mass (using the molar mass) and finally to the volume V_{oxide} (*via* the density). In case of amorphous silica, a value of 2.2 g mL^{-1} was used. The polymer concentration (and thus theoretical porosity) Φ amounts then to the ration shown in equation (S6):

$$\Phi = \frac{V_{\mathrm{BCP}}}{V_{\mathrm{BCP}} + V_{\mathrm{oxide}}} \qquad \text{(S6)}$$

In contrast, the experimental porosity P can be determined from physisorption experiments with the total (specific) pore volume $V_{\mathrm{p,\,total}}$, *i.e.*, the maximum value of the cumulative pore size distribution at large pore sizes, and the density of amorphous silica ρ_{silica} according to equation (S7):

$$P = \frac{V_{\mathrm{p,\,total}}}{V_{\mathrm{p,\,total}} + \frac{1}{\rho_{\mathrm{silica}}}} \qquad \text{(S7)}$$

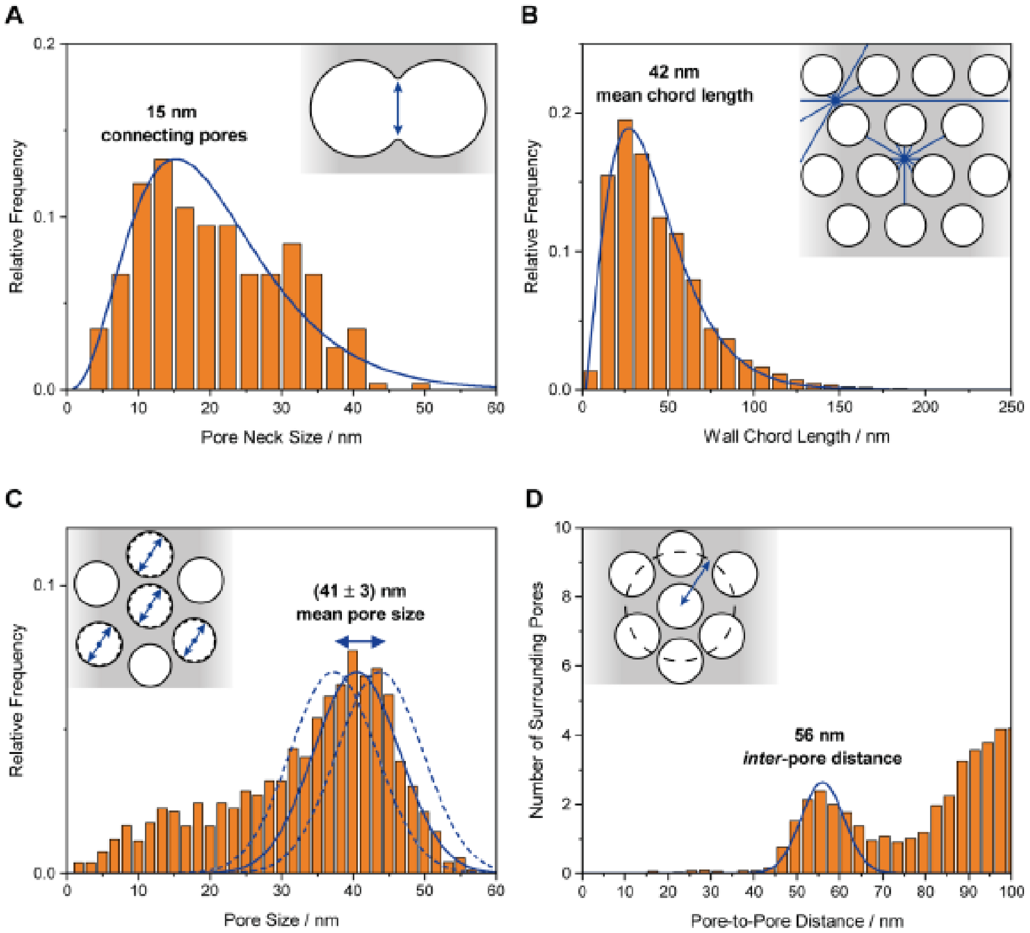

Figure S17. (A) Distribution of the pore neck size and (B) chord length distribution of the wall phase (silica) obtained from the STEM-based tomography of mesoporous silica derived from PEO$_{355}$-*b*-PHA$_{171}$ (85 vol.% template). (C) The pore size distribution with the pixel(/voxel)-size-based maximum possible error (dotted lines) and (D) the average number of surrounding mesopores in dependency on their distance to the regarded pore of the same sample are displayed together with a scheme of the pore system explaining the plotted data. The respective average distributions are shown in blue for eye guidance.

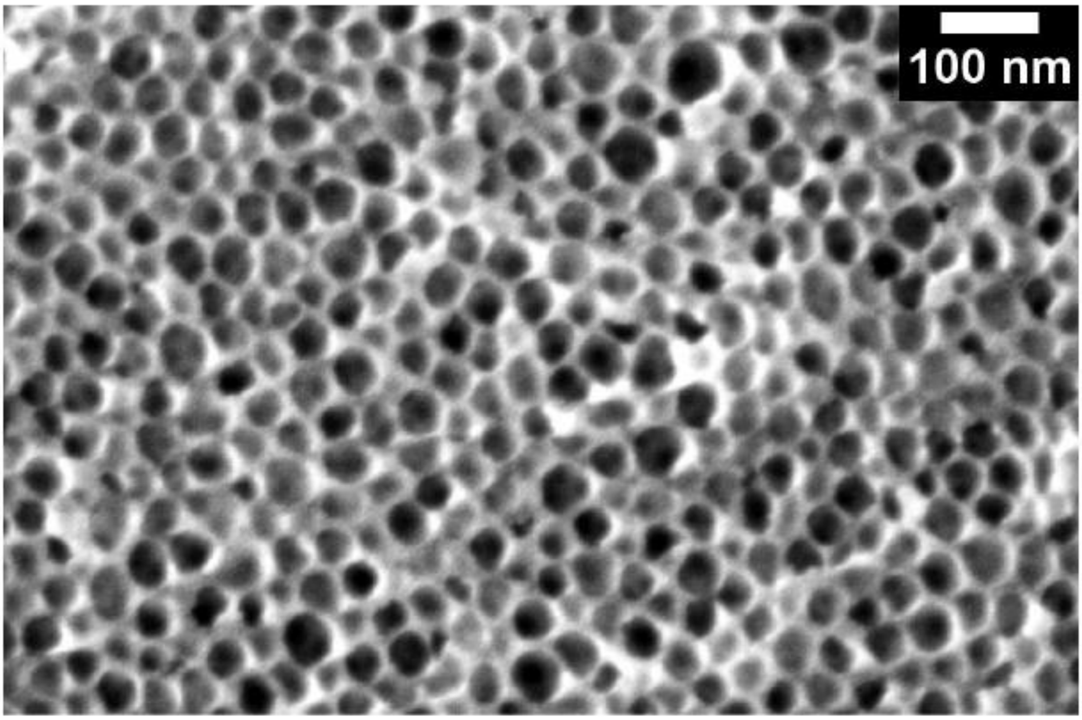

Figure S18. SEM images of mesoporous silica prepared with a PEO_{355}-*b*-PHA_{171} volume fraction of 80 vol.% providing a rough insight into the connection of the surficial mesopores to the mesopores in the sub-surface.

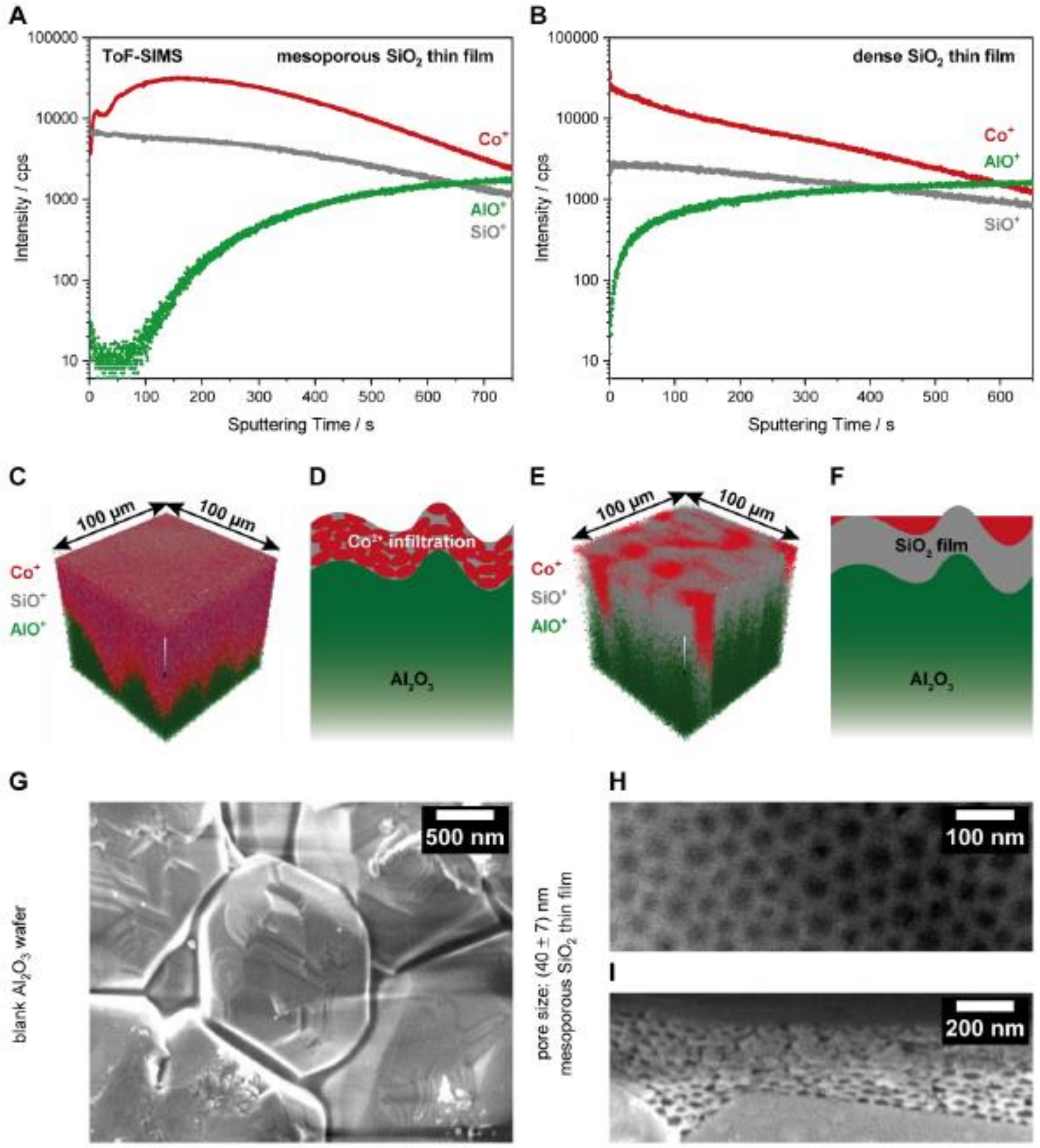

Figure S19. ToF-SIMS depth profile of (A) a PEO$_{355}$-*b*-PHA$_{171}$-derived mesoporous SiO$_2$ thin film infiltrated with a cobalt nitrate solution including the signals of the ions Co$^+$ ($m/z = 59$), SiO$^+$ (44), and AlO$^+$ (43) and (B) a dense SiO$_2$ reference film without PEO-*b*-PHA template including the signals of Co$^+$, ZrO$^+$, and SiO$^+$. The 3D overlay of the Co$^+$, SiO$^+$, and AlO$^+$ signals as well as a schematic representation of underlying situation is shown for (C and D) the mesoporous (the top of the overlay was cropped due to surface contaminations) and (E and F) the dense SiO_2 film. In addition, SEM images of the (G) pure Al_2O_3 wafer used for deposition in top-view, as well as (H) the top-view and (I) cross-section of the mesoporous SiO_2 film is given.

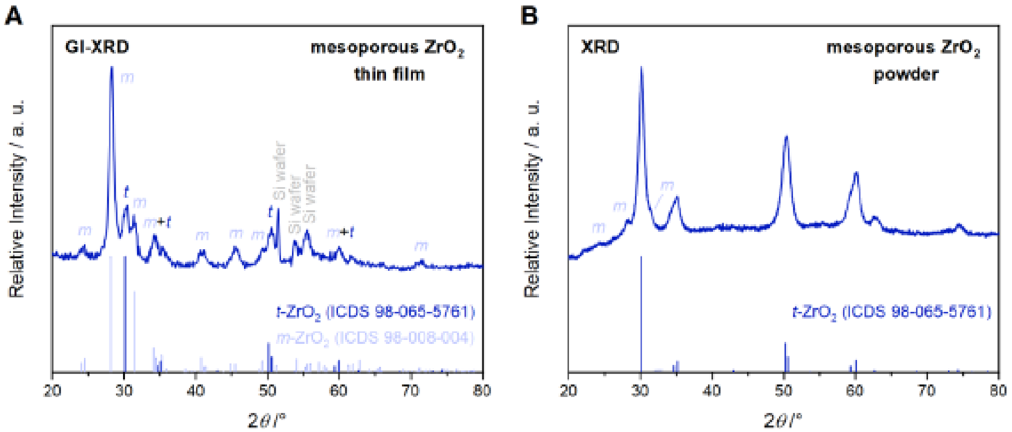

Figure S20. (A) GI-XRD pattern of the mesoporous ZrO_2 thin film and (B) powder XRD pattern of mesoporous ZrO_2 powder derived from PEO_{355}-*b*-PHA_{171}. The reference pattern for tetragonal (ICDS 98-065-5761, blue) and monoclinic (ICDS 98-008-004, light blue) ZrO_2 are given in addition, and the reflections are labeled respectively.

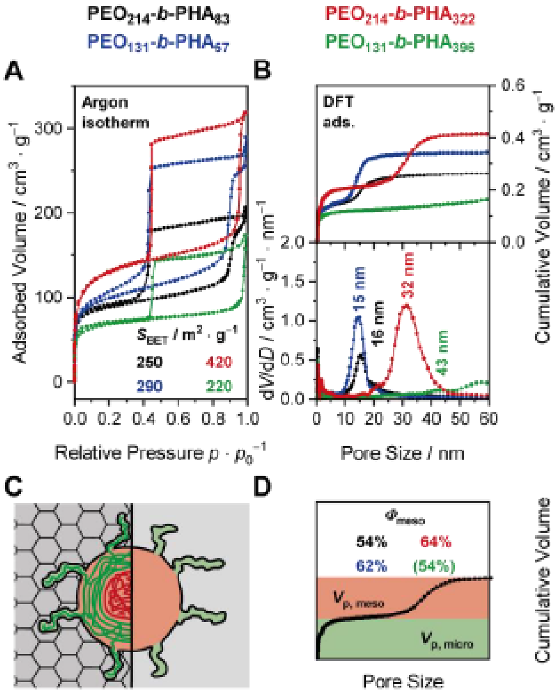

Figure S21. (A) Argon isotherms at 87 K of mesoporous silica synthesized with PEO-*b*-PHA block copolymers of varying PEO and PHA block lengths: PEO_{214}-*b*-PHA_{83} (black), PEO_{214}-*b*-PHA_{322} (red), PEO_{131}-*b*-PHA_{57} (blue), and PEO_{131}-*b*-PHA_{396} (green) as well as (B) the corresponding pore size distributions derived from the adsorption branch with an NLDFT kernel for cylindrical pores. The last sample (green) is not included in the quantitative comparison due to the pore structure most likely not resulting from a soft templating with polymer micelles leading to a blurred pore size distribution. (C) Schematic representation of the contribution of the PEO (green line) and PHA block (red line) to the mesopore (red area) and micropore volume (green area) resulting in (D) the two-step cumulative plot. Also, the mesopore contribution of the silica materials is given.

To quantify the contribution of the mesopore volume to the overall pore volume, the mesopore contribution Φ_{meso} was defined as ratio of mesopore volume $V_{\text{p, meso}}$ to total pore volume (sum of mesopore volume and micropore volume $V_{\text{p, micro}}$) as described in equation (S8):

$$\Phi_{\text{meso}} = \frac{V_{\text{p, meso}}}{V_{\text{p, meso}} + V_{\text{p, micro}}} \qquad \text{(S8)}$$

REFERENCES

(1) Beck, J. S.; Vartuli, J. C.; Roth, W. J.; Leonowicz, M. E.; Kresge, C. T.; Schmitt, K. D.; Chu, C. T. W.; Olson, D. H.; Sheppard, E. W.; McCullen, S. B.; Higgins, J. B.; Schlenker, J. L. A New Family of Mesoporous Molecular Sieves Prepared with Liquid Crystal Templates. *J. Am. Chem. Soc.* **1992**, *114*, 10834–10843.

(2) Kresge, C. T.; Leonowicz, M. E.; Roth, W. J.; Vartuli, J. C.; Beckt, J. S. Ordered Mesoporous Molecular Sieves Synthesized by a Liquid-Crystal Template Mechanism. *Nature* **1992**, *359*, 710–712.

(3) Huo, Q.; Margolese, D. I.; Stucky, G. D. Surfactant Control of Phases in the Synthesis of Mesoporous Silica-Based Materials. *Chem. Mater.* **1996**, *8*, 1147–1160.

(4) Thommes, M.; Köhn, R.; Fröba, M. Sorption and Pore Condensation Behavior of Nitrogen, Argon, and Krypton in Mesoporous MCM-48 Silica Materials. *J. Phys. Chem. B* **2000**, *104*, 7932–7943.

(5) Anderson, M. W. Simplified Description of MCM-48. *Zeolites* **1997**, *19*, 220–227.

(6) Bagshaw, S. A.; Prouzet, E.; Pinnavaia, T. J. Templating of Mesoporous Molecular Sieves by Nonionic Polyethylene Oxide Surfactants. *Science* **1995**, *269*, 1242–1244.

(7) Smarsly, B.; Polarz, S.; Antonietti, M. Preparation of Porous Silica Materials via Sol−Gel Nanocasting of Nonionic Surfactants: A Mechanistic Study on the Self-Aggregation of Amphiphiles for the Precise Prediction of the Mesopore Size. *J. Phys. Chem. B* **2001**, *105* , 10473–10483.

(8) Attard, G. S.; Glyde, J. C.; Göltner, C. G. Liquid-Crystalline Phases as Templates for the Synthesis of Mesoporous Silica. *Nature* **1995**, *378*, 366–368.

(9) Zhao, D.; Huo, Q.; Feng, J.; Chmelka, B. F.; Stucky, G. D. Nonionic Triblock and Star Diblock Copolymer and Oligomeric Sufactant Syntheses of Highly Ordered, Hydrothermally Stable, Mesoporous Silica Structures. *J. Am. Chem. Soc.* **1998**, *120*, 6024–6036.

(10) Kleitz, F.; Hei Choi, S.; Ryoo, R. Cubic Ia3d Large Mesoporous Silica: Synthesis and Replication to Platinum Nanowires, Carbon Nanorods and Carbon Nanotubes. *Chem. Commun.* **2003**, *3*, 2136.

(11) Zhang, Y.; Yang, Q.; Yang, X.; Deng, Y. One-Step Synthesis of *in-situ* N-Doped Ordered Mesoporous Titania for Enhanced Gas Sensing Performance. *Microporous Mesoporous Mater.* **2018**, *270*, 75–81.

(12) Xiao, Y.; You, S.; Yao, Y.; Zheng, T.; Lin, C.; Roth, S. V.; Müller-Buschbaum, P.; Steffen, W.; Sun, L.; Yan, C.; Gutmann, J. S.; Yin, M.; Fu, J.; Cheng, Y. Generalized Synthesis of Mesoporous Rare Earth Oxide Thin Films through Amphiphilic Ionic Block Copolymer Templating. *Eur. J. Inorg. Chem.* **2013**, *2013*, 1251–1257.

(13) Yu, C.; Yu, Y.; Zhao, D. Highly Ordered Large Caged Cubic Mesoporous Silica Structures Templated by Triblock PEO–PBO–PEO Copolymer. *Chem. Commun.* **2000**, 575–576.

(14) Thomas, A.; Schlaad, H.; Smarsly, B.; Antonietti, M. Replication of Lyotropic Block Copolymer Mesophases into Porous Silica by Nanocasting: Learning about Finer Details of Polymer Self-Assembly. *Langmuir* **2003**, *19*, 4455–4459.

(15) Lee, J.; Christopher Orilall, M.; Warren, S. C.; Kamperman, M.; DiSalvo, F. J.; Wiesner, U. Direct Access to Thermally Stable and Highly Crystalline Mesoporous Transition-Metal Oxides with Uniform Pores. *Nat. Mater.* **2008**, *7*, 222–228.

(16) Stefik, M.; Song, J.; Sai, H.; Guldin, S.; Boldrighini, P.; Orilall, M. C.; Steiner, U.; Gruner, S. M.; Wiesner, U. Ordered Mesoporous Titania from Highly Amphiphilic Block Copolymers: Tuned Solution Conditions Enable Highly Ordered Morphologies and Ultra-Large Mesopores. *J. Mater. Chem. A* **2015**, *3*, 11478–11492.

(17) Wei, J.; Wang, H.; Deng, Y.; Sun, Z.; Shi, L.; Tu, B.; Luqman, M.; Zhao, D. Solvent Evaporation Induced Aggregating Assembly Approach to Three-Dimensional Ordered Mesoporous Silica with Ultralarge Accessible Mesopores. *J. Am. Chem. Soc.* **2011**, *133*, 20369–20377.

(18) Tanaka, S.; Kaneti, Y. V.; Bhattacharjee, R.; Islam, M. N.; Nakahata, R.; Abdullah, N.; Yusa, S.; Nguyen, N.-T.; Shiddiky, M. J. A.; Yamauchi, Y.; Hossain, M. S. A. Mesoporous Iron Oxide Synthesized Using Poly(Styrene-*b*-Acrylic Acid-*b*-Ethylene Glycol) Block Copolymer Micelles as Templates for Colorimetric and Electrochemical Detection of Glucose. *ACS Appl. Mater. Interfaces* **2018**, *10*, 1039–1049.

(19) Graberg, T. Von; Hartmann, P.; Rein, A.; Gross, S.; Seelandt, B.; Röger, C.; Zieba, R.; Traut, A.; Wark, M.; Janek, J.; Smarsly, B. M. Mesoporous Tin-Doped Indium Oxide Thin Films: Effect of Mesostructure on Electrical Conductivity. *Sci. Technol. Adv. Mater.* **2011**, *12*, 1–12.

(20) Billet, J.; Vandewalle, S.; Meire, M.; Blommaerts, N.; Lommens, P.; Verbruggen, S. W.; De Buysser, K.; Du Prez, F.; Van Driessche, I. Mesoporous TiO_2 from Poly(*N,N*-Dimethylacrylamide)-*b*-Polystyrene Block Copolymers for Long-Term Acetaldehyde Photodegradation. *J. Mater. Sci.* **2020**, *55*, 1933–1945.

(21) Yu, K.; Hurd, A. J.; Eisenberg, A.; Brinker, C. J. Syntheses of Silica/Polystyrene-*block*-Poly(ethylene oxide) Films with Regular and Reverse Mesostructures of Large Characteristic Length Scales by Solvent Evaporation-Induced Self-Assembly. *Langmuir* **2001**, *17*, 7961–7965.

(22) Liang, S.; Guan, T.; Yin, S.; Krois, E.; Chen, W.; Everett, C. R.; Drewes, J.; Strunskus, T.; Gensch, M.; Rubeck, J.; Haisch, C.; Schwartzkopf, M.; Faupel, F.; Roth, S. V.; Cheng, Y.-J.; Müller-Buschbaum, P. Template-Induced Growth of Sputter-Deposited Gold Nanoparticles on Ordered Porous TiO_2 Thin Films for Surface-Enhanced Raman Scattering Sensors. *ACS Appl. Nano Mater.* **2022**, *5*, 7492–7501.

(23) Lokupitiya, H. N.; Jones, A.; Reid, B.; Guldin, S.; Stefik, M. Ordered Mesoporous to Macroporous Oxides with Tunable Isomorphic Architectures: Solution Criteria for Persistent Micelle Templates. *Chem. Mater.* **2016**, *28*, 1653–1667.

(24) Velev, O. D.; Jede, T. A.; Lobo, R. F.; Lenhoff, A. M. Porous Silica via Colloidal Crystallization. *Nature* **1997**, *389*, 447–448.

(25) Waterhouse, G. I. N.; Waterland, M. R. Opal and Inverse Opal Photonic Crystals: Fabrication and Characterization. *Polyhedron* **2007**, *26*, 356–368.

(26) Zakhidov, A. A.; Baughman, R. H.; Iqbal, Z.; Cui, C.; Khayrullin, I.; Dantas, S. O.; Marti, J.; Ralchenko, V. G. Carbon Structures with Three-Dimensional Periodicity at Optical Wavelengths. *Science* **1998**, *282*, 897–901.

(27) Chai, G. S.; Yoon, S. B.; Yu, J.-S.; Choi, J.-H.; Sung, Y.-E. Ordered Porous Carbons with Tunable Pore Sizes as Catalyst Supports in Direct Methanol Fuel Cell. *J. Phys. Chem. B* **2004**, *108*, 7074–7079.

(28) Rasmussen, C. J.; Vishnyakov, A.; Thommes, M.; Smarsly, B. M.; Kleitz, F.; Neimark, A. V. Cavitation in Metastable Liquid Nitrogen Confined to Nanoscale Pores. *Langmuir* **2010**, *26*, 10147–10157.

3.2 Publikation 2

Porosity Tuning in Soft-templated Mesoporous Silica: The Influence of Block Copolymer Composition and Concentration

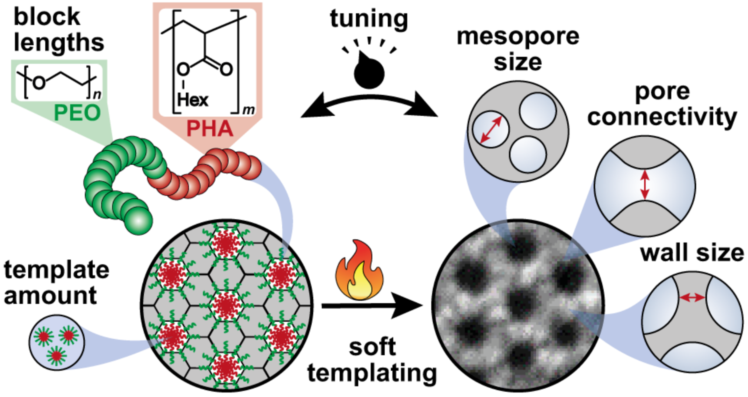

Reprinted with permission from

L. Q. Wagner, F. Breckwoldt, X. Huang, C. Kübel, X. Cheng, K. Schladitz, B. M. Smarsly, Porosity Tuning in Soft-templated Mesoporous Silica: The Influence of Block Copolymer Composition and Concentration, *Langmuir* **2025**, *41*, 30948 – 30967.

DOI: 10.1021/acs.langmuir.5c02750

LANGMUIR

pubs.acs.org/Langmuir

Article

Porosity Tuning in Soft-templated Mesoporous Silica: The Influence of Block Copolymer Composition and Concentration

Lysander Q. Wagner, Frederik Breckwoldt, Xiaohui Huang, Christian Kübel, Xiaoyin Cheng, Katja Schladitz, and Bernd M. Smarsly*

Cite This: *Langmuir* 2025, 41, 30948−30967

ABSTRACT: Macroscopic properties of mesoporous metal oxides depend on the mesopore architecture, i.e., the pore size, wall thickness, and pore connectivity. Consequently, rational preparation protocols and deep knowledge of the templating mechanism are required for systematic porosity−property studies and the intentional synthesis of an optimized pore morphology. In this work, we thus prepared a library of 17 poly(ethylene oxide)-*block*-poly(hexyl acrylate) (PEO-*b*-PHA) block copolymers of varying PEO and PHA block lengths to quantitatively deduce the effect of the individual block lengths on the mesopore size of the templated silica. The block length of the hydrophobic PHA block in the micelle core showed to enable a pore size tuning between 10 and 80 nm according to electron microscopy, physisorption, and small-angle X-ray scattering. In contrast, varying the PEO block length did not alter the pore size, but revealed that a sufficiently large PEO block is required to ensure ordered spherical mesopores. Electron tomography confirmed a spherical pore geometry and a systematic decrease in pore wall thickness upon increasing the template concentration (i.e., template-to-silica ratio) during soft templating. A statistical in-depth analysis by tomography demonstrated that this wall size decrease is accompanied by an improved pore connectivity (e.g., in terms of the coordination number of adjacent pores) and an increasing pore size. The pore size increase originates from a partial PEO collapse on the micelle core based on a pore volume analysis and occurs only above a certain threshold concentration of block copolymer. We demonstrated that this concentration can be elevated by applying soft templates featuring shorter PEO blocks, which extend the regime of wall size tuning under preservation of pore dimension and shape. Overall, these insights provide a guideline on how to tailor the pore size, wall thickness, and pore connectivity of mesoporous metal oxides and enable systematic studies concerning the optimum porosity, e.g., for electrocatalytic applications to maximize stability and activity.

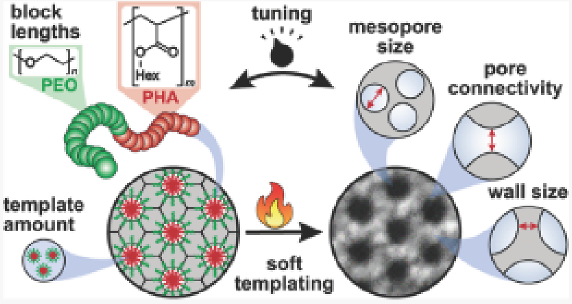

INTRODUCTION

Ordered mesoporous powders and thin films have attracted great attention in the past 30 years. As model materials with a uniform structure, they helped to understand and advance characterization methods such as gas physisorption,[1−7] mercury intrusion porosimetry,[8] and ellipsometric porosimetry,[9,10] which now enable a reliable and standardized analysis of materials with a disordered pore space. Thus, a systematic synthesis of well-ordered structures is required to expand routine techniques for pore analysis. In application, mesoporous materials take advantage of their high surface (or interface) area and large pore volume, boosting the performance of catalysts,[11−15] adsorbents,[16] gas sensors,[17,18] coatings,[19] and energy materials.[20−22] Hereby, it is important to mention that macroscopic properties like conductivity, catalytic activity, capacitance, and both thermal and mass transport show a dependency on mesoscopic parameters, namely, pore size,[23−29] wall thickness,[30] and pore connectivity.[22,31−33] Consequently, dedicated preparation protocols and closer insights into the templating behavior are required to (1) investigate porosity−property relationships systematically and (2) generate an optimized pore morphology for a desired property precisely and deliberately.

Tuning of the mesopore size is often achieved by adjusting synthesis temperature,[34−36] varying the amount[34,37] and kind[38] of acid used as a sol−gel catalyst, and using additives[12,39] or swelling agents[35,40−42] within the soft templating process. Such modifications in the synthesis protocol, however, might result in the alteration of the final skeleton material as well, e.g., its crystallite size.[43] To keep the skeleton material ideally untouched and to vary only the pore morphology, tuning the

Received: May 29, 2025
Revised: October 17, 2025
Accepted: October 27, 2025
Published: November 13, 2025

https://doi.org/10.1021/acs.langmuir.5c02750
Langmuir 2025, 41, 30948−30967

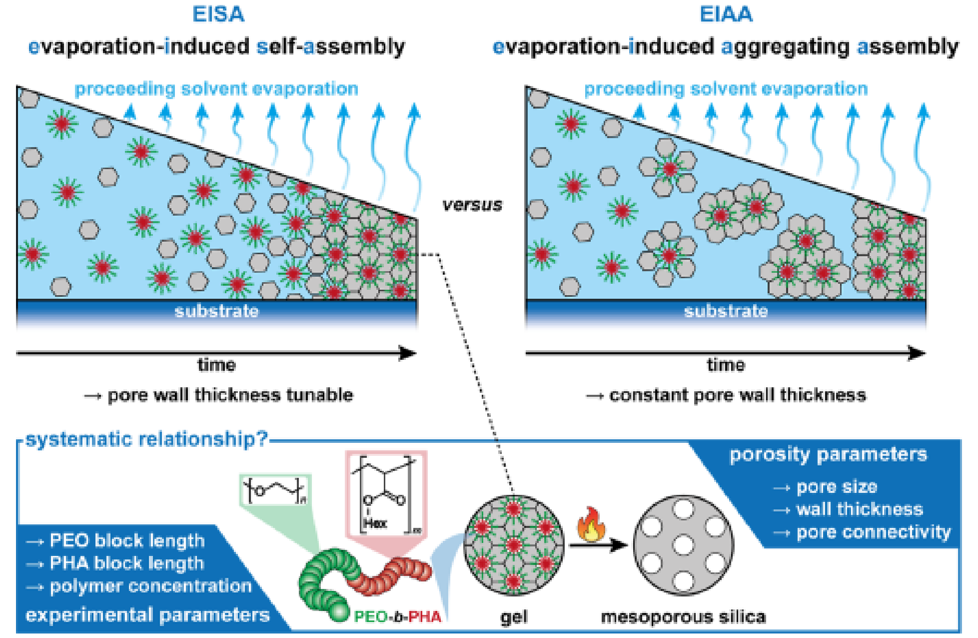

Figure 1. Schematic illustration of the EISA and EIAA mechanism for preparing mesoporous materials. In the case of EISA occurring for silica templated with PEO-*b*-PHA, the question arises how the experimental parameters (template composition and amount) are quantitatively related to structural parameters of the final mesoporous oxide.

soft template appears to be a viable option. Especially, if block copolymers are applied as structure-directing agents, variation of the block lengths represents, at first glance, a straightforward approach to adjust the pore size without changing the chemical nature of the components in the synthesis. Concerning the pore size regime, a range of 30−70 nm is of particular interest, still providing a high surface area but avoiding possible diffusion limitations of small pore networks.[44,45] Here, diblock copolymers of poly(ethylene oxide) and poly(hexyl acrylate) (PEO-*b*-PHA) appear especially suitable and superior due to their facile synthesis[46,47] and the ability to introduce large mesopores of around 50 nm in diameter.[22,46,48] Although PEO-*b*-PHA has already been used for soft templating, a precise relationship between PEO and PHA block lengths and the resulting mesopore size would further spur this field. Similarly, the question arises, which pore size region can be covered with this polymer class at all.

Besides the pore size, the pore wall thickness features a further major porosity parameter, e.g., by restricting crystallite growth within the pore wall. Tailoring the pore wall thickness is accomplished in most cases by changing the ratio between precursor and soft template.[12,47−50] This modification is only possible if soft templating follows an evaporation-induced self-assembly (EISA)[51−53] mechanism: As shown in Figure 1, the amphiphilic soft template forms micelles, which arrange themselves in a closely packed pattern during the proceeding solvent evaporation. In the space between the micelles, the (metal oxide) precursor condenses to a gel. A calcination step decomposes the template and converts the micelle pattern to an array of mesopores. If the soft template micelles are evenly dispersed within the matrix of the condensed precursor, the precursor-to-template ratio governs the micelle-to-micelle and thus the pore-to-pore distance, i.e., the pore wall thickness (as long as no phase separation occurs, i.e., precipitation of the template). Contrarily, following an evaporation-induced aggregating assembly (EIAA)[54] mechanism, micelles and precursors assemble in dispersion (Figure 1) and hence do not allow a wall size tuning by varying the template amount. While Stefik and co-workers reported an independent adjustment of pore and wall size for soft templating of Nb_2O_5 with PEO-*b*-PHA,[47,48,50] we observed an increase in pore size in silica following an EISA approach upon increasing the template amount.[46] Shao et al. observed a similar trend with Pluronic polymer P123 used for soft templating of titanium dioxide.[25] Also, studies on poly(isoprene)-*block*-poly(ethylene oxide) confirm an influence of the metal precursor amount on the local PEO environment, yielding different mesopore sizes and morphologies.[55−57] This apparent contradiction demonstrates that the influence of the template-to-precursor ratio is complex and evokes the question of how the soft template amount affects the pore space, i.e., pore size, wall size, and pore connectivity, over a broad range for a given block copolymer (BCP). Indeed, micelle kinetics and the solvent used to disperse them play an important role, as equilibration of micelles by polymer chain exchange depends on the block length[58] N and the interaction parameter[59] χ between the solvent and the solvophobic block in the micelle core. Thus, depending on the χN barrier for chain exchange (being very low in case of Pluronic P123 and very high for PEO-*b*-PHA, for instance, when presuming a hydrophilic solvent), BCP micelles can equilibrate according to their environment (dynamic micelles) or are kinetically trapped (persistent micelles).[60,61] Using the latter in soft templating, the pore size is expected to be locked to a constant value, whereas solvents enabling chain exchange (dynamic micelles) or even full micelle-core/solvent interactions (templating by BCP coassembly) might lead to fluctuating average pore sizes different from the value obtained by persistent micelle templating.[62] With dynamic micelles as a soft template, the micelle and thus pore

https://doi.org/10.1021/acs.langmuir.5c02750
Langmuir 2025, 41, 30948−30967

size deviate in both directions (up to 10−20% smaller or larger compared to the persistent micelle case[40,47,50,63]), which e.g., depends on the thermodynamic equilibrium size for a given (solvent) composition and temperature.[64−70] If this thermodynamic situation changes (or is changed intentionally) during the soft templating process, then a dynamic micelle will adjust its size accordingly (as long as chain exchange is sufficiently fast). In contrast, a persistent micelle maintains a constant aggregation number.

Besides the micelle kinetics, also the polymer block constituting the micelle corona can affect the pore size: If solvation is not sufficient to fully embed the solvophilic block as a single chain inside the pore wall phase or the micelle core is enlarged featuring a larger core surface area, which needs to be stabilized, a fraction of the corona block will collapse on the micelle core leading to an increase in mesopore size.[71]

In this study, we thus tackle the role of (1) the block lengths of PEO-*b*-PHA copolymers and (2) the template amount in soft templating. Therefore, we prepared a library of 17 different samples of PEO-*b*-PHA comprising four different PEO block lengths and different PHA block lenghts, and employed them in the soft templating of silica. Characterizing the mesoporous powders by electron microscopy, nitrogen physisorption, and small-angle X-ray scattering (SAXS), we derive a quantitative relation between the individual block lengths and the pore size and reveal which of the synthesized PEO-*b*-PHA polymers can be used for generating spherical mesopores, and which pore size regime can be covered. This empirical relationship is then discussed in terms of fundamental principles of polymer physics. Soft templating with different amounts of PEO-*b*-PHA reveals the interplay of the micelle-to-micelle distance and the resulting pore size, wall thickness, and especially pore connectivity. The latter parameter was assessed by physisorption and especially by in order to unravel dependency on the PEO block length. In particular, this study intended to clarify to which extend the PEO block is a contributor to the micropore volume and possibly to the spherical mesopores and their size. Considering the similarity between soft-templated silica and zirconia in our previous study,[46] the trends observed here likely can be generalized to other metal oxides and soft templates (as long as synthesis adjustments and precursor changes do not significantly hamper micellization), providing important guidelines for all kinds of systematic studies on porosity−property relationships and for the rational synthesis of adesired mesopore structure.

■ EXPERIMENTAL SECTION

Synthesis of the Macroinitiator PEO−Br. All block copolymers used throughout this work are based on four homopolymers of α-methyl-ω-hydroxy poly(ethylene oxide) (PEO−OH) with an average molecular weight of 2 kDa, 5 kDa, 10 kDa, and 20 kDa, respectively, as provided by the supplier Sigma-Aldrich. A ^{1}H NMR end group analysis gave a number-average molecular weight (M_n) of the PEO−OH samples of 2.1 kDa (47 EO units), 6.0 kDa (137 EO units), 11.0 kDa (251 EO units), and 19.4 kDa (441 EO units), respectively.

Conversion of the PEO−OH homopolymers to the macroinitiators PEO−Br followed a Steglich esterification based on Lokupitiya et al.[48] and reported in detail in our previous study.[46] Briefly described, 1.0 equiv of PEO−OH (Sigma-Aldrich) was dissolved in a Schlenk round-bottom flask in anhydrous dichloromethane (DCM, 99.8%, Acros Organics) under argon by stirring at room temperature. Next, 1.2 equiv of 2-bromopropionic acid (99%, Acros Organics) were added with a syringe, followed by the addition of 0.4 equiv 4-dimethylaminopyridine (DMAP, ≥99%, Sigma-Aldrich) and 2.3 equiv of *N*,*N*′-dicyclohexylcarbodiimide (DCC, 99%, Sigma-Aldrich) during cooling with an ice bath. The turbid reaction mixture was stirred under an argon atmosphere at room temperature for 20 h. After excess DCC was quenched with 1 M hydrochloric acid (Grüssing GmbH), the suspension was diluted with DCM and filtered over a paper filter. The clear filtrate was concentrated under reduced pressure, and the resulting colorless residue was dissolved in tetrahydrofuran (THF, technical grade, Thermo Scientific, purified over basic aluminum oxide to remove peroxides). Precipitating twice in a 10-fold volume of cold diethyl ether (being cooled with an ice bath) and drying in a vacuum oven at 40 °C for 1 day delivered a colorless powder with a yield of 81% (20 kDa), 91% (10 kDa), 78% (5 kDa), and 89% (2 kDa).

In addition, a second PEO−OH sample (20 kDa according to Sigma-Aldrich, 16.4 kDa and 372 EO units according to NMR) was converted to PEO−Br with a yield of 88% as a reference for gel permeation chromatography (GPC) and dynamic light scattering (DLS) studies (see below).

Synthesis of the PEO-*b*-PHA Copolymers. The PEO-*b*-PHA block copolymers were synthesized by a supplemental activator reducing agent atom transfer radical polymerization (SARA ATRP), as recently described.[46] A copper wire being activated in a mixture of methanol and concentrated hydrochloric acid[72,73] and wrapped around a stirring bar served as a reducing agent. In a typical reaction, 1.0 equiv of PEO−Br and 3.0 equiv of tris(2-pyridylmethyl)amine (TPMA, >98.0%, TCI CO.) were dissolved in anhydrous *N*,*N*-dimethylformamide (DMF, 99.8%, Acros Organics) by stirring at 40 °C in a Schlenk round-bottom flask in an inert atmosphere. After adding 1.5 equiv of $CuBr_2$ (>99%, water-free, Acros Organics) under flowing argon, a freeze−pump−thaw cycle was carried out before injecting respective amounts (typically 10% more than the targeted degree of polymerization) of hexyl acrylate (98%, Sigma-Aldrich, purified from inhibitors by passing over basic aluminum oxide) into the solution. Following two further freeze−pump−thaw cycles, the copper-coated stirring bar was introduced under flowing argon, and the green solution was stirred at 70 °C under an argon atmosphere for 18 h. The obtained orange gel was diluted with THF and passed over a column of basic aluminum oxide. After removing the solvent with a rotary evaporator, the clear gel was dissolved in THF and precipitated in a 10-fold volume of cold methanol (cooled with an ethyl acetate/liquid nitrogen freezing mixture) twice. The colorless to yellow residue was transferred to a Petri dish and dried in a vacuum oven at 40 °C overnight. In the case of PEO_{047}-Br-based copolymers, the precipitate was recovered by centrifugation at 5000 rpm for 5 min instead of filtration over a Büchner funnel. On average, around 60% of the expected mass (sum of macroinitiator and monomer) was obtained in the form of a colorless to yellow gel. All batches, including the amount of chemicals each, are listed in Table S1, while characterization by NMR and GPC is given in the Supporting Information.

Synthesis of Mesoporous SiO_2 Powders. Mesoporous SiO_2 powders were prepared by soft templating in analogy to our past article.[46] In this sol−gel synthesis, relying on the studies of Weller et al.[74] and Cop et al.,[75] the corresponding amount of soft template (see Table S2)—namely, PEO-*b*-PHA or PIB_{50}-*b*-PEO_{45} (BASF)[27,75−78]—was dissolved by ultrasonication at 37 kHz and 40 °C in 1 mL of absolute ethanol (99.8%, Fisher Chemical) within 40 min. Meanwhile, 130 μL of tetraethyl orthosilicate (TEOS, 98%, Sigma-Aldrich) was dissolved in 0.5 mL absolute ethanol by stirring at room temperature in a 5 mL PTFE cup. Both the clear polymer solution and 40 μL of deionized water were added to the metal oxide precursor. After 5 min of stirring, 10 μL of a concentrated hydrochloric acid (37 wt %) were added prior to stirring for 1 h at room temperature. The clear solution was kept at 40 °C under a glass dome for 2 days, followed by a second drying step in a vacuum oven at 40 °C for 1 day. The colorless gel was calcined at 350 °C for 1 h to remove the soft template, and at 500 °C for 4 h to obtain the final metal oxide (heating ramp each: 2 K min^{-1}), resulting in *circa* 35 mg of a colorless powder after grinding in an agate mortar.

Characterization Techniques. Proton-nuclear magnetic resonance (^{1}H NMR) spectra were acquired in $CDCl_3$ at 25 °C with Bruker AVANCE II 400 MHz and Bruker AVANCE III 400 MHz HD as well

https://doi.org/10.1021/acs.langmuir.5c02750
Langmuir 2025, 41, 30948−30967

as a Bruker Ascend AVANCE 4 Neo 7 700 MHz spectrometer and evaluated with MestReNova 14.1.2. All signals were referenced to the solvent signal at $\delta = 7.26$ ppm. GPC with simultaneous UV (TSP UV 1000) and differential refractive index (Shodex RI-101) detection was executed at room temperature using tetrahydrofuran as an eluent at a flow rate of 0.5 mL min^{-1}. The stationary phase consisted of a 300 mm × 8 mm PSS SDV linear M column packed with 3 μm particles (molecular weight range of 1×10^2 to 1×10^6 Da). Prior to the injection of a 100 μL sample solution containing around 0.15 wt % polymeric sample, it was filtered through 0.45 μm filters. Poly(styrene) standards (PSS, Mainz, Germany) were used for calibration. DLS experiments were performed on a Zetasizer Nano series instrument from Malvern. For each measurement, sample solutions with around 1 mg mL^{-1} polymer in ethanol and methanol, respectively, were characterized in three runs of 13 cycles. The data were exported using the corresponding application, Zetasizer Software.

Nitrogen physisorption experiments were carried out at 77 K on a Quadrasorb evo instrument (Quantachrome Instruments, Boynton Beach, FL) after sample degassing at 200 °C for 6 h in order to remove attached water and gases. The data obtained were analyzed with the aid of the software ASiQwin by applying a nonlocal density functional theory (NLDFT) method dedicated to nitrogen at 77 K on siliceous/oxidic materials, assuming a cylindrical pore geometry. The pore size distribution was obtained from the adsorption branch by applying a dedicated metastable adsorption branch kernel, which correctly takes into account the delay in pore condensation due to the metastable pore fluid.[2]

Scanning electron microscopy (SEM) images were obtained with a Zeiss GeminiSEM 560 microscope using an InLens detector, a working distance of 2.5 mm, and an acceleration voltage of 1 kV. To enhance the conductivity, samples were sputtered with platinum using a Leica EM ACE600 sputter coater. All images were evaluated with Fiji ImageJ software.

SAXS measurements were carried out by the laboratory SAXS instrument SAXSpoint 2.0 by Anton Paar using point-focused (spot size of 500 μm) and slit-collimated Cu Kα radiation ($\lambda = 0.1541$ nm) from a microsource operating at 50 W and a Dectris EIGER2 R 1 M hybrid pixel area X-ray detector. Powder samples were placed into an Anton Paar solid sample holder comprising a 1 mm thick metal plate with 20 square holes mounted on a motorized X/Y-stage. The sample plate was sealed at both sides with a vacuum-tight sealing tape. SAXS images of the samples and the background (sealing tapes) were recorded in vacuum (around 1 mbar and 25 °C) at a sample-to-detector distance of 575.65 mm. For each sample and background, respectively, 15 single images with 2 min exposure time each were recorded, averaged, and radially integrated in order to obtain the 1D-SAXS curves. The scattering curves were fitted using SASfit 0.94.11 with a model consisting of a form factor for spheres with a Gaussian size distribution and a lattice factor applying the implemented decoupling approximation.

Scanning transmission electron microscopy (STEM)-based tomography was executed with a Thermofisher Scientific Themis 300 transmission electron microscope equipped with probe aberration correction and operated at an acceleration voltage of 300 kV. The silica powder (around 10 mg) was ground, suspended in ethanol, and dropped on a 100 × 400 mesh carbon-coated copper grid purchased from Quantifoil Micro Tools GmbH. Gold nanoparticles ($d_{\text{Au-np}} = 12$ nm) were deposited onto the sample as fiducial markers for image alignment. The grid was cleaned twice for 30 s using a Fischione 1070 plasma cleaner in an argon−oxygen atmosphere with a power of 50%. A high-angle annular dark-field (HAADF)-STEM tilt series was acquired over a tilt range of −72° to 70° (step size: 2°) and with a pixel size of 0.81 nm using the Xplore3D software (Thermofisher Scientific) with auto focus and tracking before acquisition. A small convergence angle of roughly 8.5 mrad was used to increase the depth of focus. With the aid of the gold nanoparticles, image alignment was done in IMOD Version 4.11.7 (University of Colorado) with a residual alignment error of 0.606 nm (0.374 px). The 3D reconstruction (with a voxel size of (1.62 nm)^3) was obtained from the aligned tilt series with the simultaneous iterative reconstruction technique and 100 iterations in Inspect 3D 4.4 (Thermofisher Scientific). Denoising with a median filter in ImageJ and binarization by global thresholding in Avizo 2021.1 (Thermofisher Scientific) of the tomograms yielded an initial segmentation. The segmented volume was purified by the removal of unconnected islands smaller than 15 voxels, which originate from reconstruction artifacts. Skeletonization of a cropped region of the image stack was executed, as reported by Cheng et al.[79] using ToolIP with MAVIkit 2024 (Fraunhofer ITWM) in order to elucidate the local pore connectivity. Pore and wall size distributions were obtained with a local thickness evaluation using the corresponding plugin in ImageJ after subtracting the background with a Python code applying a rolling ball radius of 30 pixels (48.6 nm) as recently described by us.[80] While the experimental values of tilt range, unbinned pixel size, residual alignment error, voxel size of the 3D reconstruction, and the rolling ball radius given here correspond to the 85 vol % sample, the experimental details of the remaining samples (69 and 75 vol %) are listed in Table S3. Thermogravimetric studies coupled with mass spectrometry (TG-MS) were carried out in synthetic air using a STA40PC thermoscale provided by Netzsch within a temperature range from 30 to 1000 °C with a heating ramp of 2 K min^{-1} and the heating ramp used for the silica synthesis, respectively. Meanwhile, a mass spectrum covering an m/z interval between 12 and 100 was recorded constantly with the aid of a QMG451 quadrupole mass spectrometer by Balzers.

■ RESULTS AND DISCUSSION

PEO-*b*-PHA Block Copolymers. The synthesis of PEO-*b*-PHA block copolymers featuring a hydrophilic poly(ethylene oxide) and a hydrophobic poly(hexyl acrylate) block follows a two-step protocol described in our last article and summarized in Scheme S1: Steglich esterification yields the PEO−Br macroinitiator, to which the PHA block is attached by supplemental activator reducing agent atom transfer radical polymerization (SARA ATRP).[46] Studying the influence of both the PEO and the PHA block lengths on the pore size after soft templating requires a systematic matrix of block copolymers with tailored block lengths. Thus, four different PEO−Br macroinitiators were prepared starting from PEO homopolymers with average molecular weights of 20, 10, 5, and 2 kDa (as reported by the supplier). According to NMR end group analysis,[46] the degree of polymerization of the macroinitiators amounts to 441, 251, 137, and 47 EO units, respectively (see ^{1}H NMR spectra in Figures S1 and S2). From these PEO$_n$−Br macroinitiators, 18 different PEO$_n$-*b*-PHA$_m$ samples were prepared. According to NMR (Figures S1 and S2), the degrees of polymerization n and m of the PEO and PHA block, respectively, are obtained as plotted in Figure 2 and Table S4.

The PEO-*b*-PHA samples possess a polydispersity index of around 1.4 (Table S4), similar to the copolymers in our previous study.[46] In general, the GPC curves (Figure S3A) are consecutively shifted to smaller elution volumes with increasing NMR-based PHA block length, as expected from the increasing molecular weight and thus polymer size. The only exception is sample PEO$_{441}$-*b*-PHA$_{270}$ showing an almost identical GPC trace as polymer PEO$_{441}$-*b*-PHA$_{326}$ but, in addition, a higher amount of residual PEO homopolymer (shoulder at high elution volumes).[81] As a result, both the GPC-based average molecular weight and especially the NMR-based PHA block length are underestimated because both methods rely on the average over the entire sample. Hence, sample PEO$_{441}$-*b*-PHA$_{270}$ was excluded from quantitative studies on the dependency of the pore size on the block lengths and only used for concentration-dependent investigations, in which the relative pore size evolution is of importance. Due to calibration to poly(styrene) (PS), GPC is not capable of providing absolute weight distributions. However, a plot of the apparent number-weighted

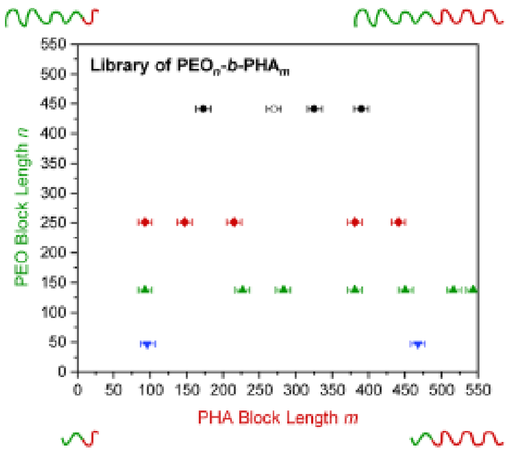

Figure 2. Library of PEO-b-PHA copolymers synthesized from PEO–Br macroinitiators with a PEO block length of 441 (black), 251 (red), 137 (green), and 47 EO units (blue). Sample PEO$_{441}$-b-PHA$_{270}$ (open symbol) was neglected for pore size evaluation due to the high polydispersity.

molecular weight from GPC against the NMR-based degree of polymerization of the PHA block still yields a linear trend. Indeed, the plots in Figure S3B confirm that all samples follow such a linear behavior with a slope of around 100 Da. Taking the molar mass of the repeating unit in the PHA block of 156 Da into account, we find that the order of magnitude is reasonable. Both the linear trend and the reasonable slope thus support that the block lengths from NMR (Figure 2) are reliable.

The soft templating process is based on the ability of PEO-b-PHA to self-assemble into spherical micelles, being converted to spherical mesopores upon calcination. In this regard, the size of the block copolymers in solution governs the pore size and is of particular relevance. However, our previous DLS study[46] showed that PEO-b-PHA does not form micelles in ethanol—the solvent used for soft templating—but dissolves as Gaussian coils. Yet, such a study using DLS (Figure 3A) is valuable to back up the block lengths obtained from NMR, as the coil size should depend on the length of both blocks. The reason why PEO-b-PHA still forms micelles upon solvent evaporation[46] in the soft templating of silica can be rationalized by the solubility of the respective polymer blocks estimated by the Hildebrand solubility parameters δ.[82−84] During the evaporation of ethanol (δ = 26.2 $\sqrt{\text{MPa}}$), the reaction mixture is enriched with the silica precursor TEOS (δ = 14.6 $\sqrt{\text{MPa}}$, calculated with an enthalpy of vaporization of 50 kJ mol^{-1}) leading to a decrease in δ of the solution and approaching the solubility of the hydrophobic PHA block (δ = 16.6 $\sqrt{\text{MPa}}$) and thus the micellization regime.[48] Following the DLS study in our previous work, micellization occurs, starting from a TEOS fraction of 80 vol %, which equals a δ = 16.9 $\sqrt{\text{MPa}}$ (upon volumetric averaging), being close to the PHA solubility. Regarding the solubility of the PEO block (δ = 20.3 $\sqrt{\text{MPa}}$),[85] PEO-b-PHA might possibly even form inverse micelles in the highly TEOS-enriched low-δ regime, being close to PHA but far away from the PEO solubility. This scenario, however, is unlikely because the (partial) hydrolysis of TEOS already occurs due to environmental humidity (to a small extent) and particularly during the synthesis due to the added water, which elevates the actual solubility parameter of the silica precursor. Also, it should be noted that the added amounts of water and hydrochloric acid further increase δ of the sol–gel mixture (away from the dynamic micelle regime), but a meaningful estimation is difficult due to the unknown amount of water removed by coevaporation with ethanol, hydrolysis of TEOS, and absorption through the silica gel.[86] Therefore, a clear statement of whether the micelles are persistent or dynamic is impossible for our synthesis. Yet, the extreme case of polymer coassembly (bulk behavior with the least solvent selectivity)[62,86] can be excluded since micellization in (TEOS-enriched) solution within an EISA mechanism was identified (prior to gelation) by cryo-electron microscopy and SAXS in solution in our previous study.[46] In contrast to ethanol, PEO-b-PHA showed micellization in methanol,[22,50] giving access to evaluate the micelle size in dependency on the PEO and PHA block length (Figure 3B).

The DLS data of the polymers dissolved in ethanol (Figures S4 and S5) clearly show an increase in hydrodynamic diameter with increasing PHA block length, but also with increasing PEO block length. This observation becomes more apparent in a plot

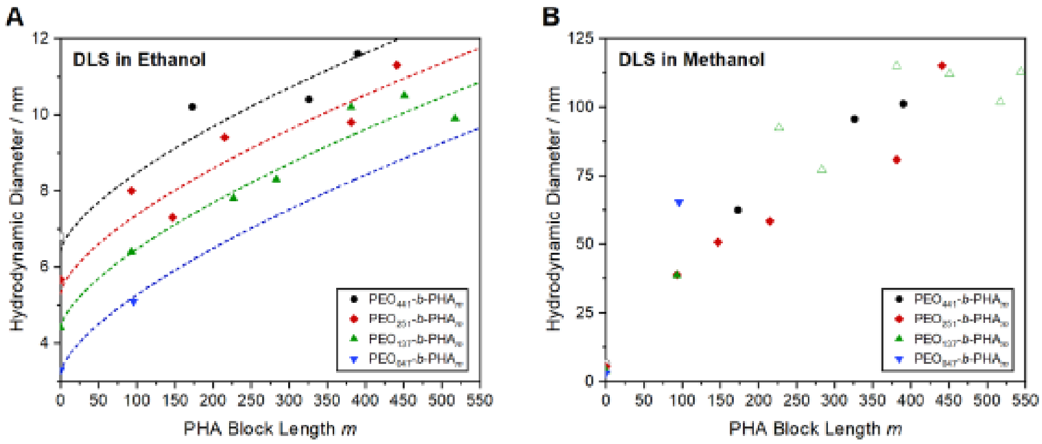

Figure 3. Hydrodynamic diameter from DLS of PEO-b-PHA copolymers of varying PEO block lengths (441 EO units in black, 251 in red, 137 in green, and 47 in blue) dissolved in (A) ethanol and (B) methanol. Entities expected to be vesicles instead of micelles (see SEM images below) are shown with open symbols. Due to a lack of sufficient amounts of PEO$_{441}$–Br, PEO$_{372}$–Br (open black circle) was investigated for comparison.

https://doi.org/10.1021/acs.langmuir.5c02750
Langmuir 2025, 41, 30948−30967

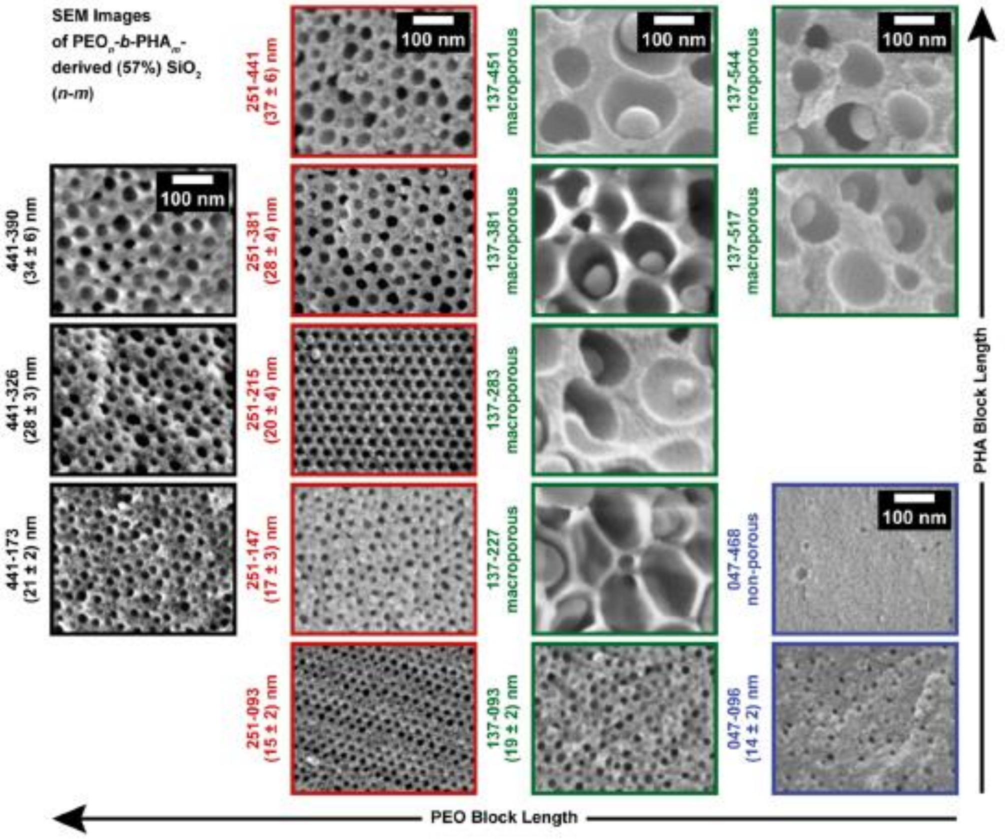

Figure 4. SEM images of mesoporous silica prepared with 57 vol % PEO$_n$-*b*-PHA$_m$ with a PEO block length of n = 441 (black), 251 (red), 137 (green), and 47 (blue), while the PHA block length m increases from the bottom to the top for each PEO block length. The mesopores are spherical in shape, as confirmed by SAXS and electron tomography.

of the average hydrodynamic diameter against the PHA block length m. In the case of all PEO block lengths, Figure 3A reveals a degressive increase of the coil size with increasing PHA block length following roughly an $m^{0.67}$ dependency. Despite the uncertainties of these measurements (ca. ± 1 nm) and the pronounced scattering of the data points in the case of large PEO blocks, the exponent in the power law (0.67) is close to Flory's exponent of 0.6 observed for dissolved PEO by DLS[87] and hints at a coiled state. Furthermore, the increase of the hydrodynamic diameter with increasing PEO block length can be clearly envisioned in Figure 3A, yielding a gradual shift of the fit curves toward higher diameters. So, the observed trends for the PEO and PHA block length variation further support the NMR-based degrees of polymerization.

Going to methanol, the entities observed by DLS are significantly larger than those in ethanol (Figures S4 and S5), except for the homopolymers (m = 0), whose hydrodynamic diameter remains the same as in ethanol. This observation confirms the self-assembly of PEO-*b*-PHA copolymers in methanol. Regarding a quantitative evaluation, an accurate scaling law is difficult to derive, as the data points are severely scattered (Figure 3B). However, the hydrodynamic diameter appears to scale linearly with the PHA block length (m^1), which is reasonable for micelles[71,88,89] although the exact exponent depends on the extent of segregation of both blocks.[90] Especially, if those block copolymer molecules are neglected that form vesicles instead of micelles (open symbols in Figure 3B) according to soft templating (see SEM evaluation below), a linear trend becomes obvious with a slope of roughly 20 nm per 100 HA units. A comparable slope (*circa* 25 nm per 100 S units) is found if the DLS-based diameter of PEO-*b*-PS micelles is plotted against the PS block length,[89] which strengthens the trend observed here. On the other hand, the influence of the PEO block length on the hydrodynamic diameter becomes less apparent, although the PEO corona is expected to have a strong contribution to the micelle size as well.[91] If sample PEO$_{251}$-*b*-PHA$_{441}$ is regarded as an outlier (e.g., if the observed entity is a vesicle), a size difference between PEO$_{441}$-*b*-PHA$_m$ and PEO$_{251}$-*b*-PHA$_m$ samples can be observed, although it is rather small. However, the degree of polymerization influences not only the micelle size but also the aggregation number,[88,90] i.e., the number of chains building the micelle. Thus, a possible change of the aggregation number upon varying the block length might compensate for the different PEO block lengths, annihilating a PEO dependency. This becomes even more complicated since the existence of a micelle equilibrium state (which can be achieved by chain exchange of dynamic micelles or promoted by sonication as performed here) or a kinetic trapping of the micelles (persistent micelles) here remains unclear from DLS alone as the presence of single chains in solution (hinting at dynamic micelles) might be overshadowed by the larger micelles possessing a higher scattering intensity than the smaller unimers.[50,59,61,64,92] Furthermore, the high sensitivity of micellization and micelle size to solvent and cosolvent effects, in which trace water/solvents in the polymer samples might alter the polarity of the medium, can cause a certain variation of the micelle size.[50] A deeper evaluation requires scattering experiments, but is not the focus of this work. Moreover, the DLS study still suggests that the micelle size can be tailored continuously over a broad range by adjusting (particularly) the PHA block length. Hence, the polymer library prepared here represents a suitable basis for a soft templating study.

Influence of the Block Lengths on the Pore Size. To understand the individual impact of the PEO and PHA block length on the pore size, the presented block copolymers were applied for soft templating of silica according to a protocol we previously reported.[46] Although direct micellization takes place in methanol (Figure 3B), we kept using ethanol as the solvent for soft templating here due to the higher solubility of PEO-*b*-PHA copolymers in ethanol compared to methanol to avoid solubility limitations upon solvent evaporation (especially during the concentration series in the next section). The benefit of mesoporous silica as a model material lies in a facile synthesis resulting in an almost ideal replica of the lyotropic phase.[93−97] In addition, we already characterized the pore structure of PEO-*b*-PHA-derived mesoporous silica in depth[46] simplifying the pore size evaluation here. Using the block copolymers in Figure 1 as soft templates in a sol−gel-based synthesis, the respective mesoporous silica powders in Figure 4 are obtained.

From SEM, it becomes obvious that not all PEO-*b*-PHA samples are able to produce mesoporous silica with spherical pore geometry. In fair alignment with our last study[46] and the concept of packing parameter,[98,99] a sufficiently large PEO block is necessary to ensure a stable spherical micelle. With decreasing PEO block length, i.e., increasing volume fraction of the PHA core, lamellae are preferred over spheres, leading to a vesicular structure. Further decrease in the PEO volume fraction theoretically results in the formation of an inverse micelle, which is, however, not stable in the hydrophilic medium of this sol−gel reaction. Consequently, a transition from micelles to vesicles occurs in PEO_{137}-*b*-PHA_m with $m > 100$, yielding macropores with nanoparticles in their center (from encapsulating hydrophilic precursor solution in the vesicle), while in the boundary case PEO_{047}-*b*-PHA_{468} almost no pores are found (Figure 4). All remaining silica samples possess an ordered mesoporous structure with spherical pores, which hints at the micellization of the underlying amphiphilic BCP templates. Silica templated with PEO_{047}-*b*-PHA_{096} represents rather a border case: Although several small mesopores are visible in the SEM image, their number appears to be rather small. Also, the nitrogen physisorption isotherm of this sample (Figure S6) reveals a majorly microporous sample. Both methods evoke the hypothesis that this BCP is at the borderline of forming stable micelles. Overall, we find that nitrogen physisorption confirms the observation from SEM, as mesoporous samples templated with micelles can be easily distinguished from those in which vesicles were present during the soft template process. The physisorption isotherms in Figure S6, which correspond to mesoporous samples (soft templates with high PEO volume fraction), possess a plateau at high relative pressures, whereas the macroporous samples (soft templates with low PEO volume fraction expected to form vesicles) do not reach such a plateau. This becomes particularly apparent in the desorption branch at high relative pressures. SAXS of the silica samples provides analogous results (Figure S8), yielding a SAXS curve with form factor oscillations in the case of mesoporous samples, a SAXS curve with a slow decay in the case of macroporous ones, and a SAXS curve with a steep decay in the case of nonporous ones.

Regarding quantitative pore size evaluation, all samples were characterized by SEM, nitrogen physisorption, and SAXS. In this regard, the same approach as in our last study[46] is used. Briefly explained, mesopore sizes from SEM were obtained by averaging a statistical sample of 50 mesopores. In the case of nitrogen physisorption, an NLDFT method [N_2 at 77 K on silica (cylindrical pores, NLDFT, adsorption branch) of the ASiQwin software], assuming cylindrical pore geometry, is applied on the adsorption branch of the nitrogen isotherms (Figure S6), which results in the pore size distributions in Figure S7. This NLDFT method correctly considers the delayed condensation due to the nucleation barrier of the vapor−liquid transition[2] but requires a correction to take the actual pore geometry into account. Multiplication with a geometrical correction factor of 1.35 for conversion of the cylindrical to a spherical pore geometry[6] provides the final mode pore size, which proved to be meaningful.[46] This approach is necessary because the nitrogen NLDFT kernel for spherical pores is not programmed yet for pores larger than 30 nm. SAXS curves were modeled with a theoretical curve using the Percus−Yevick lattice factor[46,100−103] and a form factor for polydisperse spheres, giving access to a mean pore size. Since all three methods provide comparable results (see Table S5), the following quantitative relations are based on SEM-derived pore sizes, as the SEM evaluation is straightforward, meaningful, and robust for a wide range of pore diameters. Despite being only a local method, the entire pore size regime can be covered, while physisorption and SAXS become inaccurate for large mesopores. Above a pore diameter of 40 nm, pore condensation in the isotherm is very closely shifted to a relative pressure of $p\ p_0^{-1} = 1$, so that the pore size distribution of our materials reaches the upper limit of detection and provides the same value, although the materials are different in pore size. Similarly, the form factor minimum in SAXS approaches the lower limit of detection of the scattering vector for pore diameters above 35−40 nm. In combination with the increasing polydispersity causing less pronounced form factor oscillation, an accurate pore size determination becomes challenging.

From a qualitative point of view, an increase in mesopore diameter with increasing PHA block length is clearly visible by SEM (Figure 4), physisorption (Figure S7), and SAXS (Figure S8) analysis, while the PEO block length appears to have only a minor influence. A quantitative consideration confirms this observation. As shown in Figure 5, a plot of the mesopore diameter against the PHA block length yields a common linear relation for all PEO block lengths. The pore diameter follows, in good agreement, the trend observed for the micelle size (Figure 3B), although being less scattered and being only around 30% of the micelle diameter on average. Within this set of PEO-*b*-PHA soft templates, a pore size range of roughly 15 to 40 nm can be covered, where empirically, the pore size d_p depends linearly on the PHA block length m according to eq 1.

$$d_p(\mathrm{S7\%}) = 0.06\ \mathrm{nm}\cdot m + 9.9\ \mathrm{nm} \qquad (1)$$

Note that a block length above 500 HA units is challenging to achieve (in particular, for large PEO blocks) due to the high viscosity of the BCP during polymerization. Although the synthesis of mesoporous silica here might be accomplished through dynamic micelle templating, the observed relation shows a good agreement with the pore size evolution as a

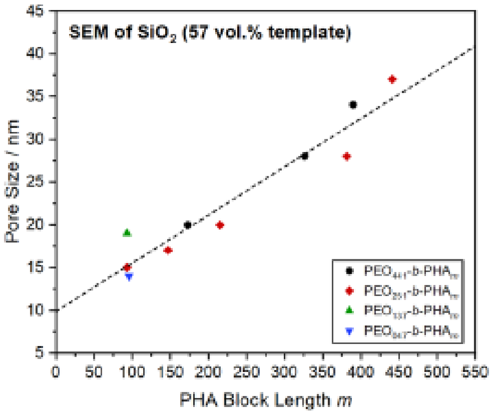

Figure 5. SEM-based pore size of mesoporous silica prepared with 57 vol % PEO$_n$-*b*-PHA$_m$ with a PEO block length of n = 441 (black), 251 (red), 137 (green), and 47 (blue) plotted against the PHA block length from NMR.

function of the PHA block length achieved with persistent PEO-*b*-PHA micelles by Stefik and co-workers (see Figure S9, note that the kind of metal oxides differ).[62] Yet, as presented there, it is important to mention that the synthesis history (stirring time, sonication, etc.) can influence the pore size as well, and thus an assignment of the targeted pore size to the polymer block length is strictly valid only for one synthesis protocol. Furthermore, it is worth mentioning that the pore size is dependent on the applied BCP concentration,[46] which will be discussed below in more detail.

The absence of a dependency on the PEO block length is surprising if studies on other soft templates like *n*-alkyl-PEO[71] are considered, in which the PEO block has a similarly large influence on the pore size as the hydrophobic block. Assuming a "three-phase model",[71,90,104] in which a fraction of the PEO block collapses on the PHA micelle core, as suggested in our last study,[46] a possible explanation can be found: A certain amount of the PEO block collapses onto the PHA core, while the remaining fraction is part of the hairy micelle corona penetrating the silica wall and ending up as a micropore channel. As a result, excess PEO does not contribute to the mesopore size but to the micropore volume (see the discussion in the last section). Thus, all mesopores experience a constant contribution of the collapsed PEO of around 10 nm to each mesopore (offset of regression function in Figure 5), irrespective of the PEO-*b*-PHA soft template. Billet et al. observed a similar behavior for titania soft-templated with block copolymers composed of poly(*N*,*N*-dimethylacrylamide) (PDMA) and PS with two different PDMA block lengths and a tailored PS block length.[105] Independent of the PDMA block length, all copolymer samples introduced mesopores, whose size depends only on the PS block length. Regarding the slope stating a pore size increase of 6 nm per 100 HA units, a comparison with studies on PEO-*b*-PS of Zhu et al. is possible. They observed a pore size increase of around 3 nm per 100 S units in mesoporous tungsten oxide,[106] which is of a similar order of magnitude to our findings, although the slope most likely depends on the size of the repeating unit and hence might be a parameter being specific for each polymer family.[16,71,105,106] A direct correlation of the slope with the size of the repeating unit is difficult, however, due to the unknown extent of stretching of the PHA chain in the micelle core and the mesopore shrinkage during calcination. All in all, PEO-*b*-PHA demonstrates a clear pore size evolution as a function of PHA block length, enabling a tailor-made pore size between 15 and 40 nm.

Influence of the Template Concentration on the Porosity. Next to the size of mesopores, the pore wall thickness features a second important structural parameter of mesoporous materials. Normally, an adjustment of the template concentration, i.e., the ratio of soft template to precursor in the soft templating process, should enable tuning of the pore wall thickness. However, while Lokupitiya et al. proposed a deliberate tailoring of the pore wall thickness upon maintaining a constant pore size by persistent micelle templating,[48] our previous study hinted at a more complex influence of the template concentration on the porosity.[46] To investigate this topic in more detail, we templated silica in a case study with PEO$_{441}$-*b*-PHA$_{270}$ over a broad range of template concentration (Figure 6). The soft template concentration is given here as polymer volume fraction Φ (in vol %) describing the ratio of BCP volume V_{BCP} to total volume (polymer volume and silica volume V_{oxide}), as shown in eq 2[107]

$$\Phi = \frac{V_{\mathrm{BCP}}}{V_{\mathrm{BCP}} + V_{\mathrm{oxide}}} \tag{2}$$

The volume of silica V_{oxide} is obtained by converting the amount of precursor to a molar amount of silica under the assumption of the full conversion of tetraethyl orthosilicate to silicon dioxide. This assumption seems reasonable since the theoretical mass of 35 mg silica per batch was obtained experimentally in most samples. Molar mass and density of amorphous silica (2.2 g mL^{-1}) then yield the desired volume. The volume of PEO-*b*-PHA V_{BCP} is generated by the division of applied polymer mass by its density ρ_{BCP}. The latter is estimated according to eq 3 by dividing the number-weighted molar mass from NMR M_{n} by the sum of the blocks' volumes (with the number of EO and HA repeating units n and m, their mass M_{EO} = 44 g mol^{-1} and M_{HA} = 156 g mol^{-1}, and the density[48] of the polymer blocks ρ_{PEO} = 1.13 g mL^{-1} and ρ_{PHA} = 1.065 g mL^{-1}, respectively)

$$\rho_{\mathrm{BCP}} = \frac{M_{\mathrm{n}}}{\frac{nM_{\mathrm{EO}}}{\rho_{\mathrm{PEO}}} + \frac{mM_{\mathrm{HA}}}{\rho_{\mathrm{PHA}}}} \tag{3}$$

The polymer volume fraction Φ according to eq 3 thus describes the theoretical porosity of the final mesoporous metal oxide. A comparison with the experimental porosity from nitrogen physisorption (Figure S10G) shows that this descriptor is meaningful, possessing a similar evolution, although a constant overestimation of about 15% is observed. A reasonable explanation represents the fact that the BCP most likely is coiled more densely in the micelle state than in the homopolymer. Consequently, the density should be higher than that in a homopolymer assumed for calculation in eq 3.

The SEM images (Figure 6A) confirm qualitatively the presence of ordered spherical mesopores over the entire concentration range, as well as a decreasing pore-to-pore distance and a pore size increase upon increasing the polymer volume fraction. Quantitatively, a plot of the pore size against the applied polymer amount (Figure 6B) reveals a more complex dependence of the pore size on the polymer volume fraction: Initially, the pore size remains the same, but when a threshold of 57 vol % is exceeded, the mesopores start to grow steadily. At 85 vol %, the pore size is twice as large as in the initial constant region.

https://doi.org/10.1021/acs.langmuir.5c02750
Langmuir 2025, 41, 30948−30967

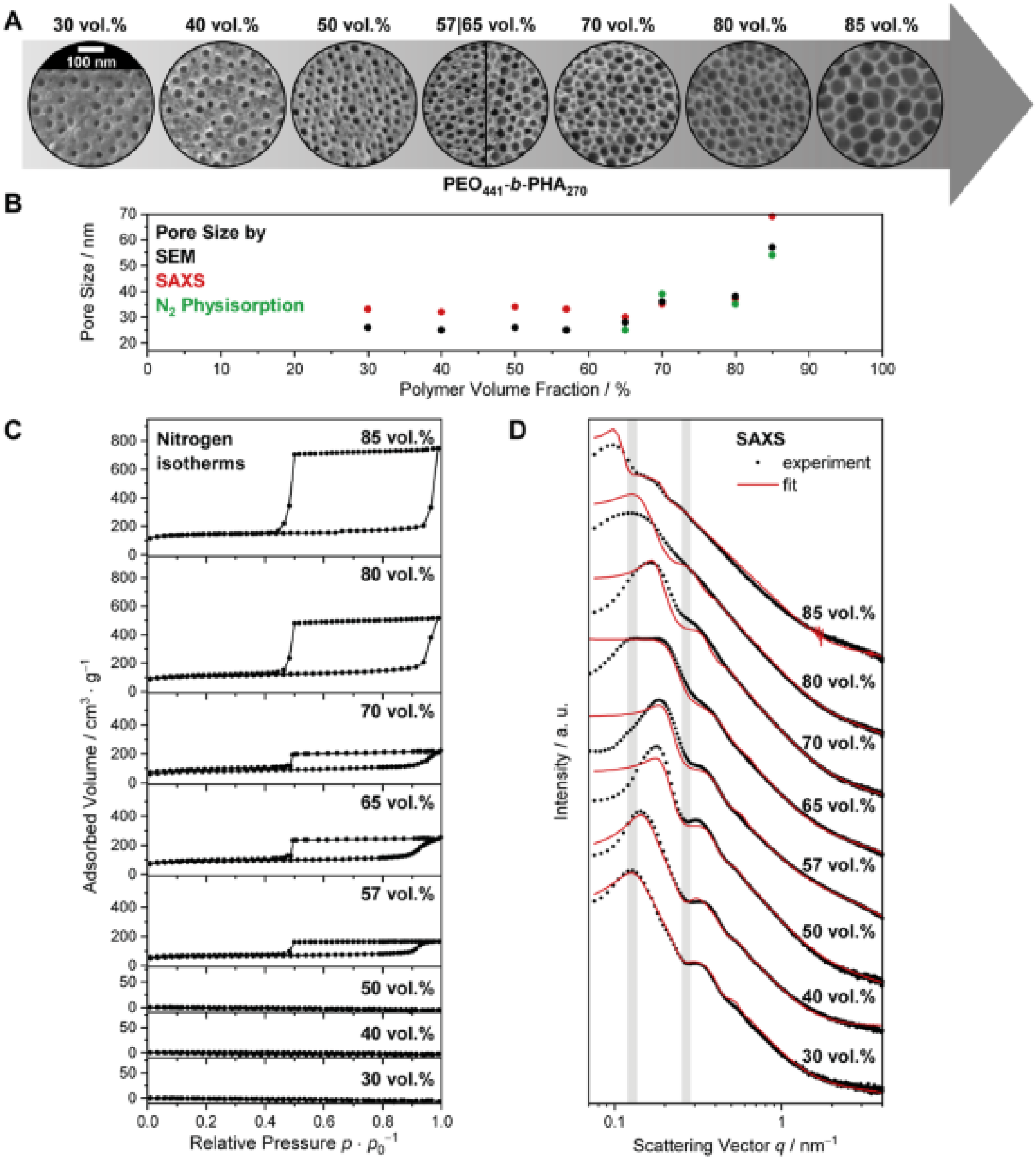

Figure 6. (A) SEM images, (B) nitrogen isotherms, and (C) SAXS curves of mesoporous silica prepared with different amounts of PEO$_{441}$-*b*-PHA$_{270}$, as well as (B) the pore size from SEM (black), physisorption (green), and SAXS (red), which depends on the applied polymer amount.

The SAXS curves in Figure 6D underline these results and show that the form factor minimum at q values of around 0.25 nm^{-1} (being mostly affected by the pore size) remains the same at low polymer volume fractions (30–65 vol %), implying a constant pore size. Simultaneously, the lattice factor maximum (0.1–0.2 nm^{-1}), being strongly connected to the pore-to-pore distance, shifts steadily toward higher q values. This trend clearly demonstrates a decreasing pore-to-pore distance and thus wall thickness upon increasing the soft template concentration and confirms that the templating procedure here must follow an EISA mechanism. Otherwise, such a continual pore wall adjustment would hardly be possible. Above 65 vol %, both form factor minimum and lattice factor maximum shift continuously toward lower q values as a result of the increasing pore size. Note that an increasing pore size leads to an increase in pore-to-pore distance as well if a wall size decrease cannot compensate for or outweigh the pore size increase. On a quantitative level, the pore size from SAXS (Figure 6B) is in good agreement with that from SEM, especially considering the uncertainty of SAXS (mostly affected by the polydispersity of the pore size) of up to 10 nm and SEM (±5 nm), which are omitted in Figure 6B for clarity but are given in Figure S10A.

Nitrogen physisorption of these samples provides insights into the underlying mechanism causing this complex pore size evolution. At low polymer volume fractions, isotherms of apparently nonporous silica are observed. However, both SEM and SAXS clearly confirm the presence of ordered mesopores in the first three samples. Only from 57 vol % onward nitrogen

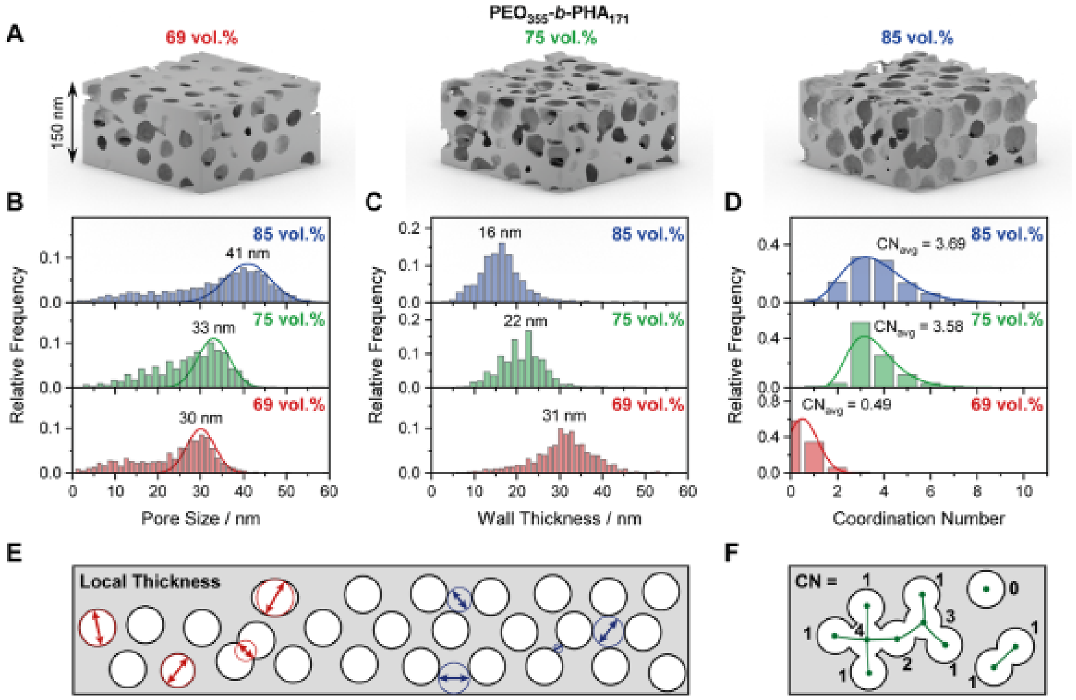

Figure 7. (A) STEM-based 3D reconstructions of mesoporous silica prepared with 69 vol % (left), 75 vol % (middle), and 85 vol % PEO$_{355}$-*b*-PHA$_{171}$ (right) and corresponding distributions of (B) pore size and (C) pore wall thickness from local thickness evaluation as well as (D) number of adjacent mesopores a single pore is connected to through a mesopore window. Mean values of each distribution are given, respectively. The (E) local thickness evaluation as well as the (F) determination of the coordination number are sketched below.

isotherms are obtained, exhibiting the expected hysteresis loop. These results indicate that the silica powders prepared with 30–50 vol % PEO$_{441}$-*b*-PHA$_{270}$ are mesoporous, but the pores are not accessible for nitrogen. The polymer concentration at which the pore system becomes accessible according to physisorption coincides with the point from which on the pore size starts to increase (57–65 vol %). Together with the findings of our previous study on PEO collapse,[46] the following mechanism can be proposed: At low soft template amounts, the hairy micelles in the gel are evenly distributed within the inorganic gel but too far apart to create an interconnected pore network. Upon increasing the amount of the soft template, the micelles approach each other until they are sufficiently close so that the PEO chains of the micelle corona penetrating the inorganic matrix can generate continuous micropore channels, which ensure an accessible mesopore space. Further increasing the soft template concentration forces the micelles to interact, leading to a collapse of PEO onto the PHA core to gradually increasing extents, which increases the resulting pore size. The PEO collapse can be explained either by avoiding entropically disfavored chain entanglement or by exceeding the solubility limit of PEO in the space between two micelles (leading to precipitation of PEO on the micelle core). Normally, PEO is expected to show miscibility over a broad (if not even the entire) range of polymer volume fractions in aqueous media. However, depending on block length and due to the presence of the inorganic precursor, a miscibility gap might be formed here for nanomaterials.[108−110] In fact, the occurrence of the PEO collapse as a microphase separation evokes the existence of a miscibility gap for such nanomaterials, behaving differently than expected from the bulk phase diagram. Indeed, the different coiling of a BCP, especially the PEO block, in dilute solution compared to a corresponding lyotropic phase is a well-established concept in polymer science.[71]

At high polymer volume fractions, the nitrogen physisorption isotherms correspond to an accessible mesopore space, provide a meaningful pore dimension (after postcorrection with a geometrical factor of 1.35) and match the results from SEM (Figure 6B). The presence of isolated voids at low polymer volume fractions also explains why no decent hysteresis loop is observed in mesoporous silica prepared with 57 vol % PEO$_{441}$-*b*-PHA$_{173}$ and PEO$_{251}$-*b*-PHA$_{093}$ (Figure S6), as this concentration marks the borderline of achieving an accessible mesopore network. Furthermore, the porosity *P* (i.e., pore volume) linearly increasing with increasing polymer volume fraction shown in Figure S10G confirms that the entire soft template is incorporated in the inorganic matrix (absence of phase segregation) in each sample and thus confirms that the sample set indeed follows the targeted series of increasing polymer volume fraction.

This study on the soft template amount used for soft templating leads to the conclusion that tailoring the wall size follows two regimes: (1) at low polymer volume fraction, the wall size can be tuned while keeping the pore size constant, whereas (2) at high polymer volume fractions, this simple "raisin-bread model", in which the micelles (or mesopores) are evenly distributed within a given inorganic volume without being changed (like raisins in a raisin bread), does not hold true anymore. Instead, the wall thickness cannot be tuned independently of the pore size. These two regions partly resolve the initial contradiction between the studies of Stefik and coworkers[47,48,50] and our studies,[46] as the Stefik group worked

https://doi.org/10.1021/acs.langmuir.5c02750
Langmuir 2025, 41, 30948−30967

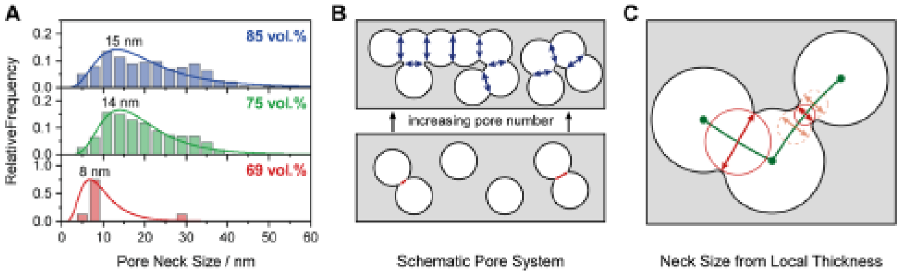

Figure 8. (A) Distribution of the pore neck size of mesoporous silica prepared with 69 vol % (bottom), 75 vol % (middle), and 85 vol % PEO$_{355}$-*b*-PHA$_{171}$ (top). Schematic representation of an exemplary pore system showing (B) the evolution of pore neck size (red and blue) upon increasing pore number, i.e., template amount (bottom to top) and (C) the underlying local thickness evaluation, in which the pore neck size represents the diameter of the smallest sphere along the pore skeleton (green) just touching the silica phase (solid red circle).

below 60−70 vol % (depending on the oxide's crystallinity and thus density: 1.9−4.3 g mL^{-1} in the case of niobia)[48,111] of the PEO-*b*-PHA template (see eq S1 in the Supporting Information for further calculations). In addition, the distinction between persistent and dynamic micelle templating needs to be considered. Since we cannot ensure a trapping of the polymer micelles (ensuring pore size conservation) like in the works of Stefik and co-workers, who applied a dedicated solvent mixture, a glassy micelle core, or cross-linked micelles to guarantee kinetic trapping,[47,48,63,112,113] a transition from the persistent micelle regime to the dynamic one, allowing chain exchange, might be present here. As a result, a pore size deviation upon varying the template amount could occur due to a transition from persistent-to-dynamic micelles, although the extent (increase by up to 120%) and systematic evolution (no significant fluctuation) of pore size change observed here appears not to be explainable by the presence of dynamic micelles alone when compared with literature values (see Figure S11).[40,47,50,63] Also, our previous study[46] revealed that the time period between micelle formation and silica gelation is rather short in this synthesis (30−60 min). While this time scale might be sufficient for micelle equilibration by chain exchange in dilute solution,[61,114] the rate of chain exchange will be significantly lower during the coassembly of micelles within a concentrating solution in this synthesis, as polymer diffusion and translocation not only depends on the block length[115−117] but is also decelerated in concentrated solutions,[118,119] in confinement,[120] and with increasing viscosity[116,121] of the solution. During gelation of silica, the viscosity of the mixture increases within minutes by 3 to 4 orders of magnitude, as shown in our previous study,[46,122] which thus most probably freezes the micelles shortly after their formation. Although an exchange of polymer chains still cannot be excluded and the determination of their rate during soft templating is a matter of future studies, a further mechanism, such as PEO collapse, appears to underlie the pore size increase here.

A quantitative consideration of the wall thickness by SAXS is challenging because overlapping micelles and thus interpenetrating spherical mesopores cause apparent pore-to-pore distances smaller than the mesopore diameter. As a result, the wall thickness determined from the pore-to-pore distance after subtraction of the pore size underestimates the actual wall dimension. Tomography based on STEM, however, is a powerful technique to not only provide a distribution of the wall thickness but also enable in-depth analysis of the pore connectivity. Tomographic reconstruction[123,124] of projection-angle-dependent STEM images of mesoporous silica prepared with different amounts of PEO$_{355}$-*b*-PHA$_{171}$ within our previous work[46] yields a three-dimensional model of the pore system. Cutouts of these models are shown in Figure 7A for the samples prepared with 69, 75, and 85 vol %. The models are expected to be accurate 3D representations of the materials due to the high tilt range, high contrast between silica and pores, a low residual alignment error of about 0.5 nm, and optimization of reconstruction and segmentation based on realistic simulations of similar systems.[125,126] By that, reliable results of nanosized features can be well resolved with a pixel size of 1.26 nm (69 vol %) and 1.62 nm (75 and 85 vol %), respectively. Following a local thickness evaluation (with the corresponding ImageJ plugin),[46,80] the pore size and wall size can be statistically evaluated by determining the diameter of the largest sphere at any point still fitting in one phase without penetrating the other (see Figure 7E).

The resulting pore size distributions in Figure 7B confirm the trend observed by SEM for PEO$_{441}$-*b*-PHA$_{270}$-derived mesoporous silica (Figure 6). By increasing the amount of PEO$_{355}$-*b*-PHA$_{171}$ used for soft templating, the mesopore size increases as well. Note that a significant contribution of small mesopores appears in the pore size distribution resulting from pores located at the particle surface and being wrongly assigned to small pore diameters by the algorithm.[46] Similar to our last study, we therefore used a Gaussian function based on the right part of the distribution (correctly assigned large mesopores) for evaluating the mean pore size (Figure 7B). In addition, the expected decrease in (local) wall thickness can be seen from the distribution in Figure 7C. In all three samples, a homogeneous wall thickness can be found, manifesting as a defined distribution, which steadily shifts to smaller sizes upon increasing the template amount. From 69 to 85 vol %, a thickness decrease by 50% (from 31 to 16 nm) is observed, giving access to a tailoring of wall size over a wide range. For comparison, Sarkar et al. observed a change in wall thickness of around 40% (12 nm vs. 7 nm) by doubling the mass ratio of metal oxide to PEO-*b*-PHA in mesoporous niobium oxide thin films (13 nm mesopores),[47] which is of a similar order of magnitude.

Beyond the pore and wall size, the physisorption study in Figure 6C hints that the polymer volume fraction has an impact on the pore connectivity and accessibility as well. Electron tomography provides the unique possibility to quantify the connection between the mesopores. Although this technique is restricted to pores above 2 nm due to the pixel size, i.e., connection through micropores cannot be evaluated, a clear difference in connection through large pore windows (>2 nm)

https://doi.org/10.1021/acs.langmuir.5c02750
Langmuir 2025, 41, 30948−30967

can be seen if comparing mesoporous silica templated with low and with high soft template amount (Figure 7D). While at 69 vol %, the majority of mesopores are isolated (coordination number of zero, see Figure 7F) and the remaining 40% of the mesopores are connected to only one or two adjacent mesopores, each mesopore is connected to four neighbors on average in the case of 75 and 85 vol %. This more pronouncedpore connectivity upon increasing the soft template amount is in good agreement with the physisorption study discussed before. Since a fast diffusion within the pore system is governed by not only the number but also especially the the size of connecting pores (necks), an evaluation of the neck size of the mesopores is equally important. Here, the local thickness evaluation of the pore system can be used for determining the bottleneck between two adjacent pores. More precisely, the pore neck size represents the smallest local thickness along the pore skeleton connecting two connected mesopores, as shown by the solid red circles in Figure 8C.[80] Following this approach, the pore neck size can be evaluated statistically, yielding a neck size distribution (Figure 8A).

Increasing the polymer volume fraction from 69 to 75 vol % not only increases the number of connecting pores but also their diameter. A reliable mean value cannot be given due to the broad distribution (the k-gamma function in Figure 8A acts rather as eye-guidance), and the number of connecting pores at 69 vol % is too small for statistical evaluations, but the few existing pore necks in this sample are still narrower than for silica templated with higher polymer amounts. Consequently, both a quantitative and a qualitative enhancement in pore connectivity can be concluded upon increasing soft template concentration, as sketched in Figure 8B. The comparably large pore neck size, especially in the case of the 75 vol % and 85 vol % samples, evokes an apparent contradiction to the pronounced cavitation phenomenon in physisorption (see isotherms in our previous study[46] and here in Figure 6 for samples prepared with high template amounts), which suggests a highly restricted pore accessibility. This contradiction can be resolved by the percolation pore model presented in our previous work,[46] in which a single dead-end of the percolation path composed of well-connected pores renders all pores of this path poorly accessible for the adsorptive. Taking the 11 mesopores of the scheme in Figure 7F as an example, the spherical pores interconnect to three subnetworks (i.e., percolation paths shown as green lines). Within these percolation paths, the pores are well-connected by the large pore necks observed in Figure 8A, but pore connectivity among individual paths and with the exterior of the particle is followed by small PEO-single-chain-induced micropore channels of 1−2 nm in diameter, restricting evaporation from the pores and causing the pronounced cavitation in the adsorption isotherms.[46] Thus, the pore neck size evaluation here is in good alignment with the previously proposed pore model.

Extending the Mesopore Size Regime. The concentration study with PEO$_{441}$-*b*-PHA$_{270}$ and PEO$_{355}$-*b*-PHA$_{171}$ as soft templates showed that the amount of BCP in soft templating influences the pore size, wall thickness, and pore connectivity. Although the pore size increase at large polymer volume fractions renders an independent wall size tuning in this regime impossible, the influence on the pore size offers the opportunity to reach even larger spherical pores than those concluded from Figure 5. Therefore, the entire polymer library was used once more for templating silica, but this time employing 85 vol % of each soft template. As shown in the SEM images in Figure S12, a similar pore morphology is obtained as in the case of 57 vol % template (Figure 4): ordered spherical pores are achieved with large PEO block lengths (*n* = 441 and 251) only, while block copolymers with short PEO and long PHA block led to rather macro- or nonporous silica. The template PEO$_{047}$-*b*-PHA$_{096}$ represents a special case again featuring some small mesopores (12 nm in size) in SEM but overall a low porosity according to nitrogen physisorption (Figure S13), featuring a mode mesopore diameter of around 27 nm. As discussed above, this might be due to the fact that this BCP is at the border of forming stable micelles. Regarding the remaining templates yielding spherical pores, a high, well-defined porosity is obtained, as confirmed by the nitrogen physisorption isotherms in Figure S13. However, in contrast to the samples prepared with 57 vol %, the pore size is twice as high, demonstrating the pore size increase to be a general trend of PEO-*b*-PHA soft templates. As explained above and shown in Table S5, the pore diameters determined from SEM, physisorption, and SAXS are in good alignment for pore sizes below 35 nm, but for larger pores, physisorption and SAXS become inaccurate. Hence, the SEM-based pore diameter was used for quantitative interpretations. Again, a plot of the pore size d_p against the PHA block length m reveals clearly a linear increase with increasing block length (Figure 9A) following the relation in eq 4

$$d_p(85\%) = 0.14\ \text{nm}\cdot m + 17.3\ \text{nm} \qquad (4)$$

Indeed, both offset and slope of the linear regression are twice as large as those in the case of the 57 vol % soft template, implying a PEO contribution of 17 nm to the mesopore size and a pore size increase of 14 nm per 100 HA units added to the PHA block of the soft template. The larger PEO contribution supports the hypothesis of a PEO collapse upon increasing polymer concentration suggested before (Figure 6) and will be discussed in more detail in the next section.

Considering that the pore size obtained with 57 vol % polymer can be regarded as the "natural" pore size achievable with the PEO-*b*-PHA copolymers according to the constant regime (1) in Figure 6A, the values resulting from 85 vol % ("expanded" pore size) represent the maximum pore size a template can introduce because higher quantities of soft template cannot be dissolved in the precursor solution. Thus, by adjusting the template concentration, a pore size tuning from 15 to 80 nm is possible with the PEO-*b*-PHA template family in the case of silica prepared in ethanolic solution. This regime represents the volume spanned by the boundary regression planes in the 3D plot shown in Figure 9B. Based on our last study with mesoporous zirconium oxide possessing the same mesopore size as silica,[46] these results might be generalized, stating that PEO-*b*-PHA can cover a mesopore size range from 10 to 80 nm, although soft template amounts have to be given in units of vol % in order to compare it along different pore skeleton materials.

To ensure that no polymer residues in the mesoporous silica samples hamper porosity evaluations, a typical (noncalcined) template/silica hybrid gel (57 vol % PEO$_{441}$-*b*-PHA$_{326}$) was exposed to the heating procedure used to prepare all samples and studied by thermogravimetric analysis (Figure S16B). Following the evolution of the mass signals assigned to released water and carbon dioxide, decomposition of the soft template starts at 250 °C and is completed at the beginning of the 500 °C dwell step. The weight loss of 36 wt % during the transformation of the hybrid material to the final oxide matches well the expected theoretical loss of 39 wt % (23.0 mg of polymer vs. 35.2 mg of SiO$_2$ assuming full conversion of TEOS). To back up a full

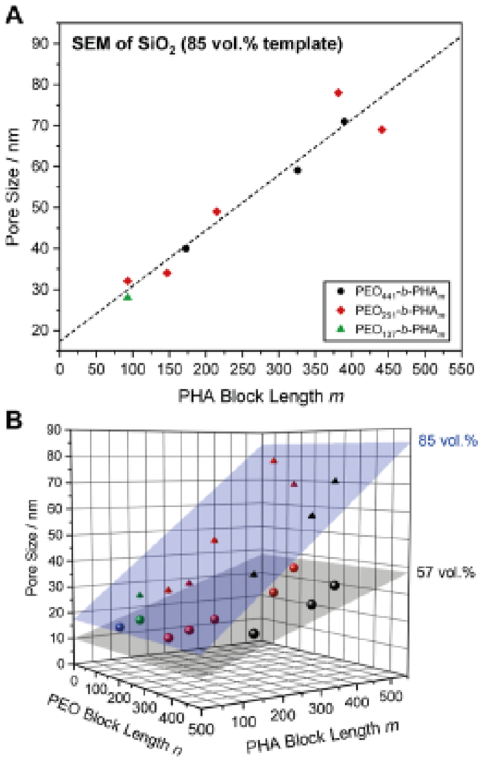

Figure 9. (A) SEM-based pore size of mesoporous silica prepared using 85 vol % PEO$_n$-*b*-PHA$_m$ with a PEO block length of $n = 441$ (black), 251 (red), and 137 (green), plotted against the PHA block length from NMR. (B) 3D Plot of the mesopore size from SEM against PEO and PHA block length for samples prepared with 57 (spheres) and 85 vol % (pyramids) soft template, including a respective fit (gray and blue plane) spanning the accessible pore size regime.

removal of the soft template, an already calcined mesoporous sample prepared with high template amounts (85 vol %) as an extreme case was heated to 1000 °C and gravimetrically studied (Figure S16A). Since only a mass loss due to the release of adsorbed water at 110 °C, but no significant intensity of the CO$_2$ mass signal can be observed, a complete PEO-*b*-PHA decomposition can be concluded.

Contribution of PEO to Micro- and Mesoporosity. Based on these insights, we are able to explain and predict the influence of the PHA and PEO block lengths as well as the polymer concentration on the porosity. In the following, we address the potential underlying reason suggested to be a PEO collapse , i.e. the formation of a layer of poorly solvated PEO chains, on the micelle core. As proposed before, the micelle core, being composed of the PHA block and collapsed PEO on top, is expected to build the mesopore, while residual PEO in the micelle corona might penetrate the inorganic wall, forming micropores. Therefore, the contribution of the micropore and mesopore volume to the total pore volume appears as a suitable descriptor to confirm a possible PEO collapse. In detail, the mesopore fraction Φ_{meso} is used for quantification here and describes the share of the mesopore volume $V_{\text{p,meso}}$ from physisorption with respect to the total pore volume (sum of mesopore volume and micropore volume $V_{\text{p,micro}}$), as described in eq 5

$$\Phi_{\text{meso}} = \frac{V_{\text{p, meso}}}{V_{\text{p, meso}} + V_{\text{p, micro}}} \qquad (5)$$

In the case of ordered mesoporous silica, the cumulative pore size distribution from physisorption typically possesses a distinct shape, as shown in the inset (top right) of Figure 10A. So, $V_{\text{p,micro}}$, and $V_{\text{p,meso}}$ can be extracted from the respective step heights. These volumes can be inserted into eq 5, yielding the relative share Φ_{meso}. Applying this procedure to the pore size distributions shown in Figures S7 and S14, respectively, and plotting the obtained values against the respective PHA block length leads to Figure 10. Within this templating study, three parameters were changed: (1) the PHA block length, (2) the PEO block length, and (3) the BCP concentration. Each of them influences the mesopore fraction Φ_{meso}, as summarized in the inset of Figure 10B.

1. An increase in PHA block length while keeping the PEO block length constant is expected to swell the micelle core.

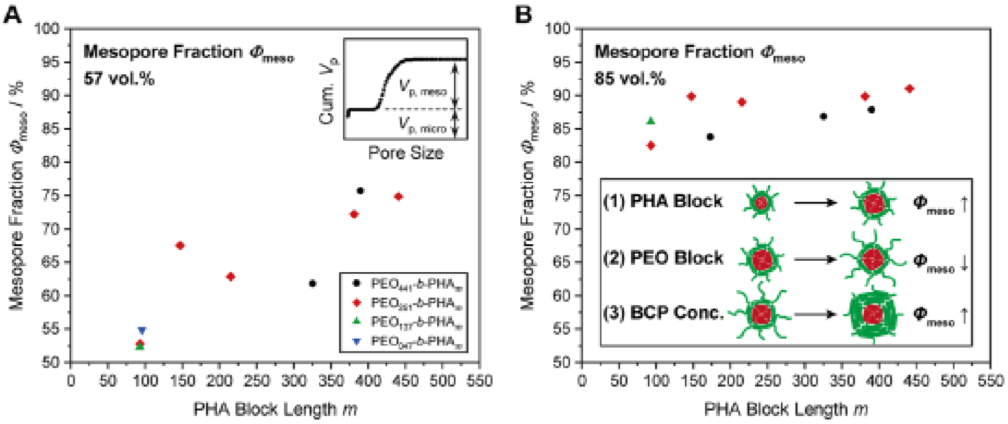

Figure 10. Mesopore fraction as a ratio of mesopore volume to total pore volume (that means the ratio of $V_{\text{p,meso}}$ to the sum of $V_{\text{p,meso}}$ and $V_{\text{p,micro}}$ shown in the inset) of mesoporous silica prepared with (A) 57 vol % and (B) 85 vol % PEO$_n$-*b*-PHA$_m$ with a PEO block length of $n = 441$ (black), 251 (red), 137 (green), and 47 (blue) plotted against the PHA block length from NMR. Schematic illustration of the expected trends of the mesopore fraction with (1) increasing PHA block length, (2) increasing PEO block length, and (3) increasing BCP concentration is shown in the inset on the right.

https://doi.org/10.1021/acs.langmuir.5c02750
Langmuir 2025, 41, 30948−30967

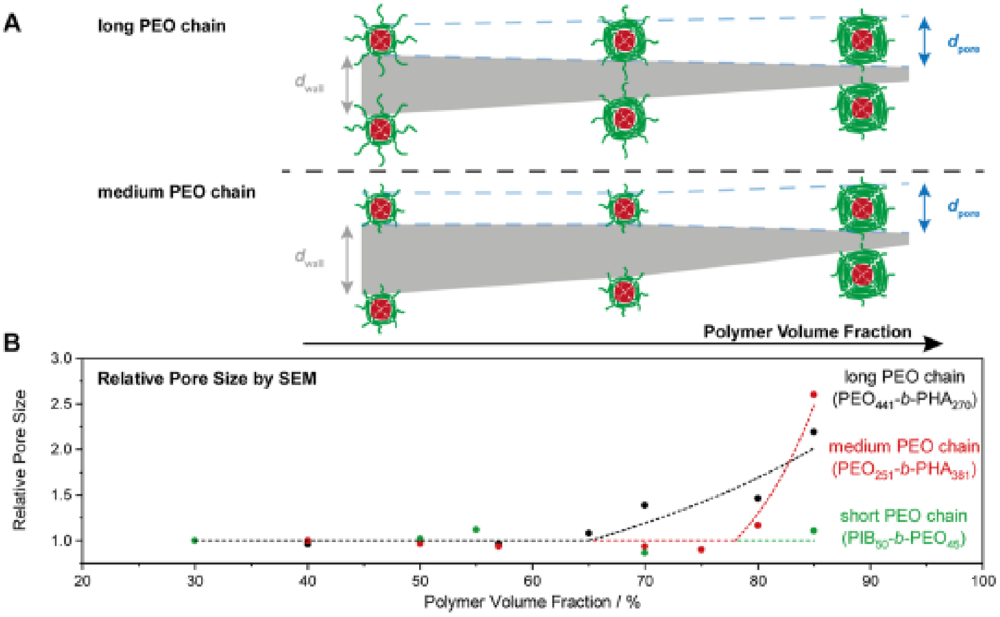

Figure 11. (A) Schematic evolution of pore and wall size with increasing polymer concentration, i.e., decreasing micelle-to-micelle distance for two different PEO block lengths. (B) SEM-based relative pore size (pore size divided by the initial pore size at 30 vol %) versus the polymer concentration of PEO_{441}-*b*-PHA_{270} (black), PEO_{251}-*b*-PHA_{381} (red), and PIB_{50}-*b*-PEO_{45} (green) used for soft templating of mesoporous silica.

Thus, the mesopore volume increases, whereas the micropore volume remains unchanged, leading to an increase in Φ_{meso} with increasing block length *m*, which is indeed observed for both concentrations and for all PEO block lengths. This effect is more pronounced in the case of the 57 vol % soft template (overall increase of ~20% versus <10% in the case of 85 vol % BCP), which can be attributed to a secondary effect being superimposed: Upon increasing the PHA block length, the micelle core expands, and by that, more PHA is exposed to the surface of the micelle core (increase in micelle core surface area). In order to ensure screening of the hydrophobic core from the hydrophilic environment, more PEO collapses on the core, and less PEO will contribute to the micropore volume, resulting in a further increase of Φ_{meso}. In the case of 85 vol %, a high amount of PEO is already collapsed on the micelle core, and thus additional collapse upon increasing *m* does not appear. As a result, this secondary effect is less pronounced or no longer occurs.

2. Increasing the PEO block length, keeping the PHA block length constant, should enlarge the micropore volume, leaving the mesopore volume untouched. Consequently, the mesopore fraction Φ_{meso} should be smaller for samples prepared with a larger PEO block (unless there is no phase separation because PEO cannot be solvated fully by the solvent/precursor). Looking at Figure 10A, this trend is less apparent due to the data points being more scattered than for 85 vol %, but regarding the latter in Figure 10B this effect is slightly recognizable. Although the difference is rather small, Φ_{meso} increases along the sequence of PEO_n-*b*-PHA_m-derived silica of decreasing PEO block length (from $n = 441$ to 251 to 137).
3. The last effect revolves around the variation of the template concentration and, by that, tackles the central hypothesis of PEO collapse. A collapse of EO units on the core is expected to cause an increase in mesopore volume (pore size increases) parallel to a decrease in micropore volume (fewer EO units contribute to single-chain templating). As a result, the mesopore contribution Φ_{meso} should increase. Comparing Figure 10A with Figure 10B, this effect appears to be particularly striking: all samples templated with an 85 vol % soft template show a larger Φ_{meso} than all silica samples prepared with a 57 vol % polymer. On average, Φ_{meso} increases by 20 percentage points upon increasing the polymer volume fraction from 57 to 85 vol %. Similarly, a continuous increase in Φ_{meso} simultaneous to a starting pore size increase above 60 vol % is visible in PEO_{441}-*b*-PHA_{270}-derived silica in the systematic concentration row (Figure S10G). These observations confirm that Φ_{meso} is a suitable descriptor for investigating the templating behavior and strongly support the hypothesis of PEO collapse causing the pore size increase at high polymer volume fractions.

The hypothesis of a constant amount of collapsed PEO in order to shield the PHA core from the hydrophilic surroundings is supported by the constant offsets in Figures 5 and 9 for all PEO block lengths and the slight PEO block influence on Φ_{meso} (trend (2) in Figure 10B). However, if this hypothesis holds true and the entire residual PEO block penetrates the inorganic pore wall, the polymer volume fraction at which the pore size starts to increase should depend on the PEO block length. As illustrated in Figure 11A, a higher soft template concentration is required to initiate a micelle−micelle interaction in the case of a shorter PEO block than in the case of a longer one. While the latter faces PEO chain entanglement at a lower polymer concentration, a BCP with a shorter PEO block still enables a wall size tuning under preservation of the pore size.

To investigate this postulation, the former concentration study with PEO_{441}-*b*-PHA_{270} (Figure 6) is extended by a similar series with a BCP possessing a shorter PEO block (PEO_{251}-*b*-PHA_{381}) and a template with a very short PEO block (PIB_{50}-*b*-PEO_{45}); the latter is preferred over PEO-*b*-PHA templates with a PEO block length of 137 and 47, as they do not lead to a well-ordered pattern of spherical mesopores over a broad concentration range.

Since the three soft templates of this concentration study induce mesopores of different pore size regimes, a comparison is only possible after normalization of the average pore size by the initial one observed at the lowest polymer volume fraction. By evaluation of the SEM images (Figure S17) of the mesoporous silica samples templated with PEO_{251}-*b*-PHA_{381} and poly(isobutylene)-*block*-poly(ethylene oxide) (PIB_{50}-*b*-PEO_{45}) and respective normalization, the evolution of the relative pore size along increasing polymer concentration can be compared with the former concentration study. As shown in Figure 11B, the transition from regime (1) of constant pore size to the pore size increase in regime (2) depends on the PEO block length. While the soft template with long PEO block starts to show a BCP-concentration-induced pore size increase from 65 vol % onward, the medium PEO block shifts this behavior to higher polymer volume fractions (~75 vol %), and with a short PEO block, no influence of the concentration on the pore size is observed at all. This study not only confirms the aforementioned hypothesis of a constant PEO collapse (already suggested from the constant offset in Figures 5 and 9) but also implies that the regime of wall size tuning under pore size conservation can be adjusted by the choice of the PEO block length. This is an important feature for studies in which the influence of only the wall size needs to be investigated. In conclusion, a large PEO block is important to guarantee solubility of the soft template for a large pore size but limits the regime of an independent wall size tuning.

■ CONCLUSION

In this study, we systematically varied the PEO and PHA block lengths and concentration of poly(ethylene oxide)-*block*-poly(hexyl acrylate) (PEO-*b*-PHA) block copolymers in soft templating of silica. We found this soft template class to produce spherical mesopores in a pore diameter range of 10−80 nm with a change by 6 nm per 100 HA units at low and 14 nm per 100 HA units at high template concentrations. Applying a polymer library of 17 copolymers with four different PEO and tailored PHA block lengths shows a large PEO block to be necessary to avoid vesicle formation and to ensure ordered mesoporous morphologies. In the latter, the pore wall thickness scales inversely with the soft template concentration according to SEM, nitrogen physisorption, SAXS, and electron tomography. In addition, the higher the template concentration, the more enhanceder the pore connectivity and the larger the mesopores exceeding a certain threshold (of about 60 vol % in the case of the largest PEO block). This threshold marks the soft template concentration, below which the wall size can be tailored under preservation of the pore size (Figure 12). Using three different block copolymers featuring different PEO block lengths as soft templates, we demonstrate the threshold concentration shifts to higher values when the PEO block is shorter, which enlarges the concentration range of independent wall size tuning. A pore volume analysis confirmed that a partial collapse of the PEO block in the micelle corona onto the PHA core causes the pore size to increase above the threshold template concentration. This PEO collapse leading to a loss of microporosity represents an important effect governing the pore size, which needs to be considered in soft templating with amphiphilic block copolymers.

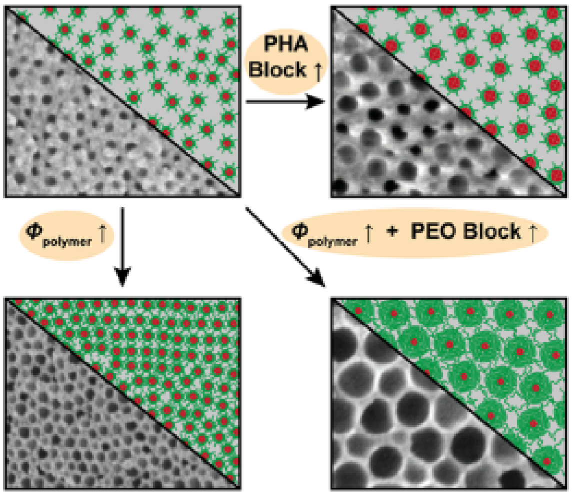

Figure 12. Schematic summary of the observed trends in soft templating of silica with PEO-*b*-PHA templates, in which the sketched micelle arrangement is contrasted to exemplary SEM images after calcination. An increase in PHA block size (top left to top right) increases the mesopore size, while an increase in template concentration yields a decrease in pore wall thickness under conservation of pore size in the case of small PEO blocks (top left to bottom left). If the PEO block is sufficiently large, an increasing template concentration additionally leads to an increase in pore size due to the collapse of the PEO block on the PHA core (top left to bottom right).

Upon varying the soft template amount, we identified a pore volume fraction of 55−60 vol % according to physisorption (considering micro- and mesopores) and 75 vol % according to tomography (considering only mesopores) to be necessary to obtain an accessible and interconnected pore system. Compared with a cubic close packing possessing a filled volume of 74%, the threshold determined by tomography considering only the spherical mesopores (and no micropores) becomes geometrically reasonable. This pore fraction can be regarded as the percolation threshold, above which enough pores are interconnected to form a continuously open pore network and might be a universal guide for mesoporous materials with spherical pores in general, in which an accessible pore system is (un)desired.

The quantitative pore size relations and the interplay between soft template concentration and wall thickness, pore size, and pore connectivity studied here represent important experimental guidelines to achieve a targeted porosity deliberately and to set up systematic studies on porosity−property relationships.

■ ASSOCIATED CONTENT

Supporting Information

The Supporting Information is available free of charge at https://pubs.acs.org/doi/10.1021/acs.langmuir.5c02750.

Image stacks of the STEM-based reconstructions of the silica particles (ZIP)

Additional experimental details on the reagent amounts; ^{1}H NMR spectra, GPC traces, and DLS spectra of all block copolymers; SEM images, nitrogen isotherms (including pore size distributions), and SAXS curves of all mesoporous silica powders; polymer characterization and pore size evaluation of all samples in tabular form (PDF)

AUTHOR INFORMATION

Corresponding Author

Bernd M. Smarsly – *Institute of Physical Chemistry, Justus Liebig University, Giessen D-35392, Germany; Center of Materials Research, Justus Liebig University, Giessen D-35392, Germany;* orcid.org/0000-0001-8452-2663; Email: bernd.smarsly@phys.chemie.uni-giessen.de

Authors

Lysander Q. Wagner – *Institute of Physical Chemistry, Justus Liebig University, Giessen D-35392, Germany; Center of Materials Research, Justus Liebig University, Giessen D-35392, Germany;* orcid.org/0009-0007-9366-6969

Frederik Breckwoldt – *Institute of Physical Chemistry, Justus Liebig University, Giessen D-35392, Germany; Center of Materials Research, Justus Liebig University, Giessen D-35392, Germany;* orcid.org/0009-0004-4284-820X

Xiaohui Huang – *Institute of Nanotechnology, Karlsruhe Institute of Technology, Eggenstein-Leopoldshafen D-76344, Germany; Department of Materials and Earth Science, Technical University Darmstadt, Darmstadt D-64287, Germany*

Christian Kübel – *Institute of Nanotechnology, Karlsruhe Institute of Technology, Eggenstein-Leopoldshafen D-76344, Germany; Department of Materials and Earth Science, Technical University Darmstadt, Darmstadt D-64287, Germany; Karlsruhe Nano Micro Facility, Karlsruhe Institute of Technology, Eggenstein-Leopoldshafen D-76344, Germany;* orcid.org/0000-0001-5701-4006

Xiaoyin Cheng – *Fraunhofer Institute for Industrial Mathematics, Kaiserslautern D-67663, Germany*

Katja Schladitz – *Fraunhofer Institute for Industrial Mathematics, Kaiserslautern D-67663, Germany*

Complete contact information is available at: https://pubs.acs.org/10.1021/acs.langmuir.5c02750

Author Contributions

The manuscript was written through the contributions of all authors. All authors have given approval to the final version of the manuscript.

Funding

The research was financially supported by the Funds of the Chemical Industry.

Notes

The authors declare no competing financial interest.

ACKNOWLEDGMENTS

The authors thank Raoul Brand and Rafael Meinusch (both Justus Liebig University) for gas physisorption experiments as well as Sascha Prentzel and Helmut Schlaad (both University of Potsdam) for GPC measurements. They also thank the Karlsruhe Nano Micro Facility (KNMFi) for providing access to the TEM instrument as well as the CERIC–ERIC Consortium for access to experimental facilities and financial support. L.W. thanks the Funds of the Chemical Industry (FCI) for financial support. X.H. acknowledges the China Scholarship Council (CSC) for the support of her Ph.D. at Karlsruhe Institute of Technology and the Technical University of Darmstadt. This work was supported by the Center for Materials Research (ZfM) at Justus-Liebig-University Giessen.

REFERENCES

(1) Thommes, M.; Köhn, R.; Fröba, M. Sorption and Pore Condensation Behavior of Nitrogen, Argon, and Krypton in Mesoporous MCM-48 Silica Materials. *J. Phys. Chem. B* **2000**, *104*, 7932–7943.

(2) Thommes, M.; Smarsly, B.; Groenewolt, M.; Ravikovitch, P. I.; Neimark, A. V. Adsorption Hysteresis of Nitrogen and Argon in Pore Networks and Characterization of Novel Micro- and Mesoporous Silicas. *Langmuir* **2006**, *22*, 756–764.

(3) Rasmussen, C. J.; Vishnyakov, A.; Thommes, M.; Smarsly, B. M.; Kleitz, F.; Neimark, A. V. Cavitation in Metastable Liquid Nitrogen Confined to Nanoscale Pores. *Langmuir* **2010**, *26*, 10147–10157.

(4) Velasco, L. F.; Guillet-Nicolas, R.; Dobos, G.; Thommes, M.; Lodewyckx, P. Towards a Better Understanding of Water Adsorption Hysteresis in Activated Carbons by Scanning Isotherms. *Carbon* **2016**, *96*, 753–758.

(5) Kube, S. A.; Turke, K.; Ellinghaus, R.; Wallacher, D.; Thommes, M.; Smarsly, B. M. Pore Size Gradient Effect in Monolithic Silica Mesopore Networks Revealed by In-Situ SAXS Physisorption. *Langmuir* **2020**, *36*, 11996–12009.

(6) Thommes, M.; Schlumberger, C. Characterization of Nanoporous Materials. *Annu. Rev. Chem. Biomol. Eng.* **2021**, *12*, 137–162.

(7) Haidar, A. F.; Belet, A.; Goderis, B.; Léonard, A. F.; Gommes, C. J. Small-Angle Scattering Indicates Equilibrium Instead of Metastable Capillary Condensation in SBA-15 Mesoporous Silica. *Langmuir* **2024**, *40*, 17444–17453.

(8) Felipe, C.; Rojas, F.; Kornhauser, I.; Thommes, M.; Zgrablich, G. Mechanistic and Experimental Aspects of the Structural Characterization of Some Model and Real Systems by Nitrogen Sorption and Mercury Porosimetry. *Adsorpt. Sci. Technol.* **2006**, *24*, 623–643.

(9) Boissiere, C.; Grosso, D.; Lepoutre, S.; Nicole, L.; Bruneau, A. B.; Sanchez, C. Porosity and Mechanical Properties of Mesoporous Thin Films Assessed by Environmental Ellipsometric Porosimetry. *Langmuir* **2005**, *21*, 12362–12371.

(10) Rosu, D. M.; Ortel, E.; Hodoroaba, V. D.; Kraehnert, R.; Hertwig, A. Ellipsometric Porosimetry on Pore-Controlled TiO_2 Layers. *Appl. Surf. Sci.* **2017**, *421*, 487–493.

(11) Hartmann, P.; Lee, D. K.; Smarsly, B. M.; Janek, J. Mesoporous TiO_2: Comparison of Classical Sol-Gel and Nanoparticle Based Photoelectrodes for the Water Splitting Reaction. *ACS Nano* **2010**, *4*, 3147–3154.

(12) Bernsmeier, D.; Ortel, E.; Polte, J.; Eckhardt, B.; Nowag, S.; Haag, R.; Kraehnert, R. Versatile Control over Size and Spacing of Small Mesopores in Metal Oxide Films and Catalytic Coatings via Templating with Hyperbranched Core–Multishell Polymers. *J. Mater. Chem. A* **2014**, *2*, 13075–13082.

(13) Luna, A. L.; Matter, F.; Schreck, M.; Wohlwend, J.; Tervoort, E.; Colbeau-Justin, C.; Niederberger, M. Monolithic Metal-Containing TiO_2 Aerogels Assembled from Crystalline Pre-Formed Nanoparticles as Efficient Photocatalysts for H_2 Generation. *Appl. Catal., B* **2020**, *267*, 118660.

(14) Kang, Y.; Tang, Y.; Zhu, L.; Jiang, B.; Xu, X.; Guselnikova, O.; Li, H.; Asahi, T.; Yamauchi, Y. Porous Nanoarchitectures of Nonprecious Metal Borides: From Controlled Synthesis to Heterogeneous Catalyst Applications. *ACS Catal.* **2022**, *12*, 14773–14793.

(15) Fried, D. I.; Tropp, K.; Fröba, M. On the Way to Cofactor Regeneration in Nanopores: Tailoring Porous Materials for Glucose-6-Phosphate Dehydrogenase Immobilization. *ChemCatChem* **2013**, *5*, 931–938.

(16) Hamaed, A.; Hoang, T. K. A.; Trudeau, M.; Antonelli, D. M. Optimization of Hydrogen Storage Capacity in Silica-Supported Low Valent Ti Systems Exploiting Kubas Binding of Hydrogen. *J. Organomet. Chem.* **2009**, *694*, 2793–2800.

(17) Sun, X.; Hao, H.; Ji, H.; Li, X.; Cai, S.; Zheng, C. Nanocasting Synthesis of In_2O_3 with Appropriate Mesostructured Ordering and

Enhanced Gas-Sensing Property. *ACS Appl. Mater. Interfaces* **2014**, *6*, 401−409.

(18) Burgess, I. B.; Koay, N.; Raymond, K. P.; Kolle, M.; Lončar, M.; Aizenberg, J. Wetting in Color: Colorimetric Differentiation of Organic Liquids with High Selectivity. *ACS Nano* **2012**, *6*, 1427−1437.

(19) Reid, B.; Taylor, A.; Chen, Y.; Schmidt-Hansberg, B.; Guldin, S. Robust Operation of Mesoporous Antireflective Coatings under Variable Ambient Conditions. *ACS Appl. Mater. Interfaces* **2018**, *10*, 10315−10321.

(20) Bach, U.; Lupo, D.; Comte, P.; Moser, J. E.; Weissörtel, F.; Salbeck, J.; Spreitzer, H.; Grätzel, M. Solid-State Dye-Sensitized Mesoporous TiO_2 Solar Cells with High Photon-to-Electron Conversion Efficiencies. *Nature* **1998**, *395*, 583−585.

(21) Kreissl, J. J. A.; Petit, J.; Oppermann, R.; Cop, P.; Gerber, T.; Joos, M.; Abert, M.; Tübke, J.; Miyazaki, K.; Abe, T.; Schröder, D. Electrochemical Lithiation/Delithiation of ZnO in 3D-Structured Electrodes: Elucidating the Mechanism and the Solid Electrolyte Interphase Formation. *ACS Appl. Mater. Interfaces* **2021**, *13*, 35625−35638.

(22) Glatthaar, C.; Wang, M.; Wagner, L. Q.; Breckwoldt, F.; Guo, Z.; Zheng, K.; Kriechbaum, M.; Amenitsch, H.; Titirici, M.-M.; Smarsly, B. M. Lignin-Derived Mesoporous Carbon for Sodium-Ion Batteries: Block Copolymer Soft Templating and Carbon Microstructure Analysis. *Chem. Mater.* **2023**, *35*, 10416−10433.

(23) Weller, T.; Sann, J.; Marschall, R. Pore Structure Controlling the Activity of Mesoporous Crystalline $CsTaWO_6$ for Photocatalytic Hydrogen Generation. *Adv. Energy Mater.* **2016**, *6*, 1600208−1600209.

(24) Oveisi, H.; Anand, C.; Mano, A.; Al-Deyab, S. S.; Kalita, P.; Beitollahi, A.; Vinu, A. Inclusion of Size Controlled Gallium Oxide Nanoparticles into Highly Ordered 3D Mesoporous Silica with Tunable Pore Diameters and Their Unusual Catalytic Performance. *J. Mater. Chem.* **2010**, *20*, 10120.

(25) Shao, J.; Yang, S.; Lei, L.; Cao, Q.; Yu, Y.; Liu, Y. Pore Size Dependent Hysteresis Elimination in Perovskite Solar Cells Based on Highly Porous TiO_2 Films with Widely Tunable Pores of 15−34 nm. *Chem. Mater.* **2016**, *28*, 7134−7144.

(26) Karandikar, P. R.; Lee, Y.-J.; Kwak, G.; Woo, M. H.; Park, S.-J.; Park, H.-G.; Ha, K.-S.; Jun, K.-W. Co_3O_4@Mesoporous Silica for Fischer−Tropsch Synthesis: Core−Shell Catalysts with Multiple Core Assembly and Different Pore Diameters of Shell. *J. Phys. Chem. C* **2014**, *118*, 21975−21985.

(27) Von Graberg, T.; Hartmann, P.; Rein, A.; Gross, S.; Seelandt, B.; Röger, C.; Zieba, R.; Traut, A.; Wark, M.; Janek, J.; Smarsly, B. M. Mesoporous Tin-Doped Indium Oxide Thin Films: Effect of Mesostructure on Electrical Conductivity. *Sci. Technol. Adv. Mater.* **2011**, *12*, 025005−025012.

(28) Cook, J. B.; Kim, H.-S.; Lin, T. C.; Robbennolt, S.; Detsi, E.; Dunn, B. S.; Tolbert, S. H. Tuning Porosity and Surface Area in Mesoporous Silicon for Application in Li-Ion Battery Electrodes. *ACS Appl. Mater. Interfaces* **2017**, *9*, 19063−19073.

(29) Wang, J.; Zhang, K.; Bogaerts, A.; Meynen, V. 3D Porous Catalysts for Plasma-Catalytic Dry Reforming of Methane: How Does the Pore Size Affect the Plasma-Catalytic Performance? *Chem. Eng. J.* **2023**, *464*, 142574.

(30) Van den Bergh, W.; Lokupitiya, H. N.; Vest, N. A.; Reid, B.; Guldin, S.; Stefik, M. Nanostructure Dependence of T-Nb_2O_5 Intercalation Pseudocapacitance Probed Using Tunable Isomorphic Architectures. *Adv. Funct. Mater.* **2021**, *31*, 2007826.

(31) Weller, T.; Timm, J.; Deilmann, L.; Doerr, T. S.; Greve, C.; Cherevan, A. S.; Beaucage, P. A.; Wiesner, U. B.; Herzig, E. M.; Eder, D.; Marschall, R. Effects of Periodic Pore Ordering on Photocatalytic Hydrogen Generation with Mesoporous Semiconductor Oxides. *Small Struct.* **2022**, *4*, 2200184.

(32) Liu, Y.; Li, W.; Shen, D.; Wang, C.; Li, X.; Pal, M.; Zhang, R.; Chen, L.; Yao, C.; Wei, Y.; Li, Y.; Zhao, Y.; Zhu, H.; Wang, W.; El-Toni, A. M.; Zhang, F.; Zhao, D. Synthesis of Mesoporous Silica/Reduced Graphene Oxide Sandwich-Like Sheets with Enlarged and "Funneling" Mesochannels. *Chem. Mater.* **2015**, *27*, 5577−5586.

(33) Sallard, S.; Schröder, M.; Boissière, C.; Dunkel, C.; Etienne, M.; Walcarius, A.; Oekermann, T.; Wark, M.; Smarsly, B. M. Bimodal Mesoporous Titanium Dioxide Anatase Films Templated by a Block Polymer and an Ionic Liquid: Influence of the Porosity on the Permeability. *Nanoscale* **2013**, *5*, 12316.

(34) Vinu, A.; Srinivasu, P.; Miyahara, M.; Ariga, K. Preparation and Catalytic Performances of Ultralarge-Pore TiSBA-15 Mesoporous Molecular Sieves with Very High Ti Content. *J. Phys. Chem. B* **2006**, *110*, 801−806.

(35) Li, Y.; Yi, J.; Kruk, M. Tuning of the Temperature Window for Unit-Cell and Pore-Size Enlargement in Face-Centered-Cubic Large-Mesopore Silicas Templated by Swollen Block Copolymer Micelles. *Chem.—Eur. J.* **2015**, *21*, 12747−12754.

(36) Hiremath, V.; Shiferraw, B. T.; Seo, J. G. MgO Insertion Endowed Strong Basicity in Mesoporous Alumina Framework and Improved CO_2 Sorption Capacity. *J. CO2 Util.* **2020**, *42*, 101294.

(37) Yang, B.; Guo, C.; Chen, S.; Ma, J.; Wang, J.; Liang, X.; Zheng, L.; Liu, H. Effect of Acid on the Aggregation of Poly(ethylene oxide)−Poly(propylene oxide)−Poly(ethylene oxide) Block Copolymers. *J. Phys. Chem. B* **2006**, *110*, 23068−23074.

(38) Loreto, S.; Vanrompay, H.; Mertens, M.; Bals, S.; Meynen, V. The Influence of Acids on Tuning the Pore Size of Mesoporous TiO_2 Templated by Non-Ionic Block Copolymers. *Eur. J. Inorg. Chem.* **2018**, *2018*, 62−65.

(39) Zhang, W.-H.; Zhang, L.; Xiu, J.; Shen, Z.; Li, Y.; Ying, P.; Li, C. Pore Size Design of Ordered Mesoporous Silicas by Controlling Micellar Properties of Triblock Copolymer $EO_{20}PO_{70}EO_{20}$. *Microporous Mesoporous Mater.* **2006**, *89*, 179−185.

(40) Sarkar, A.; Thyagarajan, A.; Cole, A.; Stefik, M. Widely Tunable Persistent Micelle Templates *via* Homopolymer Swelling. *Soft Matter* **2019**, *15*, 5193−5203.

(41) Trivedi, M.; Peng, F.; Xia, X.; Sepulveda-Medina, P. I.; Vogt, B. D. Control of Pore Size in Ordered Mesoporous Carbon-Silica by Hansen Solubility Parameters of Swelling Agent. *Langmuir* **2019**, *35*, 14049−14059.

(42) Alvarez-Fernandez, A.; Fornerod, M. J.; Reid, B.; Guldin, S. Solvent Vapor Annealing for Controlled Pore Expansion of Block Copolymer-Assembled Inorganic Mesoporous Films. *Langmuir* **2022**, *38*, 3297−3304.

(43) Yu, J.; Wang, G.; Cheng, B.; Zhou, M. Effects of Hydrothermal Temperature and Time on the Photocatalytic Activity and Microstructures of Bimodal Mesoporous TiO_2 Powders. *Appl. Catal., B* **2007**, *69*, 171−180.

(44) Rodrigues, N. T.; Alves Aarão Reis, F. D. Adsorption of Diffusing Tracers, Apparent Tortuosity, and Application to Mesoporous Silica. *Langmuir* **2024**, *40*, 11371−11380.

(45) Fried, D. I.; Brieler, F. J.; Fröba, M. Designing Inorganic Porous Materials for Enzyme Adsorption and Applications in Biocatalysis. *ChemCatChem* **2013**, *5*, 862−884.

(46) Wagner, L. Q.; Prates da Costa, E.; Glatthaar, C.; Breckwoldt, F.; Zecca, M.; Centomo, P.; Huang, X.; Kübel, C.; Schlaad, H.; Kriechbaum, M.; Amenitsch, H.; Thommes, M.; Smarsly, B. M. Poly(ethylene oxide)-*block*-poly(hexyl acrylate) Copolymers as Templates for Large Mesopore Sizes – A Detailed Porosity Analysis. *Chem. Mater.* **2023**, *35*, 9879−9899.

(47) Sarkar, A.; Stefik, M. How to Make Persistent Micelle Templates in 24 h and Know It Using X-Ray Scattering. *J. Mater. Chem. A* **2017**, *5*, 11840−11853.

(48) Lokupitiya, H. N.; Jones, A.; Reid, B.; Guldin, S.; Stefik, M. Ordered Mesoporous to Macroporous Oxides with Tunable Isomorphic Architectures: Solution Criteria for Persistent Micelle Templates. *Chem. Mater.* **2016**, *28*, 1653−1667.

(49) Yong, M. J. Q.; Wong, A. S. W.; Ho, G. W. Mesophase Ordering and Macroscopic Morphology Structuring of Mesoporous TiO_2 Film. *Mater. Chem. Phys.* **2009**, *116*, 563−568.

(50) Sarkar, A.; Evans, L.; Stefik, M. Expanded Kinetic Control for Persistent Micelle Templates with Solvent Selection. *Langmuir* **2018**, *34*, 5738−5749.

(51) Lu, Y.; Fan, H.; Stump, A.; Ward, T. L.; Rieker, T.; Brinker, C. J. Aerosol-Assisted Self-Assembly of Mesostructured Spherical Nanoparticles. *Nature* **1999**, *398*, 223−226.

(52) Brinker, C. J.; Lu, Y.; Sellinger, A.; Fan, H. Evaporation-Induced Self-Assembly: Functional Nanostructures Made Easy. *Adv. Funct. Mater.* **1999**, *11*, 579−585.

(53) Grosso, D.; Cagnol, F.; Soler-Illia, G. J.; de, A. A.; Crepaldi, E. L.; Amenitsch, H.; Brunet-Bruneau, A.; Bourgeois, A.; Sanchez, C. Fundamentals of Mesostructuring Through Evaporation-Induced Self-Assembly. *Adv. Funct. Mater.* **2004**, *14*, 309−322.

(54) Wei, J.; Wang, H.; Deng, Y.; Sun, Z.; Shi, L.; Tu, B.; Luqman, M.; Zhao, D. Solvent Evaporation Induced Aggregating Assembly Approach to Three-Dimensional Ordered Mesoporous Silica with Ultralarge Accessible Mesopores. *J. Am. Chem. Soc.* **2011**, *133*, 20369−20377.

(55) Templin, M.; Franck, A.; Du Chesne, A.; Leist, H.; Zhang, Y.; Ulrich, R.; Schädler, V.; Wiesner, U. Organically Modified Aluminosilicate Mesostructures from Block Copolymer Phases. *Science* **1997**, *278*, 1795−1798.

(56) Ulrich, R.; Chesne, A. Du; Templin, M.; Wiesner, U. Nano-Objects with Controlled Shape, Size, and Composition from Block Copolymer Mesophases. *Adv. Mater.* **1999**, *11*, 141−146.

(57) De Paul, S. M.; Zwanziger, J. W.; Ulrich, R.; Wiesner, U.; Spiess, H. W. Structure, Mobility, and Interface Characterization of Self-Organized Organic−Inorganic Hybrid Materials by Solid-State NMR. *J. Am. Chem. Soc.* **1999**, *121*, 5727−5736.

(58) Choi, S.-H.; Lodge, T. P.; Bates, F. S. Mechanism of Molecular Exchange in Diblock Copolymer Micelles: Hypersensitivity to Core Chain Length. *Phys. Rev. Lett.* **2010**, *104*, 047802.

(59) Ma, Y.; Lodge, T. P. Poly(methyl methacrylate)-*block*-poly(*n*-butyl methacrylate) Diblock Copolymer Micelles in an Ionic Liquid: Scaling of Core and Corona Size with Core Block Length. *Macromolecules* **2016**, *49*, 3639−3646.

(60) Nicolai, T.; Colombani, O.; Chassenieux, C. Dynamic Polymeric Micelles *versus* Frozen Nanoparticles Formed by Block Copolymers. *Soft Matter* **2010**, *6*, 3111.

(61) Lantz, K. A.; Sarkar, A.; Littrell, K. C.; Li, T.; Hong, K.; Stefik, M. Cavitation Enables Switchable and Rapid Block Polymer Exchange under High-χN Conditions. *Macromolecules* **2018**, *51*, 6967−6975.

(62) Stefik, M. Single-Variable Porous Nanomaterial Series from Polymer Structure-Directing Agents. *J. Mater. Res.* **2022**, *37*, 25−42.

(63) Williams, E. R.; McMahon, P. L.; Reynolds, J. E.; Snider, J. L.; Stavila, V.; Allendorf, M. D.; Stefik, M. Tailored Porous Carbons Enabled by Persistent Micelles with Glassy Cores. *Mater. Adv.* **2021**, *2*, 5381−5395.

(64) Lokupitiya, H. N.; Stefik, M. Cavitation-Enabled Rapid and Tunable Evolution of High-χN Micelles as Templates for Ordered Mesoporous Oxides. *Nanoscale* **2017**, *9*, 1393−1397.

(65) Nagarajan, R. "Non-Equilibrium" Block Copolymer Micelles with Glassy Cores: A Predictive Approach Based on Theory of Equilibrium Micelles. *J. Colloid Interface Sci.* **2015**, *449*, 416−427.

(66) Honda, C.; Hasegawa, Y.; Hirunuma, R.; Nose, T. Micellization Kinetics of Block Copolymers in Selective Solvent. *Macromolecules* **1994**, *27*, 7660−7668.

(67) Honda, C.; Abe, Y.; Nose, T. Relaxation Kinetics of Micellization in Micelle-Forming Block Copolymer in Selective Solvent. *Macromolecules* **1996**, *29*, 6778−6785.

(68) Goldmints, I.; Holzwarth, J. F.; Smith, K. A.; Hatton, T. A. Micellar Dynamics in Aqueous Solutions of PEO−PPO−PEO Block Copolymers. *Langmuir* **1997**, *13*, 6130−6134.

(69) Kositza, M. J.; Bohne, C.; Alexandridis, P.; Hatton, T. A.; Holzwarth, J. F. Dynamics of Micro- and Macrophase Separation of Amphiphilic Block-Copolymers in Aqueous Solution. *Macromolecules* **1999**, *32*, 5539−5551.

(70) Lund, R.; Willner, L.; Monkenbusch, M.; Panine, P.; Narayanan, T.; Colmenero, J.; Richter, D. Structural Observation and Kinetic Pathway in the Formation of Polymeric Micelles. *Phys. Rev. Lett.* **2009**, *102*, 188301.

(71) Smarsly, B.; Polarz, S.; Antonietti, M. Preparation of Porous Silica Materials via Sol−Gel Nanocasting of Nonionic Surfactants: A Mechanistic Study on the Self-Aggregation of Amphiphiles for the Precise Prediction of the Mesopore Size. *J. Phys. Chem. B* **2001**, *105*, 10473−10483.

(72) Kopeć, M.; Yuan, R.; GottliebAbreuSongWang, E. C. M. R. Y. Z.; Coelho, J. F. J.; Matyjaszewski, K.; Kowalewski, T. Z. F. J.; Coelho, J.; Matyjaszewski, K.; Kowalewski, T. Polyacrylonitrile-*b*-Poly(butyl acrylate) Block Copolymers as Precursors to Mesoporous Nitrogen-Doped Carbons: Synthesis and Nanostructure. *Macromolecules* **2017**, *50*, 2759−2767.

(73) Fantin, M.; Isse, A. A.; Venzo, A.; Gennaro, A.; Matyjaszewski, K. Atom Transfer Radical Polymerization of Methacrylic Acid: A Won Challenge. *J. Am. Chem. Soc.* **2016**, *138*, 7216−7219.

(74) Weller, T.; Deilmann, L.; Timm, J.; Dörr, T. S.; Beaucage, P. A.; Cherevan, A. S.; Wiesner, U. B.; Eder, D.; Marschall, R. A Crystalline and 3D Periodically Ordered Mesoporous Quaternary Semiconductor for Photocatalytic Hydrogen Generation. *Nanoscale* **2018**, *10*, 3225−3234.

(75) Cop, P.; Maile, R.; Sun, Y.; Khalid, O.; Djerdj, I.; Esch, P.; Heiles, S.; Over, H.; Smarsly, B. M. Impact of Aliovalent/Isovalent Ions (Gd, Zr, Pr, and Tb) on the Catalytic Stability of Mesoporous Ceria in the HCl Oxidation Reaction. *ACS Appl. Nano Mater.* **2020**, *3*, 7406−7419.

(76) Cop, P.; Celik, E.; Hess, K.; Moryson, Y.; Klement, P.; Elm, M. T.; Smarsly, B. M. Atomic Layer Deposition of Nanometer-Sized CeO$_2$ Layers in Ordered Mesoporous ZrO$_2$ Films and Their Impact on the Ionic/Electronic Conductivity. *ACS Appl. Nano Mater.* **2020**, *3*, 10757−10766.

(77) Cop, P.; Hess, K.; Werner, S.; Meinusch, R.; Smarsly, B. M.; Kozuka, H. Comparison of In-Plane Stress Development in Sol−Gel- and Nanoparticle-Derived Mesoporous Metal Oxide Thin Films. *Langmuir* **2019**, *35*, 16427−16437.

(78) Cop, P.; Kitano, S.; Niinuma, K.; Smarsly, B. M.; Kozuka, H. In-Plane Stress Development in Mesoporous Thin Films. *Nanoscale* **2018**, *10*, 7002−7015.

(79) Cheng, X.; Föhst, S.; Redenbach, C.; Schladitz, K. Detecting Branching Nodes of Multiply Connected 3D Structures. *Proceedings of the Mathematical Morphology and its Applications to Signal and Image Processing: 14th international symposium, ISMM 2019; Saarbrücken, Germany, July 8−10, 2019*; Burgeth, B., Kleefeld, A., Naegel, B., Passat, N., Perret, B., Eds.; Springer International Publishing: Cham, 2019; Vol. *11564*, pp 441−455.

(80) Prates da Costa, E.; Huang, X.; Kübel, C.; Cheng, X.; Schladitz, K.; Hofmann, A.; Göbel, U.; Smarsly, B. M. Effects of Hydrothermal Treatment on Mesopore Structure and Connectivity in Doped Ceria-Zirconia Mixed Oxides. *Langmuir* **2023**, *39*, 177−191.

(81) Kim, K.; Strong, J.; Sarkar, S. D.; Nguyen, D.; Dau, H.; Al-Aman, D. A. A.; Dadashi-Silab, S.; Harth, E.; Matyjaszewski, K. Polyethylene-poly(methyl acrylate) Block Copolymers from PACE-SARA ATRP: Utilizing Polyolefin Active Ester Exchange-Based Macroinitiators in Atom Transfer Radical Polymerization. *Macromolecules* **2025**, *58*, 1337−1348.

(82) Hildebrand, J. H. Solubility. xii. regular solutions. *J. Am. Chem. Soc.* **1929**, *51*, 66−80.

(83) Hildebrand, J. H. Order from Chaos. *Science* **1965**, *150*, 441−450.

(84) Abboud, J. M.; Notari, R. Critical Compilation of Scales of Solvent Parameters. Part I. Pure, Non-Hydrogen Bond Donor Solvents. *Pure Appl. Chem.* **1999**, *71*, 645−718.

(85) Fernández-Berridi, M. J.; Otero, T. F.; Guzmán, G. M.; Elorza, J. M. Determination of the Solubility Parameter of Poly(ethylene oxide) at 25°C by Gas-Liquid Chromatography. *Polymer* **1982**, *23*, 1361−1366.

(86) Stefik, M.; Song, J.; Sai, H.; Guldin, S.; Boldrighini, P.; Orilall, M. C.; Steiner, U.; Gruner, S. M.; Wiesner, U. Ordered Mesoporous Titania from Highly Amphiphilic Block Copolymers: Tuned Solution Conditions Enable Highly Ordered Morphologies and Ultra-Large Mesopores. *J. Mater. Chem. A* **2015**, *3*, 11478−11492.

(87) Devanand, K.; Selser, J. C. Asymptotic Behavior and Long-Range Interactions in Aqueous Solutions of Poly(ethylene oxide). *Macromolecules* **1991**, *24*, 5943−5947.

(88) Holder, S. J.; Durand, G. G.; Yeoh, C.; Illi, E.; Hardy, N. J.; Richardson, T. H. The Synthesis and Self-assembly of ABA Amphiphilic Block Copolymers Containing Styrene and Oligo(ethylene glycol) Methyl Ether Methacrylate in Dilute Aqueous Solutions: Elevated Cloud Point Temperatures for Thermoresponsive Micelles. *J. Polym. Sci., Part A:Polym. Chem.* **2008**, *46*, 7739−7756.

(89) Fesenmeier, D. J.; Kim, H. C.; Kim, S.; Won, Y. Determination of Block Copolymer Micelle Core T_g Using ^{1}H NMR Transverse (T_2) Relaxation Measurements of Micelle Coronas. *Macromolecules* **2023**, *56*, 9156−9163.

(90) Förster, S.; Zisenis, M.; Wenz, E.; Antonietti, M. Micellization of Strongly Segregated Block Copolymers. *J. Chem. Phys.* **1996**, *104*, 9956−9970.

(91) Reboul, J.; Nugay, T.; Anik, N.; Cottet, H.; Ponsinet, V.; In, M.; Lacroix-Desmazes, P.; Gérardin, C. Synthesis of Double Hydrophilic Block Copolymers and Induced Assembly with Oligochitosan for the Preparation of Polyion Complex Micelles. *Soft Matter* **2011**, *7*, 5836.

(92) Gupta, S.; Liberman, L.; Lodge, T. P. Role of Distance from Equilibrium in the Fragmentation Kinetics of Block Copolymer Micelles. *Macromolecules* **2023**, *56*, 4874−4883.

(93) Hentze, H.-P.; Krämer, E.; Berton, B.; Förster, S.; Antonietti, M.; Dreja, M. Lyotropic Mesophases of Poly(ethylene oxide)-*b*-Poly(butadiene) Diblock Copolymers and Their Cross-Linking To Generate Ordered Gels. *Macromolecules* **1999**, *32*, 5803−5809.

(94) Bagshaw, S. A.; Prouzet, E.; Pinnavaia, T. J. Templating of Mesoporous Molecular Sieves by Nonionic Polyethylene Oxide Surfactants. *Science* **1995**, *269*, 1242−1244.

(95) Thomas, A.; Schlaad, H.; Smarsly, B.; Antonietti, M. Replication of Lyotropic Block Copolymer Mesophases into Porous Silica by Nanocasting: Learning about Finer Details of Polymer Self-Assembly. *Langmuir* **2003**, *19*, 4455−4459.

(96) Prouzet, E.; Pinnavaia, T. J. Synthese Mesoporöser Silicate Mit wurmlochartigen Strukturmotiven unter Verwendung von nichtionischen Detergentien: Steuerung der Porengröße durch Variation der Synthesetemperatur. *Angew. Chem.* **1997**, *109*, 533−536.

(97) Tanev, P. T.; Pinnavaia, T. J. A Neutral Templating Route to Mesoporous Molecular Sieves. *Science* **1995**, *267*, 865−867.

(98) Israelachvili, J. N.; Mitchell, D. J.; Ninham, B. W. Theory of Self-Assembly of Hydrocarbon Amphiphiles into Micelles and Bilayers. *J. Chem. Soc., Faraday Trans. 2* **1976**, *72*, 1525.

(99) Cummins, C.; Lundy, R.; Walsh, J. J.; Ponsinet, V.; Fleury, G.; Morris, M. A. Enabling Future Nanomanufacturing through Block Copolymer Self-Assembly: A Review. *Nano Today* **2020**, *35*, 100936.

(100) Percus, J. K.; Yevick, G. J. Analysis of Classical Statistical Mechanics by Means of Collective Coordinates. *Phys. Rev.* **1958**, *110*, 1−13.

(101) Ashcroft, N. W.; Lekner, J. Structure and Resistivity of Liquid Metals. *Phys. Rev.* **1966**, *145*, 83−90.

(102) Wertheim, M. S. Exact Solution of the Percus-Yevick Integral Equation for Hard Spheres. *Phys. Rev. Lett.* **1963**, *10*, 321−323.

(103) Weidmann, C.; Brezesinski, K.; Suchomski, C.; Tropp, K.; Grosser, N.; Haetge, J.; Smarsly, B. M.; Brezesinski, T. Morphology-Controlled Synthesis of Nanocrystalline η-Al_2O_3 Thin Films, Powders, Microbeads, and Nanofibers with Tunable Pore Sizes from Preformed Oligomeric Oxo-Hydroxo Building Blocks. *Chem. Mater.* **2012**, *24*, 486−494.

(104) Antonietti, M.; Heinz, S.; Schmidt, M.; Rosenauer, C. Determination of the Micelle Architecture of Polystyrene/Poly(4-Vinylpyridine) Block Copolymers in Dilute Solution. *Macromolecules* **1994**, *27*, 3276−3281.

(105) Billet, J.; Vandewalle, S.; Meire, M.; Blommaerts, N.; Lommens, P.; Verbruggen, S. W.; De Buysser, K.; Du Prez, F.; Van Driessche, I. Mesoporous TiO_2 from Poly(*N*,*N*-dimethylacrylamide)-*b*-polystyrene Block Copolymers for Long-Term Acetaldehyde Photodegradation. *J. Mater. Sci.* **2020**, *55*, 1933−1945.

(106) Zhu, Y.; Zhao, Y.; Ma, J.; Cheng, X.; Xie, J.; Xu, P.; Liu, H.; Liu, H.; Zhang, H.; Wu, M.; Elzatahry, A. A.; Alghamdi, A.; Deng, Y.; Zhao, D. Mesoporous Tungsten Oxides with Crystalline Framework for Highly Sensitive and Selective Detection of Foodborne Pathogens. *J. Am. Chem. Soc.* **2017**, *139*, 10365−10373.

(107) Alberius, P. C. A.; Frindell, K. L.; Hayward, R. C.; Kramer, E. J.; Stucky, G. D.; Chmelka, B. F. General Predictive Syntheses of Cubic, Hexagonal, and Lamellar Silica and Titania Mesostructured Thin Films. *Chem. Mater.* **2002**, *14*, 3284−3294.

(108) Saeki, S.; Kuwahara, N.; Nakata, M.; Kaneko, M. Upper and Lower Critical Solution Temperatures in Poly(ethylene glycol) Solutions. *Polymer* **1976**, *17*, 685−689.

(109) Oh, S. Y.; Yang, H. E.; Bae, Y. C. Molecular Simulations and Thermodynamic Modeling for Closed-Loop Phase Miscibility of Aqueous PEO Solutions. *Macromol. Res.* **2013**, *21*, 921−930.

(110) Karlström, G. A New Model for Upper and Lower Critical Solution Temperatures in Poly(ethylene oxide) Solutions. *J. Phys. Chem.* **1985**, *89*, 4962−4964.

(111) Stefik, M.; Mahajan, S.; Sai, H.; Epps, T. H.; Bates, F. S.; Gruner, S. M.; DiSalvo, F. J.; Wiesner, U. Ordered Three- and Five-Ply Nanocomposites from ABC Block Terpolymer Microphase Separation with Niobia and Aluminosilicate Sols. *Chem. Mater.* **2009**, *21*, 5466−5473.

(112) Williams, E. R.; Ruff, C. X.; Stefik, M. Unimer Suppression Enables Supersaturated Homopolymer Swollen Micelles with Long-Term Stability after Glassy Entrapment. *Soft Matter* **2024**, *20*, 2288−2300.

(113) Collins, C. S.; Zhang, M.; Sturgill, C.; Ruff, C. X.; Melton, B.; Stefik, M. Photo-Crosslinked Persistent Micelle Templates with near Universal Solvent Compatibility. *Mater. Adv.* **2025**, *6*, 4881−4892.

(114) Larison, T.; Williams, E.; Collins, C. S.; Pingali, S. V.; Stefik, M. Bimodal Rates for Cavitation-Induced Chain Exchange Between Micelles. *Macromolecules* **2023**, *56*, 7818−7826.

(115) Wisnudel, M. B.; Torkelson, J. M. Effect of Chain Length on Rates of Diffusion-Limited Small Molecule-Polymer and Polymer-Polymer Reactions: Phosphorescence Quenching Studies. *J. Polym. Sci., Part B: Polym. Phys.* **1996**, *34*, 2999−3008.

(116) Tian, P.; Smith, G. D. Translocation of a Polymer Chain across a Nanopore: A Brownian Dynamics Simulation Study. *J. Chem. Phys.* **2003**, *119*, 11475−11483.

(117) Pajevic, S.; Bansil, R.; Konak, C. Diffusion of Linear Polymer Chains in Methyl Methacrylate Gels. *Macromolecules* **1993**, *26*, 305−312.

(118) Anastasiadis, S. H.; Chrissopoulou, K.; Fytas, G.; Appel, M.; Fleischer, G.; Adachi, K.; Gallot, Y. Self-diffusivity of Diblock Copolymers in Solutions in Neutral Good Solvents. *Acta Polym.* **1996**, *47*, 250−264.

(119) Borodin, O.; Bedrov, D.; Smith, G. D. Concentration Dependence of Water Dynamics in Poly(ethylene oxide)/Water Solutions from Molecular Dynamics Simulations. *J. Phys. Chem. B* **2002**, *106*, 5194−5199.

(120) Luo, M.-B.; Yang, Q.-H.; Zhang, C.-Y.; Wu, F. Study on the Diffusion of Polymer in Long Cylindrical Tubes. *Polymer* **2016**, *101*, 192−198.

(121) Kowert, B. A. Diffusion of Polymethylene Chain Molecules in Nonpolar Solvents. *J. Phys. Chem. B* **2020**, *124*, 3716−3723.

(122) Meinusch, R.; Ellinghaus, R.; Hormann, K.; Tallarek, U.; Smarsly, B. M. On the Underestimated Impact of the Gelation Temperature on Macro- and Mesoporosity in Monolithic Silica. *Phys. Chem. Chem. Phys.* **2017**, *19*, 14821−14834.

(123) Weyland, M.; Midgley, P. A.; Thomas, J. M. Electron Tomography of Nanoparticle Catalysts on Porous Supports: A New Technique Based on Rutherford Scattering. *J. Phys. Chem. B* **2001**, *105*, 7882−7886.

(124) Ercius, P.; Alaidi, O.; Rames, M. J.; Ren, G. Electron Tomography: A Three-Dimensional Analytic Tool for Hard and Soft Materials Research. *Adv. Mater.* **2015**, *27*, 5638−5663.

(125) Wang, W.; Svidrytski, A.; Wang, D.; Villa, A.; Hahn, H.; Tallarek, U.; Kübel, C. Quantifying Morphology and Diffusion

Properties of Mesoporous Carbon From High-Fidelity 3D Reconstructions. *Microsc. Microanal.* 2019, *25*, 891−902.

(126) Huang, X.; Hlushkou, D.; Wang, D.; Tallarek, U.; Kübel, C. Quantitative Analysis of Mesoporous Structures by Electron Tomography: A Phantom Study. *Ultramicroscopy* 2023, *243*, 113639.

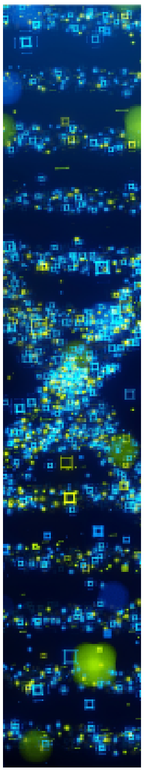

https://doi.org/10.1021/acs.langmuir.5c02750
Langmuir 2025, 41, 30948−30967

Supporting Information

Porosity Tuning in Soft-templated Mesoporous Silica: The Influence of Block Copolymer Composition and Concentration

Lysander Q. Wagner[a,b], *Frederik Breckwoldt*[a,b], *Xiaohui Huang*[c,d], *Christian Kübel*[c,d,e], *Xiaoyin Cheng*[f], *Katja Schladitz*[f], *and Bernd M. Smarsly*[a,b]*

a. Institute of Physical Chemistry, Justus Liebig University, Heinrich-Buff-Ring 17, D-35392 Giessen, Germany

b. Center of Materials Research, Justus Liebig University, Heinrich-Buff-Ring 16, D-35392 Giessen, Germany

c. Institute of Nanotechnology, Karlsruhe Institute of Technology, Hermann-von-Helmholtz-Platz 1, D-76344 Eggenstein-Leopoldshafen, Germany

d. Department of Materials and Earth Science, Technical University Darmstadt, Peter-Grünberg-Straße 2, D-64287 Darmstadt, Germany

e. Karlsruhe Nano Micro Facility, Karlsruhe Institute of Technology, Hermann-von-Helmholtz-Platz 1, D-76344 Eggenstein-Leopoldshafen, German

f. Fraunhofer Institute for Industrial Mathematics, Fraunhofer-Platz 1, D-67663 Kaiserslautern, Germany

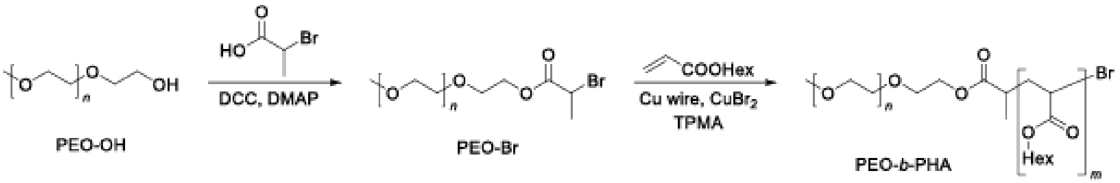

Scheme S1. Two-step synthesis of PEO-*b*-PHA block copolymers by a SARA ATRP.

Table S1. Overview on the amounts of macroinitiator (PEO-Br), monomer (hexyl acrylate), ligand (TPMA), $CuBr_2$, and solvent (DMF) used for the SARA ATRP reactions in this study.

Sample	PEO-Br	Monomer	TPMA	$CuBr_2$	DMF
PEO$_{441}$-*b*-PHA$_{390}$	2001 mg	8.30 mL	88 mg	35 mg	6 mL
PEO$_{441}$-*b*-PHA$_{326}$	2000 mg	6.60 mL	89 mg	34 mg	6 mL
PEO$_{441}$-*b*-PHA$_{270}$	1999 mg	5.60 mL	89 mg	35 mg	6 mL
PEO$_{441}$-*b*-PHA$_{173}$	1999 mg	3.51 mL	88 mg	34 mg	6 mL
PEO$_{251}$-*b*-PHA$_{441}$	500 mg	4.35 mL	44 mg	17 mg	5 mL
PEO$_{251}$-*b*-PHA$_{381}$	1000 mg	6.71 mL	88 mg	33 mg	6 mL
PEO$_{251}$-*b*-PHA$_{215}$	500 mg	2.41 mL	43 mg	17 mg	5 mL
PEO$_{251}$-*b*-PHA$_{147}$	500 mg	1.83 mL	44 mg	17 mg	5 mL
PEO$_{251}$-*b*-PHA$_{093}$	2001 mg	3.37 mL	175 mg	67 mg	10 mL
PEO$_{137}$-*b*-PHA$_{544}$	300 mg	3.35 mL	9 mg	3 mg	5 mL
PEO$_{137}$-*b*-PHA$_{517}$	300 mg	3.35 mL	17 mg	7 mg	5 mL
PEO$_{137}$-*b*-PHA$_{451}$	500 mg	5.58 mL	7 mg	3 mg	5 mL
PEO$_{137}$-*b*-PHA$_{381}$	500 mg	5.60 mL	87 mg	33 mg	5 mL
PEO$_{137}$-*b*-PHA$_{283}$	500 mg	4.92 mL	87 mg	34 mg	5 mL
PEO$_{137}$-*b*-PHA$_{227}$	501 mg	3.67 mL	88 mg	35 mg	5 mL
PEO$_{137}$-*b*-PHA$_{093}$	500 mg	1.73 mL	87 mg	34 mg	5 mL
PEO$_{047}$-*b*-PHA$_{468}$	250 mg	9.67 mL	36 mg	14 mg	6 mL
PEO$_{047}$-*b*-PHA$_{096}$	1000 mg	7.80 mL	160 mg	63 mg	5 mL

Table S2. Amount of each soft template used for preparing mesoporous silica of varying porosity (polymer volume fraction Φ in vol.%).

Soft Template	57 vol.%	85 vol.%	Soft Template	Amount	Φ
PEO$_{441}$-*b*-PHA$_{390}$	23 mg	98 mg	**PEO$_{441}$-*b*-PHA$_{270}$**	7 mg	30 vol.%
PEO$_{441}$-*b*-PHA$_{326}$	23 mg	98 mg		11 mg	40 vol.%
PEO$_{441}$-*b*-PHA$_{270}$	23 mg	98 mg		17 mg	50 vol.%
PEO$_{441}$-*b*-PHA$_{173}$	23 mg	99 mg		32 mg	65 vol.%
PEO$_{251}$-*b*-PHA$_{441}$	23 mg	97 mg		41 mg	70 vol.%
PEO$_{251}$-*b*-PHA$_{381}$	23 mg	98 mg		69 mg	80 vol.%
PEO$_{251}$-*b*-PHA$_{215}$	23 mg	98 mg	**PEO$_{251}$-*b*-PHA$_{381}$**	12 mg	40 vol.%
PEO$_{251}$-*b*-PHA$_{147}$	23 mg	99 mg		17 mg	50 vol.%
PEO$_{251}$-*b*-PHA$_{093}$	24 mg	100 mg		40 mg	70 vol.%
PEO$_{137}$-*b*-PHA$_{544}$	23 mg	97 mg		52 mg	75 vol.%
PEO$_{137}$-*b*-PHA$_{517}$	23 mg	97 mg		69 mg	80 vol.%
PEO$_{137}$-*b*-PHA$_{451}$	23 mg	97 mg	**PIB$_{50}$-*b*-PEO$_{45}$**	7 mg	30 vol.%
PEO$_{137}$-*b*-PHA$_{381}$	23 mg	98 mg		16 mg	50 vol.%
PEO$_{137}$-*b*-PHA$_{283}$	23 mg	98 mg		20 mg	55 vol.%
PEO$_{137}$-*b*-PHA$_{227}$	23 mg	97 mg		38 mg	70 vol.%
PEO$_{137}$-*b*-PHA$_{093}$	23 mg	99 mg		91 mg	85 vol.%
PEO$_{047}$-*b*-PHA$_{468}$	23 mg	97 mg			
PEO$_{047}$-*b*-PHA$_{096}$	23 mg	99 mg			

Table S3. Experimental details of the STEM-based tomography.

Sample	Tilt Range	Pixel Size	Residual Error	Voxel Size	Ball Radius
69 vol.%	–74° to 66°	0.63 nm	0.477 nm	$(1.26\ \text{nm})^3$	40 px
75 vol.%	–74° to 68°	0.81 nm	0.573 nm	$(1.62\ \text{nm})^3$	30 px

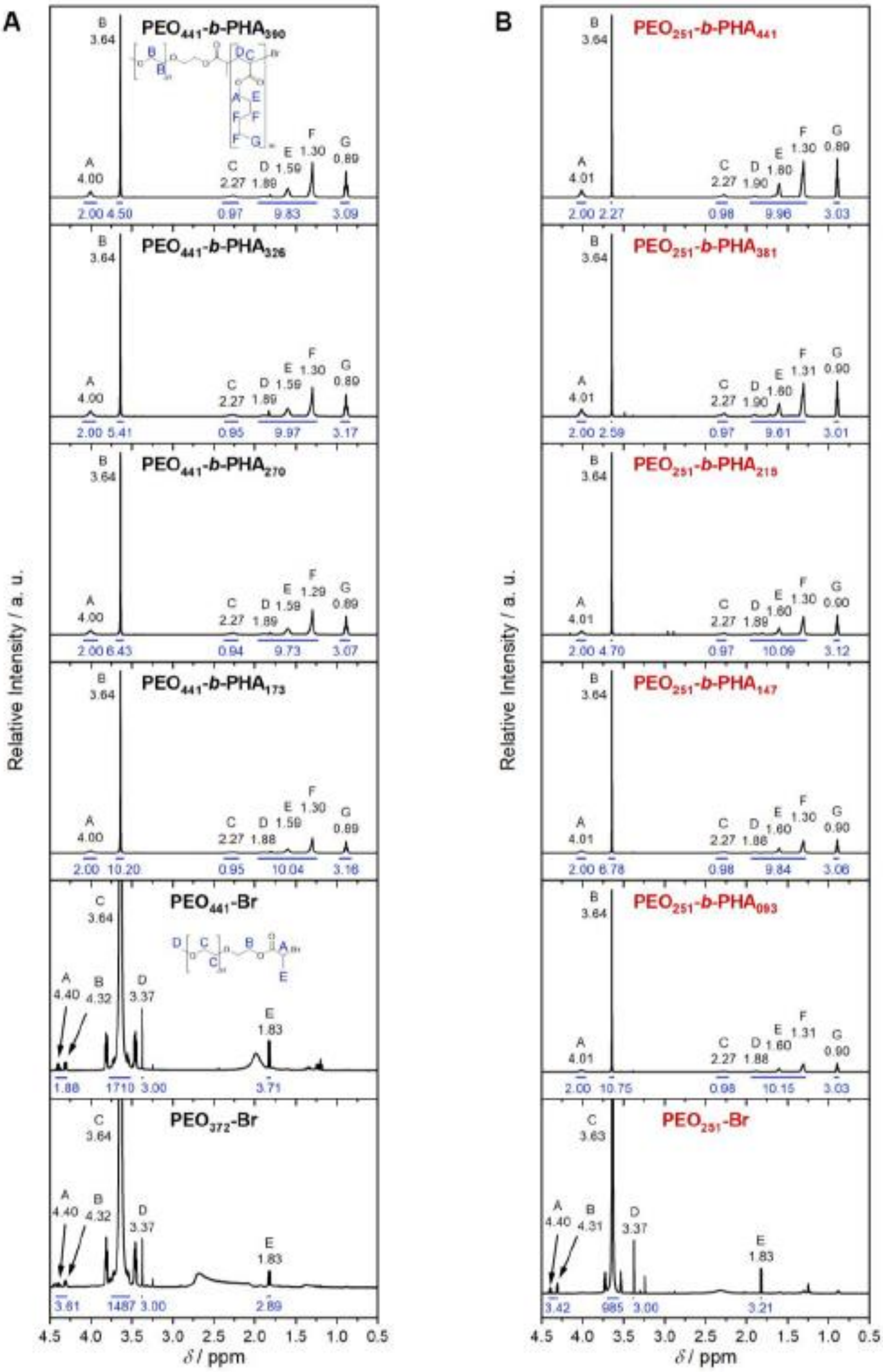

Figure S1. ^{1}H NMR (400 and 700 MHz) spectra of PEO-Br macroinitiators (20 kDa, black and 10 kDa, red) and PEO-*b*-PHA block copolymers based on them in $CDCl_3$.

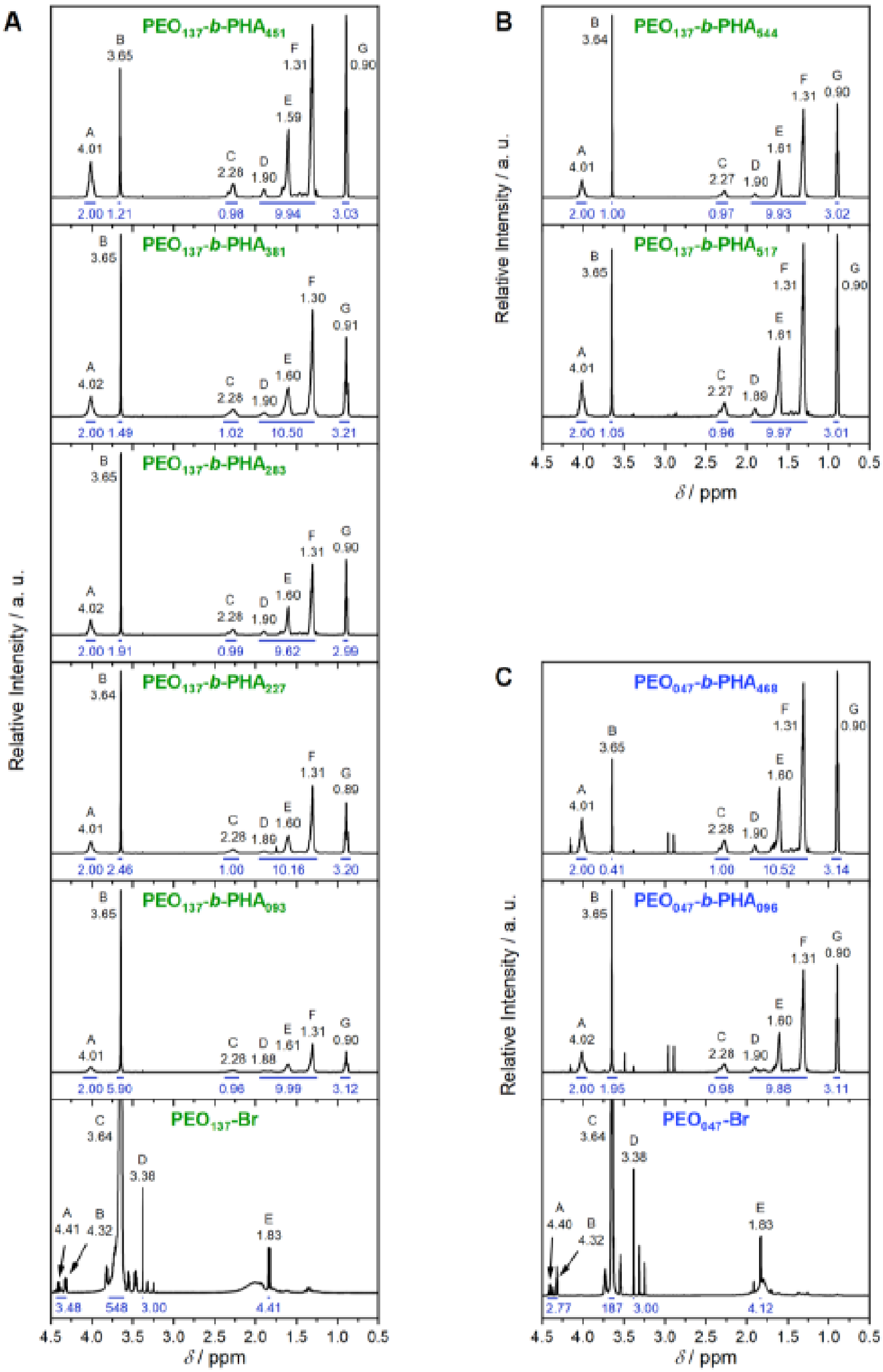

Figure S2. ^{1}H NMR (400 and 700 MHz) spectra of PEO-Br macroinitiators (5 kDa, green and 2 kDa, blue) and PEO-*b*-PHA block copolymers based on them in CDCl$_3$.

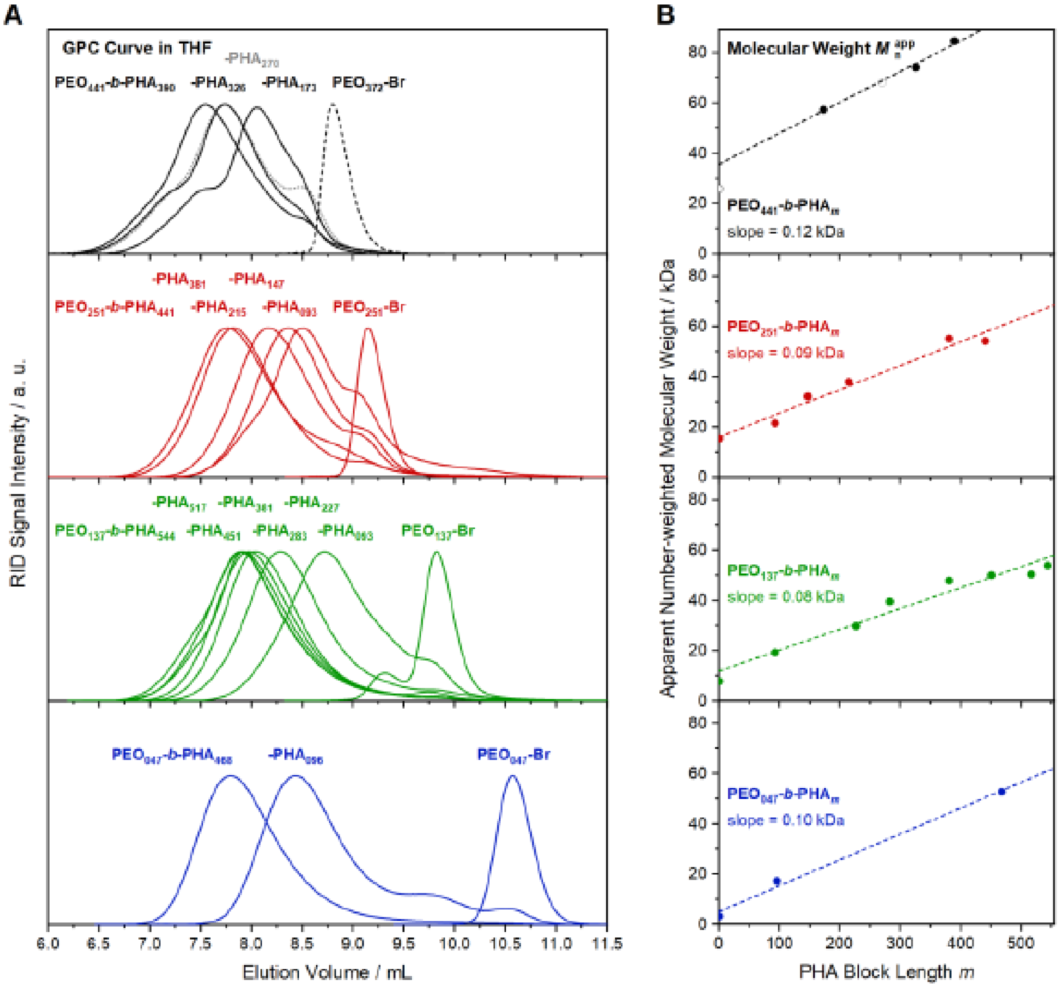

Figure S3. (A) GPC RI traces of the PEO-*b*-PHA block copolymers and the underlying macroinitiators of varying PEO block length (441 EO units in black, 251 in red, 137 in green, and 47 in blue) in THF. Labelling follows increasing PHA block length from right to left in accordance with the shift of the corresponding curve to lower elution volumes. The GPC curve of PEO_{372}-Br (dashed line) is given as references due to the absence of sufficient amounts of PEO_{441}-Br for characterization. (B) Plot of each apparent number-weighted molecular weight from GPC against the NMR-based PHA block length with a linear fit (dashed line) each. Open symbols indicate the reference PEO_{372}-Br sample and the block copolymer excluded from the soft templating matrix.

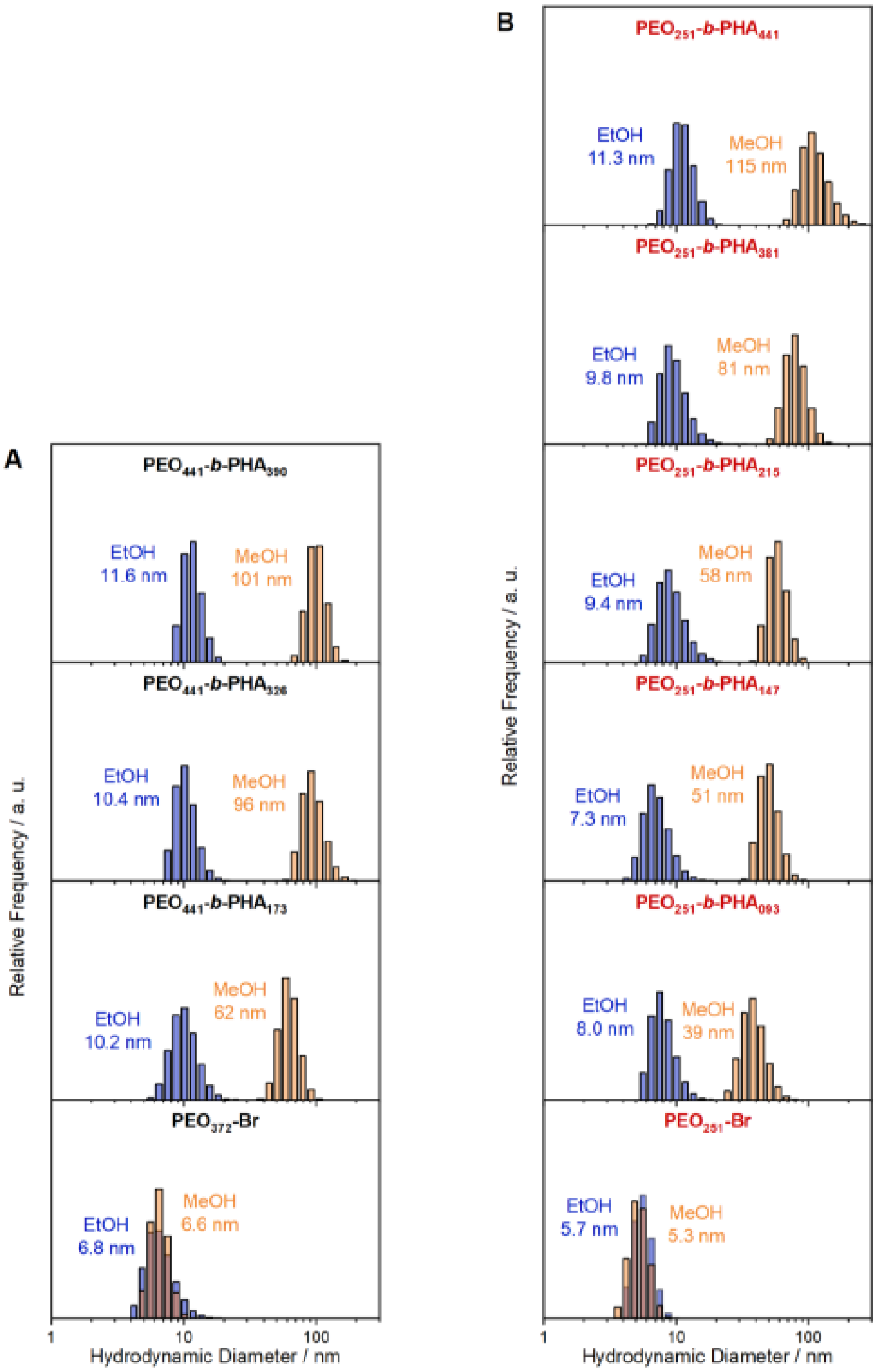

Figure S4. DLS data of PEO-Br macroinitiators (20 kDa and 10 kDa) and PEO-*b*-PHA block copolymers based on them in ethanol (blue) and in methanol (orange).

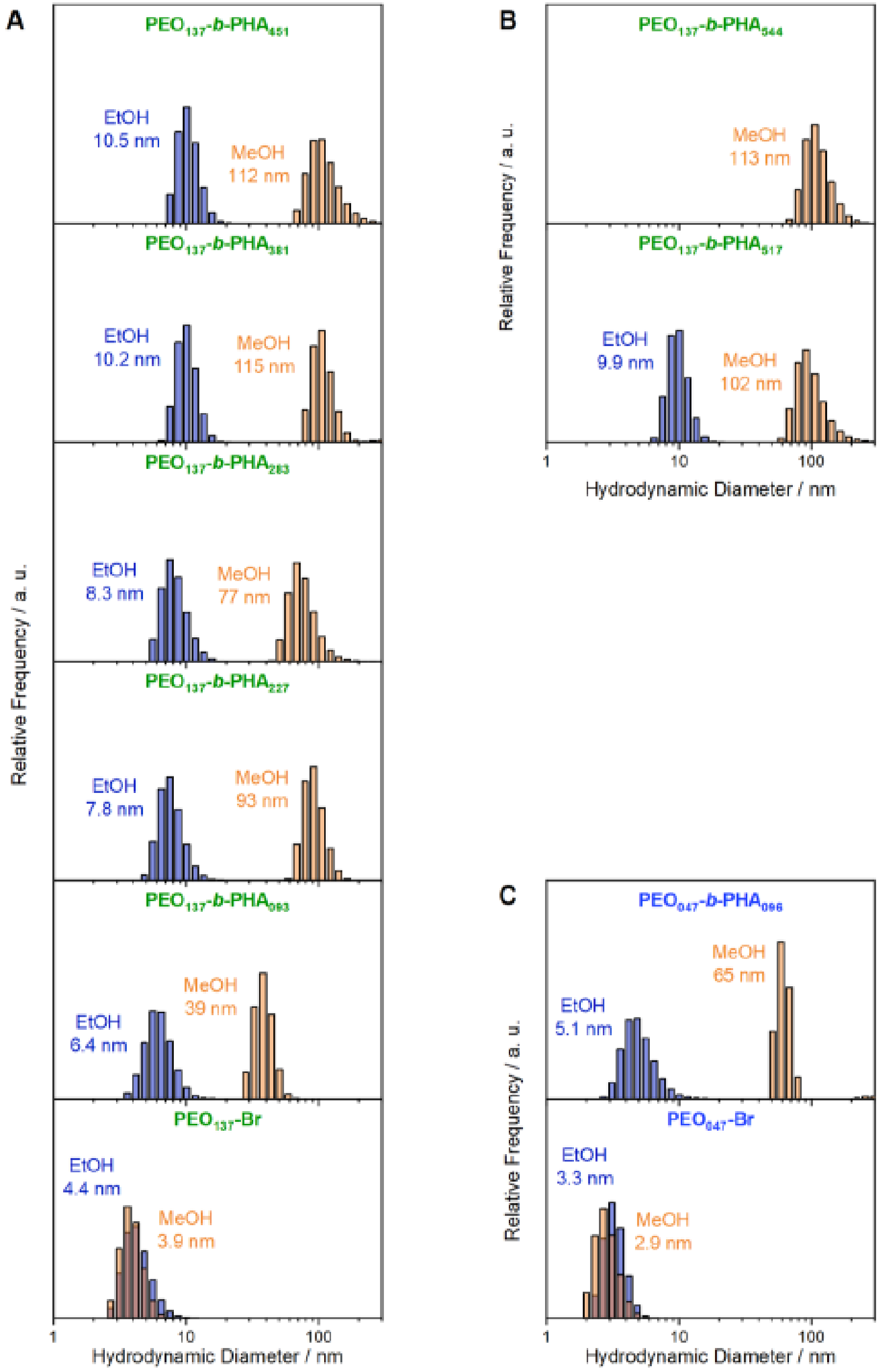

Figure S5. DLS data of PEO-Br macroinitiators (5 kDa and 2 kDa) and PEO-*b*-PHA block copolymers based on them in ethanol (blue) and in methanol (orange).

Table S4. Overview on all polymers prepared throughout this work including number-average molecular weight (M_n) from NMR, apparent number-average molecular weight (M_n^{app}) and polydispersity index ($Đ$) from GPC, and hydrodynamic size in ethanol and methanol from DLS.

Sample	M_n / kDa	M_n^{app} / kDa	$Đ$	d_{DLS}(EtOH) / nm	d_{DLS}(MeOH) / nm
PEO$_{441}$-*b*-PHA$_{390}$	80.5	84.6	1.51	11.6	101
PEO$_{441}$-*b*-PHA$_{326}$	70.5	74.0	1.50	10.4	96
PEO$_{441}$-*b*-PHA$_{270}$	61.7	68.0	1.52	11.7	86
PEO$_{441}$-*b*-PHA$_{173}$	46.6	57.3	1.13	10.2	62
PEO$_{372}$-Br	16.6	25.7	1.03	6.8	6.6
PEO$_{251}$-*b*-PHA$_{441}$	80.1	54.2	1.67	11.3	115
PEO$_{251}$-*b*-PHA$_{381}$	70.7	55.1	1.55	9.8	81
PEO$_{251}$-*b*-PHA$_{215}$	44.8	37.9	1.39	9.4	58
PEO$_{251}$-*b*-PHA$_{147}$	34.2	32.2	1.31	7.3	51
PEO$_{251}$-*b*-PHA$_{093}$	25.8	21.5	1.54	8.0	39
PEO$_{251}$-Br	11.3	15.7	1.03	5.7	5.3
PEO$_{137}$-*b*-PHA$_{544}$	91.1	53.9	1.60	–	113
PEO$_{137}$-*b*-PHA$_{517}$	86.9	50.3	1.57	9.9	102
PEO$_{137}$-*b*-PHA$_{451}$	76.6	50.0	1.57	10.5	112
PEO$_{137}$-*b*-PHA$_{381}$	65.7	47.9	1.45	10.2	115
PEO$_{137}$-*b*-PHA$_{283}$	50.4	39.5	1.44	8.3	77
PEO$_{137}$-*b*-PHA$_{227}$	41.7	29.8	1.54	7.8	93
PEO$_{137}$-*b*-PHA$_{093}$	20.7	19.2	1.41	6.4	39
PEO$_{137}$-Br	6.2	7.8	1.10	4.4	3.9
PEO$_{047}$-*b*-PHA$_{468}$	75.3	52.7	1.58	–	–
PEO$_{047}$-*b*-PHA$_{096}$	17.3	17.2	1.79	5.1	65
PEO$_{047}$-Br	2.3	3.2	1.04	3.3	2.9

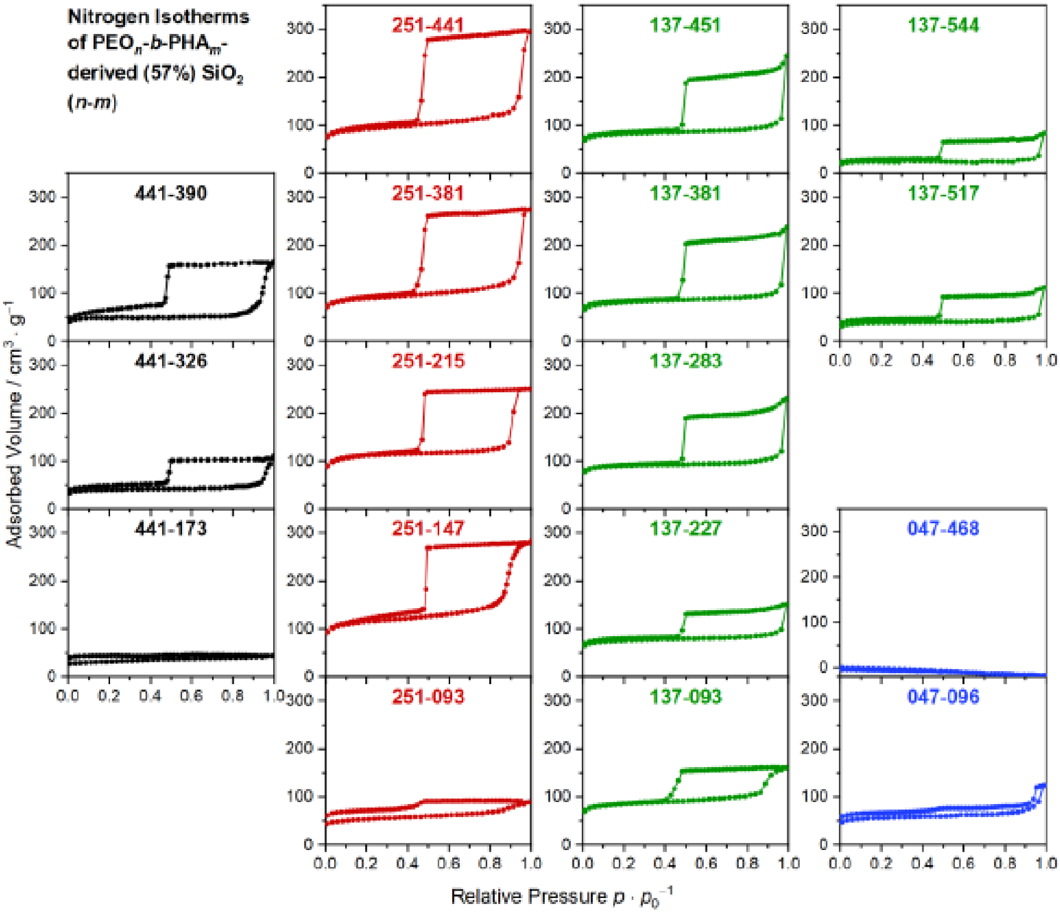

Figure S6. Nitrogen isotherms at 77 K of mesoporous silica prepared with 57 vol.% PEO$_n$-b-PHA$_m$ with a PEO block length of n = 441 (black), 251 (red), 137 (green), and 47 (blue) while the PHA block length m increases from the bottom to the top each.

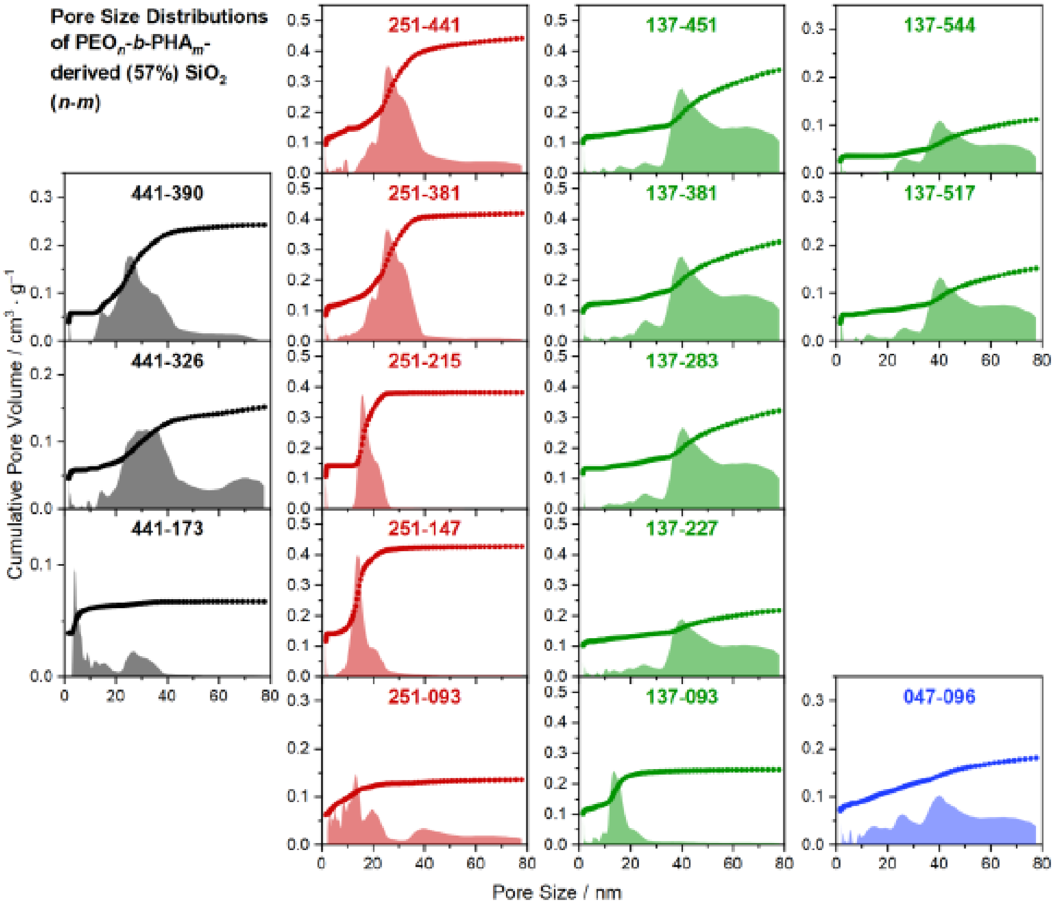

Figure S7. Pore size distributions of mesoporous silica prepared with 57 vol.% PEO$_n$-b-PHA$_m$ with a PEO block length of n = 441 (black), 251 (red), 137 (green), and 47 (blue) derived from the adsorption branch with an NLDFT kernel for cylindrical pores. The cumulative plot (filled symbols) is given in absolute values while the differential plot (filled area) is displayed in arbitrary units for eye guidance.

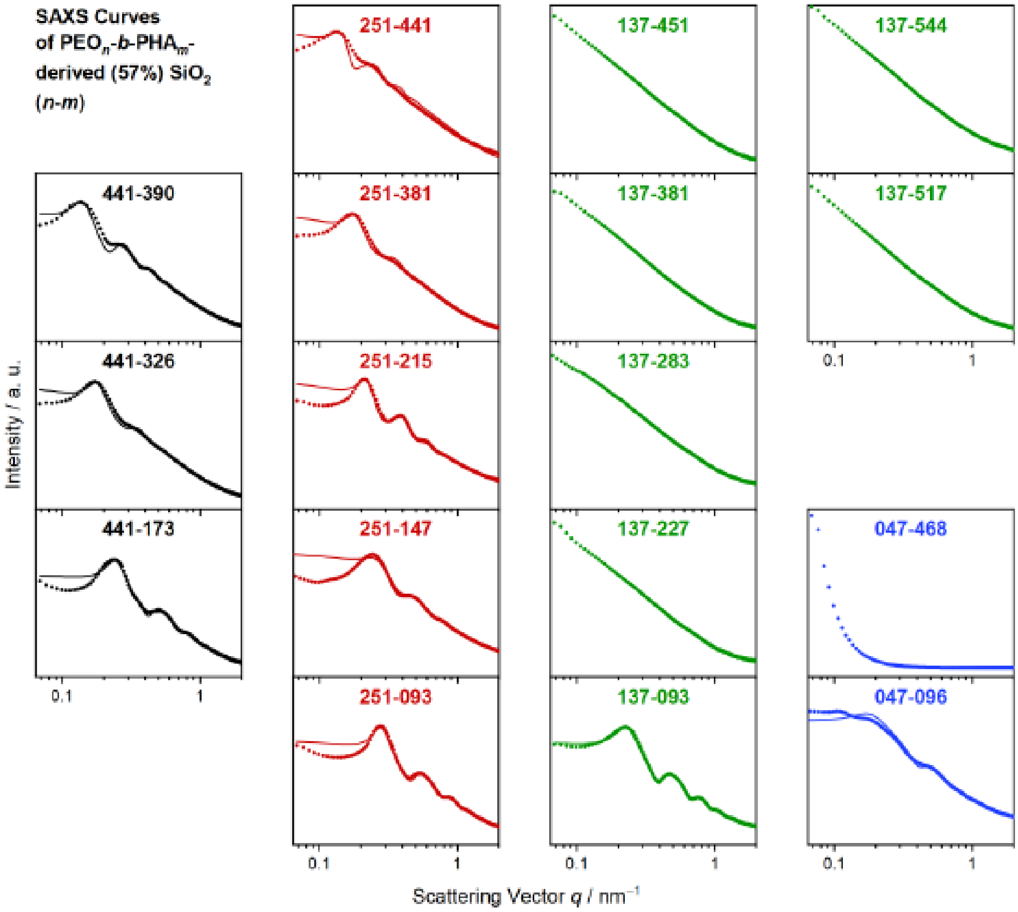

Figure S8. SAXS curves of mesoporous silica prepared with 57 vol.% PEO$_n$-*b*-PHA$_m$ with a PEO block length of $n = 441$ (black), 251 (red), 137 (green), and 47 (blue) while the PHA block length m increases from the bottom to the top each. Experimental data (dots) are fitted (solid lines) according to a Percus-Yevick model for spherical pores.

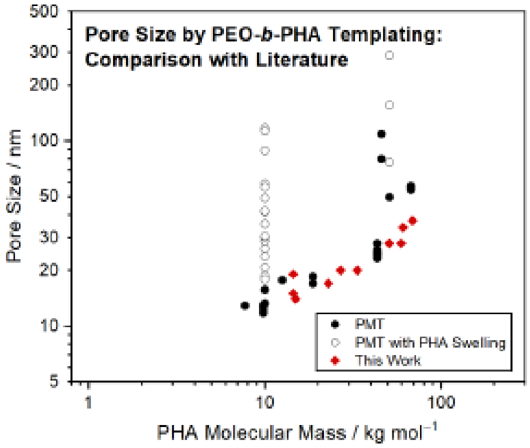

Figure S9. Comparison of the pore size of mesoporous materials obtained with PEO-*b*-PHA block copolymers of different PHA block lengths by soft templating with 57 vol.% template in this work (red diamonds) and by persistent micelle templating (PMT) without (filled black circles) and with PHA homopolymer swelling (open black circles) reported by Stefik and co-workers.[1–9] Note that some macroporous samples prepared by homopolymer swelling possess multimodal pore size distributions as summarized and categorized elsewhere.[1]

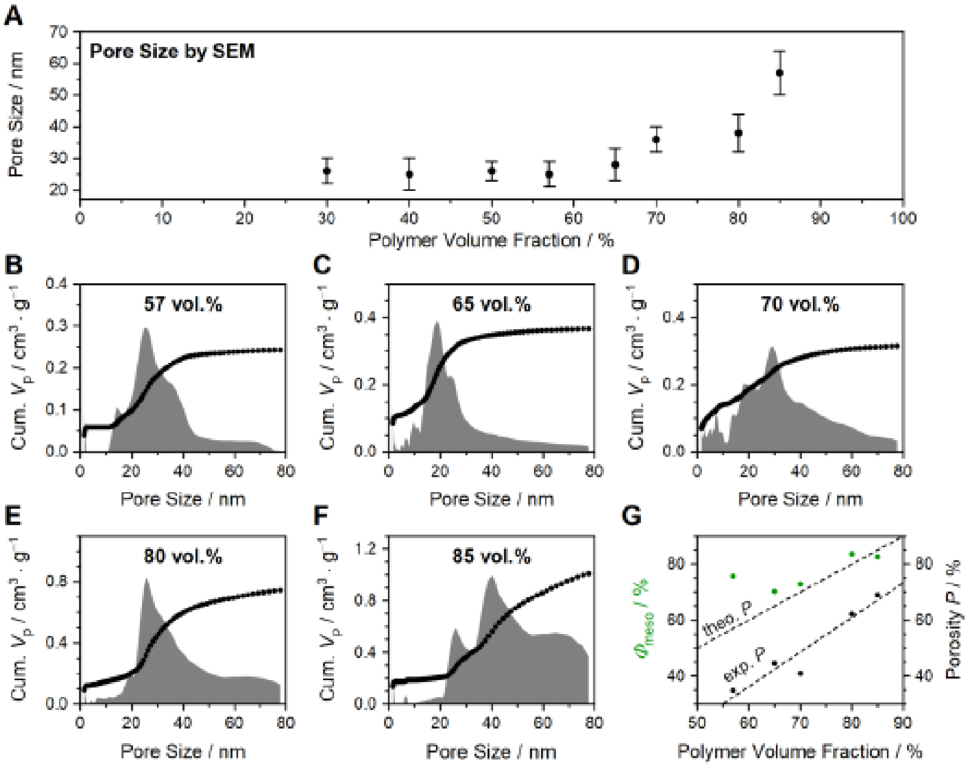

Figure S10. (A) Pore size and its standard deviation obtained from SEM of mesoporous silica prepared with different amounts of PEO$_{441}$-*b*-PHA$_{270}$ as well as the pore size distribution derived from the adsorption branch of the nitrogen (77 K) isotherm with an NLDFT kernel for cylindrical pores for the samples prepared with (B) 57, (C) 65, (D) 70, (E) 80, (F) 85 vol.% soft template. (G) Experimental porosity (black dots) and share of the mesopore volume (green dots) compared to the total pore volume both obtained from physisorption in dependency on the polymer volume fraction. The experimental porosity follows a linear fit (lower dashed line) and is contrasted to the theoretical evolution (upper dashed line).

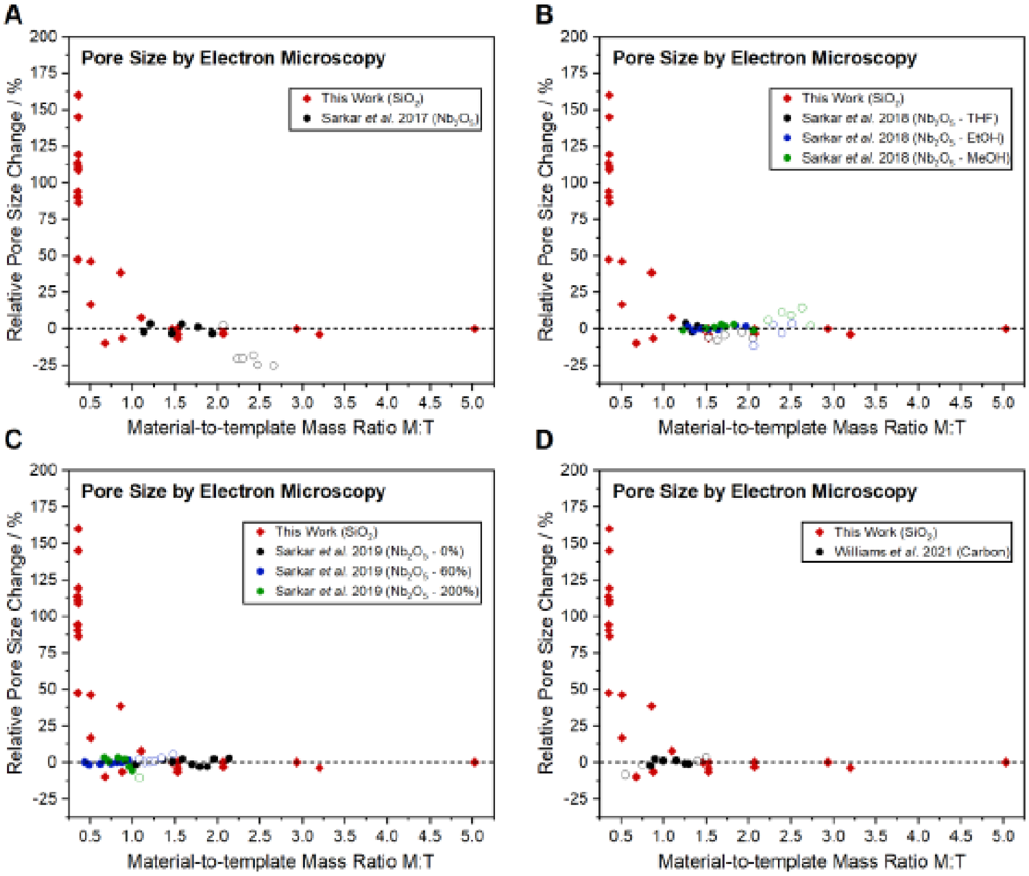

Figure S11. Comparison of relative pore size changes upon varying the template amount (the mass of final mesoporous material assuming full conversion in relation to the mass of soft template) observed in this study (red diamonds) to pore sizes found in literature for mesoporous materials templated with persistent micelles (filled circles) and dynamic micelles (open circles). The average pore diameter found by (A – C) SEM and (D) TEM in mesoporous niobia soft-templated with PEO-*b*-PHA (A) in tetrahydrofuran (THF),[4] (B) in THF, ethanol, and methanol, respectively,[6] and (C) with PEO-*b*-PHA swollen with different amounts of PHA homopolymer in ethanol[8] and (D) in mesoporous carbon templated with PEO-*b*-PS[10] are referenced to their respective pore size by persistent micelle templating and contrasted to SEM-based pore sizes (referenced to each pore size obtained with the lowest template amount) of mesoporous silica prepared in this study.

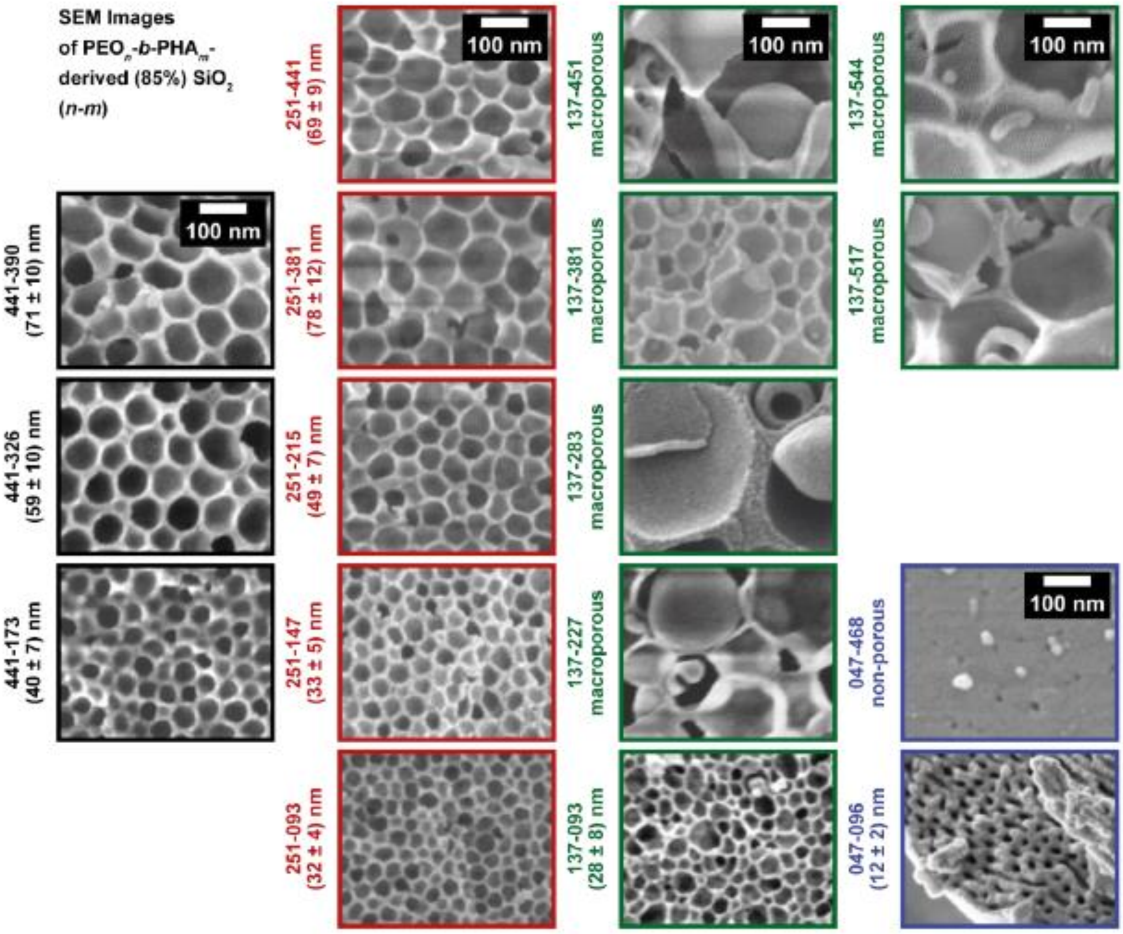

Figure S12. SEM images of mesoporous silica prepared with 85 vol.% PEO$_n$-*b*-PHA$_m$ with a PEO block length of $n = 441$ (black), 251 (red), 137 (green), and 47 (blue) while the PHA block length m increases from the bottom to the top each.

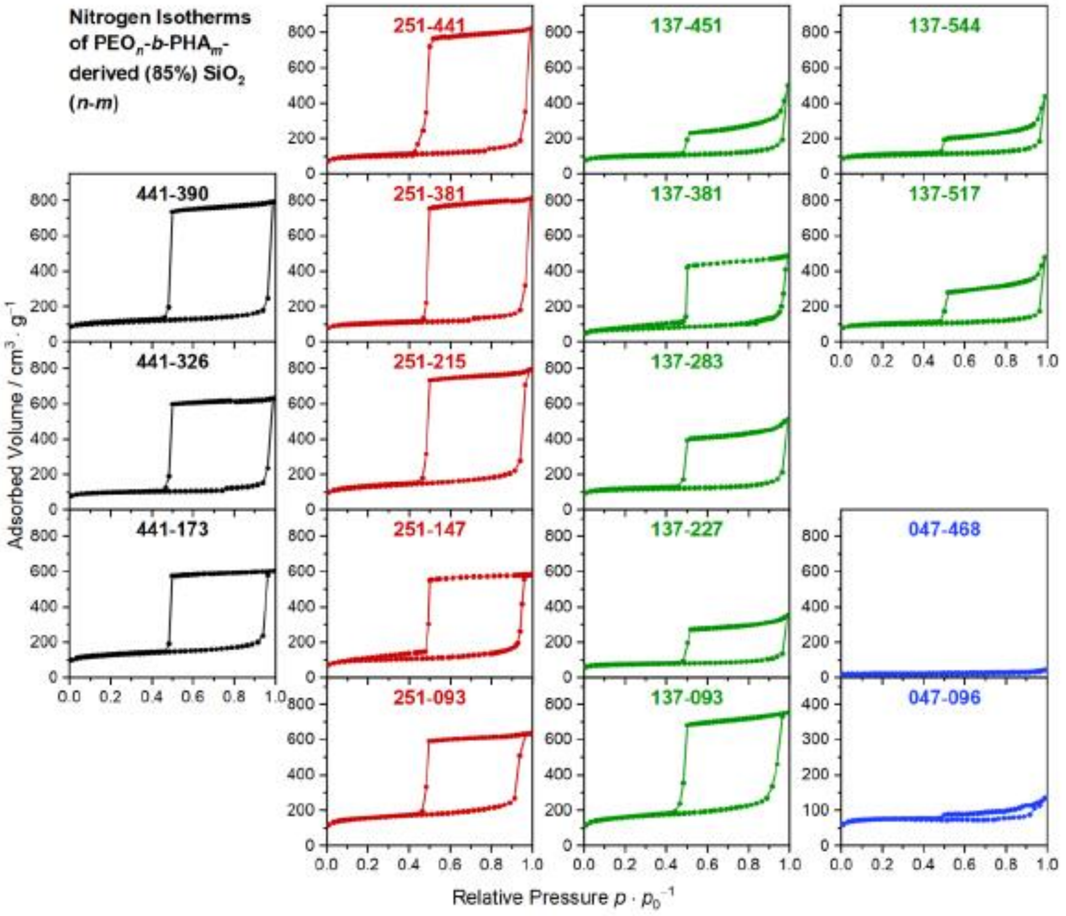

Figure S13. Nitrogen isotherms at 77 K of mesoporous silica prepared with 85 vol.% PEO$_n$-*b*-PHA$_m$ with a PEO block length of $n = 441$ (black), 251 (red), 137 (green), and 47 (blue) while the PHA block length m increases from the bottom to the top each.

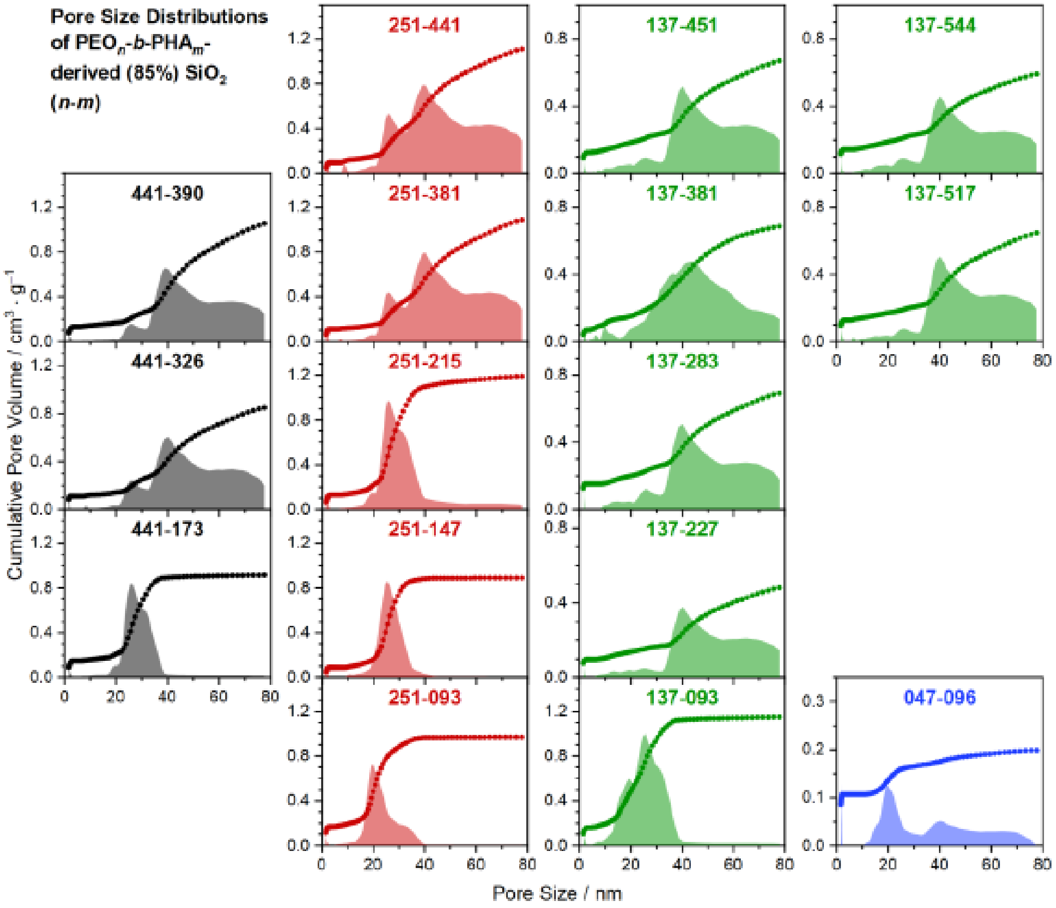

Figure S14. Pore size distributions of mesoporous silica prepared with 85 vol.% PEO$_n$-*b*-PHA$_m$ with a PEO block length of n = 441 (black), 251 (red), 137 (green), and 47 (blue) derived from the adsorption branch with an NLDFT kernel for cylindrical pores. The cumulative plot (filled symbols) is given in absolute values while the differential plot (filled area) is displayed in arbitrary units for eye guidance.

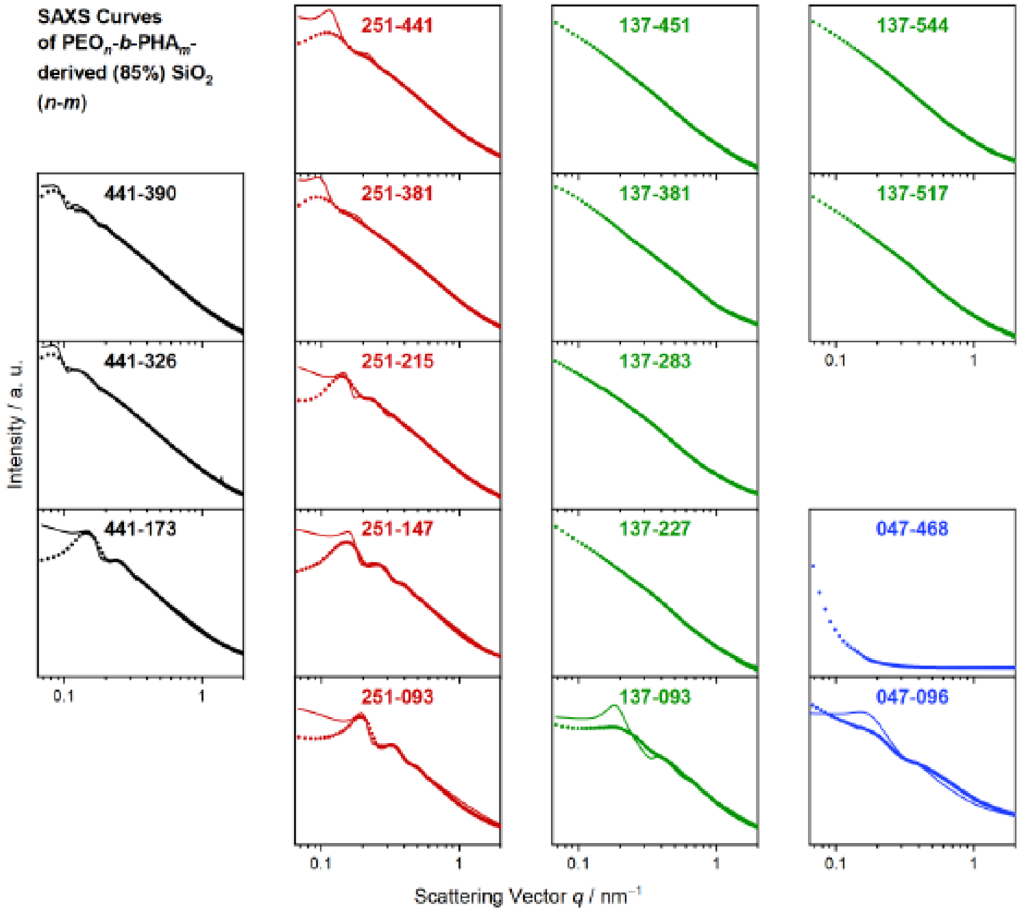

Figure S15. SAXS curves of mesoporous silica prepared with 85 vol.% PEO$_n$-*b*-PHA$_m$ with a PEO block length of $n = 441$ (black), 251 (red), 137 (green), and 47 (blue) while the PHA block length m increases from the bottom to the top each. Experimental data (dots) are fitted (solid lines) according to a Percus-Yevick model for spherical pores.

Table S5. Pore size (in nm) of all mesoporous silica powders possessing ordered arrays of spherical mesopores prepared with 57 and 85 vol.% soft template. Values from SEM were obtained by measuring the pore diameter of 50 pores and determining its standard deviation, values from nitrogen physisorption result from an NLDFT-based pore size distribution relying on the adsorption branch (mode value and full width at half maximum) after multiplication with a geometrical correction factor of 1.35 (spherical *versus* cylindrical pore geometry), and values from SAXS were received after fitting with a Percus-Yevick model for spherical pores.

	Pore Size (57 vol.%) / nm			Pore Size (85 vol.%) / nm		
Template	SEM	Phys	SAXS	SEM	Phys	SAXS
PEO$_{441}$-*b*-PHA$_{390}$	34 ± 6	34 ± 7	41 ± 10	71 ± 10	54 ± 8	85 ± 20
PEO$_{441}$-*b*-PHA$_{326}$	28 ± 3	43 ± 13	30 ± 10	59 ± 10	54 ± 8	85 ± 22
PEO$_{441}$-*b*-PHA$_{173}$	21 ± 2	–	21 ± 5	40 ± 7	38 ± 7	46 ± 14
PEO$_{251}$-*b*-PHA$_{441}$	37 ± 6	34 ± 4	49 ± 10	69 ± 9	54 ± 9	50 ± 22
PEO$_{251}$-*b*-PHA$_{381}$	28 ± 4	34 ± 6	31 ± 13	78 ± 12	54 ± 8	66 ± 26
PEO$_{251}$-*b*-PHA$_{215}$	20 ± 4	21 ± 3	30 ± 8	49 ± 7	39 ± 7	51 ± 13
PEO$_{251}$-*b*-PHA$_{147}$	17 ± 3	19 ± 3	23 ± 8	33 ± 5	34 ± 5	45 ± 11
PEO$_{251}$-*b*-PHA$_{093}$	15 ± 2	18 ± 3	20 ± 5	32 ± 4	26 ± 5	36 ± 10
PEO$_{137}$-*b*-PHA$_{093}$	19 ± 2	18 ± 3	23 ± 5	28 ± 8	29 ± 8	27 ± 9
PEO$_{047}$-*b*-PHA$_{096}$	14 ± 2	–	21 ± 8	12 ± 2	27 ± 4	26 ± 12

Table S6. Overview on the specific surface area S_{BET} of all silica samples (in $\mathrm{m^2\,g^{-1}}$) as determined by the BET approach from the respective physisorption isotherm.

Soft Template	57 vol.%	85 vol.%	Soft Template	Φ	S_{BET} / $\mathrm{m^2\,g^{-1}}$
PEO$_{441}$-*b*-PHA$_{390}$	200	410	**PEO$_{441}$-*b*-PHA$_{270}$**	30 vol.%	–
PEO$_{441}$-*b*-PHA$_{326}$	150	370		40 vol.%	–
PEO$_{441}$-*b*-PHA$_{270}$	240	540		50 vol.%	–
PEO$_{441}$-*b*-PHA$_{173}$	120	490		65 vol.%	330
PEO$_{251}$-*b*-PHA$_{441}$	350	370		70 vol.%	290
PEO$_{251}$-*b*-PHA$_{381}$	340	390		80 vol.%	400
PEO$_{251}$-*b*-PHA$_{215}$	430	480			
PEO$_{251}$-*b*-PHA$_{147}$	440	360			
PEO$_{251}$-*b*-PHA$_{093}$	200	580			
PEO$_{137}$-*b*-PHA$_{544}$	100	410			
PEO$_{137}$-*b*-PHA$_{517}$	150	380			
PEO$_{137}$-*b*-PHA$_{451}$	320	370			
PEO$_{137}$-*b*-PHA$_{381}$	310	260			
PEO$_{137}$-*b*-PHA$_{283}$	350	450			
PEO$_{137}$-*b*-PHA$_{227}$	300	280			
PEO$_{137}$-*b*-PHA$_{093}$	330	580			
PEO$_{047}$-*b*-PHA$_{468}$	–	60			
PEO$_{047}$-*b*-PHA$_{096}$	220	290			

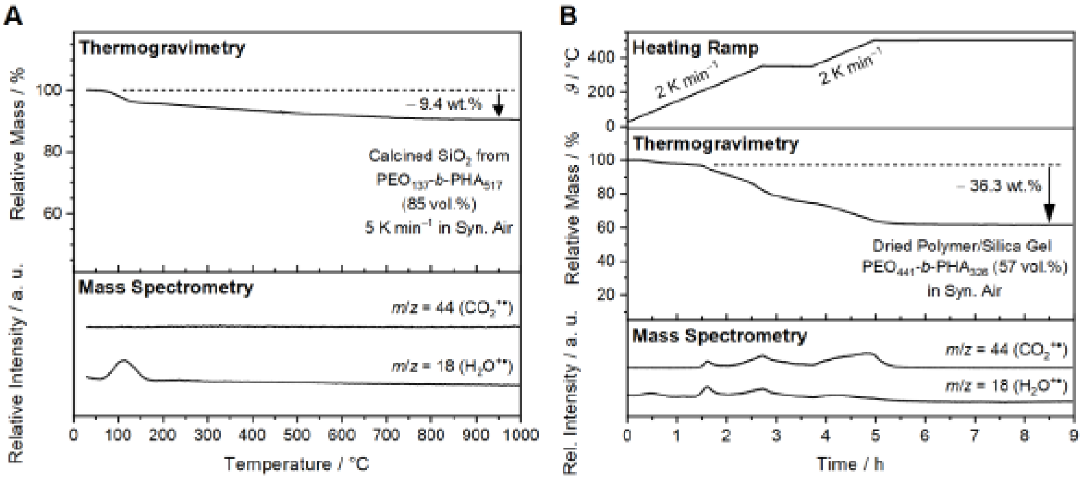

Figure S16. Thermogravimetric curve of (A) mesoporous silica prepared with 85 vol.% PEO_{137}-*b*-PHA_{517} measured in synthetic air with a heating ramp of 5 K min^{-1} and (B) of a dried PEO-*b*-PHA/silica hybrid gel with 57 vol.% PEO_{441}-*b*-PHA_{326} measured in synthetic air according to the heating ramp used for all syntheses. In addition, the intensity evolution of the mass signals corresponding to an *m*/*z* ratio of 18 (water) and 44 (CO_2) are shown below (note that all data in (B) are plotted against the elapsed time leading to discontinuances at each dwell time of the heating ramp).

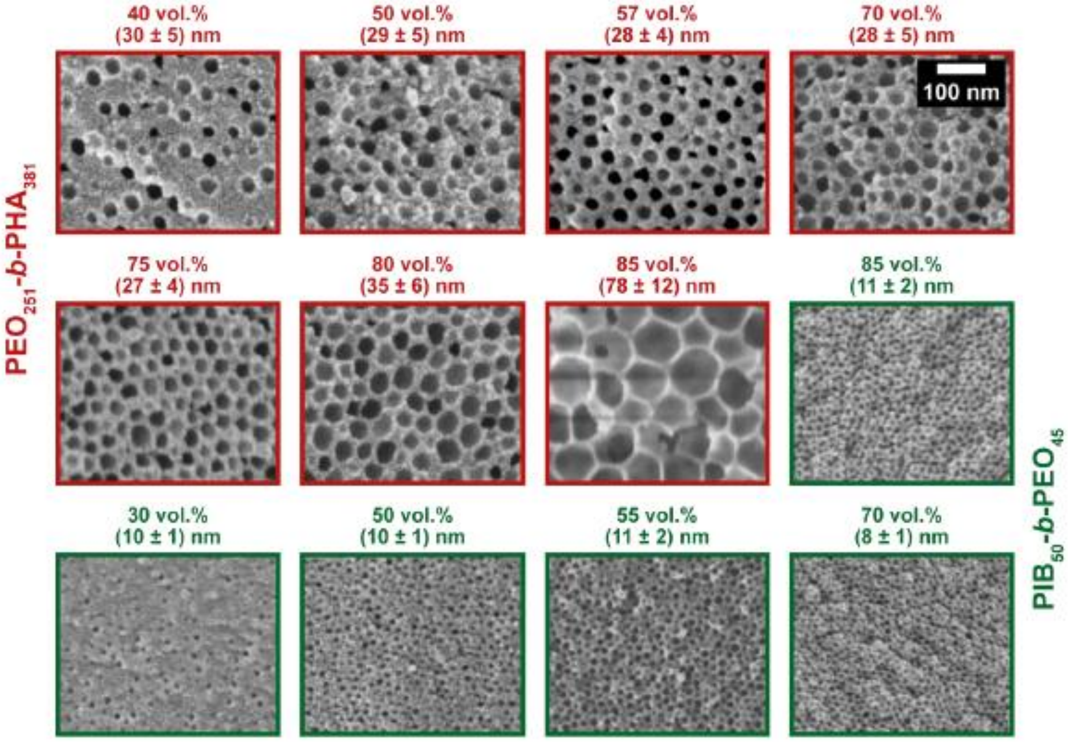

Figure S17. SEM images of mesoporous silica prepared with different amounts of PEO_{251}-*b*-PHA_{381} (red) and PIB_{50}-*b*-PEO_{45} (green), respectively. The respective polymer amount and resulting pore size is displayed above each image.

Since the volume of a material can be determined by dividing its mass by its density, the template concentration sometimes given in literature as the mass ratio (M:T) of the oxide assuming full conversion of the precursor to the mass of the soft template used can be converted to the polymer volume fraction Φ by equation **(S1)** if the density of the oxide ρ_{oxide} and soft template ρ_{BCP} are known:

$$\Phi = \frac{1}{1 + (\text{M:T})\,\dfrac{\rho_{\text{BCP}}}{\rho_{\text{oxide}}}} \qquad \textbf{(S1)}$$

REFERENCES

(1) Stefik, M. Single-Variable Porous Nanomaterial Series from Polymer Structure-Directing Agents. *J. Mater. Res.* **2022**, *37*, 25–42.

(2) Lokupitiya, H. N.; Jones, A.; Reid, B.; Guldin, S.; Stefik, M. Ordered Mesoporous to Macroporous Oxides with Tunable Isomorphic Architectures: Solution Criteria for Persistent Micelle Templates. *Chem. Mater.* **2016**, *28*, 1653–1667.

(3) Peters, K.; Lokupitiya, H. N.; Sarauli, D.; Labs, M.; Pribil, M.; Rathouský, J.; Kuhn, A.; Leister, D.; Stefik, M.; Fattakhova-Rohlfing, D. Nanostructured Antimony-Doped Tin Oxide Layers with Tunable Pore Architectures as Versatile Transparent Current Collectors for Biophotovoltaics. *Adv. Funct. Mater.* **2016**, *26*, 6682–6692.

(4) Sarkar, A.; Stefik, M. How to Make Persistent Micelle Templates in 24 Hours and Know It Using X-Ray Scattering. *J. Mater. Chem. A* **2017**, *5*, 11840–11853.

(5) Lokupitiya, H. N.; Stefik, M. Cavitation-Enabled Rapid and Tunable Evolution of High- χN Micelles as Templates for Ordered Mesoporous Oxides. *Nanoscale* **2017**, *9*, 1393–1397.

(6) Sarkar, A.; Evans, L.; Stefik, M. Expanded Kinetic Control for Persistent Micelle Templates with Solvent Selection. *Langmuir* **2018**, *34*, 5738–5749.

(7) Lantz, K. A.; Clamp, N. B.; van den Bergh, W.; Sarkar, A.; Stefik, M. Full Gamut Wall Tunability from Persistent Micelle Templates via Ex Situ Hydrolysis. *Small* **2019**, *15*, 1–10.

(8) Sarkar, A.; Thyagarajan, A.; Cole, A.; Stefik, M. Widely Tunable Persistent Micelle Templates via Homopolymer Swelling. *Soft Matter* **2019**, *15*, 5193–5203.

(9) Bergh, W.; Lokupitiya, H. N.; Vest, N. A.; Reid, B.; Guldin, S.; Stefik, M. Nanostructure Dependence of T-Nb_2O_5 Intercalation Pseudocapacitance Probed Using Tunable Isomorphic Architectures. *Adv. Funct. Mater.* **2021**, *31*, 2007826.

(10) Williams, E. R.; McMahon, P. L.; Reynolds, J. E.; Snider, J. L.; Stavila, V.; Allendorf, M. D.; Stefik, M. Tailored Porous Carbons Enabled by Persistent Micelles with Glassy Cores. *Mater. Adv.* **2021**, *2*, 5381–5395.

3.3 Publikation 3

On the Interpretation of Physisorption Isotherms: Connectivity *versus* Accessibility of Mesopore Networks

to be submitted

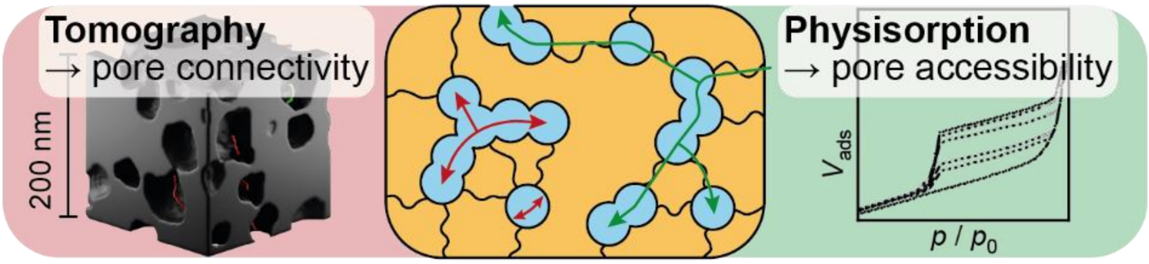

L. Q. Wagner, L. Brauch, C. Kübel, X. Cheng, K. Schladitz, B. M. Smarsly, On the Interpretation of Physisorption Isotherms: Connectivity *versus* Accessibility of Mesopore Networks, *to be submitted*.

On the Interpretation of Physisorption Isotherms: Connectivity *versus* Accessibility of Mesopore Networks

Lysander Q. Wagner[a,b], *Lucas Brauch*[c,d,e], *Christian Kübel*[c,d,e], *Xiaoyin Cheng*[f], *Katja Schladitz*[f], *and Bernd M. Smarsly*[a,b]*

Mesoporous materials feature a high pore volume and large surface area. However, the pore connectivity governs to which extent this pore volume can be used in application, *e.g.*, as hetereogeneous catalyst. Observing a network effect in physisorption isotherms, we usually have a picture of poorly connected mesopores in mind. In this study, we contrast gas physisorption and electron tomography for studying the pore connectivity of powders with spherical mesopores and see that this simple picture does not hold true. We investigated three mesoporous powders (hard carbon, SiO_2, and ZrO_2) soft-templated with the same poly(ethylene oxide)-*block*-poly(hexyl acrylate) copolymer. While physisorption reveals a significantly better pore connectivity in the ZrO_2 sample compared to the carbon powder, the 3D reconstruction from STEM-based tomography shows the opposite result. By evaluating the pore system in depth with electron microscopy, small-angle X-ray scattering, physisorption, and tomography, we demonstrate that this contradiction is only an apparent one since physisorption provides information on the global pore network accessibility whereas electron tomography gives insights into the local pore connectivity. This didactic case study shows that using physisorption isotherms alone can be misleading, and both physisorption and electron tomography are required to obtain a full picture of the pore system.

Introduction

Mesoporous materials promise great potential in several fields of material science such as catalysis,[1–10] sensing,[11,12] and energy storage[13–15] due to the large surface area and pore volume they possess. Some possible devices, however, can only benefit from the latter if the pore network is readily accessible. For instance, a mesoporous catalyst will never outperform an unstructured analogue if the reactants cannot access the interior of the pore space;[16–19] the same holds true for, *e.g.*, the electrochemical accessibility of mesoporous

---

a) Institute of Physical Chemistry, Justus Liebig University, Heinrich-Buff-Ring 17, D-35392 Giessen, Germany
b) Center of Materials Research, Justus Liebig University, Heinrich-Buff-Ring 16, D-35392 Giessen, Germany
c) Institute of Nanotechnology, Karlsruhe Institute of Technology, Hermann-von-Helmholtz-Platz 1, D-76344 Eggenstein-Leopoldshafen, Germany
d) Department of Materials and Earth Science, Technical University Darmstadt, Peter-Grünberg-Straße 2, D-64287 Darmstadt, Germany
e) Karlsruhe Nano Micro Facility, Karlsruhe Institute of Technology, Hermann-von-Helmholtz-Platz 1, D-76344 Eggenstein-Leopoldshafen, German
f) Fraunhofer Institute for Industrial Mathematics, Fraunhofer-Platz 1, D-67663 Kaiserslautern, Germany

model electrodes in dye-sensitized solar cells.[20] In contrast, sodium-ion batteries represent an example, in which an inaccessible mesopore space of the anode material seems to be superior over an accessible one.[14] Thus, the accessibility of a single mesopore, and the entire pore system in general, is of utmost importance with respect to the performance of an applied mesoporous material. Therefore, it is crucial to be capable of accurately and reliably studying the pore accessibility of and pore connectivity within a mesoporous system.

At this stage, it is important to point out that the term "pore connectivity" is used for mesoporous materials since *circa* 30 years,[21,22] however, a clear definition of this parameter (*e.g.*, by the IUPAC) is missing so far. The parameter is partly referred to the number of pores connected to a given pore and sometimes assigned to the size of the connecting pores. Due to this ambiguity, we initially use the term "pore connectivity" in quotation marks.

While mesoporous materials are routinely investigated in terms of pore size by electron microscopy, gas adsorption, small-angle X-ray scattering (SAXS), and mercury porosimetry, "pore connectivity" studies require elaborated characterization techniques.[23] Here, the isotherm obtained from gas physisorption experiments provides some hints on the pore network. In case of an open mesoporous network, spontaneous pore filling in the adsorption branch is delayed due to a nucleation barrier if the mesopores exceed a width of about 4 nm. Since emptying of the pore in the desorption branch occurs in equilibrium over a descending meniscus, a type IV isotherm with an H1-type hysteresis loop according to the IUPAC classification is obtained.[24–27] If the evaporation of the fluid inside a mesopore is restricted by a narrow pore neck, *i.e.*, if a network effect is present, the pore emptying in the desorption branch will be shifted to smaller relative pressures causing a broadening of the hysteresis loop. Here, emptying of pore neck and underlying cavity can take place together at the pressure associated with the pressure needed to empty the neck (pore blocking), or both entities are emptied *via* a spontaneous nucleation and growth of gas bubbles in the fluid because the latter reaches its limit of stability (cavitation). The second case of cavitation-induced evaporation happens if the pore neck underscores a critical width (4 – 5 nm in case of nitrogen at 77 K), whose emptying in equilibrium would require a pressure below the stability limit of the fluid. For both evaporation mechanisms, the delayed evaporation yields an H2(a)-type hysteresis loop.[23,26,28] The two cases can be discriminated experimentally by two approaches: (1) a comparison of desorption-branch-based pore size distributions measured with different adsorptives[29] and (2) evaluation of the shape of desorption scans recorded by a hysteresis scanning.[30,31] Answering the question if pore blocking or cavitation is predominant sounds very academic at first glance but is of big importance since in case of pore blocking, a pore neck size distribution of restricting pore necks can be obtained while in case of cavitation, only the statement that the necks are below the critical size can be concluded.

Besides the size of restricting pore necks, possible pore size gradients and the connection between adjacent pores can be evaluated when a physisorption measurement is coupled with an *in-situ* SAXS measurement.[31] Even deeper insight into the average connectivity (such as the number of neighboring pores and the disorder of the pore network) of a pore system can be gained with a recently reported percolation model, which fits experimental hysteresis scanning curves based on several network parameters.[32] Moreover, novel evaluation methods like the percolation-effect-integrated differential hysteresis scanning allow quantification of "pore connectivity" (like neck size distributions and the degree of constriction) in hierarchically porous systems.[33] With this approach, pore neck sizes can be contrasted to the size of the corresponding underlying cavity.

A further characterization method for elucidating the "pore connectivity" represents electron tomography, which delivers a three-dimensional (3D) view on the pore system at the nanoscale without any assumptions about the pore geometry.[34–36] In contrast to gas physisorption, tomography is not restricted to accessible pores and resolves even isolated ones. In particular, if the set of angle-dependent images acquired with scanning transmission electron microscopy (STEM) is processed with a dedicated algorithm like the discrete algebraic reconstruction technique (DART), a 3D model of high precision at the nanoscale is obtained, which can resolve the local connection of mesopores.[37,38] Albeit being a local analysis, a reliable textural analysis of the pore system is possible by statistically evaluating the pore size (following a local thickness approach) and connectivity (following a skeletonization approach). As a result, a pore size distribution of the (connecting) pore necks as well as a distribution of the number of connected, adjacent pores (coordination number of a pore) can be derived.[38–40]

Regarding the pore size distribution, gas physisorption and STEM-based tomography showed a good agreement,[39,41] however, in terms of "pore connectivity", our previous studies on soft-templated mesoporous silica revealed an inconsistency: While STEM-based tomography clearly confirms an improved "pore connectivity" if more soft template is used during the synthesis, *i.e.*, more mesopores are incorporated into the metal oxide,[42] the physisorption isotherms still possess the same pronounced cavitation in all samples implying a poor pore accessibility.[41] The question arises how these results can be brought together. Therefore, we devote in this study attention to a comparison between physisorption and tomography for "pore connectivity" analysis at a systematic level to answer the questions which information both techniques actually provide, which limitations they have, and how they can be combined. By employing three different mesoporous model materials – mesoporous carbon and SiO_2, which are expected to be poorly accessible,[41,43] and mesoporous ZrO_2, which is expected to be better accessible[41] – we first provide a guideline how to reliably and quickly determine the pore size of different materials with large spherical mesopores by physisorption and back up the results by electron microscopy, SAXS, and tomography. Then, the pore connectivity and accessibility are contrasted by detailed physisorption and tomographical experiments to reveal possible deviations and derive a clear model of the pore model consisting of percolation paths (being composed of well-connected pores in case of the samples here), which exhibits different extents of accessibility as visualized with the aid of tomography. This work not only helps to understand the underlying pore model of soft-templated mesoporous materials but, even more important, demonstrates that both physisorption and tomography are required to obtain a full picture of the pore model, as one method alone might be misleading, and extends the analysis of pore systems.

Results and Discussion

Characterization of the Mesopore System

A systematic study on "pore connectivity" in mesoporous materials requires a sample set of comparable pore geometry but of different "pore connectivity". Since our previous study suggested a rather open pore structure in case of crystalline metal oxides (namely, zirconium dioxide) compared to rather isolated silica,[41] we choose mesoporous SiO_2 and ZrO_2 powders as model materials. In addition, we expand the study with a further material class, mesoporous carbon, whose "pore

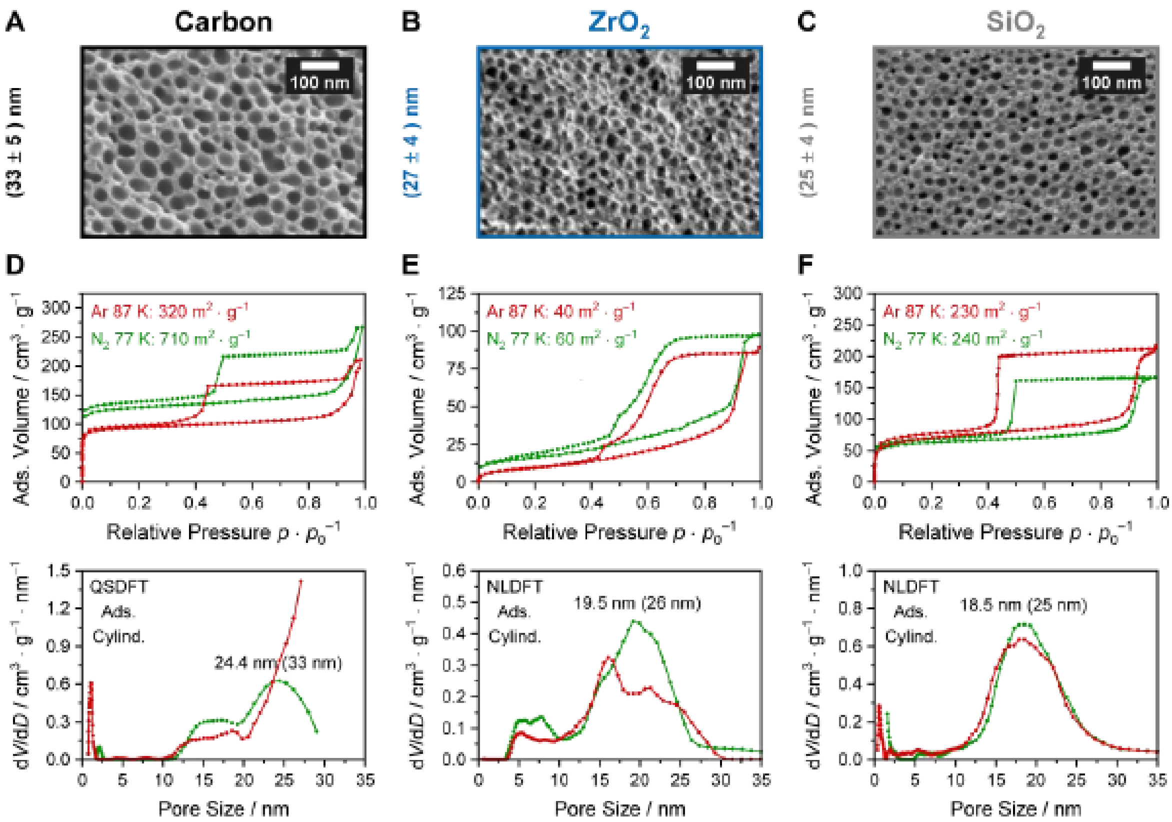

Figure 1. (A – C) SEM images, (D – F) nitrogen (77 K, green) and argon (87 K, red) isotherms of mesoporous carbon (left), ZrO_2 (middle), and SiO_2 (right), and respective pore size distributions obtained from the corresponding adsorption branch with a DFT kernel for carbon and silica, respectively, assuming a cylindrical pore geometry. The average mesopore size by SEM is given next to the respective image while the mode pore size according to physisorption is displayed in the pore size distribution for a cylindrical pore geometry and for a spherical pore geometry in brackets (resulting from multiplication with a geometrical correction factor of 1.35).

connectivity” can be tailored towards both isolated[14] and accessible[43] mesopores.

The mesoporous materials were prepared with a soft templating procedure using a poly(ethylene oxide)-*block*-poly(hexyl acrylate) block copolymer (PEO-*b*-PHA) prepared in our last study.[42] With this PEO_{441}-*b*-PHA_{270} (subscripts denote the number of repeating units) soft template sample, we obtained mesoporous silica with spherical mesopores of 25 nm in diameter. The soft templating process bases on the evaporation-induced self-assembly (EISA) mechanism,[44–46] in which micellization of the amphiphilic block copolymer occurs upon solvent evaporation. So, the hydrophobic PHA block in the micelle core is separated from the hydrophilic precursor/solvent phase by the hydrophilic PEO block in the micelle corona.[47] These micelles arrange themselves in an ordered, close-packed array upon further solvent evaporation leading to an ordered pattern of mesopores after thermal removal of the polymer micelles. The solid skeleton material is formed within a sol-gel reaction in case of the metal oxides, and within a thermopolymerization and carbonization[48–50] of the resol resin in inert atmosphere in case of the non-graphitic carbon. Scanning electron microscopy (SEM) confirms an ordered pore structure with spherical mesopores in all three samples. By averaging over 50 pores in the respective SEM image in **Figure 1**, a comparable mesopore size of 33 nm (carbon), 27 nm (ZrO_2), and 25 nm (SiO_2) is obtained in accordance with our previous work.[42] The slightly larger pore size in case of carbon may be due to the different pore formation mechanism and skeleton materials (sol-gel reaction under ambient conditions *vs.* carbonization under inert conditions) possessing different extents of pore shrinkage (difference between template size and resulting pore size) during calcination/carbonization. Also, a difference in soft template concentration can explain this deviation as the mesopore size increases with the template concentration.[42] Due to the different density of the skeleton materials and different conversions of the precursors, a perfect alignment of the pore volume cannot be guaranteed.

Physisorption experiments confirm the findings obtained by SEM as all argon (87 K) and nitrogen (77 K) isotherms possess a type IV shape of mesoporous materials according to the IUPAC definition.[26] Regarding the H2-type hysteresis loops, a pronounced network effect is striking,[25,26] which will be discussed in more detail below along the "pore connectivity". In general, physisorption experiments with argon are more accurate than with nitrogen[23,26] but both adsorptives were employed here due to the insufficient fitting of the argon quenched solid density functional theory (QSDFT)[51,52] kernel for carbon materials beyond relative pressures of 0.93 here (see the comparison between measured and fitted isotherm in **Figure S2**). Since the majority of data points of the adsorption branch, which contribute to the mesopore filling ($p/p_0 > 0.9$), are not captured by the evaluation model, the pore size distribution from the argon isotherm in **Figure 1D** is not suitable for determining the mesopore size of such large mesopores here. The remaining pore size distributions, however, provide meaningful results. Because of the network effect causing a delayed evaporation, the adsorption branch was used for evaluation, and corresponding QSDFT (in case of carbon) and non-local density functional theory (NLDFT, in case of the metal oxides) kernels assuming a cylindrical pore geometry were applied on the adsorption branches of the argon and nitrogen isotherms, respectively. The resulting pore size distributions from nitrogen (carbon, ZrO_2, and SiO_2) and argon (ZrO_2 and SiO_2) physisorption yield a mode mesopore size, which, however, needs to be corrected since the mesopores possess a spherical pore shape instead of a cylindrical geometry. In case of nitrogen adsorption on mesoporous silica, a shift by 35% towards larger pore sized were found when changing the assumed pore geometry from cylinders to spheres.[53] This correction factor of 1.35 proved to be suitable in our previous studies[42,43] and shifts the pore size of the SiO_2 sample in **Figure 1** from 19 nm to 25 nm, which is in perfect agreement with the SEM-derived value. Although this correction factor is formally only valid for silica, the mode pore sizes of carbon (33 nm) and ZrO_2 (26 nm) after geometrical correction (with a factor of 1.35) match surprisingly well with the results by SEM. Consequently, the factor of 1.35 seems to be applicable for these two materials as well.

Direct application of an evaluation model assuming spherical pores is less straightforward here. The Quantachrome software ASiQwin features spherical/ cylindrical hybrid kernels for carbon and silica for argon and nitrogen isotherms, respectively, but they either are programmed for a smaller pore size range than the cylindrical equivalents (0.35 – 40 nm instead of 0.35 nm – 100 nm) and encounter difficulties in case of such large pores (in case of silica) or show a poor fitting of the data in the pore filling regime as shown in **Figure S2** (in case of carbon). As shown in the pore size distributions in **Figure S1**, the cylindrical/spherical kernel (assuming small cylindrical and large spherical mesopores) for carbon (both argon and nitrogen) and silica (only nitrogen) are indeed shifted to a larger pore size of about 45 nm and 33 nm, respectively, compared to the distributions obtained for cylindrical pores but do not fit the adsorption branch beyond $p/p_0 = 0.9$ (see **Figure S2**). Thus, six to nine crucial data points of the hysteresis loop are not included in the evaluation process resulting in an inaccurate pore size distribution similar to that of carbon in **Figure 1D** (argon, cylindrical geometry). In case of the NLDFT method for silica with argon at 87 K assuming a hybrid geometry, a proper fitting is achieved. However, this evaluation method describes spherical/cylindrical pores, *i.e.*, assumes the opposed case of small spherical pores (< 2 nm), which connect large cylindrical mesopores (> 2 nm). As a result, the same pore size distribution is obtained as by assuming cylindrical pores only except a small shift of the micropores by 0.3 nm in case of the SiO_2 sample. A detailed overview over the DFT kernels used and their definition and pore size regimes can be found in **Table S1** in the Supporting Information. As a result, for such large spherical mesopores, the evaluation of physisorption isotherms by assuming a cylindrical pore geometry and post-correction apparently offers the highest level of accuracy.

An accurate confirmation of a spherical pore shape requires a method providing a three-dimensional view on the pore system. In this regard, STEM-based tomography is a versatile tool to visualize the sample in 3D on a nanoscale. As shown in **Figure 2**, a tilt series of angle-dependent STEM images is acquired and computed to a 3D model *via* an iterative reconstruction technique. From this model, several structural features can be statistically evaluated: from the local thickness (the diameter of a sphere at a given pixel just fitting into one phase without penetrating the second phase), both the pore size and wall thickness can be resolved locally, and the number of mesopores being connected to a given mesopore (coordination number) can be determined, as well as the size of the pore neck between two connected pores. The cutouts of the reconstructed mesoporous systems in **Figure 2** clearly demonstrate a spherical pore geometry in all three samples. In addition, a difference in the extent of "pore connectivity" can be envisioned qualitatively from the

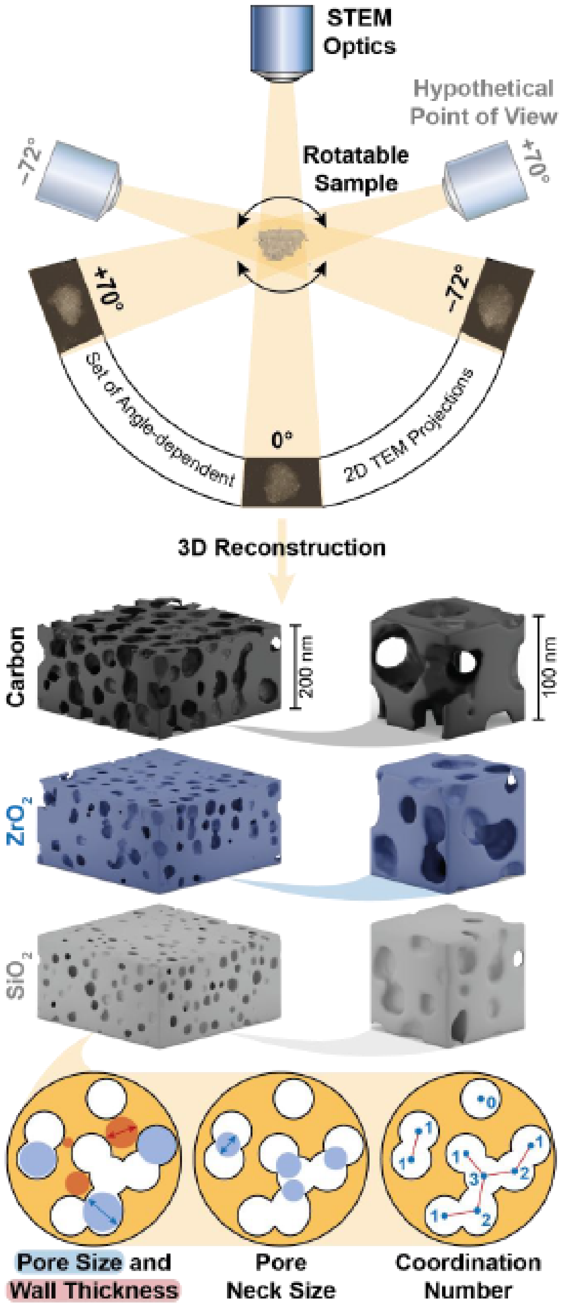

Figure 2. Principal of STEM-based tomography delivering a 3D model of the mesopore system after reconstructing angle-dependent STEM images. Cutouts of the 3D models of mesoporous carbon (black), ZrO_2 (blue), and SiO_2 (gray) are visualized as well as possible structural features that can be derived from them.

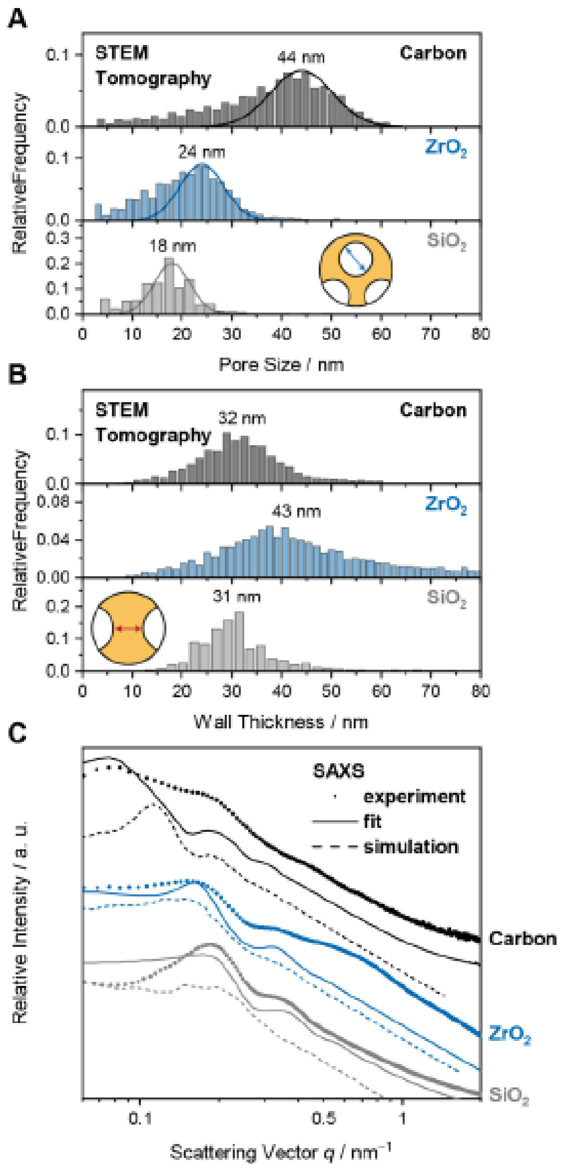

Figure 3. (A) Pore size and (B) wall thickness distribution from a local thickness evaluation of the STEM-based tomography data for carbon (black), ZrO_2 (blue), and SiO_2 (gray) together with the respective average value. The (C) SAXS data of mesoporous carbon (black), ZrO_2 (blue), and SiO_2 (gray) are given together with a fitted scattering curve (solid line) according to a Percus-Yevick model for spherical pores and a simulated curve (dashed line) derived from the STEM-based reconstruction.

models, which will be described in-depth below.

The STEM-based reconstruction bases on a single particle and thus could be affected by local inhomogenities. In order to back up that the considered particle is representative for the entire sample, a comparison of the tomography data with a further global method, such as small-angle X-ray scattering (SAXS), is reasonable. Therefore, a SAXS curve is simulated from the STEM-based reconstructions (representing a 3D distribution of electron density) following a Python script previously reported by our group[40] and contrasted to experimental SAXS data of the samples (**Figure 3C**). The scattering data exhibit two important features as frequently observed in our former studies:[42,43] a maximum at low *q* values connected to the lattice factor (and thus pore-to-pore distance) followed by a form factor minimum connected to the pore size. As a consequence of the smaller particle size in case of the metal oxides used for tomography, the simulated scattering curve is less accurate than for the carbon sample. Still, all three simulated data are in good agreement with the experimental ones in terms of the aforementioned features. The only exception represents the lattice factor maximum of the simulated curve for mesoporous carbon being shifted to larger *q* values compared to the experimental curve. This implies that the pores are a bit closer to each other in the STEM-based model than in the overall sample. The misfit hints at a certain level of inhomogeneity in the sample, which does not mean that the material is principally bad but such deviations need to be kept in mind. Otherwise, the good agreement underlines the suitability of the particles selected for reconstruction.

Structural parameters like the pore size can be derived from the SAXS curve by fitting the experimental data with a theoretical function based on a Percus-Yevick structure factor.[41,54–57] Due to the low number of form factor oscillations in the experimental SAXS data, the pore size determination becomes less accurate. Yet, the obtained mesopore sizes of 57 nm (carbon), 32 nm (ZrO_2), and 31 nm (SiO_2) follow the same trend that was observed by SEM and physisorption before, *i.e.*, slightly larger mesopores in ZrO_2 compared to SiO_2 and the largest pore size in case of carbon. The absolute values are reasonable considering the large polydispersity, and since we observed a slight overestimation of the mesopore size obtained from SAXS data with this Percus-Yevick approach already in previous samples of similar pore structure.[42] Another striking feature in case of the ZrO_2 sample comprises the deviation of both the simulated and theoretical curve from the experimental data in the *q* range between 0.5 and 1 nm^{-1} in **Figure 3C**. From the position, a structure (pore or particle) between 6 nm and 13 nm in size is expected to scatter in this *q* range, which matches with the small fraction of small mesopores (5 – 10 nm in diameter) in the pore size distribution from physisorption in **Figure 1E**. As no micropores are contained in this sample in contrast to the other two mesoporous samples (carbon and SiO_2) according to physisorption, a micropore widening upon crystallization can be expected, as suggested in a former study,[41] which yields small mesopore channels contributing to the scattering curve.

Evaluating the pore size with the aid of the STEM-based reconstructions (containing about 1000 mesopores each) supports the previous findings and confirm the absolute values found by SEM and physisorption, especially in case of the metal oxides. Following the local thickness approach described above delivers a mesopore size of 44 nm (carbon), 24 nm (ZrO_2), and 18 nm (SiO_2). **Table 1** summarizes the results of all characterization methods so far. Still, it is important to mention that the determination of a well-defined average value for the size of the spherical mesopores by tomography is hampered by (1) the small connecting pore throats possessing a small local thickness and (2) the mesopores laying at the particle surface, which are assigned only to the small pore size that is contained in the particle space by the local thickness algorithm. Both contributions lead to the asymmetric shape of the pore size distribution in **Figure 3A**. Since the local thickness evaluation can be conducted on the pore wall phase as well, the (local) wall thickness can be statistically evaluated. As depicted in **Figure 3B**, all mesoporous samples feature a similar pore wall thickness of about 30 – 40 nm. This is an important aspect because a clear comparison of the “pore connectivity” would not be possible otherwise. As shown in our last study, the “pore connectivity” increases upon bringing the pores into closer contact (decreasing the pore wall thickness by applying higher amounts of soft template).[42] That means the comparable wall thickness here gives access to draw conclusions on the influence of the material itself (amorphous or crystalline metal oxide *vs.* non-graphitic carbon) on the “pore connectivity”, which will be investigated in more detail in the next section.

Table 1. Overview on the average mesopore size (in nm) of mesoporous carbon, ZrO_2, and SiO_2 determined with different characterization methods.

Pore size (in nm) obtained from	Carbon	ZrO_2	SiO_2
SEM	33 ± 5	27 ± 4	25 ± 4
Physisorption	33 ± 4	26 ± 7	25 ± 5
SAXS	57 ± 17	32 ± 12	31 ± 14
Tomography	44 ± 8	24 ± 5	18 ± 4

Network Analysis by Physisorption and Tomography

Both physisorption and tomography do not only provide information on pore size and shape but give also valuable insights into the “pore connectivity”. With the aid of physisorption, an open (readily accessible)

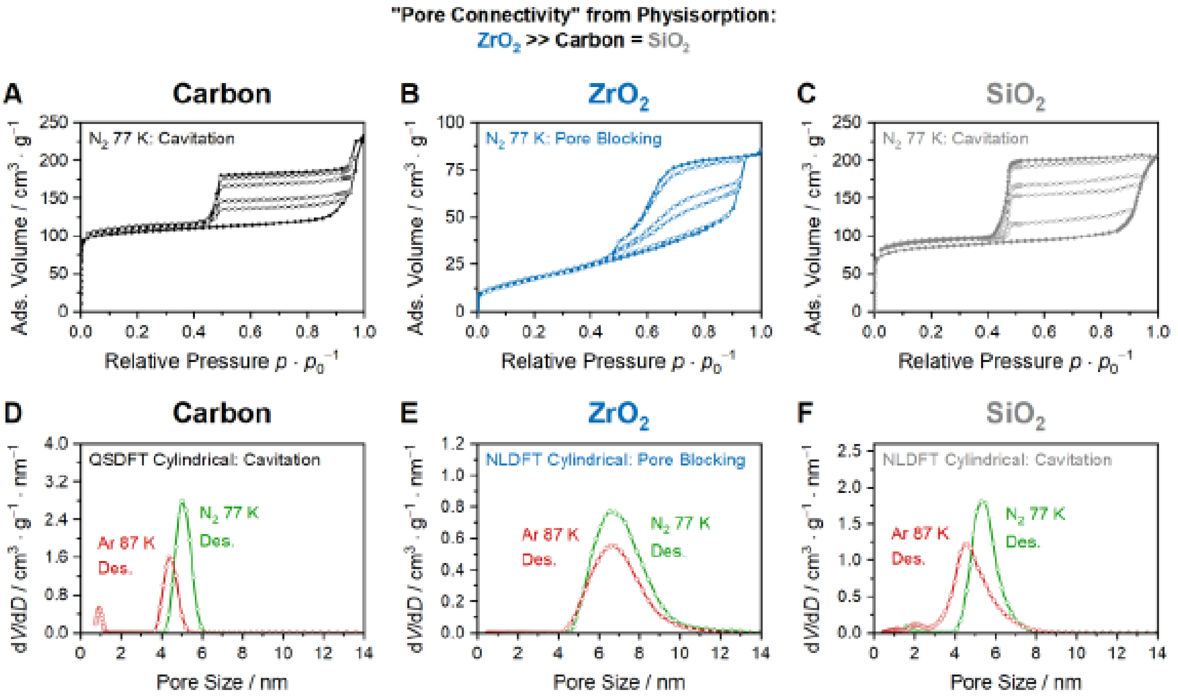

Figure 4. Nitrogen hysteresis scans at 77 K (after thermal compensation, see Supporting Information) of (A) mesoporous carbon (black), (B) ZrO_2 (blue), and (C) SiO_2 (gray) composed of a boundary loop (filled symbols) and four desorption scans (open symbols) each. Partial adsorption branches are omitted for clarity. On the bottom, the pore size distributions obtained from the desorption branch of the argon (red) and nitrogen (green) isotherm with a DFT kernel for cylindrical pores are contrasted to each other for mesoporous (D) carbon, (E) ZrO_2, and (F) SiO_2.

pore network can be distinguished from a restricted pore system, whose pore necks are so small that evaporation of the adsorptive out of the mesopore is delayed (network effect).[28] In the latter case, two possibilities are discriminated: emptying of the underlying pore occurs at the relative pressure, at which the smaller neck is emptied (pore blocking), and in case of sufficiently small necks (5 – 7 nm for N_2 at 77 K), emptying of the pore requires such a small pressure due to the small pore neck that the condensed adsorptive undershoots a critical relative pressure and becomes metastable leading to sudden emptying of the entire pore (cavitation).[23,26,28] Performing a hysteresis scanning experiment, *i.e.*, recording partial isotherms after subsequently less pore filling, represents a qualitative method to elucidate the "pore connectivity".[30,31] While all partial desorption scans converge in the lower closure point of the hysteresis loop in case of pore blocking, the shape of a straight line until the relative cavitation pressure, at which sudden evaporation occurs, is preserved for all scanning curves in case of cavitation. As shown in **Figure 4A** and **C**, the mesoporous carbon and mesoporous silica sample yield the typical shape of desorption scanning curves governed by cavitation. Hence, the large spherical mesopores in these materials are connected by very small pore necks below 5 – 7 nm. Taking the pore size distributions in **Figure 1** into account, the connecting pores are then most likely the 1 nm micropores. In case of zirconia, however, a different behavior is observed: all scanning curves in **Figure 4B** converge in the lower closure point suggesting a pore blocking. Consequently, larger pore necks such as the 5 – 10 nm mesopores in the pore size distribution (**Figure 1E**) cause the delayed evaporation in this sample. The larger pore necks in case of ZrO_2 imply that the pore system is better accessible than that of mesoporous carbon and SiO_2. Still, it should be mentioned that the small step in the ZrO_2 isotherm at $p/p_0 = 0.5$ in the desorption branch resemble a H5 hysteresis loop with a small fraction of cavitation thus hinting at a small residual amount of blocked pores, which are emptied by cavitation.[25,26] Nevertheless, the majority of the large mesopores is governed by pore blocking.

The suggested network effects are supported by the pore size distribution comparison in **Figure S4**. In general, the delayed evaporation due to the small pore necks in both pore blocking and cavitation leads to a shift of the pore size distribution derived from the desorption branch towards smaller pore sizes. The resulting mismatch between the pore size distributions derived from the adsorption and desorption branch is indicative of the presence of a network effect and is clearly visible in all three samples here (upper half of **Figure S4**). Comparing the desorption-derived distributions obtained from physisorption measurements with different adsorptives enables a discrimination between the two network effects (lower half of **Figure S4** and **Figure 4**).[29] While desorption occurs at the relative pressure corresponding to the emptying of the restricting pore neck in case of pore blocking, the position of the desorption-based pore size distribution is only governed by the pore neck size but is independent of the adsorptive. In case of cavitation, the sudden pore emptying is thermodynamically controlled by the metastability of the adsorptive and thus depends on the adsorptive. Therefore, the mismatch between the distributions obtained from nitrogen and argon measurements in case of mesoporous carbon and SiO_2, respectively, confirm the cavitation-driven desorption. In case of ZrO_2, both distributions coincide and confirm a pore blocking mechanism here. As a result, the desorption-based pore size distributions in **Figure 4E** describe a pore neck size distribution confirming the pore necks with a mode diameter of 7 nm to cause the restricted evaporation as suggested above.

The direct visualization of the pore system in 3D by STEM-tomography provides access to statistically evaluate both the size (pore neck size) and the number (coordination number, CN) of pore connections regardless of whether they are restricting or not. This is an important difference to physisorption, with which no information on connectivity of freely accessible mesopores can be concluded.[23] With tomography, the only limit is set by the pixel (/voxel) size of about 2 nm here, which renders the resolution of micropores impossible. Thus, the coordination number only considers connecting pores of mesopore dimensions. The distribution of the coordination number in **Figure 5A** reveal a rather poorly connected mesopore system in case of the metal oxides. While the SiO_2 sample is composed of 35% isolated mesopores (CN = 0) and 65% of mesopores connected to a pair (CN = 1), the ZrO_2 sample shows only a slightly higher level of connectivity with 14% of mesopores with a CN > 1. In both cases, an average CN below one demonstrates that a large network of interconnected mesopores cannot be built up. However, the mesoporous carbon sample reveals a surprisingly well-connected pore system. With only 10% of isolated mesopores and an average CN above two, a numerically well-connected network can be found as already expected from the 3D model in **Figure 2**. Taking the local thickness into consideration, the size of the pore neck connecting two adjacent mesopores can be determined each. Looking at their size distribution in **Figure 5B**, both metal oxides comprise similarly small pore necks of about 15 nm in diameter. This pore neck size is still larger than that observed by physisorption but since only the small pore necks causing networks effects are seen there, and tomography cannot resolve the small micropores, these larger values in **Figure 5B**

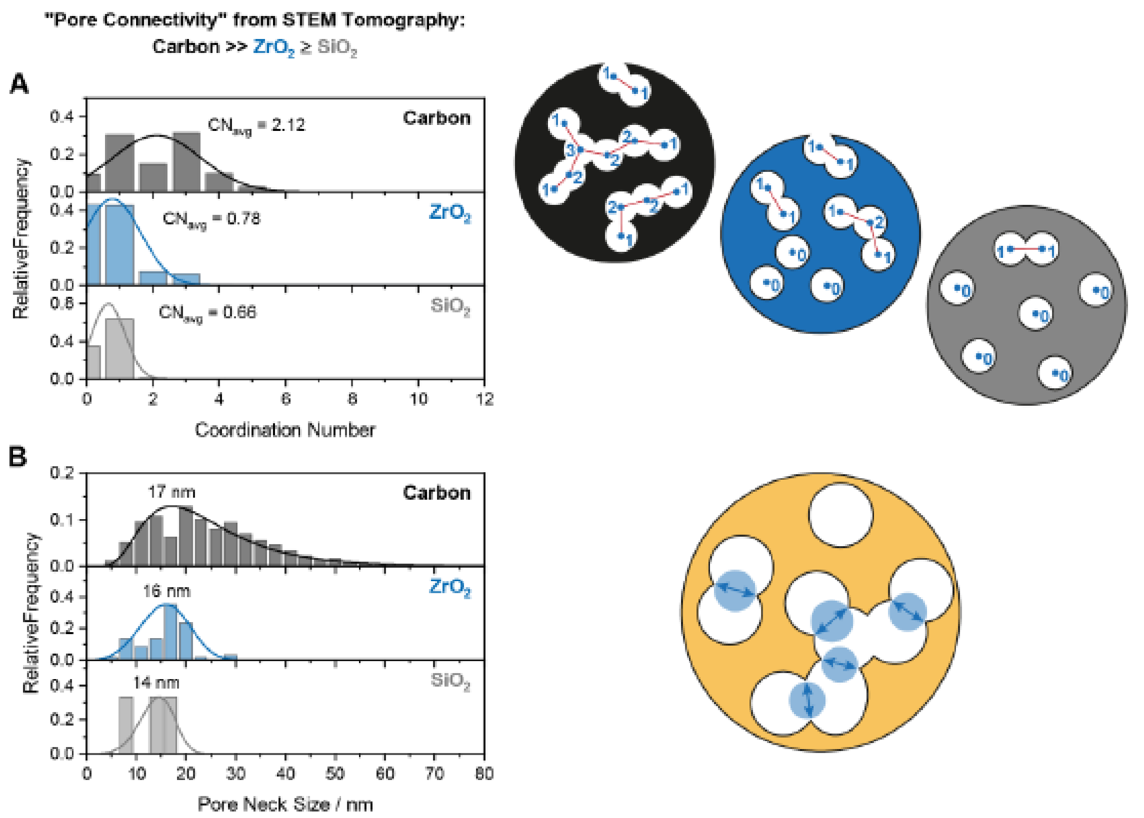

Figure 5. Distribution of the (A) pore coordination number (number of mesopores connected to a given mesopore) and (B) the size of the pore necks of carbon (black), ZrO_2 (blue), and SiO_2 (gray) derived from the STEM-based tomography data. Each average value is given above the respective distribution.

are reasonable. The mesoporous carbon sample, however, possesses not only significantly more connected pores but also their size is larger than in case of the metal oxides. Thus, from STEM-based tomography, a well-connected pore network can be concluded in case of carbon while the metal oxides feature rather isolated mesopores.

We observed a similar misfit between physisorption- and tomography-based "pore connectivity" in mesoporous silica, in which an increase in soft template amount increased the porosity without altering the pronounced cavitation phenomenon (also observed here for silica and carbon).[41] Meanwhile, the "pore connectivity" in terms of coordination number and pore neck size was significantly increased upon using more soft template resulting in complete removal of isolated mesopores (CN = 0).[42]

This evaluation of the "pore connectivity" evokes the question why the carbon sample comprises a poorly-connected mesopore system according to physisorption while tomography suggests an open, well-connected pore network and *vice versa* in case of the ZrO_2 sample. Can this contradiction be resolved or is one method wrong?

Are Physisorption and Tomography Contradictory?

To understand the outcome of this connectivity study, it is important to reconsider the information both characterization methods can provide. On the one hand, physisorption describes the connectivity between a pore inside a solid sample and the exterior (gas phase outside the particle). Thus, the overall accessibility of a pore (network) (which can be a micro- or

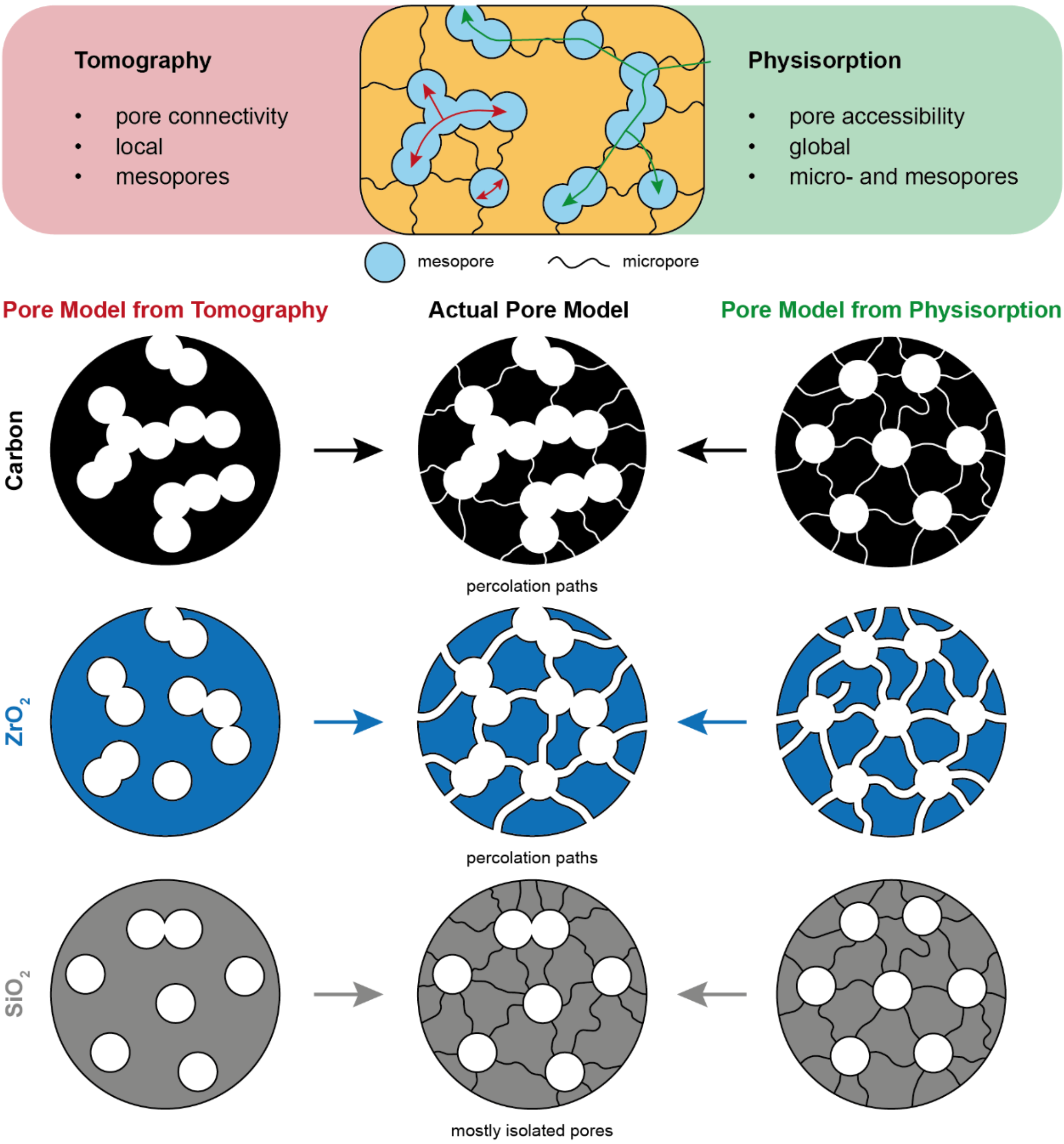

Figure 6. Comparison between information on pore network obtained from electron tomography and gas physisorption (top) and schematic representation of each sample's pore model derived from tomography and physisorption, respectively, and considering both methods (bottom).

mesopore) is regarded (green arrow in **Figure 6**). On the other hand, STEM-based tomography reveals the local connection between mesopores (including also isolated pores) by providing a 3D model on a nanoscale level (red arrow in **Figure 6**). However, due to the limited pixel (/voxel) size, micropores are not resolved. That means, the STEM-based reconstruction shows the local mesopore connectivity instead of the global pore accessibility from physisorption as contrasted in **Figure 6**.

Keeping this in mind, the contradiction between the results from physisorption and tomography is only an apparent one. Indeed, in case of an ideally homogeneous pore system with perfectly distributed mesopores as shown in the top part in **Figure 7**, both methods are expected to end up with the same result of an either open or isolated pore system. However,

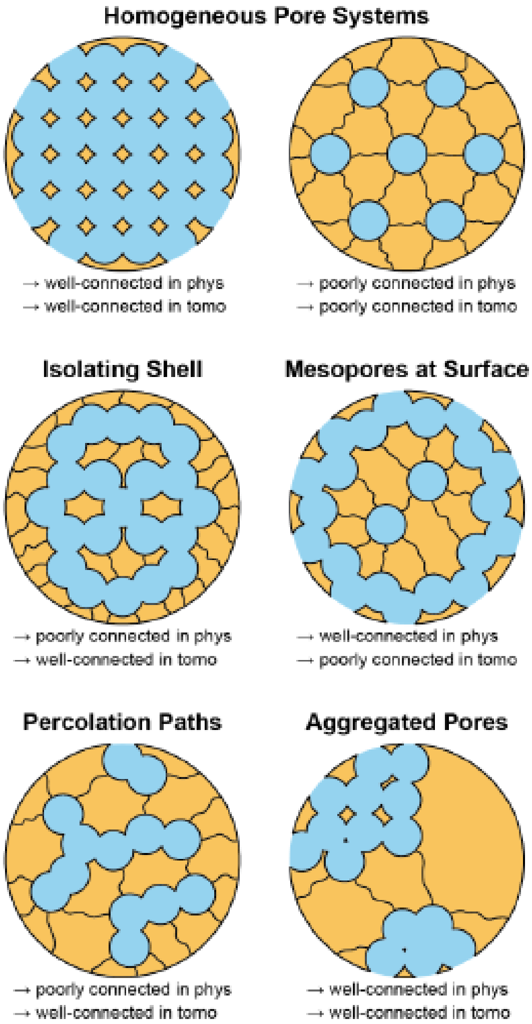

Figure 7. Schematic overview on possible pore systems with an (in)homogeneous spatial distribution of the mesopores and their expected impact on the pore connectivity observed in physisorption (phys) and STEM-based tomography (tomo).

in an actual mesoporous system, inhomogeneities with respect to the spatial distribution of mesopores can occur as stressed during the SAXS evaluation in **Figure 3C**. For instance, if a particle containing a well-connected mesopore network possesses a rather dense shell containing only micro- but no mesopores (**Figure** 7), physisorption experiments would result in networks effect while tomography would yield a high level of connectivity. *Vice versa*, a particle with an enrichment of mesopores on the particle surface would lead to a well-accessible pore system in physisorption but to poorly connected mesopores in the particle center according to tomography. A further possibility to obtain poorly accessible but well-connected mesopores represents the existence of percolation paths of mesopores, which are interconnected by large pore necks within the percolation path, but connected to other percolation paths or the exterior gas phase by micropore channels (**Figure** 7). Lastly, an aggregation of mesopores as a consequence of a phase separation or evaporation-induced aggregating assembly[58] for example could occur yielding domains of well/poorly accessible and well-connected mesopores (and non-porous domains) depending on the location of the aggregated pores inside the particle (particle surface or core) and region investigated by tomography.

Here, the two cases of an isolating shell and of mesopores mainly at the particle surface in **Figure** 7 can be ruled out on the basis of STEM-based tomography. Already the selected slices of the reconstructed particles in **Figure S5** reveal a rather even spatial distribution of mesopores. Also, a few mesopores at the particle surface (especially, in case of the carbon sample) show a connection between the exterior phase and the interior pore system on the mesoscale excluding the isolating shell model. Furthermore, an aggregation of mesopores cannot be envisioned from tomography neither. Although the images of the SiO_2 sample in **Figure S5** exhibit a small region containing no mesopores, the dimension of this zone is too small to dominate the STEM-based results. Thus, the aggregated pore model seems unlikely as well. As both the carbon and ZrO_2 sample yield an apparently contradicting outcome in terms of physisorption and tomography analysis, the percolation path model represents the only remaining model being capable of explaining the observed deviation. The large mesopores are well-connected within a percolation path yielding a

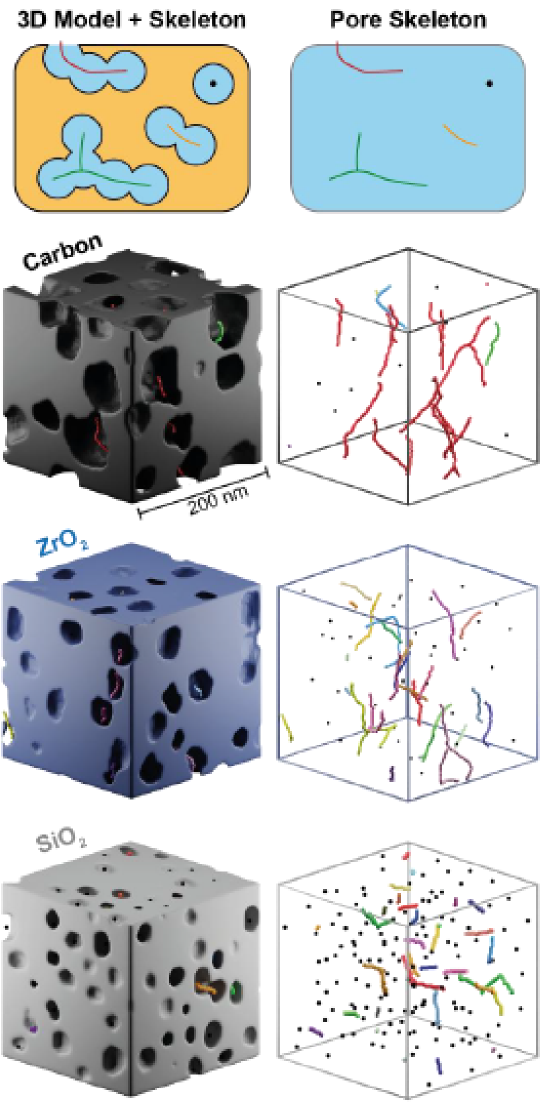

Figure 8. Schematic representation (top) and STEM-based reconstruction including visualization of the pore skeleton of mesoporous carbon (black), ZrO_2 (blue), and SiO_2 (gray) on the bottom. All percolation paths that are connected within or outside the depicted cut-out are displayed in the same color. Isolated mesopores are shown as black spheres.

high coordination number in STEM-based tomography. However, as long as each percolation path is connected with other percolation paths and – in particular – the exterior volume only by a narrow pore channel, a network effect will be observed in physisorption. Since these channels possess a diameter of about 1 nm in case of carbon and SiO_2 according to physisorption (**Figure 1D** and **F**), a pronounced cavitation-based hysteresis is obtained. In case of ZrO_2, theses micropore channels are expanded to *ca.* 7 nm (**Figure 1E** and **Figure 4E**), which still restricts evaporation, but leads to a pore blocking phenomenon instead of cavitation. The existence of these percolation paths can be visualized by using the pore skeleton deduced from tomography. The skeletonization approach follows an iteratively thinning of the pore phase until a one-voxel thick pathway (*i.e.*, the backbone) of the pore system remains (red pathway in **Figure 8**, the respective color-coded percolation paths (one color per percolation path) among the isolated mesopores (black spheres) are clearly visible, particularly in case of the metal oxides, and provide an illustrative confirmation of the percolation path model. The extent of these percolation paths increases from SiO_2 to ZrO_2 to carbon. In case of SiO_2, an almost isolated case as shown in **Figure 7** can be assumed. In case of the well-connected carbon sample, long inter-connected pathways can be found. In detail, the skeleton analysis with the ImageJ software reveals within the analyzed region (750 nm x 700 nm x 450 nm) for the mesoporous carbon sample (see **Figure S6**) 343 isolated pores (10% of all pores, see **Figure 5A**), one main percolation path with already 1172 branches but still 183 further percolation paths (composed of 1 – 17 branches) being isolated from the main network. This analysis clearly proves that the percolation model is proper to describe the pore model here. The reason why the 7 nm thick pore channels in case of ZrO_2 are not resolved in the STEM-based 3D model probably is the pixel (/voxel) size of 1.6 nm in combination with the binarization of the TEM images: If a large number of only 3 – 5 voxel thick channels are evenly distributed within the ZrO_2 wall, a solid wall with a lower electron contrast on average will be observed in the electron image. Upon reconstructing the particle, each voxel is assigned to either a pore or a pore wall (binarization), in which the ZrO_2 wall including the small channels might be fully assigned to a dense wall without pores. The general existence of these channels, clearly confirmed by physisorption, can be guessed, however, from a close-up SEM image of the spherical mesopores (**Figure S7**). Despite the rough structure, a few pore channels of *ca.* 6 nm in diameter within the large spherical mesopores can be resolved in mesoporous ZrO_2 but not in the other two samples (which still reveal a rough pore wall). Yet, the low resolution of the interior pore wall makes an unambiguous statement impossible but the SEM images seem to support the hypothesis that the PEO-single-chain-induced pore channels are larger in case of ZrO_2 than in case of carbon and SiO_2.

This study demonstrates that gas physisorption and STEM-based tomography are neither competing nor contradicting methods but complementary ones providing a full picture of the pore network when combined together (see bottom of **Figure 6**). In terms of pore connection, both methods give a different view on the pore system with physisorption describing the pore (network) accessibility from the exterior (including both micro- and mesopores) while tomography describes the local connectivity considering only mesopores. Employing only one of the two methods is possible but it should be kept in mind that irregularities of the mesopores can occur: For instance, from physisorption of the here presented mesoporous ZrO_2 sample alone, a well-connected mesopore pattern as shown in the top left of **Figure** 7 could be deduced although the spherical mesopores are actually barely merging (see STEM tomography). Similarly, a poorly connected mesopore system as shown in the top right of **Figure** 7 could be derived in case of carbon based on physisorption although the mesopores are actually merged together to a large network. In particular with physisorption as routine technique, network effects like cavitation are commonly associated with poorly connected pores and not with a highly interconnected pore network as visualized by the tomography-based pore skeleton, which entirely changes the picture of the pore system one has in mind. As a result, both techniques are required for a full understanding, not only in these soft-templated samples but in general for mesoporous materials.

Conclusion

In this work, we investigated the pore system of mesoporous carbon, SiO_2, and ZrO_2 powders soft-templated with a poly(ethylene oxide)-*block*-poly(hexyl acrylate) block copolymer and contrasted gas physisorption and electron tomography as analysis techniques for pore connectivity analysis. A detailed comparative characterization by physisorption, SEM, SAXS, and tomography showed that the pore size determination for such large spherical mesopores by physisorption is most reliable by assuming a cylindrical pore geometry and post-correction with a factor of 1.35 to consider a spherical pore geometry. The pore connectivity from physisorption following an adsorptive comparison and hysteresis scanning revealed a low pore accessibility in case of carbon and SiO_2 while the ZrO_2 sample possessed noticeably larger pore necks. Contrarily, STEM-based tomography showed a rather isolated pore system in case of the metal oxides whereas the carbon powder contained a well-connected pore network. This apparent contradiction was resolved by reconsidering the different views both methods provide: the overall pore accessibility by physisorption and the local pore connectivity by electron tomography. The introduction of a pore model comprising percolation paths of well-connected mesopores, which are connected to other percolation paths or the exterior by the small restricting pore channels observed in physisorption, harmonizes both characterization methods and can be illustratively visualized.

This case study demonstrates on the basis of three mesoporous model materials that the usage of gas physisorption for pore connectivity studies alone can be misleading. Especially in case of real materials possessing a certain degree of inhomogeneity in the pore structure, both physisorption and electron tomography are required to obtain a full picture of the pore system.

Supporting Information

The authors have cited additional references within the Supporting Information.[59–61]

Acknowledgements

The authors thank Raoul Brand and Rafael Meinusch (both Justus Liebig University) for gas physisorption measurements and Eric Prates da Costa for assistance with visualizing the pore skeleton from electron tomography. The Karlsruhe Nano Micro Facility (KNMFi) is acknowledged for providing access to the TEM instrument as well as the CERIC-ERIC Consortium for the access to the SAXS setup at the Technical University of Graz. Also, L. W. thanks the Funds of the Chemical Industry (FCI) for financial support.

References

(1) Yarulina, I.; De Wispelaere, K.; Bailleul, S.; Goetze, J.; Radersma, M.; Abou-Hamad, E.; Vollmer, I.; Goesten, M.; Mezari, B.; Hensen, E. J. M.; Martínez-Espín, J. S.; Morten, M.; Mitchell, S.; Perez-Ramirez, J.; Olsbye, U.; Weckhuysen, B. M.; Van Speybroeck, V.; Kapteijn, F.; Gascon, J. Structure–Performance Descriptors and the Role of Lewis Acidity in the Methanol-to-Propylene Process. *Nat. Chem.* **2018**, *10*, 804–812.

(2) Wang, Y.; Arandiyan, H.; Scott, J.; Bagheri, A.; Dai, H.; Amal, R. Recent Advances in Ordered Meso/Macroporous Metal Oxides for Heterogeneous Catalysis: A Review. *J. Mater. Chem. A* **2017**, *5*, 8825–8846.

(3) Cop, P.; Maile, R.; Sun, Y.; Khalid, O.; Djerdj, I.; Esch, P.; Heiles, S.; Over, H.; Smarsly, B. M. Impact of Aliovalent/Isovalent Ions (Gd, Zr, Pr, and Tb) on the Catalytic Stability of Mesoporous Ceria in the HCl Oxidation Reaction. *ACS Appl. Nano Mater.* **2020**, *3*, 7406–7419.

(4) Kang, Y.; Tang, Y.; Zhu, L.; Jiang, B.; Xu, X.; Guselnikova, O.; Li, H.; Asahi, T.; Yamauchi, Y. Porous Nanoarchitectures of Nonprecious Metal Borides: From Controlled Synthesis to Heterogeneous Catalyst Applications. *ACS Catal.* **2022**, *12*, 14773–14793.

(5) Luna, A. L.; Matter, F.; Schreck, M.; Wohlwend, J.; Tervoort, E.; Colbeau-Justin, C.; Niederberger, M. Monolithic Metal-Containing TiO_2 Aerogels Assembled from Crystalline Pre-Formed Nanoparticles as Efficient Photocatalysts for H_2 Generation. *Appl. Catal. B Environ.* **2020**, *267*, 118660.

(6) Weller, T.; Sann, J.; Marschall, R. Pore Structure Controlling the Activity of Mesoporous Crystalline $CsTaWO_6$ for Photocatalytic Hydrogen Generation. *Adv. Energy Mater.* **2016**, *6*, 1–9.

(7) Weller, T.; Deilmann, L.; Timm, J.; Dörr, T. S.; Beaucage, P. A.; Cherevan, A. S.; Wiesner, U. B.; Eder, D.; Marschall, R. A Crystalline and 3D Periodically Ordered Mesoporous Quaternary Semiconductor for Photocatalytic Hydrogen Generation. *Nanoscale* **2018**, *10*, 3225–3234.

(8) Fried, D. I.; Brieler, F. J.; Fröba, M. Designing Inorganic Porous Materials for Enzyme Adsorption and Applications in Biocatalysis. *ChemCatChem* **2013**, *5*, 862–884.

(9) Hartmann, P.; Lee, D. K.; Smarsly, B. M.; Janek, J. Mesoporous TiO_2: Comparison of Classical Sol-Gel and Nanoparticle Based Photoelectrodes for the Water Splitting Reaction. *ACS Nano* **2010**, *4*, 3147–3154.

(10) Bernsmeier, D.; Ortel, E.; Polte, J.; Eckhardt, B.; Nowag, S.; Haag, R.; Kraehnert, R. Versatile Control over Size and Spacing of Small Mesopores in Metal Oxide Films and Catalytic Coatings via Templating with Hyperbranched Core–Multishell Polymers. *J. Mater. Chem. A* **2014**, *2*, 13075–13082.

(11) Sun, X.; Hao, H.; Ji, H.; Li, X.; Cai, S.; Zheng, C. Nanocasting Synthesis of In_2O_3 with Appropriate Mesostructured Ordering and Enhanced Gas-Sensing Property. *ACS Appl. Mater. Interfaces* **2014**, *6*, 401–409.

(12) Burgess, I. B.; Koay, N.; Raymond, K. P.; Kolle, M.; Lončar, M.; Aizenberg, J. Wetting in Color: Colorimetric Differentiation of Organic Liquids with High Selectivity. *ACS Nano* **2012**, *6*, 1427–1437.

(13) Bach, U.; Lupo, D.; Comte, P.; Moser, J. E.; Weissörtel, F.; Salbeck, J.; Spreitzer, H.; Grätzel, M. Solid-State Dye-Sensitized Mesoporous TiO_2 Solar Cells with High Photon-to-Electron Conversion Efficiencies. *Nature* **1998**, *395*, 583–585.

(14) Glatthaar, C.; Wang, M.; Wagner, L. Q.; Breckwoldt, F.; Guo, Z.; Zheng, K.; Kriechbaum, M.; Amenitsch, H.; Titirici, M.-M.; Smarsly, B. M. Lignin-

Derived Mesoporous Carbon for Sodium-Ion Batteries: Block Copolymer Soft Templating and Carbon Microstructure Analysis. *Chem. Mater.* **2023**, *35*, 10416–10433.

(15) Kreissl, J. J. A.; Petit, J.; Oppermann, R.; Cop, P.; Gerber, T.; Joos, M.; Abert, M.; Tu, J.; Miyazaki, K.; Abe, T.; Schröder, D. Electrochemical Lithiation/ Delithiation of ZnO in 3D-Structured Electrodes : Elucidating the Mechanism and the Solid Electrolyte Interphase Formation. *ACS Appl. Mater. Interfaces* **2021**, *13*, 35625–35638.

(16) Weller, T.; Timm, J.; Deilmann, L.; Doerr, T. S.; Greve, C.; Cherevan, A. S.; Beaucage, P. A.; Wiesner, U. B.; Herzig, E. M.; Eder, D.; Marschall, R. Effects of Periodic Pore Ordering on Photocatalytic Hydrogen Generation with Mesoporous Semiconductor Oxides. *Small Struct.* **2022**, *31*, 2200184.

(17) Trommer, A.; Hessling, J.; Schreiner, P. R.; Schönhoff, M.; Smarsly, B. M. Influence of the Mesoporosity of Silica Carrier Materials on the Performance of an Immobilized Organocatalyst in Heterogeneous Catalysis. *ACS Appl. Mater. Interfaces* **2025**, *17*, 24283–24299.

(18) Neff, P.; Chen, J.-Y.; Burrows, R.; Brunelli, N. A. Investigating Cooperative Interactions for the Nitroaldol Reaction and Condensation: Clarifying the Impact of Microporosity and Pore Size on Catalytic Activity of Mesoporous Aminosilica Materials. *Microporous Mesoporous Mater.* **2025**, *397*, 113762.

(19) Tallarek, U.; Hochstrasser, J.; Ziegler, F.; Huang, X.; Kübel, C.; Buchmeiser, M. R. Olefin Ring-closing Metathesis under Spatial Confinement: Morphology–Transport Relationships. *ChemCatChem* **2021**, *13*, 281–292.

(20) Sallard, S.; Schröder, M.; Boissière, C.; Dunkel, C.; Etienne, M.; Walcarius, A.; Oekermann, T.; Wark, M.; Smarsly, B. M. Bimodal Mesoporous Titanium Dioxide Anatase Films Templated by a Block Polymer and an Ionic Liquid: Influence of the Porosity on the Permeability. *Nanoscale* **2013**, *5*, 12316.

(21) De Witte, B.; Vercruysse, K.; Aernouts, K.; Verwimp, P.; Uytterhoeven, J. B. N_2-Adsorption on Amorphous Aluminosilicates: Application of the Kelvin Equation and the t-Plot Analysis for Mixed Micro-Mesoporous Materials. *J. Porous Mater.* **1996**, *2*, 307–313.

(22) Kainourgiakis, M. E.; Stubos, A. K.; Konstantinou, N. D.; Kanellopoulos, N. K.; Milisic, V. A Network Model for the Permeability of Condensable Vapours through Mesoporous Media. *J. Memb. Sci.* **1996**, *114*, 215–225.

(23) Schlumberger, C.; Thommes, M. Characterization of Hierarchically Ordered Porous Materials by Physisorption and Mercury Porosimetry—A Tutorial Review. *Adv. Mater. Interfaces* **2021**, *8*, 2002181.

(24) Ball, P. C.; Evans, R. Temperature Dependence of Gas Adsorption on a Mesoporous Solid: Capillary Criticality and Hysteresis. *Langmuir* **1989**, *5*, 714–723.

(25) Thommes, M. Physical Adsorption Characterization of Nanoporous Materials. *Chemie-Ingenieur-Technik* **2010**, *82*, 1059–1073.

(26) Thommes, M.; Kaneko, K.; Neimark, A. V.; Olivier, J. P.; Rodriguez-Reinoso, F.; Rouquerol, J.; Sing, K. S. W. Physisorption of Gases, with Special Reference to the Evaluation of Surface Area and Pore Size Distribution (IUPAC Technical Report). *Pure Appl. Chem.* **2015**, *87*, 1051–1069.

(27) Kleitz, F.; Bérubé, F.; Guillet-Nicolas, R.; Yang, C.-M.; Thommes, M. Probing Adsorption, Pore Condensation, and Hysteresis Behavior of Pure Fluids in Three-Dimensional Cubic Mesoporous KIT-6 Silica. *J. Phys. Chem. C* **2010**, *114*, 9344–9355.

(28) Ravikovitch, P. I.; Neimark, A. V. Experimental Confirmation of Different Mechanisms of Evaporation from Ink-Bottle Type Pores: Equilibrium, Pore Blocking, and Cavitation. *Langmuir* **2002**, *18*, 9830–9837.

(29) Thommes, M.; Smarsly, B.; Groenewolt, M.; Ravikovitch, P. I.; Neimark, A. V. Adsorption Hysteresis of Nitrogen and Argon in Pore Networks and Characterization of Novel Micro- and Mesoporous Silicas. *Langmuir* **2006**, *22*, 756–764.

(30) Coasne, B.; Galarneau, A.; Pellenq, R. J. M.; Di Renzo, F. Adsorption, Intrusion and Freezing in Porous Silica: The View from the Nanoscale. *Chem. Soc. Rev.* **2013**, *42*, 4141–4171.

(31) Kube, S. A.; Turke, K.; Ellinghaus, R.; Wallacher, D.; Thommes, M.; Smarsly, B. M. Pore Size Gradient Effect in Monolithic Silica Mesopore Networks Revealed by *In-Situ* SAXS Physisorption. *Langmuir* **2020**, *36*, 11996–12009.

(32) Söllner, J.; Neimark, A. V.; Thommes, M. Development and Application of an Advanced Percolation Model for Pore Network Characterization by Physical Adsorption. *Langmuir* **2024**, *40*, 23146–23168.

(33) Wang, Z.; Huang, J.; Jiang, G.; Ji, T.; Lin, H.; Mu, L.; Zhu, J. Quantification of Pore Connectivity in Hierarchically Porous Carbon by Percolation Effect Integrated Differential Hysteresis Scanning. *Chem. Mater.* **2025**, *37*, 1337–1348.

(34) Midgley, P. A.; Dunin-Borkowski, R. E. Electron Tomography and Holography in Materials Science. *Nat. Mater.* **2009**, *8*, 271–280.

(35) Weyland, M.; Midgley, P. A.; Thomas, J. M. Electron Tomography of Nanoparticle Catalysts on Porous Supports: A New Technique Based on Rutherford Scattering. *J. Phys. Chem. B* **2001**, *105*, 7882–7886.

(36) Ercius, P.; Alaidi, O.; Rames, M. J.; Ren, G. Electron Tomography: A Three-Dimensional Analytic

Tool for Hard and Soft Materials Research. *Adv. Mater.* **2015**, *27*, 5638–5663.

(37) Huang, X.; Hlushkou, D.; Wang, D.; Tallarek, U.; Kübel, C. Quantitative Analysis of Mesoporous Structures by Electron Tomography: A Phantom Study. *Ultramicroscopy* **2023**, *243*, 113639.

(38) Wang, W.; Svidrytski, A.; Wang, D.; Villa, A.; Hahn, H.; Tallarek, U.; Kübel, C. Quantifying Morphology and Diffusion Properties of Mesoporous Carbon From High-Fidelity 3D Reconstructions. *Microsc. Microanal.* **2019**, *25*, 891–902.

(39) Prates da Costa, E.; Huang, X.; Kübel, C.; Cheng, X.; Schladitz, K.; Hofmann, A.; Göbel, U.; Smarsly, B. M. Effects of Hydrothermal Treatment on Mesopore Structure and Connectivity in Doped Ceria-Zirconia Mixed Oxides. *Langmuir* **2023**, *39*, 177–191.

(40) Prates da Costa, E.; Huang, X.; Kübel, C.; Cheng, X.; Schladitz, K.; Hofmann, A.; Göbel, U.; Smarsly, B. M. Tuning Mesopore Accessibility of $Ce_{0.18}Zr_{0.64}Y_{0.15}La_{0.03}O_{2-\delta}$ by Hydrothermal Post-Treatment—A Case Study for Ceria-Based Oxidation Storage Materials. *Langmuir* **2023**, *39*, 17664–17679.

(41) Wagner, L. Q.; Prates da Costa, E.; Glatthaar, C.; Breckwoldt, F.; Zecca, M.; Centomo, P.; Huang, X.; Kübel, C.; Schlaad, H.; Kriechbaum, M.; Amenitsch, H.; Thommes, M.; Smarsly, B. M. Poly(ethylene oxide)-*block*-poly(hexyl acrylate) Copolymers as Templates for Large Mesopore Sizes — A Detailed Porosity Analysis. *Chem. Mater.* **2023**, *35*, 9879–9899.

(42) Wagner, L. Q.; Breckwoldt, F.; Huang, X.; Kübel, C.; Cheng, X.; Schladitz, K.; Smarsly, B. M. Porosity Tuning in Soft-Templated Mesoporous Silica: The Influence of Block Copolymer Composition and Concentration. *Langmuir* **2025**, *41*, 30948–30967.

(43) Wagner, L. Q.; Schober, J.; Dippell, P.; Glatthaar, C.; Mekhilef, S.; Schäfer, D.; Hergert, H.; Rohnke, M.; Elm, M. T.; Smarsly, B. M. Mesoporous Carbon Thin Films with Large Mesopores as Model Material for Electrochemical Applications. *Adv. Funct. Mater.* **2025**. DOI: 10.1002/adfm.202521031.

(44) Lu, Y.; Fan, H.; Stump, A.; Ward, T. L.; Rieker, T.; Brinker, C. J. Aerosol-Assisted Self-Assembly of Mesostructured Spherical Nanoparticles. *Nature* **1999**, *398*, 223–226.

(45) Brinker, C. J.; Lu, Y.; Sellinger, A.; Fan, H. Evaporation-Induced Self-Assembly: Functional Nanostructures Made Easy. *Adv. Funct. Mater.* **1999**, *11*, 579–585.

(46) Grosso, D.; Cagnol, F.; Soler-Illia, G. J. de A. A.; Crepaldi, E. L.; Amenitsch, H.; Brunet-Bruneau, A.; Bourgeois, A.; Sanchez, C. Fundamentals of Mesostructuring Through Evaporation-Induced Self-Assembly. *Adv. Funct. Mater.* **2004**, *14*, 309–322.

(47) Lokupitiya, H. N.; Jones, A.; Reid, B.; Guldin, S.; Stefik, M. Ordered Mesoporous to Macroporous Oxides with Tunable Isomorphic Architectures: Solution Criteria for Persistent Micelle Templates. *Chem. Mater.* **2016**, *28*, 1653–1667.

(48) Meng, Y.; Gu, D.; Zhang, F.; Shi, Y.; Cheng, L.; Feng, D.; Wu, Z.; Chen, Z.; Wan, Y.; Stein, A.; Zhao, D. A Family of Highly Ordered Mesoporous Polymer Resin and Carbon Structures from Organic−Organic Self-Assembly. *Chem. Mater.* **2006**, *18*, 4447–4464.

(49) Chuenchom, L.; Kraehnert, R.; Smarsly, B. M. Recent Progress in Soft-Templating of Porous Carbon Materials. *Soft Matter* **2012**, *8*, 10801.

(50) Šebenik, A.; Osredkar, U.; Vizovišek, I. Study of the Reaction between Resorcinol and Formaldehyde. *Polymer* **1981**, *22*, 804–806.

(51) Neimark, A. V.; Lin, Y.; Ravikovitch, P. I.; Thommes, M. Quenched Solid Density Functional Theory and Pore Size Analysis of Micro-Mesoporous Carbons. *Carbon* **2009**, *47*, 1617–1628.

(52) Cychosz, K. A.; Guo, X.; Fan, W.; Cimino, R.; Gor, G. Y.; Tsapatsis, M.; Neimark, A. V.; Thommes, M. Characterization of the Pore Structure of Three-Dimensionally Ordered Mesoporous Carbons Using High Resolution Gas Sorption. *Langmuir* **2012**, *28*, 12647–12654.

(53) Thommes, M.; Schlumberger, C. Characterization of Nanoporous Materials. *Annu. Rev. Chem. Biomol. Eng.* **2021**, *12*, 137–162.

(54) Weidmann, C.; Brezesinski, K.; Suchomski, C.; Tropp, K.; Grosser, N.; Haetge, J.; Smarsly, B. M.; Brezesinski, T. Morphology-Controlled Synthesis of Nanocrystalline η-Al_2O_3 Thin Films, Powders, Microbeads, and Nanofibers with Tunable Pore Sizes from Preformed Oligomeric Oxo-Hydroxo Building Blocks. *Chem. Mater.* **2012**, *24*, 486–494.

(55) Percus, J. K.; Yevick, G. J. Analysis of Classical Statistical Mechanics by Means of Collective Coordinates. *Phys. Rev.* **1958**, *110*, 1–13.

(56) Ashcroft, N. W.; Lekner, J. Structure and Resistivity of Liquid Metals. *Phys. Rev.* **1966**, *145*, 83–90.

(57) Wertheim, M. S. Exact Solution of the Percus-Yevick Integral Equation for Hard Spheres. *Phys. Rev. Lett.* **1963**, *10*, 321–323.

(58) Wei, J.; Wang, H.; Deng, Y.; Sun, Z.; Shi, L.; Tu, B.; Luqman, M.; Zhao, D. Solvent Evaporation Induced Aggregating Assembly Approach to Three-Dimensional Ordered Mesoporous Silica with Ultralarge Accessible Mesopores. *J. Am. Chem. Soc.* **2011**, *133*, 20369–20377.

(59) Tanaka, S.; Katayama, Y.; Tate, M. P.; Hillhouse, H. W.; Miyake, Y. Fabrication of Continuous Mesoporous Carbon Films with Face-Centered Orthorhombic Symmetry through a Soft Templating Pathway. *J. Mater. Chem.* **2007**, *17*, 3639.

(60) Cheng, X.; Föhst, S.; Redenbach, C.; Schladitz, K. Detecting Branching Nodes of Multiply Connected 3D Structures. *Proceedings of the Mathematical*

Morphology and its Applications to Signal and Image Processing: 14th international symposium, ISMM 2019; Saarbrücken, Germany, July 8−10, 2019; Burgeth, B., Kleefeld, A., Naegel, B., Passat, N., Perret, B., Eds.; Springer International Publishing: Cham ***2019***, *11564, 441–455.*

(61) Schmidt-Rohr, K. Simulation of Small-Angle Scattering Curves by Numerical Fourier Transformation. *J. Appl. Crystallogr.* **2007**, *40*, 16–25.

Entry for the Table of Contents

Observing a network effect in physisorption isotherms, we usually have a picture of poorly connected mesopores in mind. Here, we contrast gas physisorption and electron tomography for studying the pore connectivity of mesoporous powders and see that this simple picture does not hold true. Instead, well-connected mesopores can still be found by tomography. We demonstrate that both methods are required to derive a clear picture of the pore system.

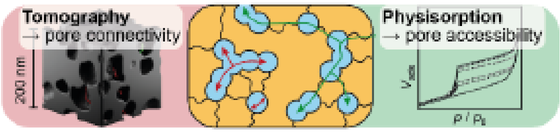

Keywords: pore connectivity • mesoporous • physisorption • electron tomography • soft templating

Supporting Information

On the Interpretation of Physisorption Isotherms: Connectivity *versus* Accessibility of Mesopore Networks

Lysander O. Wagner[a,b], *Lucas Brauch* [c,d,e], *Christian Kübel*[c,d,e], *Xiaoyin Cheng*[f], *Katja Schladitz* [f],

and Bernd M. Smarsly[a,b]*

a. Institute of Physical Chemistry, Justus Liebig University, Heinrich-Buff-Ring 17, D-35392 Giessen, Germany
b. Center of Materials Research, Justus Liebig University, Heinrich-Buff-Ring 16, D-35392 Giessen, Germany
c. Institute of Nanotechnology, Karlsruhe Institute of Technology, Hermann-von-Helmholtz-Platz 1, D-76344 Eggenstein-Leopoldshafen, Germany
d. Department of Materials and Earth Science, Technical University Darmstadt, Peter-Grünberg-Straße 2, D-64287 Darmstadt, Germany
e. Karlsruhe Nano Micro Facility, Karlsruhe Institute of Technology, Hermann-von-Helmholtz-Platz 1, D-76344 Eggenstein-Leopoldshafen, German
f. Fraunhofer Institute for Industrial Mathematics, Fraunhofer-Platz 1, D-67663 Kaiserslautern, Germany

Experimental Section

Synthesis of mesoporous carbon powders

The preparation of the non-graphitic carbon powder followed a protocol based on Tanaka *et al.*[1] and adjusted in our recent study.[2] In a 4 mL glass vial, 114 mg of the soft template PEO_{441}-*b*-PHA_{270} (synthesized in a previous study[3]) were dissolved in 1.7 mL of absolute ethanol (99.8%, Fisher Chemicals) by sonication for 120 min at 40 °C and 37 kHz. In a second vial, 198 mg of resorcinol (99%, Sigma Aldrich) were dissolved in 522 µL of deionized water upon stirring at room temperature for 20 min. After adding 18 µL of a 5 M hydrochloric acid (made from 583 µL of water and 417 µL of a fuming hydrochloric acid purchased from Fluka) to the carbon precursor, the polymer solution was added as well followed by the addition of 164 µL of triethyl orthoacetate (97%, Thermo Scientific) and 198 µL of a 37 wt.% aqueous formaldehyde solution (10 – 15% methanol as stabilizer, Sigma Aldrich) after brief stirring. The reaction mixture was stirred for 30 min at 30 °C prior to casting into a Petri dish. The solution was dried for 23 h at 80 °C in a drying oven yielding an intensely orange brittle residue. The latter was scratched off and transferred to a crucible. After carbonization in a muffle furnace in nitrogen atmosphere (3 h at 400 °C, 2 h at 900 °C, 1 $K\ min^{-1}$ heating rate each) together with a second crucible filled with ~2 g of copper powder (99%, Acros Organics) as sacrificial reducing agent and grinding, 102 mg of a black powder were obtained.

Synthesis of mesoporous ZrO_2 powders

The ZrO_2 powder was prepared in the style of a protocol proposed by Cop *et al.*[4] and similar to our previous work.[5] 161 mg of $ZrOCl_2 \cdot 8H_2O$ (98%, Alfa Aesar) were dissolved in a mixture of 330 µL of absolute ethanol and 330 µL of 2-methoxy ethanol (>99.9%, Sigma Aldrich) by sonication at 40 °C and 37 kHz for 30 min. In a second vial, 15 mg of PEO_{441}-*b*-PHA_{270} were dissolved in 660 µL of absolute ethanol and 170 µL of a concentrated acetic acid (99%, Carl Roth GmbH) in the same manner. Both solutions were combined, stirred for 10 min at room temperature, and 10 µL of water were added. After further 10 min of stirring, the solution was stored at 40 °C under a glass dome for two days. The gel was further dried in a vacuum oven at 40 °C for 24 h prior to calcination at 350 °C for 1 h and at 500 °C for 4 h (heating ramp each: 2 K min^{-1}) yielding 27 mg of a gray powder.

Synthesis of mesoporous SiO_2 powders

Mesoporous SiO_2 powders were prepared by soft templating in analogy to our past article.[5] In this sol-gel synthesis relying on the studies of Weller *et al.*[6] and Cop *et al.*,[4] 23 mg of PEO_{441}-*b*-PHA_{270} were dissolved by ultrasonication at 37 kHz and 40 °C in 1 mL of absolute ethanol within 40 min. Meanwhile, 130 µL of tetraethyl orthosilicate (TEOS, 98%, Sigma Aldrich) were dissolved in 0.5 mL absolute ethanol by stirring at room temperature in a 5 mL PTFE cup. Both the clear polymer solution and 40 µL of deionized water were added to the metal oxide precursor. After 5 min of stirring, 10 µL of concentrated hydrochloric acid (37 wt.%) were added prior to stirring for 1 h at room temperature. The clear solution was processed the same way the ZrO_2 powder was dried and calcined resulting in *circa* 35 mg of a colorless powder after grinding in an agate mortar.

Characterization techniques

Nitrogen physisorption experiments were carried out at 77 K on a *Quadrasorb evo* (*Quantachrome Instruments*, Boynton Beach, FL) while argon physisorption experiments were performed at 87 K on an *Autosorb iQ* (*Quantachrome Instruments*, Boynton Beach, FL). The data obtained were analyzed with the aid of the software *ASiQwin* by applying non-local density functional theory (NLDFT) on siliceous/oxidic materials and quenched solid DFT (QSDFT) methods on carbonaceous materials dedicated to nitrogen and argon at 77 K and 87 K, respectively, assuming a cylindrical pore geometry. In all cases, the pore size distribution was obtained from the adsorption branch by applying a dedicated metastable adsorption branch kernel, which correctly takes into account the delay in pore condensation due to metastable pore fluid.[7] In case of the nitrogen measurements for obtaining the hysteresis scans, the long measurement time results in a temperature profile along the measurement tube being significantly different than in the reference tube. Therefore, a linear background is observed in the isotherm (see **Figure S3**), which was subtracted manually to match the initial boundary isotherm (thermal compensation). All metal oxide samples were degassed at 200 °C for 6 h while the carbon sample was degassed at 80 °C for 12 h in order to remove attached water and gases prior measuring. Scanning electron microscopy (SEM) images were obtained with a *Zeiss GeminiSEM 560* microscope using an *InLens* detector, a working distance of 2.5 mm, and an acceleration voltage of 1 kV. To enhance the conductivity, samples were sputtered with platinum using a *Leica EM ACE600* sputter coater. All images were evaluated with the *Fiji ImageJ* software. Small-angle X-ray scattering (SAXS) measurements were carried with the laboratory SAXS instrument *SAXSpoint 2.0* by *Anton Paar* using point-focused (spot size of 500 μm) and slit-collimated Cu Kα radiation ($\lambda = 0.1541$ nm) from a microsource operating at 50 W and a *Dectris EIGER2 R 1M* hybrid pixel area X-ray detector. Powder samples were placed into an *Anton Paar* solid sample holder comprising a 1 mm thick metal plate with 20 squared holes mounted on a motorized X/Y-stage. The sample plate was sealed at both sides with a vacuum-tight sealing tape. SAXS images of the samples and the background (sealing tapes) were recorded in vacuum (around 1 mbar and 25 °C) at a sample-to-detector distance of 575.65 mm.

Per each sample and background, respectively, 15 single images with two minutes exposure time each were recorded, averaged, and radially integrated in order to obtain the 1D-SAXS curves. The scattering curves were fitted using the software *SASfit 0.94.11* with a model consisting of a form factor for spheres with a Gaussian size distribution and a lattice factor applying the implemented decoupling approximation. Scanning transmission electron microscopy (STEM)-based tomography was executed with a *Thermofisher Scientific Themis 300* transmission electron microscope equipped with probe aberration correction and operated at an acceleration voltage of 300 kV. Each powder (around 10 mg) was ground, suspended in *ca.* 5 mL of absolute ethanol, and about three drops of the suspension were dropped on a 100 x 400 mesh carbon-coated copper grid purchased from *Quantifoil Micro Tools GmbH*. Gold nanoparticles ($d_{\text{Au-np}}$ = 6.5 nm) were deposited onto the sample as fiducial markers for image alignment. The grid was cleaned twice for 30 s using a *Fischione 1070* plasma cleaner in argon-oxygen atmosphere with a power of 50%. A high-angle annular dark-field (HAADF)-STEM tilt series was acquired over a tilt range of −74° to 64° (step size: 2°) and with a pixel size of 1.61 nm using the *Xplore3D* software (*Thermofisher Scientific*) with auto focus and tracking before acquisition. A small converge angle of roughly 8.5 mrad was used to increase the depth of focus. With the aid of the gold nanoparticles, image alignment was done in *IMOD Version 4.11.7* (*University of Colorado*) with a residual alignment error of 0.699 nm (0.434 px). The 3D reconstruction (with a voxel size of $(1.61\text{ nm})^3$) was obtained from the aligned tilt series with the simultaneous iterative reconstruction technique (SIRT) and 100 iterations in *Inspect 3D 4.4* (*Thermofisher Scientific*). Denoising with a median filter in *ImageJ* and binarization by global thresholding in *Avizo 2021.1* (*Thermofisher Scientific*) of the tomograms yielded an initial segmentation. The segmented volume was purified by removal of unconnected islands smaller than 15 voxels, which originate from reconstruction artifacts.

Skeletonization of a cropped region of the image stack was executed as reported by Cheng *et al.*[8] using *ToolIP with MAVIkit 2024* (*Fraunhofer ITWM*) in order to elucidate the local pore connectivity. Pore and wall size distributions were obtained with a local thickness evaluation using the corresponding plugin in *ImageJ* after subtracting the background with a *Python* code applying a rolling ball radius of 15 pixels (24.2 nm) as recently described by us.[9] Simulation of the scattering curves based on a cropped cube of the reconstruction followed a numerical Fourier transformation[10] and a Python-based code as reported elsewhere in detail.[11]

Supplemental Data

Table S1. Overview on and details about the DFT evaluation models used for deducing the pore size distributions from the respective physisorption isotherms (according to the *ASiQwin* operating manual). The value in the pore scheme of the hybrid kernels reflects the upper limit of the small pores and the lower limit of the large pores (transition pore size).

Adsorptive	Adsorbent	Branch (Method)	Pore Geometry	Pore Size Range	Pore Scheme
Ar at 87 K	Carbon	Adsorption (QSDFT)	Cylindrical	< 27 nm	
Ar at 87 K	Carbon	Adsorption (QSDFT)	Cylindrical/ spherical	< 50 nm	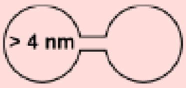
N_2 at 77 K	Carbon	Adsorption (QSDFT)	Cylindrical	< 33 nm	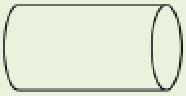
N_2 at 77 K	Carbon	Adsorption (QSDFT)	Cylindrical/ spherical	< 50 nm	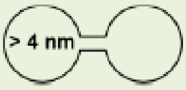
Ar at 87 K	Silica	Adsorption (NLDFT)	Cylindrical	0.35 – 100 nm	
Ar at 87 K	Silica	Adsorption (NLDFT)	Spherical/ cylindrical	0.35 – 40 nm	
N_2 at 77 K	Silica	Adsorption (NLDFT)	Cylindrical	0.35 – 100 nm	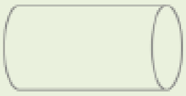
N_2 at 77 K	Silica	Adsorption (NLDFT)	Cylindrical/ spherical	0.35 – 40 nm	

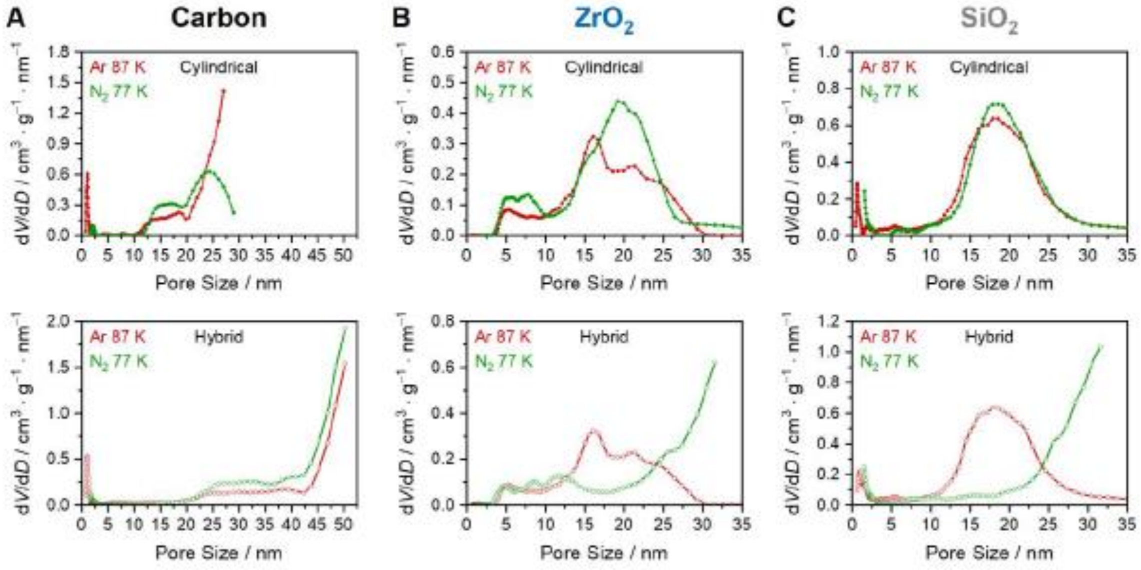

Figure S1. Pore size distributions of mesoporous (A) carbon, (B) ZrO_2, and (C) SiO_2 derived from the adsorption branch of nitrogen (77 K, green) and argon (87 K, red) isotherms with a DFT kernel for cylindrical pores (top) and a hybrid kernel assuming spherical/cylindrical pores (bottom).

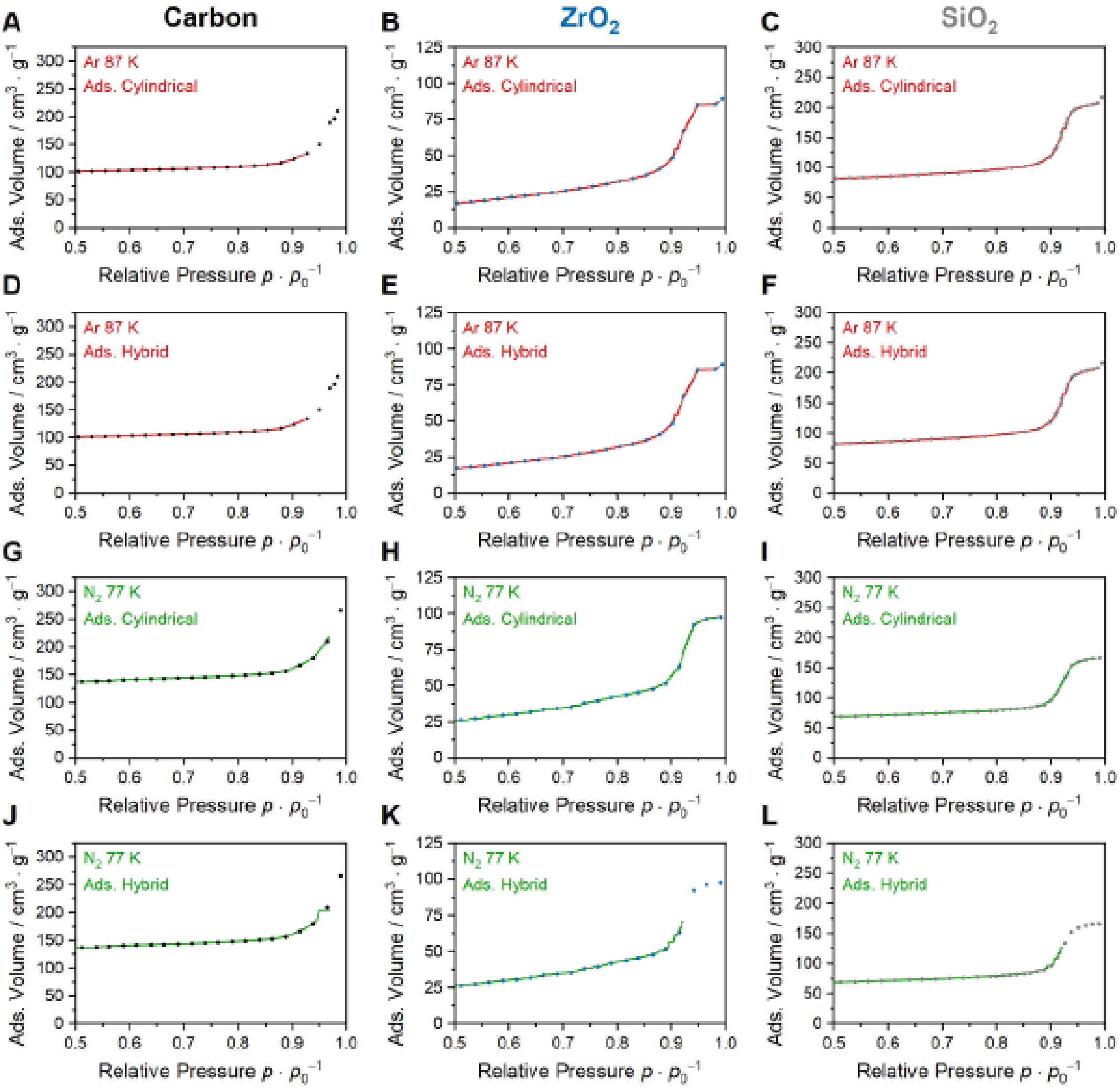

Figure S2. Comparison between measured (dotted line) and fitted isotherms (solid line) of mesoporous carbon (left), ZrO_2 (middle), and SiO_2 (right). The fitted isotherms base on eight different DFT kernels applied on the adsorption branch each: (A, D, G, J) a QSDFT kernel for carbonaceous materials while for the remaining plots an NLDFT kernel for siliceous materials was used; the hybrid kernels in (D, J, K, and L) assume a cylindrical/spherical pore geometry while in (E and F) a spherical/cylindrical geometry is assumed.

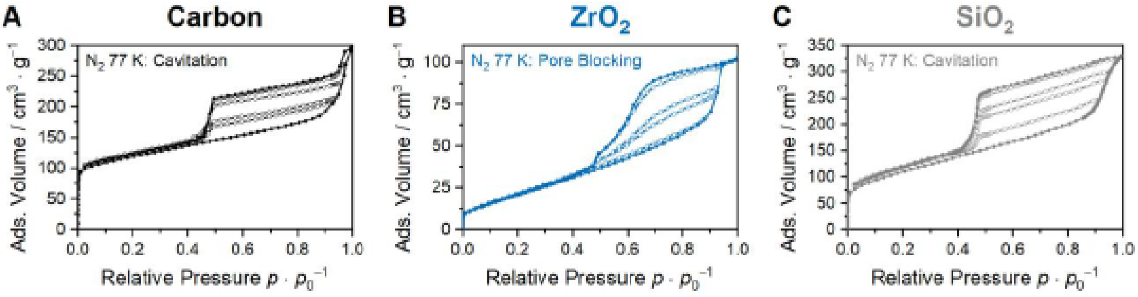

Figure S3. Nitrogen hysteresis scans at 77 K (without thermal compensation) of (A) mesoporous carbon (black), (B) ZrO_2 (blue), and (C) SiO_2 (gray) composed of a boundary loop (filled symbols) and four desorption scans (open symbols) each. Partial adsorption branches are omitted for clarity.

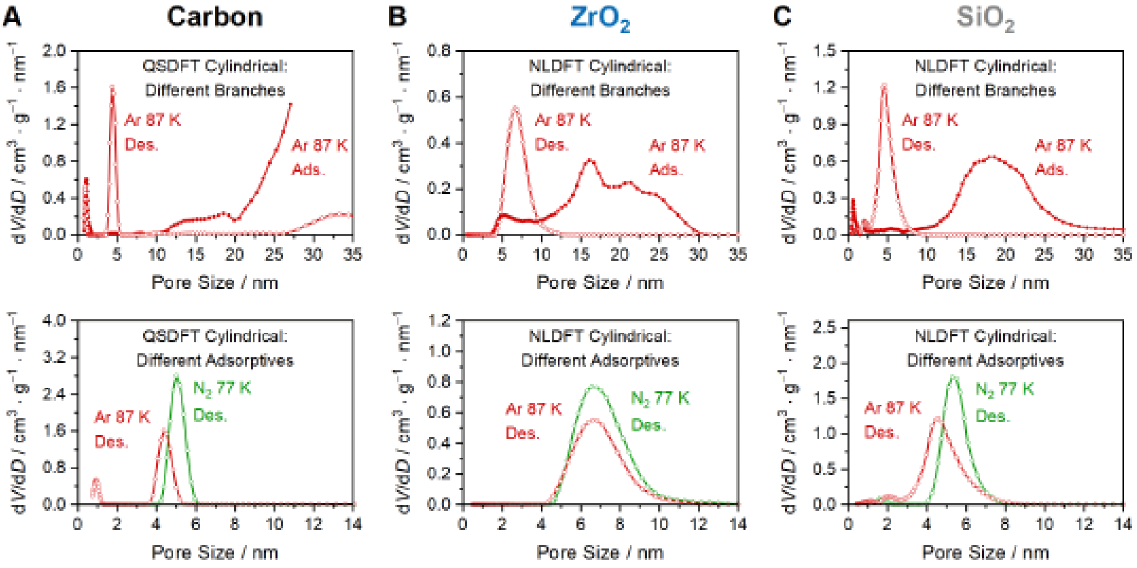

Figure S4. Comparison of the pore size distributions of mesoporous (A) carbon, (B) ZrO_2, and (C) SiO_2 derived from the adsorption branch (filled symbols) and desorption branch (open symbols) of the argon isotherm with a DFT kernel for cylindrical pores (top) and comparison of the pore size distributions obtained from the desorption branch of the argon (red) and nitrogen (green) isotherm with a DFT kernel for cylindrical pores (bottom).

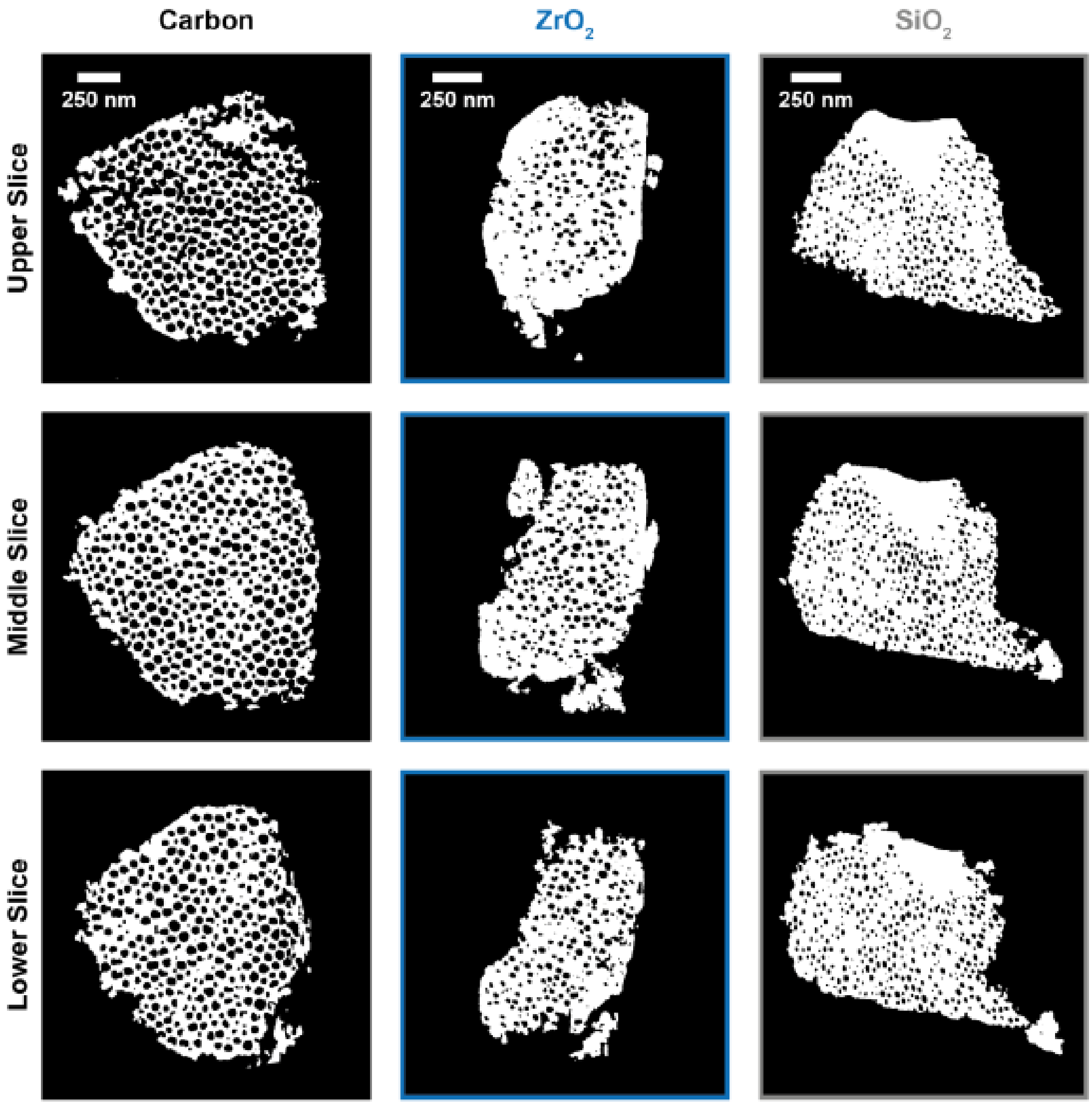

Figure S5. Selected slices along the *z*-axis through the entire 3D-reconstructed particle of mesoporous carbon (left), ZrO_2 (middle), and SiO_2 (right) obtained from STEM-based tomography.

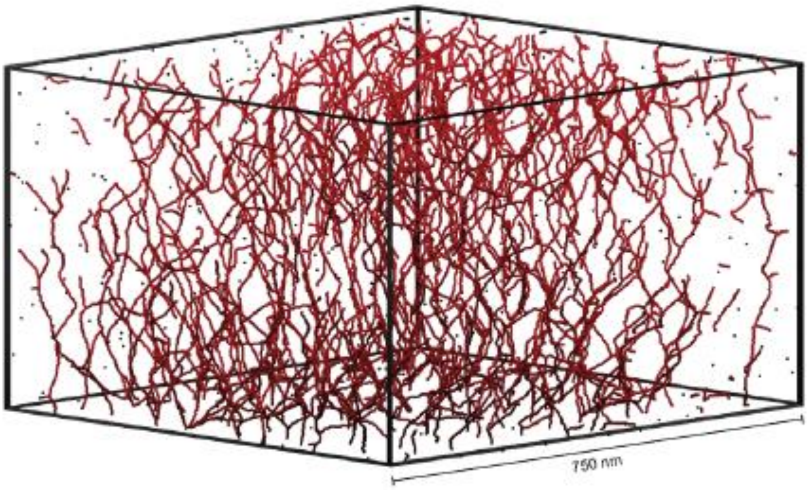

Figure S6. Visualization of the pore skeleton of mesoporous carbon obtained from STEM-based tomography. While the entire pore skeleton is shown in red, isolated pores are given as black dots.

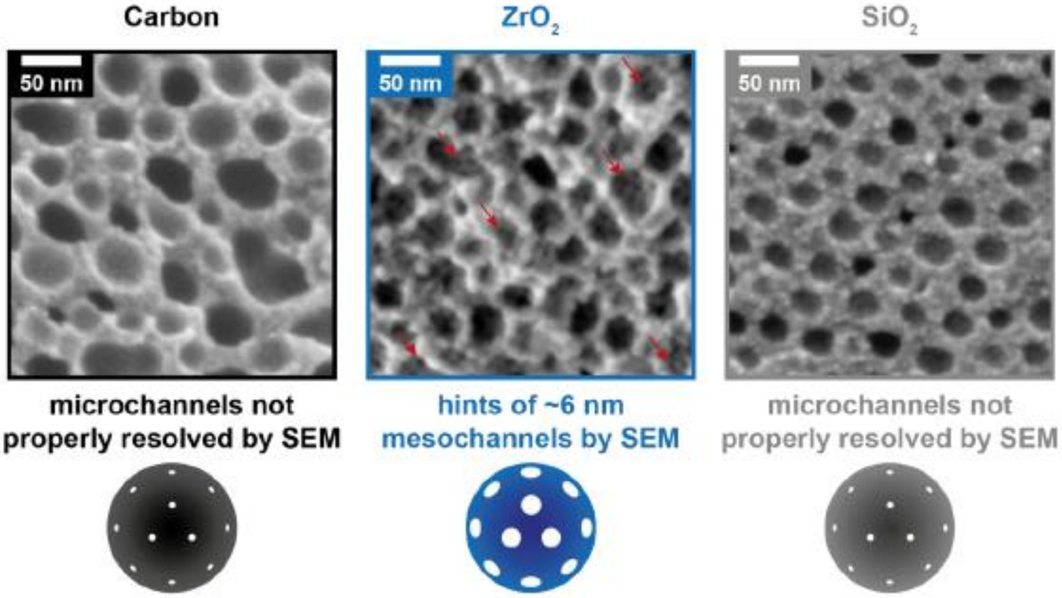

Figure S7. SEM images of mesoporous carbon (left), ZrO_2 (middle), and SiO_2 (right) and schematic representation of a single spherical mesopore containing differently sized PEO-induced channels. Red arrows in the SEM image of mesoporous ZrO_2 highlight these channels.

References

(1) Tanaka, S.; Katayama, Y.; Tate, M. P.; Hillhouse, H. W.; Miyake, Y. Fabrication of Continuous Mesoporous Carbon Films with Face-Centered Orthorhombic Symmetry through a Soft Templating Pathway. *J. Mater. Chem.* **2007**, *17*, 3639.

(2) Wagner, L. Q.; Schober, J.; Dippell, P.; Glatthaar, C.; Mekhilef, S.; Schäfer, D.; Hergert, H.; Rohnke, M.; Elm, M. T.; Smarsly, B. M. Mesoporous Carbon Thin Films with Large Mesopores as Model Material for Electrochemical Applications. *Adv. Funct. Mater.* **2025**. DOI: 10.1002/adfm.202521031.

(3) Wagner, L. Q.; Breckwoldt, F.; Huang, X.; Kübel, C.; Cheng, X.; Schladitz, K.; Smarsly, B. M. Porosity Tuning in Soft-Templated Mesoporous Silica: The Influence of Block Copolymer Composition and Concentration. *Langmuir* **2025**, *41*, 30948–30967.

(4) Cop, P.; Maile, R.; Sun, Y.; Khalid, O.; Djerdj, I.; Esch, P.; Heiles, S.; Over, H.; Smarsly, B. M. Impact of Aliovalent/Isovalent Ions (Gd, Zr, Pr, and Tb) on the Catalytic Stability of Mesoporous Ceria in the HCl Oxidation Reaction. *ACS Appl. Nano Mater.* **2020**, *3*, 7406–7419.

(5) Wagner, L. Q.; Prates da Costa, E.; Glatthaar, C.; Breckwoldt, F.; Zecca, M.; Centomo, P.; Huang, X.; Kübel, C.; Schlaad, H.; Kriechbaum, M.; Amenitsch, H.; Thommes, M.; Smarsly, B. M. Poly(ethylene oxide)-*block*-poly(hexyl acrylate) Copolymers as Templates for Large Mesopore Sizes ─ A Detailed Porosity Analysis. *Chem. Mater.* **2023**, *35*, 9879–9899.

(6) Weller, T.; Deilmann, L.; Timm, J.; Dörr, T. S.; Beaucage, P. A.; Cherevan, A. S.; Wiesner, U. B.; Eder, D.; Marschall, R. A Crystalline and 3D Periodically Ordered Mesoporous Quaternary Semiconductor for Photocatalytic Hydrogen Generation. *Nanoscale* **2018**, *10*, 3225–3234.

(7) Thommes, M.; Smarsly, B.; Groenewolt, M.; Ravikovitch, P. I.; Neimark, A. V. Adsorption Hysteresis of Nitrogen and Argon in Pore Networks and Characterization of Novel Micro- and Mesoporous Silicas. *Langmuir* **2006**, *22*, 756–764.

(8) Cheng, X.; Föhst, S.; Redenbach, C.; Schladitz, K. Detecting Branching Nodes of Multiply Connected 3D Structures. *Proceedings of the Mathematical Morphology and its Applications to Signal and Image Processing: 14th international symposium, ISMM 2019; Saarbrücken, Germany, July 8−10, 2019; Burgeth, B., Kleefeld, A., Naegel, B., Passat, N., Perret, B., Eds.; Springer International Publishing: Cham* ***2019****, 11564, 441–455.*

(9) Prates da Costa, E.; Huang, X.; Kübel, C.; Cheng, X.; Schladitz, K.; Hofmann, A.; Göbel, U.; Smarsly, B. M. Effects of Hydrothermal Treatment on Mesopore Structure and Connectivity in Doped Ceria-Zirconia Mixed Oxides. *Langmuir* **2023**, *39*, 177–191.

(10) Schmidt-Rohr, K. Simulation of Small-Angle Scattering Curves by Numerical Fourier Transformation. *J. Appl. Crystallogr.* **2007**, *40*, 16–25.

(11) Prates da Costa, E.; Huang, X.; Kübel, C.; Cheng, X.; Schladitz, K.; Hofmann, A.; Göbel, U.; Smarsly, B. M. Tuning Mesopore Accessibility of $Ce_{0.18}Zr_{0.64}Y_{0.15}La_{0.03}O_{2-\delta}$ by Hydrothermal Post-Treatment─A Case Study for Ceria-Based Oxidation Storage Materials. *Langmuir* **2023**, *39*, 17664–17679.

3.4 Publikation 4

Mesoporous Carbon Thin Films with Large Mesopores as Model Material for Electrochemical Applications

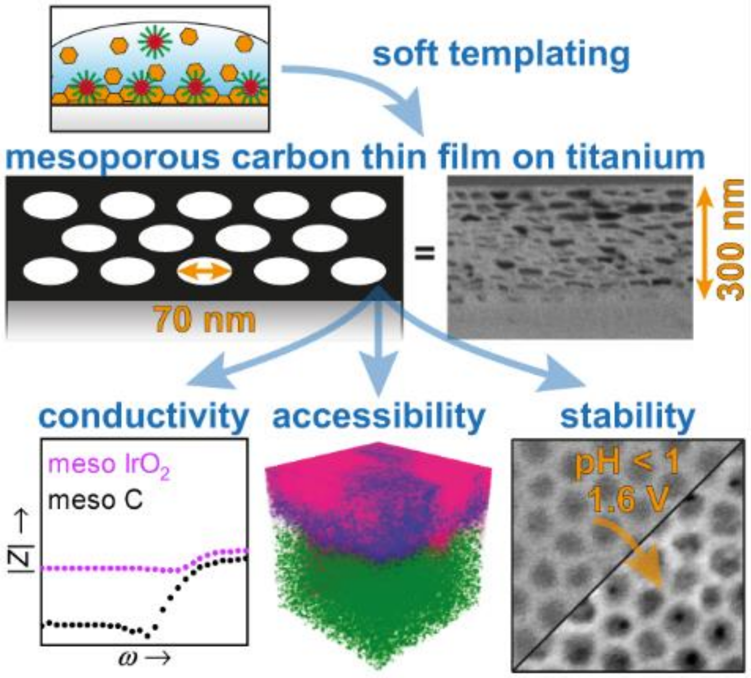

Reprinted with permission from

<u>L. Q. Wagner</u>, J. Schober, P. Dippell, C. Glatthaar, S. Mekhilef, D. Schäfer, H. Hergert, M. Rohnke, M. T. Elm, B. M. Smarsly, Mesoporous Carbon Thin Films with Large Mesopores as Model Material for Electrochemical Applications, *Adv. Funct. Mater.* **2025**, e21031.

DOI: 10.1002/adfm.202521031

RESEARCH ARTICLE

ADVANCED FUNCTIONAL MATERIALS
www.afm-journal.de

Mesoporous Carbon Thin Films with Large Mesopores as Model Material for Electrochemical Applications

*Lysander Q. Wagner, Joshua Schober, Pascal Dippell, Chantal Glatthaar, Smail Mekhilef, David Schäfer, Hannes Hergert, Marcus Rohnke, Matthias T. Elm, and Bernd M. Smarsly**

The synthesis of mesoporous carbon thin films is proposed on titanium plates with well-ordered 70 nm mesopores via soft templating of resol resins with poly(ethylene oxide)-*block*-poly(hexyl acrylate) copolymers. Surprisingly, regular carbonization in pure argon suffers from a metal substrate corrosion not yet observed in literature. This corrosion phenomenon is investigated by secondary ion mass spectrometry, electron microscopy, and X-ray diffraction, and it is identified that the introduction of carbon monoxide into the carbonization atmosphere as successful approach to suppress substrate corrosion without changing microstructure, composition, or pore structure of the non-graphitic carbon. The model electrodes, which consist of a 200–300 nm thick mesoporous carbon layer, the titanium substrate, and a 200 nm thick titanium carbide interphase, are tested for their suitability as electrocatalyst support: The electric transport through and along the thin film is investigated by impedance and Hall measurements and contrasted to similarly mesoporous IrO_2 thin films. Accessibility of the pore system and electrochemical stability under acidic water-splitting conditions are studied by SIMS and cyclovoltammetry, respectively. The mesoporous carbon thin films reveal a conductivity similar to IrO_2, high stability, and (tunable) accessibility, rendering them a promising model system for several applications like electrocatalysis and sodium-ion batteries.

1. Introduction

In the framework of energy transition, hydrogen might play a major role for temporary energy storage if so-called green energy (from wind or solar power plants) is converted to hydrogen in case of an oversupply. This hydrogen can be stored easily until the energy demand requires a reconversion of the chemical energy into electric energy.[1,2] In acidic water electrolysis, though, precious catalyst materials are needed, like iridium dioxide for the anodic oxygen evolution reaction (OER).[1] To save critical and expensive materials, a substitution by a non-critical yet conducting catalyst support is desired, on which the actual catalyst is deposited in small quantities (for instance, by atomic layer deposition).

Ordered mesoporous carbon seems to be a particularly promising model material as a catalyst support due to the large surface area,[3,4] a high mechanical and chemical durability,[5] and its abundance. Consequently, mesoporous carbon has been studied for several applications, even beyond water splitting. As summarized in **Figure 1**, such mesoporous carbon films can be used among others for pollutant removal (like heavy metal ions),[6] heterogeneous catalysis (e.g., olefin hydration),[7] gas storage (for instance, hydrogen storage for fuel cell vehicles),[8] electrocatalysis,[4] and electrode materials for capacitors[4,8] and sodium-ion batteries.[4]

While in the first three applications a metal substrate is not required (but from an industrial point of view desirable when considering stainless steel reactors), a conductive substrate is mandatory for the remaining three applications (as an electrocatalyst, capacitor, or battery material) to ensure an electric contact. For this reason, we present a specially designed synthesis of carbon thin films with well-ordered 70 nm mesopores optimized for a metal substrate. Please note that the large spherical pores in this study (partly) lie in the macropore regime according to the IUPAC definition of mesopores (2–50 nm). However, the term “mesopores” is still used herein to avoid confusion with very large pores (hundreds of nanometers) when talking of “macropores”, and with hierarchical pore systems when talking of “meso-/macropores”. The synthesis is not trivial due to possible substrate corrosion, which we identified as an unexpected obstacle and might have been overseen in previous studies. The majority

L. Q. Wagner, J. Schober, P. Dippell, C. Glatthaar, S. Mekhilef, D. Schäfer, M. Rohnke, B. M. Smarsly
Institute of Physical Chemistry
Justus Liebig University
35392 Giessen, Germany
E-mail: bernd.smarsly@phys.chemie.uni-giessen.de

L. Q. Wagner, P. Dippell, C. Glatthaar, D. Schäfer, H. Hergert, M. Rohnke, M. T. Elm, B. M. Smarsly
Center of Materials Research
Justus Liebig University
35392 Giessen, Germany

H. Hergert, M. T. Elm
Institute of Experimental Physics I
Justus Liebig University
35392 Giessen, Germany

The ORCID identification number(s) for the author(s) of this article can be found under https://doi.org/10.1002/adfm.202521031

DOI: 10.1002/adfm.202521031

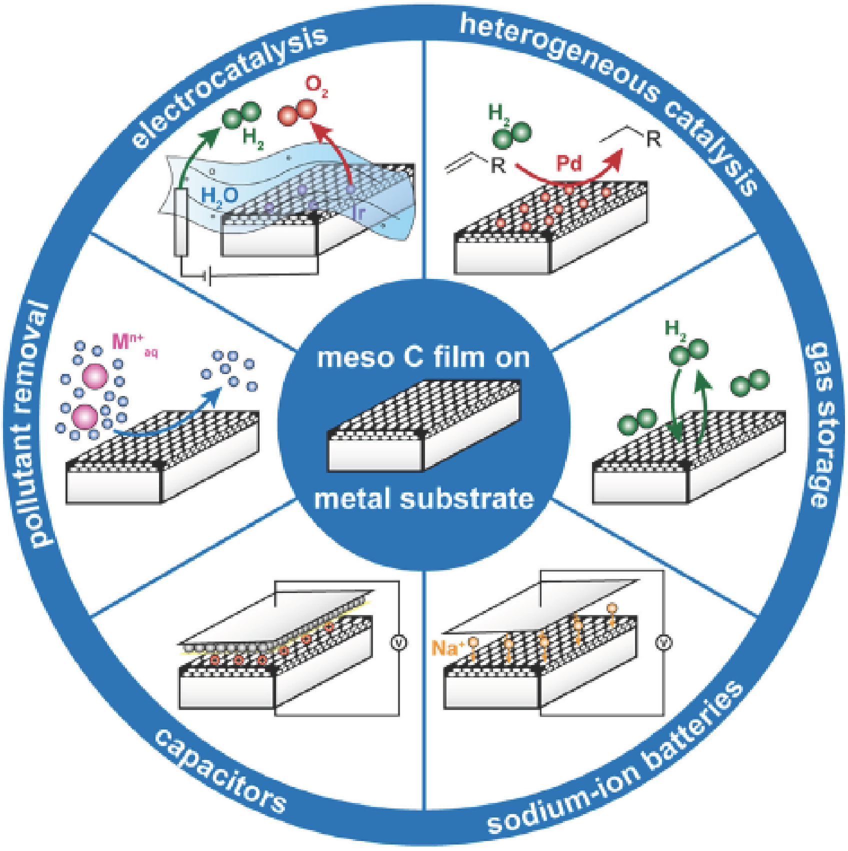

Figure 1. Possible applications of mesoporous carbon thin films deposited on metal substrates.

of articles on resin-derived carbon thin films base on samples prepared on silicon wafers, quartz glass, glassy carbon, and poly(ethylene terephthalate),[9–27] in which no alterations of the substrate were observed. Even works about carbon deposited on metal substrates such as stainless steel[7] and copper[28] do not report such a corrosion, which either might not have occurred there or remained undiscovered underneath the thick carbon film of 400–700 nm in size.

The template-based preparation of porous carbon materials seems to be well established, but there are still challenges in the synthesis, which are related to the transition from organic precursors (here: phenolic resins) to an amorphous and finally crystalline ("graphitic") carbon. It was particularly Helmut Cölfen who–as a pioneer–proposed and finally proved the groundbreaking idea that even highly ionic crystalline solids, such as $CaCO_3$,[29] may form through an amorphous particle, emphasizing the relevance of such pre-nucleation clusters[30–33] for the final material in nature. Interestingly, this concept holds true for the carbonization of organic materials, as some hydrocarbon-based materials, upon high-temperature treatment up to 3000 °C, form graphite while surprisingly others stay at the stage of non-graphitic carbons.[34,35] Those graphene-based carbon materials which do convert into graphite, namely "mesophase pitch" for instance, in essence, can – or need to – be interpreted as "mesocrystals" according to the concept introduced by Helmut Cölfen.[36–38] Since the conversion into graphite requires the parallel mutual arrangement of graphene stacks, and since their dimension commonly is on the nanometer scale, concepts of "non-classical crystallization" must be included for understanding the transition from amorphous to crystalline carbon via the intermediate formation of such "graphene mesocrystals".

Also, the templating of carbons using block copolymers involves questions similar to Cölfen's studies on manipulating biomineralization of basic inorganic compounds by block copolymers: the block copolymer micelles used as templates here might interact with the surrounding carbon precursor and also form carbonaceous species and thereby affect the transformation of amorphous carbon into graphene sheets, i.e., a "crystallization" process.[33,39–41] Thus, we try to elucidate – similar to the polymer-mediated biomineralization and "non-classical crystallization" – the impact of the block copolymers on the carbonization.

Although soft templating is used for preparing mesoporous carbon for 20 years,[42] most studies are restricted to small mesopores below 10 nm achieved with Pluronics polymers,[4,5,7,28,43–46] which might suffer from slow diffusion of reactants through the pore system.[47,48] The step toward larger mesopores of 30–70 nm comprising a still high surface area and ideally, a less restricted mass flow within the mesopores is possible by using different soft templates such as poly(ethylene oxide)-*block*-poly(styrene) (PEO-*b*-PS),[3,49] poly(styrene)-*block*-poly(4-vinylpyridine) (PS-*b*-P4VP),[42] and poly(ethylene oxide)-*block*-poly(hexyl acrylate) (PEO-*b*-PHA)[50] block copolymers. With the aid of the latter, we recently investigated the pore structure in mesoporous powders of metal oxides,[51] and successfully realized the synthesis and characterization of lignin-derived mesoporous hard carbons with variable pore sizes between 20 and 50 nm, applying soft templates of the PEO-*b*-PHA family.[52] However, these hard carbons possessed only isolated spherical mesopores, which appear to be beneficial for application in sodium-ion batteries[52] but are disadvantageous for electrocatalytic applications, in which pore accessibility for reactants has to be ensured. Otherwise, the catalytic activity decreases consecutively upon lowering the accessibility of the pore structure as recently shown for mesoporous carbon particles prepared from poly(styrene)-*block*-poly(dimethylsiloxane) copolymers.[53]

With regard to electrochemical applications, the synthesis of hard carbons with large mesopores[3,52] has to be combined with a protocol for obtaining mesoporous carbon with accessible pores[9] and then converted to a thin film procedure. Frequently studied carbon materials – typically, derived from phenolic resins – feature an accessible pore system in contrast to the aforementioned lignin-derived carbon and were already prepared in form of a thin film in the past[7,28,42,46] even though pore shape and/or size differed from that targeted here (large spherical mesopores of 70 nm in diameter). In literature, the majority of ordered mesoporous carbon films used as support for electrocatalysis were applied for the cathodic hydrogen evolution reaction (HER) so far but not for the anodic OER counterpart.[7,54] The obvious reason represents the fact that carbon typically gets oxidized to carbon dioxide (and partly carbon monoxide and surface oxygen species as well) if an oxidative (anodic) potential is applied.[55–59] Yet, carbon possesses a large variety in its chemical nature (e.g., graphitic in contrast to non-graphitic carbon), and so, carbon's stability in electrocatalysis differs as well, e.g., with a delayed carbon corrosion in case of graphitized carbon felts (corrosion starting from 1.2 V vs. RHE instead of $E_0 = 0.2$ V).[56,58] Therefore, a resorcinol-derived mesoporous hard carbon thin film might be sufficient to withstand the harsh electrocatalytic conditions of the acidic OER (i.e., pH of 1 and 1.2–1.4 V vs. RHE). By using a self-synthesized PEO_{372}-*b*-PHA_{180} block copolymer as soft template, we successfully prepared both mesoporous powders and thin films with circa 70 nm spherical pores on titanium plates.

Combining secondary ion mass spectrometry, electron microscopy, and X-ray diffraction, the substrate corrosion and strategies to avoid it were explored. Based on thermogravimetry coupled with mass spectrometry, we comprehend how the resin is transformed to the final carbon material while the (also organic) soft template is decomposed. Contrasting these findings to gas physisorption experiments of templated and non-templated carbon powders, we propose a detailed picture of the observed pore system, in which the intrinsic micropores of the resorcinol-derived hard carbon might play a major role in connecting the spherical mesopores. Next to an in-depth characterization of the carbon microstructure of the powder material by Raman spectroscopy and X-ray diffraction, we investigate the resulting properties of the thin film counterpart: While infiltration with a tracing electrolyte reveals insights into pore accessibility, the electric conductivity is studied by impedance spectroscopy and Hall measurements, and the stability under OER conditions is tested by cyclic voltammetry and electron microscopy. By these experiments, we study if mesoporous carbon thin films might fulfill the prerequisites of an electrocatalyst support – namely, an accessible pore system combined with a stable and conductive carbon skeleton, and thus might act as a promising material for electrocatalytic applications like the acidic OER.

2. Results and Discussion

2.1. Synthesis of Mesoporous Carbon

Ordered mesoporous carbon powders and thin films were prepared by a soft templating approach according to Tanaka et al.[9] based on a resorcinol-formaldehyde resin as a carbon precursor. The amphiphilic block copolymer PEO_{372}-*b*-PHA_{180} (subscripts denote the number of repeating units according to the NMR analysis in Figure S1, Supporting Information) applied as soft template was obtained by a supplemental activator reducing agent atom transfer radical polymerization (SARA ATRP) analogue to our recent study.[51] As illustrated in **Figure 2**, resorcinol and the soft template are independently dissolved prior to the combination and addition of triethyl orthoacetate (as pore-stabilizing agent[9]), and an aqueous formaldehyde solution (as cross-linker). For the synthesis of powders, which are required as a reference for deeper structural characterizations, the solution was directly dried in an oven, while for the preparation of the thin films, the reaction mixture was spin-coated on a polished titanium plate (as a conductive substrate) before drying. In both routes, drying at 80 °C promotes acid-catalyzed thermopolymerization of resorcinol and formaldehyde, yielding a resol resin in the space between the soft template.[60–62] The resin is then converted to a non-graphitic carbon (NGC) during the following heating step under an inert gas atmosphere, whereas the soft template is removed. The soft templating process, based in case of both powder and thin film on the evaporation-induced self-assembly (EISA) mechanism:[51,63–65] The block copolymer, which dissolves initially as a statistical coil in ethanol, undergoes micellization upon solvent evaporation (at 80 °C).[51] These micelles arrange themselves in an ordered, closed-packed array during proceeding evaporation and decompose selectively in the anaerobic carbonization step, yielding a mesoporous carbon pattern.

The soft templating procedure is not straightforward as it requires a selective built-down of only one organic phase (soft template) within a second stable one (resin), and the question thus arises if the soft template fully decomposes during the heating procedure. To answer this question, we coupled a thermogravimetric study with mass spectrometry of the released products (TG-MS), which reveals the underlying processes. The TG-MS experiment tells not only which fragments are released at which temperature but is also capable of checking the overall suitability of the heating ramp used in the synthesis, i.e., if the dwell times are properly chosen. Following the TG curves of the pure template, the pure resin, and the reaction mixture containing both (**Figure 3**) along the heating ramp, four steps become apparent: (1) removal of residual solvents and volatile species, (2) extrusion

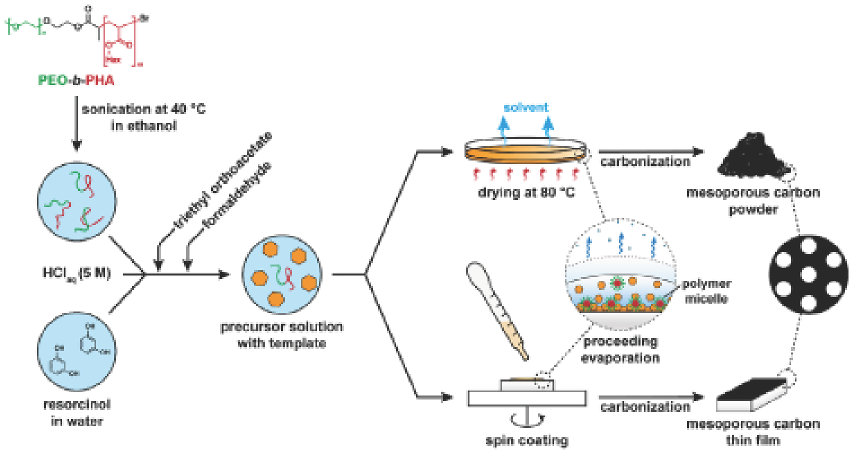

Figure 2. Overview on the synthesis of mesoporous carbon powders and thin films from resorcinol-formaldehyde (resol) resins with poly(ethylene oxide)-*block*-poly(hexyl acrylate) as soft template.

of water (by further condensation), (3) template decomposition, and (4) heteroatom removal during carbonization.

Until ≈200 °C (below 175 min), a mass loss of 10% (reaction mixture) and 12% (pure resin) is detected, which can be attributed to solvent removal following the MS signal of the water radical cations ($m/z = 18$) and the ethanol fragments (e.g., $m/z = 31$). In the case of ethanol, the fragment ion with $m/z = 31$ (protonated formaldehyde) is more reliable than the ion with $m/z = 27$ (ethylene cation), which also shows an increased intensity below 200 °C but could be confused with the ethylene cation released from the PHA block according to the fragmentation pattern in Scheme S1 (Supporting Information). Additionally, the release of residual formaldehyde ($m/z = 30$) can be found in this regime at ≈80 °C (see pure resol scan in Figure S2B, Supporting Information). Starting from 200 °C (after 175 min), a second water release step occurs ($m/z = 18$), which can be attributed to further condensation reaction in the resol resin. Indeed, ^{13}C-NMR studies of Meng et al. confirm further cross-linking in phenolic resins below 350 °C.[60] These yield a mass loss of circa 16% (reaction mixture) and 23% (pure resin), respectively. However, in the case of the reaction mixture, this step overlaps with the decomposition of the soft template (circa 18% mass loss) starting from 300 °C (275 min). The choice of unambiguous tracing ions indicating template removal arises from the proposed fragmentation pattern in Scheme S1 (Supporting Information) and is confirmed by the individual TG-MS scan of the pure template in Figure S2A (Supporting Information): Following a thermal depolymerization of the PHA block and subsequent electron impact ionization, a hexyl acrylate cation is formed, which can be built down to either a hexyl cation ($m/z = 85$) or an ethylene cation ($m/z = 27$). Both ions are clearly detectable (Figure S2A, Supporting Information) and possess an almost identical intensity evolution (both position and shape) during heating. Thus, a common source of both ions, such as the PHA block built down, is reasonable rendering these ions suitable for tracking the PHA block decomposition. The PEO block can be combusted according to two mechanisms shown in Scheme S1 (Supporting Information): either a thermal depolymerization releasing ethylene oxide cations ($m/z = 44$) or via α-C–H transfers[66] yielding several small aldehydes and alcohols. Among these, the generated ethanol produces the same fragment ions as the solvent before, which is the reason why an ion with $m/z = 31$ is observed next to the ethylene oxide cation ($m/z = 44$) in Figure S2A (Supporting Information) and Figure 3. Due to PEO's hygroscopic character, a water release ($m/z = 18$) can be detected during PEO decomposition. Since this signal is also found in the scan of the pure soft template (Figure S2A, Supporting Information), this ion can be assigned to the polymer and not to further resin cross-linking in Figure 3. Also, the intensity evolution of signals 44, 31, and 18 are all centered at 390 °C (Figure S2A, Supporting Information), hinting at a common source. From this individual scan, it becomes apparent that PEO decomposes slightly (≈10 °C) before the PHA block. Regarding the scan of the reaction mixture in Figure 3, both PEO and PHA combustion can be confirmed while monitoring the PEO fragments ($m/z = 44$ and $m/z = 31$), parallel water release from hydrophilic PEO ($m/z = 18$), and PHA fragments ($m/z = 27$), indicating removal of the entire template (both polymer blocks). A final mass loss of 14% (reaction mixture) and 19% (pure resin) starting from 450 °C (605 min) can be assigned to heteroatom removal from the resin following the cations $m/z = 44$ and $m/z = 18$ as shown in the fragmentation pattern in Scheme S1 (Supporting Information). Such further cross-linking of the aromatic benzene rings at higher temperatures is in alignment with ^{13}C-NMR and infrared spectra in the literature.[60]

A quantitative consideration of the mass losses is challenging because the starting composition (exact mass ratio of polymer to resin) used for TG-MS (after drying at 80 °C) is unknown. A semi-quantitative comparison between the reaction mixture and pure resin, however, is possible if a normalization on the first or last mass loss is performed (**Table 1**).

Normalizing on the first mass loss (10%) of the reaction mixture (last column in Table 1), which is especially in the case of the pure resin, relatively well separated from the pronounced condensation step, the 14% loss in the mixture is contrasted to 16% (initially 19%) mass loss in the pure resin. This suggests a more advanced heteroatom removal in the non-templated

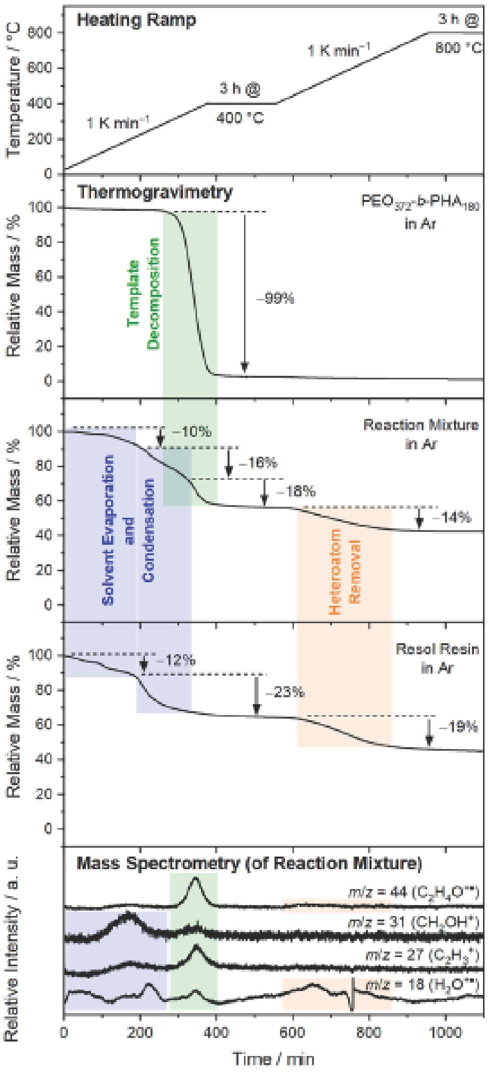

Figure 3. (Middle) Thermogravimetric analysis of the pure soft template, the reaction mixture, and the reaction mixture without soft template (pure resol resin) measured in argon following (top) the heating ramp used for the synthesis. In addition, (bottom) the evolution of the MS signals related to the release of water, ethanol, ethylene oxide, and PHA fragments from the reaction mixture are displayed, and processes describing solvent evaporation and condensation reactions (blue), polymer decomposition (green), and heteroatom removal during carbonization (orange) are highlighted.

sample, which is in alignment with our recent study.[52] Also, kinetic studies of Vogt and co-workers derived from infrared spectroscopy confirm a delayed cross-linking of the resin in the presence of a soft template.[10] However, a mass loss of ≈18% in the reaction mixture connected to polymer decomposition (second column in Table 1) hints at an incomplete template removal since a value of 25 – 37% is expected. This expected value derives from a gravimetric consideration if the weight fraction of all components in the initial reaction mixture is regarded (Figure 4). Following the recipe of a mesoporous powder in the experimental section, the soft template contributes 4.4 wt.% to the mixture. Assuming that ethanol, water, the aqueous formaldehyde solution, and the 5 M hydrochloric acid (composed of 0.7 wt.% water and 0.1 wt.% HCl compared to the entire mixture) represent volatile components during drying at 80 °C, 82.3 wt.% of the mixture's mass are removed while 17.7 wt.% remain in the resin residue after drying. The share of the soft template to the mixture is thus increased to 25% after removal of the volatile species (4.4 wt.% vs. 17.7 wt.%). In the actual synthesis, the weight of the mixture after drying dropped even stronger than the expected values in Figure 4. Both the batch with and without soft template experienced a weight loss being 5 wt.% higher although residual solvent is still present in the resin according to TG-MS (Figure 3). The reason might be the release of water during thermopolymerization and thus condensation of resorcinol and formaldehyde.[62] Consequently, the share of soft template in the resin could increase to even 37% (4.4 wt.% vs. 12.0 wt.%) yielding overall the aforementioned expected mass loss of 25–37%. Even though this argumentation claims soft template residues to be present in the final NGC (or a fraction of template being carbonized as well), an (at least partly) degradation of both blocks can be clearly concluded. Yet, NMR studies in literature demonstrated that PEO can be entirely decomposed within a phenolic resin.[60]

Table 1. Observed mass losses of the templated (meso) and non-templated sample (dense) according to thermogravimetry during (1) solvent evaporation, (2) condensation, (3) template removal, and (4) carbonization. Additionally, these experimental values are normalized to the mass loss of the dense sample during carbonization (fourth column) and to the mass loss of the mesoporous sample during solvent evaporation (fifth column) for comparison.

	observed Δm_{rel}		corrected Δm_{rel}	
step	meso	dense	meso	dense
(1)	−10%	−12%	−14%	−10%
(2)	−16%	−23%	−22%	−19%
(3)	−18%	–	−24%	–
(4)	−14%	−19%	−19%	−16%

Alternatively, if a similar carbonization behavior in both samples is assumed, i.e., normalization on the last mass loss (of 19%) of the pure resin (third column in Table 1), 24% (initially 18%) of mass is lost due to the soft template suggesting a full template removal if compared to the theoretical values discussed above. In summary, the analysis of the TG curves leads to the interpretation that either carbonization is less advanced while template residues might be present or that the soft template is fully removed, assuming a similarly advanced carbonization of the NGC skeleton in both the non-templated and mesoporous carbon. Although the question of a quantitative template removal cannot be answered accurately, this TG-MS study still confirms the suitability of the heating ramp as a plateau is reached both after template and after heteroatom removal, implying that longer heating steps would not lead to further improvements.

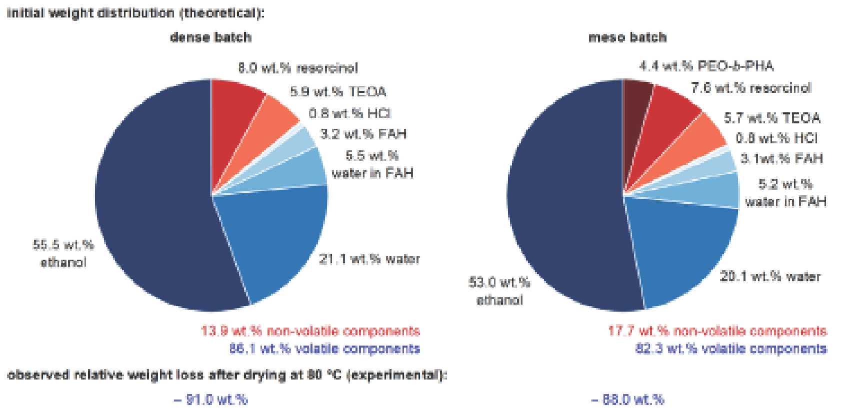

Figure 4. Weight distribution of all components in the synthesis of (left) non-templated and (right) soft-templated carbon according to the protocol in the experimental section, with TEOA describing triethyl orthoacetate, HCl describing hydrochloric acid, and FAH describing an aqueous formaldehyde solution. All non-volatile species are displayed in red colors, while volatile components are shown in blue. In addition, the relative mass loss from starting the reaction to the resin residue after drying is given at the bottom each.

2.2. Carbon Microstructure

Verifying the presence of graphene stacks formed during carbonization (at 800 °C) and required for electric conductivity, and a possibly larger extent of these stacks in the non-templated sample requires a detailed carbon microstructure analysis. The electron image in **Figure** 5A obtained by transmission electron microscopy (TEM) confirms that graphene stacks are present in the mesoporous carbon powder at a local level, but a statistical and reliable interpretation at a global level is only possible by other methods. In this regard, Raman spectroscopy can help to give a first statement. However, due to the small sample quantity in a thin film, this characterization is restricted to the powder state. Both samples possess a pronounced D (≈1340 cm^{-1}) and G band (≈1590 cm^{-1}) in the Raman spectra (Figure 5C) as well as the typical overtones between 2500 and 3000 cm^{-1} frequently observed in non-graphitic carbon.[52,67–70]

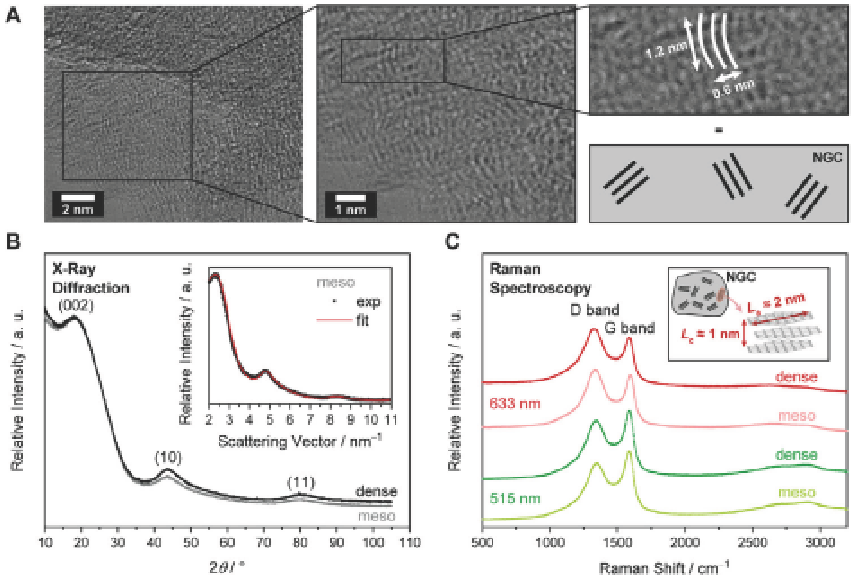

Figure 5. A) TEM image of mesoporous carbon powder with an exemplary graphene stack highlighted in white; the microstructure of this non-graphitic carbon (NGC) is sketched underneath. B) XRD patterns of non-templated (black) and mesoporous (gray) carbon powder (black) carbonized at 800 °C, as well as a fit of the latter according to an algorithm based on Ruland and Smarsly (ref.[76]) in the inset. C) Raman spectra of the non-templated (dark color) and mesoporous powder (light color) measured with an excitation wavelength of 633 nm (red) and 515 nm (green) shown with a scheme of an average graphene stack in NGC based on the XRD and Raman spectroscopy results in the inset.

The presence of the graphitic lattice mode (G band) and the defect-based D1 band already confirms the presence of graphene stacks, but their evaluation is only possible by a deconvolution of the overlapping D4, D1, D3, and G band (the D2 band is not expected here due to the comparably low carbonization temperature[52,69,71,72]). Applying two excitation wavelengths (633 and 515 nm) bakes up the evaluation as multiple correlation curves can be used for determining the intensity ratio of the D1 to the G band.[67] The deconvolution (Figure S3, Supporting Information) yields the D1 and G band position (633 nm) as well as the intensity ratio of the D1 to the G band I_{D1} I_G^{-1} (both 633 and 515 nm), from which the extent of the graphene sheets can be estimated by comparison with the empirical correlation curves of Schuepfer et al.[67] and Osswald et al.[72] shown in Figure S4 (Supporting Information). Comparing the non-templated (dense) sample with the mesoporous one, the G band is slightly shifted to larger wavenumbers while the D1 band is shifted to smaller values; also, the intensity ratio I_{D1} I_G^{-1} is a bit higher. All these trends hint at a slightly larger layer extent in case of the non-templated sample. The larger graphene sheet extent in the non-templated powder confirms the assumption of a lower heteroatom removal drawn from TG-MS and is in alignment with our previous study[52] on lignin-derived hard carbons. In absolute values, however, the effect is rather small: Depending on the applied correlation curve, an average graphene layer extent L_a of 2.5–3.5 nm is obtained (see Table S1, Supporting Information) with the dense sample possessing a slightly larger L_a value (by 0.1–0.2 nm). Yet, a recent wide-angle neutron scattering study showed that the correlation curve in Figure S4A (Supporting Information) overestimated L_a,[72] and a value of 1.3 nm might be more reasonable. Generally, the Raman-based estimation is affected by two major drawbacks: (1) Defects influence the Raman spectrum and thus, the regarded correlations depend on the applied carbon precursor.[67] This becomes particularly apparent from the deviation of the empirical values from the calibration curve in Figure S4C (Supporting Information) and the difference between pitch- and resin-based carbons[67] hampering the evaluation of the 515 nm spectra. (2) Furthermore, the correlation curves of G band position and intensity ratio are not universal, i.e., yield two L_a values in most cases. In this work, the smaller layer extent of 1.5–3.5 nm is rather obviously preferred over the large one beyond 8 nm according to comparable carbon samples in literature prepared at a low carbonization temperature (800 °C), resulting in ≈2 nm graphene layers.[52,67] Additionally, the TEM image in Figure 5A shows only occasionally small graphene stacks of $L_a = 1.5$ nm in diameter, supporting this theory. Nevertheless, the graphene layer extent from Raman spectroscopy possesses a large uncertainty and hence needs further confirmation.

Wide-angle X-ray scattering (WAXS), therefore, is a powerful tool to not only validate the Raman-based L_a value but also to gain deeper insights into various microstructure parameters of such turbostratic carbons.[73,74] By fitting the WAXS data with an algorithm based on Ruland and Smarsly[74] with the aid of the *OctCarb* script[75] and the GNU *Octave* software,[76] the average graphene layer extent L_a, the average interlayer spacing a_3, and the average stack height L_c can be determined among others (Table S2, Supporting Information). Doing that, the WAXS data in Figure 5B comprising the (002) reflection from inter- as well as the (10) and (11) reflection from intralayer scattering can be fitted as shown in the inset for the mesoporous powder (and Figure S5, Supporting Information for the non-templated sample), which delivers slightly more advanced graphene stacks in the non-templated carbon with $L_a = 1.9$ nm (vs. mesoporous carbon: $L_a = 1.8$ nm), $a_3 = 0.37$ nm (meso: 0.37 nm), and $L_c = 0.74$ nm (meso: 0.84 nm). Thus, the aforementioned hypothesis of a slightly restricted carbonization due to soft templating is confirmed, as well as the presence of nano-sized graphene stacks in both samples. In conclusion, graphene stacks of ≈2 nm in width and 1 nm in height can be found in this non-graphitic carbon, corresponding to the illustrated stack in the inset of Figure 5B and agreeing with both the example in the TEM image in Figure 5A and comparable samples in literature[52,67] carbonized at 800 °C. These graphene stacks play an important role in introducing electric conductivity into the material and thus are necessary for an application as an electrocatalyst support.

2.3. Morphological Investigation of the Mesopore Structure

So far, the carbon microstructure has been intensively investigated, but not the targeted mesoporous morphology. Concerning the powder sample, several characterization tools are applicable such as (scanning and transmission) electron microscopy (SEM and TEM) and gas physisorption. Both the SEM and TEM image in **Figure 6A** and B reveal an ordered pore system with spherical pores of 60 nm in diameter. Taking our previous studies of PEO-*b*-PHA-derived metal oxides[51] and carbon[52] into account, pore size and shape observed in this work are in good agreement with the previous works. The fact that the TEM-based pore size is slightly larger than the SEM-based one – although still being within the experimental error comparable – might be due to a systematic underestimation of SEM-derived pore sizes because the breaking plane resulting in the spherical cavities at the surface (observed in Figure 6A) in most cases does not cut the spherical pore along the center, i.e., along the maximum perimeter.

In contrast to a thin film, a powder sample enables a precise physisorption measurement, drawing a global picture of the pore structure. The nitrogen isotherm (Figure 6C) supports the presence of a mesoporous material according to the hysteresis loop. Although a significant cavitation phenomenon becomes apparent, claiming a poor pore accessibility through narrow bottlenecks analogous to comparable silica powders,[51] the significant mesopore volume confirms that the mesopore network is accessible at all in difference to comparable lignin-derived carbons.[52] Furthermore, the isotherm states that a significant number of micropores is present as well, which could be assigned to micropore channels induced by PEO single chains similar to mesoporous silica samples.[51] However, a comparison with the nitrogen isotherm of the non-templated carbon powder (black dots in Figure 6C) evokes the hypothesis that these micropores originate from intrinsic cracks of the hard carbon. These intrinsic micropores featuring a larger surface area than mesopores of the same pore volume also explain the higher specific surface area of the non-templated sample compared to the mesoporous one in Figure 6C. The micropore volume of both powders matches almost perfectly, whereas lignin-derived hard carbons do not possess any (accessible) microporosity if prepared

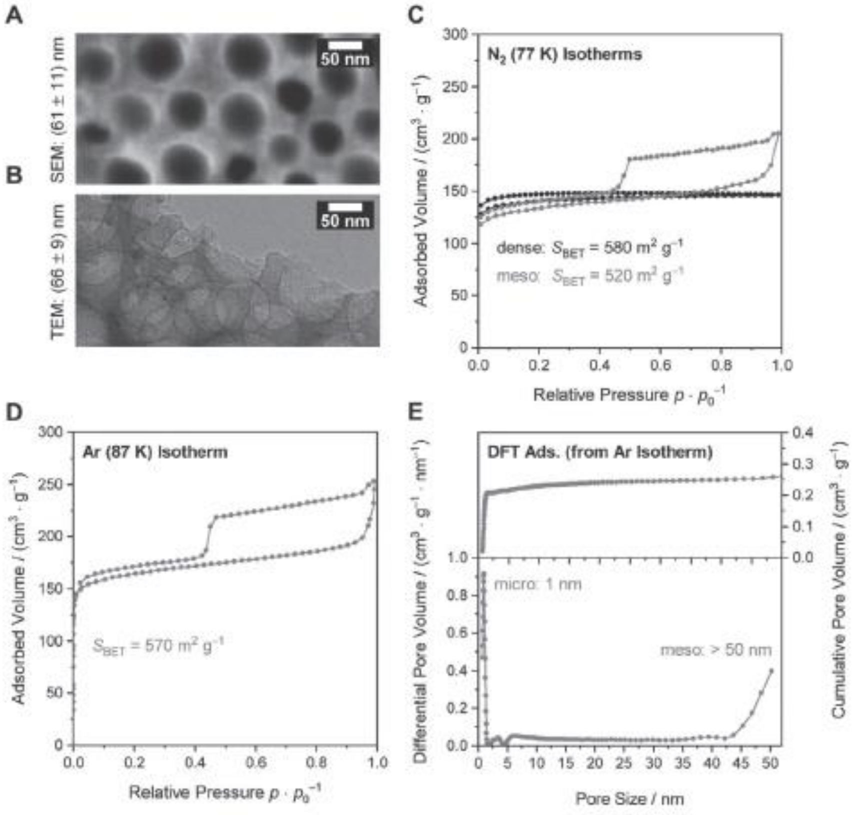

Figure 6. A) SEM and B) TEM image of mesoporous carbon powder. In addition, C) the nitrogen isotherms at 77 K of the mesoporous powder (gray) is contrasted to that of the non-templated (dense) one (black). The D) argon isotherm at 87 K of the mesoporous sample and (E) the corresponding pore size distribution obtained from the adsorption branch applying a QSDFT hybrid kernel for cylindrical/spherical pores are shown for deeper pore analysis as well.

without a soft template.[52] If prepared in a mesoporous fashion, different amounts of microporosity are observed by physisorption depending on the template used to prepare these lignin-derived carbons.[52] Still, the MS signal ($m/z = 44$) in Figure 3 clearly confirms a PEO decomposition here, which is in alignment with NMR studies of resin-derived carbons in literature,[60] but apparently does not increase the micropore volume per gram carbon compared to the non-templated reference powder. This contradiction can be resolved by the templating model sketched in **Figure 7**: Upon heating at 80 °C, the solvent evaporates while cross-linking of the carbon precursor takes place simultaneously. As a result, a closely packed pattern of polymer micelles forms,

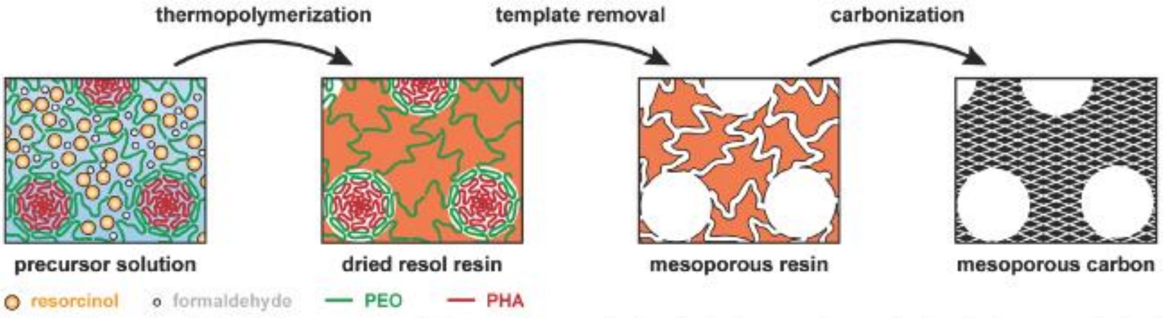

Figure 7. Schematic evolution of the pore structure during template removal and carbonization converting template-based micropores to intrinsic micropores.

embedded in the resol resin. During the first heating ramp under inert atmosphere, the soft template is removed (see TG-MS study in Figure 3), yielding a pore structure in which mesopores are connected by micropore channels. This situation depicted in the third image of Figure 7, represents the pore structure of amorphous mesoporous silica.[51] Increasing the temperature even further leads to a collapse of these micropores, while intrinsic micropores are formed during carbonization. These intrinsic micropores are often interpreted as voids between graphene stacks according to a house-of-cards model,[77–79] and indeed, a significant microporosity is frequently observed in comparable hard carbons.[3,60] Consequently, a homogeneously microporous carbon skeleton is obtained, explaining the same amount of micropore volume in the mesoporous carbon as for the non-templated powder. This represents a major difference to lignin-derived hard carbons and might explain the presence of isolated mesopores in them while applying a comparable PEO-*b*-PHA copolymer as soft template. If this carbon precursor system intrinsically does not form a comparable high number of micropores as phenolic resins, which might be responsible for connection and thus accessibility of the large mesopores, an isolated (meso)pore system is obtained. Note that the schematic representation in Figure 7 focuses on the evolution of the micropores during heating and does no state that all mesopores are only connected by micropores, as shown here. The possibility of mesopore connection through larger mesopore windows derived from micelle overlapping observed in silica[51] might also occur here as well.

In order to determine the pore size by physisorption, a detailed argon isotherm was recorded at 87 K (Figure 6D). The presence of micropores of 1 nm in size is clearly confirmed by the DFT-based pore size distribution in Figure 6E, which also reveals the presence of larger cavities above 40 nm in diameter. Although the QSDFT hybrid kernel applied on the adsorption branch is expected to be particularly suitable for spherical mesopores connected by cylindrical micropores,[80] an accurate pore size determination is challenging in this case because current QSDFT evaluation models have been programmed for pore sizes only up to 50 nm yet. Hence, a mode pore size above 50 nm can be concluded to be in alignment with electron microscopy, but an exact value cannot be given with this method here.

2.4. Substrate Corrosion in Mesoporous Carbon Thin Films

Transferring the powder synthesis to mesoporous carbon thin films requires spin coating of the same precursor solution onto a defined substrate. When using a titanium plate as substrate, which is necessary in electrocatalysis to ensure electric contact, however, bright tarnished spots are obtained on the otherwise deep black carbon coating (expected for non-graphitic carbon) after carbonization in a tube furnace with continuous argon flux. The surface scans in Figure S6 (Supporting Information) acquired by secondary ion mass spectrometry (SIMS) confirm the presence of titanium oxide species on the surface. The overlay of the C_4^- ($m/z = 48.00$) and TiO_2^- ($m/z = 79.94$) ion signals clearly demonstrates the presence of two separated phases: the non-graphitic carbon and a titanium species – possibly titanium oxide. Also, if a blank, polished Ti substrate without any carbon coating is annealed under analogous conditions, a tarnished surface is obtained, yielding fragment ions composed of titanium and oxygen in SIMS (Figure S6, Supporting Information). Since SIMS only provides information on the elemental composition, an assignment of the actual phases remains unclear. For this reason, X-ray diffraction under grazing incidence (GIXRD) of the annealed substrate and the mesoporous carbon film is needed to understand the origin of the titanium species. The GIXRD patterns in Figure S6 (Supporting Information) unambiguously show the expected occurrence of substrate-related reflections (e.g., the main reflection of Ti metal at $2\theta = 40°$) as well as the presence of TiO_2 (rutile structure), as can be seen from the reflections at $2\theta = 27°$ and 54° in both the annealed substrate and the carbon thin film. The carbon phase almost drowns out due to the little amount of carbon and the low scattering intensity of the rather amorphous NGC phase. A small background observed in XRD around $2\theta = 20°$ can be assigned to the carbon coating. These experiments strongly hint that the corrosion of the Ti substrate (i.e., formation of TiO_2) is responsible for the surface impurity leading to the tarnished appearance of the thin films. Several attempts were investigated to mitigate this corrosion, and we discovered that the introduction of 15 vol.% of carbon monoxide to the inert feed gas during carbonization was sufficient to prevent the formation of oxide particles (see the Supporting Information for more details). When carbonized in such an Ar/CO mixture, neither TiO_2-related ions are found by SIMS nor corresponding reflections by GIXRD (Figure S6, Supporting Information). While SIMS confirms the surface to be composed solely of non-graphitic carbon, the GIXRD pattern features, in addition to Ti-related reflections, several signals that can be assigned to titanium carbide (located at $2\theta = 36$, 42, and 60°). These can be found in the pattern of the carbon film carbonized in pure argon as well, but the absence of Ti-containing ions in the SIMS surface scan of the apparently non-corroded thin film raises the question where TiC is located. To tackle this question, depth profiles of the mesoporous carbon thin films carbonized in pure Ar and the Ar/CO mixture, respectively, were recorded by SIMS (**Figure 8**A,B). Here, the intensity profiles of all mass signals were normalized and stacked for a better overview.

In case of the thin film carbonized in pure argon (Figure 8A), many titanium/oxygen species like TiO^- and TiO_2^- (but also TiO_3^- in Figure S17A, Supporting Information) and heavy carbon fragments like C_4^- (and also C_7^- in Figure S17A, Supporting Information) can be found near the surface. Overall, the intensity evolution of the carbon- and titania-based ions shows a comparable sigmoidal trend of a decay ≈700 nm in depth upon ongoing sputtering. Yet, a small deviation between these two kinds of fragments becomes apparent between 400 and 600 nm with an increase in carbon-based signal intensity next to a small decrease in titania-based signal intensity. This observation can be explained with TiO_2 particles on the former surface of the thin film (see SEM images in **Figure 9**; Figures S8,S9, and S13, Supporting Information) leading to a relative enrichment of titania-derived ions at the (former) surface and a relative enrichment of carbon-based signals underneath the (former) surface after sputtering through these surface particles and reaching the actual carbon film. Generally, the evolution of the signal's intensities claims for a surface layer composed of hard carbon and TiO_2 with the latter being the dominating species. After further sputtering (> 600 nm), the aforementioned signals become weaker whereas

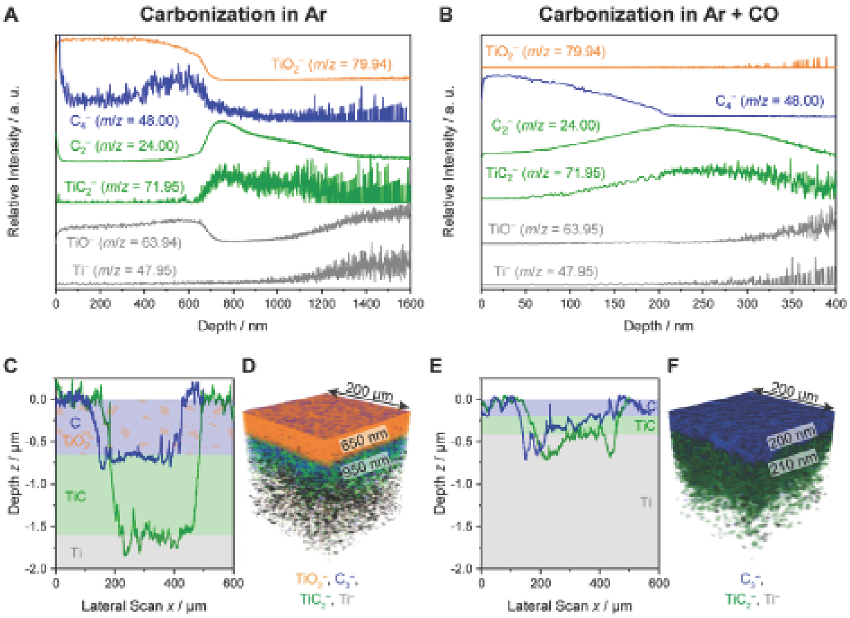

Figure 8. SIMS depth profiles of mesoporous carbon thin films on titanium substrates carbonized in A) pure argon and B) a mixture of 85 vol.% argon and 15 vol.% CO comprising the evolution of the ion signals assigned to the TiO_2 phase (in orange), the hard carbon phase (in blue), the TiC phase (in green), and the metal substrate (in gray) with proceeding sputtering. The (C and E) AFM scans of the sputter craters before reaching the TiC interphase (blue) and the metal substrate (green), respectively, are given as well as the (D and F) 3D overlay of the TiO_2^-, C_3^-, TiC_2^-, and Ti^- signal with the respective layer thickness from AFM.

the ion signals of lighter carbon fragments like C_2^- (and also C_3^- in Figure S17A, Supporting Information) and titanium/carbon species like TiC_2^- (and also TiC^- in Figure S17A, Supporting Information) become more intense. The parallel intensity trend of these two kinds of fragments hint at the appearance of the TiC phase observed by GIXRD (Figure S6, Supporting Information). Moreover, the opposed intensity evolution of the light vs. the heavy carbon fragments evokes the hypothesis that non-graphitic carbon, possessing small graphene stacks (see Figure 5), decomposes preferentially into larger carbon species while the carbide only forms small carbon anions (see Figure S17C, Supporting Information). This might be reasonable since larger carbon species most likely are more challenging to from starting from the rock salt structure of TiC than from a large carbon network, i.e., a non-graphitic carbon containing aromatic ring structures. For depths > 1200 nm, the TiC-related ion signals become less intense or at least their signal noise increases in parallel to an increase of the TiO^- and Ti^- ion count, which can be assigned to the crossing of the TiC/Ti interface and a penetration of the metallic substrate. Consequently, a mixed C/TiO_2 surface layer and a TiC interphase on top of the metallic substrate can be concluded from the depth profiles in Figure 8A, which becomes obvious in the 3D overlay of the TiO_2^-, C_3^-, TiC_2^-, and Ti^- ion signals in Figure 8D, confirming a layered structure. The thickness of the respective layers requires an additional measurement. The atomic force microscope (AFM) implemented in the SIMS setup enables topographic analyses of the created sputter craters. When sputtering is stopped at the inflection point of the signal intensity evolution (e.g., the TiO_2^- signal evolution), the sputter crater can be assumed to end at the interface between two phases. Thus, the two depth profiles in Figure S17A,C (Supporting Information) correspond to sputter craters terminating at the interface between the C/TiO_2 and TiC phases and the interface between TiC and the substrate, respectively. The corresponding height profiles of the sputter craters obtained from AFM in Figure 8C give access to the layer thickness by measuring the height difference each. As a result, the fluence (sputter ion exposure) can be converted to the depth (*x*-axis) in Figure 8A and B (since the sputter rate of each layer is known through the measured layer thickness), and an overall structure of a 650 nm thick C/TiO_2 surface layer above a 950 nm thick TiC interphase is obtained for the corroded sample.

The carbon thin film carbonized in an Ar/CO mixture, however, gives no indication of any TiO_2 at the surface (Figure 8B), which can be concluded from the initial absence of TiO^- and TiO_2^- ions. On the contrary, only carbon-based fragments can be found (C_3^-, C_4^-, and C_7^- in Figure S17B, Supporting Information) following all the same trend. Surprisingly, the C_3^- signal follows the trend of the heavier carbon fragments and not that of the carbide-derived ones as observed in the corroded sample in Figure 8A. Apparently, the ionizability of this ion is significantly increased by the absence of TiO_2 in the hard carbon matrix. Underneath the carbon phase at 200 nm, the evolution of the observed ion signals is very similar to those in the corroded sample. Thus, a pure hard carbon phase on the titanium substrate with a TiC interphase between them, possessing again a layered structure (see the 3D overlay in Figure 8F) can be concluded by this SIMS analysis. Performing a similar AFM study of the sputter craters leads to strikingly thinner layers

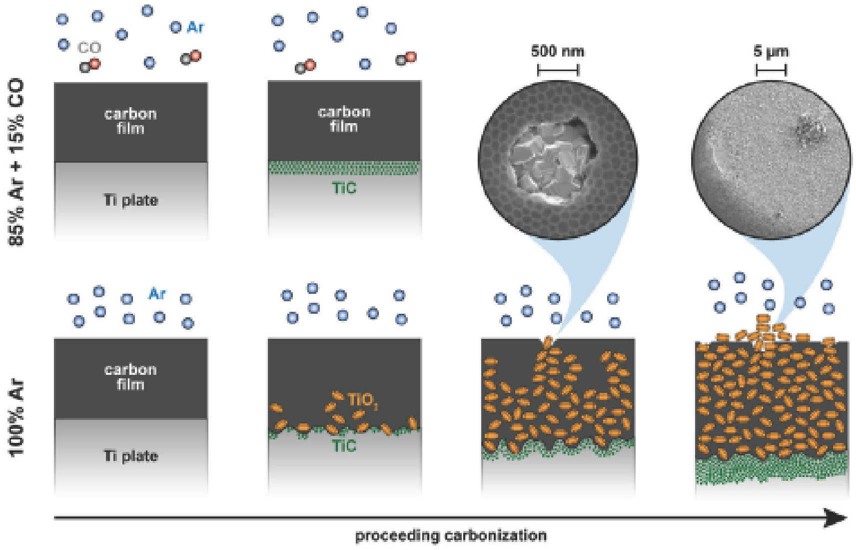

Figure 9. Proposed corrosion mechanism of the titanium substrate if no reducing agent is mixed to the inert feed gas (below) including two SEM images of the titanium oxide particles. In case of an Ar/CO atmosphere (top), only a thin TiC interphase is formed.

compared to the corroded sample: a 200–300 nm thick hard carbon thin film above a 210 nm thick TiC interphase is observed. Measuring the film thickness of the carbon layer is hampered by the crack at a lateral position of ≈200 µm (blue profile in Figure 8E) but from the remaining crater, a thickness between 200 and 300 nm can be concluded, which is confirmed qualitatively by SEM of the cross-section of an analogous carbon film on silicon yielding a thickness between 300 and 400 nm (see below). The reliability of the AFM scans is supported by monitoring the depth profile in the forward and backward direction being in good alignment as shown in Figure S18 (Supporting Information).

The reason that both the mesoporous carbon film and the TiC interphase are tremendously thinner may be the absence of the substrate corrosion by TiO_2 formation. As shown in Figure 9, the oxide forms in the shape of nano-sized particles, and according to the proposed corrosion mechanism, their formation roughens the substrate surface, which makes it more prone to the formation of carbide at the interface. Combining the results from SIMS and the synthesis optimization in the Supporting Information, oxygen traces (from either the feed gas or – more likely – the metal substrate containing 0.25% oxygen according to the supplier) cause the formation of TiO_2 at the metal surface during carbonization. These oxide particles grow through the carbon matrix, break through the surface, and spill over the thin film surface like a volcanic eruption. This coverage of the sample surface with TiO_2 could explain the shape of the C_4^--depth profile in Figure 8A possessing a maximum at ≈500 nm. After sputtering the surficial oxide particles embedding some residual carbon, the actual hard carbon layer (≈300 to 400 nm estimated from the depth profile) infiltrated with TiO_2 is uncovered, showing a similar film thickness as the non-corroded thin film. If a sufficient amount (15 vol.%) of CO as a reducing agent is introduced to the feed gas, the TiO_2 formation is inhibited, the flat carbon film is allowed to carbonize without perturbation, and a homogeneously thin TiC interphase is built at the interface.

To ensure that the introduction of CO into the inert atmosphere does not change the chemical nature of the non-graphitic carbon, mesoporous carbon powders were prepared under different carbonization atmospheres. As shown in Figure S19A (Supporting Information), the XRD patterns look alike irrespective of the resin was carbonized in nitrogen (muffle oven), argon, or a mixture of 85 vol.% argon and 15 vol.% CO (both tube furnace). Consequently, the choice of inert gas does not affect the microstructure of the non-graphitic carbon. To elucidate if possible changes in oxygen content occur when CO is employed as reducing agent, a dried resin and two carbon powders obtained from it after carbonization in pure argon and a Ar/CO mixture, respectively, were analyzed by X-ray photoelectron spectroscopy (XPS). The spectra in Figure S19 (Supporting Information) confirm the expected heteroatom removal upon carbonization leading to an decrease in oxygen content from 24 at.% to 14 at.% (Ar) and 15 at.% (Ar + CO), respectively. However, the elemental composition of both carbonized materials is very similar so that no influence of the CO introduction can be found. Also, this experiment demonstrates that the beneficial role of CO during corrosion inhibition is not due to the direct reduction of the resin but rather due to trapping of oxygen traces before they can react with the titanium metal. Consequently, there is no indication that CO chemically influences the non-graphitic carbon and solely prevents the substrate from being oxidized.

The general formation of titanium carbide at the interface between resin and metal substrate is not surprising if the phase diagram of carbon and titanium is taken into account. At high temperatures like 800 °C, the formation of TiC is thermodynamically expected.[81,82] Yet, the question remains whether this TiC interphase impedes the electrocatalytic application of the mesoporous carbon thin film carbonized in an Ar/CO mixture –, e.g., if the interphase acts as electric insulator. Indeed, TiC is considered as a good electric conductor and thus is investigated as supercapacitor and electrocatalyst support itself.[83–85] However, to check the suitability of the proposed thin film prepared on a metal substrate for later applications, the electric conductivity, electrochemical stability, and pore accessibility need to be studied in more detail.

2.5. Properties of Mesoporous Carbon Thin Films

Summing up, the successful synthesis of a flat and ordered-mesoporous hard carbon thin film with nano-sized graphene stacks (microstructure in Figure 5), a film thickness of 200–300 nm, and 70 nm spherical mesopores (Figure 9 and see below) was shown. Yet, for application as electrocatalyst support, the carbon thin film must fulfil the following features: (1) the carbon layer has to be electrically conductive, (2) the film has to withstand harsh electrocatalytic conditions (e.g., pH 1 and 1.2 V anodic potential in OER), and (3) the mesoporous network has to be accessible for catalyst deposition and the catalysis in general.

2.5.1. Electric Transport

In order to investigate the electric transport through the non-graphitic carbon, we measured the in-plane resistance (along the surface) of the mesoporous carbon thin film and the transport through the carbon thin film (perpendicular to the surface) and the respective substrate (both a titanium plate and a silicon wafer). While the first measurement provides information on the electric properties of only the thin film, the latter includes coating and substrate (and possible interfaces), providing a figure of merit for the actual electrocatalytic application, in which the sample is contacted from the backside. As an internal benchmark, the carbon film is compared with an analogously mesoporous iridium dioxide (IrO_2) thin film – a typical electrocatalyst for acidic OER.[86–92] The IrO_2 thin film was synthesized (both on silicon and titanium substrates) with the same soft template employed for the carbon analogue, following usual sol-gel procedures[51,92] for metal oxide thin films modified in terms of solvents to ensure micellization of PEO-*b*-PHA[50] (see Experimental Section). The GIXRD data in Figure S20A (Supporting Information) show the main reflections of IrO_2 (at $2\theta = 28$ and $35°$) in agreement with the depicted reference pattern although their intensity is rather low and overshadowed by the substrate's reflections due to the small quantity of sample and the low crystallinity after calcination at 350 °C.[92] Similarly, the Raman spectrum (Figure S20B, Supporting Information) confirms the presence of IrO_2 because the expected E_g band (at 570 cm^{-1}), B_{2g}, and A_{1g} (both overlapping at 750 cm^{-1}) are observed.[93] The mesoporous morphology is verified by SEM (Figure S20C, Supporting Information), revealing spherical pores of 79 nm in diameter similar to those in the carbon sample. Compared to the latter, the metal oxide thin film is noticeably thinner, with a film thickness of 48 nm according to ellipsometry. The X-ray reflectometry (XRR) scan (Figure S20D, Supporting Information) gives rise to a higher value though. The average distance between the Kiessig fringes of 0.056 nm^{-1} hints at a film thickness of 113 nm,[94] and indeed, fitting of the scan for the mesoporous film in Figure S20D (Supporting Information) yields a thickness of 98 nm. In addition, the porosity of the thin film can be determined based on the critical wave vector q_c originating from the difference in electron density at the air/IrO_2 interface.[95–97] While a non-templated IrO_2 thin film (Figure S20D, Supporting Information) leads to $q_c = 0.618$ nm^{-1} (corresponding to a density of 6.70 g cm^{-3}), the introduction of mesopores into the IrO_2 phase lowers the average electron density, causing a reduction in q_c.[96,98,99] If a sufficiently high porosity is present so that the electron density of the thin film comes below that of the silicon substrate, the mesoporous film becomes a waveguide, and two critical wave vectors are observed: one of the thin film (here: $q_c = 0.244$ nm^{-1}) and one of the substrate (here: $q_c = 0.315$ nm^{-1}).[96,100] From the thin film's q_c, an electron density of 420 nm^{-3} can be determined (see Supporting Information for more details), which corresponds to a porosity of 84% when compared with the electron density of crystalline tetragonal IrO_2 (2700 nm^{-3}). Alternatively, the density obtained from fitting the experimental XRR curve (1.55 g cm^{-3}) can be related to the density of the non-templated sample, yielding a porosity of 77%, which should be more reasonable due to the low crystallinity of IrO_2 synthesized here. Compared to this evaluation, the refractive index of the mesoporous thin film ($n = 1.68$) measured with ellipsometry delivers a porosity of 55% when compared with crystalline IrO_2 ($n = 2.50$)[101] according to the Bruggemann effective medium approximation[102,103] (BEMA). This deviation evokes the assumption that this ellipsometry evaluation model becomes inaccurate for mesoporous samples, in particular, as the film thickness determined by XRR (9.9 nm) and ellipsometry (11.7 nm) are in good agreement in the case of the non-templated sample. In the case of the mesoporous sample, evaluation of the XRR data becomes more challenging because of the superposition of the reflectivity curve with Bragg peaks originating from the ordered array of mesopores. The spherical pores, which are compressed along the film normal, possessing an ellipsoidal shape,[20,28,102] are stacked layer-wise with a defined pore wall between each pore layer, causing periodically appearing Bragg peaks.[96,99,104] Their position q gives access to the layer period (pore-to-pore distance) being equal to $2\pi\ i\ q^{-1}$ if their order i is known. In the case of the curve of the mesoporous film in Figure S20D (Supporting Information), a broad background at ≈0.35 nm^{-1} can be observed, leading to a deviation between the simulated and experimental reflectivity curve. Assuming a second order Bragg peak (the first order one would be hidden in the specular region below q_c), a layer period of 36 nm is obtained, which matches very well the lateral pore-to-pore distance found in the mesoporous carbon film (see SEM cross-section in Figure 11A below) being composed of a pore height of 20 – 25 nm and a 10 nm thick wall. Thus, the mesoporous IrO_2 thin film seems to be a suitable comparison sample for the carbon-based one in terms of pore morphology.

The transport perpendicular through the thin film (including substrate) was determined using electrochemical impedance spectroscopy (EIS) after mounting the thin films into a metal screw clamp, as sketched in **Figure 10C** and exemplified in the photos in Figure S21 (Supporting Information). Within an internal comparison, the aforementioned mesoporous carbon and mesoporous IrO_2 thin films (both deposited on polished titanium plates) were contrasted to a blank, polished titanium plate (conductor) and a silicon wafer (semiconductor) as border cases on a conductivity scale. It is important to mention that only effective

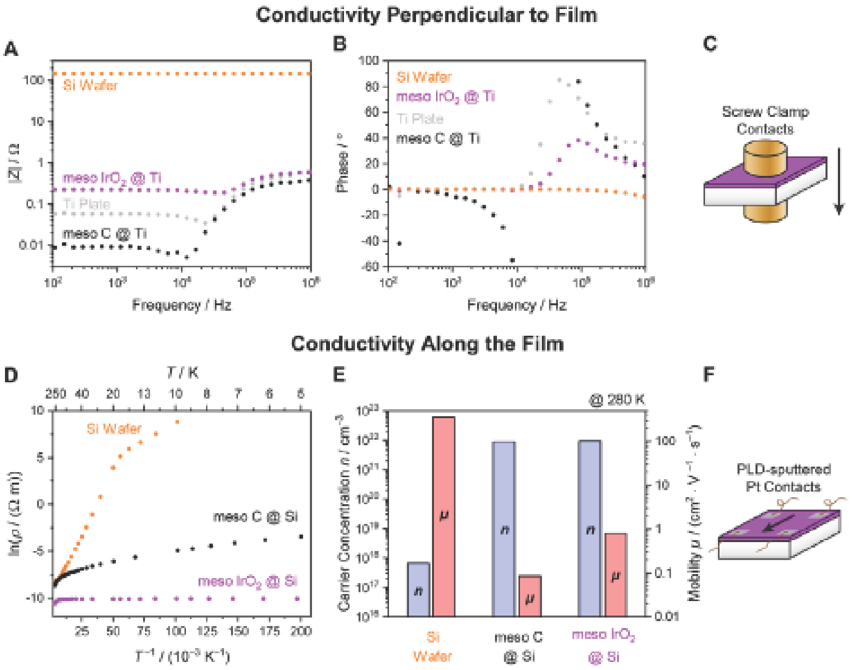

Figure 10. A,B) Bode plot of the impedance spectra of a silicon wafer (orange), a titanium substrate (gray), and a mesoporous hard carbon (black) and IrO_2 thin film (violet) deposited on titanium, recorded at room temperature in transversal direction as shown in C) the sketch of an exemplary sample. D) Arrhenius plot of the resistivity of mesoporous carbon and IrO_2 thin films deposited on silicon wafers, and E) the corresponding charge carrier concentration (blue) and mobility (red) at 280 K determined by a Hall measurement in van-der-Pauw geometry, as illustrated in F) the scheme of a thin film.

impedances and conductivities are measured for the mesoporous samples here and not the material-specific values of the solid skeleton material (i.e., pure carbon and pure IrO_2) as porosity decreases the effective conductivity compared to a non-porous sample.[105] Yet, due to the similar morphology of both samples, the internal comparison based on the effective values is sufficient.

At high frequencies, the impedance spectrum of the silicon wafer is governed by capacitive contributions, which can be seen by the negative phase in the Bode plot (Figure 10B) and negative imaginary values in the Nyquist plot (Figure S22D, Supporting Information). Contrarily, the impedance of the metal-based samples is dominated by inductive contributions in the high frequency region (arising probably from the setup) leading to a positive phase (Figure 10B) in the Bode plot and positive imaginary parts in the Nyquist plot (Figure S22, Supporting Information). However, with decreasing frequency, this inductive contribution diminishes, and the properties of the thin films control the impedance. At low frequencies, the phase of all samples approaches zero so that the impedance is fully governed by its real part, i.e., an ohmic resistance. Therefore, the absolute value of the impedance measured at low frequencies in Figure 10A corresponds to the resistance of the entire sample (thin film and substrate) in transversal direction following the trend: mesoporous carbon (9 mΩ) < Ti (56 mΩ) < mesoporous IrO_2 (215 mΩ) << Si (145 Ω). These values demonstrate that a model electrode made from a mesoporous hard carbon thin film deposited on a titanium plate possesses a similarly low resistance, i.e., high electric conductivity, as an IrO_2-based model electrode applicable for electrocatalysis. It should be noted that the measured resistance value of the highly conductive samples (such as the metal-based samples) is affected by large uncertainties due to a contact resistance contribution. As the pressure for the screw contacts clamping the samples could not be controlled in a defined way, even small variations in the contact resistance between electrodes and sample may dominate the overall impedance at low frequencies. Thus, the results for the samples with a resistance below roughly 1 Ω are less reliable than those for silicon wafer with a significantly higher resistance. This explains why the mesoporous carbon sample features surprisingly a lower resistance than the parent metal plate expected to yield the highest conductivity. The same holds true for the IrO_2 sample, which is expected to be more conductive than non-graphitic carbon,[87,106] although the formation of a thin less conductive TiO_2 layer on the backside of the substrate during calcination in air might also be responsible for a lower overall conductivity of the IrO_2 sample. Nevertheless, a low resistance in both the carbon and IrO_2 sample can be concluded from this experiment, whose reliability is supported by the temperature-dependent impedance measurements (Figure S23A, Supporting Information) of a mesoporous carbon thin film on silicon (this substrate was used to increase reliability of the obtained resistance). The Arrhenius plot of the measured resistance (Figure S23B, Supporting Information) shows a change in the dominant transport mechanism at 263 K, at which the activation energy increases from 12.4 meV (low temperatures) to 26.2 meV (high temperatures). This behavior is reported for other thin films on silicon and can be explained with a release of charge carriers trapped at the Si/coating interface upon exceeding a threshold temperature.[107] This confirms that indeed the transport through thin film and substrate was measured with the screw clamp setup.

An unambiguous comparison between solely non-graphitic carbon and IrO_2 with regard to their electric transport properties requires an in-plane conductivity measurement, i.e., along the mesoporous thin film. For this reason, the substrate, the mesoporous carbon sample, and the IrO_2 counterpart were sputtered with platinum in all four corners using pulsed-laser deposition and contacted with conducting silver and copper wires each prior to performing transport measurements in van-der-Pauw geometry as shown in the sketched sample in Figure 10F and the photos in Figure S21 (Supporting Information). Silicon was used as substrate due to its comparably high electric resistivity, which ensures that the measured transport properties are dominated by the properties of the deposited thin film layer. The temperature-dependent resistance measurement of the Si substrate (without external magnetic field) yields the transport behavior expected for n-doped silicon (orange data in Figure 10D; determined values in Figure S23C, Supporting Information):[108–110] At low temperatures (<20 K), conduction follows a tunneling-controlled hopping mechanism between the donor states with a very low activation barrier (6.5 meV). With increasing temperatures, the donor-based charge carriers are consecutively thermally activated with an activation energy of $E_A = 23.9$ meV (corresponding to a dopant energy level of $E_D = 2\ E_A = 47.8$ meV[108] and being in good alignment with 46 meV as expected for phosphorus[111] as dopant). Finally, at high temperatures (>100 K), a plateau is found originating from the saturation of the carrier concentration when all donor-based charge carriers are thermally activated from the donor into the conduction band. The fact that the sheet resistance R of the mesoporous samples (Figure S23C, Supporting Information) neither coincides with the resistance of the silicon substrate nor shows a comparable temperature behavior confirms that the measured resistance is dominated by the mesoporous thin film, i.e., the transport indeed occurs in the thin film, and a contribution from the substrate can be neglected. When multiplying the sheet resistance by the thickness of the layer in which the transport occurs (Si: 450 µm, carbon: 300 nm, and IrO_2: 50 nm), the corresponding (thickness-independent) resistivity ρ can be estimated. The Arrhenius plot of ρ in Figure 10D shows that the mesoporous IrO_2 film has one order of magnitude higher in-plane conductivity than the mesoporous hard carbon film (at 280 K, $\rho = 2.37 \times 10^{-5}\ \Omega$ m and $\rho = 1.67 \times 10^{-4}\ \Omega$ m, respectively) in contrast to the transversal measurement. The general temperature dependency reveals a transport behavior in both thin films with a pronounced hopping regime (plateau) at low temperatures followed by a steep decrease with increasing T being characteristic for highly doped semiconductors.[112] In the case of mesoporous carbon, the slope in the low temperature region is higher than in case of mesoporous IrO_2, which hints at a very broad impurity band.[108] This is reasonable as there are various possible defects (acting as dopants) in non-graphitic carbon[67] (leading to the pronounced D band in Figure 5C), probably higher in concentration and with less-defined energy levels than in the metal oxide[87,90] (e.g., oxygen vacancies).

When applying an external magnetic field, the charge carrier concentration n and their mobility μ can be determined by Hall measurements (Figure 10E). The values determined for the silicon substrate are in excellent agreement with values reported for phosphorus-doped silicon[113] and confirm the overall reliability of this method. In case of the mesoporous samples, a comparable charge carrier density n is observed for mesoporous IrO_2 (9.36×10^{21} cm^{-3}) and mesoporous hard carbon (8.79×10^{21} cm^{-3}) at 280 K but a noticeably higher resistivity is measured in case of mesoporous carbon. This discrepancy in resistivity between the carbon- and IrO_2-based samples in Figure 10D indicates a lower mobility of the charge carriers in the mesoporous carbon compared to IrO_2 (0.086 vs. 0.787 cm^2 V^{-1} s^{-1}). Although the carrier densities appear to be very high, both n and μ of the IrO_2 sample are in very good alignment with results reported by Sachse et al.[87] for mesoporous IrO_2 thin films. From all these experiments, it can be concluded that mesoporous carbon itself shows a slightly lower conductivity than the comparative IrO_2 model system, but can compete with the latter when regarding the entire model electrode, including the metal substrate.

2.5.2. Electrochemical Stability

The stability of the mesoporous carbon is of crucial importance for electrocatalysis if used as a catalyst support. Although the carbon support would be protected from the electrolyte by the actual catalyst (e.g., a thin layer of IrO_2) in real electrocatalysis, direct exposure to the acidic electrolyte while applying an oxidizing potential acts as a stress test to study the stability of the non-graphitic carbon. Therefore, a mesoporous carbon thin film on titanium was built in an electrochemical flow cell made from poly(ether ether ketone) (PEEK), contacted from the backside with a stainless steel plate, and flushed with 0.5 M sulfuric acid (flow rate of 2 mL min^{-1}) as sketched in **Figure 11D**. As a stability protocol, a long-term cyclovoltammetry (CV) within a (OER-active) potential regime of 1.45 and 1.60 V (vs. SHE) was adapted from Duran et al., who studied the stability of porous IrO_2 in acidic water splitting.[114] The evolution of the current density together with SEM images of the pore system after different polarization times give insight into the electrochemical stability of the porous system. Here, two analogous carbon thin films were analyzed: one for a short-term polarization (75 min) and one for a long-term measurement for 24 h.

Before exposing the film to the harsh OER conditions, an ordered mesoporous structure with spherical pores of 69 nm in diameter can be observed by SEM at the surface (Figure 11E) and throughout the entire film (film thickness of 370 nm) when analyzing the cross-section of an analogous carbon reference film on silicon (Figure 11A). On a macroscopic level, the carbon film appears homogeneously black, as shown in the photo in Figure 11B. If this film experiences a linearly swept anodic potential under acidic conditions, a small periodically oscillating current density of a few µA cm^{-2} can be recorded (Figure 11J; Figure S24, Supporting Information). This current is expected to originate mainly from the carbon corrosion reaction (CCR) shown in

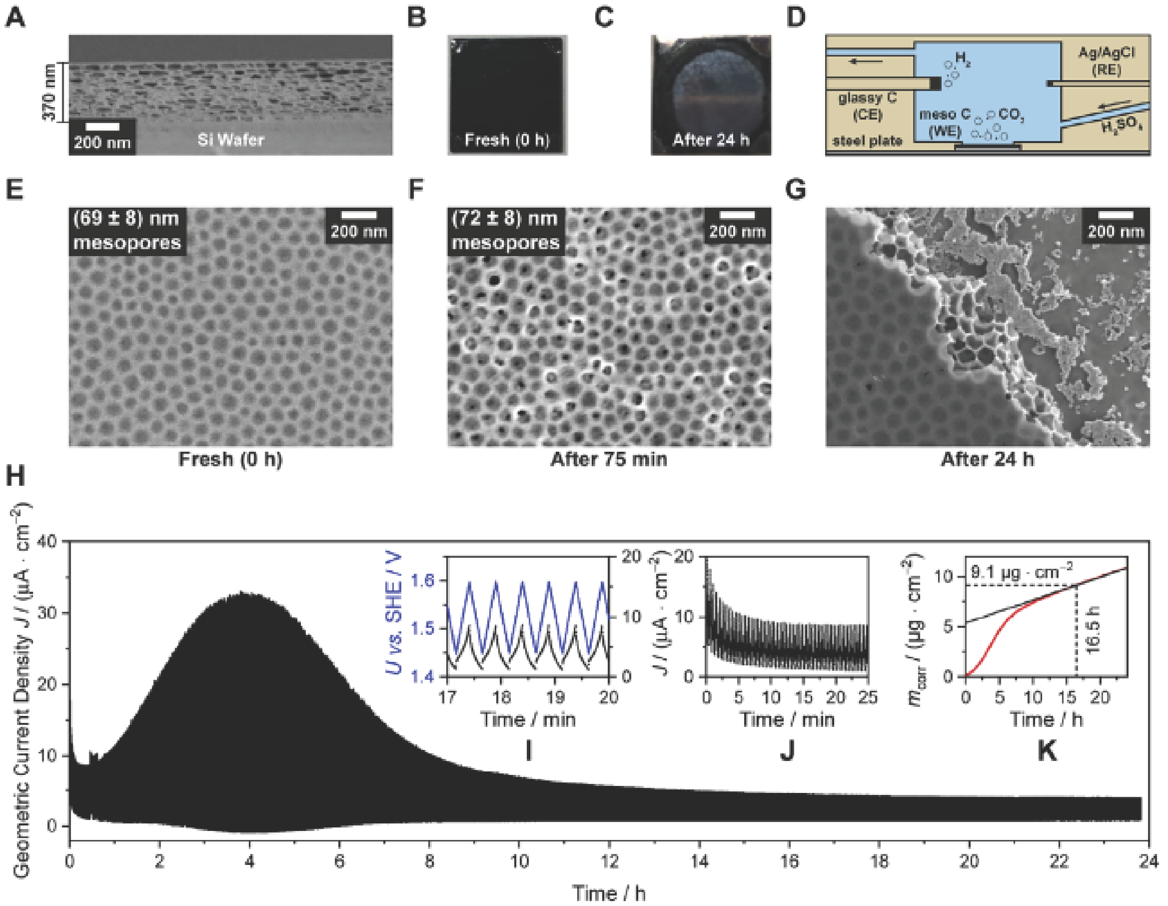

Figure 11. SEM images of A) the cross-section and E) top-view of a pristine mesoporous carbon thin film on titanium and F) one after 75 min and G) after 24 h of cyclic polarization between 1.45 and 1.60 V against SHE in D) an electrochemical flow cell. Photos of B) the fresh film before and C) after 24 h of polarization are displayed together with H) the monitored geometric current density. The insets show the evolution of the current density (black) in a I) 3 min and J) 25 min time interval upon applying a cycled linear potential (blue) recorded with 0.01 V s^{-1} as well as K) the mass of corroded carbon (red) after integration of the current density and conversion following the Faradaic law under the assumption of pure carbon corrosion without side reactions.

Equation 1, which was confirmed to be the dominating reaction starting from 1.4 V vs. SHE for different carbon materials according to differential electrochemical mass spectrometry (DEMS).[57,58,115] The contribution of the OER only becomes significant above 1.6 V vs. SHE in the case of carbon.[115]

$$C + 2H_2O \rightarrow CO_2 + 4H^+ + 4e^- \tag{1}$$

The evolution of the current density shows an initial decay before reaching a state of constant current (between 20 and 75 min in Figure S24D, Supporting Information). This initial decrease can be explained by the establishment of a stable concentration profile of the reactants and products near the electrode surface, as typically observed in chronoamperometry and described by the Cotrell equation.[116] Such a trend is slightly discernible in the studies on porous IrO_2 with the analogue cycling protocol as well.[114] After polarization for 75 min (150 CV cycles), no significant morphological changes occur. The SEM image in Figure 11F reveals a pore size being slightly larger (72 nm), possibly due to a minimal enlargement upon consecutive carbon corrosion, but the deviation is not significant if the polydispersity of the pore size is considered. Additionally, the CV scans between 0.2 and 1.7 V vs. SHE before and after polarization (Figure S24C, Supporting Information) of the mesoporous carbon film are almost identical featuring a small reductive current and a larger oxidative current at the borders, which can be assigned to the HER and CCR, respectively.[57,58] Hence, no severe change in carbon occurred. Yet, the pore structure in the SEM image in Figure 11F appears slightly better connected as more pore necks of the sub-surficial pores can be observed compared to the initial state (Figure 11E).

When performing a long-term cycling on a second sample, a different evolution in current density is found (Figure 11H): Initially, the current density shows the trend discussed before

(Figure 11J). However, after the region of constant current density, J starts to increase after 1 h and reaches a maximum at 4 h prior to decreasing until a constant region is established again after 14 h of polarization. Assuming a proceeding carbon corrosion, this behavior can be explained by an opening of the formerly (rather) isolated mesopores (see Figure 7) by electrochemical etching, which results in an increase in exposed/accessible surface area, leading to an increase in corrosion current density. While the CCR continues, non-graphitic carbon material is consecutively degraded, which results in a decrease in surface area after a certain point. Thus, an apex followed by a decrease in J is found until no carbon is present anymore. Regarding the macroscopic appearance of the sample (shiny circle in Figure 11C) as well as the mesoscopic morphology at the border between carbon being exposed and not exposed to the electrochemical cell by SEM (Figure 11G) after 24 h of polarization (2900 cycles), a complete degradation of the mesoporous thin film can be clearly confirmed. The final region of constant J after 14 h is then most likely a consequence of the uniform leaching of the substrate. Understandably, the CV scans of the sample before and after 24 h of polarization do not coincide anymore, as the carbon layer is removed completely (Figure S24A, Supporting Information). Assuming that only the CCR as a four-electron process takes place as expected from DEMS studies,[57,58] the current density in Figure 11H can be integrated to obtain the transferred charge Q and converted to the mass of corroded carbon m_{corr} as a function of reaction time following Faraday's law (red curve in Figure 11K). After 16.5 h, the sigmoidal growth curve merges into a linear behavior (which can be assigned to substrate corrosion). These data imply that the overall amount of 9 $\mu g\,cm^{-2}$ of mesoporous carbon is fully corroded after ≈16.5 h.

Overall, this study demonstrates that the mesoporous non-graphitic carbon itself is not long-term stable under OER conditions. Still, a remarkably long time is needed to significantly corrode the carbon material, especially considering the large surface area of this porous system (see Figure 6D) and the CCR that is expected to occur already at 207 mV vs. SHE[58] according to thermodynamics. Furthermore, the carbon is protected by a layer of the actual catalyst in electrocatalysis and thus is not in contact with the electrolyte needed to decompose the carbon support. Even if a few small uncoated spots of the support should be exposed to the electrolyte, severe corrosion would require a long time due to the small exposed area, and the catalytic activity should not be significantly reduced as long as electric conduction over the pore wall is still ensured. Indeed, recent studies of carbon hybrid materials for electrocatalysis confirm a promising stability in both acidic[117] and alkaline[118] water electrolysis. Therefore, the mesoporous carbon in this study remains a promising support for electrocatalysis with regard to stability.

2.5.3. Accessibility of the Pore System

Concerning the last prerequisite, i.e., the accessibility, the mesoporous carbon thin films (both before and after 75 min of corrosion) were infiltrated with a tracing electrolyte, and the spatial ion distribution within the mesoporous system was monitored in 3D by SIMS. Similar to previous studies on metal oxide thin films,[51,119] the appearance of tracing ions deep inside the thin film acts as marker for an interconnected and accessible pore system. By that, the mutual accessibility of the fresh film can be checked as well as a possible increase in accessibility upon brief carbon corrosion. In this study, however, cobalt nitrate could not be used as tracing electrolyte (in contrast to the previous studies) as the carbon film shows only appropriate ion counts in negative ion mode while Co^{2+} ions need to be measured in positive ion mode. Thus, an easily detectable, soluble, stable, and unambiguous (that means an ion that can only be assigned to the added salt) anion probe is required. Therefore, lithium tetrafluoroborate ($LiBF_4$) was used instead. Using SIMS, the depth profiles were recorded, and the evolution of the carbon-based (here, following a small and a heavy carbon fragment) and TiC-based (C_2^- and TiC_2^-) signals was investigated, similar to the measurements in Figure 8 but extended by the $Li_2F_3^-$ and BF_4^- signals of the tracing electrolyte. As shown in **Figure 12A** for the fresh carbon film before carbon corrosion, the $LiBF_4$-derived fragments can be found within the hard carbon thin film but their signals do not show a congruent trend to the carbon-based signals. This implies that the tracer penetrated the carbon film roughly up to the top 20 – 30% but was not capable of fully accessing the entire mesoporous coating. In this qualitative study, no further AFM experiments were carried out, and, hence, the signal evolution is plotted against the fluence of ions sputtering the surface instead of the actual depth. This becomes more apparent from the 3D overlay in Figure 12B, confirming the surficial infiltration of the carbon film by $LiBF_4$. As a result, the fresh hard carbon thin film possesses only low accessibility.

However, after 75 min of electrochemical corrosion, the mesoporous carbon samples yield a different result. In this case, the $Li_2F_3^-$ profile in Figure 12D evolves in parallel to the carbon-derived fragments. The intensity fluctuations of the mass signals close to the surface (decay and increase of $Li_2F_3^-$ signal intensity, local maximum of BF_4^- signal intensity, and initial increase in carbon signal intensity between a fluence of 0 and $2 \times 10^{16}\ cm^{-2}$) most likely originate from the precipitation of residual lithium salts, fluorides, and BF_4-containg species at the surface of the thin film as confirmed by the surface images in Figure S25 (Supporting Information). Nevertheless, the high intensity of the $LiBF_4$-derived signals until the carbon/TiC interface demonstrates a complete infiltration of the mesoporous carbon, which is further supported by the 3D overlay in Figure 12C. This experiment also confirms the previous assumption of an increase in pore accessibility upon electrochemical corrosion, presumed on the basis of SEM and the evolution of the corrosion current density in Figure 11. Consequently, the initially poor accessibility of the mesoporous hard carbon thin film can be overcome by applying a short electrochemical etching to widen the pore throats. The accessibility thus obtained is mandatory for application to ensure an even coating (e.g., by atomic layer deposition) or catalysis without diffusion limitation. Yet, even without etching, the pristine mesoporous carbon with isolated pores is still promising for other applications, such as sodium-ion batteries, in which isolated mesopores proved to be beneficial.[52]

In summary, ordered mesoporous hard carbon thin films on titanium possessing spherical pores with 70 nm in diameter showed to be electrically conductive, sufficiently stable under acidic and oxidizing conditions, and accessible for probe

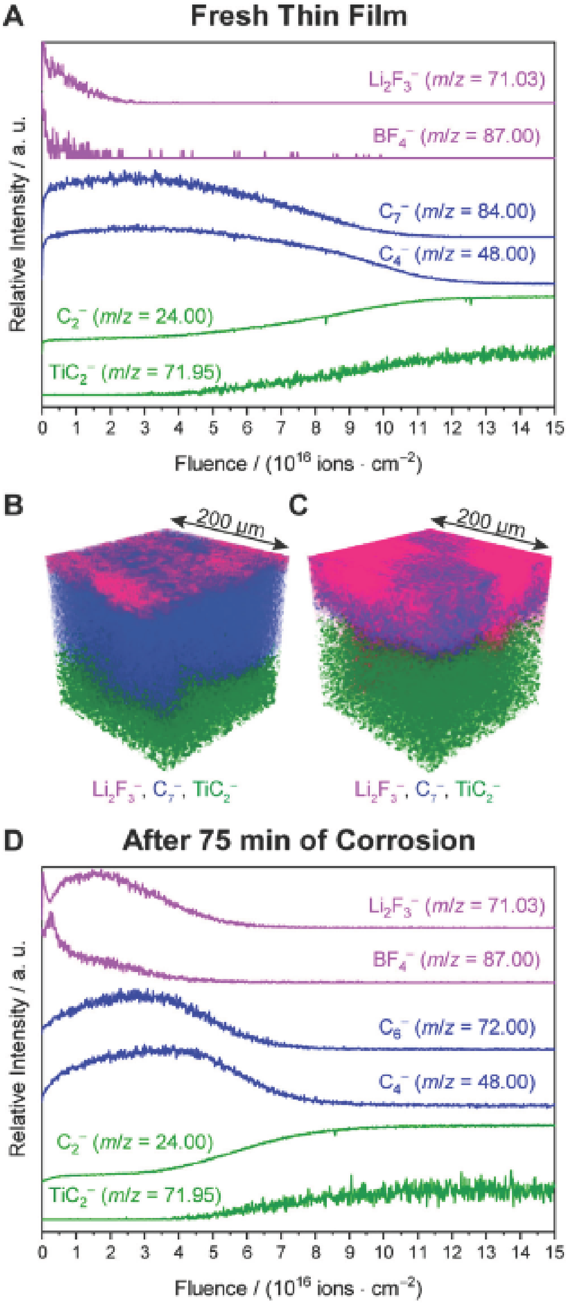

Figure 12. Accessibility of mesoporous carbon thin films. SIMS depth profiles of A) a fresh and D) a briefly electrochemically corroded mesoporous carbon thin film on titanium infiltrated with a $LiBF_4$ tracing electrolyte comprising the evolution of the ion signals assigned to the $LiBF_4$ phase in violet, the hard carbon phase in blue, and the TiC phase in green as well as the 3D overlay of the $Li_2F_3^-$, C_7^-, and TiC_2^- signal of the B) fresh and C) briefly corroded sample after infiltration.

molecules after brief electrochemical corrosion, rendering them a promising support for electrocatalytic applications.

3. Conclusion

Having experienced Helmut Cölfen as a colleague for many years, we are grateful for his courage to bring a seemingly naïve question onto the stage of materials science, namely, how simple inorganic crystalline substances are formed from molecular entities and how the crystallization can be manipulated. In particular, his passion in emphasizing the necessity for understanding the nature and relevance of the amorphous state in nucleation and crystallization was an important momentum for us to elucidate the transition of amorphous carbon into graphene-like materials. As an important part of our study, we addressed the important question of the fate and role of block copolymers in the carbonization process, which we would certainly have ignored if one of the authors (B.S.) had not been exposed to Helmut Cölfen's work for several years. The fact that organic additives – even in small amounts – may affect the nucleation and crystallization of classic inorganic salts, was put forward by Helmut and represents a relevant question in our studies on carbon, too.

This study thus aimed at the preparation and deep characterization of mesoporous carbon thin films with high electric conductivity on metallic substrates, which are suitable for electrochemical applications. While we confirmed an ordered mesoporous structures (with 70 nm mesopores) with the aid of gas physisorption and electron microscopy, we elucidated the formation and sp^2-based microstructure of the non-graphitic carbon by TG-MS, XRD, Raman spectroscopy, and TEM images. Employing ToF-SIMS, GIXRD, and SEM, we observed an unexpected and severe substrate corrosion leading to a significant incorporation of TiO_2 into the carbon material when carbonized in pure argon. A mixture of 85 vol.% argon and 15 vol.% CO showed to be mandatory to avoid substrate oxidation yielding a homogeneous mesoporous carbon film separated from the substrate by a thin carbide interphase. XPS and XRD experiments confirmed that CO influences neither the carbon microstructure nor composition.

The corrosion-free carbon thin films were tested for their suitability as model supports for electrocatalysis in terms of electric conductivity, stability, and accessibility. Regarding electric transport, the carbon thin film demonstrated to be able to compete with analogously porous IrO_2 model electrodes as shown by impedance and Hall measurements. The initial poor accessibility of the carbon thin film (deduced from SIMS depth profiling after infiltration with a tracing solution) was successfully overcome by short-term polarization under (acidic and oxidizing) OER conditions, under which the carbon samples generally revealed a surprisingly high stability even in an uncoated (i.e., unprotected) state.

These properties render the mesoporous carbon thin film a promising support for electrocatalysis (e.g., in water splitting), on which a catalytically active material (such as IrO_2) can be deposited as atomically thin layers to reduce the overall loading of active yet precious materials. In the future, two questions need to be addressed: On the one hand, if a metal oxide like IrO_2 can be deposited as a homogenous layer onto carbon at all, and on the other hand, if the resulting electrocatalyst can keep up with pure IrO_2 catalysts in terms of activity and stability. Beyond this application, the presented work acts as a general, extensive guideline for characterizing non-graphitic carbon thin films, which can be used for several systematic studies in electrochemistry (e.g., sodium-ion batteries) due to their well-defined structure.

The presented work benefited from Helmut Cölfen also in regards how to perform studies involving self-assembled materials and complex analytics: First, one should be courageous to ask basic questions, especially when it comes to crystallization. Second, collaboration in cutting-edge analytics, especially in such demanding fields as self-assembled materials, works best on the basis of a friendly partnership and respectful cooperation. Thus, our complex analytical studies would not have been possible without such unselfish collaboration of many co-workers, which also was one of the outstanding character traits Helmut was known for and by which he certainly had a significant impact on many colleagues and students, who had the pleasure to work with him.

4. Experimental Section

Synthesis of the Soft Template: The PEO-*b*-PHA block copolymer was prepared by a two-step procedure analogous to the previous study[51] and based on the initial report of Lokupitiya et al.[50] α-Methyl-ω-hydroxy poly(ethylene oxide) (PEO-OH) with an average molecular weight of 20 kDa (as provided by the supplier) was purchased from Sigma-Aldrich. According to ^{1}H-NMR end group analysis (Figure S1A, Supporting Information), the number-weighted molecular weight (M_n) of PEO-OH amounts to 16.6 kDa (372 EO units) with a polydispersity index of 1.03 based on gel permeability chromatography (Figure S1B, Supporting Information). Experimental details on the Steglich esterification yielding the macroinitiator PEO-Br and subsequent supplemental activator reducing agent radical atom transfer polymerization (SARA ATRP) can be found in the last article,[51] while only a brief description is given here.

For macroinitiator synthesis, 4.000 g (0.20 mmol, 1.0 eq) poly(ethylene oxide) methyl ether (PEO-OH, 20 kDa, Sigma Aldrich) were dissolved in 10 mL anhydrous dichloromethane (DCM, 99.8%, Acros Organics) under argon in a 50 mL round bottom flask by stirring at room temperature. After adding 22 µL (0.24 mmol, 1.2 eq) 2-bromopropionic acid (99%, Acros Organics), 10 mg (0.08 mmol, 0.4 eq) 4-dimethylaminopyridine (DMAP, ≥ 99%, Sigma Aldrich), and 95 mg (0.46 mmol, 2.3 eq) *N*,*N*'-dicyclohexylcarbodiimide (DCC, 99%, Sigma Aldrich) to the colorless solution, it was stirred for 20 h at room temperature under argon atmosphere. Excess DCC was quenched with 5 µL of a 1 M hydrochloric acid (Grüssing GmbH), and the turbid reaction mixture was diluted with 50 mL DCM, filtered, and concentrated under reduced pressure. The colorless residue was dissolved in 10 mL tetrahydrofuran (THF, technical grade, Thermo Scientific) and precipitated twice in 250 mL cold diethyl ether. Drying in a vacuum oven at 40 °C for 18 h resulted in 3.552 g (0.18 mmol, 88%) of a colorless powder.

The PEO-*b*-PHA block copolymer was synthesized by a supplemental activator reducing agent atom transfer radical polymerization (SARA ATRP) with a pretreated[120,121] copper wire wrapped around the stirring bar as reducing agent. In a 100 mL Schlenk round bottom flask, 1.000 g (0.05 mmol, 1.0 eq) PEO-Br, 44 mg (0.15 mmol, 3.0 eq) tris(2-pyridylmethyl)amine (TPMA, >98.0%, TCI CO.), 11 mg (0.05 mmol, 1.0 eq) $CuBr_2$ (>99%, water free, Acros Organics), and 2.4 mL (13.64 mmol, 274 eq) hexyl acrylate (98%, Sigma Aldrich) were dissolved in 3.2 mL anhydrous *N*,*N*-dimethylformamide (DMF, 99.8%, Acros Organics) and stirred at 70 °C for 16 h under argon atmosphere. The dark orange gel was dissolved in 80 mL THF, passed over a column of basic alumina, concentrated under reduced pressure, and precipitated twice in 200 mL cold methanol (cooled with an ethyl acetate/liquid nitrogen freezing mixture). The fine colorless precipitation was recovered by filtration over a Büchner funnel and transferred to a Petri dish prior to drying in a vacuum oven at 40 °C for 15 h leading to 1.698 g of a yellow gel. The PHA's degree of polymerization was determined to be 180 (PEO_{372}-*b*-PHA_{180}) according to ^{1}H-NMR in $CDCl_3$ (Figure S1C, Supporting Information) while the polydispersity index amounts to 1.55 according to gel permeability chromatography (Figure S1D, Supporting Information). Note that both the apparent number-weighted molecular weight of 60.2 kDa and the polydispersity from GPC are overestimated due to residual PEO-Br macroinitiator, which, however, does not interfere with the soft templating process.[51]

Synthesis of Mesoporous Carbon Powders: In a 4 mL glass vial, 190 mg of the soft template were dissolved in 2.9 mL absolute ethanol (99.8%, Fisher Chemicals) by sonication for 40 min at 40 °C and 37 kHz. In a second vial, 330 mg resorcinol (99%, Sigma Aldrich) were dissolved in 870 µL deionized water upon stirring at room temperature for 20 min. After adding 30 µL of a 5 M hydrochloric acid (made from 583 µL water and 417 µL fuming hydrochloric acid purchased from Fluka) to the carbon precursor, the polymer solution was added as well followed by the addition of 275 µL triethyl orthoacetate (97%, Thermo Scientific) and 330 µL of a 37 wt.% aqueous formaldehyde solution (10 – 15% methanol as stabilizer, Sigma Aldrich) after brief stirring. The reaction mixture was stirred for 60 min at 40 °C prior to casting into a Petri dish. The slightly orange solution was dried at 80 °C in a drying oven, yielding an intensely orange brittle residue. The latter was scratched off and transferred to a crucible. After carbonization in a muffle furnace in nitrogen atmosphere (3 h at 400 °C, 3 h at 800 °C, 1 K min^{-1} heating rate each) together with a second crucible filled with ≈200 mg copper powder (99%, Acros Organics) as sacrificial reducing agent and grinding, 125 mg of a black powder were obtained.

In case of the non-templated powder (referred to as dense reference), the same protocol was applied replacing, however, the polymer solution by the same volume of pure absolute ethanol.

Preparation of Mesoporous Carbon Thin Films: Prior to spin coating, the titanium plates (10 mm x 10 mm, 1 mm thickness, 99.2%, Evek GmbH) were deburred with P400 silicon carbide paper and polished to a mirror finish with an *AutoMet 300* polishing machine by *Buehler* using polycrystalline colloidal diamond suspensions of consecutively decreasing size. The detailed protocol comprises in-phase polishing with 260 and 130 rpm (rotation rate of lower and upper rotor, respectively) with 15, 1, and 0.05 µm diamond colloids for 30, 20, and 10 min, respectively, and an applied force of 15, 15, and 10 N to press the titanium plates against the lower rotor. Following polishing, the substrates were cleaned by ultrasonication in acetone (to remove residual wax used to attach the substrates to the polishing machine), water, ethanol, and acetone for 10 min at 37 kHz each. Before use, all substrates were further cleaned in a UV ozone cleaner (*Ossila*) for 10 min.

Regarding spin coating, the same reaction mixture was used as for the preparation of mesoporous powders. Yet, instead of casting into a Petri dish, the solution was sonicated at 37 kHz for 5 min and used for spin coating with a *SCC-200* spin coater from *KLM*. Here, 30 drops (≈250 µL) were dropped within 60 s with a Pasteur pipette on the polished Ti plates rotating with 15 rps. After further 2 min of rotation, the films were transferred to a pre-heated furnace for drying, in which they were kept for 12 h at 80 °C. Carbonization was performed in a tube furnace (*Nabertherm*) in a mixture of flowing argon (85 mL min^{-1}) and carbon monoxide (15 mL min^{-1}) using the same heating ramp applied for the powders.

Preparation of Mesoporous IrO_2 Thin Films: Reference samples of mesoporous IrO_2 thin films on polished titanium plates and silicon wafers, respectively, were prepared by spin coating. First, 15 mg of the PEO-*b*-PHA soft template were dissolved in a mixture of 500 µL of DMF (technical grade) and 100 µL of THF (technical grade) by sonication at 37 kHz and 40 °C for 30 min (the vessel was sealed with a tap and Parafilm to avoid solvent evaporation). In the case of the non-templated sample, the pure solvent mixture was used instead. Thereafter, 20 mg of $IrCl_4 \cdot 2H_2O$ (99.9%, 52% Ir, abcr) were dissolved in a mixture of 500 µL of absolute ethanol and 100 µL of hydrochloric acid (fuming, ≥37%, Fluka) by stirring at room temperature for a few minutes. The polymer solution was added dropwise to the precursor solution with a glass pipette within 5 s, and the resulting deep purple solution was stirred for a further 2 min. Upon spin coating, 50 μL of the reaction solution was deposited on the respective substrate (cleaned in a UV ozone cleaner for 10 min before coating) rotating with 15 rps. After 2 min of rotation with 15 rps, the samples were rotated with 50 rps for 1 s to remove excess precursor solution before transferring to an oven pre-heated to 90 °C. After drying at this temperature for 2 h, the thin film were calcined at 130 °C for 1 h and 350 °C for 6 h (heating rate: 0.13 and 0.61 K min^{-1}).

Characterization Techniques: Proton-nuclear magnetic resonance (^{1}H NMR) spectra were measured using an *Avance II 400 MHz HD* by *Bruker* in CDCl$_3$ at 25 °C. All spectra were evaluated with *MestReNova 14.1.2* and referenced to the solvent peak at $\delta = 7.26$ ppm. Gel permeability chromatography (GPC) of the macroinitiator and the block copolymer was executed with tetrahydrofuran as eluent at room temperature and with a flow rate of 0.5 mL min^{-1}. The instrument was equipped with a UV (*TSP UV 1000*) and a simultaneous differential refractive index detector (*Shodex RI-101*) as well as a 300 mm x 8 mm *PSS SDV linear M* column packed with 3 μm particles (10^2–10^6 Da molar mass regime). The polymer solution samples (circa 0.15 wt.% polymer in THF) were filtered through a 0.45 μm filter before 100 μL were injected. Calibration was performed with poly(styrene) standards purchased from *PSS* (Mainz, Germany). Thermogravimetric studies coupled with mass spectrometry (TG-MS) were carried out in argon using a *STA40PC thermoscale* provided by *Netzsch* (resolution of 2 μg and thus $\Delta m_{\mathrm{rel}} = 0.01\%$) within a temperature range from 30 to 1000 °C with a heating ramp of 5 K min^{-1} and the heating ramp used for the carbon synthesis, respectively. Meanwhile, a mass spectrum covering an m/z interval between 12 and 100 was recorded constantly with the aid of a *QMG451* quadrupole mass spectrometer by *Balzers*. Raman spectra were acquired at room temperature with a *Renishaw inVia* Raman microscope in backscattering geometry using an excitation wavelength of 633 nm and 515 nm, respectively. Spectra were recorded with a charge-couple device (CCD) detector in a spectral range of 100–3200 cm^{-1} with a step size of 2 cm^{-1}, integrating five scans of 10 s exposure time each. Powder X-ray diffraction (XRD) of the carbon powders was performed with a *PANalytical Empyrean Series 2* diffractometer in Bragg-Bretano geometry under ambient conditions in a 2θ range of 5 to 115° with monochromatized Cu Kα radiation ($\lambda = 1.5406$ Å, a Ni filter for suppression of Cu Kβ radiation). The optics consisted of 1° anti-scatter slits, a 0.5° divergence slit, and 0.04 rad sollar slits. XRD data were exported with *High Score Plus* and analyzed with an algorithm based on Ruland and Smarsly[74] implemented in the *OctCarb* script[75] in *GNU Octave*.[76] Scanning electron microscopy (SEM) images were obtained with a *Zeiss GeminiSEM 560* microscope using an *InLens* detector, a working distance of 2.5 mm, and an acceleration voltage of 1 kV. To enhance the conductivity, samples were coated with platinum using a *Leica EM ACE600* sputter coater. In the case of cross-sectional imaging, the samples were contacted with conducting silver varnish before sputtering. All images were evaluated with the *Fiji ImageJ* software. Nitrogen physisorption isotherms were recorded at 77 K on an *Autosorb iQ* by *Quantachrome Instruments* (Boynton Beach, USA, FL). The data were analyzed with the *ASiQwin* software applying a quenched solid density functional theory (QSDFT) kernel, assuming a carbon material with cylindrical pores. All samples were degassed for 12 h at 80 °C to remove attached gases and water before each measurement. Time-of-flight secondary ion mass spectrometry (ToF-SIMS) studies were carried out on a *M6 Plus* instrument by *IONTOF GmbH* (Münster, Germany), in which a ToF-SIMS and an in situ scanning probe microscopy (SPM) module are combined. The instrument is equipped with a 30 keV bismuth liquid metal ion gun (LMIG, nanoprobe 50) for analysis, and a gas cluster ion beam (GCIB) for depth profiling. All measurements, which include surface imaging and depth profiling, were performed in negative polarity using Bi$_3^+$ primary ions with an energy of 30 keV. Moreover, the surfaces were flooded with low-energy electrons for all measurements to avoid surface charging. For surface imaging of the carbon thin films, the fast-imaging mode (unbunched mode, full width at half maximum (FWHM) of $m/\Delta m = 7390$ at $m/z = 48.00$ (C$_4^-$)) was used in combination with the delayed extraction analyzer setting, to allow 2D studies of the morphology and chemical environment of the thin film surfaces. The analysis area was 200 μm × 200 μm, and the plane was rasterized with (512 × 512) pixels. The primary ion current was ≈0.04 pA with a cycle time of 50 μs. Depth profiles were recorded in spectrometry mode (bunched mode, FWHM of $m/\Delta m = 14044$ at $m/z = 48.00$ (C$_4^-$)) providing a high signal intensity, and were combined with the high mass resolution setting of the analyzer, which enables simultaneously a high mass resolution. In order to record the 3D composition and the accessibility of the mesoporous thin films, Ar$_{1000}$-cluster (cluster distribution with a maximum at 1000 Ar atoms) with an energy of 10 keV were used for sputtering. For analysis, an area of 200 μm × 200 μm was placed in the sputter crater of 300 μm × 300 μm. The larger sputter crater was chosen to avoid crater wall effects on the extracted secondary ions. Every analysis plane of the depth profile was rasterized with (128 × 128) pixels, and between three sputters, six analysis frames were performed after waiting for 1 s in random raster mode. The primary ion current was ≈0.4–0.5 pA and the sputter current was 9.0 nA at a duty cycle of 100 μs. AFM line scans of the sputter crater were performed with the in situ SPM module of the *M6 Plus*. Line scans were recorded with a Ni cantilever with a pyramidal boron-doped diamond tip in intermittent contact mode. The whole data recording and analysis of the SIMS and SPM measurements were carried out with the *SurfaceLab 7.4* software (*IONTOF GmbH*). Prior to analysis of the pore accessibility, both carbon thin films were immersed by a 1 M tracing solution. For this purpose, 9 mg LiBF$_4$ (98%, Sigma Aldrich) were dissolved in 1 mL isopropanol upon stirring at room temperature for 5 min. One drop of the colorless tracing solution was dropped on every sample with the aid of a Pasteur pipette, and the films were dried under ambient conditions for 15 min. After careful removal of remaining droplets with a tissue, the samples were further dried in an oven at 80 °C for 5 h. Phase composition of the IrO$_2$ thin film was studied by grazing incidence X-ray diffraction (GIXRD) using an *XRDynamic 500* diffractometer by *Anton Paar* with an incidence angle of 2°. A 2θ range of 10 until 90° was covered with a step size of 0.01° and a scanning time of 100 s per step. The optics were composed of a Cu Kα ($\lambda = 1.5406$ Å) X-ray source, a divergence slit of 0.03°, a beam mask of 10 mm, and a primary and secondary solar slit of 0.05 rad each. The Raman spectrum was recorded with a *Senterra* spectroscope by *Bruker* equipped with a laser of 532 nm wavelength and a power of 20 mW. After co-addition of 30 scans of 10 s each in the spectral range of 80–4450 cm^{-1}, the data were exported with the corresponding *OPUS* software. The thickness and refractive index of the IrO$_2$ thin film were measured with a *SE400Adv* laser ellipsometer by *Sentech* equipped with a 633 nm HeNe laser. Angles of 55, 65, and 75° were used for the measurement, and a model consisting of an overlaying air layer ($n = 1.0000$), a 100 nm IrO$_2$ ($n = 2.5000$) deposition layer, and a silicon substrate ($n = 3.8714$) was assumed. X-ray reflectometry (XRR) of metal oxide thin films on silicon wafers was carried out on a *Rigaku SmartLab* diffractometer operated with a Cu Kα ($\lambda = 1.5406$ Å) X-ray generator (power of 9 kW and voltage of 45 kV). The optics of the parallel-beam geometry comprised a 0.05 mm incident slit, a Ge(220) monochromator, a 5 mm length-limiting slit, a 0.1 mm receiving slit, and a 2.5° Soller slit. The $2\theta/\omega$ scans were recorded with a scan speed of 0.4° min^{-1} and a step size of 0.01° in a 2θ range from 0 to 6° with a *HyPix3000(H)* detector. All XRR curves were fitted with the corresponding *SmartLab Studio II* software, assuming a model composed of a Si substrate (density of 2.329 g cm^{-3} and roughness of 0.5 nm), an SiO$_2$ interface (thickness of 2 nm according to ellipsometry), and an IrO$_2$ thin film. The electrochemical properties of the mesoporous thin films were investigated on both Ti and Si substrates at room temperature and on Si wafers between −50 and 50 °C (every 5 °C). In this regard, electrochemical impedance spectroscopy (EIS) perpendicular to the thin film surface was performed in a frequency range between 10^7 and 10 Hz with an *Alpha-A* impedance bridge from *Novocontrol Technologies GmbH & Co. KG* and an AC amplitude of 100 mV. In-plane electric transport measurements along the thin film surface were performed on silicon wafers in van-der-Pauw geometry. Platinum was used as electrical contacts, which was deposited at all four corners of the specimen using pulsed laser deposition (PLD). The deposition was conducted at room temperature under argon atmosphere ($p = 2$ Pa) with a *Coherent* KrF excimer laser ($\lambda = 248$ nm) using 10000 pulses with an energy of 400 mJ each and a repetition rate of 6 Hz. The PLD mask resulted in deposition of square-shaped platinum contacts (2 mm x 2 mm) in the thin film's corner with a distance of 0.5 mm to each edge. The transport measurements were conducted using a superconducting magnetic system from *Oxford*

Instruments equipped with a variable temperature insert. The temperature-dependent resistivity was measured in the temperature range between 10 and 280 K using a current varying between 10 nA and 10 mA depending on the resistivity of the sample. Hall measurements were performed at 280 K varying the magnetic field between −10 T and +10 T perpendicular to the samples' surface. The electrochemical stability of the carbon thin film was tested in a custom-made PEEK flow cell equipped with a glassy carbon counter electrode (3 mm carbon disk cladded with 3 mm PEEK, eDAQ) and an Ag/AgCl reference electrode (2 mm wide leakless miniature electrode filled with 3.4 M KCl, eDAQ). The carbon sample on polished titanium was contacted from the backside (i.e., the Ti metal substrate) with a stainless steel lid closing the flow cell. The 0.5 M sulfuric acid used as electrolyte (prepared with 486 mL of deionized water and 14 mL of a 95% sulfuric acid purchased from VWR Chemicals) was pumped through the cell using a *BT100-3J* peristaltic pump (*Longer*) equipped with a *DG-1-6* pump head with a flow rate of 2 mL min^{-1} (motor rotation of 10.6 rpm). Cyclic voltammetry (CV) was performed with an *Autolab PGSTAT302N* potentiostat by *Metrohm*, and all electrode potentials were corrected for the Ohmic (iR) drop and given vs. the standard hydrogen electrode (SHE) throughout this article. Conditioning of the carbon sample was executed by recording 50 CV cycles between 0.10 and 1.50 V and 40 cycles between 1.25 and 1.40 V against the reference electrode with a scan rate of 0.05 V s^{-1}. After equilibration of the open-circuit potential (OCP), the actual CV scans (0.01 V s^{-1}) were measured. X-ray photoelectron spectroscopy (XPS) measurements were conducted with a *PHI 5000 VersaProbe IV* Scanning ESCA Microprobe (*Physical Electronics*) using monochromatized Al Kα X-ray radiation (hν = 1486.6 eV) in high power mode (with a beam diameter of 200 µm, an X-ray power of 50 W, and an X-ray lamp voltage of 15 kV). Carbon powders were filled in a Teflon sample cap and attached to the XPS sample holder with an isolating tape. Survey spectra were recorded with time steps of 50 ms, a step size of 0.2 eV, and an analyzer pass energy of 140 eV. The sample surface was charge-neutralized with slow electrons and argon ions, and the pressure was kept between 10^{-7} and 10^{-6} Pa during the measurement. All spectra were analyzed using the *CasaXPS* software.

Supporting Information

Supporting Information is available from the Wiley Online Library or from the author.

Acknowledgements

The authors thank Raoul Brand and Rafael Meinusch (both Justus Liebig University) for gas physisorption measurements, Sascha Prentzel and Helmut Schlaad (both University of Potsdam) for GPC experiments, and Mengnan Wang (Swansea University) for TEM measurements. Furthermore, Matteo Crisci is acknowledged for XPS measurements as well as Florian Rink for PLD sputtering and Limei Klar for recording Raman spectra of the carbon powders (all Justus Liebig University). L.W. thanks the Funds of the Chemical Industry (FCI) and C.G. the German Academic Scholarship Foundation for financial support each. B.S. and M.R. acknowledge funding by the German Research Foundation (DFG) within the project 390874152 (POLiS Cluster of Excellence). M.T.E. acknowledges financial support by the Heisenberg Program of the DFG (498993886, grant no. EL 863/6-1). M.R. thanks the Federal Ministry of Education and Research (BMBF) for funding of the SIMS-AFM machine within the ProGraL project (grant no. 03XP0427).

Open access funding enabled and organized by Projekt DEAL.

Conflict of Interest

The authors declare no conflict of interests.

Author Contributions

The manuscript was written through contributions of all authors. All authors have given approval to the final version of the manuscript.

Data Availability Statement

The raw data of this study are openly available in Zenodo: https://doi.org/10.5281/zenodo.17591320.

Keywords

amorphous-to-crystalline transition, block copolymers, electric transport, electrocatalysis, hard carbons, mesoporous carbon, secondary ion mass spectrometry, soft templating

Received: August 11, 2025
Revised: September 25, 2025

[1] J. Kibsgaard, I. Chorkendorff, *Nat. Energy* **2019**, *4*, 430.
[2] M. Carmo, D. L. Fritz, J. Mergel, D. Stolten, *Int. J. Hydrogen Energy* **2013**, *38*, 4901.
[3] Y. Deng, Y. Cai, Z. Sun, D. Gu, J. Wei, W. Li, X. Guo, J. Yang, D. Zhao, *Adv. Funct. Mater.* **2010**, *20*, 3658.
[4] M. R. Benzigar, S. N. Talapaneni, S. Joseph, K. Ramadass, G. Singh, J. Scaranto, U. Ravon, K. Al-Bahily, A. Vinu, *Chem. Soc. Rev.* **2018**, *47*, 2680.
[5] X. Wang, C. Liang, S. Dai, *Langmuir* **2008**, *24*, 7500.
[6] D. Gang, Z. Uddin Ahmad, Q. Lian, L. Yao, M. E. Zappi, *Chem. Eng. J.* **2021**, *403*, 126286.
[7] D. Bernsmeier, L. Chuenchom, B. Paul, S. Rümmler, B. Smarsly, R. Kraehnert, *ACS Catal.* **2016**, *6*, 8255.
[8] H. Nishihara, T. Kyotani, *Adv. Mater.* **2012**, *24*, 4473.
[9] S. Tanaka, N. Nishiyama, Y. Egashira, K. Ueyama, *Chem. Commun.* **2005**, 2125.
[10] Y. Zhang, Z. Qiang, B. D. Vogt, *RSC Adv.* **2014**, *4*, 44858.
[11] S. Kataoka, T. Yamamoto, Y. Inagi, A. Endo, M. Nakaiwa, T. Ohmori, *Carbon* **2008**, *46*, 1358.
[12] B. D. Vogt, V. L. Chavez, M. Dai, M. R. C. Arreola, L. Song, D. Feng, D. Zhao, G. M. Perera, G. E. Stein, *Langmuir* **2011**, *27*, 5607.
[13] A. Labiano, M. Dai, W.-S. Young, G. E. Stein, K. A. Cavicchi, T. H. Epps, B. D. Vogt, *J. Phys. Chem. C* **2012**, *116*, 6038.
[14] J. Xue, G. Singh, Z. Qiang, A. Karim, B. D. Vogt, *Nanoscale* **2013**, *5*, 7928.
[15] T. Kimura, A. M. Emre, K. Kato, Y. Hayashi, *J. Mater. Chem. A* **2013**, *1*, 15135.
[16] Z. Qiang, Y. Guo, H. Liu, S. Z. D. Cheng, M. Cakmak, K. A. Cavicchi, B. D. Vogt, *ACS Appl. Mater. Interfaces* **2015**, *7*, 4306.
[17] D. Bernsmeier, M. Bernicke, E. Ortel, R. Schmack, J. Polte, R. Kraehnert, *J. Catal.* **2017**, *355*, 110.
[18] D. Bernsmeier, R. Sachse, M. Bernicke, R. Schmack, F. Kettemann, J. Polte, R. Kraehnert, *J. Catal.* **2019**, *369*, 181.
[19] R. Sachse, D. Bernsmeier, R. Schmack, I. Häusler, A. Hertwig, K. Kraffert, J. Nissen, R. Kraehnert, *Catal. Sci. Technol.* **2020**, *10*, 2057.
[20] J. Schuster, R. Köhn, A. Keilbach, M. Döblinger, H. Amenitsch, T. Bein, *Chem. Mater.* **2009**, *21*, 5754.
[21] Z. Qiang, J. Xue, G. E. Stein, K. A. Cavicchi, B. D. Vogt, *Langmuir* **2013**, *29*, 9950.
[22] Z. Qiang, Y. Zhang, Y. Wang, S. M. Bhaway, K. A. Cavicchi, B. D. Vogt, *Carbon* **2015**, *82*, 51.

[23] J. Jin, N. Nishiyama, Y. Egashira, K. Ueyama, *Chem. Commun* **2009**, 1371.

[24] D. Feng, Y. Lv, Z. Wu, Y. Dou, L. Han, Z. Sun, Y. Xia, G. Zheng, D. Zhao, *J. Am. Chem. Soc.* **2011**, *133*, 15148.

[25] S. Tanaka, A. Doi, N. Nakatani, Y. Katayama, Y. Miyake, *Carbon* **2009**, *47*, 2688.

[26] L. Song, D. Feng, N. J. Fredin, K. G. Yager, R. L. Jones, Q. Wu, D. Zhao, B. D. Vogt, *ACS Nano* **2010**, *4*, 189.

[27] T. Mitome, Y. Uchida, Y. Egashira, N. Nishiyama, *Colloids Surfaces A Physicochem. Eng. Asp.* **2014**, *449*, 51.

[28] S. Tanaka, Y. Katayama, M. P. Tate, H. W. Hillhouse, Y. Miyake, *J. Mater. Chem.* **2007**, *17*, 3639.

[29] D. Gebauer, A. Völkel, H. Cölfen, *Science* **2008**, *322*, 1819.

[30] D. Gebauer, H. Cölfen, *Nano Today* **2011**, *6*, 564.

[31] D. Gebauer, M. Kellermeier, J. D. Gale, L. Bergström, H. Cölfen, *Chem. Soc. Rev.* **2014**, *43*, 2348.

[32] J. J. De Yoreo, P. U. P. A. Gilbert, N. A. J. M. Sommerdijk, R. L. Penn, S. Whitelam, D. Joester, H. Zhang, J. D. Rimer, A. Navrotsky, J. F. Banfield, A. F. Wallace, F. M. Michel, F. C. Meldrum, H. Cölfen, P. M. Dove, *Science* **2015**, *349*, 498.

[33] A.-W. Xu, Y. Ma, H. Cölfen, *J. Mater. Chem.* **2007**, *17*, 415.

[34] A. Oberlin, *Carbon* **1984**, *22*, 521.

[35] F. Badaczewski, M. O. Loeh, T. Pfaff, S. Dobrotka, D. Wallacher, D. Clemens, J. Metz, B. M. Smarsly, *Carbon* **2019**, *141*, 169.

[36] R. Song, H. Cölfen, *Adv. Mater.* **2010**, *22*, 1301.

[37] M. Jehannin, A. Rao, H. Cölfen, *J. Am. Chem. Soc.* **2019**, *141*, 10120.

[38] M. Niederberger, H. Cölfen, *Phys. Chem. Chem. Phys.* **2006**, *8*, 3271. .

[39] T. Wang, A. Xu, H. Cölfen, *Angew. Chem., Int. Ed.* **2006**, *45*, 4451.

[40] L.-B. Mao, H.-L. Gao, H.-B. Yao, L. Liu, H. Cölfen, G. Liu, S.-M. Chen, S.-K. Li, Y.-X. Yan, Y.-Y. Liu, S.-H. Yu, *Science* **2016**, *354*, 107.

[41] F. C. Meldrum, H. Cölfen, *Chem. Rev.* **2008**, *108*, 4332.

[42] C. Liang, K. Hong, G. A. Guiochon, J. W. Mays, S. Dai, *Angew. Chem., Int. Ed.* **2004**, *43*, 5785.

[43] Y. Meng, D. Gu, F. Zhang, Y. Shi, H. Yang, Z. Li, C. Yu, B. Tu, D. Zhao, *Angew. Chem., Int. Ed.* **2005**, *44*, 7053.

[44] E. Axente, M. Sopronyi, C. Matei Ghimbeu, C. Nita, A. Airoudj, G. Schrodj, F. Sima, *Carbon* **2017**, *122*, 484.

[45] S. Herou, M. C. Ribadeneyra, R. Madhu, V. Araullo-Peters, A. Jensen, P. Schlee, M. Titirici, *Green Chem.* **2019**, *21*, 550.

[46] X. Sun, W. Huang, C. Yang, F. Qi, J. Chen, N. Zhao, X. OuYang, *ACS Appl. Energy Mater.* **2023**, *6*, 6826.

[47] N. T. Rodrigues, F. D. Alves, A. Reis, *Langmuir* **2024**, *40*, 11371.

[48] A. Liang, C. Liu, P. S. Branicio, *Langmuir* **2024**, *40*, 10868.

[49] Y. Deng, T. Yu, Y. Wan, Y. Shi, Y. Meng, D. Gu, L. Zhang, Y. Huang, C. Liu, X. Wu, D. Zhao, *J. Am. Chem. Soc.* **2007**, *129*, 1690.

[50] H. N. Lokupitiya, A. Jones, B. Reid, S. Guldin, M. Stefik, *Chem. Mater.* **2016**, *28*, 1653.

[51] L. Q. Wagner, E. Prates da Costa, C. Glatthaar, F. Breckwoldt, M. Zecca, P. Centomo, X. Huang, C. Kübel, H. Schlaad, M. Kriechbaum, H. Amenitsch, M. Thommes, B. M. Smarsly, *Chem. Mater.* **2023**, *35*, 9879.

[52] C. Glatthaar, M. Wang, L. Q. Wagner, F. Breckwoldt, Z. Guo, K. Zheng, M. Kriechbaum, H. Amenitsch, M.-M. Titirici, B. M. Smarsly, *Chem. Mater.* **2023**, *35*, 10416.

[53] H. Oh, Y. J. Lee, E. J. Kim, J. Park, H.-E. Kim, H. Lee, H. Lee, B. J. Kim, *Nanoscale* **2024**, *16*, 879.

[54] D. Bernsmeier, M. Bernicke, E. Ortel, A. Bergmann, A. Lippitz, J. Nissen, R. Schmack, P. Strasser, J. Polte, R. Kraehnert, *ChemElectroChem* **2017**, *4*, 221.

[55] J. Willsau, J. Heitbaum, *J. Electroanal. Chem.* **1984**, *161*, 93.

[56] S. J. Ashton, M. Arenz, *Electrochem. Commun.* **2011**, *13*, 1473.

[57] L. Eifert, Z. Jusys, R. Banerjee, R. J. Behm, R. Zeis, *ACS Appl. Energy Mater.* **2018**, *1*, 6714.

[58] L. Eifert, Z. Jusys, R. J. Behm, R. Zeis, *Carbon* **2020**, *158*, 580.

[59] M. Schilling, A. Ershov, R. Debastiani, K. Duan, K. Köble, S. Scherer, L. Lan, A. Rampf, T. Faragó, M. Zuber, A. Cecilia, S. Liu, C. Liu, T. Baumbach, J. Li, P. Sui, R. Zeis, *Energy Adv* **2024**, *3*, 997.

[60] Y. Meng, D. Gu, F. Zhang, Y. Shi, L. Cheng, D. Feng, Z. Wu, Z. Chen, Y. Wan, A. Stein, D. Zhao, *Chem. Mater.* **2006**, *18*, 4447.

[61] L. Chuenchom, R. Kraehnert, B. M. Smarsly, *Soft Matter* **2012**, *8*, 10801.

[62] A. Šebenik, U. Osredkar, I. Vizovišek, *Polymer* **1981**, *22*, 804.

[63] Y. Lu, H. Fan, A. Stump, T. L. Ward, T. Rieker, C. J. Brinker, *Nature* **1999**, *398*, 223.

[64] C. J. Brinker, Y. Lu, A. Sellinger, H. Fan, *Adv. Funct. Mater.* **1999**, *11*, 579.

[65] D. Grosso, F. Cagnol, G. J. de, A. A. Soler-Illia, E. L. Crepaldi, H. Amenitsch, A. Brunet-Bruneau, A. Bourgeois, C. Sanchez, *Adv. Funct. Mater.* **2004**, *14*, 309.

[66] M. A. Soto-Oviedo, R. S. Lehrle, I. W. Parsons, M. A. De Paoli, *Polym. Degrad. Stab.* **2003**, *81*, 463.

[67] D. B. Schuepfer, F. Badaczewski, J. M. Guerra-Castro, D. M. Hofmann, C. Heiliger, B. Smarsly, P. J. Klar, *Carbon* **2020**, *161*, 359.

[68] A. C. Ferrari, D. M. Basko, *Nat. Nanotechnol.* **2013**, *8*, 235.

[69] A. Sadezky, H. Muckenhuber, H. Grothe, R. Niessner, U. Pöschl, *Carbon* **2005**, *43*, 1731.

[70] A. Kaniyoor, S. Ramaprabhu, *AIP Adv.* **2012**, *2*, 032183.

[71] R. Vidano, D. B. Fischbach, *J. Am. Ceram. Soc.* **1978**, *61*, 13.

[72] O. Osswald, M. O. Loeh, F. M. Badaczewski, T. Pfaff, H. E. Fischer, A. Franz, J. Hoffmann, M. Reehuis, P. J. Klar, B. M. Smarsly, *C* **2023**, *9*, 27.

[73] K. Faber, F. Badaczewski, W. Ruland, B. M. Smarsly, *Zeitschrift für Anorg. und Allg. Chemie* **2014**, *640*, 3107.

[74] W. Ruland, B. Smarsly, *J. Appl. Crystallogr.* **2002**, *35*, 624.

[75] O. Osswald, B. M. Smarsly, *C* **2022**, *8*, 78.

[76] J. W. Eaton, D. Bateman, S. Hauberg, R. Wehbring, **2023**.

[77] R. E. Franklin, *Proc. R. Soc. London. Ser. A* **1951**, *209*, 196.

[78] D. A. Stevens, J. R. Dahn, *J. Electrochem. Soc.* **2000**, *147*, 1271.

[79] Y. Youn, B. Gao, A. Kamiyama, K. Kubota, S. Komaba, Y. Tateyama, *npj Comput. Mater.* **2021**, *7*, 48.

[80] M. Thommes, C. Schlumberger, *Annu. Rev. Chem. Biomol. Eng.* **2021**, *12*, 137.

[81] K. Frisk, *Calphad* **2003**, *27*, 367.

[82] D. A. Andersson, P. A. Korzhavyi, B. Johansson, *Calphad* **2008**, *32*, 543.

[83] S. Saha, B. M. Rajbongshi, V. Ramani, A. Verma, *Int. J. Hydrogen Energy* **2021**, *46*, 12801.

[84] W. Yan, Y. Zhang, L. Chen, J. Luo, P. Pang, X. Zhang, B. Liao, M. Ying, *Diam. Relat. Mater.* **2021**, *120*, 108628.

[85] S.-Y. Lin, X. Zhang, *J. Power Sources* **2015**, *294*, 354.

[86] T. Weber, J. Pfrommer, M. J. S. Abb, B. Herd, O. Khalid, M. Rohnke, P. H. Lakner, J. Evertsson, S. Volkov, F. Bertram, R. Znaiguia, F. Carla, V. Vonk, E. Lundgren, A. Stierle, H. Over, *ACS Catal.* **2019**, *9*, 6530.

[87] R. Sachse, M. Pflüger, J.-J. Velasco-Vélez, M. Sahre, J. Radnik, M. Bernicke, D. Bernsmeier, V.-D. Hodoroaba, M. Krumrey, P. Strasser, R. Kraehnert, A. Hertwig, *ACS Catal.* **2020**, *10*, 14210.

[88] H. Over, *ACS Catal.* **2021**, *11*, 8848.

[89] D. D. Matienzo, D. Settipani, E. Instuli, T. Kallio, *Catalysts* **2020**, *10*, 92.

[90] W. Li, J. Lv, D. Liu, W. Cai, X. Chen, Q. Huang, L. Wang, B. Wang, *Chem. Mater.* **2023**, *35*, 3892.

[91] D. Bernsmeier, M. Bernicke, R. Schmack, R. Sachse, B. Paul, A. Bergmann, P. Strasser, E. Ortel, R. Kraehnert, *ChemSusChem* **2018**, *11*, 2367.

[92] M. Bernicke, E. Ortel, T. Reier, A. Bergmann, J. Ferreira De Araujo, P. Strasser, R. Kraehnert, *ChemSusChem* **2015**, *8*, 1908.

[93] Y. S. Huang, S. S. Lin, C. R. Huang, M. C. Lee, T. E. Dann, F. Z. Chien, *Solid State Commun.* **1989**, *70*, 517.
[94] A. Baptiste, A. Gibaud, J. F. Bardeau, K. Wen, R. Maoz, J. Sagiv, B. M. Ocko, *Langmuir* **2002**, *18*, 3916.
[95] A. Gibaud, S. Hazra, *Curr. Sci.* **2000**, *78*, 1467.
[96] S. Dourdain, J. F. Bardeau, M. Colas, B. Smarsly, A. Mehdi, B. M. Ocko, A. Gibaud, *Appl. Phys. Lett.* **2005**, *86*, 113108.
[97] S. Dourdain, A. Mehdi, J. F. Bardeau, A. Gibaud, *Thin Solid Films* **2006**, *495*, 205.
[98] Y. Minhao, M. J. Henderson, A. Gibaud, *Thin Solid Films* **2009**, *517*, 3028.
[99] A. Gibaud, S. Dourdain, G. Vignaud, *Appl. Surf. Sci.* **2006**, *253*, 3.
[100] Y. P. Feng, S. K. Sinha, E. E. Fullerton, G. Grübel, D. Abernathy, D. P. Siddons, J. B. Hastings, *Appl. Phys. Lett.* **1995**, *67*, 3647.
[101] A. K. Goel, G. Skorinko, F. H. Pollak, *Phys. Rev. B* **1981**, *24*, 7342.
[102] C. Boissiere, D. Grosso, S. Lepoutre, L. Nicole, A. B. Bruneau, C. Sanchez, *Langmuir* **2005**, *21*, 12362.
[103] P. Cop, K. Hess, S. Werner, R. Meinusch, B. M. Smarsly, H. Kozuka, *Langmuir* **2019**, *35*, 16427.
[104] D. A. Doshi, A. Gibaud, V. Goletto, M. Lu, H. Gerung, B. Ocko, S. M. Han, C. J. Brinker, *J. Am. Chem. Soc.* **2003**, *125*, 11646.
[105] J. K. Eckhardt, C. Heiliger, M. T. Elm, *ACS Appl. Mater. Interfaces* **2023**, *15*, 35332.
[106] M. Einert, C. Wessel, F. Badaczewski, T. Leichtweiß, C. Eufinger, J. Janek, J. Yuan, M. Antonietti, B. M. Smarsly, *Macromol. Chem. Phys.* **2015**, *216*, 1930.
[107] A. Kanapitsas, C. Tsonos, D. Triantis, I. Stavrakas, C. Anastasiadis, P. Photopoulos, P. Pissis, V. Em Vamvakas, *Thin Solid Films* **2010**, *518*, 2357.
[108] C. Michel, S. D. Baranovskii, P. J. Klar, P. Thomas, B. Goldlücke, *Appl. Phys. Lett.* **2006**, *89*, 2.
[109] T. F. Rosenbaum, R. F. Milligan, M. A. Paalanen, G. A. Thomas, R. N. Bhatt, W. Lin, *Phys. Rev. B* **1983**, *27*, 7509.
[110] I. B. Olenych, L. S. Monastyrskii, O. I. Aksimentyeva, Y. I. Eliyashevskyy, I. S. Girnyk, M. S. Rudko, *Mol. Cryst. Liq. Cryst.* **2020**, *700*, 88.
[111] C. Jagannath, Z. W. Grabowski, A. K. Ramdas, *Phys. Rev. B* **1981**, *23*, 2082.
[112] M. T. Elm, P. Uredat, J. Binder, L. Ostheim, M. Schäfer, P. Hille, J. Müßener, J. Schörmann, M. Eickhoff, P. J. Klar, *Nano Lett.* **2015**, *15*, 7822.
[113] W. R. Thurber, R. L. Mattis, Y. M. Liu, J. J. Filliben, *J. Electrochem. Soc.* **1980**, *127*, 1807.
[114] S. Duran, A. Grimaud, M. Faustini, J. Peron, *Chem. Mater.* **2023**, *35*, 8590.
[115] H. Liu, Q. Xu, C. Yan, *Electrochem. Commun.* **2013**, *28*, 58.
[116] M. D. Hawley, S. W. Feldberg, *J. Phys. Chem.* **1966**, *70*, 3459.
[117] L. Zeng, B. Yuan, Q. Zhou, *Langmuir* **2024**, *40*, 24696.
[118] T. Shen, X. Chen, Z. Hu, Z. Yan, L. Yang, H. Sun, R. Zhang, H.-Y. Yu, *Langmuir* **2025**, *41*, 694.
[119] P. Hartmann, D. K. Lee, B. M. Smarsly, J. Janek, *ACS Nano* **2010**, *4*, 3147.
[120] M. Kopeć, R. Yuan, E. Gottlieb, C. M. R. Abreu, Y. Song, Z. Wang, J. F. J. Coelho, K. Matyjaszewski, T. Kowalewski, *Macromolecules* **2017**, *50*, 2759.
[121] M. Fantin, A. A. Isse, A. Venzo, A. Gennaro, K. Matyjaszewski, *J. Am. Chem. Soc.* **2016**, *138*, 7216.

Supporting Information

Mesoporous Carbon Thin Films with Large Mesopores as Model Material for Electrochemical Applications

Lysander Q. Wagner[a,b], *Joshua Schober*[a], *Pascal Dippell*[a,b], *Chantal Glatthaar*[a,b], *Smail Mekhilef*[a], *David Schäfer*[a,b], *Hannes Hergert*[b,c], *Marcus Rohnke*[a,b], *Matthias T. Elm*[b,c], *and Bernd M. Smarsly*[a,b]*

a. Institute of Physical Chemistry, Justus Liebig University, Heinrich-Buff-Ring 17, D-35392 Giessen, Germany
b. Center of Materials Research, Justus Liebig University, Heinrich-Buff-Ring 16, D-35392 Giessen, Germany
c. Institute of Experimental Physics I, Justus Liebig University, Heinrich-Buff-Ring 16, D-35392 Giessen, Germany

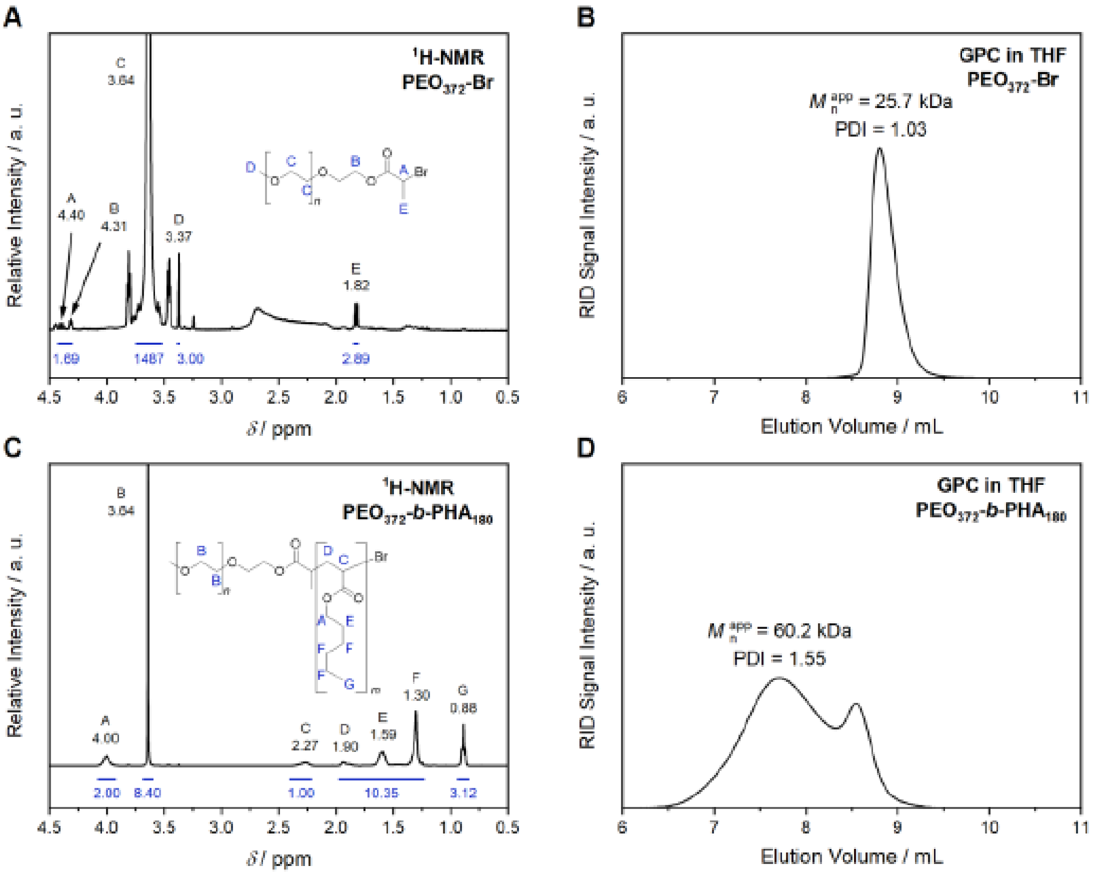

Figure S1. ^{1}H-NMR (400 MHz) spectrum of (A) the PEO-Br macroinitiator (20 kDa) and (C) the PEO-*b*-PHA block copolymer in $CDCl_3$. The peaks are assigned according to the given structure. In addition, the respective GPC curves of (B) the initiator and (D) the block copolymer measured in THF are presented with the apparent number-weighted molecular weight and the polydispersity index each.

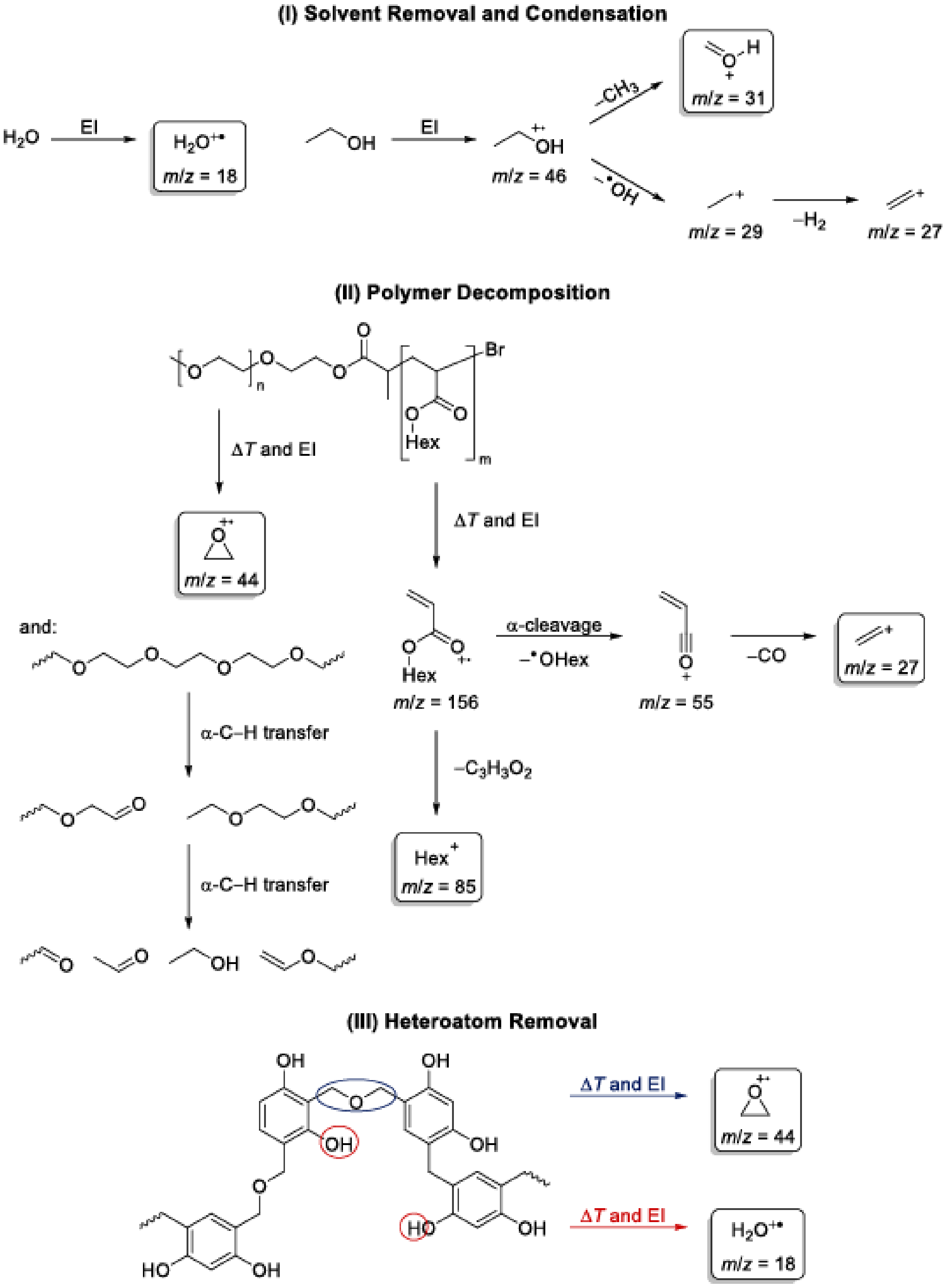

Scheme S1. Fragmentation pattern of the applied solvents, block copolymer, and resol resin induced by electron impact ionization (EI) yielding the detected cations highlighted by boxes.

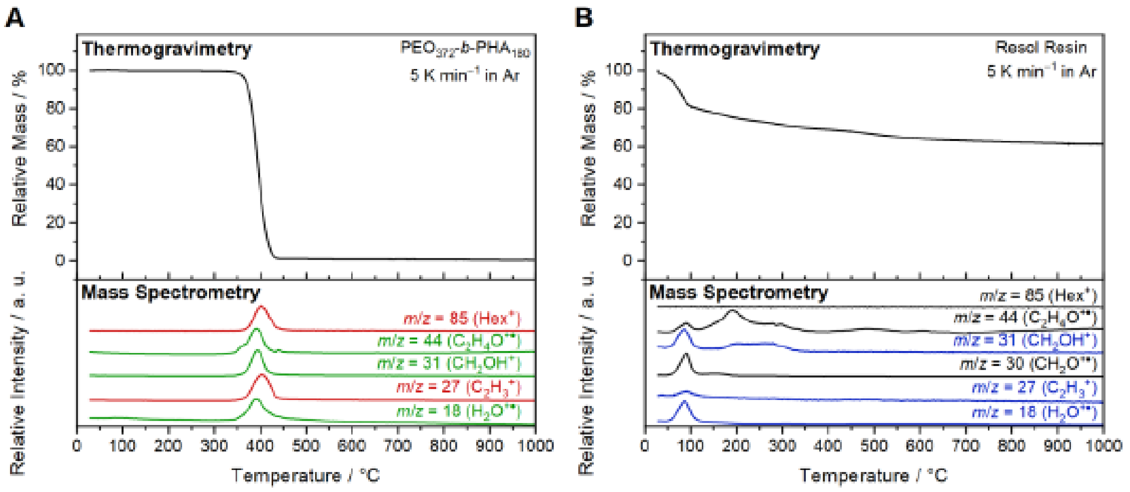

Figure S2. Thermogravimetric curves and evolution of the MS signal intensity of selected fragment cations during heating of (A) the block copolymer and (B) the pure resol resin measured with a heating ramp of 5 K min^{-1} in argon. MS signals assigned to the PEO block are given in green, the PHA block in red, solvents in blue, and the resin in black.

Table S1. G and D1 band position and intensity ratio (D1 to G band) of mesoporous and non-templated carbon powder measured with an excitation wavelength of 633 and 515 nm given with the resulting average graphene layer extent L_a obtained from them by empirical correlations. Values in brackets stem from the WANS-based curve (G band) or lay out of the calibration range and thus are approximated (remaining ones).

Sample	G band	L_a / nm	D1 band	L_a / nm	$I_{D1}\ I_G^{-1}$	L_a / nm
633 nm - meso	1589 cm^{-1}	2.6 (1.3)	1335 cm^{-1}	3.0	1.3	3.4
633 nm - dense	1590 cm^{-1}	2.7 (1.3)	1328 cm^{-1}	(3.0)	1.4	3.6
515 nm - meso	1589 cm^{-1}	–	1345 cm^{-1}	–	1.0	(3.0)
515 nm - dense	1589 cm^{-1}	–	1340 cm^{-1}	–	1.0	(3.0)

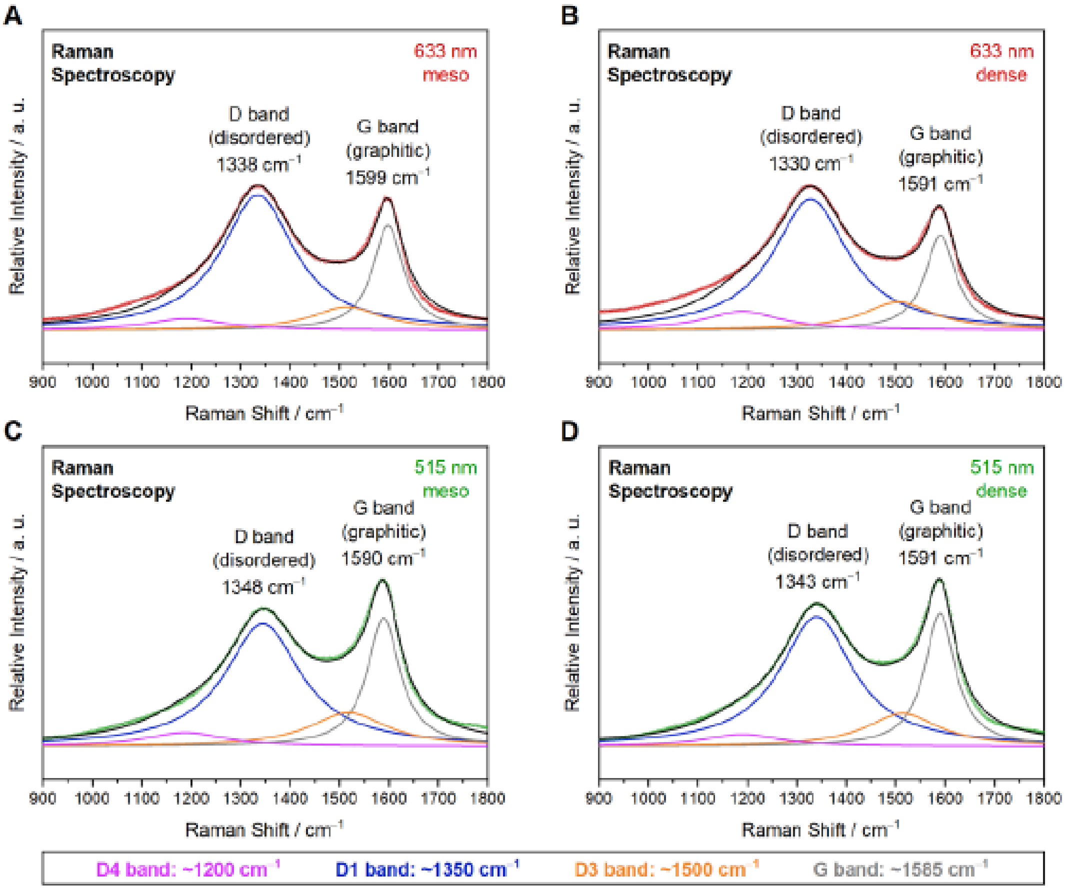

Figure S3. Raman spectra of a (A and C) mesoporous and (B and D) non-templated carbon powder measured with an excitation wavelength of (A and B) 633 nm (red) and (C and D) 515 nm (green). The spectra are fitted (black) with a superposition of four Lorentzian functions representing the D4 (pink), D1 (blue), D3 (orange), and G band (gray).

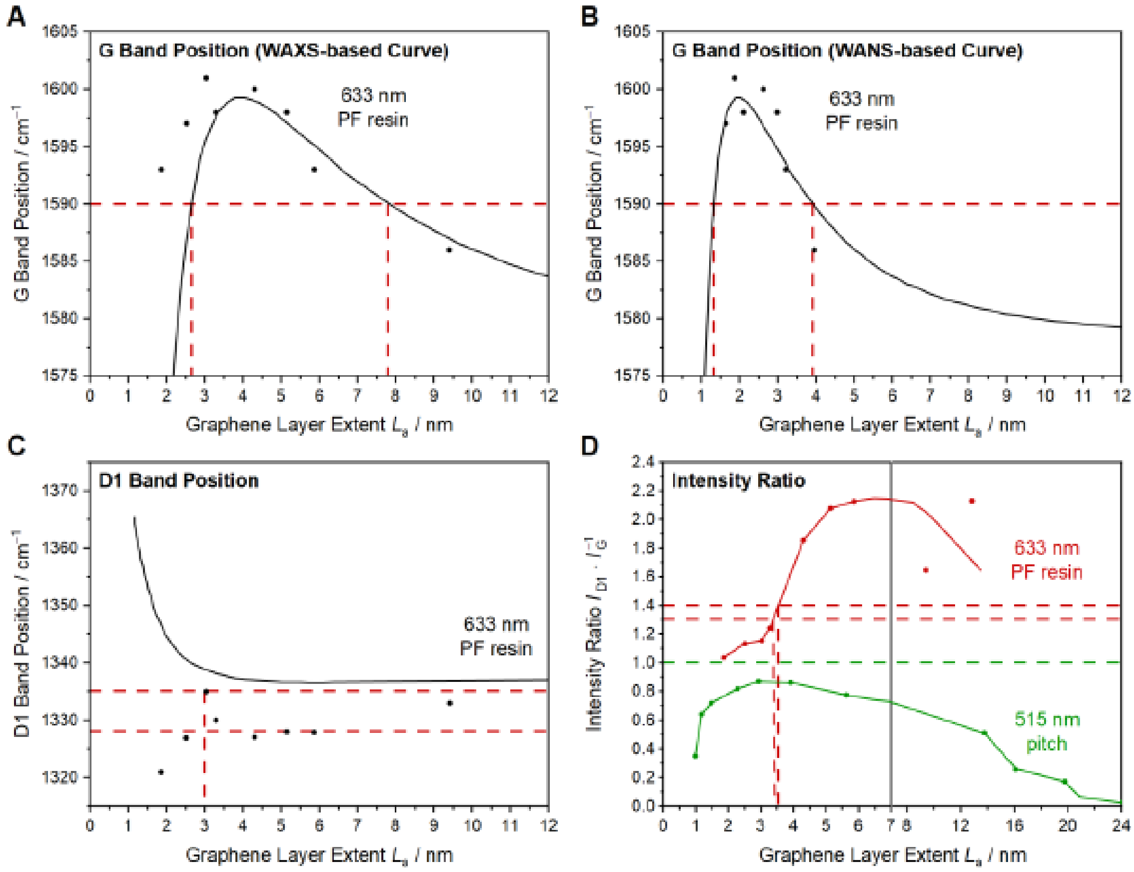

Figure S4. Empirical correlations between (A and B) G band position, (C) D1 band position, and (D) the intensity ration of the D1 to G band and the average graphene layer extent L_a according to (A, C, and D) Schuepfer *et al.*[1] and (B) Osswald *et al.*[2] The experimental values observed in this work are indicated with a dashed line.

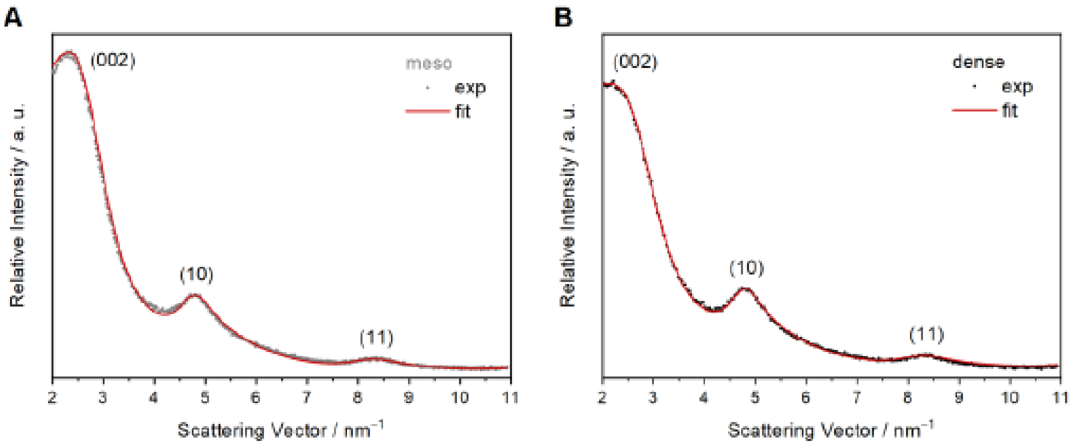

Figure S5. Powder XRD pattern of a (A) mesoporous and (B) non-templated carbon powder fitted (red) with an algorithm according to Ruland and Smarsly.[3]

Table S2. Structural parameters of mesoporous and non-templated carbon powder obtained by fitting the respective XRD pattern. The parameters comprise the average graphene layer extent L_a, the average C–C bond length l_{CC} with its standard deviation σ_1, the average stack height L_c, and the average interlayer spacing a_3 with its standard deviation σ_3.

	Layer Parameters			**Stacking Parameters**		
Sample	**L_a / nm**	**l_{CC} / nm**	**σ_1 / nm**	**L_c / nm**	**a_3 / nm**	**σ_3 / nm**
meso	1.75	0.14	0.02	0.84	0.37	0.07
dense	1.85	0.14	0.02	0.74	0.37	0.07

As a synthesis of mesoporous thin films deposited on titanium plates (1 mm x 1 mm) under similar conditions as that of carbon powders leads to corrosion of the substrate (tarnished areas of the carbon film, at which small particles grow through the film according to SEM, see **Figure 9** and **Figure S6**), several attempts were tested to prevent this corrosion.

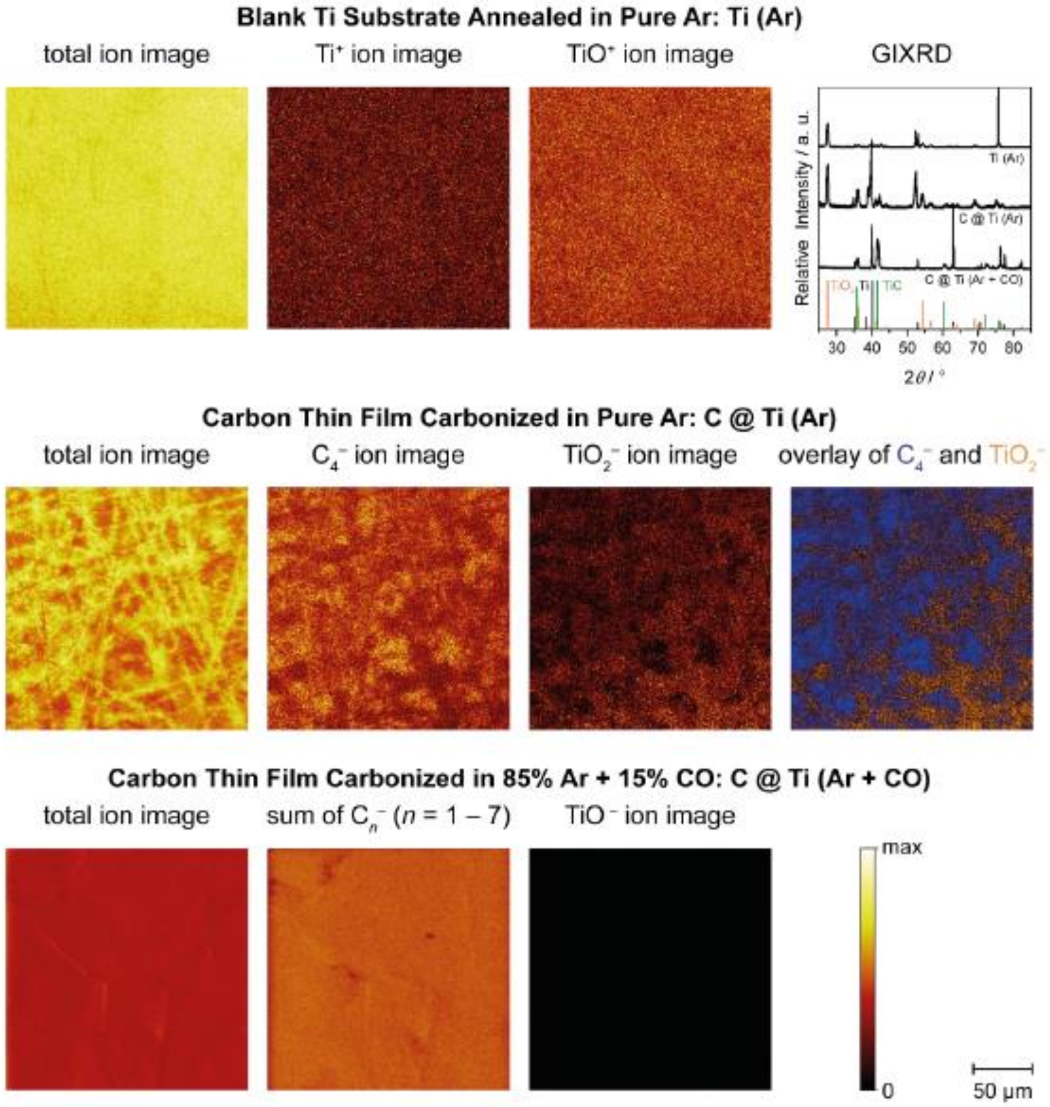

Figure S6. SIMS surface images (200 µm x 200 µm, each normalized to the respective total ion image) of (top) a polished titanium substrate annealed in pure argon at 800 °C, (middle) a mesoporous carbon thin film carbonized in pure argon atmosphere, and (bottom) a similar film carbonized in a mixture of argon and carbon monoxide. Next to the total ion images, single ion images of the carbon- and TiO_2-related ions normalized to the total ion count are given as well as GIXRD patterns of all three samples together with the reference patterns of Ti (ICSD 98-004-3614, black), TiO_2 (rutile, ICSD 98-020-2241, orange) and TiC (ICSD 98-000-1546, green).

Adjustment of the carbonization part of the heating ramp might be reasonable because the TG-MS study in **Figure 2** evoke the hypothesis that such a long carbonization step is not necessary. A shortening of the latter should decrease the time, the substrate is exposed to the harsh (possibly corrosive) conditions of 800 °C. A mesoporous carbon thin film carbonized for only one hour (**Figure** S7 middle) appeared even more tarnished than the reference sample (**Figure** S7 left). However, a reduction of the dwell time by one hour and halving of the heating time (2 K min^{-1} instead of 1 K min^{-1}) leads to less tarnished carbon thin film. This experiment might show that the heating period from 400 to 800 °C, in which the carbon structure is not yet evolved, is responsible for corrosion of the substrate and an increase in heating rate helps to mitigate corrosion. One the hand, the inconstant results with the second film (**Figure** S7 middle) and the still significant corrosion claim that this adjustment is not appropriate to prevent substrate corrosion.

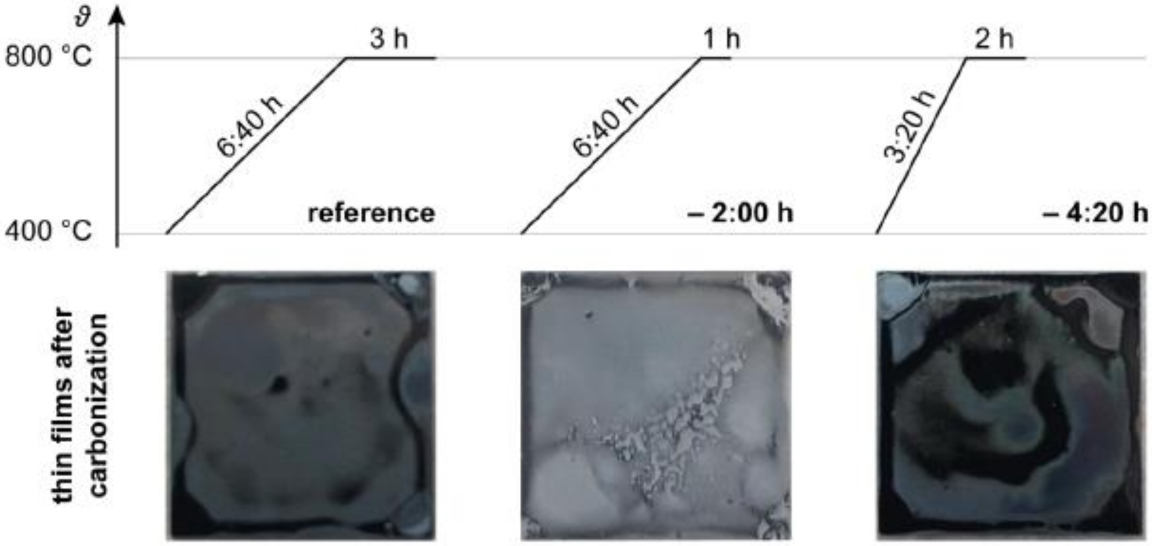

Figure S7. Photographs of carbon thin films on titanium plates (1 mm x 1 mm) after carbonization according to the heating ramps shown above.

If the pyrolysis gases formed during carbonization cause oxidation of the titanium substrate, their contact time with the samples should be minimize to suppress substrate corrosion. Therefore, three different flow rates of the inert feed gas were probed. Although the contrast in the photos in **Figure S8** do not display the tarnished surface properly, neither a doubling nor a quadrupling of the argon flux yield a smooth shiny black carbon coating. This corrosion is further supported by an SEM image of the sample carbonized in an argon flow of 200 mL min^{-1} (**Figure S8** middle) revealing a full coverage of the mesoporous surface with oxide particles.

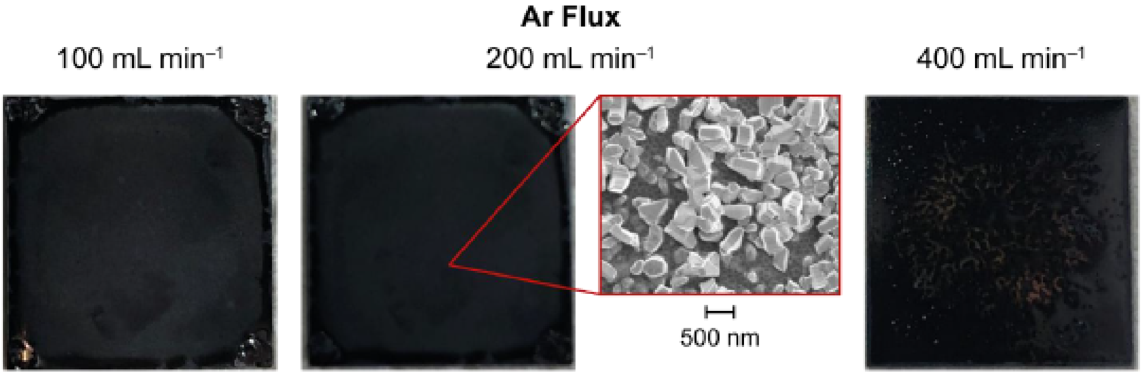

Figure S8. Photographs of carbon thin films on titanium plates (1 mm x 1 mm) after carbonization with different argon flow rates as indicated above. In addition, an SEM image of the sample carbonized in a medium argon stream shows the corrosion of the substrate.

When several samples are carbonized simultaneously, the thin films closer to the exhaust appear less tarnished. One possible explanation could be that the reaction products released during carbonization inhibit the corrosion of titanium. To validate this hypothesis, a closed alumina crucible was used instead of an open one (**Figure S9**). The idea is to keep the reaction atmosphere saturated with pyrolysis gas. If these suppress corrosion, the film should appear less tarnished after carbonization. However, both the photo and the SEM images clearly demonstrate that the corrosion is tremendously more pronounced in case of a closed crucible (even if it was filled with argon before insertion in the furnace to reduce the amount of residual oxygen). Thus, this optimization attempt is not suitable.

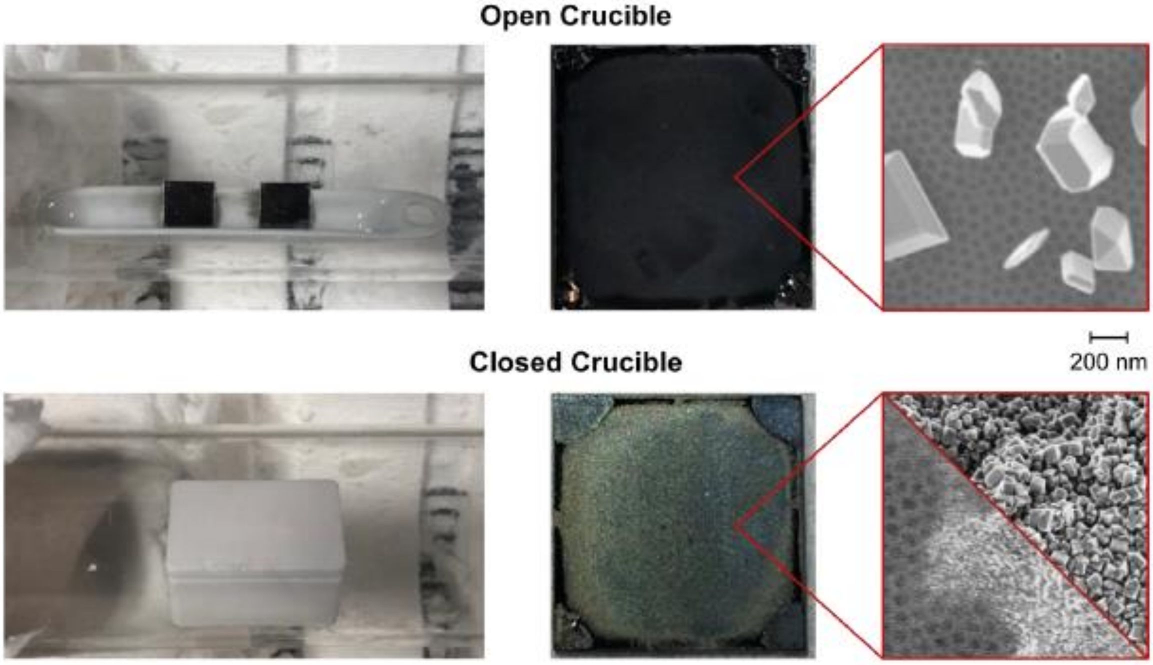

Figure S9. Comparison of carbonization results using an (top) open and (bottom) closed crucible. A photograph of the respective setup and the obtained carbon thin film is given together with three SEM images of the surface structure on the nanoscale.

The possible oxygen sources causing titanium oxidation are either reaction products released from the resin or oxygen traces in the feed gas or oxygen traces in the metal substrate itself (0.25% according to supplier). If the feed gas represents the problem, a sacrificial oxygen trap such as a crucible filled with copper powder (similar to the synthesis of carbon powders) as shown in **Figure S10** (left) should catch oxygen traces before they affect the metal substrate leading to a less tarnished carbon coating. However, both films in **Figure S10** (right) appear strongly corroded although the copper powder did not undergo any change in color. These findings clearly falsify the initial hypothesis of oxygen traces in the feed gas as reason for corrosion and render this adjustment inappropriate.

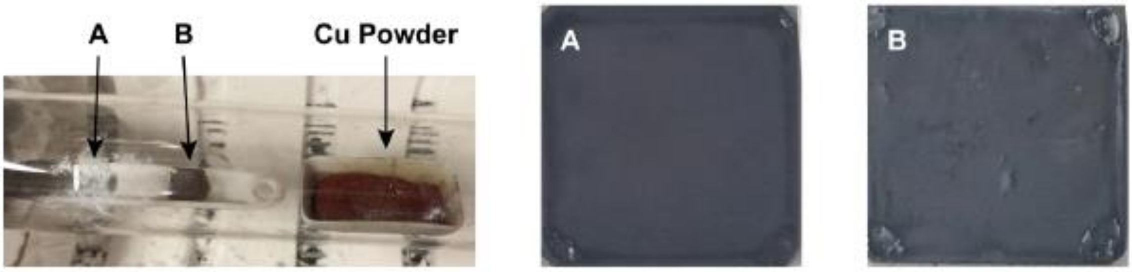

Figure S10. Carbonization of carbon thin films using copper powder as oxygen trap with photographs showing the setup and the thin films obtained after carbonization.

A further idea to mitigate substrate corrosion is the introduction of a protection layer on top of the polished titanium plate. For this reason, a thin layer of gold (around 200 nm) was deposited *via* pulsed-laser deposition (PLD) on a polished titanium plate, and in addition, a polished titanium plate and polished stainless steel plate were annealed in air for 2 h at 600 °C (5 K min^{-1}) to receive a passivating layer[4] of oxide boosting film quality. All three systems were tested in carbonization at 800 °C in argon but according to the film appearance and SEM images (**Figure S11**), no improvement was achieved. In all cases, no smooth mesoporous coating is obtained.

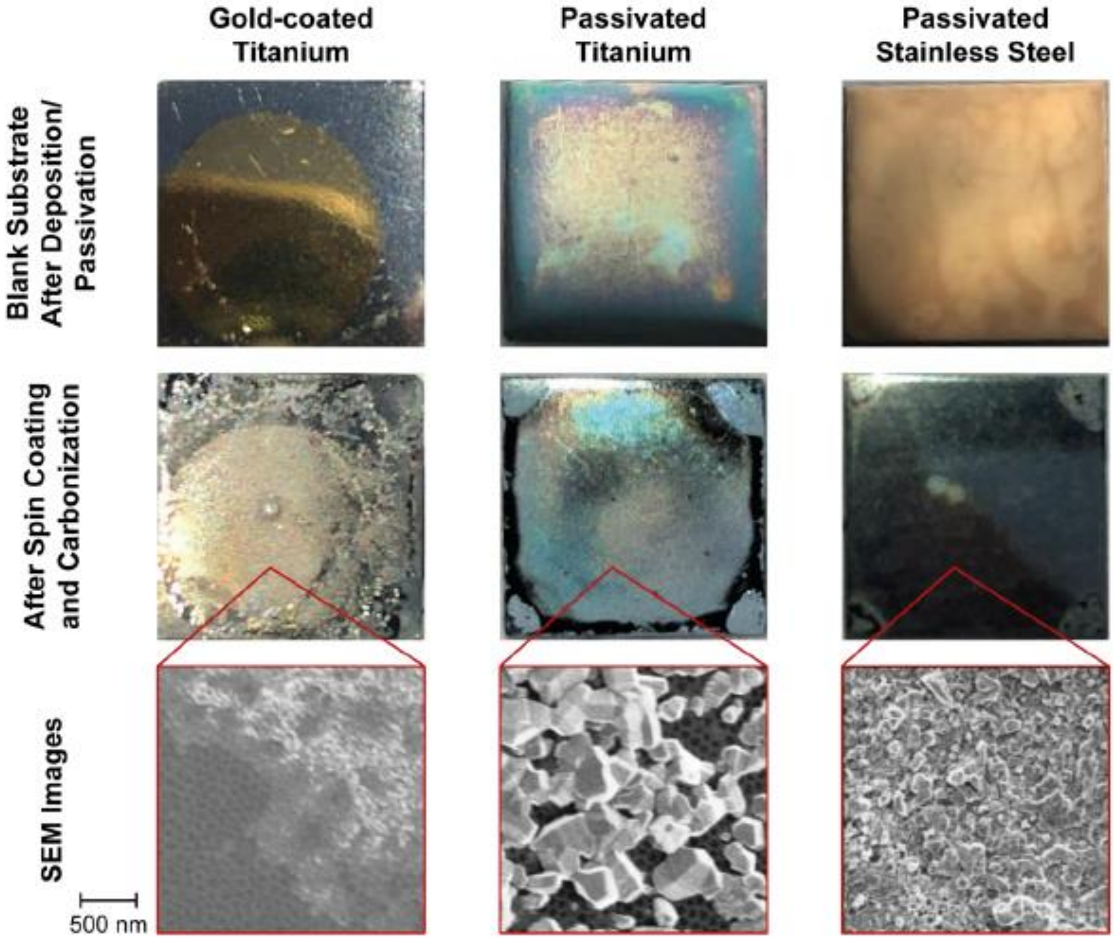

Figure S11. Photographs of different substrates and carbon thin films after carbonization deposited on them as well as SEM images showing the surface structure on the nanoscale. As substrates, (left) a polished titanium plate coated with a gold layer by PLD, (middle) a polished titanium plate annealed for 2 h at 600 °C in air, and (right) a polished stainless steel plate passivated analogously were employed.

To annihilate possible oxygen sources released from either the substrate or the resin, a further promising approach could be the usage of a reductive carbonization atmosphere. Therefore, the argon feed gas was mixed with hydrogen to different extents. As shown in **Figure S12**, mesoporous carbon thin films appear less tarnished if 2 or 4 vol.% hydrogen are employed but from SEM, the surficial particles being characteristic for substrate corrosion are still present. In addition, surprisingly many cracks in the thin film are observed. Apparently, the small hydrogen molecule is capable of penetrating the substrate and makes substrate and/or thin film brittle. Consequently, this approach is not suitable.

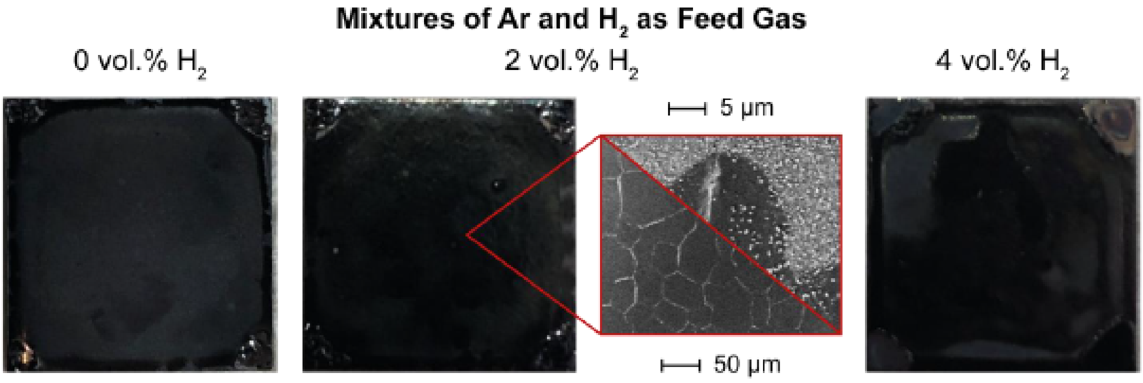

Figure S12. Photographs of carbon thin films on titanium plates (1 mm x 1 mm) after carbonization in argon and different mixtures of argon and hydrogen, respectively, as labeled above. In addition, an SEM image of the sample carbonized in an atmosphere containing 4 vol.% hydrogen is displayed.

An alternative reducing agent that should not possess such embrittlement abilities is carbon monoxide (CO). Therefore, mixtures of argon and CO with different volumetric ratios were tested to prevent substrate corrosion. While 2 vol.% of CO do not significantly decrease the degree of corrosion, 10 vol.% yield an almost perfect carbon coating (see **Figure S13**). With SEM, only a few spots can be found, at which corrosion occurred. Further increase in CO amount to 15 vol.% leads to an evenly black hard carbon coating, which shows also on a nanoscale no traces of substrate corrosion and no cracks. Hence, CO is able of inhibiting the corrosion of the substrate although high amounts are required.

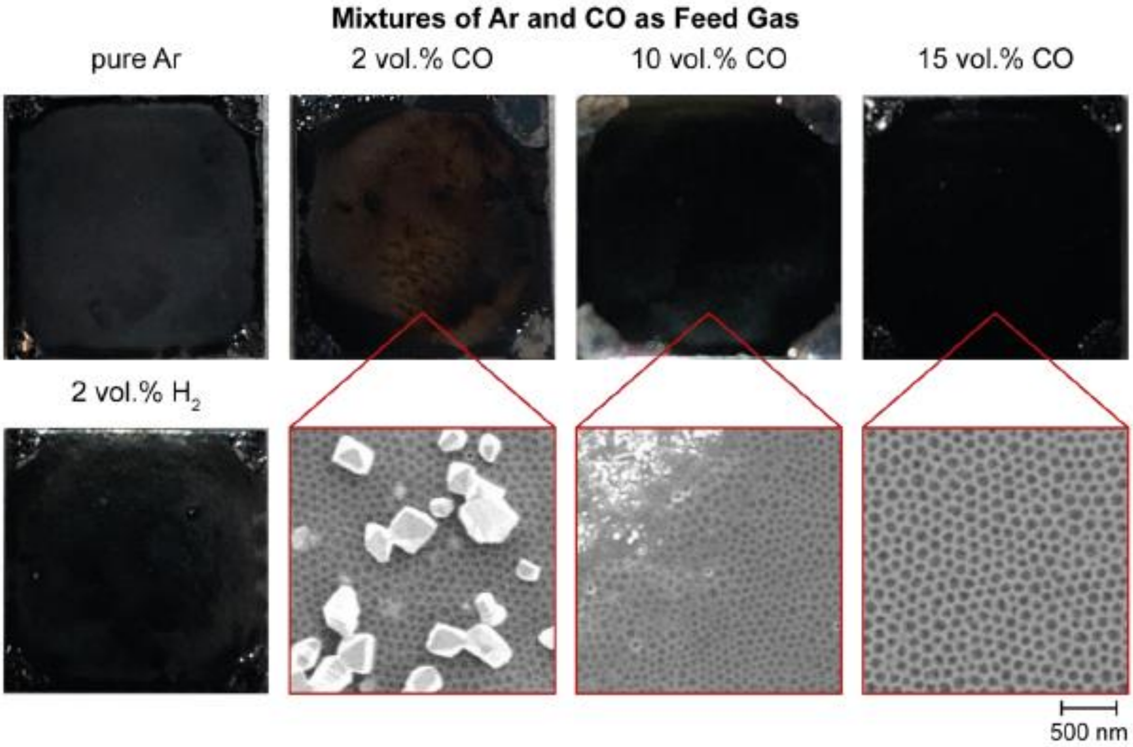

Figure S13. Photographs of carbon thin films on titanium plates (1 mm x 1 mm) after carbonization in different mixtures of argon and carbon monoxide (and two further atmospheres for comparison) as written above. In addition, SEM images of the surface structure are given to evaluate the degree of corrosion.

To check how many samples can be prepared reproducibly without corrosion, eight titanium plates coated with resol resin were distributed along the tube of the tube furnace and carbonized in a mixture of argon and CO. For comparison, two analogue samples were carbonized in argon only to estimate the degree of corrosion. As shown in **Figure S14** (top), corrosion occurs in all cases in pure argon but the extent clearly depends on the tube position: The sample closer to the exhaust suffers less from corrosion than the one near the entrance. A similar trend of film quality is observed for the carbonization under reducing atmosphere. The five carbon films laying in the tube half close to the exhaust possess a homogeneous black coating, while the remaining half at the entrance suffers from delamination and inhomogeneities (see **Figure S14** bottom). Thus, the carbon thin films should be prepared in the exhaust half of the tube to ensure a homogeneous carbon coating.

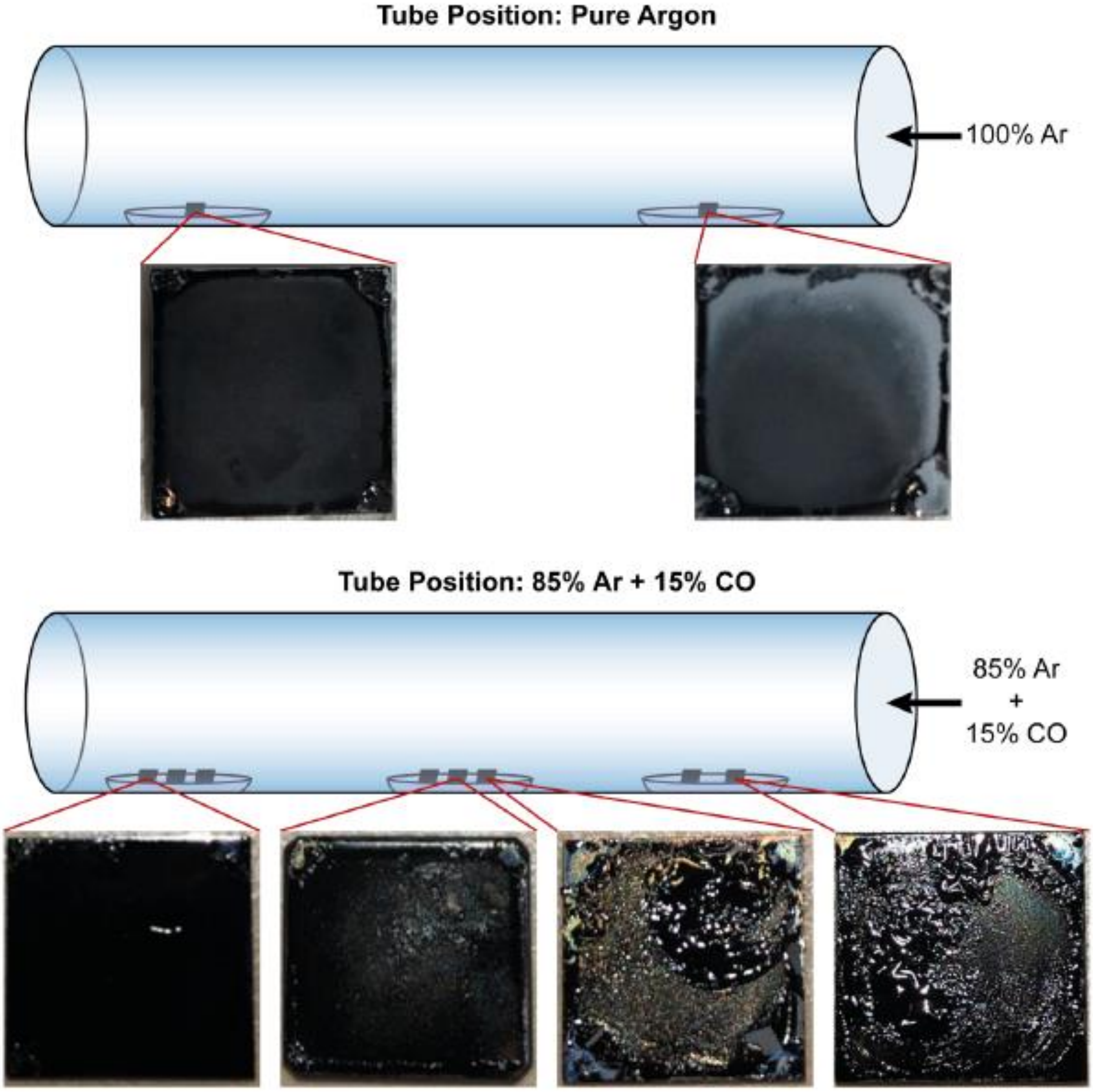

Figure S14. Photographs and SEM images of carbon thin films on titanium plates (1 mm x 1 mm) after carbonization in (top) pure argon and (bottom) a mixture of 85 vol.% argon and 15 vol.% carbon monoxide, respectively, at different positions in the tube furnace.

A possible reason might be a temperature gradient along the tube. The gas flowing through the hot tube needs some time to reach the temperature of the glass wall. According to the temperature dependency of the Boudouard equilibrium (see **Figure S15**), a temperature below 800 °C might decrease the CO concentration into the feed gas below the required 15 vol.% (see comparison of different CO concentrations in **Figure S13**).

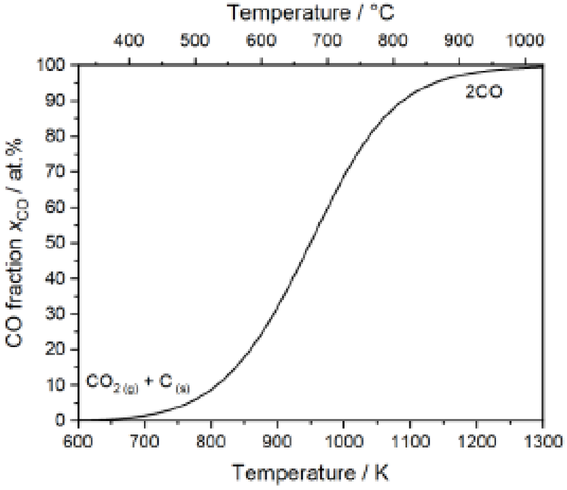

Figure S15. Temperature dependency of the Boudouard equilibrium between carbon monoxide and the disproportionation products carbon dioxide and carbon.

Within a reference experiment, exposing the blank titanium substrate to different atmospheres (nitrogen, argon, and a mixture of argon and CO) provides access to two conclusion: (1) Whether oxygen traces in the resin cause the substrate corrosion and (2) which influence the gas atmosphere has on the pure substrate. As shown in **Figure S16**, a carbonization in nitrogen leads to a shiny golden metal plate. Based on the color, this is most likely due to the formation of titanium nitride. Comparing the other two metal plates, a severe corrosion in pure argon took place while in the Ar/CO mixture the homogeneous surface was preserved (albeit the mirror finish disappeared, which could also be due to a sintering at the high temperature of 800 °C). Combined with the absence of a non-corroded sample after employing copper as oxygen trap (see **Figure S10**), the oxygen traces contained in the titanium plate seem to be responsible for the corrosion. In addition, this experiment clearly confirms that the introduction of CO into the feed gas suppresses the oxidation of the substrate.

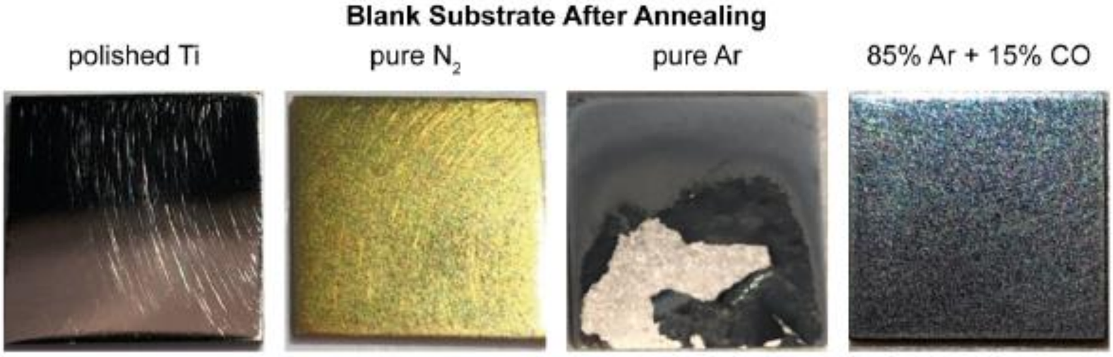

Figure S16. Photographs of polished titanium plates (1 mm x 1 mm) before and after annealing in different atmospheres as indicated above.

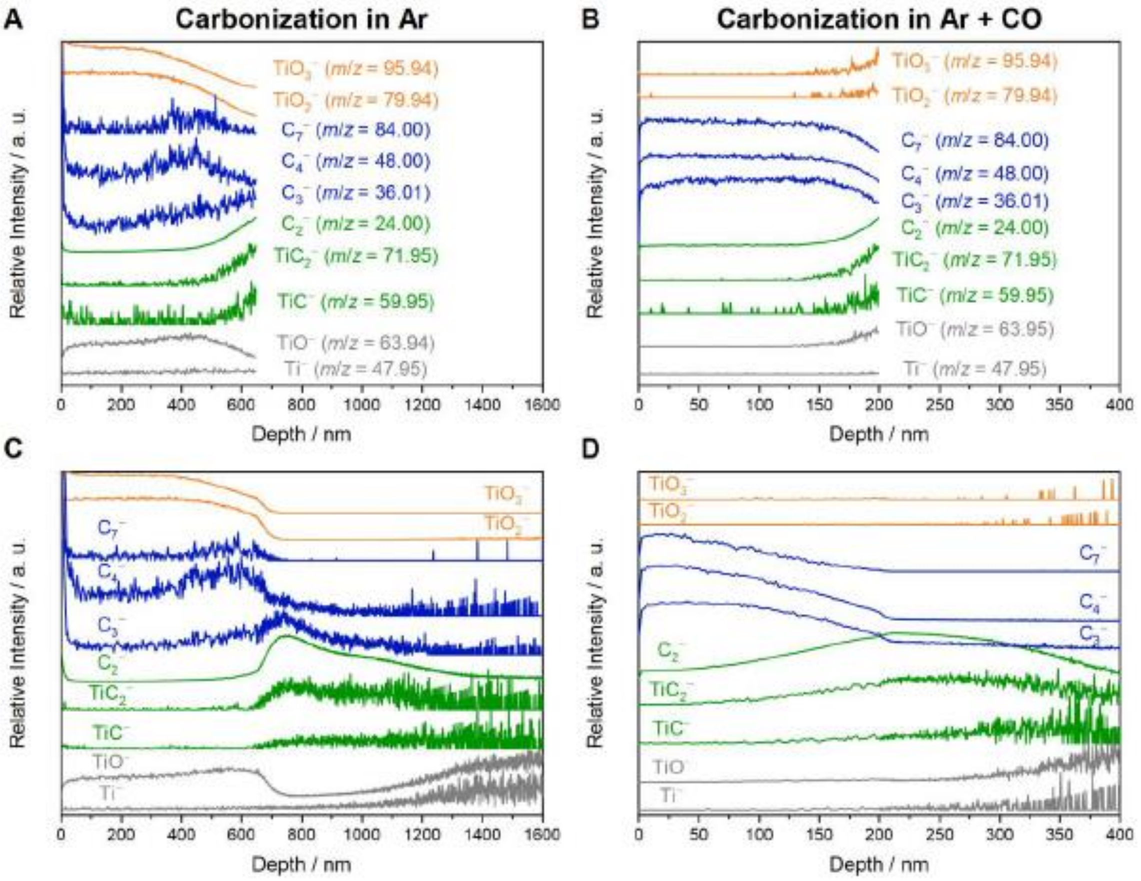

Figure S17. SIMS depth profiles of a mesoporous carbon thin film carbonized (A) in pure argon and (B) in a mixture of 85 vol.% argon and 15 vol.% CO, which were sputtered until the beginning of the TiC interphase as well as (C and D, respectively) the profiles at a second spot each, which were sputtered until the metal substrate was reached. All ions related to TiO_2 are given in orange, the hard carbon film in blue, the TiC interphase in green, and the metal substrate in gray.

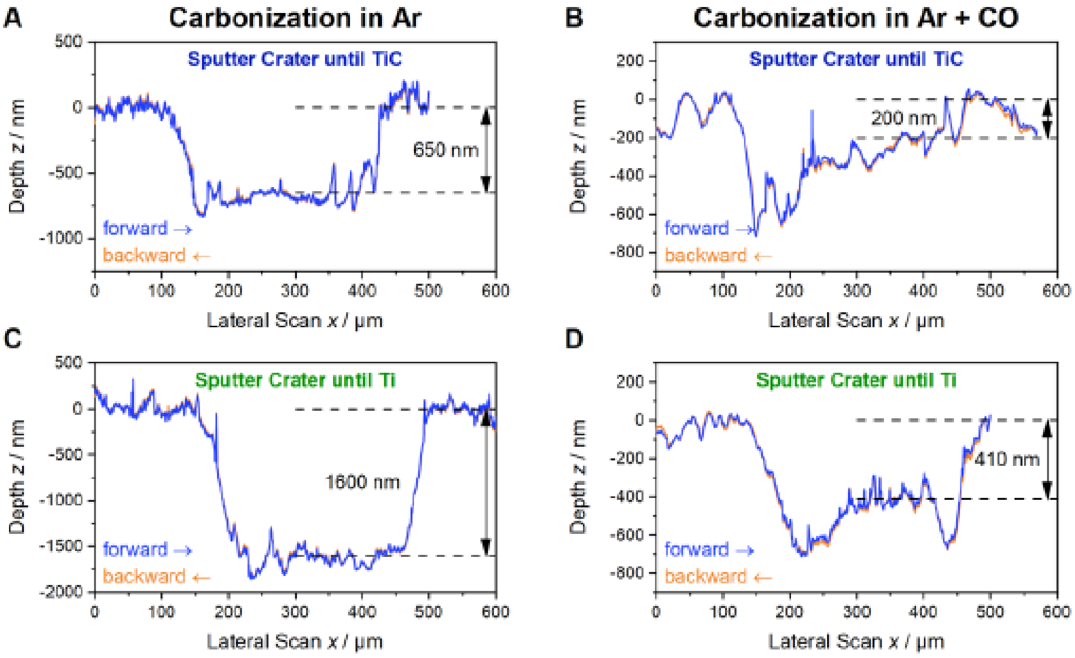

Figure S18. AFM-based topographic scans of the sputter crater in forward (blue) and backward direction (orange) of mesoporous carbon thin films carbonized in (A and C) argon and (B and D) a mixture of argon and CO, respectively, and sputtered until the TiC interphase and Ti substrate, respectively.

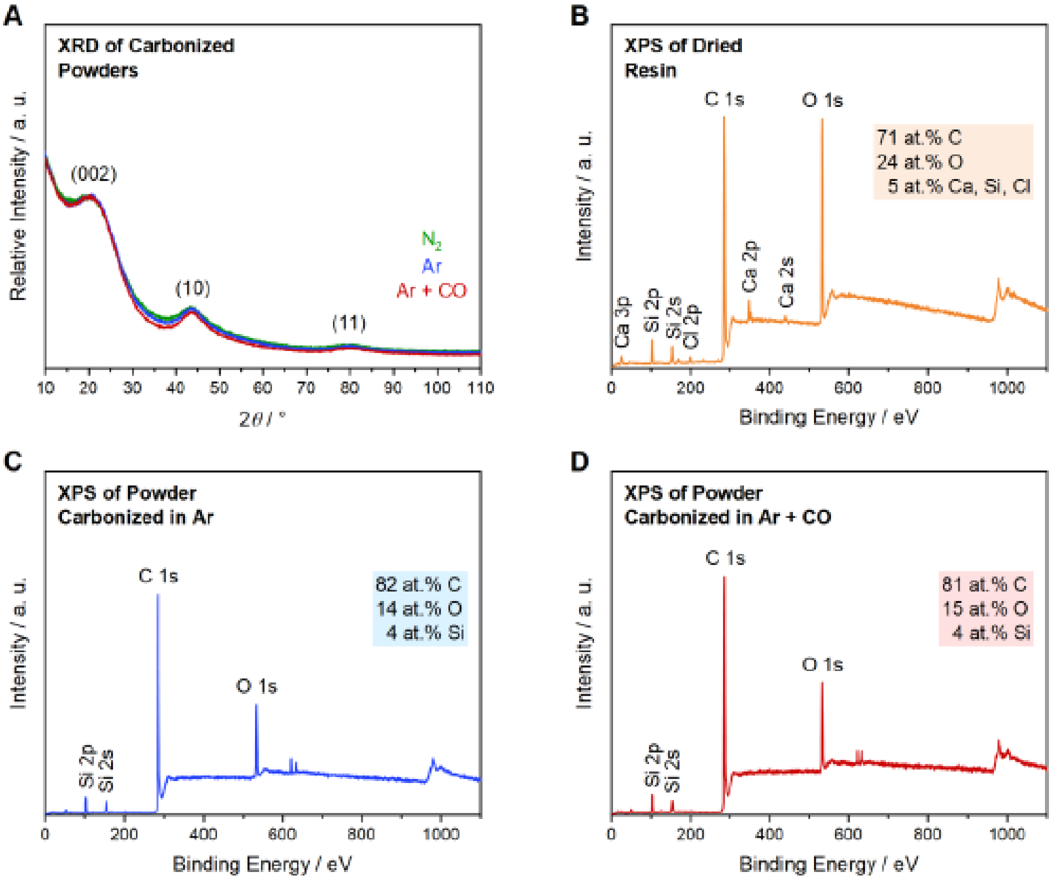

Figure S19. (A) To the (002) reflection normalized XRD patterns of mesoporous carbon powders carbonized at 800 °C in nitrogen (green), argon (blue), and a mixture of 85% argon and 15% CO (red). X-ray photoelectron spectra of (B) a non-templated dried resin, (C) a carbon powder carbonized in argon, and (D) a carbon powder carbonized in a mixture of 85% argon and 15% CO, both prepared from the resin displayed in (B). Labeling of each peak and elemental composition are given for each survey spectrum.

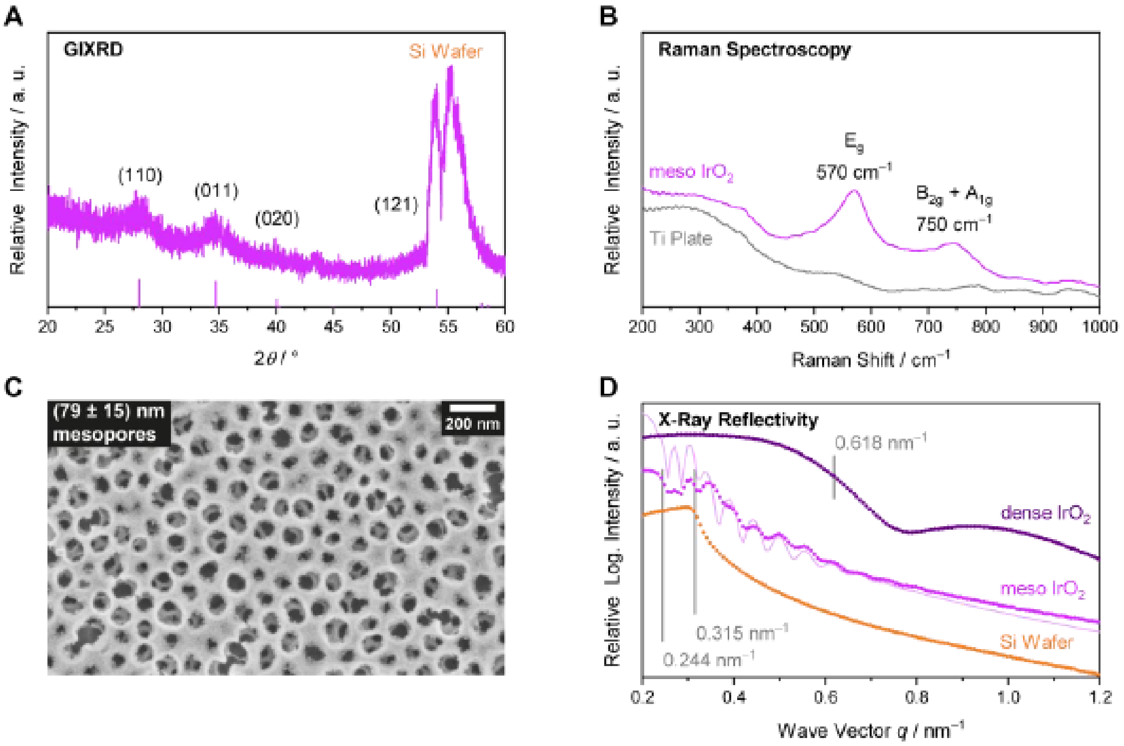

Figure S20. Characterization of the mesoporous IrO_2 reference film including (A) a GIXRD with a reference pattern for tetragonal IrO2 (ICSD 98-005-6009, violet) and labeling of the four main reflections as well as the substrate-related ones, (B) Raman spectra of both the sample (violet) and the blank substrate (gray), (C) an SEM image in top-view, and (D) XRR scans of the substrate (orange), the mesoporous (violet) and a non-templated IrO_2 thin film (deep purple) together with the fitted curve (light violet) of the mesoporous sample. The critical angles assigned to mesoporous IrO_2, the silicon substrate, and dense IrO_2 are highlighted with gray lines, respectively.

The XRR data were recorded in 2θ but are given here in dependency on the wave vector q according to equation **(S1)** inserting the X-ray wavelength λ of 0.154 nm.

$$q = \frac{4\,\pi}{\lambda} \cdot \sin\left(\frac{2\theta}{2}\right) \qquad \textbf{(S1)}$$

The determination of the density ρ (in electrons per nm^3) from the critical wave vector q_c is possible following equation **(S2)**, in which r_e describes the classic radius of the electron (2.813 x 10^{-6} nm). Using the same equation, the expected critical wave vector can be predicted if the electron density is calculated from the volume of the material's unit cell and the number of electrons inside it.

$$\rho = \frac{q_c^2}{16\,\pi\,r_e} \qquad \textbf{(S2)}$$

In case of the mesoporous sample, its average density ρ_{meso} can be used to obtain the porosity P (volume fraction of pores) when contrasting ρ_{meso} to the dense material's density ρ_{dense} as shown in equation **(S3)**.

$$P = \frac{\rho_{\text{dense}} - \rho_{\text{meso}}}{\rho_{\text{dense}}} \qquad \textbf{(S3)}$$

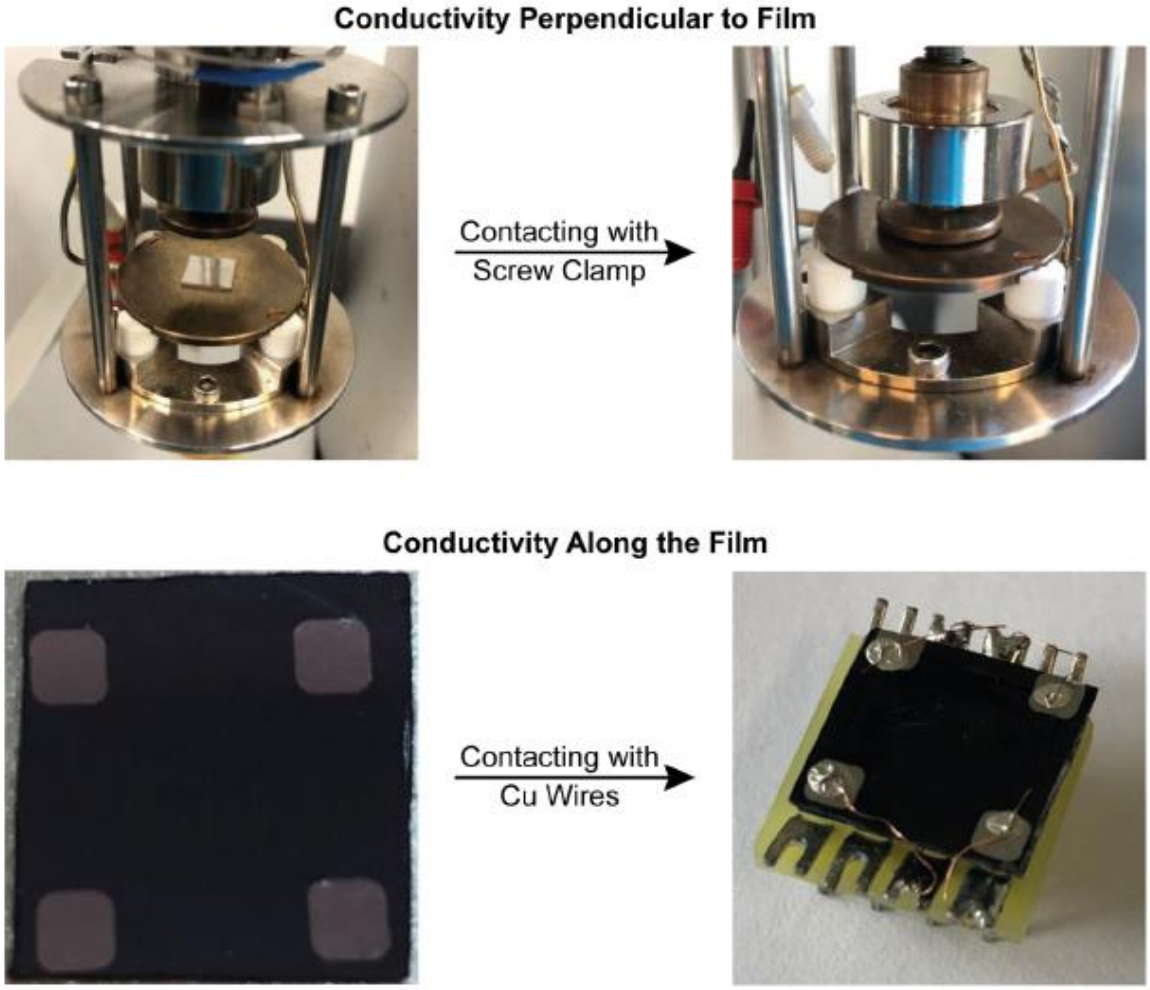

Figure S21. Setup for measuring the electric transport (top) perpendicular and (bottom) along the thin film surface. For the first measurement, the thin film sample is mounted into a metal screw clamp. In case of the in-plane measurement, platinum is deposited in all corners of the thin film by pulsed-laser deposition and then contacted with conducting silver and copper wires.

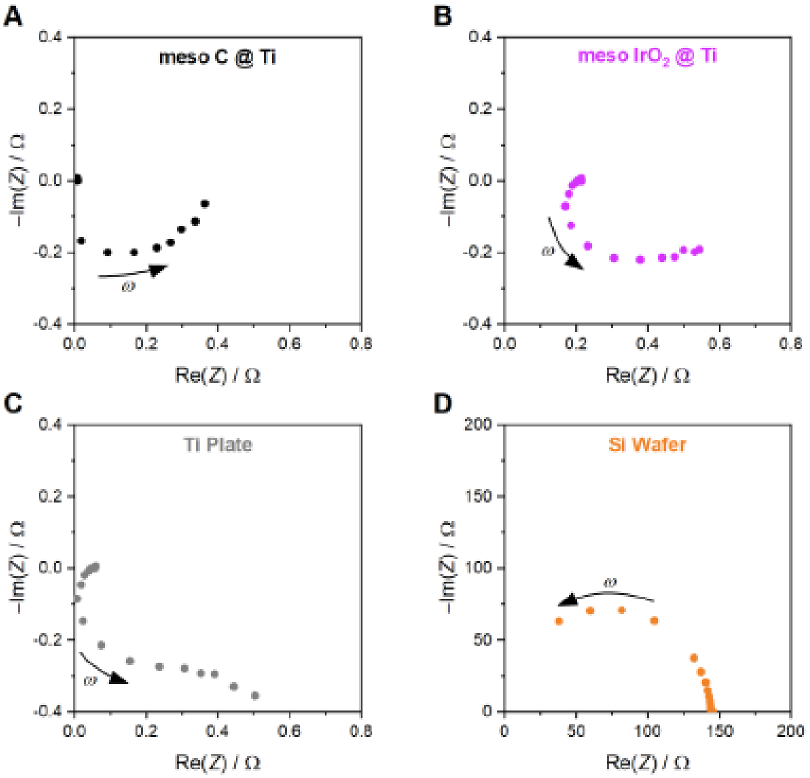

Figure S22. Nyquist plots of the impedance spectra at room temperature of (A) a mesoporous carbon thin film on titanium carbonized in a mixture of argon and CO, (B) a mesoporous IrO_2 thin film on titanium, (C) a blank, polished titanium substrate, and (D) a blank silicon wafer. The arrows indicate the direction of increasing frequency.

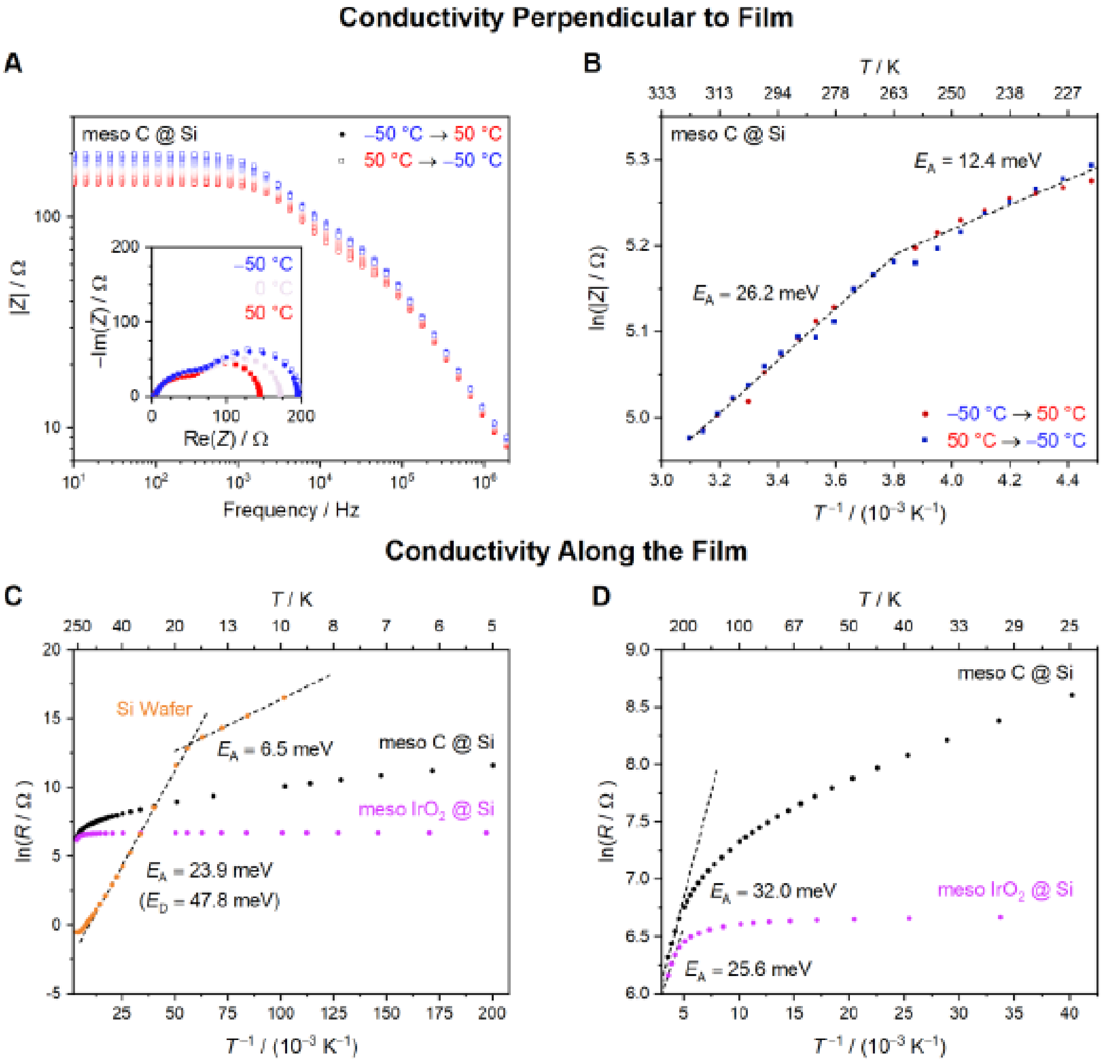

Figure S23. (A) Bode and Nyquist (inset) plot of the impedance spectra of a mesoporous carbon thin film deposited on a silicon wafer measured at different temperatures between –50 and 50 °C in transversal direction and (B) the Arrhenius plot of the resistance measured at low frequencies with the apparent activation barriers determined from the slopes of the linear fits. (C and D) Arrhenius plot of the lateral sheet resistance of a silicon wafer (orange), and a mesoporous hard carbon (black) and IrO_2 thin film (violet) deposited on silicon recorded in van-der-Pauw geometry along the sample surface at temperatures between 5 and 280 K. Apparent activation energies were determined from the slope of corresponding linear fits.

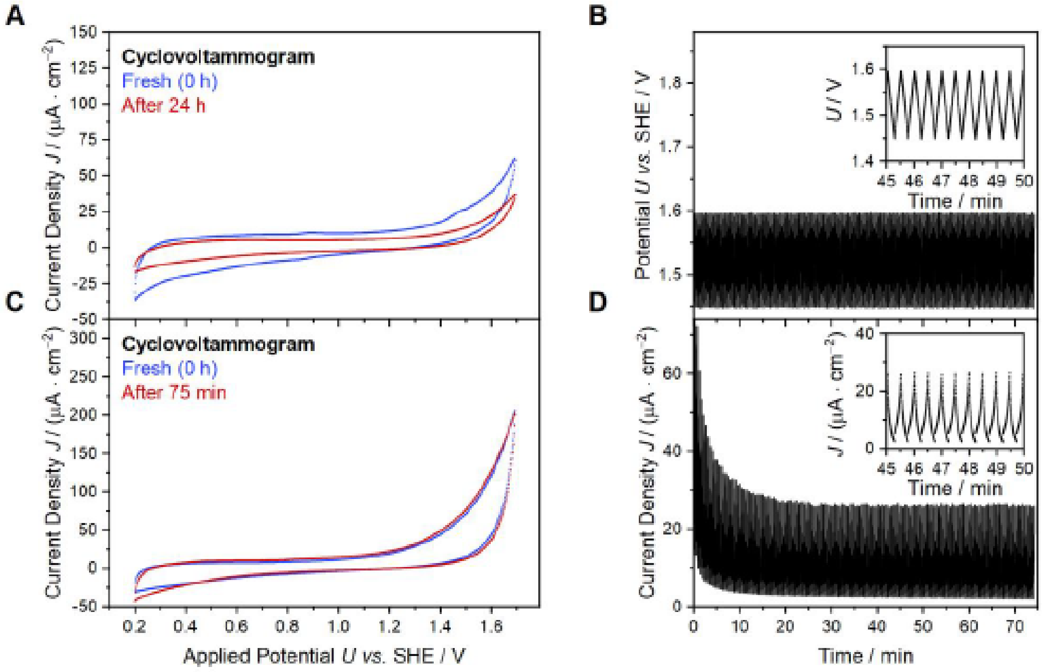

Figure S24. CV scans of two mesoporous carbon thin films on titanium carbonized in a mixture of argon and CO recorded with 0.05 V s^{-1} in 0.5 M H_2SO_4 and a flow rate of 2 mL min^{-1} before (blue) and after (red) continuous cycling between 1.45 and 1.60 V against SHE. While one sample underwent (C) short-term cycling (75 min, 150 cycles), the other was exposed to (A) long-term cycling for 24 h (2900 cycles). The (B) applied potential and (D) measured current density of the short-term measurement are given together with a respective zoomed-in cutout in the inset.

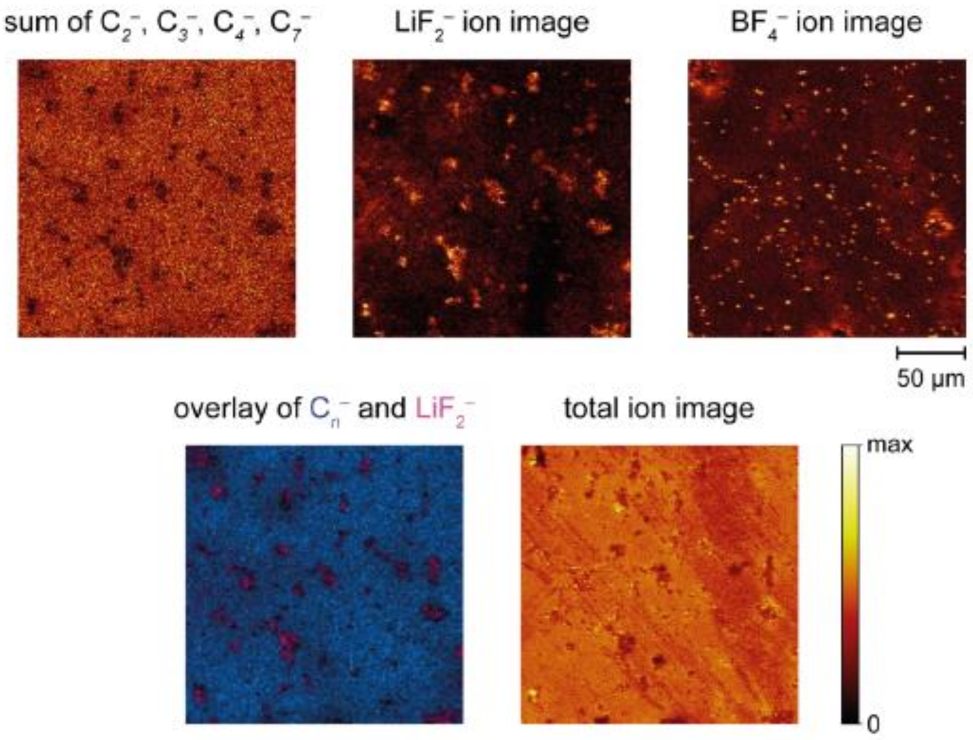

Figure S25. SIMS surface images (200 µm x 200 µm) of a mesoporous carbon thin film carbonized in a mixture of argon and carbon monoxide and infiltrated with a $LiBF_4$ solution after electrochemical cycling between 1.45 and 1.60 V against SHE for 75 min. Next to the total ion images, single ion images of the carbon- and $LiBF_4$-related ions normalized to the total ion count are given together with an overlay image showing the residual salt (violet) on the carbon surface (blue).

REFERENCES

(1) Schuepfer, D. B.; Badaczewski, F.; Guerra-Castro, J. M.; Hofmann, D. M.; Heiliger, C.; Smarsly, B.; Klar, P. J. Assessing the Structural Properties of Graphitic and Non-Graphitic Carbons by Raman Spectroscopy. *Carbon* **2020**, *161*, 359–372.

(2) Osswald, O.; Loeh, M. O.; Badaczewski, F. M.; Pfaff, T.; Fischer, H. E.; Franz, A.; Hoffmann, J.; Reehuis, M.; Klar, P. J.; Smarsly, B. M. On the Highly Ordered Graphene Structure of Non-Graphitic Carbons (NGCs)—A Wide-Angle Neutron Scattering (WANS) Study. *C* **2023**, *9*, 27.

(3) Ruland, W.; Smarsly, B. X-Ray Scattering of Non-Graphitic Carbon: An Improved Method of Evaluation. *J. Appl. Crystallogr.* **2002**, *35*, 624–633.

(4) Sokolov, S.; Ortel, E.; Radnik, J.; Kraehnert, R. Influence of Steel Composition and Pre-Treatment Conditions on Morphology and Microstructure of TiO_2 Mesoporous Layers Produced by Dip Coating on Steel Substrates. *Thin Solid Films* **2009**, *518*, 27–35.

4 Fazit und Ausblick

Das Ziel dieser Arbeit bestand in der Etablierung einer Bibliothek mesoporöser Materialien, deren Porensystem gezielt variiert werden kann und die somit systematische Studien zwischen morphologischen Parametern und elektrochemischen Eigenschaften ermöglichen. Hierfür gilt es insbesondere zwei Fragen zu beantworten: (1) Wie kann das Porensystem von über *Soft Templating* synthetisierten mesoporösen Materialien maßgeschneidert und zuverlässig charakterisiert werden? (2) Sind solche Materialien für elektrochemische Anwendungen geeignet?

Zur Beantwortung der ersten Frage wurde zunächst das Block-Copolymer PEO-*b*-PHA über eine optimierte Polymersynthese hergestellt und als Templat zur Synthese mesoporösen Silikas verwendet. Hierbei zeigte eine umfassende morphologische Charakterisierung mittels REM, Physisorption, SAXS und Tomographie, dass diese Templatfamilie nicht nur in der Lage ist, große Mesoporen von etwa 40 nm zu erzielen, sondern offenbarte auch ein genaues Bild des Porensystems bestehend aus Mikro- und Mesoporen. In einer zweiten Studie wurde aufbauend auf der nun etablierten Polymersynthese und Methodik zur Untersuchung großer Mesoporen eine Matrix aus PEO-*b*-PHA-Copolymeren mit variabler PEO- und PHA-Blocklänge synthetisiert und zur Templatierung herangezogen. Während die Modulation der PHA-Blocklänge eine gezielte Einstellung der Porengröße zwischen 10 – 80 nm ermöglichte, bestimmte die Templatkonzentration die Wanddicke und Porenkonnektivität. Die geschlussfolgerten experimentellen Leitfäden zum bewussten Design des Porensystems erlauben die gezielte Synthese einer bestimmten Porenstruktur sowie die systematische Variation morphologischer Parameter für allerlei Porositätsstudien.

Ein Vergleich eines mit PEO-*b*-PHA templatierten Pulvers aus Silika mit einem ähnlich templatiertem aus Kohlenstoff legte in einer weiteren Studie nahe, dass die Porenstruktur im Oxid hinsichtlich der Konnektivität analog zu der im mesoporösen Kohlenstoff ist. Diese Erkenntnis deutet darauf hin, dass die zuvor gewonnenen Ergebnisse zum gezielten Porendesign auch für das elektrochemisch interessante Material Kohlenstoff gelten. Außerdem zeigte die tiefgehende Untersuchung der Porenkonnektivität, dass sowohl Physisorptionsexperimente als auch Elektronentomographie notwendig sind, um ein vollständiges Bild der Konnektivität zu erhalten.

In einer letzten Studie wurde der zweiten Frage bezüglich der Anwendbarkeit solcher mesoporöser Materialien in der Elektrochemie nachgegangen. Dafür wurde ein mesoporöser Dünnfilm aus Iridiumoxid und aus Kohlenstoff hergestellt und im Hinblick auf deren elektrische Leitfähigkeit verglichen. Der Kohlenstofffilm zeigte hierbei eine zum Oxid vergleichbar hohe Leitfähigkeit, und im Rahmen anschließender Messungen auch eine hohe elektrochemische Stabilität unter sauren und oxidativen Bedingungen, sowie ein zugängliches Porensystem. Diese Untersuchung stellt nicht nur eine Blaupause zur Charakterisierung von mesoporösen Kohlenstoff dar, sondern bestätigt auch, dass diese Kohlenstofffilme als Modellsystem für elektrochemische Studien (zum Beispiel als Trägermaterial in der sauren Elektrokatalyse) vielversprechend sind.

Die hier gezeigten Arbeiten legen lediglich die Grundlagen für anwendungsbezogene Porositätsstudien, weshalb kommende Arbeiten den Fokus auf elektrokatalytisch aktive Materialien wie Iridiumoxid legen sollten. Aufbauend auf den Grundsätzen zum Porendesign aus der zweiten Publikation und der Synthese von mesoporösen Iridiumoxidfilmen aus der vierten Publikation stellen die Synthese einer definierten Matrix aus Dünnfilmen mit variabler Porengröße und Wanddicke und dessen Untersuchung in der sauren Wasserelektrolyse hinsichtlich katalytischer Aktivität und Stabilität die nächsten Schritte dar. Auf diese Weise kann die für die Elektrokatalyse optimale (aktivste und stabilste) Porenstruktur identifiziert werden. Weiterhin kann künftig mittels der Kohlenstofffilme aus der vierten Publikation untersucht werden, ob sich über Atomlagenabscheidung eine nanometerdicke Schicht aus Iridiumoxid auf Kohlenstoff abscheiden und in der Elektrokatalyse nutzen lässt. Dadurch könnte (vor allem bei Kenntnis der optimalen Porenstruktur) ein vielversprechender Modellkatalysator für die Wasserelektrolyse erhalten werden, der minimale Mengen des kritischen Iridiums benötigt bei optimaler katalytischer Aktivität und Stabilität.

Die Erkenntnisse dieses Promotionsprojekts sind allerdings nicht nur auf Studien zur sauren Wasserelektrolyse mit Iridiumoxid beschränkt, sondern können auf sämtliche Anwendungsgebiete mesoporöser Materialien übertragen werden. Da mesoporöser Kohlenstoff zum Beispiel auch in Kondensatoren oder Natrium-Ionen-Batterien untersucht wird, bilden die hier dargestellten Ergebnisse ein Fundament für allerlei Studien, in denen die makroskopischen Eigenschaften eines mesoporösen Modellsystems mit seinen morphologischen Parametern (Porengröße und Wanddicke) korreliert werden soll.

5 Literaturverzeichnis

[1] J. Kibsgaard, I. Chorkendorff, *Nat. Energy* **2019**, *4*, 430–433.

[2] M. Carmo, D. L. Fritz, J. Mergel, D. Stolten, *Int. J. Hydrogen Energy* **2013**, *38*, 4901–4934.

[3] T. Weber, T. Ortmann, D. Escalera-López, M. J. S. Abb, B. Mogwitz, S. Cherevko, M. Rohnke, H. Over, *ChemCatChem* **2020**, *12*, 855–866.

[4] C. Minke, M. Suermann, B. Bensmann, R. Hanke-Rauschenbach, *Int. J. Hydrogen Energy* **2021**, *46*, 23581–23590.

[5] C. P. Liu, E. H. Vang, T. Priamushko, C. Roiron, S. Cherevko, P. Atanassov, *ACS Catal.* **2025**, *15*, 7956–7965.

[6] A. Song, Y. Chen, B. Ghosh, H. Yang, *Chem. Mater.* **2025**, 37, 9153–9164.

[7] E. Ortel, T. Reier, P. Strasser, R. Kraehnert, *Chem. Mater.* **2011**, *23*, 3201–3209.

[8] M. Bernicke, E. Ortel, T. Reier, A. Bergmann, J. Ferreira de Araujo, P. Strasser, R. Kraehnert, *ChemSusChem* **2015**, *8*, 1908–1915.

[9] L. Li, M. Krissanasaeranee, S. W. Pattinson, M. Stefik, U. Wiesner, U. Steiner, D. Eder, *Chem. Commun.* **2010**, *46*, 7620–7622.

[10] M. Ternan, *Can. J. Chem. Eng.* **1987**, *65*, 244–249.

[11] N. T. Rodrigues, F. D. Alves Aarão Reis, *Langmuir* **2024**, *40*, 11371–11380.

[12] A. Liang, C. Liu, P. S. Branicio, *Langmuir* **2024**, *40*, 10868–10883.

[13] A. Trommer, J. Hessling, P. R. Schreiner, M. Schönhoff, B. M. Smarsly, *ACS Appl. Mater. Interfaces* **2025**, *17*, 24283–24299.

[14] T. Weller, J. Sann, R. Marschall, *Adv. Energy Mater.* **2016**, *6*, 1–9.

[15] H. Oveisi, C. Anand, A. Mano, S. S. Al-Deyab, P. Kalita, A. Beitollahi, A. Vinu, *J. Mater. Chem.* **2010**, *20*, 10120.

[16] J. Shao, S. Yang, L. Lei, Q. Cao, Y. Yu, Y. Liu, *Chem. Mater.* **2016**, *28*, 7134–7144.

[17] P. R. Karandikar, Y.-J. Lee, G. Kwak, M. H. Woo, S.-J. Park, H.-G. Park, K.-S. Ha, K.-W. Jun, *J. Phys. Chem. C* **2014**, *118*, 21975–21985.

[18] T. von Graberg, P. Hartmann, A. Rein, S. Gross, B. Seelandt, C. Röger, R. Zieba, A. Traut, M. Wark, J. Janek, B. M. Smarsly, *Sci. Technol. Adv. Mater.* **2011**, *12*, 1–12.

[19] J. B. Cook, H.-S. Kim, T. C. Lin, S. Robbennolt, E. Detsi, B. S. Dunn, S. H. Tolbert, *ACS Appl. Mater. Interfaces* **2017**, *9*, 19063–19073.

[20] J. Wang, K. Zhang, A. Bogaerts, V. Meynen, *Chem. Eng. J.* **2023**, *464*, 142574.

[21] W. van den Bergh, H. N. Lokupitiya, N. A. Vest, B. Reid, S. Guldin, M. Stefik, *Adv. Funct. Mater.* **2021**, *31*, 2007826.

[22] C. Glatthaar, M. Wang, L. Q. Wagner, F. Breckwoldt, Z. Guo, K. Zheng, M. Kriechbaum, H. Amenitsch, M.-M. Titirici, B. M. Smarsly, *Chem. Mater.* **2023**, *35*, 10416–10433.

[23] S. Yoon, S. M. Oh, C. W. Lee, J. H. Ryu, *J. Electroanal. Chem.* **2011**, *650*, 187–195.

[24] T. Weller, J. Timm, L. Deilmann, T. S. Doerr, C. Greve, A. S. Cherevan, P. A. Beaucage, U. B. Wiesner, E. M. Herzig, D. Eder, R. Marschall, *Small Struct.* **2022**, *31*, 2200184.

[25] Y. Liu, W. Li, D. Shen, C. Wang, X. Li, M. Pal, R. Zhang, L. Chen, C. Yao, Y. Wei, Y. Li, Y. Zhao, H. Zhu, W. Wang, A. M. El−Toni, F. Zhang, D. Zhao, *Chem. Mater.* **2015**, *27*, 5577–5586.

[26] S. Sallard, M. Schröder, C. Boissière, C. Dunkel, M. Etienne, A. Walcarius, T. Oekermann, M. Wark, B. M. Smarsly, *Nanoscale* **2013**, *5*, 12316.

[27] J. K. Eckhardt, C. Heiliger, M. T. Elm, *ACS Appl. Mater. Interfaces* **2023**, *15*, 35332–35341.

[28] L. R. Meza, S. Das, J. R. Greer, *Science* **2014**, *345*, 1322–1326.

[29] T. Priamushko, R. Guillet-Nicolas, M. Yu, M. Doyle, C. Weidenthaler, H. Tüysüz, F. Kleitz, *ACS Appl. Energy Mater.* **2020**, *3*, 5597–5609.

[30] M. Stefik, *J. Mater. Res.* **2022**, *37*, 25–42.

[31] M. Frisch, M. H. Raza, M. Ye, R. Sachse, B. Paul, R. Gunder, N. Pinna, R. Kraehnert, *Adv. Mater. Interfaces* **2022**, *9*, 2102035.

[32] L. Zeng, B. Yuan, Q. Zhou, *Langmuir* **2024**, *40*, 24696–24705.

[33] T. Shen, X. Chen, Z. Hu, Z. Yan, L. Yang, H. Sun, R. Zhang, H.-Y. Yu, *Langmuir* **2025**, *41*, 694–703.

[34] A. E. Danks, S. R. Hall, Z. Schnepp, *Mater. Horizons* **2016**, *3*, 91–112.
[35] M. Kakihana, *J. Sol-Gel Sci. Technol.* **1996**, *6*, 7–55.
[36] D. M. Schleich, *Solid State Ionics* **1994**, *70–71*, 407–411.
[37] J. Livage, *New J. Chem.* **2001**, *25*, 1.
[38] T. Graham, *J. Chem. Soc.* **1864**, *17*, 318–327.
[39] G. J. Owens, R. K. Singh, F. Foroutan, M. Alqaysi, C.-M. Han, C. Mahapatra, H.-W. Kim, J. C. Knowles, *Prog. Mater. Sci.* **2016**, *77*, 1–79.
[40] H. Y. Hsueh, C. T. Yao, R. M. Ho, *Chem. Soc. Rev.* **2015**, *44*, 1974–2018.
[41] D. Bokov, A. Turki Jalil, S. Chupradit, W. Suksatan, M. Javed Ansari, I. H. Shewael, G. H. Valiev, E. Kianfar, *Adv. Mater. Sci. Eng.* **2021**, DOI: 10.1155/2021/5102014.
[42] L. L. Hench, J. K. West, *Chem. Rev.* **1990**, *90*, 33–72.
[43] P. J. Flory, *Faraday Discuss. Chem. Soc.* **1974**, *57*, 7.
[44] A. L. Luna, F. Matter, M. Schreck, J. Wohlwend, E. Tervoort, C. Colbeau-Justin, M. Niederberger, *Appl. Catal. B Environ.* **2020**, *267*, 118660.
[45] J. Gonthier, T. Rilling, E. Scoppola, F. Zemke, A. Gurlo, P. Fratzl, W. Wagermaier, *Chem. Mater.* **2023**, *35*, 7683–7693.
[46] F. Matter, M. Niederberger, *Chem. Mater.* **2023**, *35*, 7995–8008.
[47] W. Stöber, A. Fink, E. Bohn, *J. Colloid Interface Sci.* **1968**, *26*, 62–69.
[48] D. Gallagher, T. A. Ring, *Chimia* **1989**, *43*, 298–304.
[49] M. Nabavi, S. Doeuff, C. Sanchez, J. Livage, *J. Non. Cryst. Solids* **1990**, *121*, 31–34.
[50] N. Talebian, M. Kheiri, *Solid State Sci.* **2014**, *27*, 79–83.
[51] C. Han, J. Andersen, V. Likodimos, P. Falaras, J. Linkugel, D. D. Dionysiou, *Catal. Today* **2014**, *224*, 132–139.
[52] J. Livage, M. Henry, C. Sanchez, *Prog. Solid State Chem.* **1988**, *18*, 259–341.
[53] E. M. Valliant, F. Romer, D. Wang, D. S. McPhail, M. E. Smith, J. V. Hanna, J. R. Jones, *Acta Biomater.* **2013**, *9*, 7662–7671.
[54] M. P. Pechini, *US Patent 3330697A*, **1967**.
[55] J. A. E. Paiva, P. C. C. Daza, F. A. Rodrigues, J. F. Ortiz-Mosquera, C. R. M. da Silva, M. Montero Muñoz, R. A. M. Meneses, *Ceram. Int.* **2020**, *46*, 18419–18427.
[56] J. Lin, M. Yu, C. Lin, X. Liu, *J. Phys. Chem. C* **2007**, *111*, 5835–5845.
[57] M. Einert, M. Mellin, N. Bahadorani, C. Dietz, S. Lauterbach, J. P. Hofmann, *ACS Appl. Energy Mater.* **2022**, *5*, 717–730.
[58] M. Einert, A. Waheed, S. Lauterbach, M. Mellin, M. Rohnke, L. Q. Wagner, J. Gallenberger, C. Tian, B. M. Smarsly, W. Jaegermann, F. Hess, H. Schlaad, J. P. Hofmann, *Small* **2023**, *19*, 2205412.
[59] S. Herou, M. C. Ribadeneyra, R. Madhu, V. Araullo-Peters, A. Jensen, P. Schlee, M.-M. Titirici, *Green Chem.* **2019**, *21*, 550–559.
[60] R. T. Mayes, C. Tsouris, J. O. Kiggans Jr., S. M. Mahurin, D. W. DePaoli, S. Dai, *J. Mater. Chem.* **2010**, *20*, 8674.
[61] C. Matei Ghimbeu, L. Vidal, L. Delmotte, J.-M. Le Meins, C. Vix-Guterl, *Green Chem.* **2014**, *16*, 3079.
[62] L. Chuenchom, R. Kraehnert, B. M. Smarsly, *Soft Matter* **2012**, *8*, 10801.
[63] A. Šebenik, U. Osredkar, I. Vizovišek, *Polymer* **1981**, *22*, 804–806.
[64] Y. Meng, D. Gu, F. Zhang, Y. Shi, L. Cheng, D. Feng, Z. Wu, Z. Chen, Y. Wan, A. Stein, D. Zhao, *Chem. Mater.* **2006**, *18*, 4447–4464.
[65] A. J. J. de Breet, W. Dankelman, W. G. B. Huysmans, J. de Wit, *Die Angew. Makromol. Chemie* **1977**, *62*, 7–31.
[66] T. Y. Ma, L. Liu, Z. Y. Yuan, *Chem. Soc. Rev.* **2013**, *42*, 3977–4003.
[67] V. Malgras, J. Tang, J. Wang, J. Kim, N. L. Torad, S. Dutta, K. Ariga, M. S. A. Hossain, Y. Yamauchi, K. C. W. Wu, *J. Nanosci. Nanotechnol.* **2019**, *19*, 3673–3685.
[68] G. M. Jenkins, K. Kawamura, *Nature* **1971**, *231*, 175–176.
[69] A. Oberlin, *Carbon* **1984**, *22*, 521–541.
[70] F. Badaczewski, M. O. O. Loeh, T. Pfaff, S. Dobrotka, D. Wallacher, D. Clemens, J. Metz, B. M. Smarsly, *Carbon* **2019**, *141*, 169–181.
[71] X. Wang, C. Liang, S. Dai, *Langmuir* **2008**, *24*, 7500–7505.

[72] M.-M. Titirici, R. J. White, N. Brun, V. L. Budarin, D. S. Su, F. del Monte, J. H. Clark, M. J. MacLachlan, *Chem. Soc. Rev.* **2015**, *44*, 250–290.

[73] S. H. Yu, X. J. Cui, L. L. Li, K. Li, B. Yu, M. Antonietti, H. Cölfen, *Adv. Mater.* **2004**, *16*, 1636–1640.

[74] P. Cop, R. Maile, Y. Sun, O. Khalid, I. Djerdj, P. Esch, S. Heiles, H. Over, B. M. Smarsly, *ACS Appl. Nano Mater.* **2020**, *3*, 7406–7419.

[75] D. I. Fried, K. Tropp, M. Fröba, *ChemCatChem* **2013**, *5*, 931–938.

[76] X. Sun, H. Hao, H. Ji, X. Li, S. Cai, C. Zheng, *ACS Appl. Mater. Interfaces* **2014**, *6*, 401–409.

[77] I. B. Burgess, N. Koay, K. P. Raymond, M. Kolle, M. Lončar, J. Aizenberg, *ACS Nano* **2012**, *6*, 1427–1437.

[78] DECHEMA Gesellschaft für Chemische Technik und Biotechnologie e.V., *Membranen für die Trenntechnik - Anwendungspotenziale für Deutschland*, **2022**, *Positionspapier*.

[79] R. G. Jones, C. K. Ober, T. Hayakawa, C. K. Luscombe, N. Stingelin, *Pure Appl. Chem.* **2020**, *92*, 1861–1891.

[80] D. H. Everett, *Pure Appl. Chem.* **1972**, *31*, 577–638.

[81] H. Yu, M. Liu, Q. Lu, Y. Yu, D. Zhao, X. Li, *J. Phys. Chem. C* **2024**, *128*, 19945–19961.

[82] A. -H. Lu, F. Schüth, *Adv. Mater.* **2006**, *18*, 1793–1805.

[83] Y. Liu, J. Goebl, Y. Yin, *Chem. Soc. Rev.* **2013**, *42*, 2610–2653.

[84] R. Ryoo, S. H. Joo, S. Jun, *J. Phys. Chem. B* **1999**, *103*, 7743–7746.

[85] O. D. Velev, T. A. Jede, R. F. Lobo, A. M. Lenhoff, *Nature* **1997**, *389*, 447–448.

[86] B. T. Holland, C. F. Blanford, A. Stein, *Science* **1998**, *281*, 538–540.

[87] M. -M. Titirici, A. Thomas, M. Antonietti, *Adv. Funct. Mater.* **2007**, *17*, 1010–1018.

[88] J. Chen, Y. Cao, D. Xie, J. Wang, X. Wu, Y. Tang, Y. Wang, *Batter. Supercaps* **2025**, e202500665, DOI: 10.1002/batt.202500665.

[89] K. Nakanishi, *J. Porous Mater.* **1997**, *4*, 67–112.

[90] S. H. Joo, S. J. Choi, I. Oh, J. Kwak, Z. Liu, O. Terasaki, R. Ryoo, *Nature* **2001**, *412*, 169–172.

[91] C. Yao, W. Wang, P. Wang, M. Zhao, X. Li, F. Zhang, *Adv. Mater.* **2018**, *30*, 1704833.

[92] A. S. Deshpande, D. G. Shchukin, E. Ustinovich, M. Antonietti, R. A. Caruso, *Adv. Funct. Mater.* **2005**, *15*, 239–245.

[93] X. Xue, B. Li, *Nanomaterials* **2025**, *15*, 472.

[94] H. Yang, D. Zhao, *J. Mater. Chem.* **2005**, *15*, 1217–1231.

[95] Z. Wang, Y. Li, Q. Li, *Front. Energy* **2025**, *19*, 599–618.

[96] J. Wang, K. Zhang, S. Kavak, S. Bals, V. Meynen, *Chem. – A Eur. J.* **2023**, *29*, e202202670.

[97] D. Zou, S. Ma, R. Guan, M. Park, L. Sun, J. J. Aklonis, R. Salovey, *J. Polym. Sci. Part A Polym. Chem.* **1992**, *30*, 137–144.

[98] T. Wang, O. Sel, I. Djerdj, B. Smarsly, *Colloid Polym. Sci.* **2006**, *285*, 1–9.

[99] G. I. N. Waterhouse, M. R. Waterland, *Polyhedron* **2007**, *26*, 356–368.

[100] G. J. d. A. A. Soler-Illia, E. L. Crepaldi, D. Grosso, C. Sanchez, *Curr. Opin. Colloid Interface Sci.* **2003**, *8*, 109–126.

[101] C. Cummins, R. Lundy, J. J. Walsh, V. Ponsinet, G. Fleury, M. A. Morris, *Nano Today* **2020**, *35*, 100936.

[102] C. Liang, K. Hong, G. A. Guiochon, J. W. Mays, S. Dai, *Angew. Chem. Int. Ed.* **2004**, *43*, 5785–5789.

[103] C. T. Kresge, M. E. Leonowicz, W. J. Roth, J. C. Vartuli, J. S. Beckt, *Nature* **1992**, *359*, 710–712.

[104] J. S. Beck, J. C. Vartuli, W. J. Roth, M. E. Leonowicz, C. T. Kresge, K. D. Schmitt, C. T. W. Chu, D. H. Olson, E. W. Sheppard, S. B. McCullen, J. B. Higgins, J. L. Schlenker, *J. Am. Chem. Soc.* **1992**, *114*, 10834–10843.

[105] S. A. Bagshaw, E. Prouzet, T. J. Pinnavaia, *Science* **1995**, *269*, 1242–1244.

[106] P. T. Tanev, T. J. Pinnavaia, *Science* **1995**, *267*, 865–867.

[107] G. S. Attard, J. C. Glyde, C. G. Göltner, *Nature* **1995**, *378*, 366–368.

[108] M. Barón, R. F. T. Stepto, *Pure Appl. Chem.* **2002**, *74*, 493–509.

[109] E. Fleischmann, R. Zentel, *Angew. Chem. Int. Ed.* **2013**, *52*, 8810–8827.

[110] G. J. de A. A. Soler-Illia, C. Sanchez, B. Lebeau, J. Patarin, *Chem. Rev.* **2002**, *102*, 4093–4138.

[111] F. S. Bates, G. H. Fredrickson, *Phys. Today* **1999**, *52*, 32–38.

[112] S. Förster, M. Antonietti, *Adv. Mater.* **1998**, *10*, 195–217.

[113] C. Li, Q. Li, Y. V. Kaneti, D. Hou, Y. Yamauchi, Y. Mai, *Chem. Soc. Rev.* **2020**, *49*, 4681–4736.

[114] F. Kleitz, S. Hei Choi, R. Ryoo, *Chem. Commun.* **2003**, *3*, 2136.

[115] T. Weller, L. Deilmann, J. Timm, T. S. Dörr, P. A. Beaucage, A. S. Cherevan, U. B. Wiesner, D. Eder, R. Marschall, *Nanoscale* **2018**, *10*, 3225–3234.

[116] M. Kopeć, R. Yuan, E. Gottlieb, C. M. R. Abreu, Y. Song, Z. Wang, J. F. J. Coelho, K. Matyjaszewski, T. Kowalewski, *Macromolecules* **2017**, *50*, 2759–2767.

[117] Y. Lu, H. Fan, A. Stump, T. L. Ward, T. Rieker, C. J. Brinker, *Nature* **1999**, *398*, 223–226.

[118] C. J. Brinker, Y. Lu, A. Sellinger, H. Fan, *Adv. Funct. Mater.* **1999**, *11*, 579–585.

[119] D. Grosso, F. Cagnol, G. J. de A. A. Soler-Illia, E. L. Crepaldi, H. Amenitsch, A. Brunet-Bruneau, A. Bourgeois, C. Sanchez, *Adv. Funct. Mater.* **2004**, *14*, 309–322.

[120] J. Wei, H. Wang, Y. Deng, Z. Sun, L. Shi, B. Tu, M. Luqman, D. Zhao, *J. Am. Chem. Soc.* **2011**, *133*, 20369–20377.

[121] H. Yang, A. Kuperman, N. Coombs, S. Mamiche-Afara, G. A. Ozin, *Nature* **1996**, *379*, 703–705.

[122] M. Ogawa, *Chem. Commun.* **1996**, 1149–1150.

[123] E. L. Crepaldi, G. J. de A. A. Soler-Illia, D. Grosso, P.-A. Albouy, C. Sanchez, *Chem. Commun.* **2001**, 1582–1583.

[124] S. Tanaka, N. Nishiyama, Y. Egashira, K. Ueyama, *Chem. Commun.* **2005**, 2125–2127.

[125] A. S. Deshpande, N. Pinna, B. Smarsly, M. Antonietti, M. Niederberger, *Small* **2005**, *1*, 313–316.

[126] S. C. Warren, F. J. DiSalvo, U. Wiesner, *Nat. Mater.* **2007**, *6*, 156–161.

[127] P. Cop, K. Hess, S. Werner, R. Meinusch, B. M. Smarsly, H. Kozuka, *Langmuir* **2019**, *35*, 16427–16437.

[128] J. Zhang, Y. Deng, J. Wei, Z. Sun, D. Gu, H. Bongard, C. Liu, H. Wu, B. Tu, F. Schüth, D. Zhao, *Chem. Mater.* **2009**, *21*, 3996–4005.

[129] D. Bernsmeier, E. Ortel, J. Polte, B. Eckhardt, S. Nowag, R. Haag, R. Kraehnert, *J. Mater. Chem. A* **2014**, *2*, 13075–13082.

[130] H. N. Lokupitiya, A. Jones, B. Reid, S. Guldin, M. Stefik, *Chem. Mater.* **2016**, *28*, 1653–1667.

[131] A. Sarkar, M. Stefik, *J. Mater. Chem. A* **2017**, *5*, 11840–11853.

[132] A. Sarkar, L. Evans, M. Stefik, *Langmuir* **2018**, *34*, 5738–5749.

[133] K. A. Lantz, N. B. Clamp, W. van den Bergh, A. Sarkar, M. Stefik, *Small* **2019**, *15*, 1–10.

[134] E. R. Williams, P. L. McMahon, J. E. Reynolds, J. L. Snider, V. Stavila, M. D. Allendorf, M. Stefik, *Mater. Adv.* **2021**, *2*, 5381–5395.

[135] J. G. Werner, Y. Li, U. Wiesner, *Small Sci.* **2023**, *3*, 2300074.

[136] Y. Zhu, Y. Zhao, J. Ma, X. Cheng, J. Xie, P. Xu, H. Liu, H. Liu, H. Zhang, M. Wu, A. A. Elzatahry, A. Alghamdi, Y. Deng, D. Zhao, *J. Am. Chem. Soc.* **2017**, *139*, 10365–10373.

[137] J. Billet, S. Vandewalle, M. Meire, N. Blommaerts, P. Lommens, S. W. Verbruggen, K. de Buysser, F. du Prez, I. van Driessche, *J. Mater. Sci.* **2020**, *55*, 1933–1945.

[138] P. C. A. Alberius, K. L. Frindell, R. C. Hayward, E. J. Kramer, G. D. Stucky, B. F. Chmelka, *Chem. Mater.* **2002**, *14*, 3284–3294.

[139] M. J. Q. Yong, A. S. W. Wong, G. W. Ho, *Mater. Chem. Phys.* **2009**, *116*, 563–568.

[140] S. Y. Choi, M. Mamak, N. Coombs, N. Chopra, G. A. Ozin, *Adv. Funct. Mater.* **2004**, *14*, 335–344.

[141] P. Holmqvist, P. Alexandridis, B. Lindman, *J. Phys. Chem. B* **1998**, *102*, 1149–1158.

[142] S. Rasappa, L. Schulte, D. Borah, H. Hulkkonen, S. Ndoni, T. Salminen, R. Senthamaraikanan, M. A. Morris, T. Niemi, *Microelectron. Eng.* **2018**, *192*, 1–7.

[143] G. Wanka, H. Hoffmann, W. Ulbricht, *Macromolecules* **1994**, *27*, 4145–4159.

[144] A. Vinu, P. Srinivasu, M. Miyahara, K. Ariga, *J. Phys. Chem. B* **2006**, *110*, 801–806.

[145] Y. Li, J. Yi, M. Kruk, *Chem. – A Eur. J.* **2015**, *21*, 12747–12754.

[146] V. Hiremath, B. T. Shiferraw, J. G. Seo, *J. CO2 Util.* **2020**, *42*, 101294.

[147] S. Loreto, H. Vanrompay, M. Mertens, S. Bals, V. Meynen, *Eur. J. Inorg. Chem.* **2018**, *2018*, 62–65.

[148] B. Yang, C. Guo, S. Chen, J. Ma, J. Wang, X. Liang, L. Zheng, H. Liu, *J. Phys. Chem. B* **2006**, *110*, 23068–23074.

[149] J. H. Pan, X. S. Zhao, W. I. Lee, *Chem. Eng. J.* **2011**, *170*, 363–380.

[150] W.-H. Zhang, L. Zhang, J. Xiu, Z. Shen, Y. Li, P. Ying, C. Li, *Microporous Mesoporous Mater.* **2006**, *89*, 179–185.

[151] P. Schmidt-Winkel, C. J. Glinka, G. D. Stucky, *Langmuir* **2000**, *16*, 356–361.

[152] J. L. Blin, C. Otjacques, G. Herrier, B.-L. Su, *Langmuir* **2000**, *16*, 4229–4236.

[153] L. Huang, M. Kruk, *Chem. Mater.* **2015**, *27*, 679–689.

[154] Y. Deng, J. Liu, C. Liu, D. Gu, Z. Sun, J. Wei, J. Zhang, L. Zhang, B. Tu, D. Zhao, *Chem. Mater.* **2008**, *20*, 7281–7286.

[155] A. Sarkar, A. Thyagarajan, A. Cole, M. Stefik, *Soft Matter* **2019**, *15*, 5193–5203.

[156] M. Trivedi, F. Peng, X. Xia, P. I. Sepulveda-Medina, B. D. Vogt, *Langmuir* **2019**, *35*, 14049–14059.

[157] A. Alvarez-Fernandez, M. J. Fornerod, B. Reid, S. Guldin, *Langmuir* **2022**, *38*, 3297–3304.

[158] F. Kleitz, F. Bérubé, R. Guillet-Nicolas, C.-M. Yang, M. Thommes, *J. Phys. Chem. C* **2010**, *114*, 9344–9355.

[159] N. A. Seaton, *Chem. Eng. Sci.* **1991**, *46*, 1895–1909.

[160] R. Cimino, K. A. Cychosz, M. Thommes, A. V. Neimark, *Colloids Surfaces A Physicochem. Eng. Asp.* **2013**, *437*, 76–89.

[161] M. Pérez-Mendoza, J. González, C. A. Ferreiro-Rangel, M. M. Lozinska, D. Fairén-Jiménez, T. Düren, P. A. Wright, N. A. Seaton, *J. Phys. Chem. C* **2014**, *118*, 10183–10190.

[162] A. Galarneau, H. Cambon, F. Di Renzo, R. Ryoo, M. Choi, F. Fajula, *New J. Chem.* **2003**, *27*, 73–79.

[163] B. de Witte, K. Vercruysse, K. Aernouts, P. Verwimp, J. B. Uytterhoeven, *J. Porous Mater.* **1996**, *2*, 307–313.

[164] C. Vercaemst, M. Ide, H. Friedrich, K. P. de Jong, F. Verpoort, P. Van Der Voort, *J. Mater. Chem.* **2009**, *19*, 8839.

[165] D. Kuang, T. Brezesinski, B. Smarsly, *J. Am. Chem. Soc.* **2004**, *126*, 10534–10535.

[166] O. Sel, A. Brandt, D. Wallacher, M. Thommes, B. Smarsly, *Langmuir* **2007**, *23*, 4724–4727.

[167] J. Yu, G. Wang, B. Cheng, M. Zhou, *Appl. Catal. B Environ.* **2007**, *69*, 171–180.

[168] B. Smarsly, S. Polarz, M. Antonietti, *J. Phys. Chem. B* **2001**, *105*, 10473–10483.

[169] D. Zhao, J. Feng, Q. Huo, N. Melosh, G. H. Fredrickson, B. F. Chmelka, G. D. Stucky, *Science* **1998**, *279*, 548–552.

[170] C. G. Göltner, B. Berton, E. Krämer, M. Antonietti, *Chem. Commun.* **1998**, 2287–2288.

[171] A. Thomas, H. Schlaad, B. Smarsly, M. Antonietti, *Langmuir* **2003**, *19*, 4455–4459.

[172] M. Groenewolt, T. Brezesinski, H. Schlaad, M. Antonietti, P. W. Groh, B. Iván, *Adv. Mater.* **2005**, *17*, 1158–1162.

[173] C. Reitz, J. Haetge, C. Suchomski, T. Brezesinski, *Chem. Mater.* **2013**, *25*, 4633–4642.

[174] M. Templin, A. Franck, A. du Chesne, H. Leist, Y. Zhang, R. Ulrich, V. Schädler, U. Wiesner, *Science* **1997**, *278*, 1795–1798.

[175] J. Lee, M. Christopher Orilall, S. C. Warren, M. Kamperman, F. J. DiSalvo, U. Wiesner, *Nat. Mater.* **2008**, *7*, 222–228.

[176] M. Stefik, J. Song, H. Sai, S. Guldin, P. Boldrighini, M. C. Orilall, U. Steiner, S. M. Gruner, U. Wiesner, *J. Mater. Chem. A* **2015**, *3*, 11478–11492.

[177] A. A. Zakhidov, R. H. Baughman, Z. Iqbal, C. Cui, I. Khayrullin, S. O. Dantas, J. Marti, V. G. Ralchenko, *Science* **1998**, *282*, 897–901.

[178] G. S. Chai, S. B. Yoon, J.-S. Yu, J.-H. Choi, Y.-E. Sung, *J. Phys. Chem. B* **2004**, *108*, 7074–7079.

[179] J. G. Werner, T. N. Hoheisel, U. Wiesner, *ACS Nano* **2014**, *8*, 731–743.

[180] Y. Liu, W. Teng, G. Chen, Z. Zhao, W. Zhang, B. Kong, W. N. Hozzein, A. A. Al-Khalaf, Y. Deng, D. Zhao, *Chem. Sci.* **2018**, *9*, 7705–7714.

[181] K. Yu, A. J. Hurd, A. Eisenberg, C. J. Brinker, *Langmuir* **2001**, *17*, 7961–7965.

[182] S. Liang, T. Guan, S. Yin, E. Krois, W. Chen, C. R. Everett, J. Drewes, T. Strunskus, M. Gensch, J. Rubeck, C. Haisch, M. Schwartzkopf, F. Faupel, S. V. Roth, Y.-J. Cheng, P. Müller-Buschbaum, *ACS Appl. Nano Mater.* **2022**, *5*, 7492–7501.

[183] G. Pan, W. Xie, S. Liang, T. Tian, S. Yin, L. Li, A. Buyan-Arivjikh, J. Zhang, T. Baier, Z. Xu, M. Schwartzkopf, S. Koyiloth Vayalil, S. V. Roth, Y. Deng, P. Müller-Buschbaum, *Adv. Funct.*

Mater. **2025**, e05935, DOI: 10.1002/adfm.202505935.
[184] S. Tanaka, Y. V. Kaneti, R. Bhattacharjee, M. N. Islam, R. Nakahata, N. Abdullah, S. Yusa, N.-T. Nguyen, M. J. A. Shiddiky, Y. Yamauchi, M. S. A. Hossain, *ACS Appl. Mater. Interfaces* **2018**, *10*, 1039–1049.
[185] S. A. Hesse, K. E. Fritz, P. A. Beaucage, E. M. Susca, J. Suntivich, U. Wiesner, *Macromol. Chem. Phys.* **2023**, *224*, 1–14.
[186] J. Wei, Z. Sun, W. Luo, Y. Li, A. A. Elzatahry, A. M. Al-Enizi, Y. Deng, D. Zhao, *J. Am. Chem. Soc.* **2017**, *139*, 1706–1713.
[187] R. Spann, D. Boucher, *J. Polym. Sci.* **2023**, *61*, 503–514.
[188] L. P. D. Ratcliffe, B. E. McKenzie, G. M. D. Le Bouëdec, C. N. Williams, S. L. Brown, S. P. Armes, *Macromolecules* **2015**, *48*, 8594–8607.
[189] D. M. Day, L. R. Hutchings, *Eur. Polym. J.* **2021**, *156*, 110631.
[190] Y. Deng, J. Wei, Z. Sun, D. Zhao, *Chem. Soc. Rev.* **2013**, *42*, 4054–4070.
[191] A. Halperin, *Macromolecules* **1987**, *20*, 2943–2946.
[192] S. Förster, M. Zisenis, E. Wenz, M. Antonietti, *J. Chem. Phys.* **1996**, *104*, 9956–9970.
[193] J. H. Hildebrand, *J. Am. Chem. Soc.* **1929**, *51*, 66–80.
[194] J. H. Hildebrand, *Science* **1965**, *150*, 441–450.
[195] J. M. Abboud, R. Notari, *Pure Appl. Chem.* **1999**, *71*, 645–718.
[196] L. Atanase, G. Riess, *Polymers* **2018**, *10*, 62.
[197] S. Saeki, N. Kuwahara, M. Nakata, M. Kaneko, *Polymer* **1976**, *17*, 685–689.
[198] G. Karlström, *J. Phys. Chem.* **1985**, *89*, 4962–4964.
[199] S. Y. Oh, H. E. Yang, Y. C. Bae, *Macromol. Res.* **2013**, *21*, 921–930.
[200] J. N. Israelachvili, D. J. Mitchell, B. W. Ninham, *J. Chem. Soc. Faraday Trans. 2* **1976**, *72*, 1525.
[201] T. G. Ribelli, F. Lorandi, M. Fantin, K. Matyjaszewski, *Macromol. Rapid Commun.* **2019**, *40*, 1–44.
[202] G. Moad, E. Rizzardo, S. H. Thang, *Acc. Chem. Res.* **2008**, *41*, 1133–1142.
[203] E. Borsig, M. Lazár, M. Čapla, *Die Makromol. Chemie* **1967**, *105*, 212–222.
[204] M. K. Georges, R. P. N. Veregin, P. M. Kazmaier, G. K. Hamer, *Macromolecules* **1993**, *26*, 2987–2988.
[205] B. B. Wayland, G. Poszmik, S. L. Mukerjee, M. Fryd, *J. Am. Chem. Soc.* **1994**, *116*, 7943–7944.
[206] C. M. Fellows, R. G. Jones, D. J. Keddie, C. K. Luscombe, J. B. Matson, K. Matyjaszewski, J. Merna, G. Moad, T. Nakano, S. Penczek, G. T. Russell, P. D. Topham, *Pure Appl. Chem.* **2022**, *94*, 1093–1147.
[207] D. H. Solomon, G. Waverley, P. Cacioli, W. Hill, G. Waverley, *US Patent 4581429*, **1986**.
[208] J. Nicolas, Y. Guillaneuf, C. Lefay, D. Bertin, D. Gigmes, B. Charleux, *Prog. Polym. Sci.* **2013**, *38*, 63–235.
[209] M. Lee, T. Morigami, Y. Minoura, *J. Chem. Soc. Faraday Trans. 1 Phys. Chem. Condens. Phases* **1978**, *74*, 1738.
[210] L. E. N. Allan, M. R. Perry, M. P. Shaver, *Prog. Polym. Sci.* **2012**, *37*, 127–156.
[211] J. Chiefari, Y. K. Chong, F. Ercole, J. Krstina, J. Jeffery, T. P. T. Le, R. T. A. Mayadunne, G. F. Meijs, C. L. Moad, G. Moad, E. Rizzardo, S. H. Thang, *Macromolecules* **1998**, *31*, 5559–5562.
[212] N. P. Truong, G. R. Jones, K. G. E. Bradford, D. Konkolewicz, A. Anastasaki, *Nat. Rev. Chem.* **2021**, *5*, 859–869.
[213] J. S. Wang, K. Matyjaszewski, *J. Am. Chem. Soc.* **1995**, *117*, 5614–5615.
[214] M. Kato, M. Kamigaito, M. Sawamoto, T. Higashimura, *Macromolecules* **1995**, *28*, 1721–1723.
[215] K. Matyjaszewski, J. Xia, *Chem. Rev.* **2001**, *101*, 2921–2990.
[216] S. Perrier, D. M. Haddleton, *Macromol. Symp.* **2002**, *182*, 261–272.
[217] W. A. Braunecker, N. V. Tsarevsky, A. Gennaro, K. Matyjaszewski, *Macromolecules* **2009**, *42*, 6348–6360.
[218] M. Fantin, A. A. Isse, A. Gennaro, K. Matyjaszewski, *Macromolecules* **2015**, *48*, 6862–6875.
[219] W. Tang, A. K. Nanda, K. Matyjaszewski, *Macromol. Chem. Phys.* **2005**, *206*, 1171–1177.
[220] F. Seeliger, K. Matyjaszewski, *Macromolecules* **2009**, *42*, 6050–6055.
[221] W. Tang, Y. Kwak, W. Braunecker, N. V. Tsarevsky, M. L. Coote, K. Matyjaszewski, *J. Am. Chem. Soc.* **2008**, *130*, 10702–10713.
[222] T. G. Ribelli, M. Fantin, J.-C. Daran, K. F. Augustine, R. Poli, K. Matyjaszewski, *J. Am. Chem.*

Soc. **2018**, *140*, 1525–1534.
[223] S. Lanzalaco, M. Fantin, O. Scialdone, A. Galia, A. A. Isse, A. Gennaro, K. Matyjaszewski, *Macromolecules* **2017**, *50*, 192–202.
[224] A. J. D. Magenau, N. C. Strandwitz, A. Gennaro, K. Matyjaszewski, *Science* **2011**, *332*, 81–84.
[225] J. Mosnáček, M. Ilčíková, *Macromolecules* **2012**, *45*, 5859–5865.
[226] D. Konkolewicz, K. Schröder, J. Buback, S. Bernhard, K. Matyjaszewski, *ACS Macro Lett.* **2012**, *1*, 1219–1223.
[227] X. Pan, M. Lamson, J. Yan, K. Matyjaszewski, *ACS Macro Lett.* **2015**, *4*, 192–196.
[228] Z. Wang, Z. Wang, X. Pan, L. Fu, S. Lathwal, M. Olszewski, J. Yan, A. E. Enciso, Z. Wang, H. Xia, K. Matyjaszewski, *ACS Macro Lett.* **2018**, *7*, 275–280.
[229] K. Matyjaszewski, S. Coca, S. G. Gaynor, M. Wei, B. E. Woodworth, *Macromolecules* **1997**, *30*, 7348–7350.
[230] D. Konkolewicz, Y. Wang, M. Zhong, P. Krys, A. A. Isse, A. Gennaro, K. Matyjaszewski, *Macromolecules* **2013**, *46*, 8749–8772.
[231] D. Konkolewicz, Y. Wang, P. Krys, M. Zhong, A. A. Isse, A. Gennaro, K. Matyjaszewski, *Polym. Chem.* **2014**, *5*, 4396–4417.
[232] H.-P. Hentze, E. Krämer, B. Berton, S. Förster, M. Antonietti, M. Dreja, *Macromolecules* **1999**, *32*, 5803–5809.
[233] E. Prouzet, T. J. Pinnavaia, *Angew. Chem.* **1997**, *109*, 533–536.
[234] S. Marx, D. Avnir, *Acc. Chem. Res.* **2007**, *40*, 768–776.
[235] V. Vignal, A. W. Morawski, H. Konno, M. Inagaki, *J. Mater. Res.* **1999**, *14*, 1102–1112.
[236] C. Schlumberger, M. Thommes, *Adv. Mater. Interfaces* **2021**, *8*, 2002181.
[237] C. Felipe, F. Rojas, I. Kornhauser, M. Thommes, G. Zgrablich, *Adsorpt. Sci. Technol.* **2006**, *24*, 623–643.
[238] F. Herrera, G. Rumi, P. Y. Steinberg, A. Wolosiuk, P. C. Angelomé, *ChemCatChem* **2023**, *15*, e202300490.
[239] L. A. Solovyov, *Chem. Soc. Rev.* **2013**, *42*, 3708–3720.
[240] S. Mitchell, L. Gerchow, R. Warringham, P. Crivelli, J. Pérez-Ramírez, *Small Methods* **2018**, *2*, 1–16.
[241] D. Majda, M. Zimowska, K. Tarach, K. Góra-Marek, B. D. Napruszewska, A. Michalik-Zym, *J. Therm. Anal. Calorim.* **2017**, *127*, 207–220.
[242] J. Mitchell, J. Webber, J. Strange, *Phys. Rep.* **2008**, *461*, 1–36.
[243] C. Schlumberger, L. Sandner, A. Michalowski, M. Thommes, *Langmuir* **2023**, *39*, 4611–4621.
[244] C. Boissiere, D. Grosso, S. Lepoutre, L. Nicole, A. B. Bruneau, C. Sanchez, *Langmuir* **2005**, *21*, 12362–12371.
[245] Y. Yao, A. M. Lenhoff, *J. Chromatogr. A* **2004**, *1037*, 273–282.
[246] I. Bacskay, A. Sepsey, A. Felinger, *J. Chromatogr. A* **2014**, *1339*, 110–117.
[247] C. Pfeifer, F. Cavalli, B. Huber, P. Theato, L. Barner, M. Wilhelm, *Macromol. Chem. Phys.* **2021**, *222*, e2000300.
[248] N. W. Ashcroft, J. Lekner, *Phys. Rev.* **1966**, *145*, 83–90.
[249] M. S. Wertheim, *Phys. Rev. Lett.* **1963**, *10*, 321–323.
[250] C. Weidmann, K. Brezesinski, C. Suchomski, K. Tropp, N. Grosser, J. Haetge, B. M. Smarsly, T. Brezesinski, *Chem. Mater.* **2012**, *24*, 486–494.
[251] E. Prates da Costa, X. Huang, C. Kübel, X. Cheng, K. Schladitz, A. Hofmann, U. Göbel, B. M. Smarsly, *Langmuir* **2023**, *39*, 17664–17679.
[252] S. Mascotto, D. Wallacher, A. Brandt, T. Hauss, M. Thommes, G. A. Zickler, S. S. Funari, A. Timmann, B. M. Smarsly, *Langmuir* **2009**, *25*, 12670–12681.
[253] S. A. Kube, K. Turke, R. Ellinghaus, D. Wallacher, M. Thommes, B. M. Smarsly, *Langmuir* **2020**, *36*, 11996–12009.
[254] E. Prates da Costa, X. Huang, C. Kübel, X. Cheng, K. Schladitz, A. Hofmann, U. Göbel, B. M. Smarsly, *Langmuir* **2023**, *39*, 177–191.
[255] S. Y. Lee, D. H. Cho, S. C. Song, J. Shin, J. Hwang, E. Park, S. Y. Lee, S. Kim, J. Lee, C. Song, *ACS Nano* **2023**, *17*, 22488–22498.
[256] J. Kärger, *Microporous Mesoporous Mater.* **2014**, *189*, 126–135.
[257] P. Hartmann, D. K. Lee, B. M. Smarsly, J. Janek, *ACS Nano* **2010**, *4*, 3147–3154.

[258] M. Thommes, K. Kaneko, A. V. Neimark, J. P. Olivier, F. Rodriguez-Reinoso, J. Rouquerol, K. S. W. Sing, *Pure Appl. Chem.* **2015**, *87*, 1051–1069.
[259] T. Binninger, E. Fabbri, R. Kötz, T. J. Schmidt, *J. Electrochem. Soc.* **2014**, *161*, 121–128.
[260] M. Łukaszewski, M. Soszko, A. Czerwiński, *Int. J. Electrochem. Sci.* **2016**, *11*, 4442–4469.
[261] P. C. Ball, R. Evans, *Langmuir* **1989**, *5*, 714–723.
[262] M. Thommes, *Chemie-Ingenieur-Technik* **2010**, *82*, 1059–1073.
[263] I. Langmuir, *J. Am. Chem. Soc.* **1916**, *38*, 2221–2295.
[264] I. Langmuir, *J. Am. Chem. Soc.* **1918**, *40*, 1361–1403.
[265] H. Freundlich, *Z. Phys. Chem.* **1907**, *57*, 385–471.
[266] V. P. M. Temkin, *Acta Physicochim. URSS* **1940**, *12*, 327–356.
[267] S. Brunauer, P. H. Emmett, E. Teller, *J. Am. Chem. Soc.* **1938**, *60*, 309–319.
[268] E. P. Barrett, L. G. Joyner, P. P. Halenda, *J. Am. Chem. Soc.* **1951**, *73*, 373–380.
[269] W. Thomson, *Proc. R. Soc. Edinburgh* **1872**, *7*, 63–68.
[270] L. H. Cohan, *J. Am. Chem. Soc.* **1938**, *60*, 433–435.
[271] B. V. D. B. W. Derjaguin, *Acta Physicochim. URSS* **1940**, 182–200.
[272] J. C. P. Broekhoff, J. H. de Boer, *J. Catal.* **1968**, *10*, 368–376.
[273] B. K. Peterson, J. P. R. B. Walton, K. E. Gubbins, *Int. J. Thermophys.* **1985**, *6*, 585–593.
[274] M. W. Maddox, K. E. Gubbins, *Int. J. Thermophys.* **1994**, *15*, 1115–1123.
[275] P. A. Monson, *Microporous Mesoporous Mater.* **2012**, *160*, 47–66.
[276] A. V. Neimark, P. I. Ravikovitch, *Microporous Mesoporous Mater.* **2001**, *44–45*, 697–707.
[277] P. I. Ravikovitch, A. V. Neimark, *Langmuir* **2002**, *18*, 9830–9837.
[278] A. V. Neimark, Y. Lin, P. I. Ravikovitch, M. Thommes, *Carbon* **2009**, *47*, 1617–1628.
[279] K. A. Cychosz, X. Guo, W. Fan, R. Cimino, G. Y. Gor, M. Tsapatsis, A. V. Neimark, M. Thommes, *Langmuir* **2012**, *28*, 12647–12654.
[280] M. Thommes, B. Smarsly, M. Groenewolt, P. I. Ravikovitch, A. V. Neimark, *Langmuir* **2006**, *22*, 756–764.
[281] C. J. Rasmussen, A. Vishnyakov, M. Thommes, B. M. Smarsly, F. Kleitz, A. V. Neimark, *Langmuir* **2010**, *26*, 10147–10157.
[282] B. Coasne, A. Galarneau, R. J. M. Pellenq, F. Di Renzo, *Chem. Soc. Rev.* **2013**, *42*, 4141–4171.
[283] A. V. Neimark, *Stud. Surf. Sci. Catal.*, **1991**, *62*, 67–74.
[284] K. Morishige, N. Tarui, *J. Phys. Chem. C* **2007**, *111*, 280–285.
[285] F. Casanova, C. E. Chiang, C.-P. Li, I. K. Schuller, *Appl. Phys. Lett.* **2007**, *91*, 243103.
[286] J. Söllner, A. V. Neimark, M. Thommes, *Langmuir* **2024**, *40*, 23146–23168.
[287] Z. Wang, J. Huang, G. Jiang, T. Ji, H. Lin, L. Mu, J. Zhu, *Chem. Mater.* **2025**, *37*, 1337–1348.
[288] M. Weyland, P. A. Midgley, J. M. Thomas, *J. Phys. Chem. B* **2001**, *105*, 7882–7886.
[289] P. Ercius, O. Alaidi, M. J. Rames, G. Ren, *Adv. Mater.* **2015**, *27*, 5638–5663.
[290] P. A. Midgley, R. E. Dunin-Borkowski, *Nat. Mater.* **2009**, *8*, 271–280.
[291] W. Wang, A. Svidrytski, D. Wang, A. Villa, H. Hahn, U. Tallarek, C. Kübel, *Microsc. Microanal.* **2019**, *25*, 891–902.
[292] X. Huang, D. Hlushkou, D. Wang, U. Tallarek, C. Kübel, *Ultramicroscopy* **2023**, *243*, 113639.
[293] C. Fouard, G. Malandain, S. Prohaska, M. Westerhoff, *IEEE Trans. Med. Imaging* **2006**, *25*, 1319–1328.
[294] X. Cheng, S. Föhst, C. Redenbach, K. Schladitz, *Proceedings of the Mathematical Morphology and its Applications to Signal and Image Processing: 14th international symposium, ISMM 2019; Saarbrücken, Germany, July 8−10, 2019; Burgeth, B., Kleefeld, A., Naegel, B., Passat, N., Perret, B., Eds.; Springer International Publishing: Cham* **2019**, *11564*, 441–455.
[295] U. Tallarek, J. Hochstrasser, F. Ziegler, X. Huang, C. Kübel, M. R. Buchmeiser, *ChemCatChem* **2021**, *13*, 281–292.
[296] S. Bruns, T. Müllner, M. Kollmann, J. Schachtner, A. Höltzel, U. Tallarek, *Anal. Chem.* **2010**, *82*, 6569–6575.
[297] D. Stoeckel, C. Kübel, M. O. Loeh, B. M. Smarsly, U. Tallarek, *Langmuir* **2015**, *31*, 7391–7400.
[298] E. Özkan, A. Hofmann, M. Votsmeier, W. Wang, X. Huang, C. Ku, F. Badaczewski, K. Turke, S. Werner, B. M. Smarsly, *Langmuir* **2021**, *37*, 2563–2574.
[299] T. Hildebrand, P. Rüegsegger, *J. Microsc.* **1997**, *185*, 67–75.
[300] K. Schmidt-Rohr, *J. Appl. Crystallogr.* **2007**, *40*, 16–25.